OXIDATION CHEMISTRY AND KINETICS IN SUPERCRITICAL WATER: HYDROGEN, CARBON MONOXIDE, AND GLUCOSE

by

HENRY RICHARD HOLGATE

B.S.E., Chemical Engineering, Princeton University, 1987
M.S., Chemical Engineering Practice, Massachusetts Institute of Technology, 1989

Submitted to the Department of Chemical Engineering
in Partial Fulfillment of the Requirements for the Degree of

DOCTOR OF PHILOSOPHY

at the

MASSACHUSETTS INSTITUTE OF TECHNOLOGY

February 1993

Signature of Author_____
Department of Chemical Engineering
October 23, 1992

Certified by_____
Professor Jefferson W. Tester
Thesis Supervisor

Accepted by_____
Professor Robert E. Cohen
Chairman, Committee for Graduate Students

OXIDATION CHEMISTRY AND KINETICS IN SUPERCRITICAL WATER: HYDROGEN, CARBON MONOXIDE, AND GLUCOSE

by

HENRY RICHARD HOLGATE

Submitted to the Department of Chemical Engineering
on October 23, 1992 in Partial Fulfillment of the Requirements for the
Degree of Doctor of Philosophy in Chemical Engineering

ABSTRACT

Supercritical water oxidation represents an innovative technology for complete and efficient destruction of hazardous wastes, without formation of harmful by-products. Organic compounds and oxygen are completely soluble in supercritical water at temperatures above 374 °C and pressures above 221 bar, providing a single-phase medium for rapid oxidation of organics to CO_2, H_2O, and N_2. The scale-up and reliable operation of commercial-sized process equipment require a thorough understanding of oxidation kinetics, reaction pathways, and mechanisms.

Hydrogen oxidation in supercritical water was studied in an isothermal, isobaric, tubular plug-flow reactor apparatus from 495 to 600 °C at 246 bar. Over the range of conditions studied, the reaction was globally first order in hydrogen and independent of oxygen, with an activation energy of 372±34 kJ/mol and a pronounced induction time of about 2 s at 550 °C.

Carbon monoxide oxidation in supercritical water was reexamined from 420 to 593 °C at 246 bar, to obtain updated kinetic expressions for the direct-oxidation ($CO + {}^1/_2\ O_2 \rightarrow CO_2$) and water-gas shift ($CO + H_2O \rightarrow CO_2 + H_2$) pathways. Heat-transfer experiments established the thermal histories of the reactor feeds and the histories were included in the kinetic analysis. For conditions employed in the experiments, reaction by the water-gas shift during feed preheating occurred to a negligible extent. The water-gas-shift pathway was of fractional order in CO with an activation energy of 95±3 kJ/mol, while the direct-oxidation pathway was first order in CO with an activation energy of 134±32 kJ/mol. The direct-oxidation pathway also exhibited a fractional-order dependence on oxygen not seen in an earlier study. Additional experiments at 550 and 560 °C confirmed the oxygen dependence and revealed an induction time of approximately 2 s in the oxidation reaction. Hydrogen formation by the water-gas shift pathway was strongly dependent on fuel equivalence ratio, with fuel-rich conditions favoring its formation. The water-gas shift is very slow in the complete absence of oxygen.

In the pressure range 118 to 263 bar, oxidation of both hydrogen and carbon monoxide is strongly pressure (water density) dependent, with higher densities favoring

higher oxidation rates. At 550 and 570 °C, respectively, the rates of hydrogen and carbon monoxide oxidation increased by a factor of three to five when the operating pressure was increased from 118 to 263 bar. Limited studies of hydrogen and carbon monoxide oxidation in a packed reactor showed that the additional surface area inhibits oxidation, although the magnitude of the effect implies that high-temperature results from the tubular reactor may be treated as homogeneous.

An elementary reaction model for hydrogen oxidation, with theoretically consistent modifications for high pressure, successfully reproduced observed kinetic behavior. A similar model for carbon monoxide oxidation was less successful, although hydrogen formation was well predicted. Both models captured the majority of the observed pressure dependence. The primary effect of the high water density on oxidation kinetics is the increase in the rate of the $HO_2 + H_2O \rightarrow H_2O_2 + OH$ branching reaction; the dissociations of hydrogen peroxide and the hydroperoxyl radical are also at or near their high-pressure limits. Both models exhibited high sensitivities to the rate constant and equilibrium constant for the branching reaction.

Glucose hydrolysis and oxidation occurred rapidly in supercritical water at 246 bar. A diverse set of products, present in the liquid effluent and also subject to hydrolysis, was formed. At 600 °C and a 6-second reactor residence time, glucose is completely gasified, even in the absence of oxygen. In the presence of oxygen, destruction of liquid-phase products is enhanced, with none found above 550 °C at a 6-second reactor residence time. Major products formed were acetic acid, acetonylacetone, propenoic acid, acetaldehyde, carbon monoxide, methane, ethane, ethylene, and hydrogen. Methane and hydrogen were present at temperatures up to 600 °C for reactor residence times of 6 s.

Thesis Supervisor: Jefferson W. Tester

Title: Professor of Chemical Engineering
Director, Energy Laboratory

The completion of this thesis was made possible (and enjoyable) by the contributions, tangible and otherwise, of a great number of people. While it would be impossible to name all of them, certain individuals deserve special recognition:

My advisor, Jeff Tester, for his respect and encouragement and the collegial relationship we have shared. His urging led to my involvement with the Practice School, both as a student and as an Assistant Director, an opportunity that provided a type of experience unattainable in Cambridge. I will always value our friendship and I wish him continued success.

Jeff and Marci Feerer, for creating an educational and humane environment at the Midland Station of the Practice School and for their endless, heartfelt interest in the lives of the students. I treasure their friendship and regret that MIT will no longer benefit from their many contributions.

Jean and Louise Leinroth, for an enjoyable and instructive summer at the Richmond Station of the Practice School, and for their continued friendship.

My fellow residents of 66-553, and in particular Fred Armellini and Gabe Worley, for helping to create a positive working environment that was friendly and casual yet productive. The interest in each other's work and the frequent exchange of ideas (and sarcasm) were highly constructive and appreciated (usually).

Ashley Shih, Victor Antaramian, Jay Corbett, and especially Jerry Meyer, for their extremely helpful and competent assistance with the experimental work.

Rich Shandross and Joe Marr, for being invaluable resources on elementary reaction modeling matters, from RRKM calculations to chemical kinetic software.

Professor Michael Antal, of the University of Hawaii, Professor Frederick Dryer, of Princeton University, and Dr. Charles Westbrook, of Lawrence Livermore National Laboratory, for helpful discussions and suggestions and their willingness to share their work and ideas.

My thesis committee members, Professors Jack Howard and Adel Sarofim of MIT and K.C. Swallow of MODAR, Inc., for the contributions of their time and knowledge to the improvement of the quality of this research.

The personnel at MODAR, Inc., including Glenn Hong, Bill Killilea, Dave Ordway, and Alain Bourhis, for their lasting interest in the research in our laboratory. Their contributions of equipment and experience are sincerely appreciated.

My predecessors on this project, Rich Helling and Paul Webley, for setting high standards of research and for their continued involvement in our work.

Donald Price, of NASA/Johnson Space Center, Robert Shaw, of the Army Research Office, and the Environmental Protection Agency, for their recognition of the value of our research and their financial support, without which this work would not have been possible.

The many people with whom I've participated in intramural sports, including the semi-regular departmental basketball and volleyball sessions. My thanks go to them for providing numerous hours of relaxation and the chance to interact outside of academics.

My wife, Laura, for her support and understanding and for making the last five years special in countless ways. Although I've mentioned her last, she remains first in my heart.

This thesis is dedicated to my father, who did not see its completion.

John David Holgate

April 1, 1916 — January 3, 1992

Seek simplicity but distrust it.

—A.N. Whitehead

Table of Contents

List of Figures

List of Tables

Chapter 1

Summary

1.1 Introduction

Oxidation in a supercritical water environment is an innovative technology for the rapid destruction of hazardous organic and metabolic wastes without formation of harmful by-products (Modell, 1989; Swallow *et al.*, 1989; Thomason *et al.*, 1990; Tester *et al.*, 1991). Pure water is considered supercritical if its temperature and pressure both exceed the critical values of 374.2 °C and 221 bar, respectively. At or above the critical point, the density of water is a strong function of both temperature and pressure, as are the solvation properties of water (Franck, 1970). Supercritical water acts as a dense gas, with the solvation characteristics of a non-polar organic (Connolly, 1966): organics and gases are completely miscible with supercritical water, yet inorganic salts are virtually insoluble (Martynova, 1976).

In supercritical water oxidation, the unique properties of supercritical water allow oxygen and organics to be contacted in a single phase at temperatures above 400 °C and pressures above 230 bar. Under these conditions, rapid oxidation of the organics occurs, raising the mixture temperature to 550–650 °C, where destruction proceeds rapidly and completely. Conversions of 99.99% or greater can be attained with reactor residence times of 1 minute or less. Heteroatoms are converted to mineral acids which can be

neutralized and precipitated from the mixture as salts by adding a base to the feed (Thomason and Modell, 1984).

While supercritical water oxidation was first proposed fourteen years ago, kinetic data for the oxidation of model compounds in supercritical water have only become available in recent years. Compounds studied have included carbon monoxide (Helling and Tester, 1987), methane (Webley and Tester, 1991), methanol (Webley and Tester, 1989; Webley *et al.*, 1991), and ammonia (Helling and Tester, 1988; Webley *et al.*, 1991), as well as more complex compounds such as phenol (Thornton and Savage, 1992). Of these, carbon monoxide and ammonia are important because they are intermediates in the oxidation of more complex organics and because their destruction can be the rate-limiting step in the complete conversion of the organic to CO_2 and N_2. Carbon monoxide is also the simplest model organic and its gas-phase oxidation kinetics have been well characterized.

The fundamental kinetics and mechanisms of oxidation in supercritical water remain poorly understood relative to combustion. This laboratory has been conducting kinetic oxidation experiments in supercritical water since 1983, with the mission of improving the level of understanding of the process. To that end, an isothermal, isobaric, plug-flow reactor apparatus has been constructed. Kinetic data obtained in the reactor have been correlated using global rate expressions (Helling and Tester, 1987,1988; Webley *et al.*, 1991; Webley and Tester, 1991), and have recently been used as the basis for the development of detailed elementary reaction models (Webley and Tester, 1991). While global kinetic expressions can be useful for design purposes, they contain no fundamental mechanistic information. Elementary reaction models can provide this information, if they are able to describe the data; to date, however, such models have not been able to faithfully reproduce experimental observations.

A diagram of the current experimental apparatus is shown in Figure 1.1. Dilute aqueous feed solutions of gaseous organic and oxygen are prepared by dissolving the gases in purified water in two high-pressure, 3-L saturators. Agitation is provided by pumped recirculation of the saturator liquid. Alternatively, a soluble liquid or solid organic may be fed directly to the reactor as a dilute solution. The feed solutions are delivered separately to the reactor by a duplex high-pressure feed pump. The tubular reactor is 4.71 m of 0.635-cm o.d. × 0.171-cm i.d. Inconel 625 tubing, with a total volume of 11.11 cm^3, contained in a fluidized sand bath. A packed reactor is also available, consisting of a 61.67-cm length of 0.912-cm i.d. × 1.43-cm o.d. Inconel 625 tubing packed with 200-μm Inconel beads, with a total volume of 16.0 cm^3 and a surface-area-to-volume ratio over twenty times that of the tubular reactor.

The reactor feeds are preheated separately to reaction temperature in two 2.8-m lengths of 0.159-cm o.d. × 0.108-cm i.d. Hastelloy C276 tubing (denoted "preheating tubing" in Figure 1.1) contained in the reactor sand bath. The preheated feeds meet and mix at the reactor inlet, where the oxidation reaction is initiated. Reactor temperature is taken as the average of the mixing and exit fluid temperatures; in no case do these temperatures differ by more than 8 °C and the exit temperature is always within 1 °C of the sand bath temperature. Reactor residence times range from 3.4 to 12 seconds, and are constrained by the maximum feed pump flow rate and the need to maintain turbulent flow within the reactor. Upon exiting the reactor, the reaction mixture is quenched to ambient temperature in a countercurrent shell-and-tube heat exchanger, and the pressure is reduced to ambient upon passing through the back-pressure regulator. The resulting gas and liquid phases are disengaged in a gas-liquid separator and the flow rate of each phase is measured. Compositional analysis of the gas phase is accomplished by gas chromatography using a thermal conductivity detector. High sensitivity for hydrogen is

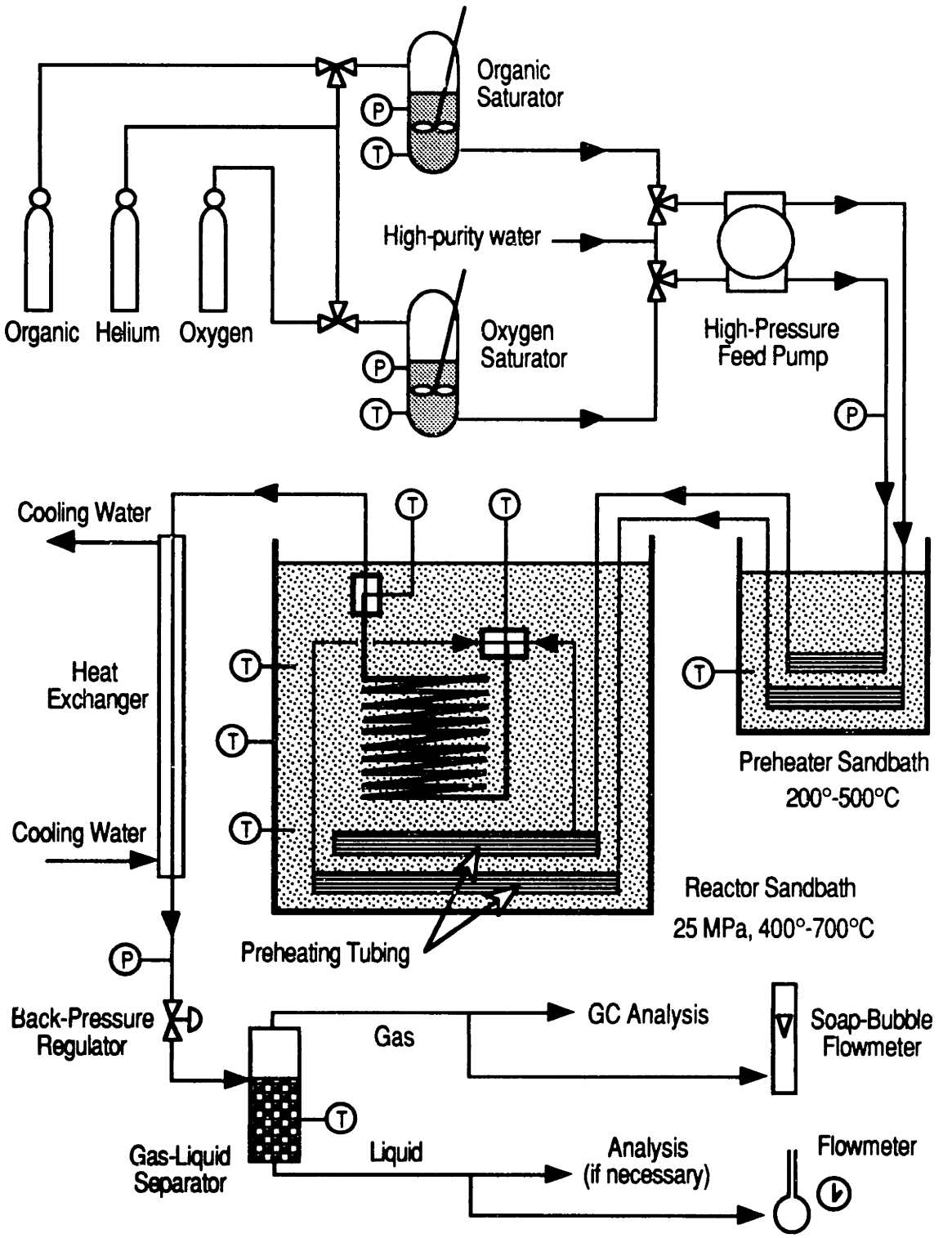

Figure 1.1 Isothermal, Plug-Flow Reactor Apparatus.

obtained by performing duplicate sample analyses in a second GC using nitrogen as the carrier gas. Liquid-phase analyses, when necessary, are accomplished by high-performance liquid chromatography with detection by UV absorption.

1.2 Objectives

The primary objective of this work was to extend the set of kinetic data for oxidation of simple compounds in supercritical water under well-defined conditions, and to use those data as the basis for development of an accurate model of the fundamental kinetic processes and mechanisms. Specific objectives are listed below:

1. Obtain kinetic data for hydrogen oxidation in supercritical water. Hydrogen is the simplest oxidizable compound; its oxidation in the gas phase has been thoroughly characterized and occurs through a well-defined mechanism. Measurement of hydrogen oxidation kinetics in supercritical water will provide an important basis for modeling and can yield insights into the effect of the supercritical water environment on the most basic oxidation mechanism.

2. Reexamine carbon monoxide oxidation in supercritical water. Carbon monoxide is important as an oxidation intermediate, since it is usually the rate-limiting step in achieving complete oxidation. As a simple, refractory molecule, accurate characterization of its oxidation kinetics is crucial. The earlier study in this laboratory of carbon monoxide oxidation in supercritical water (Helling and Tester, 1987) examined only a limited range of oxygen concentrations and lacked high analytical sensitivity for hydrogen. The importance of reaction during feed preheating also remained uncertain, Validation or improvement of the earlier data taken in our laboratory was necessary.

3. Identify the effects of pressure (density) on oxidation kinetics. Hong (1992) has enumerated the potential advantages of operating the SCWO process at lower, even

subcritical, pressures (semicritical water oxidation). The effects of decreasing pressu on oxidation rates, however, are not well known. By changing the operating pressure (water density) in a controlled, systematic manner, the kinetic effects of varying operating pressure, as well as potentially the role of water in the oxidation mechanism, can be identified.

4. Evaluate the influence of the reactor surface. Earlier studies in this laboratory identified a heterogeneous catalytic effect of the reactor surface for ammonia oxidation (Webley *et al.*, 1991). Preliminary studies in our laboratory have not revealed pronounced heterogeneous influences in the oxidation of compounds other than ammonia, but this conclusion must be verified to insure that any measured kinetic data are an accurate reflection of homogeneous oxidation mechanisms.

5. Develop and validate an elementary reaction model for hydrogen and carbon monoxide oxidation in supercritical water. Several elementary reaction models for SCWO have been compiled for more complex molecules such as methane or methanol. With new data for hydrogen and carbon monoxide oxidation, it becomes possible to develop improved models for those two simple compounds, whose oxidation mechanisms are necessarily a subset of the mechanisms for larger molecules. Development and validation of a model for hydrogen and carbon monoxide oxidation will thus provide a sound basis for the subsequent development of more complex models.

6. Investigate glucose oxidation in supercritical water. Growing interest in the use of SCWO for treatment of sludges and human waste (Takahashi *et al.*, 1989; Shanableh and Gloyna, 1991; Modell *et al.*, 1992) has demonstrated the need for kinetic data for this class of waste. While glucose is not strictly speaking a simple compound, it does represent a significant simplification of the much more complex sludge matrix and is a

good model compound for cellulosic wastes. Identification of destruction-limiting intermediates is also important for treatment optimization.

1.3 Hydrogen Oxidation in Supercritical Water

1.3.1 Experimental Results

Fifty-five hydrogen oxidation experiments were conducted at temperatures of 495 to 600 °C at a constant pressure of 246 bar. Reactor residence times ranged from 3.4 to 11.0 seconds. Inlet molar oxygen-to-hydrogen ratios were between 0.125 and 11.82, both above and below the stoichiometric ratio of 0.5; inlet concentrations were varied from approximately 0.4×10^{-6} to 4.5×10^{-6} mol/cm^3. Observed conversions ranged from 6.1 to 98.2%.

The hydrogen oxidation data were fit to a power-law rate form, with an Arrhenius expression for the rate constant, by non-linear regression to the plug-flow equation. Global reaction orders with respect to hydrogen and oxygen were not statistically different from one and zero, respectively, and the best-fit global rate expression was

$$R_{H_2} = 10^{22.8\pm2.2} \exp\left(-372\pm34/RT\right) [H_2] \qquad (1.1)$$

where the activation energy is in kJ/mol. The experimental data are shown in Figure 1.2 with the best-fit line described by Equation 1.1.

The scatter in the experimental data at 550 °C is the result of a pronounced induction time in the hydrogen oxidation reaction; at 550 °C, the observed induction time is approximately 2 seconds. The simple rate expression of Equation 1.1 cannot capture this behavior and the calculated global rate constant is therefore a function of residence time. The presence of an induction time strongly suggests the occurrence of a complex,

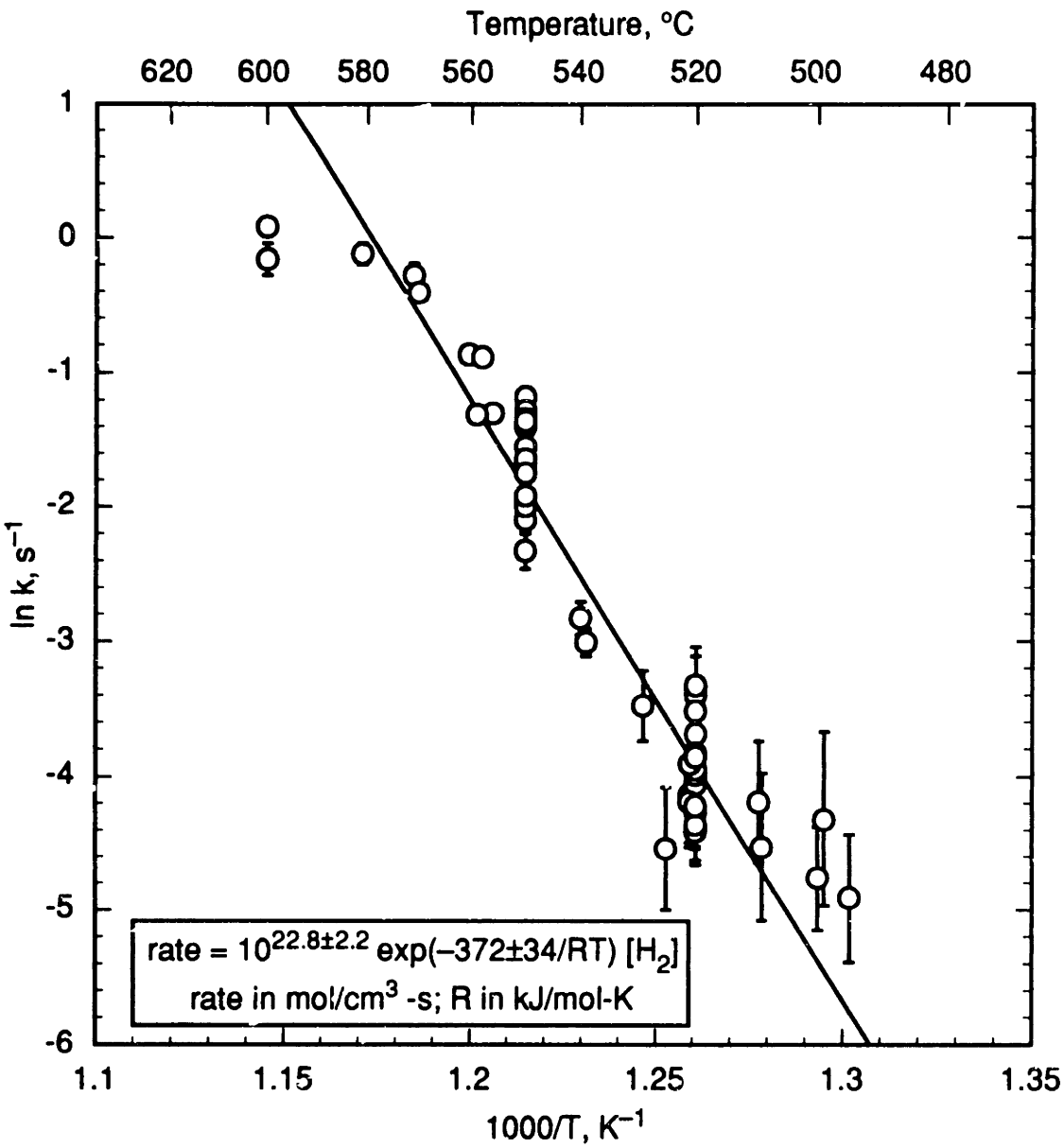

Figure 1.2 **First-Order Arrhenius Plot for Hydrogen Oxidation in Supercritical Water at 246 bars.**

free-radical mechanism and lends support to the notion th· ɔxidation in supercritical water may be described by elementary reaction models. The induction time, and the subsequent decay of hydrogen, were found to be only weakly dependent on concentration for a stoichiometric H_2-O_2 mixture at 550 °C and a threefold variation in concentration.

The effect of operating pressure on hydrogen oxidation kinetics was investigated for a stoichiometric mixture at 550 °C and pressures from 118 to 263 bar. Hydrogen and oxygen concentrations were maintained at constant values of nominally 1×10^{-6} and 0.5×10^{-6} mol/cm^3, respectively, over the entire range of pressures. A change in the operating pressure was thus effectively a change in the concentration of water in the reactor. The pressures studied correspond to water densities (concentrations) of 1.8×10^{-3} mol/cm^3 to 4.6×10^{-3} mol/cm^3, or nearly a factor-of-three variation in water concentration. Experimental results are shown in Figure 1.3, with the apparent first-order rate constant presented as a function of operating pressure (water density). The rate constant clearly increases with increasing pressure, and is roughly an order of magnitude higher at 263 bar than at 118 bar. The magnitude of this trend is tempered somewhat by the variation in the rate constant at a given operating pressure, the result of the induction time discussed earlier. Nevertheless, distinct evidence indicates that higher pressures (water concentrations) favor higher oxidation rates.

A series of experiments at 550 °C in the packed reactor was conducted to investigate the possible influence of reactor surface on observed kinetics. The high increase in surface-to-volume ratio (by a factor of 20.5) decreased the observed kinetic decay constant for hydrogen relative to that observed in the tubular reactor under identical experimental conditions. The reactor surface area thus tends to inhibit oxidation, most likely through termination of free-radical species. However, the decrease in the kinetic decay constant with added surface was only by a factor of about 6, implying

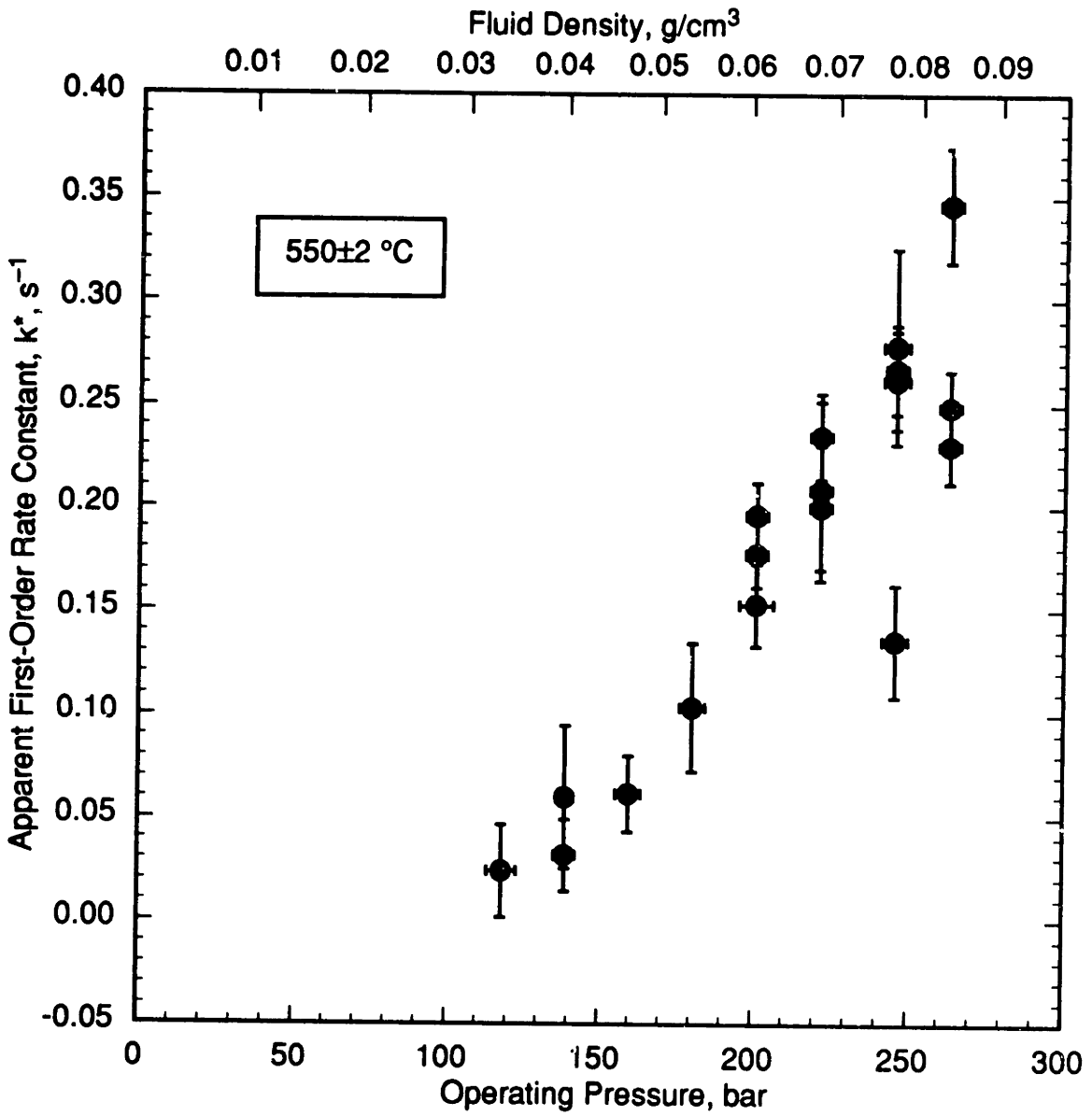

Figure 1.3 **Effects of Operating Pressure (Fluid Density) on the Apparent First-Order Rate Constant, k^*, for Hydrogen Oxidation.** Experimental conditions: 550±2 °C, $[H_2]_o$ = (1.06±0.02) × 10^{-6} mol/cm^3, $[O_2]_o$ = (0.53±0.01) × 10^{-6} mol/cm^3.

that results in the tubular reactor may be approximately treated as homogeneous for modeling purposes.

1.3.2 Elementary Reaction Modeling

Oxidation in supercritical water, at the conditions characteristic of the SCWO process (230–250 bar, 450–650 °C), is likely to proceed via free-radical mechanisms (Webley and Tester, 1991). The experimental results of the present study have therefore been modeled using gas-phase, free-radical, elementary reaction mechanisms, with certain modifications for the high-pressure SCWO environment.

The basic mechanism chosen was the validated, comprehensive carbon monoxide oxidation mechanism of Yetter, Dryer and Rabitz (1991a). The basic mechanism, modified only to include the high third-body efficiency of water, overpredicted oxidation rates for the entire range of conditions studied experimentally. On the basis of sensitivity analyses, three modifications were made to the mechanism: 1) the rate of hydrogen peroxide dissociation was set to its high-pressure limit (Brouwer *et al.*, 1987); 2) the newer rate expression for $HO_2 + HO_2 \rightarrow H_2O_2 + O_2$ from Hippler *et al.* (1990) was used, because this reaction exhibits non-Arrhenius behavior near the temperature range of the present study; and 3) thermodynamic data from the JANAF Thermochemical Tables (Chase *et al.*, 1985) were used in calculating reverse rate constants, rather than the thermodynamic data supplied by Yetter *et al.* (1991a). The first modification was validated by detailed RRKM calculations. The third modification affects the model almost exclusively through the rate of the $HO_2 + H_2O \rightarrow H_2O_2 + OH$ branching reaction, and was necessary to obtain any reasonable agreement with the data. The resulting mechanism, with these modifications, was denoted YDR91J and used to model the experimental data.

Figure 1.4 shows the excellent agreement obtained between the model predictions and the experimental data. Earlier elementary reaction models for supercritical water oxidation of more complex molecules were unable to achieve this level of agreement. Figure 1.5 compares concentration profiles for hydrogen oxidation as determined experimentally and as predicted by the model. Again the agreement is quite good, although the model slightly underpredicts both the induction time and the rate of decay of the hydrogen concentration.

Figure 1.6 illustrates the major pathways in the oxidation of hydrogen, as predicted by the model. Oxidation of hydrogen occurs by the reaction $H_2 + OH \rightarrow H_2O + H$; since this step is by nature first-order in hydrogen, so too is the overall oxidation. Oxygen participates in the mechanism through the rapid conversion of H to HO_2; since this step is fast, the overall oxidation does not depend on the oxygen concentration. HO_2 subsequently disproportionates to H_2O_2 and O_2, with the H_2O_2 dissociating to the oxidizing OH radicals. HO_2 may also react with H_2O in a branching step to form effectively three OH radicals; at steady state, the rate of this reaction is slow, although during the induction time this reaction is responsible for the creation of the radical pool.

The model also successfully captures much of the pressure dependence of the data, as shown in Figure 1.7. The variation in the rate constants of the two major pressure-dependent reactions in the mechanism ($H_2O_2 \rightarrow OH + OH$, $H + O_2 \rightarrow HO_2$), as determined by detailed calculations, are only minor over the range of pressures studied, and cannot account for the observed pressure dependence of the oxidation. Rather, the primary effect is of the change in water concentration with pressure. Since water is a reactant in the $HO_2 + H_2O \rightarrow H_2O_2 + OH$ branching reaction, the branching rate in the mechanism decreases proportionately to the decrease in the water concentration. Consequently, as pressure is reduced, the induction time is lengthened and the ultimate

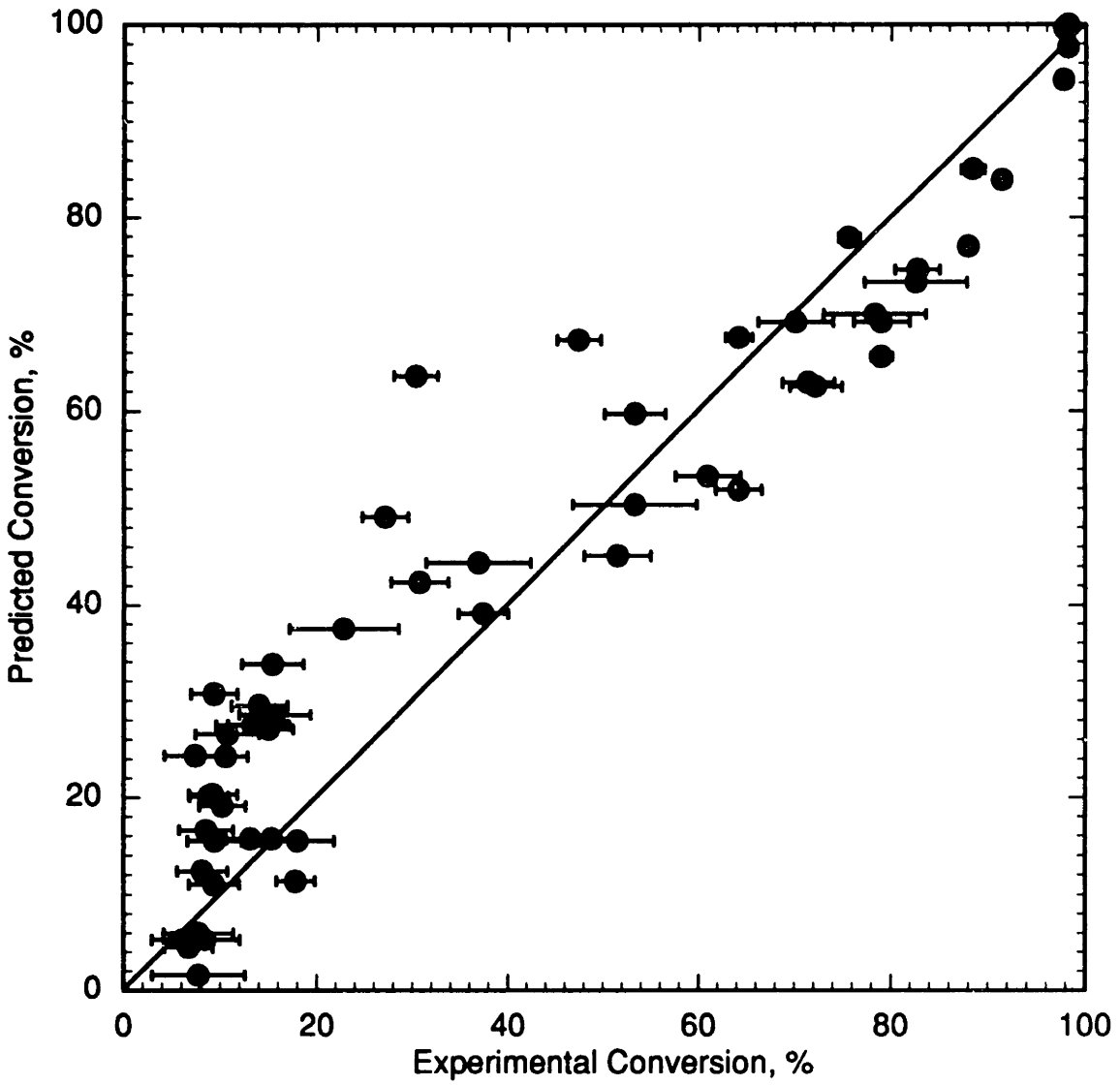

Figure 1.4 **Conversion of Hydrogen Predicted by the Modified Elementary Reaction Model of Yetter, Dryer and Rabitz (1991) with JANAF Thermochemical Data (Model YDR91J).**

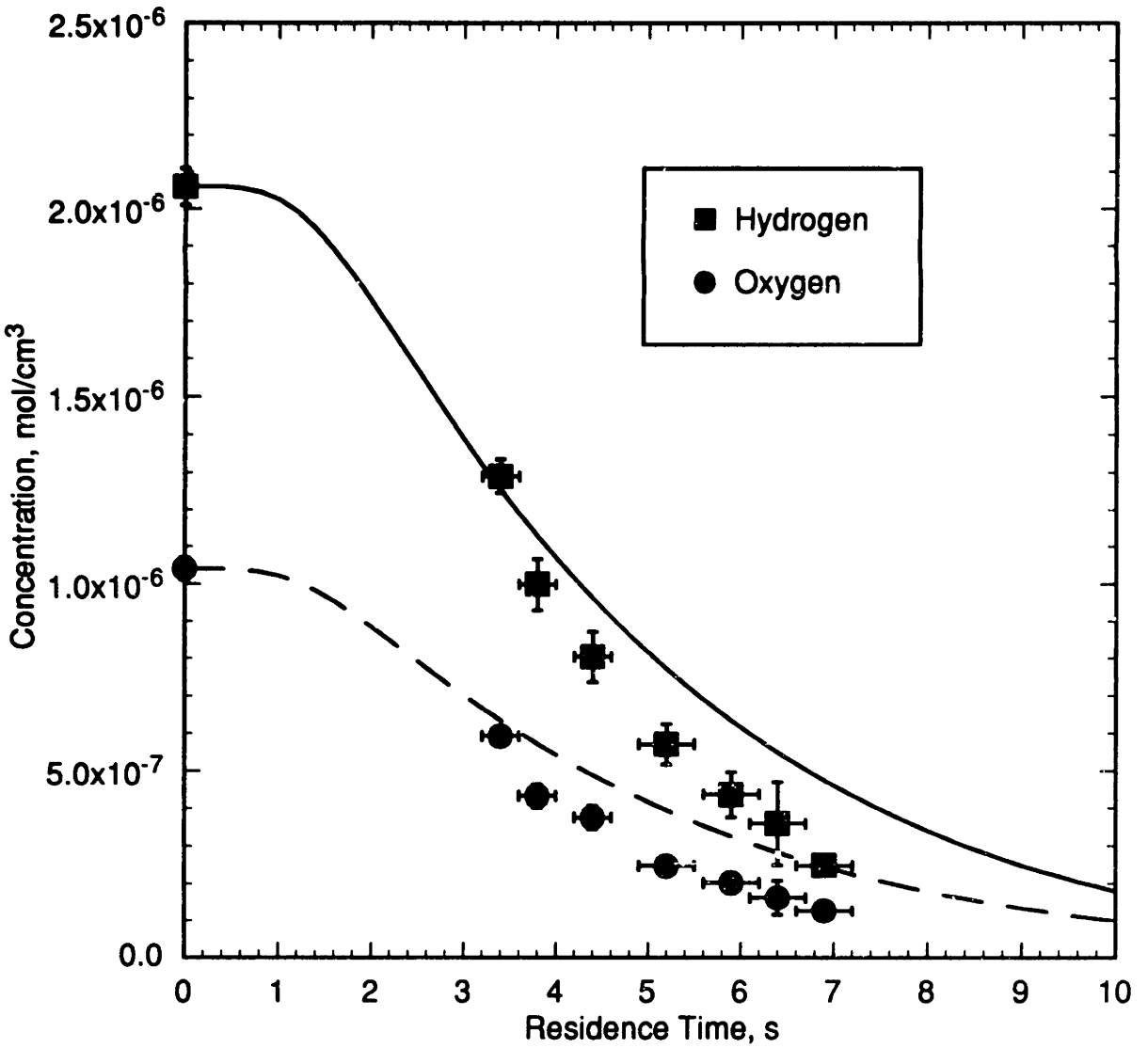

Figure 1.5 **Concentration Profiles for Stoichiometric Hydrogen Oxidation at 550±2 °C.** Symbols: experimental data, $[H_2]_o = (2.06\pm0.02) \times 10^{-6}$ mol/cm^3, $[O_2]_o = (1.04\pm0.01) \times 10^{-6}$ mol/cm^3, $[H_2O] = (4.25\pm0.08) \times 10^{-3}$ mol/cm^3. Curves: predictions of YDR91J elementary reaction model.

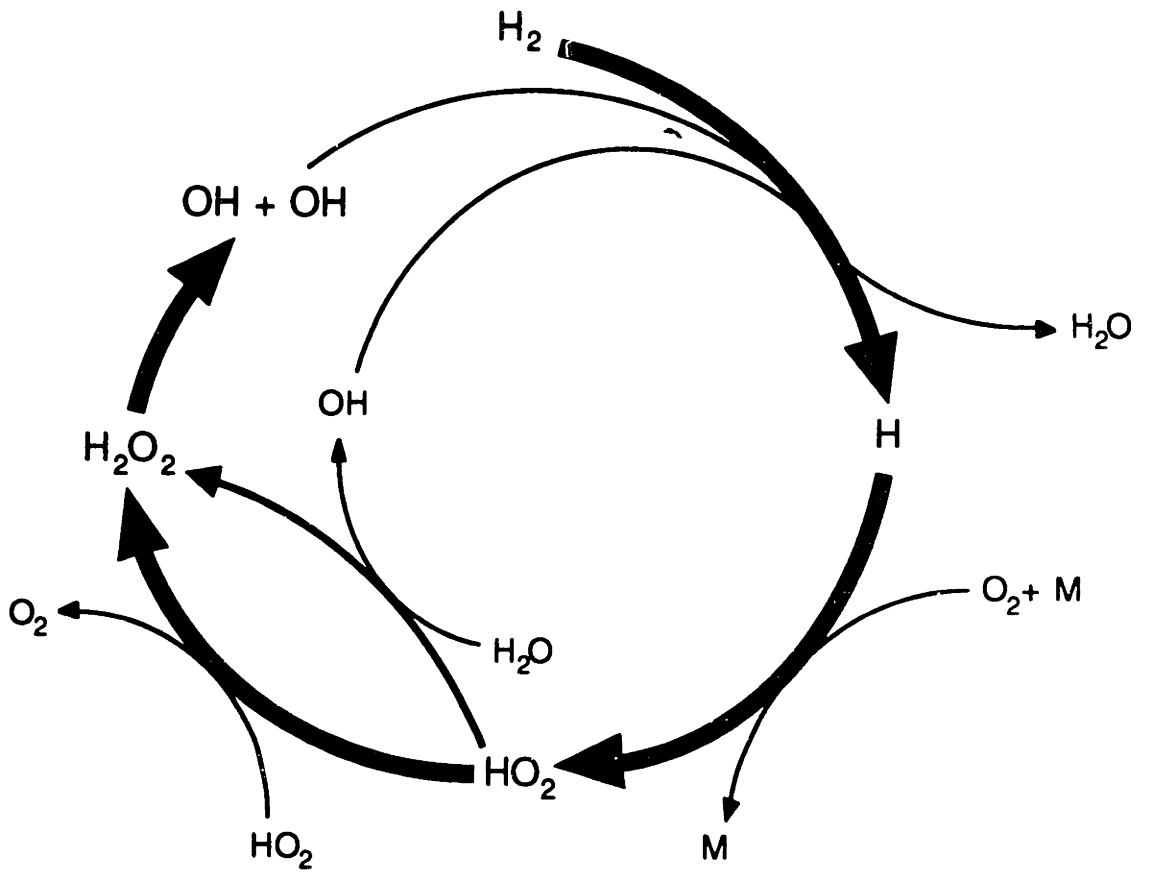

Figure 1.6 Major Free-Radical Reaction Pathways in the Elementary Reaction Network for Hydrogen Oxidation in Supercritical Water. Arrow thicknesses indicate relative rates of reactions.

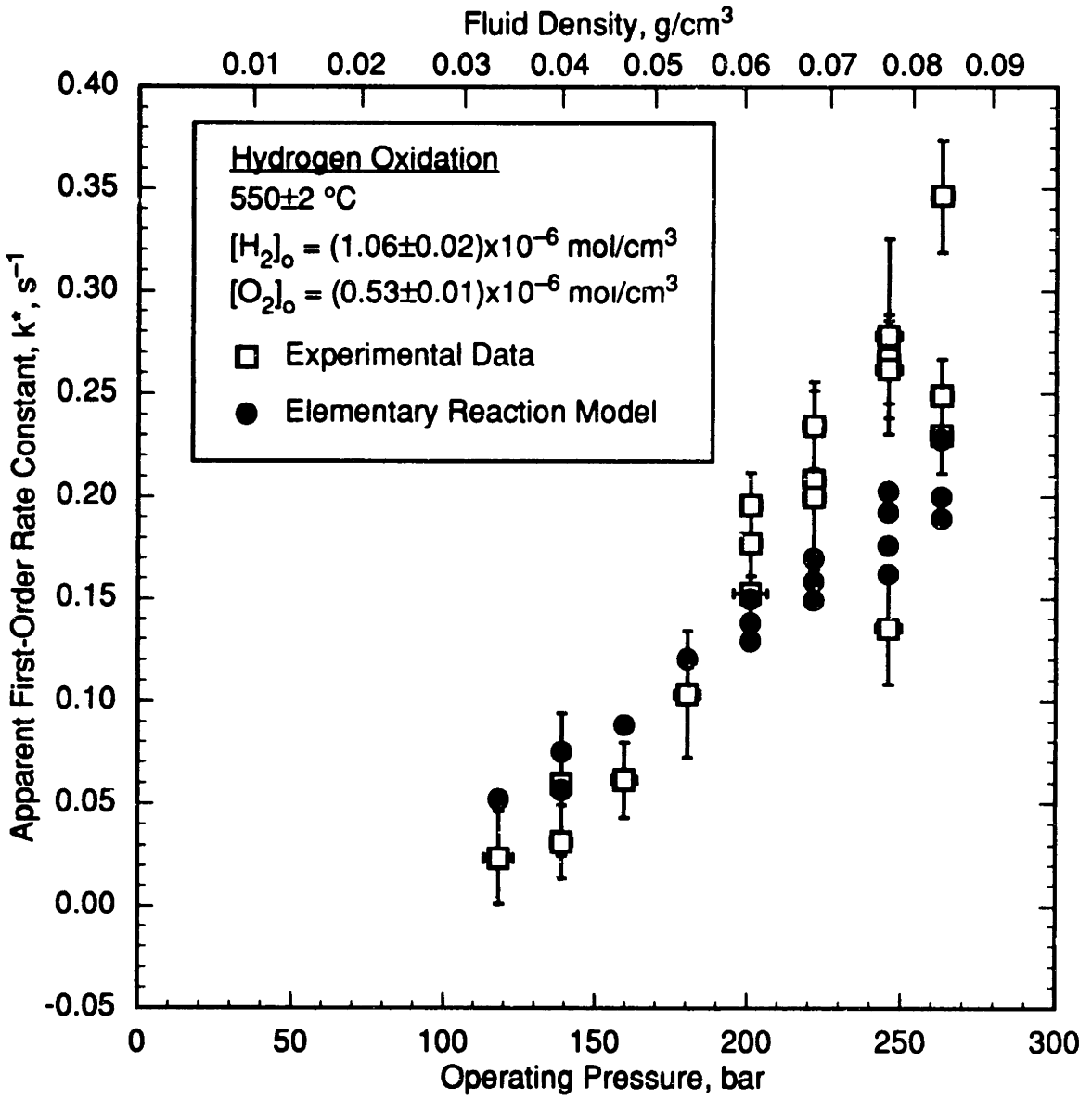

Figure 1.7 **Predicted Effects of Operating Pressure (Fluid Density) on the Apparent First-Order Rate Constant, k^*, for Hydrogen Oxidation.**
□—Experimental data from Figure 1.3;
●—Predictions of YDR91J model.

steady-state OH concentration, as determined by the net branching rate, is reduced, thereby decreasing the observed oxidation rate.

1.4 Carbon Monoxide Oxidation in Supercritical Water

1.4.1 Experimental Results

The oxidation of carbon monoxide in supercritical water was investigated in 43 experiments at 246 bar and 420 to 571 °C, at residence times of 5.0 to 12.1 seconds, with molar feed ratios of oxygen to carbon monoxide of 0.15 to 8.20, above and below the stoichiometric value of 0.5. Observed conversions ranged from 4 to 93%.

Twenty experiments were also conducted in the absence of oxygen to measure the kinetics of the global water-gas shift reaction pathway, $CO + H_2O \rightarrow CO_2 + H_2O$. Results of heat-transfer experiments were used to determine the temperature profiles of the aqueous CO feed to the reactor, and these profiles were used in the regression of the rate expression in order to account for any reaction during preheating. The resulting best-fit rate expression was

$$R_{WGS} = 10^{3.3\pm0.2} \exp(-95\pm3/RT)\,[CO]^{0.71\pm0.08} \qquad (1.2)$$

with the concentration in mol/L and the activation energy in kJ/mol. The fractional-order dependence on CO is consistent with earlier observations by Helling and Tester (1987).

Equation 1.2, in conjunction with derived feed temperature profiles, was used to calculate the extent of reaction of the carbon monoxide feed by the water-gas shift pathway during preheating in the oxidation experiments. The extent of reaction was found to be negligible in all cases, amounting to no more than 4% (Holgate *et al.*, 1992). The current experimental data were combined with the earlier data of Helling and Tester

(1987) and regressed to a global rate expression. The earlier data have been corrected with respect to temperature on the basis of the heat-transfer experiments. In determining the direct oxidation rate expression, the water-gas shift was assumed to occur in parallel and the contribution by that pathway was subtracted (Holgate *et al.*, 1992). The resulting direct-oxidation global rate expression was

$$R_{DO} = 10^{8.5\pm3.3} \exp(-134\pm32/RT)\,[CO]^{0.96\pm0.30}\,[O_2]^{0.34\pm0.24} \qquad (1.3)$$

with the units as in Equation 1.2. The experimental data and the corresponding rate expressions are shown in Figure 1.8. The first-order dependence on carbon monoxide and the fractional-order dependence on oxygen in Equation 1.3 are consistent with early global expressions for gas-phase, moist carbon monoxide oxidation (Hottel *et al.*, 1965; Dryer and Glassman, 1973; Howard *et al.*, 1973), but inconsistent with more recent gas-phase studies (Yetter *et al.*, 1991b) and the earlier study of CO oxidation in supercritical water (Helling and Tester, 1987).

Additional carbon monoxide oxidation experiments were subsequently conducted to obtain species concentration profiles, as had been obtained for hydrogen oxidation. The results are shown in Figure 1.9, where only the (normalized) carbon monoxide pro[illegible]e presented. As for hydrogen oxidation, these concentration profiles indicate that carbon monoxide oxidation proceeds only after a pronounced induction time of approximately 2 seconds. The induction time does not vary noticeably among the profiles. The three profiles obtained at 560 °C for varying fuel equivalence ratios indicate that the oxidation rate depends on the oxygen concentration. Assuming the carbon monoxide decay is first-order in CO, the variation in these three profiles can only be reconciled by an order of approximately 0.5 with respect to oxygen, which is

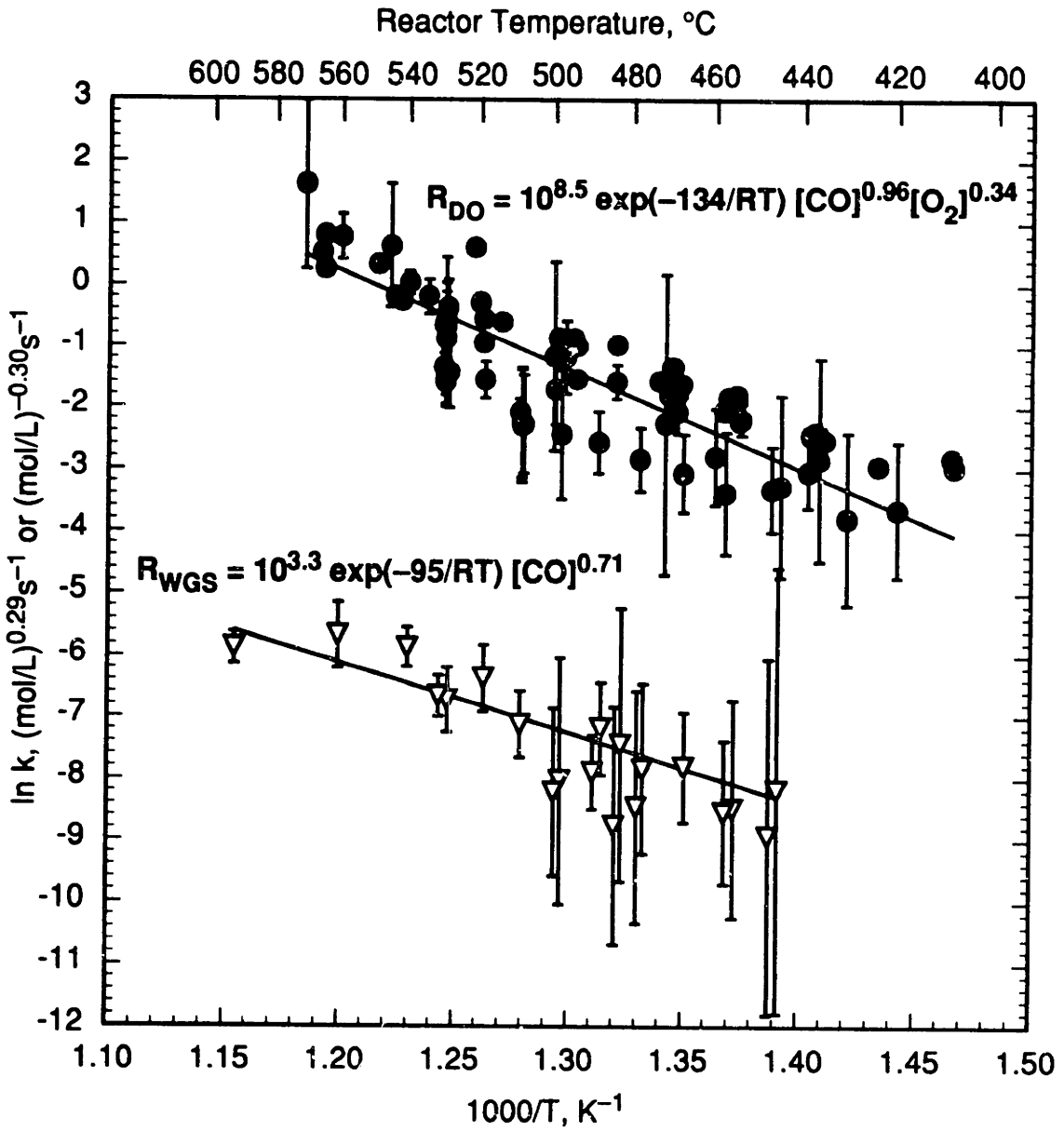

Figure 1.8 **Arrhenius Plot of Direct Oxidation and Water-Gas Shift Data, Including Global Rate Expressions.** Direct oxidation data include both the current results and the earlier results of Helling and Tester (1987).

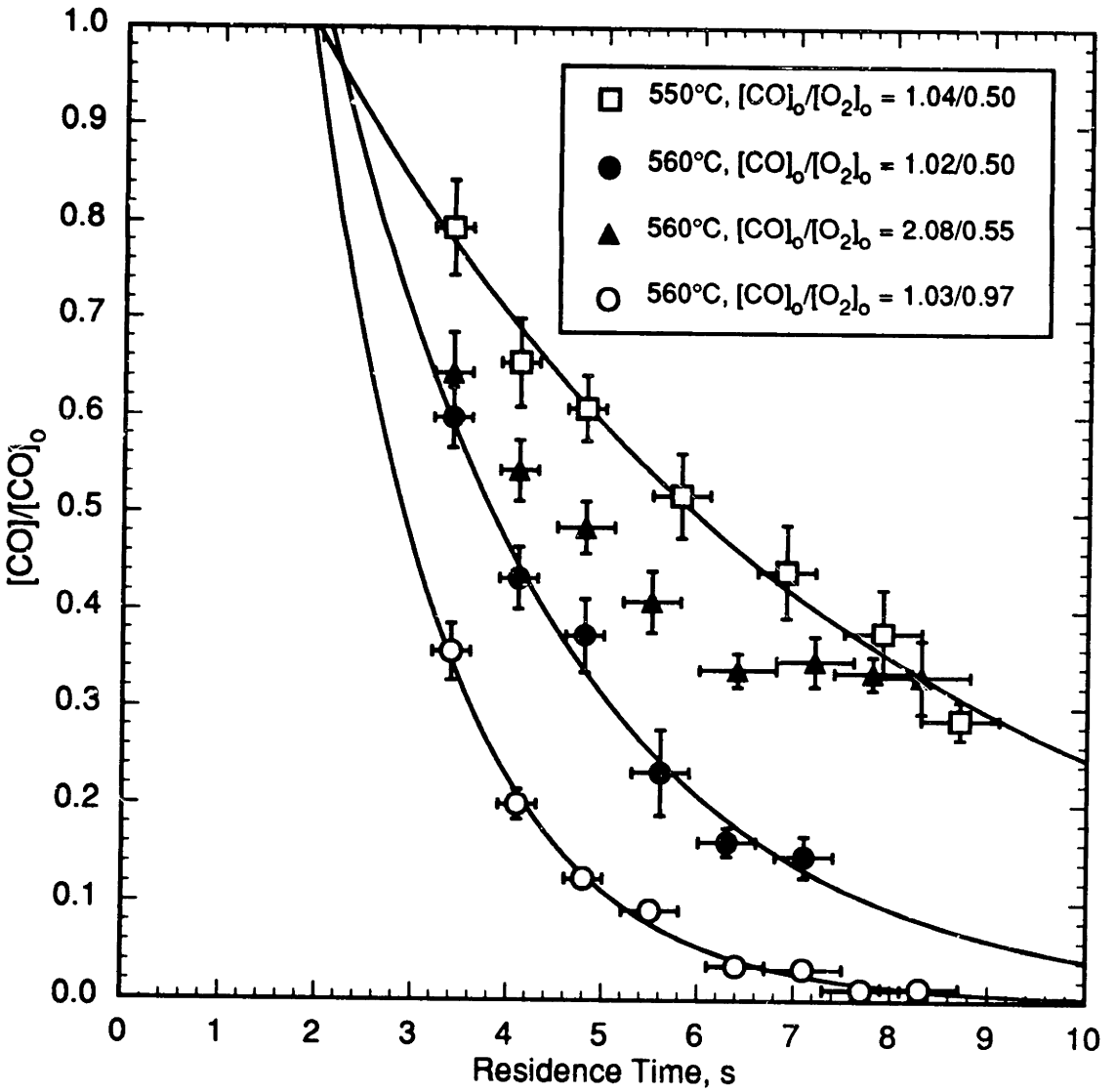

Figure 1.9 **Normalized Carbon Monoxide Decay Profiles Demonstrating Effective Induction Times and Decay Constants.**
Experimental conditions:
□—550±2 °C, $[CO]_o$ = (1.04±0.02) × 10^{-6} mol/cm^3, $[O_2]_o$ = (0.50±0.01) × 10^{-6} mol/cm^3, $[H_2O]$ = (4.25±0.08) × 10^{-3} mol/cm^3;
●—560±2 °C, $[CO]_o$ = (1.02±0.02) × 10^{-6} mol/cm^3, $[O_2]_o$ = (0.50±0.01) × 10^{-6} mol/cm^3, $[H_2O]$ = (4.16±0.07) × 10^{-3} mol/cm^3;
▲—560±3 °C, $[CO]_o$ = (2.08±0.03) × 10^{-6} mol/cm^3, $[O_2]_o$ = (0.55±0.01) × 10^{-6} mol/cm^3, $[H_2O]$ = (4.16±0.14) × 10^{-3} mol/cm^3;
○—560±2 °C, $[CO]_o$ = (1.03±0.04) × 10^{-6} mol/cm^3, $[O_2]_o$ = (0.97±0.04) × 10^{-6} mol/cm^3, $[H_2O]$ = (4.16±0.09) × 10^{-3} mol/cm^3.
Curves are exponential fits to data.

consistent with Equation 1.3. The leveling off of the fuel-rich profile occurs when oxygen has been fully depleted.

A series of experiments was conducted at operating pressures of 118 to 263 bar for a stoichiometric CO-O_2 mixture at 570 °C, with care taken to maintain constant CO and O_2 concentrations. Results for two residence times, 3.4 and 4.1 s, are shown in Figure 1.10. As for hydrogen oxidation, operating pressure (water density) has a pronounced effect on the oxidation of carbon monoxide, with the apparent first-order rate constant varying by a factor of 3 to 4 over the range of pressures studied. The slope of the curves in Figure 1.10 implies an effective reaction order with respect to water of about 1.7.

Limited experiments were also conducted in the packed reactor for stoichiometric CO oxidation at 560 °C. As for hydrogen oxidation, carbon monoxide oxidation was inhibited in the packed reactor, although the extent of inhibition was not extraordinarily high. Results for the tubular reactor at the higher temperatures were concluded to be essentially homogeneous for modeling purposes.

1.4.2 Elementary Reaction Modeling

The elementary reaction model developed for hydrogen oxidation was used as the basis for the development of a model for carbon monoxide oxidation. Basic rate constants for the additional reactions of carbon-containing species were again taken from the mechanism of Yetter *et al.* (1991a), with collisional efficiencies set to those for water. Preliminary modeling prompted the further examination of two rate constants. First, the primary CO oxidation reaction, $CO + OH \rightarrow CO_2 + H$, is known to be pressure dependent and the model of Larson *et al.* (1988) was used to calculate its rate constant under supercritical water conditions. The pressure dependence is weak for the temperatures of

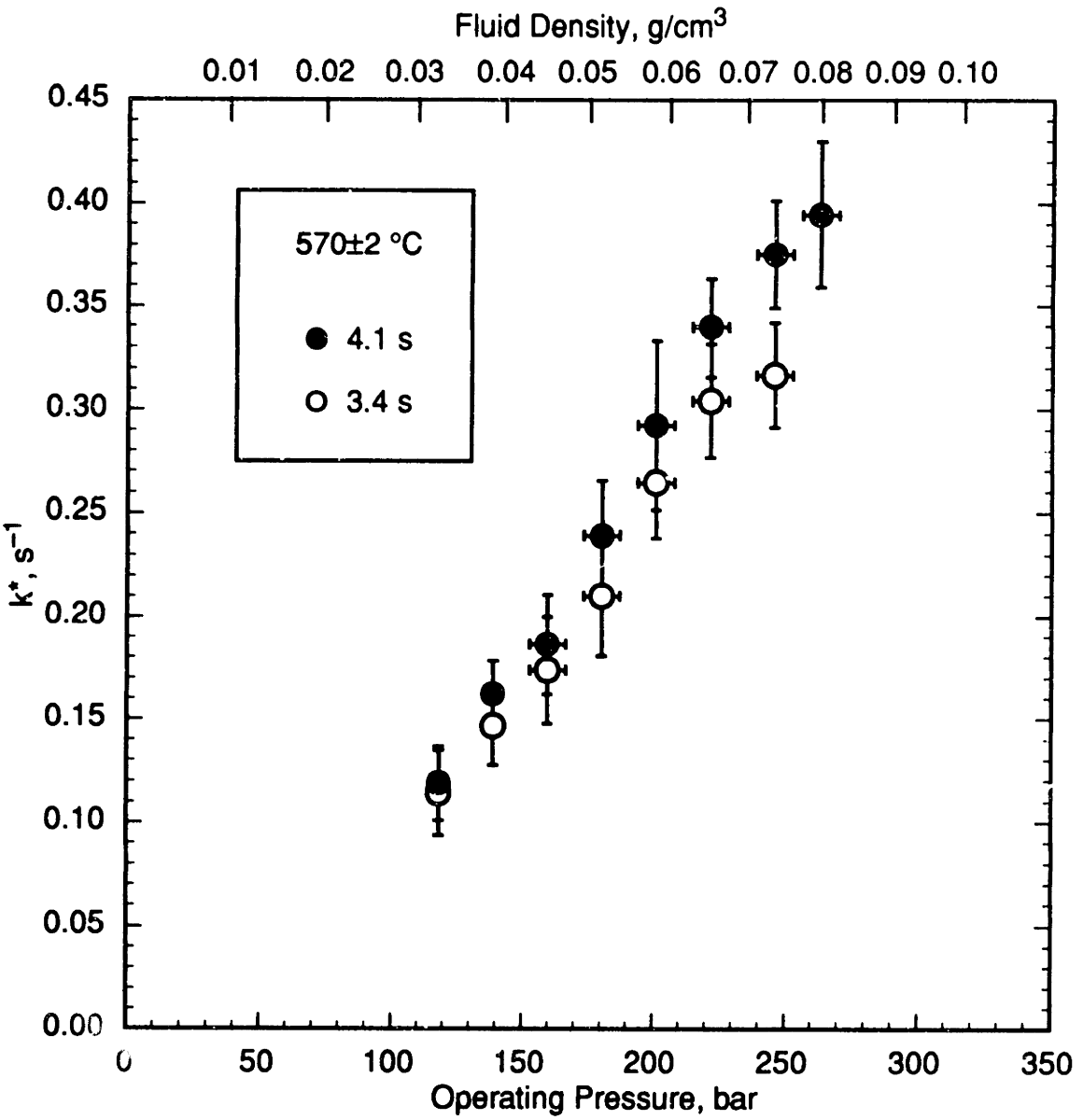

Figure 1.10 **Effects of Operating Pressure (Fluid Density) on the Apparent First-Order Rate Constant, k^*, for Carbon Monoxide Oxidation.**
Experimental conditions: 570±2 °C, $[CO]_o = (1.03 \pm 0.01) \times 10^{-6}$ mol/cm^3, $[O_2]_o = (0.51 \pm 0.01) \times 10^{-6}$ mol/cm^3. Results for two residence times (3.4 s, 4.1 s) are shown.

interest and incorporation of the pressure dependence affected the rate constant only slightly. Second, predicted hydrogen concentrations were found to be highly sensitive to the rate of the $H + O_2 \rightarrow HO_2$ reaction. Detailed modeling calculations, using the model of Cobos *et al.* (1985), showed that this reaction is in the falloff region under supercritical water conditions, and the low-pressure rate expression from the earlier model was replaced. Modeling of hydrogen oxygen with this replacement showed that predictions of hydrogen oxidation were not affected by the modification. The adapted mechanism, using JANAF thermodynamic data and also denoted YDR91J, was used for subsequent modeling of carbon monoxide oxidation.

Model predictions are shown compared to experimental oxidation data in the form of a first-order Arrhenius plot in Figure 1.11. Calculated rate constants are based on total conversion of carbon monoxide (including the water-gas shift contribution); only data from the present study are shown. While agreement between the model and data is good at the higher temperatures, the deviation is considerable at lower temperatures and the model exhibits a significantly higher global activation energy than the data (428 kJ/mol vs. 180 kJ/mol). The same data and model predictions are compared in Figure 1.12, where observed and predicted conversions of carbon monoxide are shown. Low conversions are seriously underpredicted, while higher conversions show better agreement.

The data show some evidence of a change in activation energy at about 500 °C. For example, the two stoichiometric curves in Figure 1.9, at 550 and 560 °C, imply an activation energy for the decay constant of 488 kJ/mol, much higher than the overall activation energy in Figure 1.11 but close to the model's activation energy. A different low-temperature mechanism for carbon monoxide oxidation, possibly involving heterogeneous reactions, cannot be ruled out.

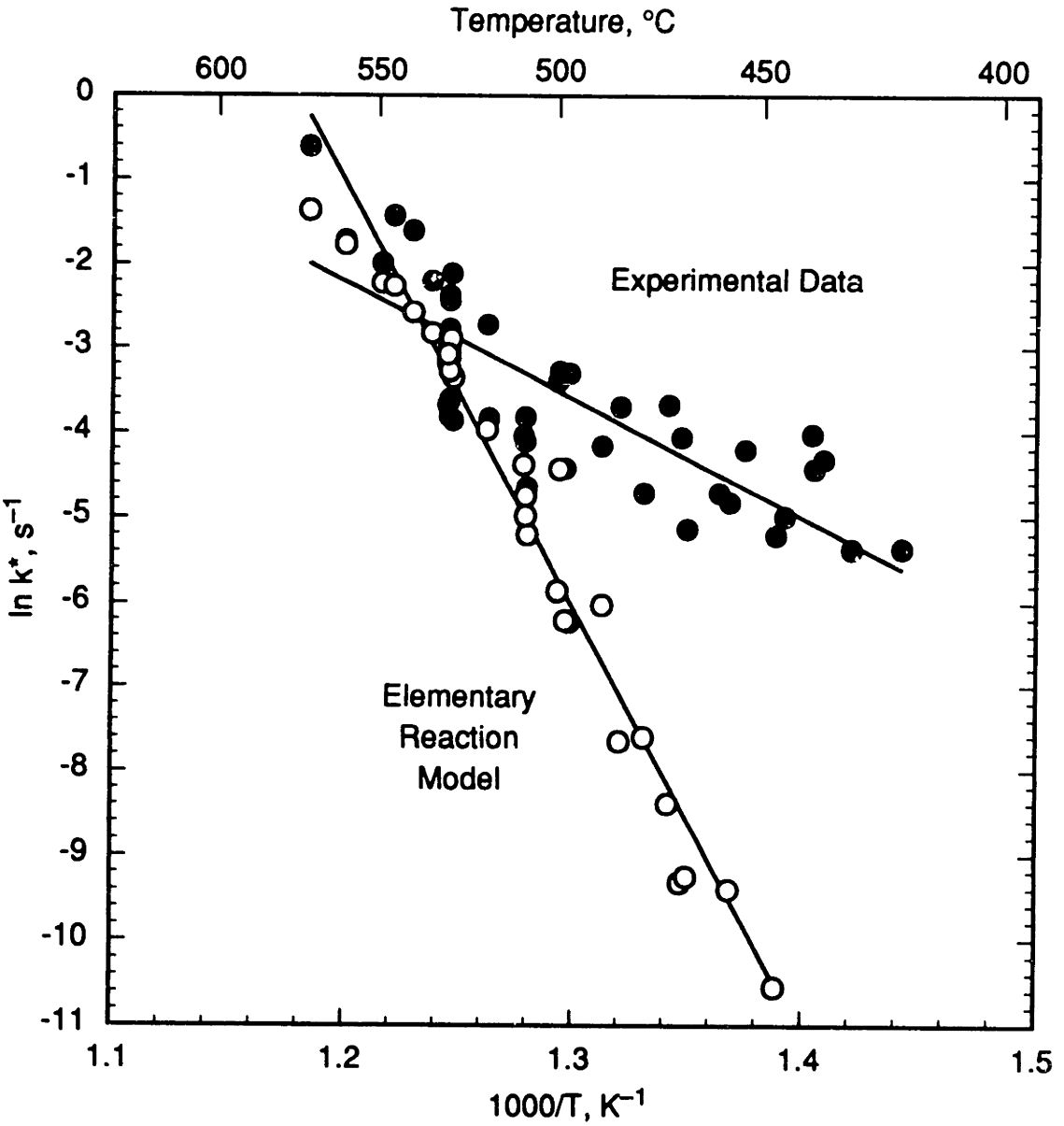

Figure 1.11 **Arrhenius Plot for Experimental Data and Elementary Reaction Model for Carbon Monoxide Oxidation in Supercritical Water at 246 bar.**

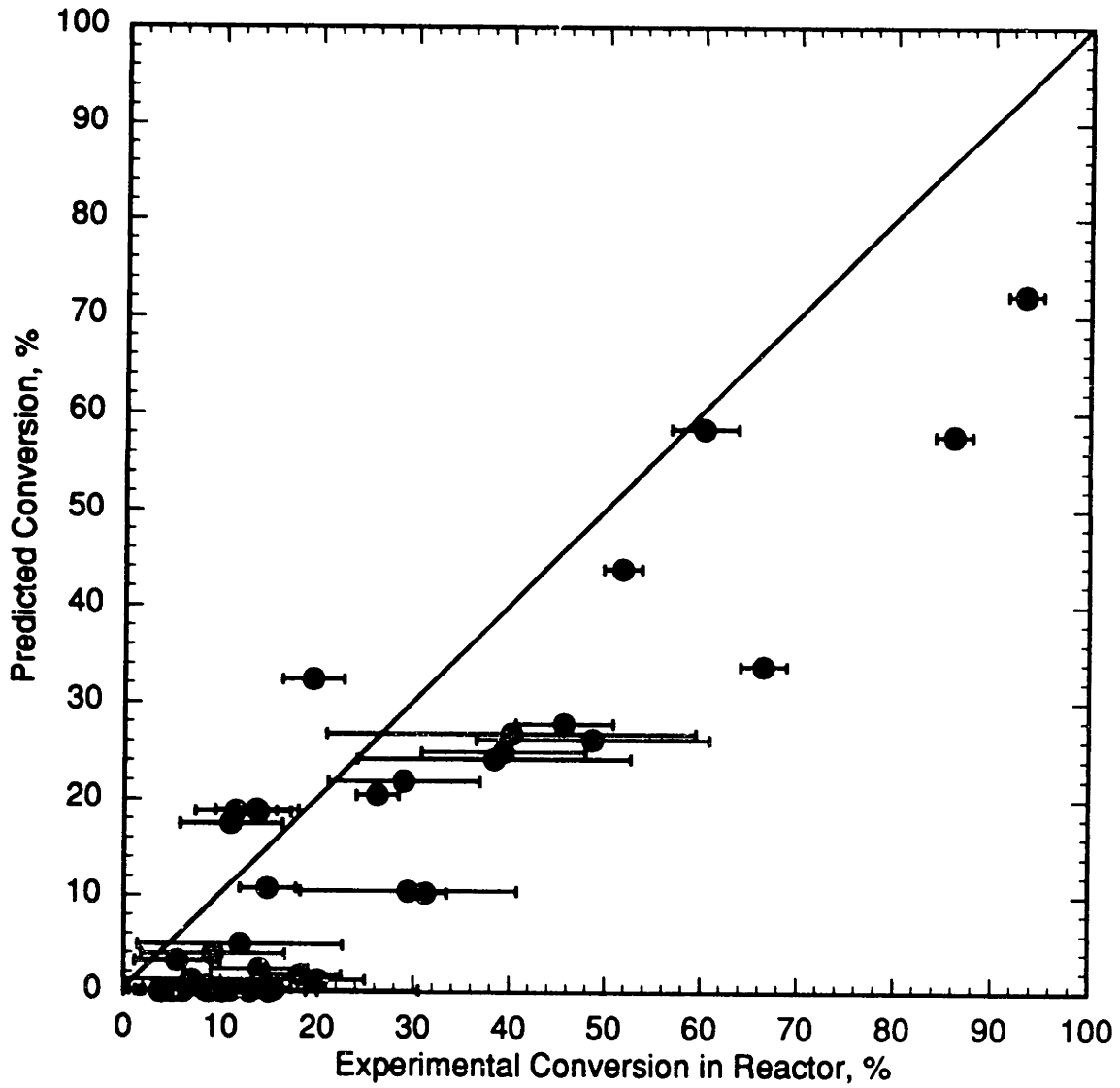

Figure 1.12 **Predicted Conversion of Carbon Monoxide from Elementary Reaction Model (Oxidation Experiments).**

Higher-temperature data, including the profiles from Figure 1.9, are quite well described by the model. Figures 1.13 through 1.15 show three full sets of concentration profiles for varying fuel equivalence ratios, all obtained at 560 °C, with the corresponding model predictions. For the stoichiometric and fuel-rich data (Figures 1.13 and 1.14), the model matches the data quite well, particularly for the fuel-rich conditions. For fuel-lean conditions (Figure 1.15), the predictions are less satisfactory, evidence of the fact that the model predicts no dependence of the oxidation rate on oxygen. Particularly encouraging in all three cases is the close agreement between the amount of hydrogen observed and predicted, even if the shapes of the hydrogen profiles are not in complete agreement. Earlier models were not able to predict this hydrogen formation. Also noteworthy is the variation with equivalence ratio in the amount of hydrogen formed. At the fuel-rich conditions (Figure 1.14), the hydrogen concentration is 50 times that at the fuel-lean conditions (Figure 1.15). On the other hand, hydrogen formation virtually ceases once oxygen has been depleted in the fuel-rich case (Figure 1.14). This behavior suggests that the rate of hydrogen formation is enhanced in the presence of oxygen, but increasing oxygen concentration decreases the amount of hydrogen formed.

The fundamental mechanisms of carbon monoxide oxidation, as predicted by the model, are illustrated in Figure 1.16. The primary mechanism is essentially identical to the mechanism for hydrogen oxidation, but with carbon monoxide as the fuel. Hydrogen formation results from the superequilibrium concentration of H atoms which drives the hydrogen-oxidizing reaction in the reverse direction. The H-atom concentration, and thus the H_2 concentration, is proportional to the relative rates of the $CO + OH \rightarrow CO_2 + H$ and $H + O_2 \rightarrow HO_2$ reactions. The failure of earlier models to predict hydrogen formation is directly traceable to the value of the $H + O_2 \rightarrow HO_2$ rate constant. For example, the low-pressure rate expression used by Webley and Tester (1991) predicts a rate constant two

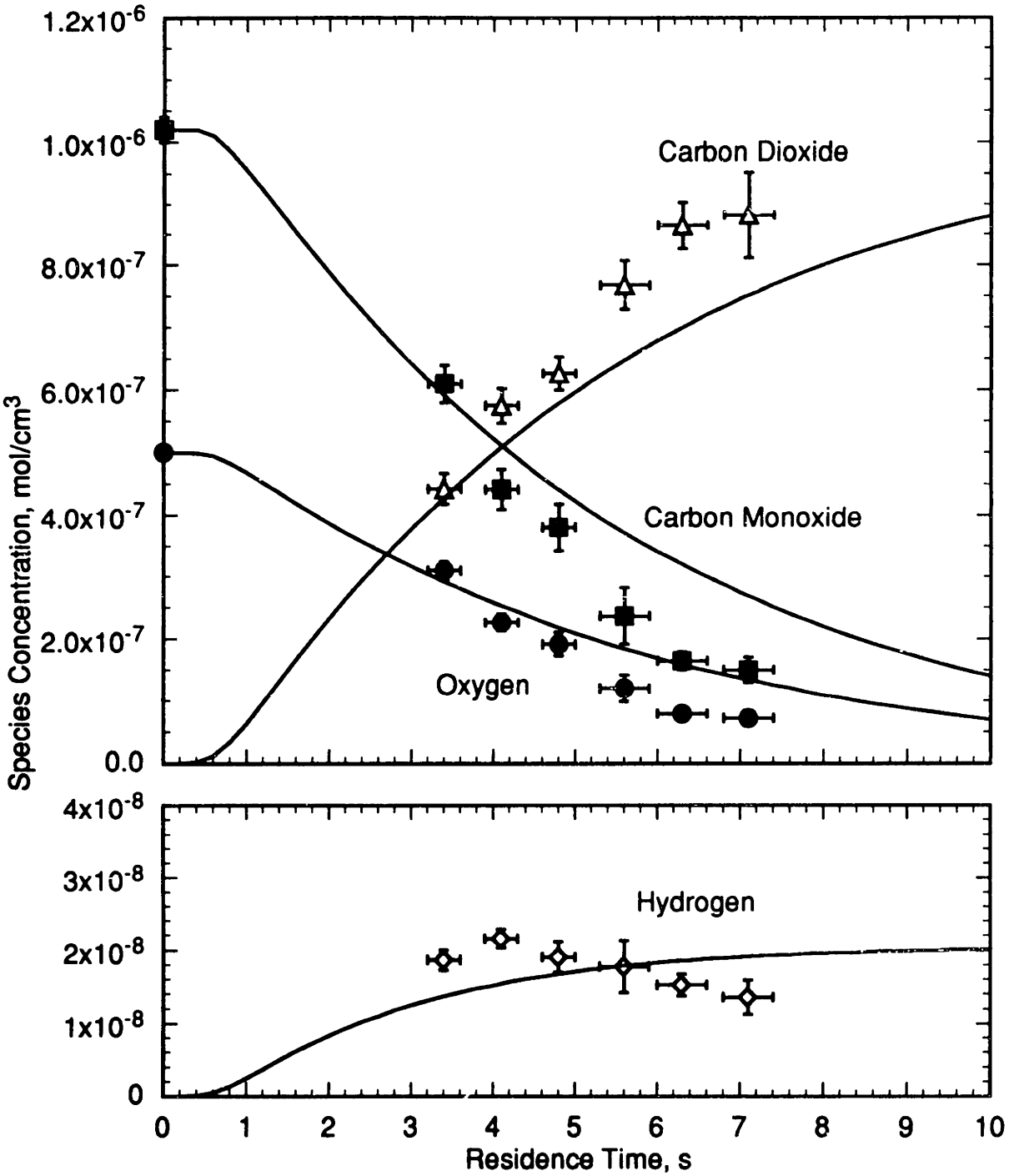

Figure 1.13 **Major Species Profiles for Stoichiometric Carbon Monoxide Oxidation at 560±2 °C.** Symbols: experimental data, $[CO]_o$ = (1.02±0.02) × 10^{-6} mol/cm^3, $[O_2]_o$ = (0.50±0.01) × 10^{-6} mol/cm^3, $[H_2O]$ = (4.16±0.07) × 10^{-3} mol/cm^3. Curves: predictions of model YDR91J.

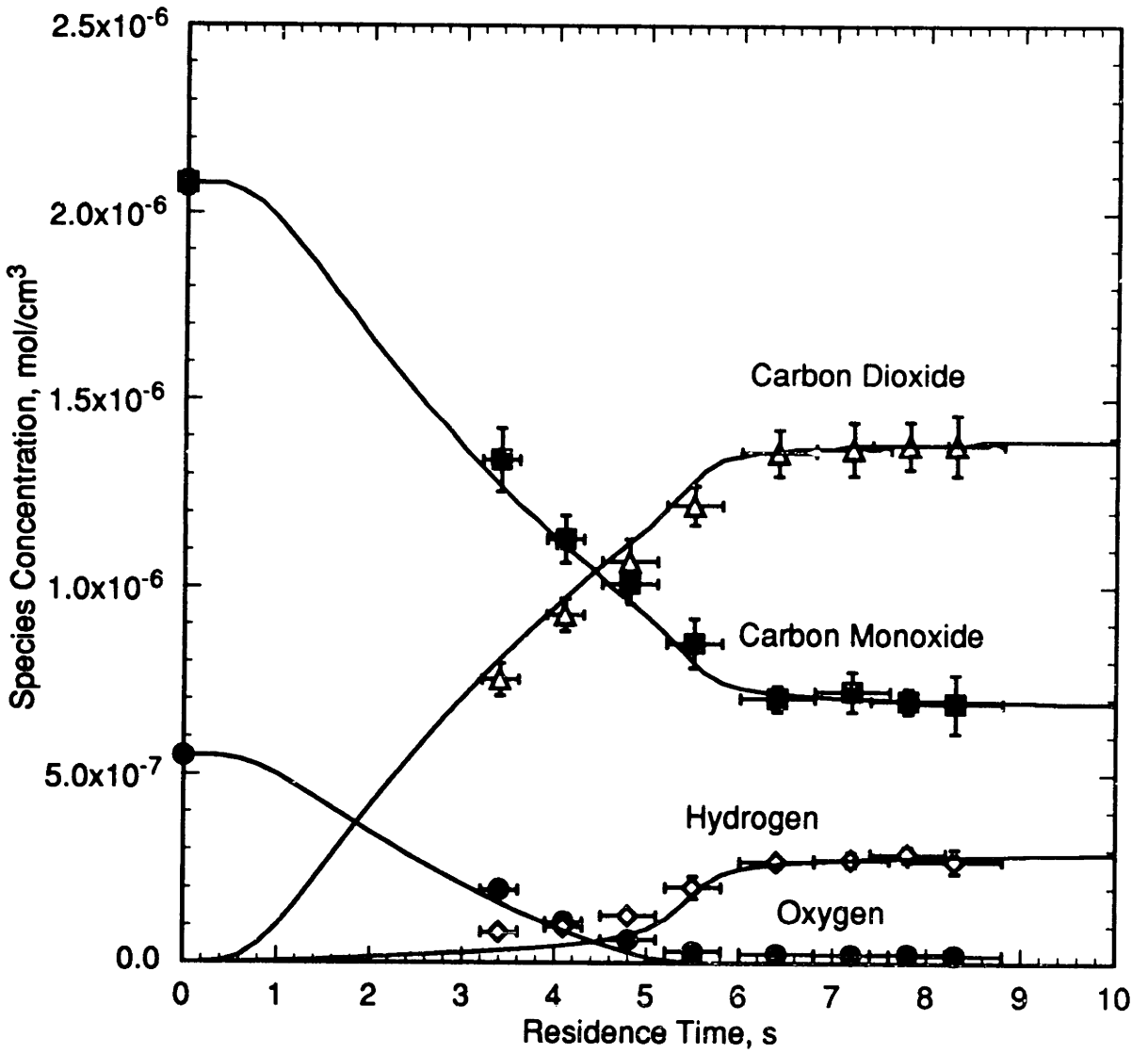

Figure 1.14 **Major Species Profiles for Substoichiometric (Fuel-Rich) Carbon Monoxide Oxidation at 560±3 °C.** Symbols: experimental data, $[CO]_o$ = (2.08±0.03) × 10^{-6} mol/cm^3, $[O_2]_o$ = (0.55±0.01) × 10^{-6} mol/cm^3, $[H_2O]$ = (4.16±0.14) × 10^{-3} mol/cm^3. Curves: predictions of model YDR91J.

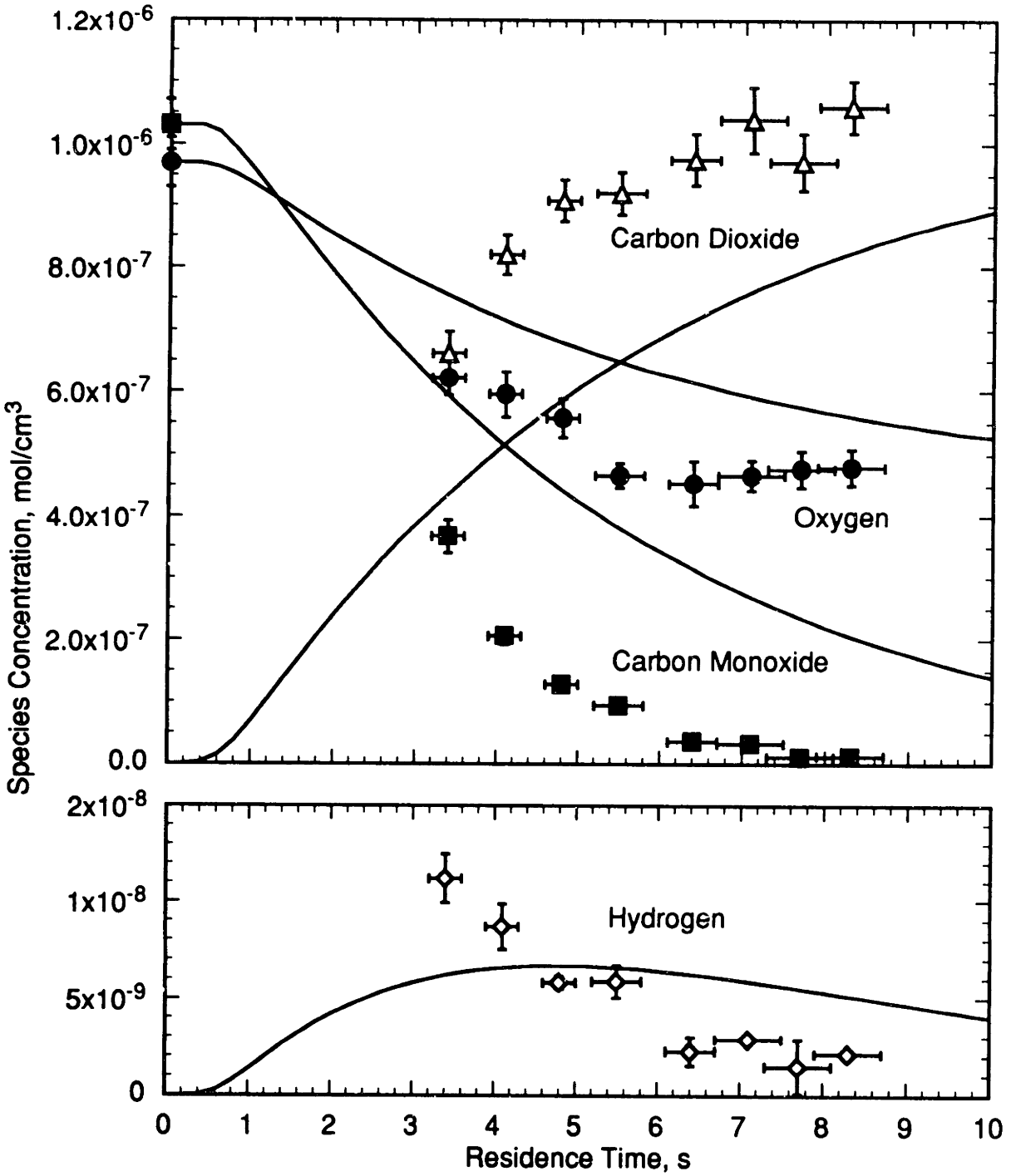

Figure 1.15 **Major Species Profiles for Superstoichiometric (Fuel-Lean) Carbon Monoxide Oxidation at 560±2 °C.** Symbols: experimental data, $[CO]_o$ = $(1.03\pm0.04) \times 10^{-6}$ mol/cm^3, $[O_2]_o = (0.97\pm0.04) \times 10^{-6}$ mol/cm^3, $[H_2O]$ = $(4.16\pm0.09) \times 10^{-3}$ mol/cm^3. Curves: predictions of model YDR91J.

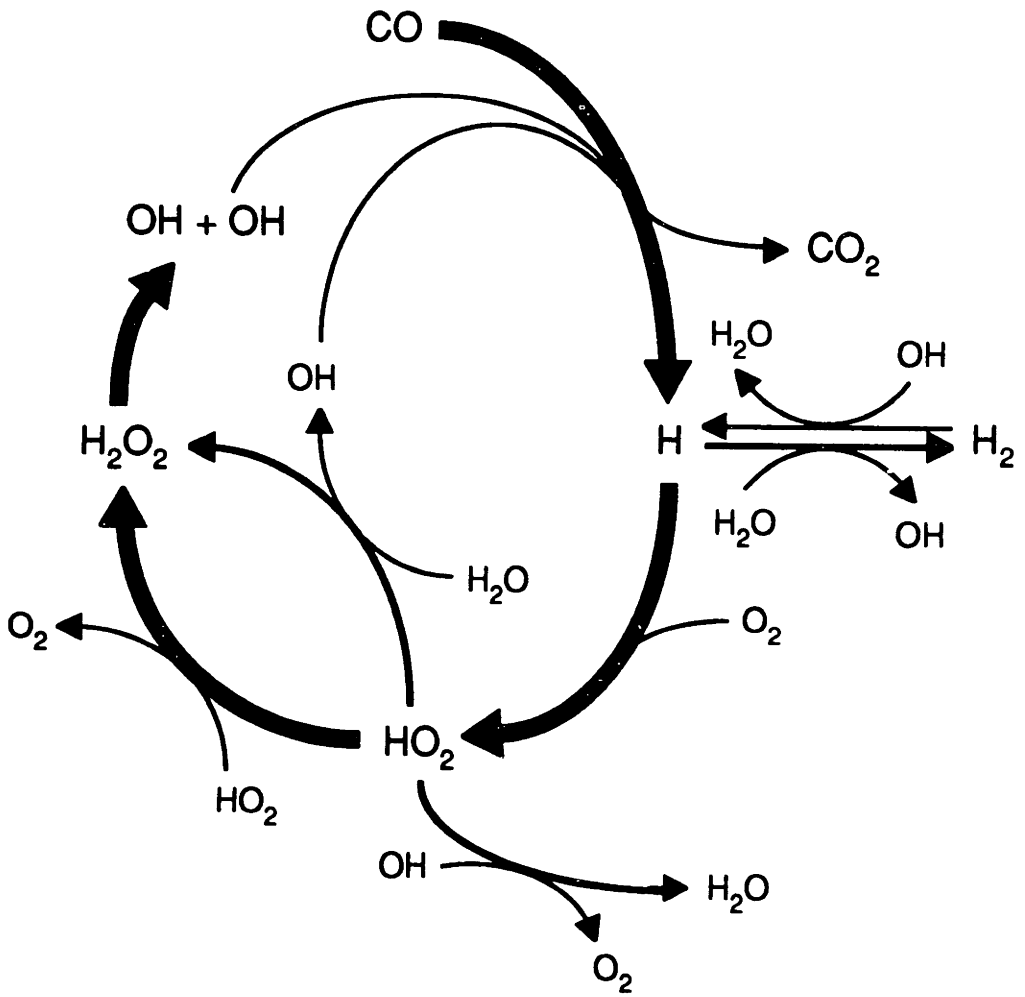

Figure 1.16 **Major Free-Radical Reaction Pathways in the Elementary Reaction Network for Carbon Monoxide Oxidation in Supercritical Water.** Arrow thicknesses indicate relative rates of reactions.

orders of magnitude higher than the falloff rate constant calculated here; hydrogen concentrations were thus two orders of magnitude lower in the earlier model.

The model for carbon monoxide oxidation also captures the majority of the pressure dependence of the data, as shown in Figure 1.17. As for hydrogen oxidation, the magnitude of the predicted pressure dependence is not as large as that of the observed dependence, but the trend is clear. Again, the primary source of the global pressure dependence is not pressure-dependent rate constants, but rather the effect of changing water concentration on the branching rate via the $HO_2 + H_2O \rightarrow H_2O_2 + OH$ reaction. The slopes of the predicted rate constants in Figure 1.17 suggest a global order with respect to water of 1, consistent with a branching rate proportional to the water concentration.

1.5 Glucose Hydrolysis and Oxidation in Supercritical Water

The hydrolysis and oxidation of glucose in supercritical water, as models for the reactions of cellulosic wastes, were studied in a limited set of experiments. In an initial set of experiments, 1×10^{-6} mol/cm^3 glucose was fed to the reactor, with and without stoichiometric (6×10^{-6} mol/cm^3) oxygen present, at a fixed residence time of 6 seconds and over the temperature range 425 to 600 °C. In this manner the hydrolysis and oxidation pathways could be examined and compared under otherwise identical conditions. Even at the lowest temperature studied, glucose concentrations in the liquid effluent (as determined enzymatically) indicated a conversion of glucose of over 90%, demonstrating the high reactivity of glucose even in the absence of oxygen and making kinetic measurements infeasible.

Both hydrolysis and oxidation of glucose produced large quantities of gas. Gasification was obviously more prevalent under oxidizing conditions, with 60% of the

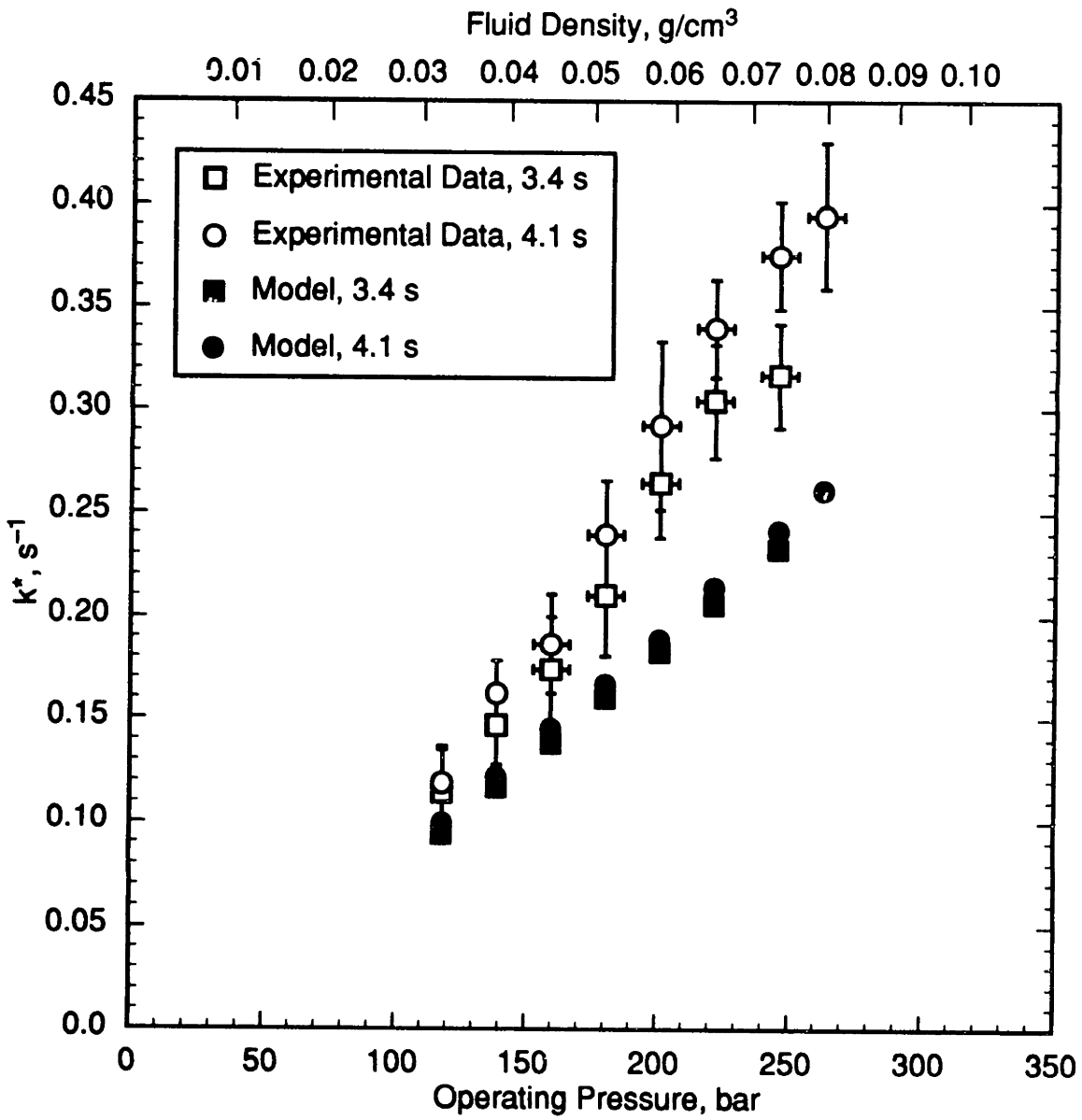

Figure 1.17 **Predicted Effects of Operating Pressure (Fluid Density) on the Apparent First-Order Rate Constant, k^*, for Carbon Monoxide Oxidation.**
□,○—Experimental data from Figure 1.10;
■,●—Predictions of YDR91J model.

glucose carbon appearing in the gaseous effluent at 425 °C, increasing to virtually 100% for temperatures of 500 °C and higher. Carbon dioxide, carbon monoxide, methane, and hydrogen were produced, with smaller quantities of ethylene and ethane. Under hydrolysis conditions, gasification was less extensive at low temperatures (~12% at 450 °C), but rose quickly to 100% at 575 to 600 °C. The same gases were found in the hydrolysis effluent, although at high temperatures hydrolysis gave almost exclusively hydrogen and carbon dioxide in a 1.7:1 ratio, indicating the presence of a fast, water-gas-shift-type pathway. These observations are generally consistent with the recently reported results of Antal and co-workers (Antal *et al.*, 1992).

Hydrolytic reactions of glucose also tended to produce large numbers of products present in the liquid effluent. Typical HPLC chromatograms for the liquid effluent from comparable hydrolysis and oxidation experiments are shown in Figure 1.18. Peak identities, when known or suspected, have been indicated. Clearly the number of liquid-phase products is greatly reduced under oxidizing conditions, with a correspondingly higher extent of gasification. Many peaks formed during glucose hydrolysis remain unidentified. Almost forty individual compounds were tested as possible hydrolysis products, on the basis of their prior identification among the products of biomass pyrolysis or carbohydrate hydrolysis. Positive identifications in the present study were made for acetaldehyde, acetic acid, acetonylacetone (2,5-hexanedione), 2-acetylfuran, formic acid, furfural (2-furaldehyde), 5-hydroxymethylfurfural, lactic acid, 5-methylfurfural, and propenoic (acrylic) acid.

Yields of identified products of glucose oxidation are shown in Figure 1.19 as a function of reactor temperature for a constant residence time of 6 seconds. Yields of liquid-phase products decrease with increasing temperature, with no liquid-phase products detected at temperatures above 550 °C. Temperatures above 550 °C are thus

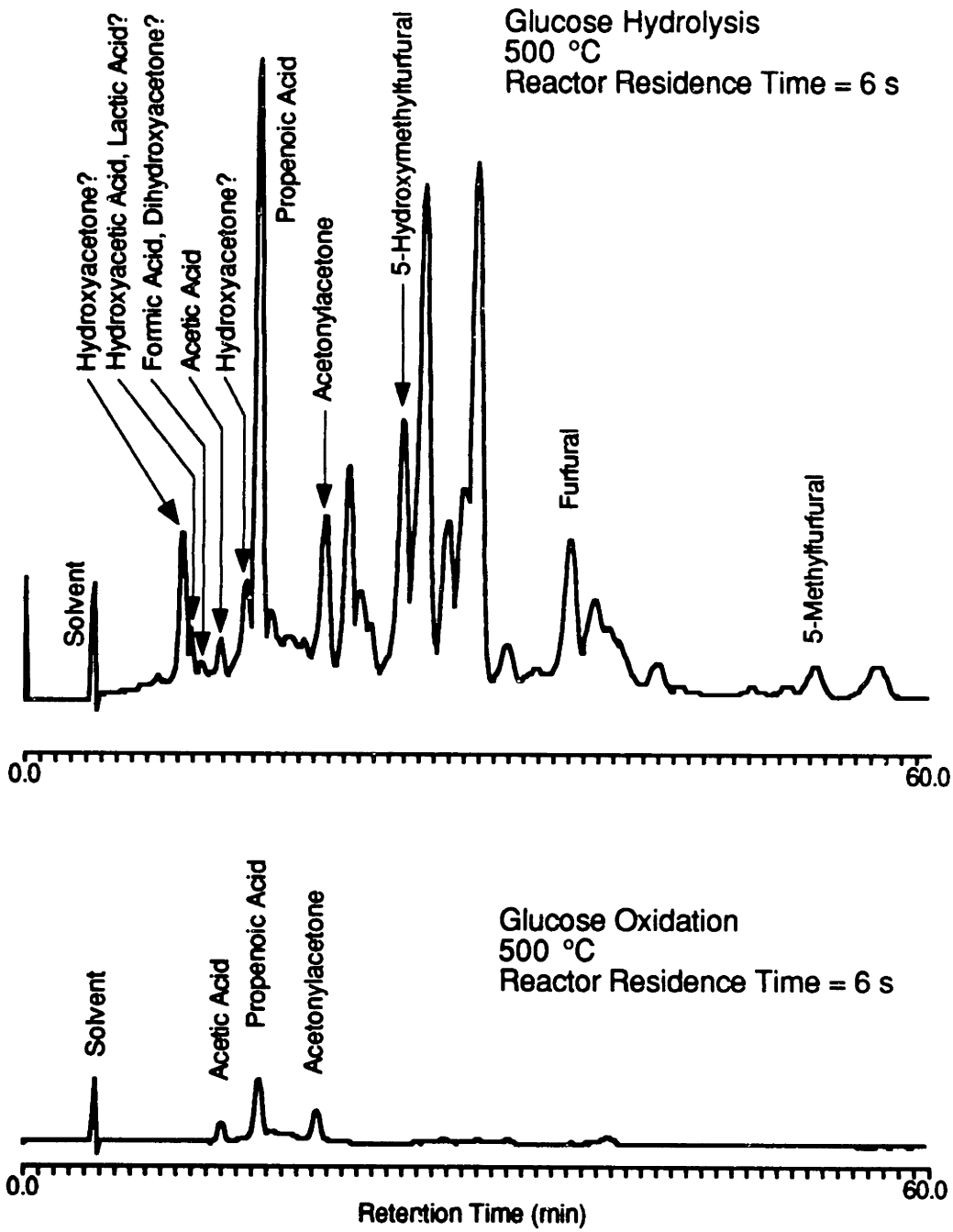

Figure 1.18 **Comparison of HPLC Chromatograms of Liquid Effluent from Glucose Hydrolysis and Oxidation in Supercritical Water.** Nominal initial conditions: 500 °C, 1×10^{-6} mol/cm^3 glucose, 6×10^{-6} mol/cm^3 oxygen (for oxidation), 6 s reactor residence time. UV detection at 210 nm.

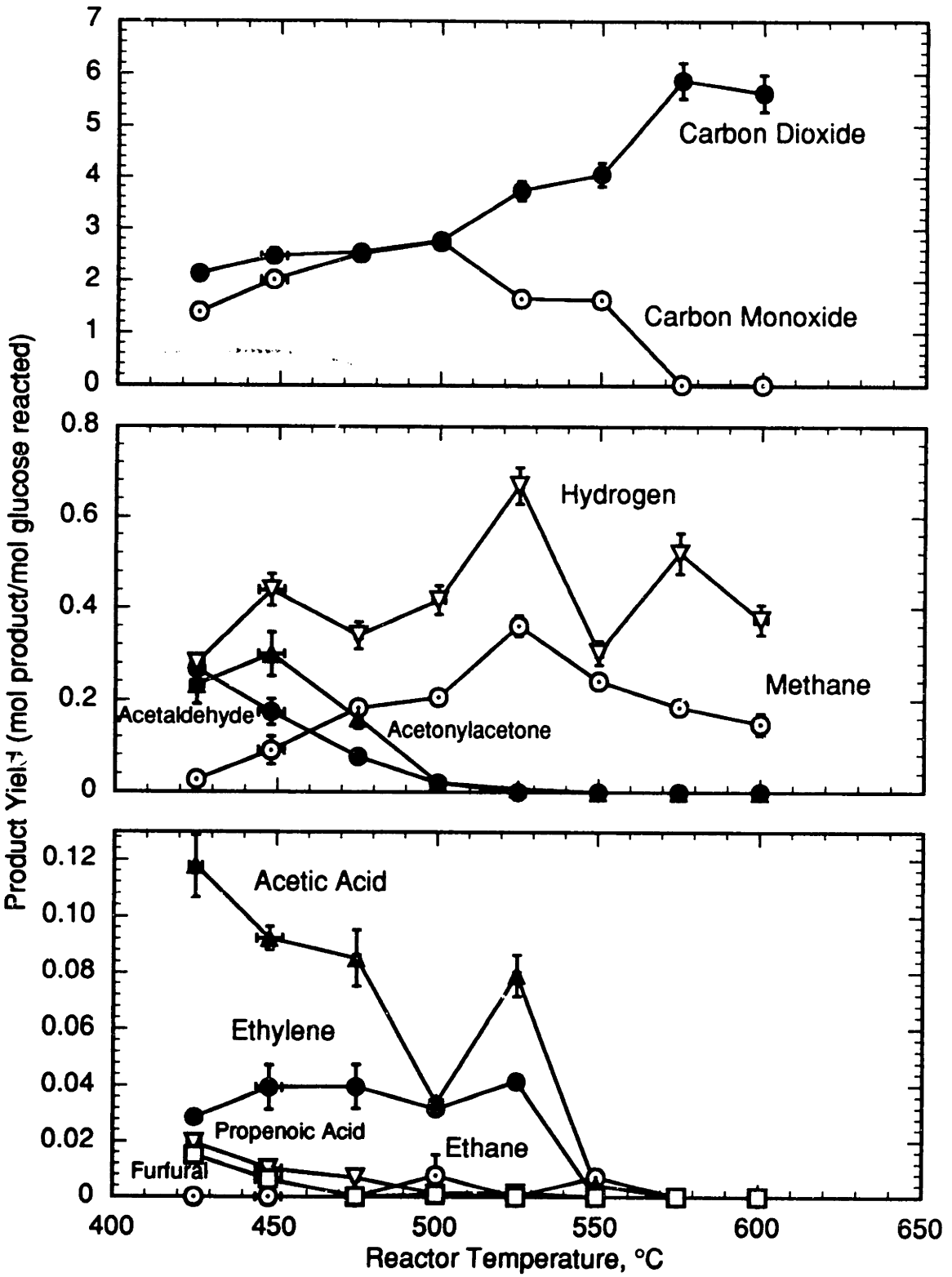

Figure 1.19 Variation of Product Yields with Temperature for Glucose Oxidation at 246 bar. Nominal initial conditions: 1×10^{-6} mol/cm^3 glucose, 6×10^{-6} mol/cm^3 oxygen, 6 s reactor residence time.

sufficient to insure complete destruction of all intermediates produced from glucose, including acetic acid and furan derivatives. At the highest temperatures, glucose is converted almost entirely to carbon dioxide, with small quantities of hydrogen and methane also present.

Figure 1.20 shows the results of a series of experiments conducted at 500 °C in order to evaluate the effect of residence time on the observed product yields. Over a span of five seconds, from 5 to 10 seconds residence time, the yields of the major products shown do not change markedly, indicating that reactions (oxidation) of these species occur relatively slowly at this temperature. On the other hand, primary decomposition or oxidation of glucose, as well as secondary destruction of the more complex intermediates, must occur quite rapidly, in the first five seconds and/or during preheating of the glucose feed. The compounds shown in Figure 1.20 therefore represent the destruction-limiting species for oxidation of glucose in supercritical water.

1.6 Conclusions

1. Measurements of oxidation kinetics. The oxidation kinetics of hydrogen in supercritical water have been examined at 246 bar and 495 to 600 °C. Over the range of conditions studied, the reaction is first order in hydrogen and independent of oxygen concentration, with a global activation energy of 372±34 kJ/mol. Carbon monoxide oxidation was investigated at 246 bar and 420 to 593 °C, over an extended range of concentrations and fuel equivalence ratios. Reaction of the carbon monoxide during preheating of the reactor feeds was found to be unimportant for the experimental conditions studied. Regression of the carbon monoxide oxidation data to a global rate form revealed a fractional-order dependence on oxygen concentration, which had not been observed earlier. The global reaction was first-order in carbon monoxide, with an

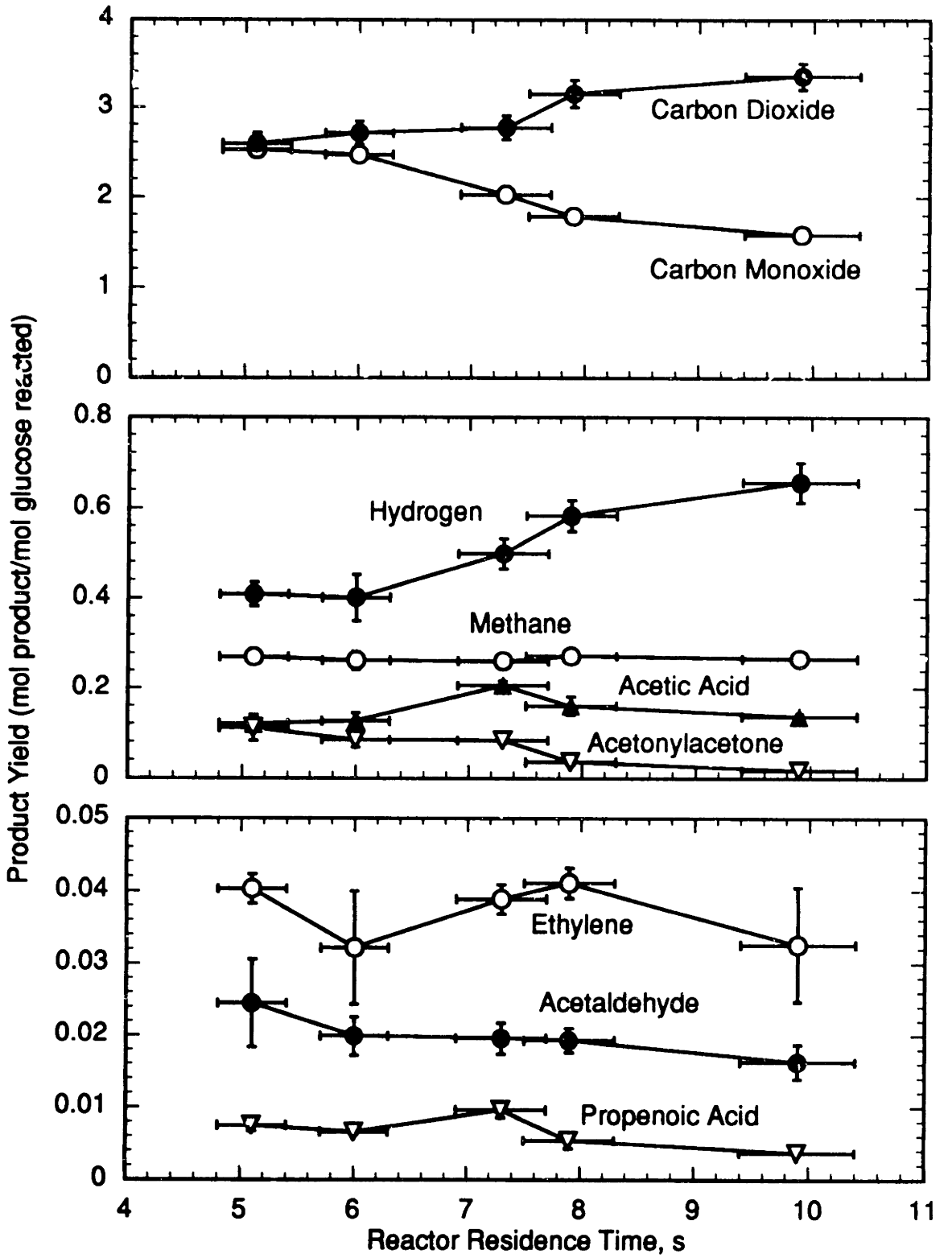

Figure 1.20 **Variation of Product Yields with Residence Time for Glucose Oxidation at 500 °C and 246 bar.** Initial concentrations: 1×10^{-6} mol/cm^3 glucose, 6×10^{-6} mol/cm^3 oxygen.

activation energy of 134±32 kJ/mol.

2. Identification of induction times. Hydrogen oxidation in supercritical water possesses a distinct induction time, which is a strong indication of a free-radical mechanism. Additional studies of carbon monoxide oxidation showed that the reaction, like hydrogen oxidation, possesses an induction time. The induction time for carbon monoxide oxidation is the same or shorter than that for hydrogen oxidation.

3. Hydrogen formation by the water-gas shift pathway. Hydrogen formation during carbon monoxide oxidation is facilitated by the presence of oxygen, and is very slow in the absence of oxygen. Hydrogen formation is strongly dependent on the fuel equivalence ratio, with fuel-rich conditions favoring its formation.

4. Global reaction modeling. The presence of an induction time complicates, and partially invalidates, global reaction modeling efforts. Attempts to extend global models for single compounds to multi-step global models for more complex compounds were not completely successful.

5. Effects of operating pressure. The oxidation of hydrogen and carbon monoxide, at 550 and 570 °C, respectively, is strongly pressure (water-density) dependent over the range 118 to 263 bar, with higher pressures favoring higher oxidation rates. This dependence suggests that a kinetic penalty is incurred for operation of the SCWO process at lower pressures.

6. Effects of reactor surface. Limited studies of hydrogen and carbon monoxide oxidation in a packed reactor showed that the additional surface area tends to inhibit oxidation, most likely through termination of free radicals. The effect of the surface was not severe, however, indicating that tubular reactor results at higher temperatures may be treated as homogeneous.

7. Elementary reaction modeling. An elementary reaction model for hydrogen oxidation, with certain modifications for high pressure, was largely successful in reproducing the experimentally observed kinetic behavior, including the effect of pressure. A similar model for carbon monoxide oxidation was somewhat less successful, exhibiting a higher overall activation energy than the data and lacking an oxygen dependence. High-temperature stoichiometric and fuel-rich data were reproduced well, however. The principal effects of the high pressure (water concentration) on the oxidation mechanism are threefold: a) the dissociation of hydrogen peroxide ($H_2O_2 \rightarrow OH + OH$) is at or near its high-pressure limit; b) the dissociation (recombination) of the hydroperoxyl radical ($H + O_2 \rightarrow HO_2$) approaches its high-pressure limit; and c) the rate of the $HO_2 + H_2O \rightarrow H_2O_2 + OH$ branching reaction is greatly accelerated by the high water concentrations (densities) present in supercritical water relative to typical gas-phase oxidation conditions.

8. Glucose hydrolysis and oxidation. Glucose hydrolysis proceeds rapidly and completely in supercritical water. The products formed are diverse but also undergo hydrolysis; at 600 °C and a 6-second reactor residence time, glucose is converted completely to gases, even in the absence of oxygen. The presence of oxygen accelerates the destruction of the intermediate products, with no liquid-phase products found above 550 °C at a 6-second reactor residence time. The major, persistent intermediate products of glucose hydrolysis and oxidation are acetic acid, acetonylacetone, propenoic acid, and acetaldehyde in the liquid effluent, and carbon monoxide, methane, ethane, ethylene, and hydrogen in the gaseous effluent. Methane and hydrogen are present in the effluent at temperatures up to 600 °C.

1.7 Recommendations

1. Modifications to the experimental apparatus are necessary to increase the range of operating conditions (concentrations and residence times) and to maximize the flexibility of the system. The range of accessible residence times needs to be extended to allow the determination of temporal concentration profiles over a wider range of temperatures. This may entail upgrading the flow capacity of the feed pump, improving the heating capability of the fluidized sand bath, and/or constructing new tubular reactors of varying sizes. In addition, a larger-diameter (lower surface area relative to fluid volume) reactor should be tested to confirm the lack of a surface influence on the kinetic data obtained in the present tubular reactor.

2. Temporal concentration profiles should be obtained for hydrogen oxidation under sub- and superstoichiometric conditions, and, if possible, for both carbon monoxide and hydrogen over an extended temperature range. These profiles should then be used for further validation of the elementary reaction models. Similar profiles should also be obtained for more complex compounds such as methane and methanol, since simple conversion data are insufficient for verification of elementary reaction models.

3. With the existing model for carbon monoxide and hydrogen oxidation as a basis, and with additional concentration-profile data, elementary reaction models should be extended to more complex model compounds. A hierarchical modeling effort with proper validation is necessary.

4. More extensive glucose experiments are needed to quantify the global oxidation kinetics and the optimum treatment conditions for cellulosic wastes. Experiments under hydrolysis conditions and at subcritical temperatures and pressures may be desirable to

identify (in terms of by-product formation) the implications of operating under conditions more typically encountered in wet-air oxidation.

5. The kinetics of oxidation of additional model compounds should be studied. In particular, acetic acid and acetaldehyde represent the next level of molecular complexity and are frequently found to be persistent intermediates. Compounds containing chlorine, sulfur, and phosphorus heteroatoms represent an important class of wastes whose oxidation kinetics in supercritical water have not been fully characterized; selection and examination of simple model compounds from this class are a logical step in the extension of the kinetic database.

6. Elementary reaction models have clearly demonstrated the important role of the hydroxyl radical in oxidation in supercritical water. As a source of these radicals, hydrogen peroxide added to the reactor feed has been shown to enhance oxidation. Careful experimental examination of this enhancement, with corresponding elementary reaction modeling, may provide important verification of the fundamental oxidation mechanisms.

Chapter 2

Introduction and Background

Increasing concern over the large quantities of human and hazardous organic wastes produced worldwide has prompted research into efficient methods for the destruction of such wastes. While the best solution is a reduction or elimination of the amount of waste generated, an effective method of waste destruction is necessary for existing wastes as well as for any additional wastes which may be produced in the future. MODAR, Inc. has developed a process for oxidizing hazardous wastes in a supercritical water environment (Modell, 1982, 1985a; Modell *et al.*, 1982; Staszak *et al.*, 1987). The supercritical water oxidation (SCWO) process represents a significant improvement over traditional destruction methods, in that it provides complete and rapid oxidation of wastes without formation of toxic by-products (Swallow *et al.*, 1989; Modell, 1989; Thomason *et al.*, 1990; Tester *et al.*, 1991). The process has also proven suitable for treatment of human metabolic wastes, and is being considered for use in life support systems on long-term spaceflights (Timberlake *et al.*, 1982; Hong *et al.*, 1987,1988).

By definition, SCWO takes place above the critical point of pure water (374 °C and 221 bar). In practice, the SCWO process brings together water, organics, and oxygen at moderate temperatures (400 °C and above) and high pressures (about 250 bar). These temperatures are high enough to induce spontaneous oxidation of the organics, and the heat of reaction raises the mixture temperature to between 550 and 650 °C, where organics are oxidized rapidly and completely, to conversions greater than 99.99% for

reactor residence times of 1 minute or less. Heteroatoms, such as chlorine, sulfur and phosphorus, are oxidized to acids which can be neutralized and precipitated as salts by adding a base to the feed (Thomason and Modell, 1984). For aqueous solutions of between 1 and 20 wt% organics, supercritical water oxidation is both more economical than controlled incineration or activated carbon treatment and more efficient than wet oxidation that takes place below the critical point (Thomason and Modell, 1984). With appropriate temperatures, pressures, and residence times, organics are oxidized completely to carbon dioxide, water, and molecular nitrogen, without formation of NO_x compounds or other toxic products of incomplete combustion. Modell *et al.* (1982) also destroyed problematic PCBs and DDT at greater than 99.99% efficiency without formation of dioxins. Johnston *et al.* (1988) oxidized synthetic pharmaceutical and biopharmaceutical wastes and achieved >99.99% destruction of total organic carbon and >99.9999% destruction of bacteria. Bramlette *et al.* (1990) successfully treated complex matrices of organics and inorganics simulating DOE mixed waste and electronics industry waste.

Oxidation in supercritical water is not limited to aqueous organics. Sludges, biomass, sewage, and soil can be slurried and fed to the reactor as a two-phase mixture. For example, treatment by SCWO has been achieved for many types of high-solids-content streams, including dioxin-containing pulp mill sludges (Hossain and Blaney, 1991; Modell *et al.*, 1992), industrial waste-treatment activated sludges (Shanableh and Gloyna, 1990), model life-support system wastes (Takahashi *et al.*, 1989), and even dioxin-contaminated soil (Thomason *et al.*, 1990). Dioxins contained in the wastes were destroyed to levels below detection. Precipitated salts and other solids can be removed from the product stream, providing a clean, high-temperature, high-pressure source of energy consisting almost entirely of CO_2, H_2O, and N_2. Heat can be recovered from the

treated process stream and used to preheat the feed, or the stream can be used in a high-efficiency Rankine cycle to generate electric power. The heat of reaction is thus partially recoverable and can be used to offset the cost of treatment. Reviews of SCWO technology have been prepared by Modell (1989), Thomason *et al.* (1990), Shaw *et al.* (1991), and Tester *et al.* (1991).

2.1 Properties of Supercritical Water

Pure water exists in a supercritical phase if both its temperature and pressure exceed the critical values of 374.3 °C and 221 bar (3200 psia). In the region near and above the critical point, the density of water (shown in Figure 2.1) changes rapidly with both temperature and pressure, and is typically intermediate between that of liquid water (1 g/cm^3) and low-pressure water vapor (0.001 g/cm^3). One should note, however, that under supercritical conditions the density of water can vary over an order of magnitude, from liquid-like (~1 g/cm^3 or higher) to more gas-like (~0.1 g/cm^3 or lower). The extension of the vapor-pressure curve beyond the critical point describes a locus of pseudocritical points, where for a given pressure the variation in density with temperature is a maximum. In general, at a particular pressure, temperatures at or below the pseudocritical point give liquid-like densities, while temperatures above the pseudocritical point give more expanded, gas-like densities. At sufficiently high reduced temperatures (T_r > ~1.3 for P_r ~ 1.1), supercritical water will obey the ideal-gas law. Typical SCWO operating conditions (nominally, 230 to 260 bar and 450 to 650 °C), shown in Figure 2.1, occupy a small fraction of the supercritical region, and lie in the expanded, lower-density regime. Since solvation properties are strongly correlated with density (Franck, 1976; Shaw *et al.*, 1991), the solvation properties of supercritical water (SCW) can vary over a wide range, and at SCWO conditions can be quite different from

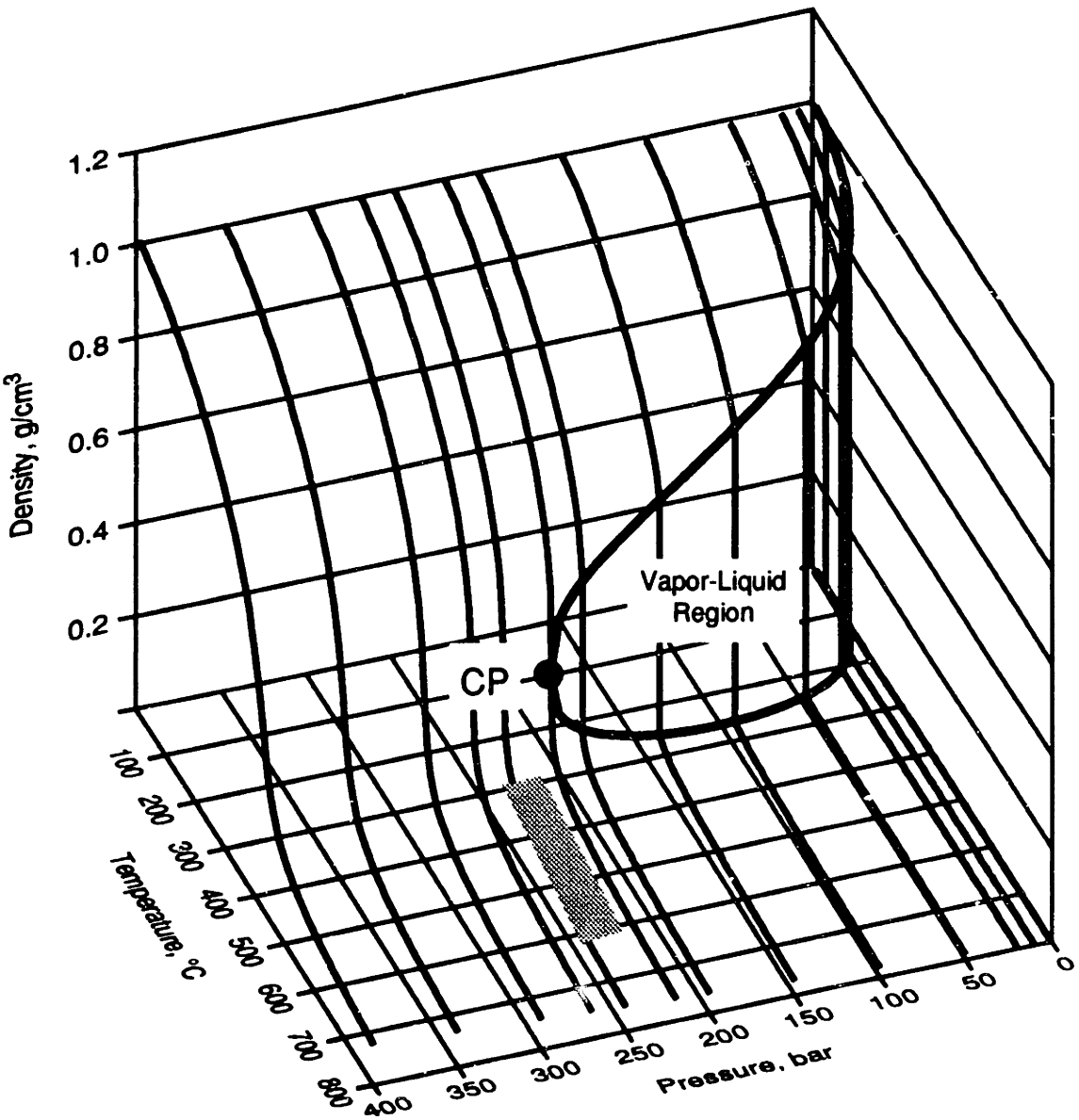

Figure 2.1 **Pressure-Temperature-Density Behavior of Pure Water.** CP denotes the critical point; the vapor-liquid region indicates conditions under which two phases are present. Density calculated from the equation of state of Haar *et al.* (1984). Shaded region indicates typical operating conditions for the SCWO process.

those of room-temperature water.

Figure 2.2 shows that the static dielectric constant of water at 250 bar decreases steadily from a room-temperature value of around 80 to about 5 to 10 in the near-critical region, and finally to 1 to 2 at 450 °C and above (Heger *et al.*, 1980; Uematsu and Franck, 1980; Franck *et al.*, 1990). Figure 2.2 also shows that the ionic dissociation constant initially increases from 10^{-14} $(mol/kg)^2$ at room temperature to 10^{-11} $(mol/kg)^2$ at 250 to 320 °C, then decreases rapidly to 10^{-18} $(mol/kg)^2$ in the near-critical regime, and finally falls to 10^{-23} $(mol/kg)^2$ or less under supercritical conditions (Marshall and Franck, 1981).

Elucidation of the solvation behavior of supercritical water has been provided by experimental and theoretical studies of the structure of water. For example, Bondarenko *et al.* (1974) used infrared absorption to study the vibrational-rotational spectra of supercritical water. With increasing temperature, the spectra of SCW began to resemble that of water vapor, with increasing rotational motion at the expense of intermolecular association; the transition from liquid-like to gas-like behavior occurred essentially along the pseudocritical locus. Gorbaty and Demianets (1983) determined pair-correlation functions for supercritical water using X-ray diffraction; the peak in the functions ascribed to hydrogen bonding decreased steadily with increasing temperature, while the peak corresponding to "non-bonded" neighbors steadily increased. Raman measurements (Kohl *et al.*, 1992) also indicate a decrease in hydrogen bonding in SCW with increasing temperature, even when the density is maintained at liquid-like values (~0.8 to 1.0 g/cm^3); with decreasing pressure and density (< 0.2 g/cm^3), the disappearance of hydrogen bonding is even more pronounced. Finally, Monte Carlo simulations of supercritical water using a realistic intermolecular potential function (Kalinichev, 1991) indicate that the intermolecular bonding energy in water decreases significantly under

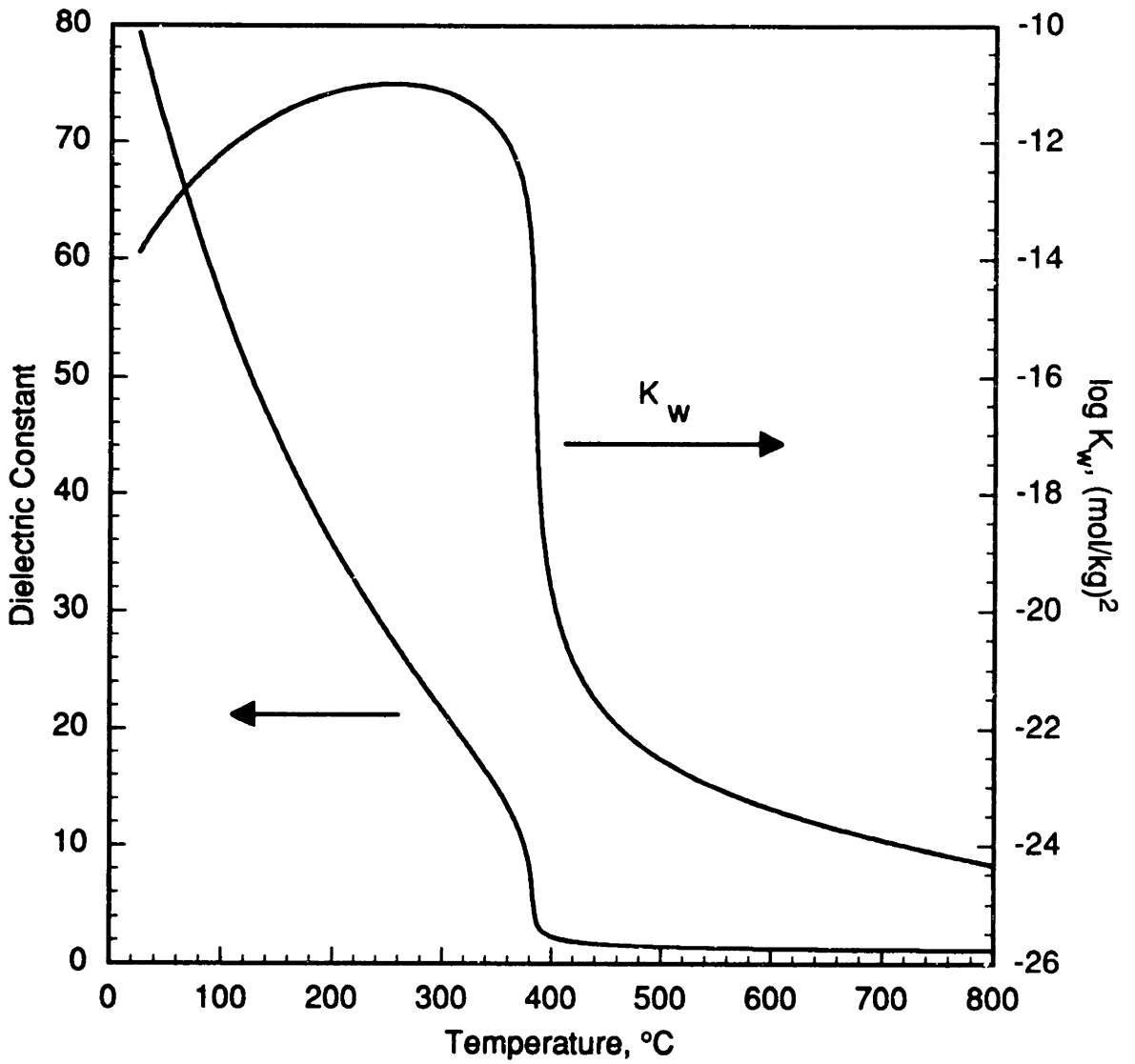

Figure 2.2 **Solvation Properties of Pure Water at 250 bar.** Properties shown are the dielectric constant ε (Uematsu and Franck, 1980) and the ionic dissociation constant K_w (Marshall and Franck, 1981).

supercritical conditions, even at liquid-like densities; similarly, radial distribution functions suggest that hydrogen-bonding interactions are weakened considerably even in high-density SCW. Taken collectively, these studies portray supercritical water as a medium which, despite its comparatively high density, possesses little short- or long-range structure and gas-like intermolecular interactions. The contrast between this behavior and that of liquid water leads naturally to the observed drastic change in solvation properties.

As a result of the low degree of hydrogen bonding, the low dielectric constant, and the low ionic dissociation constant, supercritical water at SCWO conditions acts as a non-polar dense gas, and its solvation properties resemble those of a typical hydrocarbon (Josephson, 1982). For example, organics from *n*-alkanes to aromatics exhibit high solubility in supercritical water (Connolly, 1966). Supercritical water also shows complete miscibility with "permanent" gases such as nitrogen (Japas and Franck, 1985a), oxygen and air (Japas and Franck, 1985b), and carbon dioxide (Tödheide and Franck, 1963), in addition to hydrogen (Seward and Franck, 1981) and small organics like methane (Krader and Franck, 1987). Conversely, the solubility and dissociation of inorganic salts are very low (Marshall, 1976; Martynova, 1976; Armellini and Tester, 1992). At the same time, supercritical water possesses high diffusivity (Tödheide, 1972; Lamb *et al.*, 1981) and low viscosity (Tödheide, 1972; Dudziak and Franck, 1966).

The combination of these solvation and physical properties makes supercritical water an ideal medium for oxidation of organics: oxygen and waste can be contacted in the same homogeneous phase; inorganics precipitate from the mixture, providing a means for their separation; the reaction is uninhibited by mass-transport limitations; and reaction occurs relatively rapidly at temperatures of interest.

2.2 SCWO Process Description

Figure 2.3 shows a conceptual flowsheet for the MODAR supercritical water process. Aqueous waste (1 to 20 wt% organic) is delivered to the reactor by a high-pressure feed pump. For wastes with a high solids content, a preparation step may be required in which the waste undergoes homogenization or other treatment to create a pumpable slurry or suspension of solids (Hong *et al.*, 1987; Killilea *et al.*, 1988; Modell *et al.*, 1992). If the waste is particularly dilute or if its heating value is very low, an auxiliary fuel (or a second, more concentrated waste stream) may be added to the feed to upgrade the heating value (Thomason *et al.*, 1990). Finally, if the waste contains heteroatomic groups (e.g., chlorine, sulfur, or phosphorus) which form acids upon oxidation, it may be desirable to add a caustic (NaOH) or other alkaline solution (e.g., sodium acetate) to the feed to neutralize the acids *in situ* (Swallow *et al.*, 1990; Thomason *et al.*, 1990).

Oxidant is fed separately to the reactor. The oxidant may be atmospheric air, which can easily be compressed to high pressure for injection into the reactor. Since the use of air introduces a large (diluting) volume of nitrogen into the reactor, it may be more desirable to use pure oxygen, which can be pressurized using a cryogenic pump and subsequently vaporized prior to injection into the reactor (Thomason *et al.*, 1990; Modell *et al.*, 1992). Alternatively, hydrogen peroxide can be used, although its cost is high compared to that of air or oxygen (Tester *et al.*, 1991), and on a per-mole basis it provides only half the oxygen of O_2.

Waste and oxidant are mixed at the reactor inlet, typically by injection through a concentric nozzle. Temperatures at the reactor inlet are sufficient to initiate oxidation, whereupon the heat of combustion of the waste raises the mixture temperature to 600 to 650 °C, where destruction proceeds quickly. Once the fluid mixture becomes

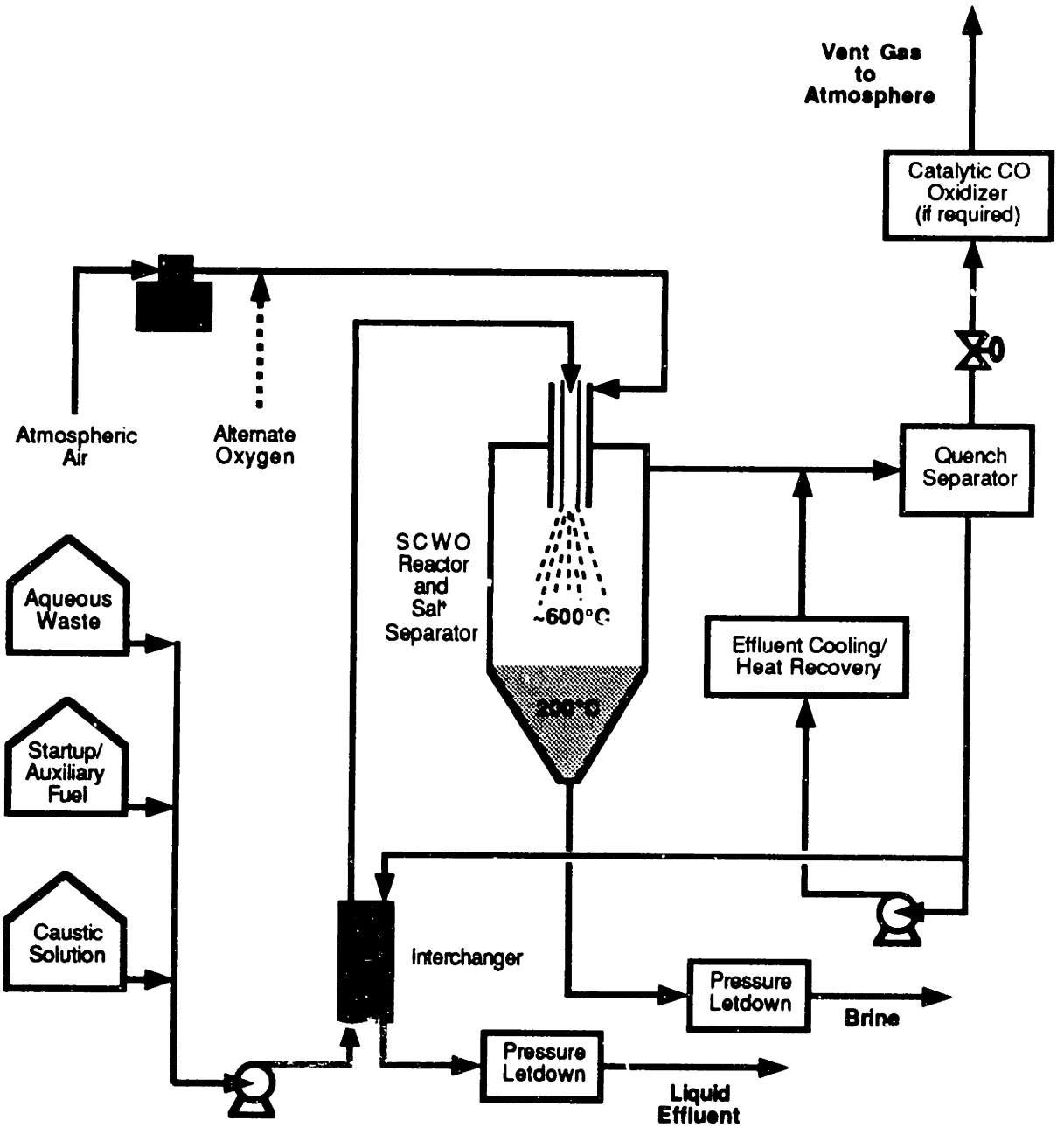

Figure 2.3 MODAR Process Flowsheet. Adapted from Barner *et al.* (1992).

supercritical, dissolved salts (present in the feed or formed during acid neutralization) become virtually insoluble and undergo rapid precipitation (Armellini and Tester, 1990,1991). In the configuration shown in Figure 2.3, precipitated solids are directed toward the bottom of the reactor/salt separator, where a low-temperature (~200 °C) brine solution is maintained; the reactor fluid phase reverses direction and exits the reactor at its top, where a filter may be installed to prevent overhead entrainment of solids (Hong, 1992). The brine solution (and accompanying solids) can be periodically purged from the reactor and replaced by a makeup of pure water (Hong *et al.*, 1989; Barner *et al.*, 1992; Killilea *et al.*, 1992). In an alternative configuration (Modell *et al.*, 1992), solids may be entrained with the reactor effluent and separated downstream, although erosion and plugging of process equipment can then become a concern, owing to the high fluid velocities required to maintain solids entrainment and the "stickiness" of solid salts under supercritical conditions (Killilea *et al.*, 1988; Hong *et al.*, 1989; Tester *et al.*, 1991).

A second-stage reactor may also be installed downstream from the primary reactor/salt separator, to insure complete oxidation of the waste once the solids have been removed (Thomason *et al.*, 1990). Auxiliary fuel may be added at this point to maintain high reactor temperatures (Killilea *et al.*, 1992). Effluent from the reactor/salt separator system is cooled, either during heat recovery or by direct quenching (Thomason *et al.*, 1990; Barner *et al.*, 1992). Any remaining solid salts will also redissolve during cooling. The low-temperature process stream then undergoes pressure letdown, which is typically carried out in multiple stages to optimize gas/liquid separation (Thomason *et al.*, 1990; Modell *et al.*, 1992). Finally, a catalytic CO oxidizer can be used, if desired, to insure complete cleanliness of the ultimate gaseous effluent.

The process flowsheet can be modified to optimize heat recovery. For example, a waste with low heating value (<4200 kJ/kg) can be blended with auxiliary fuel and/or

preheated using regenerative heat exchange (as in Figure 2.3). For a high-heating-value fuel (~4200 kJ/kg), it may be more advantageous to recover heat from the reactor effluent for steam or power generation, and to "preheat" the feed by direct mixing at the reactor inlet with a partial recycle of the hot reactor effluent (Thomason *et al.*, 1990). The use of a feed "interchanger" may also be precluded if the waste is subject to thermal degradation, such as polymerization or char formation (Barner *et al.*, 1992).

Hazardous by-products found in incinerator stack gases can be effectively controlled or almost completely eliminated in the SCWO process. Since the oxidation is carried out in an aqueous environment, the reaction medium is effectively "scrubbed" *in situ*, and acid gases (HCl, SO_2) are either neutralized or leave the reactor dissolved in the aqueous liquid effluent. Most heavy metals are converted to refractory oxides which precipitate from the reactor medium and can be removed as solids; volatile heavy metals (such as mercury) can form potentially volatile salts, but these species are confined to the liquid phase, where they can undergo post-treatment if necessary (Swallow *et al.*, 1990). Temperatures in the SCWO process are too low to favor NO_x formation (Timberlake *et al.*, 1982; Killilea *et al.*, 1992); most waste-bound (reduced) nitrogen is converted to ammonia (NH_3), which is subsequently oxidized to nitrogen (N_2) and nitrous oxide (N_2O). Waste nitrates (NO_3^-) and nitrites (NO_2^-) are reduced to N_2 and N_2O under conditions of low excess oxygen (Killilea *et al.*, 1992). At sufficiently high temperatures, N_2O is reduced to N_2 (Timberlake *et al.*, 1982; Killilea *et al.*, 1992).

Since supercritical water oxidation is carried out in a confined environment, effluent discharges can be carefully controlled. The liquid and brine effluents can be continually monitored to insure adequate waste destruction, and can be stored and recycled to the reactor should a process upset occur (Thomason *et al.*, 1992; Modell *et al.*, 1992). Effluent water polishing (e.g., removal of metal contaminants) can be

accomplished by ion exchange or other post-treatment (Hong *et al.*, 1987). A complete, up-to-date review of supercritical water oxidation technology and process development, with over 160 literature citations, is given by Tester *et al.* (1991).

2.3 Summary of Previous Kinetics Research

While supercritical water oxidation was proposed by Modell and co-workers at MIT 14 years ago, fundamental kinetic data have become available only relatively recently. Most early studies (Modell *et al.*, 1982; Timberlake *et al.*, 1982; Hong *et al.*, 1987; Johnston *et al.*, 1988) were concerned primarily with achieving high destruction efficiencies, rather than elucidating reaction mechanisms and rate dependences under well-defined temperature, pressure, and composition conditions.

2.3.1 Experimental Kinetics Studies

Table 2.1 and Figure 2.4 summarize the kinetics studies (to date) of oxidation in supercritical water which have resulted in oxidation rate expressions. Compounds studied include carbon monoxide (Helling and Tester, 1987), methane (Webley and Tester, 1991), methanol (Webley, 1989; Tester *et al.*, 1992), ammonia (Webley *et al.*, 1990,1991), ethanol (Helling and Tester, 1987), acetic acid (Wightman, 1981; Lee and Gloyna, 1990), phenol (Wightman, 1981; Thornton and Savage, 1990,1992), and acetamide (Lee and Gloyna, 1992). Figure 2.4 presents the kinetic data from the studies in Table 2.1 in the form of a first-order Arrhenius plot (in which the apparent first-order rate constant, k^*, is calculated assuming the reaction is first order in the organic alone), in order to provide a common basis for comparison of the data. Strict first-order behavior has frequently *not* been borne out experimentally; Figure 2.4 should thus not be considered a reflection of true kinetic behavior. Other studies have been conducted which did not yield complete kinetic expressions (temperature dependences and/or

$$d[C]/dt = -A \exp(-E_a/RT)\,[C]^a\,[O_2]^b\,[H_2O]^c$$

Units: kJ, mol, L, s

Compound (C)	log *A*	E_a	*a*	*b*	*c*	Conditions	Source
Carbon Monoxide	6.52	112	1	0	0	246 bar, 400–540 °C	Helling and Tester (1987)
Methane	11.4	179	0.99	0.66	0	246 bar, 560–650 °C	Webley and Tester (1991)
Methanol	26.2	409	1	0	0	246 bar, 450–550 °C	Webley (1989); Tester *et al.* (1992)
Ammonia (tubular reactor)	6.5	157	1	0	0	246 bar, 650–700 °C	Webley *et al.* (1990,1991)
Ammonia (packed reactor)	0.1	30	1	0	0	246 bar, 530–680 °C	Webley *et al.* (1990,1991)
Ethanol	21.8	340	1	0	0	246 bar, 480–540 °C	Helling and Tester (1987)
Acetic Acid	18.0	231	1	1	0	400–445 bar, 338–445 °C	Wightman (1981)
Acetic Acid*	11.5	180	1.01	0.16	0	248–355 bar, 400–530 °C	Lee and Gloyna (1990)
Phenol	5.4	64	1	1	0	296–403 bar, 284–429 °C	Wightman (1981)
Phenol	2.5	52	1	0.5	0.7	190–282 bar, 300–420 °C	Thornton and Savage (1992)
Acetamide*‡	3.6	69	1	0	0	233–339 bar, 400–525 °C	Lee and Gloyna (1992)

*H_2O_2 as oxidant. ‡Overall reaction (hydrolysis + oxidation).

Table 2.1 Global Kinetic Expressions for Oxidation of Model Compounds in Supercritical Water.

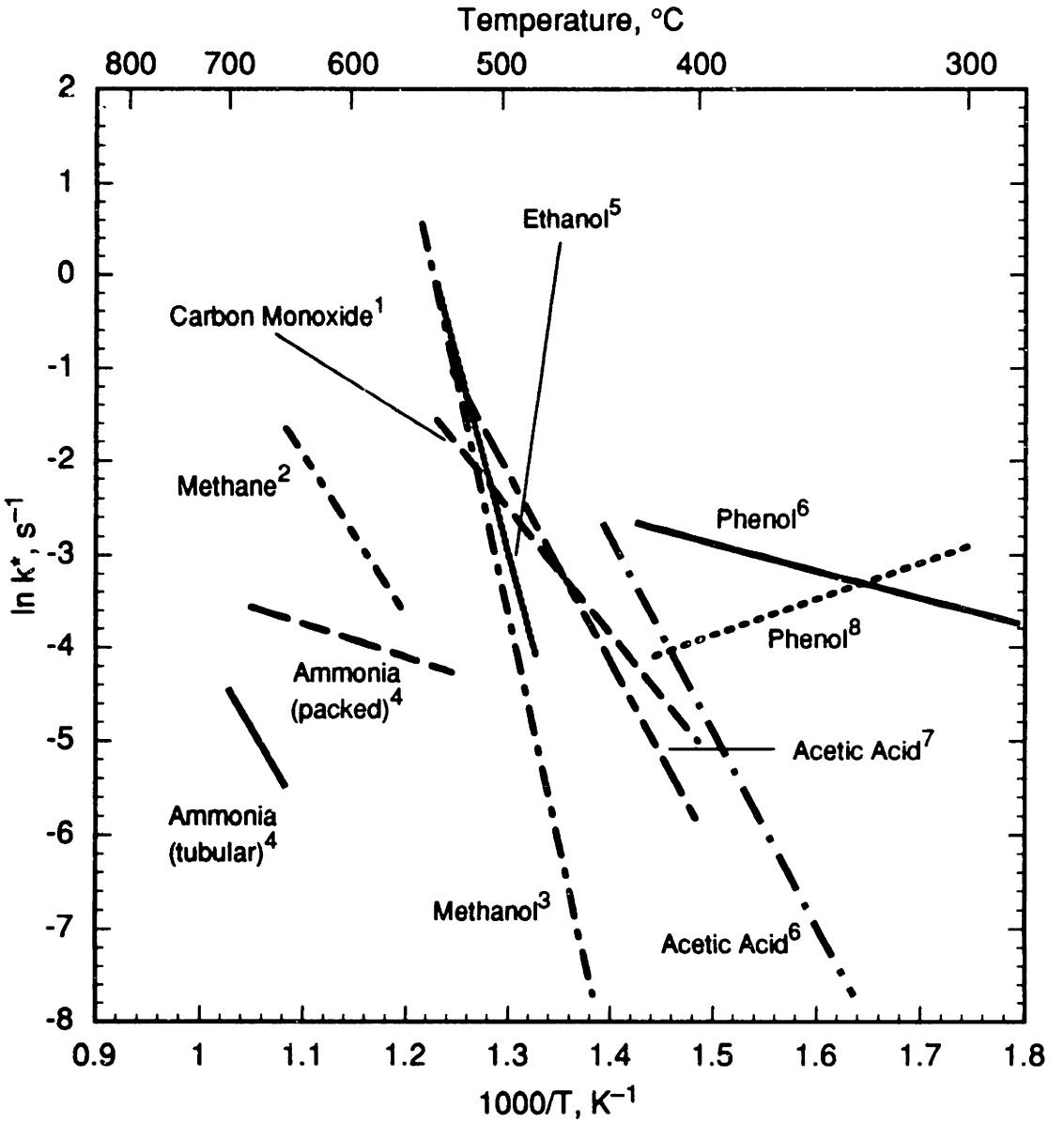

Sources:

[1]Helling and Tester (1987)
[2]Webley and Tester (1991)
[3]Webley (1989), Tester *et al.* (1992)
[4]Webley *et al.* (1990,1991)
[5]Helling and Tester (1988)
[6]Wightman (1981)
[7]Lee and Gloyna (1990)
[8]Thornton and Savage (1990)

Figure 2.4 First-Order Arrhenius Plot for Oxidation of Model Compounds in Supercritical Water.

reaction orders). Yang and Eckert (1988), for example, determined only the approximate concentration dependence of *p*-chlorophenol oxidation in supercritical water at conditions near the critical point of water, and Wightman (1981) performed individual oxidation experiments with compounds other than phenol and acetic acid. Limited data for the oxidation of several other compounds have also been reported by Lee *et al.* (1990) and Shanableh and Gloyna (1991).

Wightman (1981) was the first to report kinetic data for oxidation under supercritical water conditions. In addition to reporting results of single oxidation experiments for a variety of compounds, Wightman determined the temperature dependence of phenol and acetic acid oxidation at high supercritical pressures (296 to 445 bar) and at sub- and supercritical temperatures (284 to 445 °C). In his study, Wightman calculated rate constants using *assumed* reaction orders of unity for both the organic and oxygen. Furthermore, the pressure was not varied in a systematic manner and the reactor was not always isothermal; the kinetic results should thus be regarded as approximate. Oxidation products were not identified. The first-order lines in Figure 2.4 for Wightman's data were calculated from the raw values of conversion and residence time (Wightman, 1981).

Our laboratory has been conducting oxidation kinetics experiments in supercritical water since 1983. Helling (1986) and Helling and Tester (1987) first reported results on the oxidation of carbon monoxide in supercritical water at 246 bar and between 400 and 540 °C. They found that oxidation of CO to CO_2 occurred via two separate global pathways, direct oxidation (2.1) and the water-gas shift reaction (2.2):

$$CO + \tfrac{1}{2} O_2 \rightarrow CO_2 \qquad (2.1)$$

$$CO + H_2O \rightarrow CO_2 + H_2 \qquad (2.2)$$

Regression of Helling's data yielded the following global rate expression for carbon monoxide oxidation in supercritical water:

$$-\frac{d[CO]}{dt} = 10^{7.25\pm0.53} \exp(-120\pm7.7/RT)\,[CO]^{1.014\pm0.09}\,[O_2]^{0.03\pm0.04} \qquad (2.3)$$

where the concentrations in square brackets [ ] are in mol/L, the activation energy is in kJ/mol, the rate is in mol/L-s, and the stated errors are at the 95% confidence level. The kinetics demonstrated essentially no dependence on oxygen, hydrogen, or carbon dioxide concentration, and the assumption of kinetics first order in carbon monoxide alone was thus a good one. The Arrhenius parameter values listed in Table 2.1 were obtained from regression of the experimental data with the CO and O_2 reaction orders set identically to one and zero, respectively.

Helling attempted to separate the two oxidative pathways, and observed that the relative extent of the water-gas shift reaction, as indicated by the ratio of hydrogen to carbon dioxide in the reactor effluent, tended to decrease with increasing temperature, from about 75% at 400 °C to about 20% at 540 °C (Helling, 1986; Helling and Tester, 1987). This observation implies a lower activation energy for the water-gas shift reaction. On the basis of data for which no oxygen was fed to the reactor, Helling regressed the following rate expression for the water-gas shift portion of the overall reaction:

$$-\frac{d[CO]}{dt} = 10^{1.60\pm3.57} \exp(-62.9\pm8.6/RT)\,[CO]^{0.568\pm0.107} \qquad (2.4)$$

and for the direct oxidation reaction, on the basis of the global rate data:

$$-\frac{d[CO]}{dt} = 10^{17.4\pm1.64} \exp(-238\pm24/RT)\,[CO]^{1.87\pm0.02} \qquad (2.5)$$

Helling also attempted to determine the kinetics of oxidation of several other model compounds and mixtures, including hydrogen, ammonia, and ethanol (Helling and Tester, 1988). However, experimental limitations did not allow extensive exploration of these systems. Helling's analytical method was not sufficiently sensitive to allow accurate determination of hydrogen concentrations, and furthermore water was present in such excess that the small amount of water production could not be distinguished from the influent water. The detection of hydrogen in the products of carbon monoxide oxidation indicates that hydrogen oxidation proceeds relatively slowly in a supercritical water environment, and it may represent a rate-limiting step in the oxidation of wastes.

In those early studies in our laboratory we also examined the oxidation of ammonia:

$$2\,NH_3 + \tfrac{3}{2}\,O_2 \rightarrow N_2 + 3\,H_2O \qquad (2.6)$$

which proceeds slowly, as ammonia is quite refractory. Helling was able to achieve conversions of only about 5% at residence times of 6 to 13 s and 540 °C , the highest attainable temperature in his apparatus. Consequently, he was unable to determine kinetics for the reaction. Limited data for the oxidation of ethanol between 480 °C and 540 °C yielded the first-order rate expression given in Table 2.1 (Helling and Tester, 1988):

$$-\frac{d[C_2H_5OH]}{dt} = 10^{21.82\pm2.7} \exp(-340\pm41/RT)\,[C_2H_5OH] \qquad (2.7)$$

where the reaction orders were assumed rather than derived from data. Helling also detected carbon monoxide and acetaldehyde among the products of ethanol oxidation. The rate of ethanol oxidation was virtually unaffected by the addition of carbon monoxide or ammonia to the feed in two experiments.

Webley (1989) continued the work of Helling (1986) by examining the oxidation of methane, methanol, and ammonia in supercritical water. Helling's apparatus was modified to allow operation at temperatures up to 700 °C, and the analytical method for hydrogen detection was improved. Methane oxidation experiments were conducted over a 560 to 650 °C temperature range at 246 bar and residence times of 5.5 to 14.8 seconds. The regressed rate expression for the entire range of experimental conditions was (Webley and Tester, 1991):

$$-\frac{d[CH_4]}{dt} = 10^{11.4\pm1.1} \exp(-179.1\pm18.0/RT)\,[CH_4]^{0.99\pm0.08}\,[O_2]^{0.66\pm0.14} \qquad (2.8)$$

The reaction can thus be considered first order in methane, but the order for oxygen is clearly not zero. Webley observed carbon monoxide in the reactor effluent, accounting for 30% of the product carbon at low conversions and dropping to 5% at high conversions. Small fractions (<1%) of hydrogen were present in the product, consistent with the earlier results of Helling. In addition, no methanol or formaldehyde was found among the products of methane oxidation. Negligible conversion at 650 °C was observed for methane pyrolysis. Note that earlier reported data and rate expressions for methane oxidation (Webley and Tester, 1988; Rofer and Streit, 1988,1989) were obtained in this laboratory under poorly defined reaction conditions; those results are no longer valid and have been superseded by the newer rate expression (Equation 2.8 and Table 2.1) and data (Webley and Tester, 1991).

Methanol oxidation experiments (Webley, 1989) were carried out at 246 bar from 450 to 550 °C and at residence times of 6.9 to 10.3 seconds. Regression over the entire range of experimental conditions revealed that the reaction was, to 95% statistical confidence, first order in methanol and zero order in oxygen (Tester *et al.*, 1992):

$$-\frac{d[CH_3OH]}{dt} = 10^{26.2\pm5.8} \exp(-408.8\pm85.4/RT)\,[CH_3OH] \qquad (2.9)$$

No methane or formaldehyde was detected among the products of methanol oxidation, and negligible pyrolysis of methanol (to CO and H_2) was found at 550 °C and a 6.6-second residence time (Webley, 1989; Tester *et al.*, 1992). As is the case for methane, earlier results for methanol oxidation obtained in this laboratory (Webley and Tester, 1989; Rofer and Streit, 1989) have been superseded by the newer, more accurate data and rate expression (Webley, 1989; Tester *et al.*, 1992).

Ammonia was by far the most refractory compound studied. Oxidation did not occur at residence times of 10.8 seconds and at temperatures below 600 °C, and only 11% conversion was observed at 700 °C (Webley *et al.*, 1990,1991). Molecular nitrogen was the only major product of oxidation, with no N_2O, NO or NO_2 detected in the product gas. Small amounts of hydrogen were also found in the effluent, the result of a low degree of ammonia pyrolysis:

$$2\,NH_3 \rightarrow N_2 + 3\,H_2 \qquad (2.10)$$

The ammonia oxidation data could not be fit satisfactorily to a power-law rate expression of the form $k[NH_3]^a[O_2]^b$, and a catalytic mechanism for the reaction was postulated based on a model of Golodets (1983), in which ammonia reacts with oxygen adsorbed to

a catalyst surface. The model predicts a rate expression of the form

$$\frac{[O_2]}{\text{rate}} = a + b\frac{[O_2]}{[NH_3]} \tag{2.11}$$

The data fit the catalytic model significantly better than the homogeneous, power-law rate form cited in Table 2.1, for which the reaction orders were assumed.

The catalytic nature of ammonia oxidation prompted investigation of the extent of catalysis in that reaction and of the possibility that other oxidation reactions might be similarly catalyzed. For this purpose a high-surface-area, packed-bed reactor was constructed to replace the standard tubular reactor (see Section 4.1 for details). Single rate experiments in the packed reactor for methane and methanol oxidation showed a negligible influence of the increased surface area, although further experiments would be necessary to confirm the absence of catalysis or other surface effects.

The ammonia oxidation reaction, on the other hand, showed a significant effect of increased reactor surface. In addition, small quantities of N_2O were detected in the reactor effluent. If ammonia oxidation were entirely surface-catalyzed, the rate increase should be proportional to the surface area increase (a factor of 20). The absence of such a rate increase indicates the mechanism is only partially surface-catalyzed. Also noteworthy is the lower apparent activation energy in the packed reactor, which is consistent with catalysis theory. The extent of surface catalysis could be determined by further changing the reactor surface-to-volume ratio in a systematic manner. The power-law rate expression for ammonia oxidation in the packed reactor:

$$-\frac{d[NH_3]}{dt} = 10^{0.1\pm2.8}\exp(-30.\pm49./RT) \tag{2.12}$$

was derived with assumed reaction orders; insufficient data were available to allow a fit to the catalytic model.

Webley *et al.* (1990,1991) also conducted experiments in which they co-oxidized ammonia and methanol at 246 bar. For temperatures (480 to 530 °C), concentrations, and residence times (7 to 10 s) similar to those used in the individual oxidation experiments in the tubular reactor, the rates of co-oxidation of methanol and ammonia were not significantly different from the rates observed individually. For co-oxidation experiments in the packed reactor under similar conditions of temperature, residence time and composition, methanol oxidation rates were unchanged while ammonia oxidation rates were significantly lower than the individual rates. Thus, for the range of conditions investigated, co-oxidation of ammonia with another organic did not seem to offer a distinct improvement in the rate of ammonia oxidation, contrary to observations in practical SCWO systems (Killilea *et al.*, 1992).

Additional kinetic data from other laboratories have appeared only recently. Lee and Gloyna (1990) studied acetic acid oxidation from 400 to 530 °C and 248 to 355 bar, with hydrogen peroxide as the oxidant. The resulting best-fit rate expression was

$$-\frac{d[CH_3COOH]}{dt} = 10^{11.54\pm11.47} \exp(179.5\pm15.2/RT)\,[CH_3COOH]^{1.01\pm0.09}\,[H_2O_2]^{0.16\pm0.08} \qquad (2.13)$$

The reported error in the preexponential factor is unrealistic relative to the other parameter errors and is likely incorrect. Kinetic behavior in this study is very closely approximated by a simple first-order rate expression. Figure 2.4 shows the activation energy from this study to be in good agreement with that obtained by Wightman (1981), although the absolute values of the rates are in disagreement. Lee and Gloyna (1990)

attribute this discrepancy to errors introduced by Wightman's experimental procedures. Products of acetic acid oxidation were not identified, but formic acid was not found in the effluent. An additional study of acetic acid oxidation (Wilmanns and Gloyna, 1990) was conducted in a pilot-scale SCWO unit under inadequately defined, nonisothermal conditions; the kinetic expression from that study is thus probably not meaningful and has been omitted from Table 2.1 and Figure 2.4.

Thornton and Savage (1990,1992) reported the kinetics of phenol oxidation in supercritical water, albeit under conditions (300 to 420 °C, 190 to 282 bar) somewhat removed from the typical SCWO operating regime. A significant fraction of their data was obtained with subcritical temperatures or pressures, and many of their supercritical data were obtained at conditions below the pseudocritical point where densities are liquid-like. The high fluid densities (~0.5 g/cm^3) at the high pressures and low temperatures used in this study imply a high ionic dissociation constant for water, ~10^{-13} (mol/kg)^2 (Tanger and Pitzer, 1989). Thus it is questionable whether the same reaction mechanisms prevail under these conditions as under the lower-density (<0.1 g/cm^3), non-ionic SCWO conditions. The rate expression from the Thornton and Savage (1992) study is given in Table 2.1; estimates of parameter errors were not reported. A relatively strong dependence on water concentration was observed, owing to the significant range of sub- and pseudocritical densities examined. The apparent first-order line in Figure 2.4 was obtained from the conversion and residence time data of Thornton and Savage (1990); the apparent negative activation energy results from the failure to account for the oxygen and water dependences. There is approximate agreement (in terms of observed rates) between this study and that of Wightman (1981) for phenol, in which similar (high-pressure, low-temperature) conditions were employed. Thornton and Savage (1991) have also studied formation of certain products of phenol oxidation (including dioxins and

furans), although these studies were again conducted at sub- and pseudocritical conditions and at very long residence times (minutes to hours). The direct relevance of this study to typical SCWO conditions is not clear, since the higher temperatures employed in the SCWO process do not favor formation of these species.

Finally, Lee and Gloyna (1992) have studied acetamide oxidation in supercritical water from 400 to 525 °C and 233 to 339 bar. They found that acetamide undergoes rapid hydrolysis in supercritical water to ammonia and acetic acid, such that hydrolysis (rather than oxidation) was the dominant pathway for acetamide destruction. The proposed rate expression for reaction of acetamide, both by hydrolysis and by oxidation, was

$$-\frac{d[CH_3CONH_2]}{dt} = 10^{3.6\pm2.5} \exp(-68.8\pm3.8/RT)\,[CH_3CONH_2] \qquad (2.14)$$

A first-order model was used since regression yielded essentially zero (0.05±0.06) for the order with respect to oxidant (hydrogen peroxide), although the regressed order with respect to acetamide was slightly different from one (1.15±0.06). Products of acetamide destruction were not identified, except for ammonia and acetic acid. Results of this study have been omitted from Figure 2.4 for clarity.

Figure 2.4, while simplifying the true kinetic behavior, provides a global framework within which to evaluate the relative reactivities of the compounds studied. For example, ammonia and methane are clearly highly refractory. The oxidation of carbon monoxide, with its relatively low activation energy, becomes a rate-limiting step in the oxidation of methanol, ethanol, and acetic acid for temperatures above about 500 °C; the presence (or absence) of carbon monoxide in the SCWO effluent thus becomes a good indicator of reactor performance (Modell, 1989; Hong, 1992). The results for

phenol oxidation, although obtained at non-SCWO conditions, indicate a very low activation energy and suggest the possibility that phenol persists (as a destruction-limiting species) to high temperatures.

The rate expressions in Table 2.1 indicate the global, phenomenological approach which has been taken to date in studies of supercritical water oxidation kinetics. The prevalence of this approach is evident in a recent compilation of global rate expressions for both supercritical water oxidation and wet-air oxidation (Li *et al.*, 1991). While global rate expressions can provide a good correlation of experimental data and can be useful for design purposes, they provide little information about the fundamental mechanisms of the oxidation reactions. The observation of fractional reaction orders with respect to oxygen (for methane and phenol in Table 2.1) suggests complex reaction pathways and networks which require more detailed models.

Supercritical water oxidation carried out at temperatures above 450 °C and pressures above 230 bar bears a strong resemblance to (low-temperature, high-pressure) combustion, and recent studies suggest that the well-developed experimental and theoretical techniques of combustion science can be used to improve our fundamental understanding of the SCWO process. For example, Franck and co-workers have reported the occurrence of inverse diffusion methane-oxygen flames in supercritical water (Schilling and Franck, 1988; Franck, 1991), and these flame phenomena are currently under further study at Sandia National Laboratories (Steeper *et al.*, 1992).

2.3.2 Theoretical Modeling Studies

The logical extension of simple, one-step global rate expressions for the oxidation of model compounds is the development of multi-step global reaction mechanisms. The use of these mechanisms affords an additional level of modeling detail, in that concentrations

(yields) of oxidation intermediates can be predicted. Models of this type have been used successfully in combustion modeling (see, e.g., Westbrook and Dryer, 1981). Recently, Webley and Tester (1991) reported the results of a multi-step mechanism for methane oxidation, in which methane was oxidized to carbon monoxide, which subsequently reacted either by direct oxidation or the water-gas shift; oxidation of hydrogen produced by the water-gas shift was also included. Predictions of CH_4 destruction and CO_2 formation were good, but the multi-step model failed to predict the observed CO and H_2 concentrations with accuracy. Li *et al.* (1991) have also reported the successful use of two-step mechanisms for the oxidation of more complex wastes, including sludges; however, no attempt was made to model experimental data for formation of intermediates. While these multi-step global mechanisms allow the prediction of additional parameters, they are ultimately limited by their global nature and their lack of fundamental mechanistic information. The desire for detailed mechanistic insight has led to the development of elementary reaction models for oxidation in supercritical water.

The use of elementary reaction models to describe the fundamental chemistry of supercritical water oxidation represents another example of the application of combustion science to SCWO. Helling and Tester (1987) first attempted to model the oxidation of carbon monoxide using an elementary reaction model, since the prevailing conditions in their experiments tended to favor a free-radical reaction mechanism. They used a 21-reaction, 10-species model based on a model for gas-phase ethylene oxidation (Westbrook *et al.*, 1982), with little modification. The rate constants for the elementary reactions were not changed, but the equilibrium constants were modified to account for both the non-ideal compressibility factor of supercritical water and the effect of pressure on species entropy. This model was not able to reproduce the experimental results satisfactorily, and in most cases predicted conversions in error by a factor of 2.

Furthermore, the model failed to predict hydrogen formation, with experimental hydrogen yields typically almost two orders of magnitude higher than predicted. Finally, the model demonstrated an apparent overall activation energy much higher than that observed experimentally.

Following earlier modeling attempts initiated by Helling and Tester, Webley and Tester (1989,1991) modeled oxidation in supercritical water using free-radical elementary reaction mechanisms. However, they applied more extensive corrections to existing elementary rate data. In particular, unimolecular reaction rate theory was used to adjust the unimolecular rate constants for the high-pressure supercritical water environment. Reactions requiring the collision of a generic second or third body were assumed to have water as the collisional partner, and the rate was adjusted to account for the high collisional efficiency of water. Bimolecular reaction rate constants were largely unchanged, since they should be unaffected by pressure; however, the elementary, free-radical reaction

$$CO + OH \rightarrow CO_2 + H \qquad (2.15)$$

is known to be pressure-dependent and its rate was therefore adjusted. Equilibrium constants were corrected for the non-ideal compressibility factor of supercritical water.

Webley's (1989) elementary reaction model for methanol oxidation agreed quite well with the experimental data, matching observed conversions to within a few percent. An apparent first-order Arrhenius plot for the model was quite similar to the experimental results, although the activation energy of the model was slightly higher. The model predicted formation of formaldehyde, which was not observed experimentally; in addition, the model incorrectly predicted high selectivity toward carbon monoxide and

very little hydrogen formation. Webley and Tester's (1991) elementary reaction model for methane oxidation did not perform as well. The conversion of methane was consistently underpredicted and the formation of methanol was wrongly predicted, although the model was in fairly good agreement with the relative amounts of CO and CO_2 produced. The model again failed to predict hydrogen formation, which in the case of methane oxidation was accurate.

Rofer and Streit (1988,1989) also attempted to model the experimental results of Helling (1986) and Webley (1989) using elementary reactions, and corrected the rate constants for supercritical water pressures. In a somewhat arbitrary fashion, they further modified activation energies and the elementary reactions themselves in an effort to account for the high water density. Even with these modifications, the Rofer-Streit model for carbon monoxide oxidation overpredicted the apparent activation energy and underpredicted hydrogen formation. Curiously, their other models successfully reproduced our experimental data for methane oxidation, but were considerably less successful at matching our methanol data. Webley's (1989) models were able to match the methanol data but not those for methane.

More recent elementary reaction modeling for methanol oxidation has been conducted by Butler *et al.* (1991) and Schmitt *et al.* (1991). In those studies, a reaction mechanism was assembled from several different gas-phase oxidation mechanisms, and reaction rate constants were corrected for the high-pressure environment using unimolecular reaction rate theory. The Peng-Robinson equation of state was used to incorporate the non-ideal density of supercritical water. Model predictions were used to deduce the fundamental mechanisms of methanol oxidation; however, the model was compared only to methanol destruction data and not to rigorous kinetic data, and the

model thus cannot be considered to have been properly validated. Conclusions concerning mechanisms must therefore be regarded as preliminary.

The logical extension of kinetic oxidation studies in supercritical water, beyond the phenomenological, global approach, appears to be the development of elementary reaction models. Unfortunately, the uncertain ability to model accurately the fundamental mechanisms of supercritical water oxidation has thus far posed a significant challenge to efforts to attain a deeper understanding of the process.

Chapter 3

Objectives

The primary objective of this work was to obtain kinetic data for oxidation of simple compounds in supercritical water under well-defined conditions, and to use those data as the basis for development of accurate models of the fundamental kinetic processes and mechanisms. Specific objectives are listed below:

1. Obtain kinetic data for hydrogen oxidation in supercritical water. Hydrogen is the simplest oxidizable compound; its oxidation in the gas phase has been thoroughly characterized and occurs through a well-defined mechanism. Measurement of hydrogen oxidation kinetics in supercritical water will provide an important basis for modeling and can yield insights into the effect of the supercritical water environment on the most basic oxidation mechanism.

2. Reexamine carbon monoxide oxidation in supercritical water. Carbon monoxide is the simplest carbon-containing species, and its oxidation, like that of hydrogen, has been well characterized in the gas phase. The earlier study in this laboratory of carbon monoxide oxidation in supercritical water (Helling and Tester, 1987) examined only a limited range of oxygen concentrations and lacked high analytical sensitivity for hydrogen. The importance of reaction during feed preheating also remained uncertain. Carbon monoxide is important as an oxidation intermediate, since it is usually the rate-

limiting step in achieving complete oxidation. Accurate characterization of the oxidation kinetics of carbon monoxide, as a simple, refractory molecule, is crucial, and validation or improvement of the earlier data taken in our laboratory was necessary.

3. Identify the effects of pressure (density) on oxidation kinetics. Hong (1992) has enumerated the potential advantages of operating the SCWO process at lower, even subcritical, pressures (semicritical water oxidation). These advantages include reduced construction costs, decreased corrosion, and more favorable phase behavior of salts. The effects of decreasing pressure on oxidation rates are not well known. By changing the operating pressure (water density) in a controlled, systematic manner, the kinetic effects of varying operating pressure, as well as potentially the role of water in the oxidation mechanism, can be identified.

4. Evaluate the influence of the reactor surface. Earlier studies in this laboratory identified a heterogeneous catalytic effect of the reactor surface for ammonia oxidation (Webley *et al.*, 1990,1991). Gas-phase studies indicate that surfaces can inhibit reactions by destroying free-radical species, particularly for carbon monoxide and hydrogen oxidation. Preliminary studies in our laboratory have not revealed pronounced heterogeneous influences in the oxidation of compounds other than ammonia, but this conclusion must be verified to insure that any measured kinetic data are an accurate reflection of homogeneous oxidation mechanisms.

5. Develop and validate an elementary reaction model for hydrogen and carbon monoxide oxidation in supercritical water. Several elementary reaction models for SCWO have been compiled for more complex molecules such as methane or methanol.

With new data for hydrogen and carbon monoxide oxidation, it becomes possible to develop improved models for those two simple compounds, whose oxidation mechanisms are necessarily a subset of the mechanisms for larger molecules. Development and validation of a model for hydrogen and carbon monoxide oxidation will thus provide a sound basis for the subsequent development of more complex models.

6. Investigate glucose oxidation in supercritical water. Growing interest in the use of SCWO for treatment of sludges and human waste (Takahashi *et al.*, 1989; Shanableh and Gloyna, 1991; Modell *et al.*, 1992) has demonstrated the need for kinetic data for this class of waste. While glucose is not strictly speaking a simple compound, it does represent a significant simplification of the much more complex sludge matrix and is a good model compound for cellulosic wastes. Identification of destruction-limiting intermediates is also important for treatment optimization.

Chapter 4

Experimental Techniques

4.1 Apparatus

Experimental data were obtained in an isothermal, isobaric, plug-flow reactor apparatus, which is shown in Figure 4.1. Feed solutions are prepared in two, three-liter agitated saturators. The saturators are filled with approximately 2500 mL of high-purity water, and oxygen (Airco) and hydrogen (Airco) or carbon monoxide (Matheson CP grade) are supplied from compressed gas cylinders, with pressures adjusted to achieve the desired concentrations in the saturators. Gases are used as received without further purification. Agitation of the saturator fluid is provided by pumped recirculation using two single-head, positive-displacement pumps (LDC Analytical/Milton Roy minipumps). Overnight agitation of the saturator solutions is usually sufficient to achieve equilibrium; with the recirculation pumps at maximum flow rate (~7.5 mL/min), the contents of the saturator are completely overturned at least twice during saturation. Owing to solubility constraints, this system is able to produce only low feed concentrations of carbon monoxide, hydrogen and oxygen, on the order of 10^{-6} to 10^{-7} mol/cm^3 at the reactor inlet, compared to about 4×10^{-3} mol/cm^3 for water at 246 bar (mole fraction of water greater than 0.999). Consequently, kinetics cannot be determined over orders of magnitude in concentration; on the other hand, much higher concentrations could result in significant reaction exotherms and corresponding difficulties in maintaining reactor isothermality.

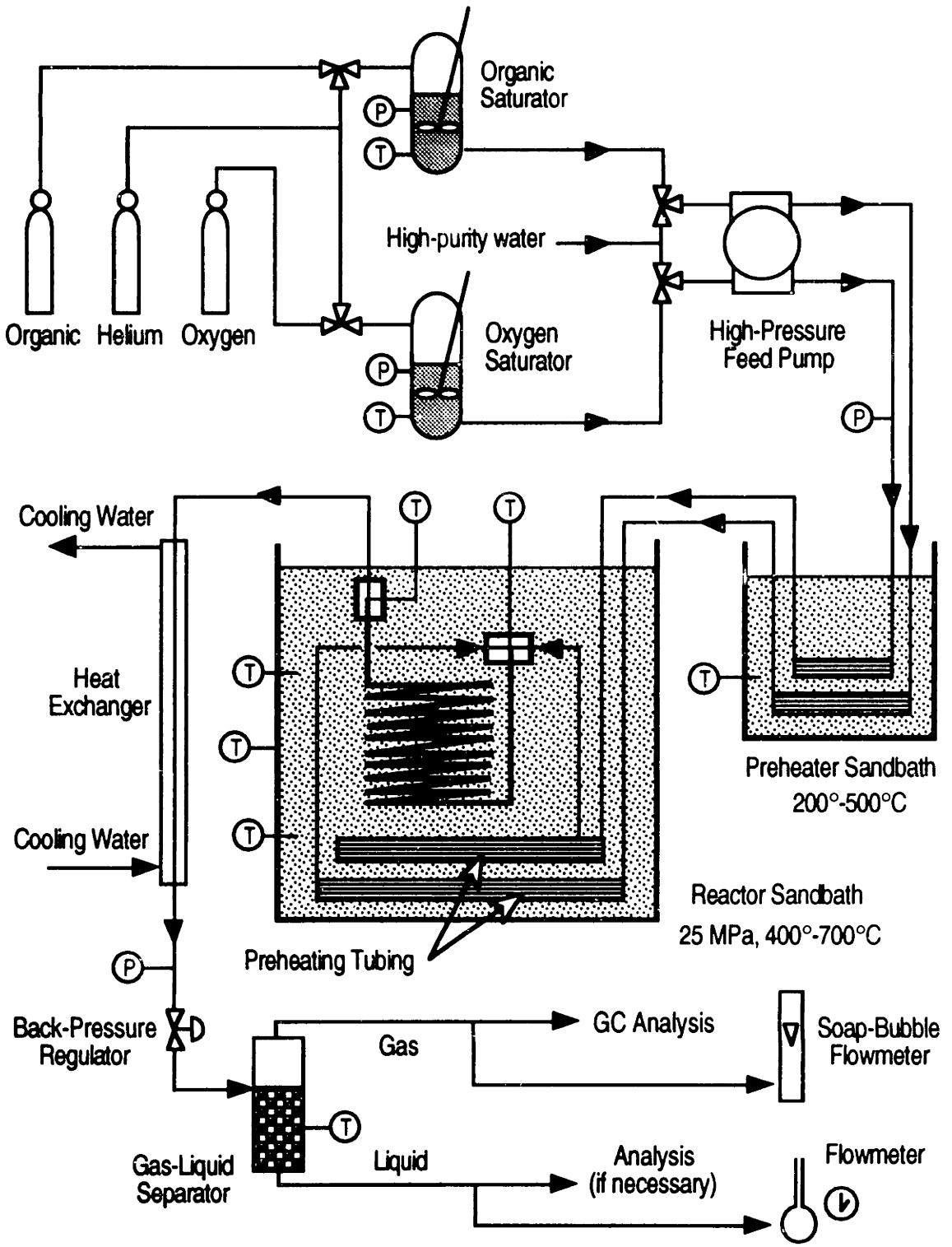

Figure 4.1 Isothermal, Plug-Flow Reactor Apparatus.

In the case of glucose, solutions of desired concentration are loaded into the organic saturator and the saturator headspace is filled with low-pressure helium; recirculation is unnecessary. Maximum glucose concentrations are constrained by the corresponding attainable oxygen concentration and not by glucose solubility.

Feed solutions are delivered to the reactor at operating pressure by a high-pressure, variable-speed, duplex feed pump (LDC Analytical/Milton Roy minipump). System pressure is controlled by a back-pressure regulator (Tescom) at the exit of the reactor product heat exchanger. The pressure is measured both by a pressure transducer (Dynisco) just upstream of the back-pressure regulator and by a pressure gauge just downstream of the feed pump. During an experiment, these two pressure measurements are the same within the natural variability of the system pressure and the readability of the pressure gauge (±3–4 bar), confirming that pressure drop through the system is negligible relative to the total operating pressures of 118 to 263 bar. During heatup of the reactor, pure water is flowed through the system, and the feeds are introduced when the system has reached operating temperature. The feeds pass through 1.5 m (5 ft.) of 1.59-mm (1/16-in.) 316 stainless steel tubing in a preheating fluidized sand bath (Techne), which is normally operated at about 200 °C; this sand bath was used in some experiments to provide additional feed preheating and to help achieve greater reactor isothermality. The feeds then enter the main fluidized sand bath (Techne), and pass through an additional 3.0 m (heated length 2.8 m) of 1.59-mm (1/16-in.) Hastelloy C276 tubing, where they are heated to reaction/sand bath temperature. At this point the feeds are mixed in a Hastelloy C276 high-pressure cross fitting (High Pressure Equipment) at the top of the reactor. The mixing of the feeds in the cross initiates the oxidation reaction. The fourth port of the cross contains a 1.59-mm (1/16-in.), Inconel-sheathed, type K thermocouple (Omega Engineering) which measures the fluid temperature at the point of

mixing. A second internal thermocouple (Inconel-sheathed, type K) is located at the exit of the reactor. Additional external thermocouples (type K) are located at the top and bottom of the reactor. Typically all thermocouple measurements are within a few degrees Celsius of each other, although the sand bath consistently exhibits a natural thermal gradient such that the bath temperature is a few degrees higher at the top than at the bottom. When temperatures differ, the average of the mixing and exit fluid temperatures is taken as the reactor temperature.

The tubular reactor is a coiled 4.71-m length of 1.71-mm (0.067-in.) I.D. × 6.35-mm (1/4-in.) O.D. Inconel 625 tubing, with an internal tubing volume of 10.82 cm^3 and a total internal volume (including fittings at the entrance and exit) of 11.11 cm^3. Reynolds numbers in the reactor are maintained above the critical value for laminar flow (2100), such that flow conditions in the reactor are always in the turbulent or transition regime. When the reacting mixture exits the reactor it immediately enters a countercurrent shell-and-tube heat exchanger where its temperature is rapidly quenched to ambient. The effluent then passes through the back-pressure regulator and is reduced to ambient pressure, at which point the products separate into two phases. A gas-liquid separator splits the streams, and it is assumed that the two streams are in equilibrium when they separate. The flow rate of gas is measured with a soap-bubble flowmeter and the liquid flow rate is measured on the basis of the time to fill a volumetric flask.

A packed-bed reactor has also been constructed to permit investigation of the influence of reactor surface area on observed kinetics. The packed reactor consists of a 61.67-cm length of 9.12-mm (0.359-in.) I.D. × 1.43-cm (9/16-in.) O.D. Inconel 625 tubing, bent into a U-shape to be accommodated by the sand bath, and with an internal volume of 40.27 cm^3. The tubing is packed with –60+100 mesh (150–250 μm) Inconel 625 beads, held in place by 10-μm Hastelloy fritted disks at the ends of the tube. The

void fraction of the packing was estimated on a density basis to be 0.39, such that the free volume in the packed tube is 15.71 cm^3; including fittings at the reactor entrance and exit, the total packed reactor volume is 16.00 cm^3. Total internal surface area of the packed reactor, based on an average particle diameter of 200 μm, is 7545 cm^2, for a surface area-to-volume ratio of 480 cm^{-1}. By comparison, the internal surface area for the open tubular reactor is 253 cm^2, for a surface area-to-volume ratio of 23.4 cm^{-1}. The packed reactor thus increases the reactor surface area by a factor of 20.5 on a volumetric basis. The packed reactor incorporates 1.43-cm (9/16-in.) × 6.35-mm (1/4-in.) Inconel 625 reducing fittings at both ends, such that the tubular and packed reactors are completely interchangeable without any further modification to the system.

The present apparatus is essentially identical to that used by Webley (1989), although several modifications have been made to improve system operability and reaction condition characterization. Specific modifications include:

1. A second internal thermocouple has been installed in the tee fitting at the reactor exit, to provide additional direct measurement of the reactor fluid temperature.
2. The one-liter saturators used by Helling (1986) and Webley (1989) have been replaced by two three-liter, 304 stainless steel sample cylinders (Hoke 8HD3000, rated to 1800 psig) to provide larger feed reservoirs and concomitant longer experimental run times.
3. The original pressure transducer indicator has been replaced by a newer model (Dynisco μPR690, 0–10,000 psig). The transducer itself remains the same.
4. A pressure gauge (Omega Engineering, 0–7,500 psig) has been installed on the oxygen feed line downstream from the feed pump. The combination of this gauge and the pressure transducer downstream from the reactor provides a direct measurement of the pressure drop through the system.

5. Analytical resources have been improved. One of the Perkin-Elmer Sigma series gas chromatographs has been replaced by a new Hewlett Packard unit, and a high-performance liquid chromatography apparatus has been added for liquid-phase analyses (details are given in Section 4.2).

4.2 Analytical Procedures

The effluent gas stream was sampled manually and analyzed using two gas chromatographs (GCs). Primary gas sample analysis was accomplished with a Hewlett Packard 5890 Series II GC, equipped with thermal conductivity and flame ionization detectors and interfaced to a Hewlett Packard Vectra computer for data acquisition and analysis. The use of helium as the carrier gas allowed accurate determination of O_2, N_2, CO, CO_2, and light hydrocarbons using the thermal conductivity detector, but detection of H_2 was poor except at high concentrations. Carrier gas flow was 20 mL/min; oven temperature was programmed to hold at 60 °C for the first 7 minutes, then rise at 40 °C/min. to 100 °C, where it was held for the remainder of the analysis; total time for the method was 14 minutes. The gas analysis scheme, developed by Helling (1986) and Webley (1989), employed two colums, a 12-ft. × 1/8-in. stainless steel column packed with 80/100 mesh Porapak T (Column I) and an 8-ft. × 1/8-in. stainless steel column packed with 60/80 mesh molecular sieve 5A (Column II), connected through an air-actuated switching valve. In the initial valve position, samples pass through Column I and then Column II; immediately after the elution of N_2 and O_2, the valve (and order of columns) is switched, such that CO and CH_4 pass through Columns I and II and Column I a second time, while CO_2 and the C_2s only pass through a single column (Column I). The order of elution with this method is H_2, O_2, N_2, CO_2, C_2H_4, C_2H_6, CH_4, C_2H_2, CO. The method thus provides relatively rapid sample analysis without sacrificing peak

resolution, although at very high CO_2 concentrations a small C_2H_4 peak may be lost. The column-switching scheme is also capable of accommodating on-line gas sample analysis, should that be desirable in future experiments.

Secondary gas sample analysis was provided by a Perkin Elmer Sigma 1B GC, also equipped with thermal conductivity and flame ionization detectors. This GC uses nitrogen as the carrier gas and was used exclusively for hydrogen and helium detection by thermal conductivity, for which it is very sensitive. [Trace amounts of helium were occasionally found in the effluent gas, either because the pure startup water and glucose feed were pressurized with helium, or because the saturator liquid was pressurized with helium for loading into the saturators.] While this GC was also equipped with the same valve-switching configuration as the Hewlett Packard GC, for H_2/He analysis the valve was left in its initial position. Nitrogen flow rate was 40 mL/min, and the oven temperature was constant at 60 °C.

Both GCs were calibrated volumetrically using samples of authentic gases. Dual 100- or 200-μL samples of the gaseous reactor effluent were analyzed simultaneously to determine the volumes of the individual gases in the samples, and the instantaneous gas composition (mole fractions) was determined from the volume fractions (volume of an individual gas divided by the sum of the volumes of all gases). The total sample volume calculated from the sum of the constituent gas volumes typically agreed with the injected sample volume to within about 5%; some discrepancy is to be expected due to calibration drift or variability in peak integration, as well as inaccuracies in injection volumes from sample to sample. Final gas compositions for an experiment were typically the average of four to six (and as many as twelve) sets of dual sample analyses.

Glucose concentrations were determined by a standard enzymatic technique (Sigma Chemical Co.) in which glucose is converted by hexokinase to glucose-6-

phosphate, which is then consumed by glucose-6-phosphate dehydrogenase with concomitant conversion of NAD to NADH. The resulting NADH concentration is equivalent to the original glucose concentration, and the NADH concentration was determined by its absorption at 340 nm using a UV/visible spectrophotometer (Shimadzu UV160U). This method is specific to glucose and is not readily subject to interference by other compounds. The method was sufficiently sensitive to allow determination of glucose concentrations in the liquid effluent as low as 5×10^{-5} mol/L.

Analysis of the liquid effluent from experiments with glucose was accomplished by isocratic high-performance liquid chromatography, using a Rainin HPXL solvent delivery system with an Interaction ORH-801 analysis column (chosen for its ability to resolve organic acids) and an Interaction Ionguard guard column. Detection was by UV absorption at 210 or 290 nm using a Rainin Dynamax UV-1 UV/visible detector. Column temperature was maintained by a Timberline column heater. The HPLC system was interfaced to a Macintosh IIsi for data acquistion and analysis. The mobile phase was 0.002 M H_2SO_4 delivered at 0.5 mL/min, with a column temperature of 65 °C; sample injection volumes were 100 μL. Peak identification was accomplished by comparison of sample peak retention times with those of standard solutions of pure compounds. Once peaks were identified, calibrations were performed with standard solutions of varying concentrations. Calibration by peak height or peak area gave equally good results; sample peaks were subsequently quantified by peak height since peak overlap frequently occurred and peak areas could not be determined accurately in all cases. Section 9.3 contains a more detailed discussion of the specific application of the HPLC method to the analysis of the effluent from glucose experiments.

4.3 Data Reduction

Sample calculations of data reduction have been given by Helling (1986) and Webley (1989) and are not reproduced in detail here. Briefly, since the gas-liquid separator is assumed to produce equilibrium between the two (liquid and gas) effluent streams, the total molar flow rate of gaseous species in the effluent must take into account the gas dissolved in the liquid. The liquid-phase composition is determined from the measured gas-phase composition by Henry's law:

$$y_i \phi_i P = H_i(T, P) x_i \tag{4.1}$$

where the gas-phase mole fraction of species i, y_i, is measured, ϕ_i, the gas-phase fugacity coefficient, is set to unity since the pressure, P, is approximately 1 bar; $H_i(T,P)$ is the Henry's law coefficient, which is a function of both temperature and pressure, and x_i is the liquid-phase mole fraction (the desired quantity). Henry's law constants, as a function of temperature for temperatures near ambient, were obtained from the literature for oxygen (Benson *et al.*, 1979), carbon monoxide (Rettich *et al.*, 1982), hydrogen, helium, nitrogen, carbon dioxide (with a correction for the dissociation of carbonic acid), ethylene, and acetylene (Wilhelm *et al.*, 1977), and methane and ethane (Rettich *et al.*, 1981). The weak pressure dependence of $H_i(T,P)$ was unimportant since the literature values were for atmospheric pressures. The liquid-phase contribution to the total effluent molar flow rate of gases was usually rather small, although for carbon dioxide the contribution was significant because of the high solubility of CO_2.

Conversions and reaction rates in our system are normally calculated on the basis of product formation (effluent concentrations) and reaction stoichiometry. For example, in the case of carbon monoxide, the conversion is given by $[CO_2]/([CO]+[CO_2])$, where

the concentrations are those in the reactor effluent and $[CO]+[CO_2]$ is equivalent to the inlet CO concentration. The inlet O_2 concentration can be calculated from the exit concentrations in a similar manner. Measurements of the reactor effluent can thus characterize completely the experimental conditions.

Inlet molar flow rates of hydrogen, carbon monoxide, and oxygen were also calculated from the liquid-phase mole fraction in the saturator, given by Henry's law, and the flow rates of the two feed streams, given by the feed pump calibration (Webley, 1989). The non-ideality of the high-pressure (8 to 110 bar) gas phase in the saturator was taken into account by inclusion of the gas-phase fugacity coefficient ϕ_i in the Henry's law calculation (Equation 4.1). Fugacity coefficients for oxygen and carbon monoxide were calculated from the Peng-Robinson equation of state with parameters from Reid *et al.* (1987). Fugacity coefficients for pure hydrogen were calculated from the expression

$$\ln \phi_i = \int_0^P \frac{Z-1}{P} dP \tag{4.2}$$

with the compressibility factor Z regressed from experimental data as a function of pressure P (Perry *et al.*, 1984). Furthermore, pressure dependences of the Henry's law constants for the saturator gases were calculated using a Poynting-type correction

$$H_i(T,P) = H_i(T,P_o)\exp[\overline{V}_{i,\infty}(P-P_o)/RT] \tag{4.3}$$

with literature values for the infinite-dilution partial molar volumes ($\overline{V}_{i,\infty}$) for oxygen (Brelvi and O'Connell, 1972), carbon monoxide (Rettich *et al.*, 1982), and hydrogen (Moore *et al.*, 1982), and with P_o, the reference pressure, taken as atmospheric. Tests of this method with the reactor at ambient temperature provided complete recovery (within

2%) of the calculated gas feed, and proved the viability of the technique.

The comparison of reactor inlet concentrations calculated from saturator conditions and those calculated from effluent concentrations provides a test of the system's performance. For carbon monoxide oxidation, quoted mass-balance closures (Tables 12.7, 12.8, and 12.10 through 12.12) indicate the extent to which the two methods for determining inlet concentrations agree; a mass-balance closure of 100% for CO or O_2 indicates perfect agreement of the two methods. For a given carbon monoxide experiment, the quoted initial concentrations are those calculated from the exit concentrations, since those quantities are essentially measured.

In the case of hydrogen oxidation, the product (water) is indistinguishable from the large amount of water already present in the reactor, and thus it is not possible to determine inlet concentrations or conversions directly from exit concentrations. For these experiments we determined conversions based on the difference between the inlet hydrogen concentration, as calculated from saturator conditions and Henry's law, and the exit hydrogen concentration, as measured experimentally. Quoted inlet concentrations for hydrogen experiments are those calculated from saturator conditions. Since the inlet and outlet concentrations must be related by reaction stoichiometry, it is possible to check the consistency of the two sets of concentrations and thus calculate an overall mass-balance closure. These mass-balance closures are reported in Tables 12.3 through 12.6. For a given hydrogen or carbon monoxide experiment, potential sources of incomplete mass-balance closures include analytical error, drift in the relative feed flow rates, and incomplete saturation of the feeds.

Quoted experimental errors are estimates based on uncertainties in measured values. All measured quantities are reported as approximate, normal, 95% confidence intervals (intervals of 2 standard deviations), and measurement uncertainties are

propagated to uncertainties in derived quantities using standard propagation-of-error formulas. Rigorously, Student's *t* distribution should be used to obtain confidence intervals, rather than the normal distribution. In many cases, however, a sufficient number of experimental measurements was made that the difference between the two distributions was negligible.

4.4 Evaluation of Reactor Performance

The reactor system in these studies is assumed to perform as an isothermal, plug-flow reactor, and experimental data are analyzed using these assumptions. Reliability of experimental results thus depends on the ability of the reactor to satisfy the assumptions. Reactor isothermality is largely assured by the temperature control provided by the fluidized sand bath, although under conditions of high flow rates the lengths of preheating tubing may not be sufficient to heat the reactor feeds completely to sand bath (reactor) temperature prior to their entering the reactor. In those cases, there will be an axial thermal gradient in the reactor, but such gradients can be neglected as long as they are not too large. Reaction exotherms are unimportant because the reactor conditions are so dilute; for the highest hydrogen and carbon monoxide concentrations used, the maximum adiabatic temperature rise is only 2 to 3 °C, which would be manifested as a negligibly small axial temperature gradient. The criteria for attainment of plug-flow conditions have been the subject of intense study, and are discussed in the context of the present system in Section 4.4.1. [Note that the existence in the reactor of axial temperature gradients, of any magnitude, does not affect ideal plug-flow behavior (Denbigh, 1965), and the requirement of (axial) reactor isothermality is entirely independent of the plug-flow requirement.] Another important issue, not always considered, is the mixing of the feeds at the reactor entrance; mixing must occur on a

time scale that is very short compared to the residence time in the reactor. This requirement is addressed in Section 4.4.2.

4.4.1 Plug-Flow Behavior

The steady-state continuity equation for species i for flow through a tube, in cylindrical coordinates and neglecting the radial velocity convective contribution and all angular (azimuthal) dependences, is

$$-\frac{d}{dz}(v(r,z)C_i)+\mathcal{D}_i\left(\frac{\partial^2 C_i}{\partial r^2}+\frac{1}{r}\frac{\partial C_i}{\partial r}+\frac{\partial^2 C_i}{\partial z^2}\right)-R_i=0 \tag{4.4}$$

where C_i is the concentration of species i, $\mathcal{D}_i$ is the diffusivity of species i in the reactor fluid, $v(r,z)$ is the axial velocity of the fluid in the tube, and r and z are the radial and axial coordinates, respectively. The term R_i accounts for formation or loss of species i by reaction. For systems in which there are multiple species of interest, there is an equation of the form of Equation 4.4 for each species. Similarly, for multiple reactions (e.g., an elementary reaction mechanism), there will be additional reaction terms (for each reaction in which the species is a participant) in the species continuity equation. Under plug-flow conditions ($v \neq v(r)$, $\partial v/\partial r = 0$), Equation 4.4 reduces to

$$-v\frac{dC_i}{dz}-C_i\frac{dv}{dz}-R_i=0 \tag{4.5}$$

The second convective term accounts for axial variation in the fluid velocity, and can be discarded for an isothermal reactor with negligible volume change on reaction. The first convective term in Equation 4.5 is essentially the temporal variation of C_i since $z/v = t$. Equation 4.5 is thus equivalent to the purely kinetic equation

$$\frac{dC_i}{dt} = -R_i \tag{4.6}$$

Numerous studies have tried to identify the conditions that insure the accuracy of the replacement of Equation 4.4 with Equation 4.6. Cutler *et al.* (1988) have recently summarized the "plug-flow criteria" resulting from those studies, and Webley (1989) evaluated the performance of our reactor system, relative to those criteria, in his studies. The primary requirements for achieving plug flow are 1) that radial (transverse) diffusion occurs rapidly enough to insure that the reactor fluid is well mixed radially; and 2) that axial (longitudinal) diffusion is slow relative to convection. The first requirement is equivalent to the criterion (Cleland and Wilhelm, 1956)

$$\frac{L\mathcal{D}}{vR^2} > 1 \tag{4.7}$$

where L and R are the reactor length and radius, respectively. This dimensionless group may be thought of as the ratio of time scales for radial diffusion to axial convection; when diffusion is much faster than convection, radial concentration profiles are smoothed rapidly and all reactive species experience the same reactor residence time. The opposite extreme occurs for laminar flow and slow diffusion, such that the radial velocity and concentration profiles are both parabolic. Under these "parabolic" conditions, there is a distribution of residence times and reactor performance (as indicated by the conversion of reactant) is deteriorated relative to the plug-flow condition; however, even under the most extreme case of parabolic profiles, observed reactor performance differs only by about 30% from the flat-profile, plug-flow case (Cleland and Wilhelm, 1956; Denbigh, 1965; Ramayya and Antal, 1989). Furthermore, under turbulent conditions the radial velocity

profile is not parabolic and is usually much flatter, with a correspondingly narrower distribution of residence times (Bosworth, 1949). Finally, there is some doubt as to the physical ability to ever attain purely parabolic velocity *and* concentration profiles under gas-like conditions, since diffusion is typically rapid enough to eliminate radial concentration gradients. Velocities high enough to eliminate diffusional flattening of the profiles will almost always lie in the turbulent regime, where profiles will be flattened anyway (Cleland and Wilhelm, 1956; Mulcahy and Pethard, 1963).

Radial concentration gradients may also be induced or enhanced by reaction occurring on time scales faster than those for radial diffusion, such that diffusion cannot eliminate gradients prior to reaction taking place. The criterion for insuring rapid radial diffusion relative to reaction is (Walker, 1961; Poirier and Carr, 1971)

$$\frac{\mathcal{D}}{k^* R^2} > 1 \tag{4.8}$$

where k^* is the (first-order) rate constant for the reaction. The dimensionless quantity in Equation 4.8 is the traditional Damköhler number, *Da*.

The value for $\mathcal{D}$ in Equations 4.7 and 4.8 must be chosen carefully since it depends on the flow regime. The frequent approximation is made that the total diffusivity $\mathcal{D}$ is given by the sum of the molecular diffusivity $\mathcal{D}_m$ and the turbulent diffusivity $\mathcal{D}_t$ (Sherwood *et al.*, 1975). Many studies of plug-flow criteria were undertaken to determine the conditions under which plug-flow reactor behavior could be achieved with laminar flow conditions ($Re < 2100$). In laminar flow, molecular diffusion is dominant and $\mathcal{D}$ is approximated by the molecular diffusivity $\mathcal{D}_m$. For higher, turbulent Reynolds numbers, as are found in the tubular reactor in the present study, turbulent (eddy) diffusion dominates and $\mathcal{D}$ should be the turbulent diffusivity, $\mathcal{D}_t$

(Kramers and Westerterp, 1963). Experimental values for neither $\mathcal{D}_m$ nor $\mathcal{D}_t$ are readily available for supercritical water systems. $\mathcal{D}_m$ can be approximated by the self-diffusivity of pure supercritical water; at 246 bar and 400 to 700 °C, $\mathcal{D}_m$ is then 0.002 to 0.007 cm^2/s (Lamb *et al.*, 1981). $\mathcal{D}_t$ is a property of the flow conditions (not the fluid itself), and is given by the product of the Lagrangian turbulence scale l_1 and the root-mean-square velocity fluctuation u' (Lewis and von Elbe, 1987):

$$\mathcal{D}_t = l_1 u' \tag{4.9}$$

The Lagrangian turbulence scale l_1 is roughly one half the Eulerian turbulence scale l_2, with l_2 at the centerline approximately given by $0.17R$, where R is the tubing radius; the turbulence intensity, u'/v, is about 3% at the centerline (Lewis and von Elbe, 1987). With these approximations, $\mathcal{D}_t$ in the tubular reactor is estimated to range from 0.008 to 0.03 cm^2/s, up to an order of magnitude higher than $\mathcal{D}_m$. Near the wall, in the laminar sublayer, turbulence is negligible and molecular diffusion is dominant. A single, characteristic value for $\mathcal{D}$ is thus difficult to choose; $\mathcal{D}_m$ gives a low estimate for the average rate of diffusion in the free stream while $\mathcal{D}_t$ overestimates diffusion near the wall.

For tubular reactor residence times of 3.4 to 13 s, velocities in the reactor are 40 to 140 cm/s. The radius of the reactor is 0.0855 cm and the length is 471 cm, for a length-to-radius ratio (L/R) of 5500. The conservative case for Equations 4.7 and 4.8 is $\mathcal{D} = \mathcal{D}_m$; since flow in the reactor is turbulent, turbulent diffusion will contribute to $\mathcal{D}$ and Equations 4.7 and 4.8 will be more easily satisfied for the higher values of $\mathcal{D}_t$. Even with the conservative assumption, Equation 4.7 is satisfied for all our experimental conditions; the dimensionless quantity ranges approximately from 2.5 to 6.7 over the range of temperatures and flow rates used in the present study. Similarly, Equation 4.8 is

satisfied (assuming $\mathcal{D} = \mathcal{D}_m$), with $Da > \sim 10$, for all but the highest values of k^* ($\sim 1\ s^{-1}$), for which $Da \sim 1$; however, such high k^* values are only rarely observed experimentally. Furthermore, the coiled configuration of the tube introduces a secondary flow (with radial components) in the tube, thereby enhancing radial mixing and reducing radial gradients (Kramers and Westerterp, 1963), and improving reactor performance relative to the criteria of Equations 4.7 and 4.8. Radial concentration and velocity gradients in the tubular reactor are therefore negligible.

The second criterion for plug flow, negligible axial diffusion, is expressed by the equivalent conditions (Azatyan, 1972; Norton, 1990)

$$\frac{-\mathcal{D}\dfrac{dC_i}{dz}}{C_i v} = -\frac{1}{C_i}\frac{dC_i}{dt}\frac{\mathcal{D}}{v^2} = \frac{k^*\mathcal{D}}{v^2} < 1 \tag{4.10}$$

The first and second expressions represent a characteristic-velocity analysis of axial diffusion and convection (Norton, 1990): the numerator in the first expression is the axial diffusive flux of species i, and the denominator is the convective flux. The second expression is a restatement of the first, with distance (z) converted to time (t). The third expression, due to Azatyan (1972), results from a dimensional scaling analysis of Equation 4.4, but can also be derived from the second expression using the definition of k^*. In evaluating Equation 4.10, one should realize that the worst case is given by the maximum (i.e., turbulent) value for $\mathcal{D}$. Furthermore, the macroscopic rate constant k^* does not provide the most rigorous test of Equation 4.10. Rather, the maximum rate of axial diffusion relative to convection occurs for low-concentration species undergoing high axial concentration gradients. This condition is most severe for free radicals at the reactor entrance, where their concentrations are very small but increase rapidly up to their

steady-state values. The sharpest gradients predicted by elementary reaction models occurred during hydrogen oxidation at 600 °C, with maximum normalized gradients (defined as $(1/C_i)dC_i/dt$) of ~100 s^{-1}. Axial diffusion thus could only be important if $\mathcal{D}$ were greater than 10 cm^2/s, which is physically unrealistic. Axial diffusion is therefore unimportant in the tubular reactor.

In the packed reactor, $\mathcal{D}$ is related to neither molecular nor turbulent diffusion, but rather to the mechanical dispersion caused by the packing. This dispersion is typically greater in the axial direction than in the radial direction by about a factor of five. Radial dispersivity is approximately $0.1vD_p$, with D_p the particle diameter of the packing (0.02 cm), while axial dispersivity is about $0.5vD_p$ (Denbigh, 1965; Kramers and Westerterp, 1963). Dispersivity values thus range from 0.08 to 1.4 cm^2/s, and the packed reactor is radially well-mixed. Furthermore, the presence of packing tends to macroscopically mix the fluid such that non-uniform velocity profiles tend to be flattened out (Denbigh, 1965; Sherwood *et al.*, 1975), as long as the reactor diameter is much larger than the particle diameter (as it is here). Finally, axial dispersion in the packed reactor can be neglected since the reactor length is much greater than the particle diameter (Denbigh, 1965); similarly, the use of the high axial dispersivities in Equation 4.10 does not alter the conclusion that axial convection is dominant.

For the conditions employed in the present study, then, both the tubular reactor and the packed reactor operate within the plug-flow regime and data obtained in the reactors may be treated using the plug-flow assumption.

4.4.2 Feed Mixing Lengths

Another important consideration in evaluating reactor performance is the time scale on which the two reactor feed streams are mixed. Meaningful data rely on the radial mixing

occurring in a time much shorter than the characteristic reaction time or the reactor residence time.

Mixing of the two reactor feeds in the current apparatus is accomplished in the high-pressure cross fitting at the reactor entrance, which acts as an opposed-flow tee mixer. The mixing geometry is shown in Figure 4.2. Because of the nature of the high-pressure fitting, the feed streams undergo several expansions and contractions both before and after the point of mixing. Of particular note are the relative diameters of the feed tubing (1.08 mm) and the reactor (1.71 mm). The original design of the mixing tee was intended primarily to introduce the feeds into the reactor, and not necessarily to achieve high-efficiency mixing of the two streams.

Experimental studies of opposed-flow tee mixers under turbulent or transitional flow conditions (Henzler, 1978) indicate that the most efficient mixing occurs for a configuration in which the two feed streams enter at high velocities via small-diameter tubes, with the mixed stream traveling at lower velocity in a larger-diameter tube. The configuration in Figure 4.2 is thus not optimal due to the constraints of the high-pressure fitting. Although the feeds initially occupy smaller-diameter tubing, immediately prior to mixing they are expanded into channels the same size as the mixed-stream channel. The feeds thus travel at velocities lower than the ultimate mixed-stream velocity. Experimental results for liquid mixing, however, indicate that even with this sub-optimal configuration the feeds are well-mixed about 20 to 40 tubing diameters downstream from the point of mixing (Uhl and Gray, 1986).

In general, mixing studies suggest that gases mix somewhat more readily than liquids, even with similar mixing configurations and Reynolds numbers; mixing lengths for gases are less than about 5 mixed-stream diameters, while liquid mixing lengths are typically 10 to 40 diameters (Henzler, 1978; Uhl and Gray, 1986). The susceptibility to

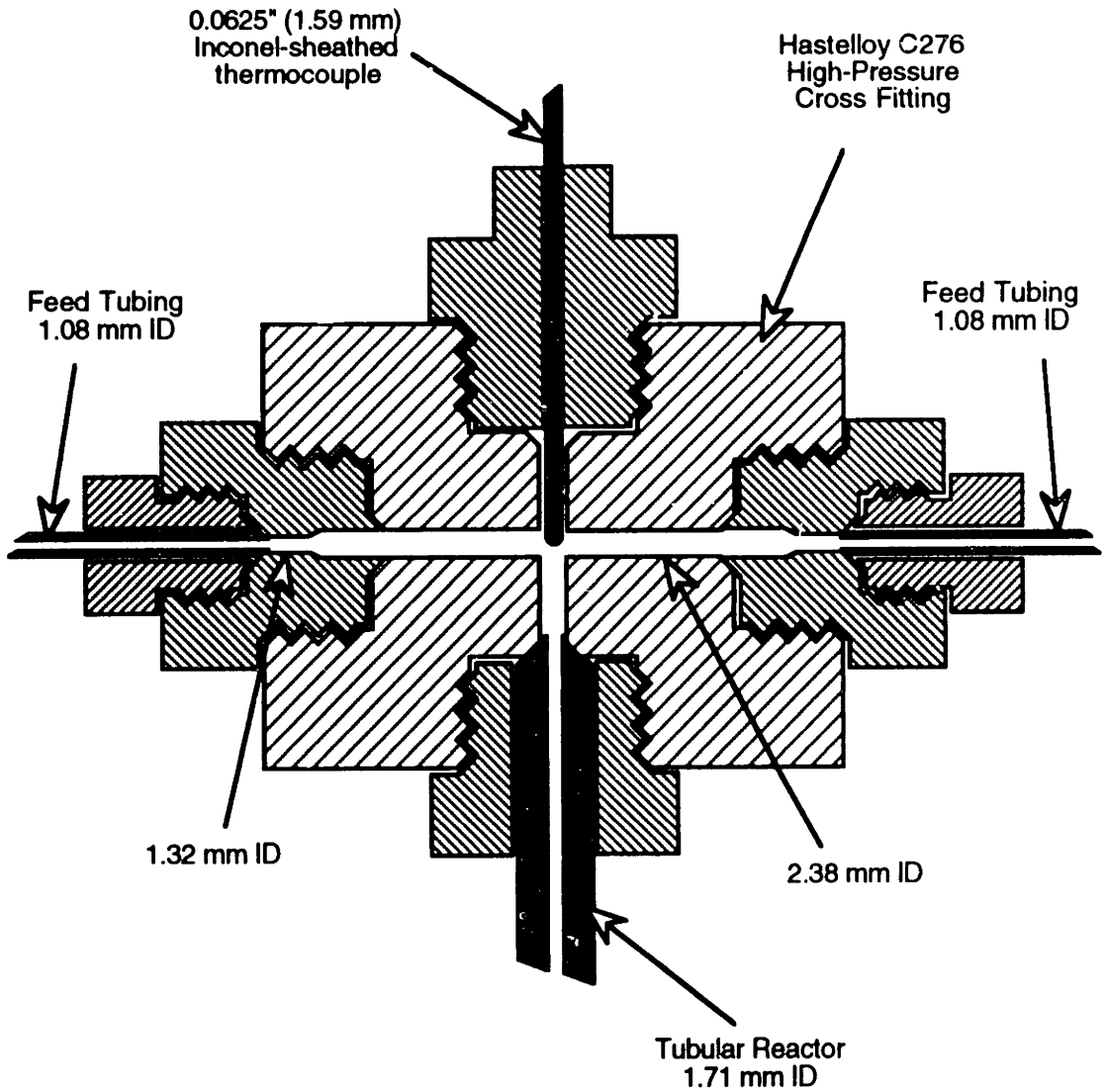

Figure 4.2 **Schematic of Mixing Tee at Reactor Entrance.** Drawn approximately to scale. Details of high-pressure fittings not shown.

mixing of supercritical water probably lies somewhere between that of a gas and that of a liquid. For a very conservative estimate, we take the mixing length to be 50 tubing diameters. Since the tubular reactor is over 2700 diameters long, this mixing length corresponds to less than 2% of the reactor length. In other words, the feeds are completely mixed in less than 2% (conservatively) of the reactor residence time. The peculiarities of the flow geometry within the mixer are also likely to induce additional turbulence and mixing, such that the true mixing length is significantly less than 2% of the tubular reactor length. In the packed reactor, radial dispersion and mixing occurs very rapidly (Section 4.4.1) and the feed mixing time is again likely to be very short relative to the reactor residence time. Hence the opposed-flow tee mixer, while not of optimal design, is sufficient to achieve rapid mixing of the reactor feeds and mixing effects may be neglected.

Chapter 5

Experimental Studies of Hydrogen Oxidation in Supercritical Water

In earlier experiments in our laboratory, Helling and Tester (1987) and Holgate *et al.* (1992) reported that carbon monoxide is oxidized to carbon dioxide by two global reaction pathways: direct oxidation (5.1) and the water-gas shift (5.2).

$$CO + \tfrac{1}{2} O_2 \rightarrow CO_2 \tag{5.1}$$

$$CO + H_2O \rightarrow CO_2 + H_2 \tag{5.2}$$

Below 430 °C, the water-gas shift accounted for a large fraction of the total oxidation of CO, as indicated by the significant amounts of hydrogen produced (see Sections 7.1 through 7.4 for further details). Since carbon monoxide is a primary intermediate in the oxidation of other organics, hydrogen may, under certain conditions, be a major product of supercritical water oxidation, and may undergo further oxidation via the following global pathway:

$$H_2 + \tfrac{1}{2} O_2 \rightarrow H_2O \tag{5.3}$$

The kinetics of hydrogen oxidation are thus important for accurate modeling of the overall oxidation process. Similarly, hydrogen has been cited as a possible auxiliary fuel,

to be used when the heating value of the waste is insufficient to achieve the desired temperatures within the reactor (Hong *et al.*, 1987); quantitative characterization of hydrogen oxidation kinetics will be needed for design purposes in such applications. Furthermore, since the mechanism for hydrogen oxidation is a subset of all other oxidation mechanisms, an understanding of the kinetics and mechanisms of hydrogen oxidation will yield insight into those more complex mechanisms. The mechanisms of gas-phase hydrogen oxidation have been well-characterized, and data for hydrogen oxidation in supercritical water will afford the opportunity to extend the well-developed hydrogen models to a high-pressure environment.

Helling (1986) attempted to measure the kinetics of hydrogen oxidation in supercritical water in our laboratory, but his analytical method for hydrogen was not sensitive enough to allow accurate determination of hydrogen conversions. He developed a rate expression for hydrogen oxidation, but its reliability is doubtful as it was based on only four data points. We have since improved our analytical sensitivity for hydrogen and have obtained a new and more reliable rate expression for hydrogen oxidation in supercritical water.

Fifty-five oxidation experiments were conducted at temperatures between 495 and 600 °C at a constant pressure of 246 bar. The pressure was chosen for consistency with earlier kinetic experiments (Helling and Tester, 1987,1988; Webley and Tester, 1991; Webley *et al.*, 1990,1991), and is representative of pressures found in the supercritical water oxidation process. Liquid flow rates at ambient conditions ranged from 5.4 to 15.2 mL/min, corresponding to reactor residence times of 3.4 to 11.0 seconds at supercritical conditions. Hydrogen concentrations at the reactor inlet varied between 0.385×10^{-6} and 3.69×10^{-6} mol/cm^3, while inlet oxygen concentrations varied between 0.409×10^{-6} and 4.55×10^{-6} mol/cm^3. Inlet molar oxygen-to-hydrogen ratios were between 0.125 and

11.82, corresponding to fuel equivalence ratios ($\phi = ([H_2]_o/[O_2]_o) / ([H_2]_o/[O_2]_o)_{stoich}$) between 0.042 and 4.01; the ratio of hydrogen to oxygen thus ranged from fuel-lean to fuel-rich. However, in no oxidation experiment was either reactant conversion-limiting; a single "pyrolysis" experiment in which oxygen was deliberately excluded from the reactor was performed. Calculations using thermodynamic properties from the JANAF Thermochemical Tables (Chase *et al.*, 1985) showed that equilibrium did not limit the conversion of hydrogen for the range of conditions studied.

A complete tabulation of experimental conditions and results is given in Tables 12.3 and 12.4. [Note that Table 12.4 contains more detailed information for certain experiments listed in Table 12.3, but does not contain data for any new or different experiments.] Observed oxidative conversions varied between 6.1 and 98.2%, with average oxidation rates (defined as the change in hydrogen concentration divided by the residence time) between 1×10^{-8} and 3.8×10^{-7} mol/cm^3-s. The mass-balance closures reported in Tables 12.3 and 12.4 (87.3 to 105.7 %, with an average value of 97.3±4.4 %) indicate the good consistency obtained between the measured and calculated hydrogen and oxygen concentrations. In the aforementioned "pyrolysis" experiment (Run 63 in Table 12.3), only hydrogen and water were fed to the reactor at 600 °C with a 4.8-second residence time; a conversion of 2% was observed, which is easily explained by reaction with the trace amount of oxygen present. This result led us to conclude that there is no significant net reaction between hydrogen and water in our experiments.

5.1 Derivation of Global Rate Expression

Kinetic results were analyzed and modeled assuming the system could be described as an isothermal plug-flow reactor. Webley (1989) tested this assumption using the criteria of Cutler *et al.* (1988) and found it to be valid for our operating regime, and further

justification for this assumption was provided in Section 4.4. The kinetic results should thus obey the plug-flow design equation:

$$\frac{\tau}{C_{i,o}} = \int_0^{X_i} \frac{dX_i}{-R_i} \qquad (5.4)$$

where

X_i = conversion of species i

R_i = reaction rate for species i

$C_{i,o}$ = initial concentration of reactant i

τ = reactor residence time

and we have assumed that the volumetric flow through the reactor is constant. This assumption is good for the dilute range of reactant concentrations studied, since water is vastly in excess (mole fraction greater than 0.999) and any volume change on reaction will have a negligible effect on the overall density. Similarly, since we have assumed isothermality and the experiments were performed isobarically (with a negligible pressure drop through the system), there is no density change of the water as it passes through the reactor. The reactor residence time thus depends only on the reactor volume, the supercritical water density, and the water mass flow rate.

In practice, Equation 5.4 requires an expression for the reaction rate R_i. For our study, we used a global rate expression of the form

$$R_{H_2} = k\,[H_2]^a\,[O_2]^b \qquad (5.5)$$

with a classical Arrhenius form assumed for k

$$k = A \exp(-E_a/RT) \qquad (5.6)$$

Water was omitted from the rate expression because its concentration did not vary significantly during an experiment (for the reasons discussed above), and because its concentration (density) is strongly coupled to the temperature. Since variations in temperature are likely to have a much larger effect on the intrinsic rate of oxidation than the corresponding variations in water concentration, it was unnecessary to include water concentration as a rate parameter.

Substituting Equations 5.5 and 5.6 into Equation 5.4, and using the global stoichiometry of Equation 5.3, the following relationship is obtained for isothermal, plug-flow conditions:

$$[H_2]_o^{a+b-1} k \tau = \int_0^X \frac{dX}{(1-X)^a (F - \frac{1}{2}X)^b} \tag{5.7}$$

where

$[\,]_o$ = inlet concentration

F = $[O_2]_o/[H_2]_o$

X = conversion of hydrogen

and k is given by Equation 5.6. Best-fit values of the rate parameters A, E_a, a, and b were determined by regressing Equation 5.7 to the experimental oxidation data in Table 12.3 using a nonlinear regression routine which employed a modified Marquardt method (Press *et al.*, 1986). The resulting best-fit rate expression, for temperature as the predicted variable (see Section 12.1), was

$$R_{H_2} = 10^{24.4\pm4.9} \exp(-390\pm60/RT)\,[H_2]^{1.1\pm0.25}\,[O_2]^{0.02\pm0.29} \tag{5.8}$$

where the rate is in mol/cm^3-s, the concentrations are in mol/cm^3, the activation energy is in kJ/mol, and the parameter uncertainties, as determined by an ANOVA routine (Press *et al.*, 1986), are at the 95% confidence level. Since the reaction order with respect to oxygen, b, was not statistically significant at this level of confidence, that parameter was eliminated from the rate expression and the remaining parameters regressed again. The new rate expression was

$$R_{H_2} = 10^{24.2\pm3.8} \exp(-388\pm51/RT)\,[H_2]^{1.1\pm0.25} \tag{5.9}$$

We now note that the reaction order with respect to hydrogen, a, is not statistically different from 1.0 at a 95% confidence level. Assumption of first-order behavior simplifies Equation 5.7 to

$$k = -\ln(1-X)/\tau \tag{5.10}$$

Since a first-order form facilitates use of the rate expression, we set a to one and regressed the remaining Arrhenius parameters for a third time. The resulting final rate expression was

$$R_{H_2} = 10^{22.8\pm2.2} \exp(-372\pm34/RT)\,[H_2] \tag{5.11}$$

Statistical analysis of the three rate forms, Equations 5.8, 5.9, and 5.11, yielded F-statistics of 157, 240, and 480, respectively. These values suggest that the additional parameters present in Equations 5.8 and 5.9 did not improve the fit of the rate expression to the data. Furthermore, the regressed Arrhenius parameters A and E_a did not vary significantly among the various rate forms, indicating that those parameters were

essentially independent of the reaction orders. Finally, the r^2 values, adjusted for the degrees of freedom, were about 0.90 for all three rate expressions. These observations led us to conclude that the simple first-order form of Equation 5.11 adequately represents the experimental data, and introduction of additional parameters does not enhance the accuracy of the global rate expression.

The experimental data are shown in Figure 5.1 in the form of a first-order Arrhenius plot, with the solid line representing the behavior predicted by the best-fit rate expression of Equation 5.11. Error bars in the figure are 95%-confidence estimates of experimental error. Experimental error is smaller for the high-temperature (high-conversion) runs because in those experiments the exit hydrogen concentration is much lower than that at the inlet. A danger in regressing data to a form like Equation 5.11 is that there is a tendency to ascribe more significance to the expression than it possesses. The regressed global rate form captures the general trend of the data, although the data do *not* strictly obey the first-order rate form, as witnessed by the slight sigmoidal shape of the Arrhenius plot. The data at 600 °C, in particular, seem to deviate from the overall linearity. This non-linearity in the global rate constant may be the result of inherent kinetic complexities, or may reflect the influence of diffusional transport on the observed kinetics. The analysis of reactor performance in Section 4.4 showed that the rate of hydrogen oxidation at 600 °C is comparable to the rate of radial diffusion within the reactor; under such conditions the diffusional limitations may compromise the reactor's ability to perform in the plug-flow regime. Moreover, if the data obeyed the regressed rate expression exactly, all data at a single temperature would be represented by a single point. The numerous data at 520 °C and 550 °C deviate from this ideal, and exhibit a degree of scatter which cannot be explained by experimental error alone.

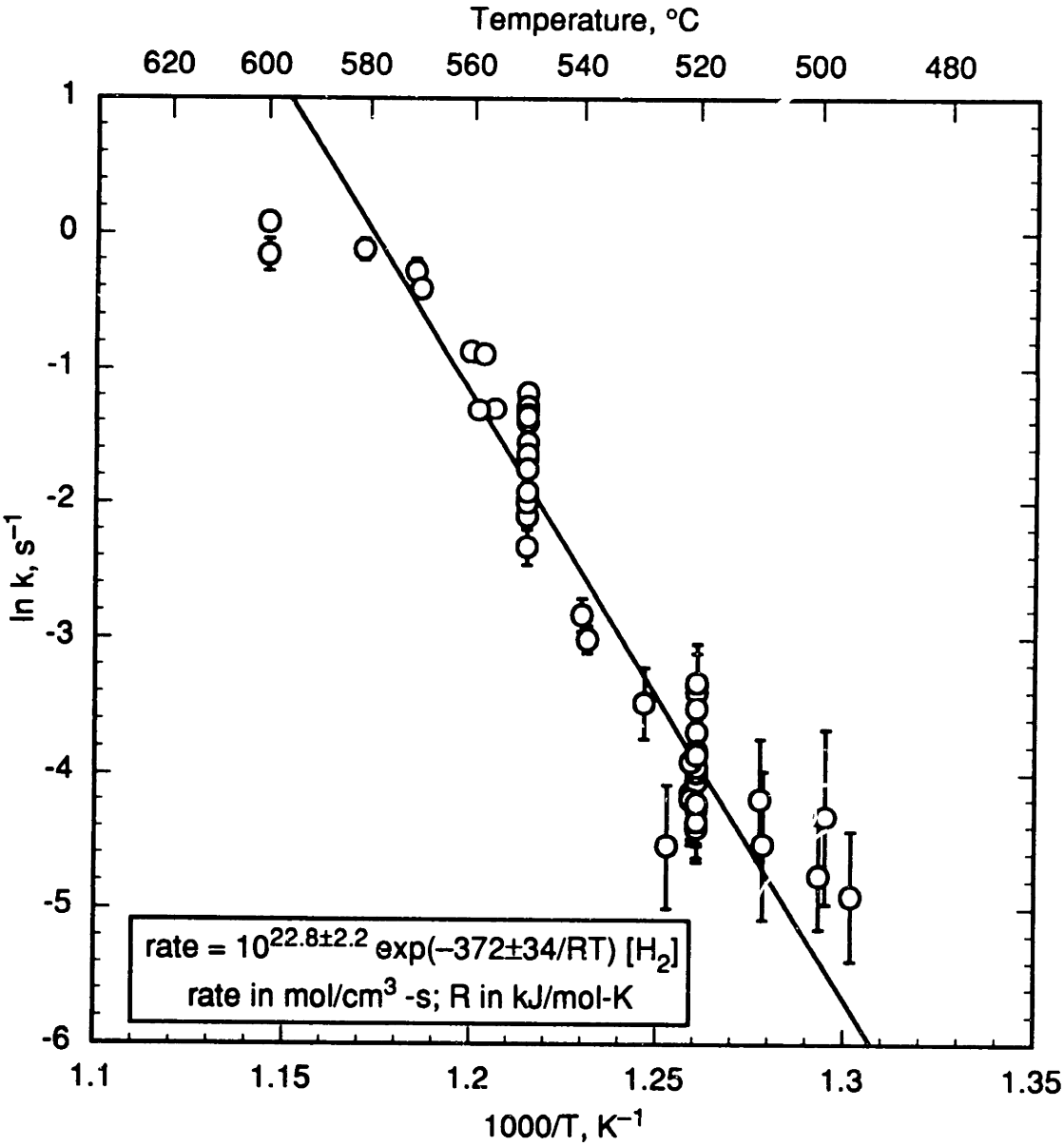

Figure 5.1 **First-Order Arrhenius Plot for Hydrogen Oxidation in Supercritical Water at 246 bar.**

The experimental observation of global hydrogen oxidation kinetics which are first order in hydrogen and independent of oxygen is not entirely surprising. In earlier studies in our laboratory, Helling and Tester (1987), in the case of carbon monoxide, and Webley and Tester (1989), in the case of methanol, observed global kinetics independent of oxygen and first-order in the organic. The reasons for this behavior are not immediately apparent; obviously at some level of dilution, the kinetics must be dependent on oxygen concentration, since oxidation cannot occur in the absence of oxygen. However, for the range of conditions studied here, including an order-of-magnitude variation in oxygen concentration and a two-order-of-magnitude variation in feed ratio, the experimental results do not exhibit an oxygen dependence.

Similar qualitative behavior has been observed by other investigators. Von Elbe and Lewis (1937) reported that the rate of the homogeneous, gas-phase reaction of hydrogen and oxygen above ~550 °C was affected equally by addition of oxygen or inert gas, indicating that oxygen did not specifically influence the reaction rate. The same independence of oxygen was observed by Gibson and Hinshelwood (1928). Observed global activation energies for gas-phase hydrogen oxidation have varied widely, from 230 kJ/mol (Baldwin and Mayor, 1958) to 540 kJ/mol and as high as 800 kJ/mol or higher (Kassel, 1937; Gibson and Hinshelwood, 1928). The general similarity to our results is encouraging; however, studies of gas-phase hydrogen oxidation are typically carried out at low (atmospheric or lower) pressures and are markedly complicated by diverse effects, including surface reactions and acceleration by steam (von Elbe and Lewis, 1937,1942; Kassel, 1937). There is little reason to expect that we should be able to extrapolate those results to our system.

In general, although the regressed global rate form of Equation 5.11 adequately reproduces the observed experimental behavior, the rate expression should be regarded as

a simplified model for correlating the experimental data, applicable only for the range of conditions studied here and containing no inherent mechanistic information.

5.2 Species Profiles

5.2.1 Variation of k^* with Residence Time

A series of experiments was conducted to investigate the possible influence of reactor residence time on the apparent first-order rate constant, k^*. If the data strictly obey Equation 5.11, k^* should be invariant with residence time. In our system, however, it is not possible to vary residence time at a given temperature and pressure without varying the flow rate through the reactor. Consequently, any observed variation in k^* with residence time could be the result of either kinetic effects or hydrodynamic effects. Flow conditions in our reactor are not completely turbulent, but rather are in the transition regime. Since the reactor velocity profiles may not be completely uniform, observed kinetic results could exhibit some dependence on flow conditions.

Results of experiments at 550 °C for a stoichiometric H_2/O_2 feed ratio are shown in Figure 5.2, with ln k^* plotted as a function of residence time; for each residence time, the corresponding experimental Reynolds number is also indicated. The lower limit of experimentally accessible residence times in the 11.1-cm^3 tubular reactor was determined by the maximum flow rate achievable with the feed pump, and the upper limit by both the lowest measurable gas flow rate and a desire to maintain turbulent or transitional flow conditions with Reynolds numbers above 2100. Figure 5.2 clearly shows that k^* increases uniformly with increasing residence time (decreasing Reynolds number).

According to Ramayya and Antal (1989), the maximum possible error in k^*, resulting from the incorrect application of the plug-flow idealization to parabolic, laminar-flow data, is about 30%, corresponding to an error of 0.3 in ln k^*. Reynolds

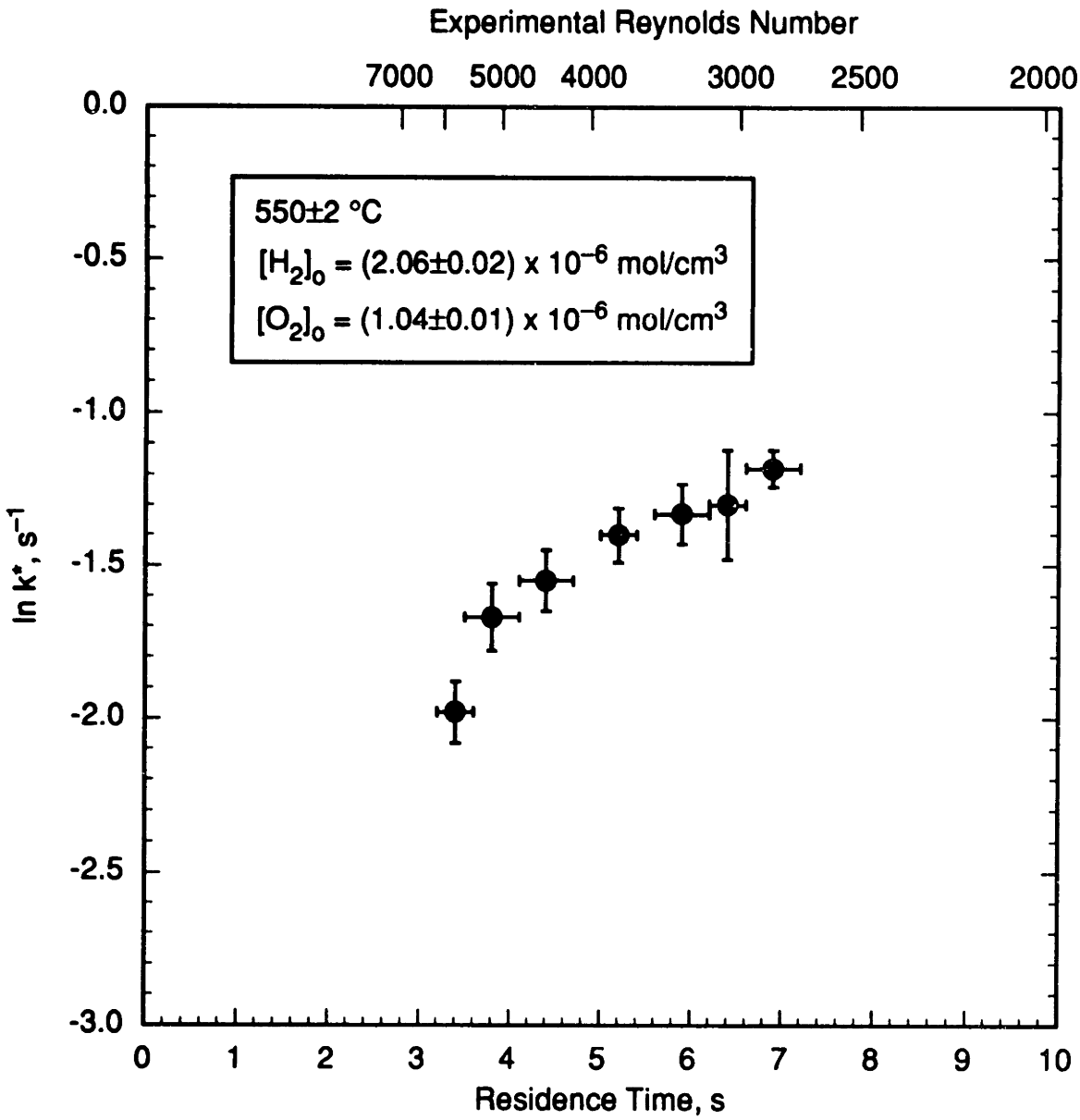

Figure 5.2 **Variation of Apparent First-Order Rate Constant, k^*, with Residence Time.** Experimental conditions as indicated; $[H_2O] = (4.25\pm0.08) \times 10^{-3}$ mol/cm^3.

numbers in the reactor for these experiments, as shown in Figure 5.2, ranged from 2700 to 5800, typical of values in all our experiments and above the range for which it is possible to sustain laminar flow. The 30% error is therefore a very conservative estimate of the maximum variation possible in our system as a result of velocity profile nonuniformities. The data in Figure 5.2, however, clearly vary by more than 30% over the range of flow conditions; ln k^* varies by nearly 1. Furthermore, Ramayya and Antal (1989) indicate that k^* should decrease when flow conditions deviate from plug flow, i.e., as they become laminar, while Figure 5.2 shows the opposite trend. The observed variation in k^* thus cannot be explained on the basis of hydrodynamic effects, but instead must be the result of kinetic behavior that is more complex than the simple first-order model of Equation 5.11. Further examination of the data revealed the source of the k^* variations.

5.2.2 Apparent Induction Times and Hydrogen Decay Profiles

The data from Figure 5.2 are replotted in Figure 5.3, along with data for two other stoichiometric H_2/O_2 mixtures at 550 °C, in the form of hydrogen concentration decay profiles as a function of residence time. Hydrogen concentrations in Figure 5.3 are normalized by the initial hydrogen concentration. The curves in Figure 5.3 represent exponential fits to the three sets of data, *with the initial concentrations omitted.* In all three data sets, the hydrogen concentration clearly follows an exponential decay characteristic of a first-order reaction, confirming our earlier conclusion from global reaction modeling. For each set of data, one can define a kinetic decay constant, k', as

$$k' = -\frac{1}{C_i}\frac{dC_i}{dt} = -\frac{d\ln C_i}{dt} \tag{5.12}$$

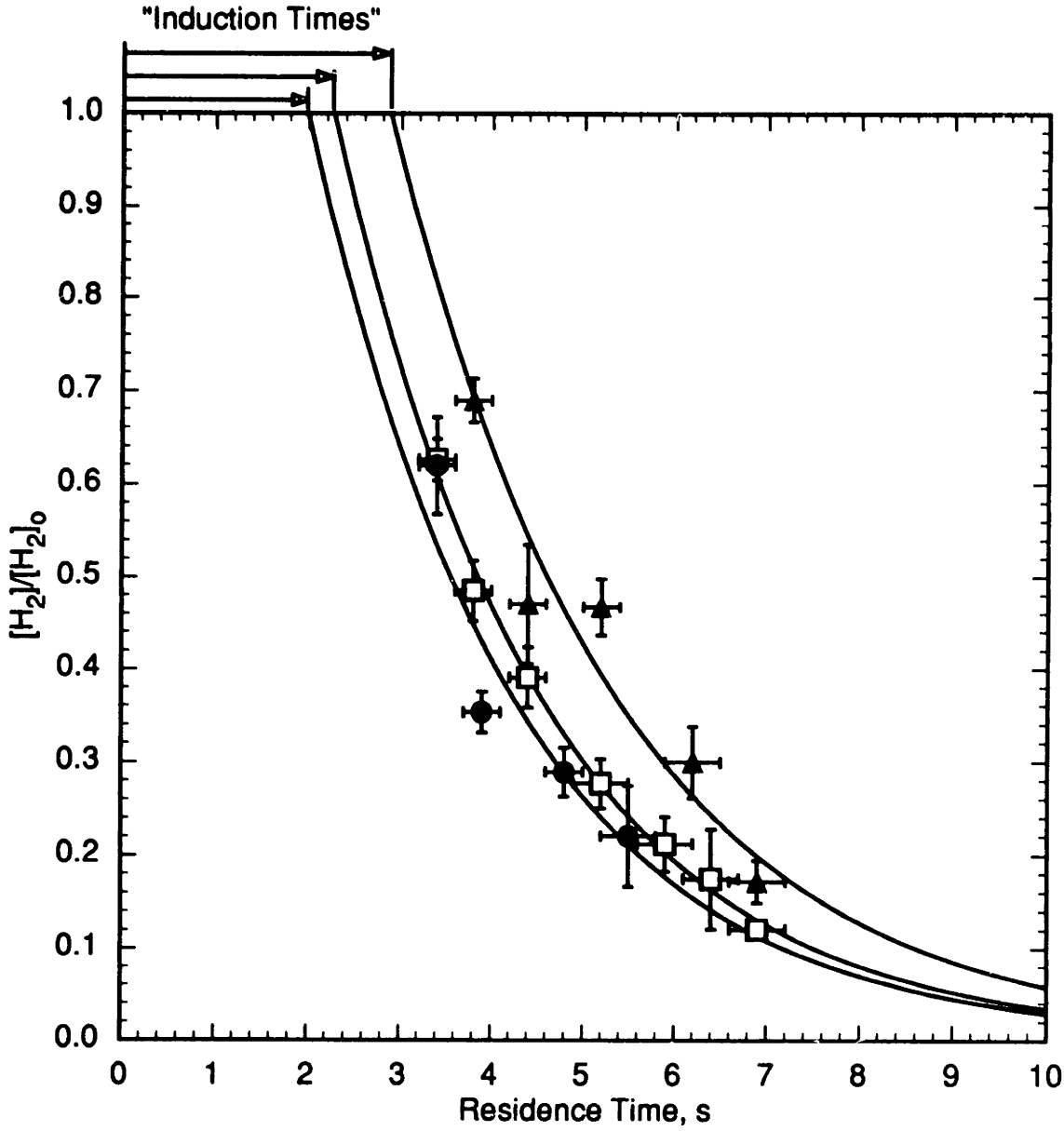

Figure 5.3 **Normalized Hydrogen Decay Profiles for Stoichiometric H_2-O_2-H_2O Mixtures, Demonstrating Effective Induction Times.** Experimental conditions: 550±2 °C; $[H_2O] = (4.25\pm0.08) \times 10^{-3}$ mol/cm^3;
▲—$[H_2]_o = (3.06\pm0.03) \times 10^{-6}$ mol/cm^3, $[O_2]_o = (1.55\pm0.02) \times 10^{-6}$ mol/cm^3;
□—$[H_2]_o = (2.06\pm0.02) \times 10^{-6}$ mol/cm^3, $[O_2]_o = (1.04\pm0.01) \times 10^{-6}$ mol/cm^3;
●—$[H_2]_o = (1.065\pm0.015) \times 10^{-6}$ mol/cm^3, $[O_2]_o = (0.54\pm0.01) \times 10^{-6}$ mol/cm^3.
Curves are exponential fits to data.

where C_i is the concentration of the species of interest (in this case, hydrogen). For a first-order decay, k' is equal to the exponential decay constant, and the concentration profile is characterized by a single value of k'; for a non-exponential decay, k' is a function of time.

Extrapolation of the regressed decay curves in Figures 5.3 back to the initial time ($t = 0$) should give the initial hydrogen concentration ($[H_2]/[H_2]_o = 1$), if the reaction truly obeys the simple rate form of Equation 5.11. This is clearly not the case. Instead, the exponential (first-order) decay does not begin until a time of 2 s or later. This apparent lag in the start of the reaction can be considered an "ignition delay" or "induction time." These results represent the first reported observation of an induction time in supercritical water oxidation. The effective induction times (τ_{ind}) for the three data sets have been indicated in Figure 5.3. Figure 5.4 shows an alternative form of Figure 5.3, in which the exponential decays have been linearized by the use of a logarithmic vertical axis; in this form, the fit of the data to an exponential decay, as well as the extrapolation of the exponential, are more apparent. All three data sets again clearly decay exponentially, and extrapolation of the fitted lines gives induction times identical to those obtained in Figure 5.3. The decay constants and induction times derived from Figures 5.3 and 5.4 are summarized in Table 5.1; reported errors are one standard deviation. Values for the induction times and decay constants were obtained from both the hydrogen concentration profiles and the oxygen profiles, which are not shown in Figures 5.3 and 5.4 but are listed in Table 12.4. For all three mixtures, induction times and decay constants derived from the two profiles are in excellent agreement. Note that all three data sets exhibit the same decay constant (k'), within regression error. On the other hand, the induction time appears to increase slightly with increasing concentration, but because the estimation error is quite large, an unequivocal conclusion is not possible.

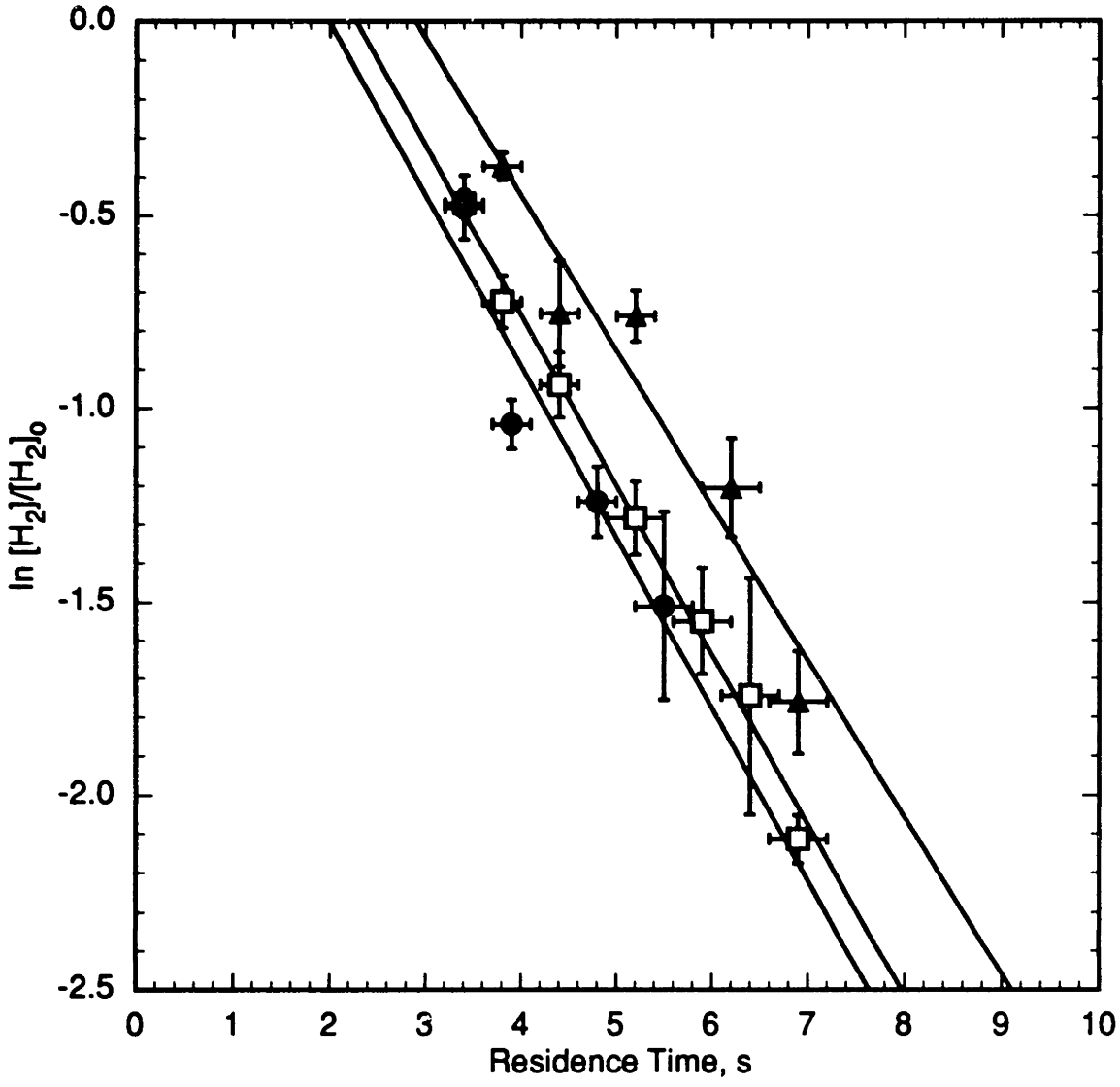

Figure 5.4 **Normalized Hydrogen Decay Profiles for Stoichiometric H_2-O_2-H_2O Mixtures, Demonstrating Effective Induction Times.** Conditions as in Figure 5.3, but concentration scale is logarithmic. Lines are linear fits to data.

Initial Conditions 10^{-6} mol/cm^3	k', s^{-1} (H_2)	k', s^{-1} (O_2)	τ_{ind}, s (H_2)	τ_{ind}, s (O_2)
$[H_2]_o = 1.06\pm0.02$ $[O_2]_o = 0.54\pm0.01$	0.44±0.11	0.47±0.08	2.0±0.6	2.0±0.5
$[H_2]_o = 2.06\pm0.02$ $[O_2]_o = 1.04\pm0.01$	0.44±0.02	0.42±0.02	2.3±0.2	1.9±0.2
$[H_2]_o = 3.06\pm0.03$ $[O_2]_o = 1.55\pm0.02$	0.40±0.07	0.42±0.07	2.9±0.7	2.6±0.6

Table 5.1 **Apparent Induction Times τ_{ind} and Decay Constants k' for Stoichiometric Hydrogen Oxidation at 550 °C and 246 bar.**

The observation of an induction time in the oxidation reaction strongly suggests the presence of a complex elementary reaction mechanism, and complicates global reaction modeling efforts. No single rate expression of the form of Equation 5.5 could capture this type of behavior. Similarly, calculation of k^* (the apparent first-order rate constant) for a given experiment assumes the reaction begins at $t = 0$, and the ignition delay results in the variations in k^* with residence time seen in Figure 5.2. Since the regressed rate form can only approximate this kinetic behavior, there is scatter in the data at 550 °C in Figure 5.1; in addition, the rate constant calculated from Equation 5.11 at 550 °C ($k = 0.15$ s^{-1}) differs significantly from the decay constants observed in Figures 5.3 and 5.4 and listed in Table 5.1 ($k' \sim 0.40$–0.45 s^{-1}), because Equation 5.11 attempts (unsuccessfully) to capture both the ignition delay and the concentration decay due to oxidation.

Earlier attempts have been made to measure induction times for gaseous hydrogen-oxygen-diluent mixtures (Schott and Kinsey, 1958; Skinner and Ringrose, 1965; Slack, 1977; Hidaka *et al.*, 1982). Since the oxygen concentration can strongly affect the induction time, measured induction times are frequently "normalized" such that the product τ_{ind} [O_2] is constant at a given temperature. This normalization suggests that the induction time should be shortened by increasing the oxygen concentration. No strong effect of oxygen was seen in our experiments (Figures 5.3 and 5.4), despite a threefold variation in oxygen concentration. If anything, τ_{ind} seems to increase slightly with increasing oxygen (and hydrogen) concentration. Although there is sufficient scatter in the data to make a definitive conclusion difficult, it seems clear that τ_{ind} is not nearly as sensitive to oxygen concentration as observed in earlier gas-phase studies. Moreover, extrapolation of the higher-temperature data of Skinner and Ringrose (1965) to the conditions of Figures 5.3 and 5.4 predicts induction times too long by an order of

magnitude. This evidence suggests that the mechanisms controlling the induction time in gas phase combustion are very different from those in supercritical water oxidation.

Finally, one should note that it is difficult to measure quantitatively induction times in a flow-reactor apparatus like ours. While fluid residence times are relatively well defined experimentally, the initiation point of the reaction ("$t = 0$") is less well characterized because of the presence of a feed mixing zone at the entrance to the reactor. As discussed earlier in Section 4.4.2, mixing times are certainly short relative to the reactor residence time; however, absolute values of effective induction times should be viewed with some reservation since induction chemistry (and hence observed induction times) can be affected by even minor concentration perturbations during mixing (Yetter *et al.*, 1985).

5.3 Effects of Operating Pressure (Fluid Density)

The potential advantages of operation of the SCWO process at lower, even subcritical, pressures have recently been outlined by Hong (1992), and include reduced construction costs, decreased corrosion, and more favorable phase behavior of salts. The effect of reduced operating pressure on the oxidation kinetics, however, is not well known. Furthermore, a systematic variation of the fluid density (water concentration), with all other conditions (reactant concentrations, temperature) held constant, can help elucidate the role of water in the oxidation mechanism.

Subsequent to the experiments described in Sections 5.1 and 5.2, a series of hydrogen oxidation experiments was conducted in which the operating pressure (and hence the water density) was varied from approximately 120 bar to 260 bar, at a constant nominal temperature of 550 °C and nominal stoichiometric reactant concentrations $[H_2]_o = 1 \times 10^{-6}$ mol/cm^3, $[O_2]_o = 0.5 \times 10^{-6}$ mol/cm^3. These conditions were chosen on the

basis of the earlier oxidation results, which indicated that a temperature of 550 °C gave hydrogen conversions of 50 to 80% for residence times of 4 to 6 s at 246 bar; this "baseline" range of conversions would allow observation of significant changes in conversion (either increasing or decreasing) as operating pressure was varied. Maximum reactant concentrations were constrained by saturator solubilities, since lower operating pressures (lower water concentrations) require a higher reactant mole fraction to maintain constant reactant concentrations. The chosen concentrations were the highest attainable for an operating pressure of 100 bar; lower concentrations were not considered since low reactant concentrations yield low effluent gas flow rates and can limit the range of experimentally accessible conditions. The maximum operating pressure, 263 bar, was set by the ratings of pressure-relief equipment (rupture disks) in the experimental system.

Results of the variable-pressure experiments are shown in Figure 5.5 and are compiled numerically in Table 12.5. Data were obtained for pressures from 118 to 263 bar, with observed hydrogen conversions ranging from 9 to 87%. An attempt to obtain data at 97.5 bar and a 2.3-s residence time was unsuccessful, with no observable conversion of hydrogen. The range of pressures examined spans the critical region, from well above the critical pressure (221 bar) to well below, and corresponds to water densities of 0.033 to 0.083 g/cm^3 (reduced densities, ρ/ρ_c, of 0.10 to 0.26), or nearly a factor-of-three variation in density. Figure 2.1 shows that the density varies smoothly with pressure at 550 °C; at pressures below 221 bar, the reaction medium is essentially a high-pressure gas phase. Figure 5.5 clearly shows that the apparent first-order rate constant, k^*, increases significantly with increasing operating pressure (water density); at 263 bar, k^* is almost an order of magnitude higher than at 118 bar. The large errors bars at the lower pressures result from the higher proportional uncertainty in the lower measured hydrogen conversion.

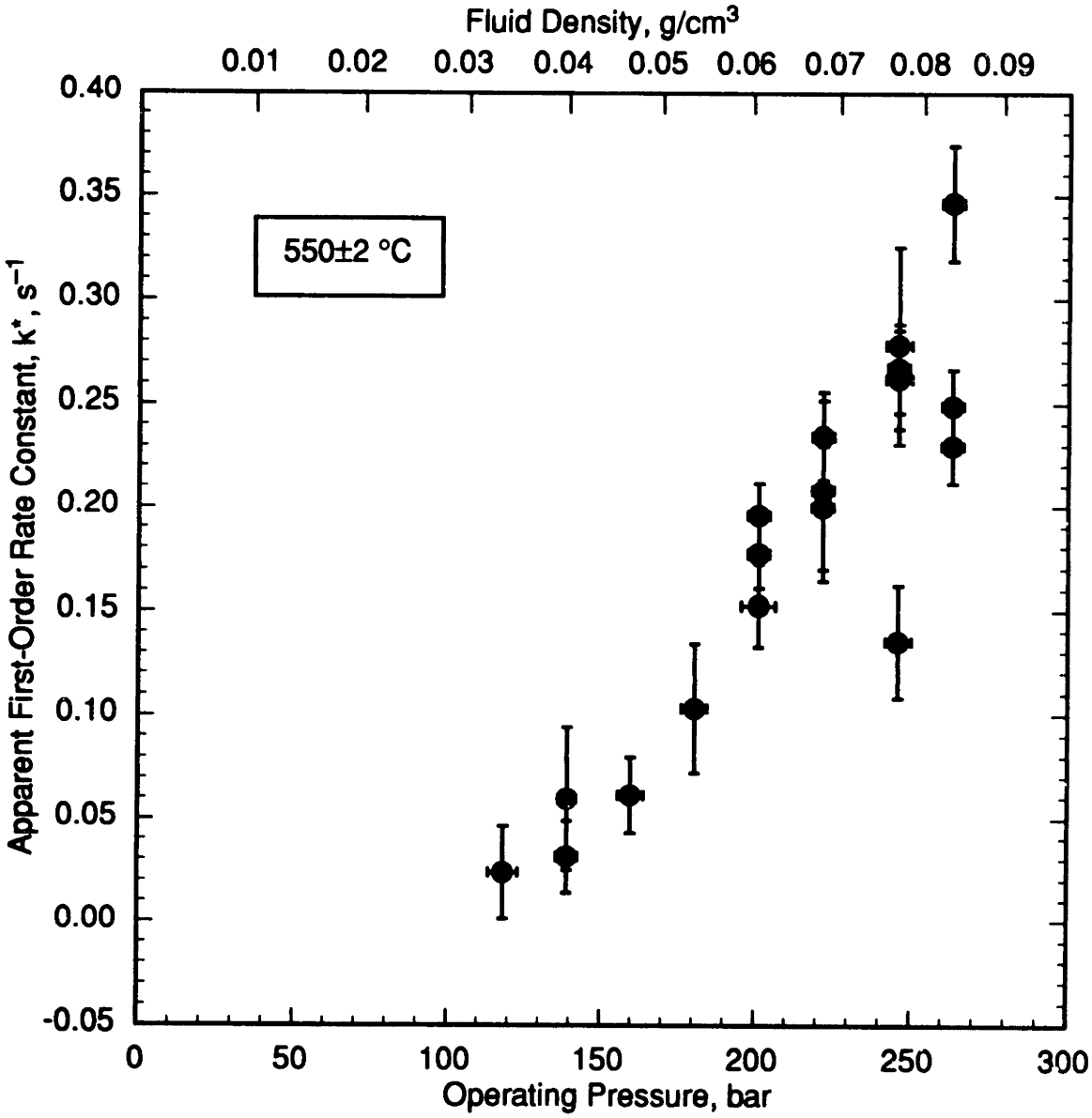

Figure 5.5 **Effects of Operating Pressure on Apparent First-Order Rate Constant, k^*, for Hydrogen Oxidation.** Experimental conditions: 550±2 °C, $[H_2]_o = (1.06\pm0.02) \times 10^{-6}$ mol/cm^3, $[O_2]_o = (0.53\pm0.01) \times 10^{-6}$ mol/cm^3.

The dramatic increase in k^* with pressure in Figure 5.5 is somewhat overemphasized by the hidden effect of varying residence time. Section 5.2 showed that, all other things being equal, k^* increases with increasing residence time owing to the presence of an induction time in the oxidation reaction. Some variation in residence time with operating pressure in Figure 5.5 was unavoidable, due to the variation in fluid density combined with flow restrictions imposed by the feed pump and the critical Reynolds number. Under high-density (high-pressure) conditions, the minimum residence time is set by the maximum pump flow rate, while at low densities the maximum residence time is set by the need to maintain *Re* above 2100. Some indication of the variation in k^* with residence time is given by the data at 201, 222, 246, and 263 bar; at each of those pressures, the various data points were obtained at different residence times. Since k^* in general increases with increasing residence time, and longer residence times tend to fall at higher pressures in Figure 5.5, the pressure dependence of k^* is somewhat exaggerated.

Figure 5.6 eliminates residence time as a confounding variable by showing k^* as a function of residence time for the various operating pressures studied. At a given residence time, the variation of k^* with operating pressure represents the "pure" pressure dependence of the rate constant. This pressure dependence is most evident at a residence time of 3.8 to 3.9 s, where studied pressures ranged from 139 to 263 bar, and is also apparent at 4.8 s, with pressures of 201 to 246 bar. The rate constant increases uniformly with pressure, except at the highest pressures studied. One should note that the data at 3.8 and 4.2 s, for pressures of 201, 222, and 246 bar, were obtained six months after the rest of the data; the slight inconsistency of those data points with earlier data are likely attributable to natural equipment variability and an inability to reproduce precisely the earlier reaction conditions. The slight anomaly of those data points should be considered

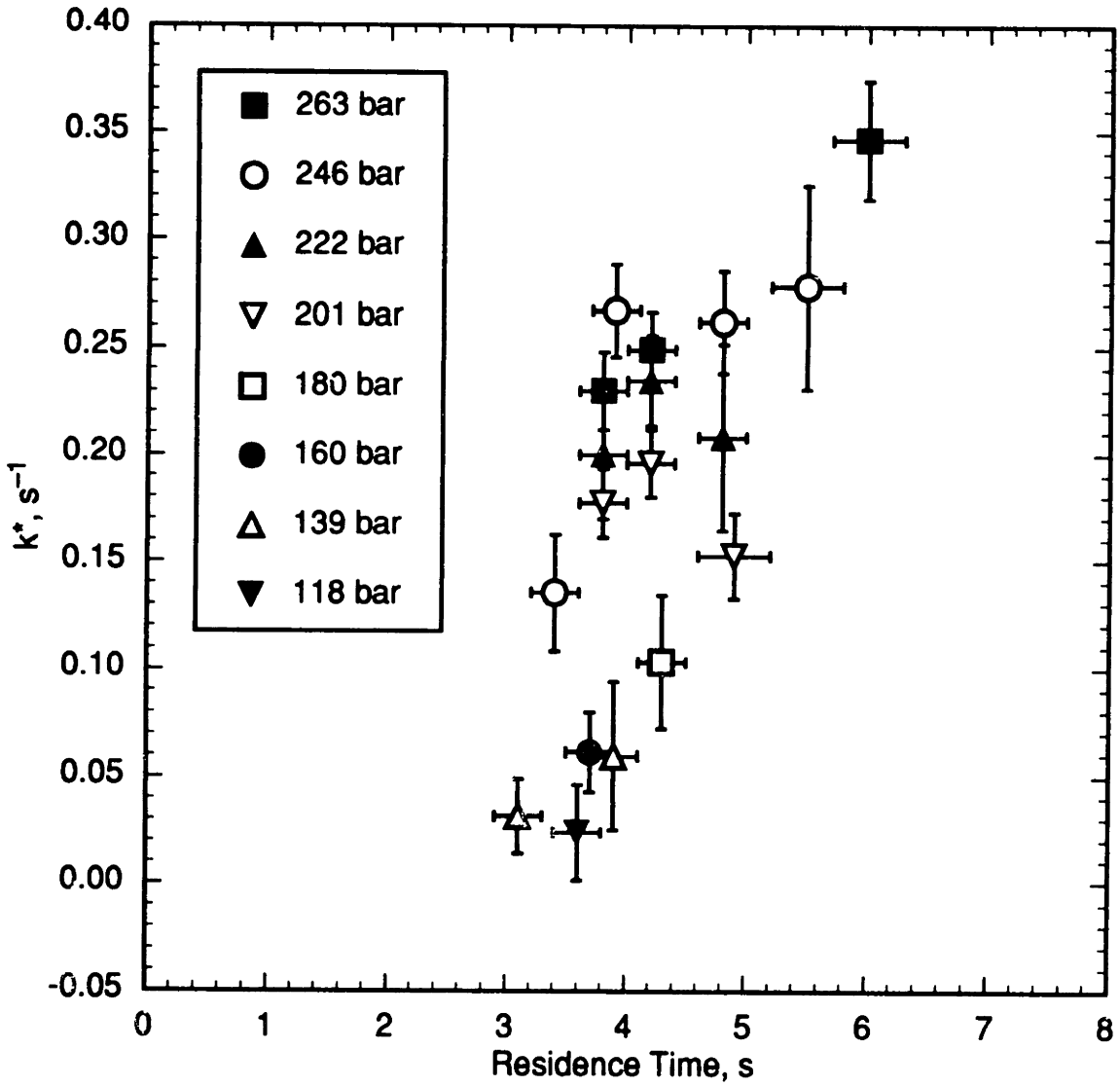

Figure 5.6 **Variation of Apparent First-Order Rate Constant, k^*, with Residence Time at Varying Operating Pressures.** Conditions as in Figure 5.5.

representative of experimental error, and should not detract from the much larger overall trend of increasing k^* with increasing pressure.

The observed trend of increasing oxidation rate with increasing pressure can be examined in the context of explosion behavior for hydrogen-oxygen mixtures. An explosion diagram for stoichiometric H_2-O_2 mixtures is shown in Figure 5.7. The sigmoidal curve delineates the boundary between the slow reaction of hydrogen with oxygen (by a chain-propagating mechanism) and the explosively fast reaction (by a chain-branching mechanism); for pressures and temperatures to the left of the curve, hydrogen and oxygen react slowly; to the right of the curve, the reaction rate becomes very fast. The explosion boundary can be divided into three limits (Lewis and von Elbe, 1987), as shown in Figure 5.7. The first limit corresponds to the quenching of chain-carrying species by vessel walls. For pressures below the first limit, mean free paths are large and frequent collisions with the vessel surface occur, destroying radical species and acting as chain-terminating steps. At pressures above the first limit (> ~0.01 bar), homogeneous reactions become important and homogeneous chain-branching steps overcome the heterogeneous chain termination at the walls. The first limit can be considered a "lower limit" to explosion. Since the first limit by nature is strongly surface-dependent, the location of the first limit (in P, T space) is subject to great uncertainty and is highly specific to the geometry and surface of the reaction vessel. At pressures well above the first limit, an upper explosion limit (the second limit) is encountered. In the explosive region between the first and second limits, chain branching occurs via the reaction

$$H + O_2 \rightarrow OH + O \qquad (5.13)$$

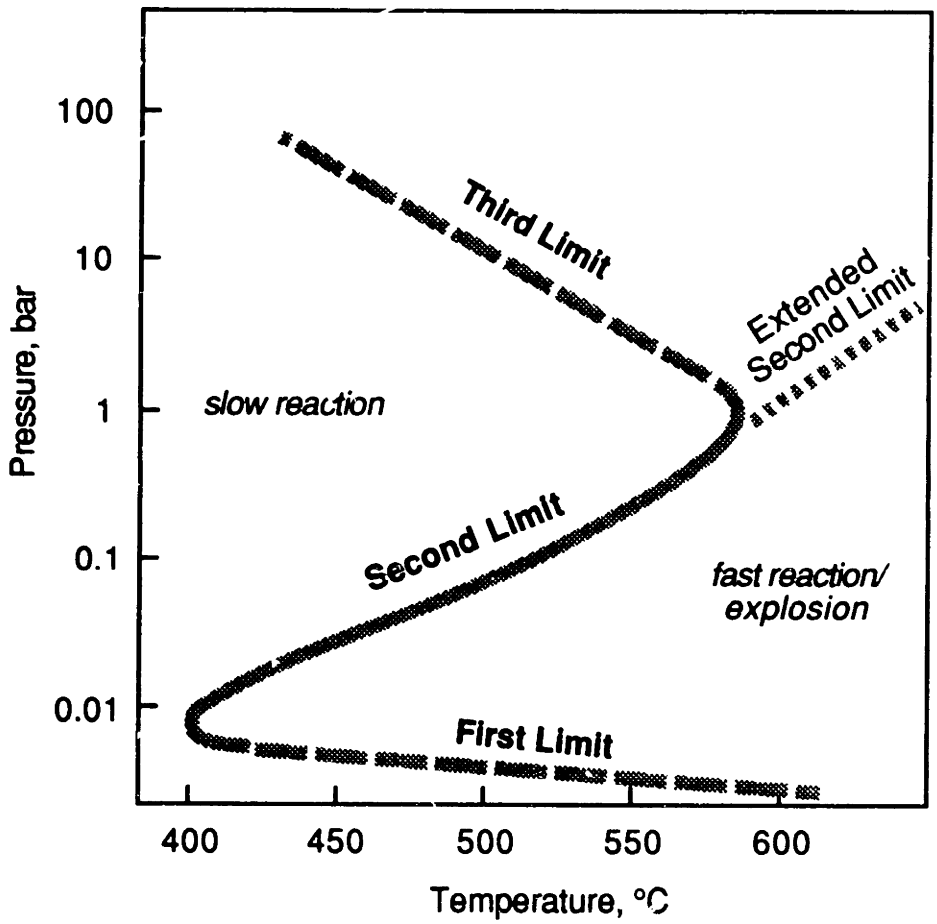

Figure 5.7 **Explosion Diagram for Stoichiometric H_2-O_2 Mixtures.** Adapted from Lewis and von Elbe (1987) and Vermeersch (1991).

At and above the second limit, the alternative reaction

$$H + O_2 + M \rightarrow HO_2 + M \qquad (5.14)$$

which depends on pressure via the third-body concentration [M], competes successfully with (5.13). Since the HO_2 radical is relatively unreactive at temperatures and pressures just above the second limit, (5.14) moderates the overall reaction rate and prevents explosive chain-branching from occurring (Lewis and von Elbe, 1987).

Increasing the pressure above the second limit results in steadily increasing reaction rates, since the rate of (5.14) continues to increase with pressure. Furthermore, as (5.14) becomes faster, reactions of HO_2 become important, including

$$HO_2 + HO_2 \rightarrow H_2O_2 + O_2 \qquad (5.15)$$

$$HO_2 + H_2 \rightarrow H_2O_2 + H \qquad (5.16)$$

H_2O_2 formed in these steps can dissociate in a pressure-dependent step to form OH radicals

$$H_2O_2 + M \rightarrow OH + OH + M \qquad (5.17)$$

As (5.17) becomes fast at higher pressures, the sequence (5.14)–(5.17) results in high production of OH radicals, and eventually (above the third limit) this sequence becomes explosive (Lewis and von Elbe, 1987). The extended second limit has recently been studied computationally (Yetter *et al.*, 1989,1991c) and experimentally (Vermeersch, 1991). This limit appears to represent the conditions under which the branching nature of (5.16)+(5.17) is moderated by the propagating nature of (5.15)+(5.17); hence the reaction

rate increases with pressure both above and below the extended second limit, but proportionally slower above the limit than below. The pressures and temperatures of the present study (495–600 °C, 118–263 bar) suggest that our operating regime lies above the third explosion limit. In no case was an explosively fast reaction observed, however; instead, the oxidation reaction occurred on time scales of seconds, and increased smoothly with increasing pressure.

In reality, the third limit is most likely not a well-defined boundary between slow and fast (explosive) reaction. The computational studies of Dougherty and Rabitz (1980) and Maas and Warnatz (1988) suggest that the third limit is an explosion boundary only for pure or concentrated H_2-O_2 mixtures, or for adiabatic conditions under which the exothermicity of the reaction serves to heat the reaction mixture to temperatures at which explosion (rapid chain branching) is unavoidable. In the presence of a large quantity of diluent (like supercritical water) and/or under isothermal conditions (the operating regime in this study), the reaction rate does not become explosively fast but rather increases steadily with increasing pressure (Dougherty and Rabitz, 1980; Maas and Warnatz, 1988). Hence the third limit is a thermal limit rather than a kinetic limit; as long as concentrated, adiabatic conditions are avoided, the third limit is merely a region of steady reaction. The present experimental observations are thus consistent with the chain-propagating mechanism of (5.14), (5.15), and (5.17), corresponding to the pressure-moderated reaction above the third limit.

5.4 Reactor Surface Effects

The gas-phase oxidation of hydrogen has long been known to be profoundly affected by the nature and the extent of the interactions between the reacting species and the surface of the reaction vessel (von Elbe and Lewis, 1937,1942; Kassel, 1937). Most frequently,

the (non-catalytic) effect of the reactor surface is to inhibit the oxidation reaction by acting as a site for termination of free radicals (Lewis and von Elbe, 1987). Surface inhibitory effects are usually most pronounced at low pressures, where molecular mean free paths are large and radical collisions with the wall are relatively frequent. At higher pressures, the homogeneous collisional frequency is higher, and homogeneous reactions increase in importance at the expense of any heterogeneous reactions.

In the present experimental system, the nominal surface area-to-volume ratio is rather high (253 cm^2/10.82 cm^3, 23.4 cm^{-1}) owing to the small diameter of the reactor; thus heterogeneous contributions to the overall reaction rate cannot be ruled out *a priori*. In previous studies in the present experimental system, using the packed-bed reactor, Webley *et al.* (1990,1991) found a pronounced catalytic effect of the reactor material (Inconel 625) on the oxidation of ammonia. Limited experiments in the packed reactor for methane, methanol, and carbon monoxide oxidation did not reveal a distinct effect of the additional surface on the observed oxidation rate, but those conclusions must be regarded as preliminary. The present experimental results for hydrogen oxidation can only be used for modeling purposes if heterogeneous contributions are small or absent, and we therefore sought to perform a definitive experiment to identify the effect of the reactor surface on observed kinetics.

A series of experiments was conducted in the packed reactor with the experimental conditions $T = 550\pm2$ °C, $[H_2]_o = (1.04\pm0.01) \times 10^{-6}$ mol/cm^3, $[O_2]_o = (0.55\pm0.01) \times 10^{-6}$ mol/cm^3. The results are shown in Figure 5.8, where they are compared to experimental results for the same conditions in the tubular reactor, shown originally in Figure 5.3. Numerical data from the packed reactor experiments are given in Table 12.6. The range of accessible residence times in the packed reactor is shifted to

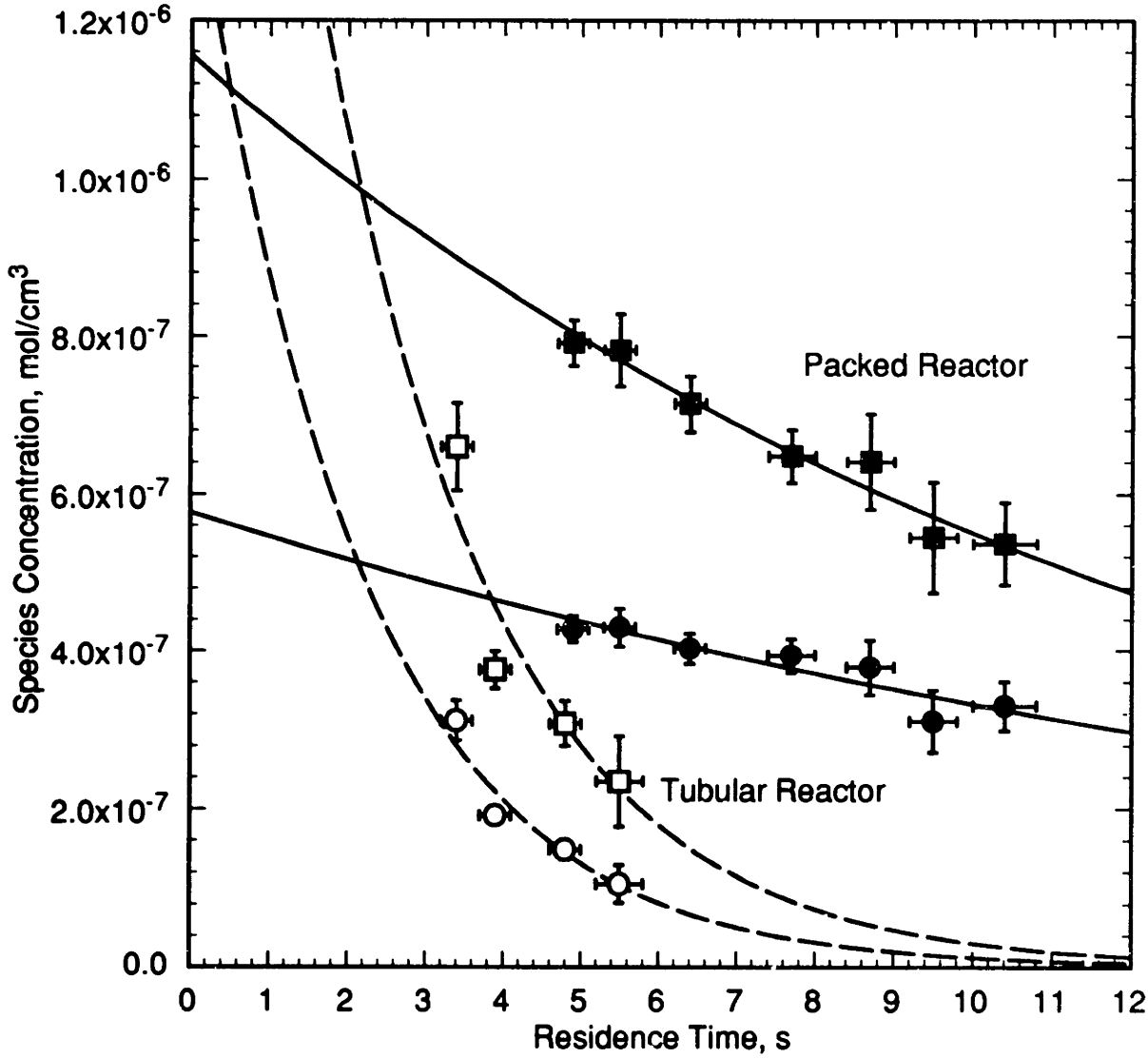

Figure 5.8 **Comparison of Concentration Profiles for Hydrogen Oxidation at 246 bar in Tubular and Packed-Bed Reactors.** Nominal experimental conditions: 550 °C, $[H_2]_o = 1 \times 10^{-6}$ mol/cm^3, $[O_2]_o = 0.5 \times 10^{-6}$ mol/cm^3. Squares: hydrogen; circles: oxygen; open symbols: tubular reactor; filled symbols: packed reactor. Curves are exponential fits to data.

somewhat longer times because of the higher free volume of the packed reactor (16.00 cm^3 vs. 11.11 cm^3 for the tubular reactor).

Figure 5.8 clearly shows that the added surface area in the packed reactor inhibits the oxidation reaction. The kinetic decay constant k' for the hydrogen profile in the packed reactor is 0.074 s^{-1}, compared to the value of 0.44 s^{-1} obtained in the open tubular reactor (see Table 5.1). The added surface area thus decreases the rate of disappearance of hydrogen by a factor of about 6. Considering that the surface area-to-volume ratio in the packed reactor is 20.5 times that of the tubular reactor (480 cm^{-1} vs. 23.4 cm^{-1}), the reduction in rate is less than directly proportional to the increase in surface area. If the observed decay constant is assumed to be proportional to the surface area-to-volume ratio in the reactor, extrapolation of the decay constant to the limit of zero surface area gives a value for k' of 0.46 s^{-1}, which is very close to that observed in the tubular reactor and well within the experimental error and the estimation error for k'. This crude approximation implies that the role of the reactor surface is sufficiently small in the tubular reactor experiments. Since heterogeneous reaction effects can be neglected, the measured kinetics reflect the true homogeneous rate of hydrogen oxidation.

In reality, the dependence of the kinetics on surface area may not be linear. In fact, rates of actual radical termination reactions may not be strictly proportional to surface area. The limit of proportionality occurs only when transport of radicals to the surface is perfect (not limited by mass transport); in this case, the surface area acts as if it were dispersed "homogeneously" throughout the reactor, and heterogeneous rate constants will be directly proportional to the amount of surface area present and independent of the actual location of the surface. If the heterogeneous reactions directly affect the ultimate concentration of the principal oxidizing radical, the overall reaction rate may also be directly proportional to the amount of surface area. In less idealized

cases, mass transfer to the wall is not perfect, and heterogeneous rates then depend on more complex system parameters (mass-transfer coefficients, diffusivities, etc.), and surface reactions are then properly modeled as a boundary condition at the surface of the reactor (Smith *et al.*, 1980). Since mass transfer from the bulk fluid to the reactor surface is likely to be more efficient in the packed reactor (Sherwood *et al.*, 1975), the influence of the added surface in the transport-limited case will be more pronounced than indicated by the simple ratio of surface areas. In that case, linear extrapolation of the decay constant to zero surface area will overestimate the difference between the tubular reactor results and the zero-surface-area result. The simple linear extrapolation of k' to zero surface area thus appears to give a reasonable, if not conservative, estimate of the effect of surface area on the tubular reactor results.

The exponential fits to the experimental data in Figure 5.8 reveal an interesting trend in the tubular and packed reactor results. The extrapolated exponential curves for the packed reactor intersect the extrapolated curves for the tubular system at concentrations corresponding approximately to the feed concentrations. Similarly, both points of intersection occur at the same residence time (~2.0 s), which corresponds to the induction time observed in the tubular reactor. Taken together, these results suggest that the induction time in the packed reactor is almost identical to that in the tubular reactor. This behavior is unexpected, since the inhibitory effect of the additional surface would presumably tend to lengthen appreciably the chemical induction time. Instead, the experimental evidence indicates that the heterogeneous reactions do not affect the kinetic behavior until the decay of hydrogen begins. This lag in heterogeneous influence is conceivable if the surface reactions are slow; during the induction period, when radical concentrations are low and rising, the rate of heterogeneous termination may be small relative to homogeneous branching. When the radicals reach their maximum or steady-

state levels, the heterogeneous rates may be sufficiently fast that they perturb (decrease) these ultimate radical concentrations. In this scenario, the induction period would be relatively unaffected by added surface area, yet the decay constant would be decreased by the reduced steady-state radical pool.

The conclusion regarding the importance of surface reactions is strictly valid only for the conditions of the packed-reactor experiments, and may not necessarily be valid under all conditions. For example, gas-phase studies of hydrogen oxidation (von Elbe and Lewis, 1937; Kassel, 1937; Gibson and Hinshelwood, 1928) found that surface reactions became important for temperatures below about 520 to 550 °C, as evidenced by a pronounced change in the activation energy for the overall reaction. No change in activation energy was found in the present study, indicating that the role of surface reactions (or lack thereof) was most likely constant over the conditions of this study.

In summary, experimental evidence strongly suggests that the hydrogen oxidation reaction has a negligibly small heterogeneous contribution in the tubular reactor. Data obtained in the tubular reactor for hydrogen oxidation can therefore be treated as purely homogeneous, and elementary reaction models for these data need not incorporate surface reactions. Future experiments should, however, attempt to verify the unimportance of surface effects using a larger-diameter reactor with a reduced surface-to-volume ratio.

Chapter 6

Elementary Reaction Modeling of Hydrogen Oxidation

6.1 Motivation

Hydrogen oxidation in supercritical water occurs through a complex mechanism consisting of many elementary reactions. The mechanism for hydrogen oxidation is a subset of all other oxidation mechanisms. An understanding of this simpler mechanism can therefore yield insight into more complex mechanisms. The development of a reaction mechanism, however, first requires a hypothesis regarding the nature of its constituent reactions.

For our typical range of operating conditions, 246 bar and 400 to 700 °C, reactions in supercritical water most likely proceed as free-radical, gas-phase reactions. Above 500 °C and at 250 bar, the transport properties of supercritical water are close to those of a gas. The self-diffusion coefficient of water at these conditions is approximately 5×10^{-3} cm^2/s and can be modeled as a dilute polar gas (Lamb *et al.*, 1981). In the range 400 to 700 °C, the viscosity ranges from 0.03 cp to 0.04 cp (Sengers and Watson, 1986), which is 25 times lower than the viscosity of room temperature water and very similar to that of a low-temperature dilute gas. The dielectric constant of supercritical water in our operating regime is greatly reduced from its value at room temperature, where ionic reactions predominate. At 500 °C and 250 bar, the dielectric

constant of water is 1.2 (Franck *et al.*, 1990), compared to its value of 78 at 25 °C and 1 bar. Similarly, the ionic dissociation constant of water (K_w) drops from 10^{-14} at subcritical conditions to approximately 10^{-23} at 450 to 600 °C (Marshall and Franck, 1981), indicating that water only weakly dissociates and poorly solvates ions in the supercritical state. Antal *et al.* (1987) conducted experiments on the dehydration of ethanol in supercritical water; for conditions where $K_w \approx 10^{-14}$, ethanol underwent rapid dehydration to ethylene in the presence of dilute Arrhenius acids, indicating an ionic mechanism. Under conditions where the ionic dissociation constant was much less than 10^{-14} (approximately10^{-20} or lower), the dehydration was not catalyzed by acids and instead a wide variety of hydrocarbons and carbon oxides, characteristic of free-radical reactions, was produced. In the non-ionic, gas-like supercritical-water region, where we have carried out our experiments, reaction intermediates are likely to be free radicals rather than ionic species. The oxidation of hydrogen in supercritical water was therefore modeled using a free-radical, gas-phase reaction mechanism.

6.2 Modeling Methodology

Many gas-phase, free-radical oxidation mechanisms are available in the literature. Typical H_2-O_2 mechanisms contain 8 species and about 20 reversible reactions, and give expressions for the forward reaction rate constants. These rate constants may be adjusted for our high-pressure environment by techniques such as RRKM theory. Reverse rate constants k_r in our models were calculated from the forward rate constants k_f using the equilibrium constant in concentration units, K_c:

$$k_r = k_f / K_c \tag{6.1}$$

The equilibrium constant K_c can in turn be calculated rigorously from the equilibrium constant in pressure units, K_p:

$$K_c = K_p K_\phi (ZRT)^{-\Sigma \nu_i} \tag{6.2}$$

where T is the temperature, R the gas constant, ν_i the stoichiometric coefficient of species i, and Z is the compressibility factor of the reacting mixture, assumed for our dilute mixtures to be that of pure supercritical water and obtained from steam tables (Haar *et al.*, 1984). Values for Z for supercritical water at the conditions of these experiments (495 to 600 °C, 118 to 263 bar) are about 0.8 or higher, so the correction resulting from the inclusion of this term is relatively minor. K_p can be calculated straightforwardly from thermodynamic data available from, for example, the JANAF Thermochemical Tables (Chase *et al.*, 1985) or other literature sources such as Yetter *et al.* (1991a). K_ϕ accounts for non-idealities and is defined as

$$K_\phi = \prod \phi_i^{\nu_i} \tag{6.3}$$

where the ϕ_i are the fugacity coefficients of each species in the mixture. For very dilute mixtures and temperatures well above the critical point, the equation of state of Christoforakos and Franck (1986) indicates that the fugacity coefficients of stable species are not significantly different from one (Webley, 1989), and for our model we have assumed that $K_\phi = 1$ for all reactions. The error introduced by this assumption is likely to be small (~30%) relative to the uncertainty associated with the rate constant values.

The various versions of the models, including forward and reverse reactions, were integrated using the Acuchem software (Braun *et al.*, 1988). Since our system was modeled as an isothermal, radially well-mixed, plug-flow reactor, only time-dependent

kinetic equations appeared in the model; no spatial transport equations were included. Model predictions were obtained by applying the experimental initial conditions to the model and then comparing the predicted numerical results with those observed experimentally. Sensitivity gradients, reaction fluxes, and pathway analyses were obtained from the SENKIN sensitivity software (Lutz *et al.*, 1988), updated to include the CHEMKIN-II kinetic software (Kee *et al.*, 1989). Duplicate solution of models using both the Acuchem and the SENKIN software confirmed that both packages gave essentially identical results (predicted concentrations the same within 0.1%). A customized driver program supplied the forward and reverse rate constants to the Acuchem and SENKIN software, with the forward rate constants calculated from kinetic rate expressions and the reverse rate constants calculated from Equations 6.1 and 6.2. Equilibrium constants K_p for the reactions were calculated from Gibbs-free-energy-of-formation data and their temperature dependences were correlated to a Gibbs-Helmholtz-type relationship

$$\log_{10} K_p = A + B/T \tag{6.4}$$

for input to the driver program, with A and B fit to data. The use of a customized driver program allowed complete control over all model parameters and simplified the process of model development and modification.

6.3 Model Development

The various hydrogen oxidation models considered in this study are listed and summarized in Table 6.1. The initial mechanism we chose was the H_2-O_2 subset of the methane oxidation mechanism developed by Webley and Tester (1991) for supercritical water oxidation. Their H_2-O_2 submechanism was based on that of Westbrook *et al.*

Model	Sources and Description
WT91	Webley and Tester (1991). Thermodynamics from JANAF Tables (Chase *et al.*, 1985).
YDR91	Yetter *et al.* (1991). Third-body-assisted reactions adjusted to include efficiency of H_2O as the exclusive third-body species, following recommendations of original sources. Thermodynamics of Yetter *et al.* (1991a).
YDR91A	Same as YDR91, but rate of $OH + OH \rightarrow H_2O_2$ set to high-pressure limit given by Brouwer *et al.* (1987), and with rate of $HO_2 + HO_2 \rightarrow H_2O_2 + O_2$ given by Hippler *et al.* (1990). Thermodynamics of Yetter *et al.* (1991a).
YDR91J	Same as YDR91A, but with thermodynamics from JANAF Tables (Chase *et al.*, 1985).
YDR91S	Same as YDR91A, but including reactions for surface destruction of HO_2 and H_2O_2. Heterogeneous reaction rates estimated from Hoare *et al.* (1967) and Hart *et al.* (1963). Thermodynamics of Yetter *et al.* (1991a).

Table 6.1 Considered Elementary Reaction Models for Hydrogen Oxidation in Supercritical Water.

(1982), but with many rate constants updated to reflect newer data. Explicit rate expressions are given in the original article (Webley and Tester, 1991). In addition, for consistency with their model, we used species thermodynamics from the JANAF Tables (Chase *et al.*, 1985). Results for this and subsequent models are shown in Figure 6.1 in the form of a first-order Arrhenius plot, where the modeling results are compared with the experimental data from Table 12.3. The Webley and Tester model (denoted WT91 in Figure 6.1) demonstrates quite good agreement with the experimental data. Unfortunately, because many of the rate constants had been modified away from their original values reported by Westbrook *et al.* (1982), the WT91 model was not based on a rigorously validated, gas-phase mechanism. In the interests of initiating a hierarchical modeling effort (Westbrook and Dryer, 1984), we sought to begin with a validated mechanism for gas-phase hydrogen oxidation, and then modify the model systematically to identify those reactions which need to be corrected to achieve reasonable agreement between the model and data. Once a hydrogen oxidation model has been validated for our conditions, more complex models can be developed.

The validated, gas-phase model we chose was the comprehensive carbon monoxide oxidation mechanism of Yetter, Dryer and Rabitz (1991a), which has recently been successfully tested for hydrogen oxidation (Vermeersch, 1991). Initially, no modifications to the model were made, other than to set the values of the third-body chaperone efficiencies to those for water, using the water chaperone efficiencies recommended by the original sources for the rate constants. Species thermodynamics were given by Yetter *et al.* (1991a). We should note here that Yetter's thermodynamics differ from the JANAF thermodynamics only in the value for the heat of formation for the hydroperoxy radical at 298 K, $\Delta H_{f,298}(HO_2)$. JANAF lists a value of 2.09 kJ/mol, while Yetter *et al.* use the value of 12.55 kJ/mol recommended by Hills and Howard

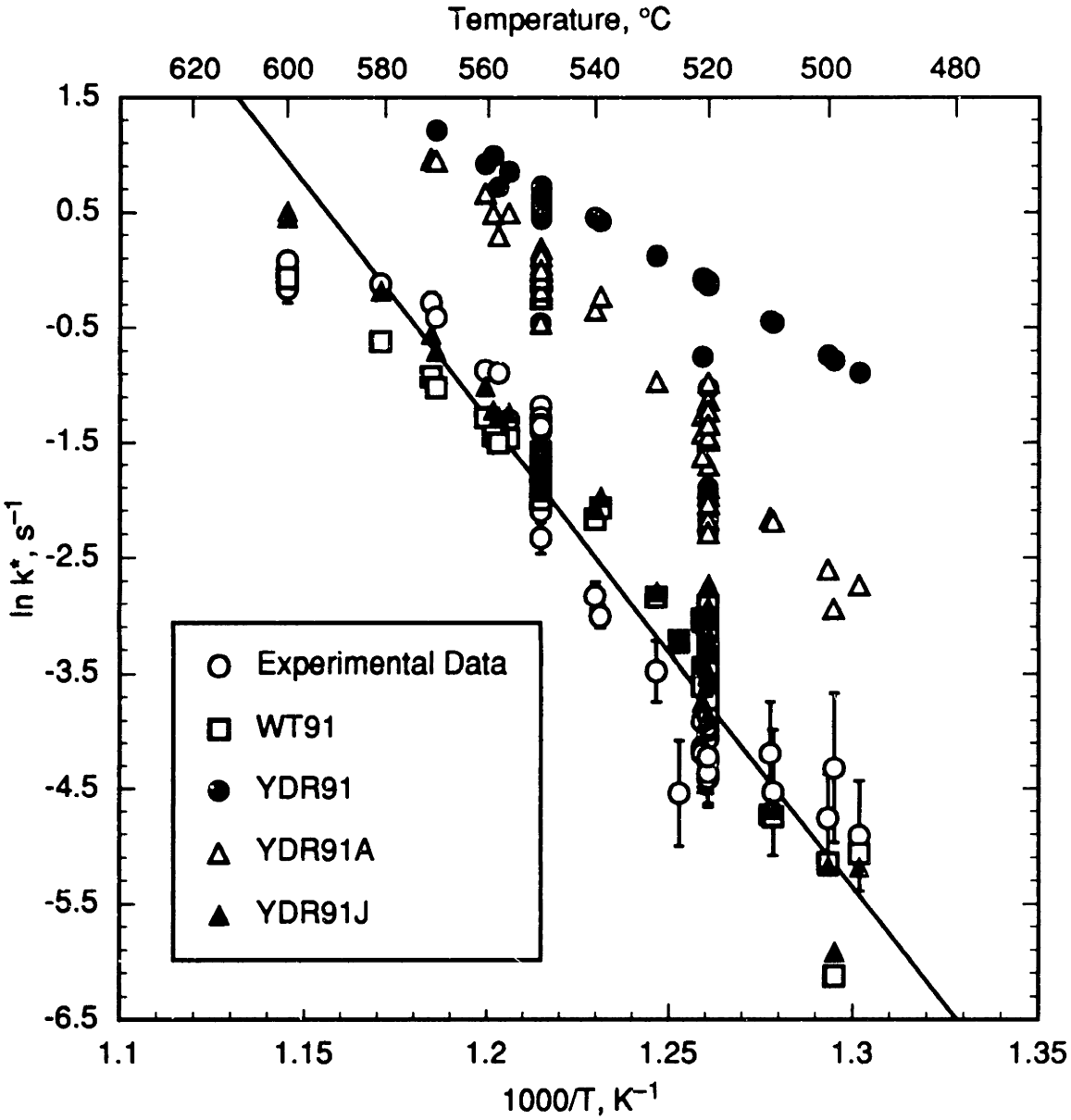

Figure 6.1 **First-Order Arrhenius Plots for Experimental Data and Elementary Reaction Models.** Line is best fit to experimental data (Equation 5.11). See text and Table 6.1 for description of models.

(1984). The essentially unmodified model of Yetter *et al.* is denoted in Table 6.1 and Figure 6.1 as YDR91. The YDR91 model drastically overpredicts reaction rates, to the extent that one or both reactants are consumed almost completely in every instance. Furthermore, the global activation energy of the model is distinctly lower than that observed experimentally. It is clear that more extensive modifications of the YDR91 model are necessary in order to apply it to our high-pressure conditions.

Based on preliminary sensitivity analyses of the WT91 and YDR91 models, two reaction rate constants were modified in the YDR91 model. First, the recombination of hydroxyl radicals to hydrogen peroxide

$$OH + OH \rightarrow H_2O_2 \tag{6.5}$$

was assumed to be in the high-pressure limit and the bimolecular rate constant of Brouwer *et al.* (1987) was used. This assumption has been validated by detailed RRKM calculations (see Section 12.2). Second, the newer rate expression of Hippler *et al.* (1990) for the disproportionation of hydroperoxyl radicals

$$HO_2 + HO_2 \rightarrow H_2O_2 + O_2 \tag{6.6}$$

was included in the model, because there is strong evidence of non-Arrhenius behavior (a minimum in the rate constant near our temperature range) for this reaction. The more complex, sum-of-exponentials rate form given by Hippler *et al.* was fit in our temperature range (495 to 600 °C) to a simpler (Arrhenius) rate form for our modeling purposes.

No other rate constants in the mechanism were modified, although several of the remaining reactions may be influenced by pressure. For example, Webley and Tester

(1991) used RRKM calculations (Webley, 1989) to establish that the rate constant for the dissociation of water,

$$H_2O + M \rightarrow OH + H + M \tag{6.7}$$

while potentially subject to falloff behavior, is still in the low-pressure (bimolecular) regime under supercritical water conditions. A similar conclusion was reached by Webley and Tester for the decomposition of hydroperoxyl radicals

$$HO_2 + M \rightarrow H + O_2 + M \tag{6.8}$$

using the model of Troe (1977). Although Webley and Tester incorporated calculated rate expressions for reactions 6.7 and 6.8 in their model, these modifications were omitted because the model was completely insensitive to the precise values of these rate constants and the inclusion of the calculated expressions had no observable effect on the model's predictions. Since the dissociation of triatomic species appears to lie within or near the low-pressure range even under the elevated pressures studied here, it is a reasonable assumption that the dissociation of smaller, diatomic species (OH, H_2, O_2), with even fewer degrees of freedom, will also remain in the low-pressure range. Dissociation or recombination reactions of OH, H_2, and O_2 were therefore taken to be in the low-pressure limit and were not modified to account for any pressure effects. Further examination of the model showed that, in any case, those three reactions proceed very slowly at these relatively low temperatures (400 to 700 °C) and do not participate to any extent in the oxidation mechanism.

The slightly altered mechanism of Yetter *et al.* used in this modeling study, incorporating the high collisional efficiency of water and including the two modified rate

constants mentioned above, contains 8 species and 19 reactions. The final values for the forward rate constant parameters are given in Table 6.2, along with their uncertainty factors and the temperature range for which the parameters are valid. Reactions which have a third body M as a participant are in the low-pressure limit and the rate constant is multiplied by the third-body concentration. For the dilute conditions of the experiments, the third-body species is assumed to be exclusively water.

The mechanism of Table 6.2 was used with the thermodynamics of Yetter *et al.* to model our data, with the results shown in Figure 6.1 and denoted YDR91A. The modified model shows significant improvement over the YDR91 model, yet reaction rates are still too fast. Setting the rate of hydroxyl radical recombination to its high-pressure limit drastically reduces predicted reaction rates, but this effect is mitigated somewhat by inclusion in the model of Hippler *et al.*'s rate expression for hydroperoxyl radical disproportionation, which tends to increase reaction rates. Interestingly, the YDR91A model has an overall activation energy that is both significantly higher than that of the YDR91 model and seemingly very near that of the experimental data. Thus the model's overall activation energy must be sensitive to either or both of the activation energies of the modified rate constants. For comparison, the fit version of the Hippler *et al.* rate expression for reaction 6.6 has an activation energy of 17.6 kJ/mol, compared to 5.8 kJ/mol for the rate expression given by Yetter *et al.* Similarly, the high-pressure-limit rate expression for reaction 6.5, when converted by thermodynamics to the dissociation rate constant, has an activation energy of 210 kJ/mol (see Section 12.2), compared to 190 kJ/mol for the activation energy of H_2O_2 dissociation in the YDR91 model. The increase in the activation energies of these two elementary reactions in the YDR91A model translates into a higher activation energy for the overall oxidation reaction.

#	Elementary Reaction	$k = A\,T^b \exp(-E_a/RT)^\dagger$ log A	b	E_a	UF [a]	Temp. Range[b]	Source
1	$H + O_2 \rightarrow OH + O$	14.28	0.0	68.8	2	962–2577	1
2	$O + H_2 \rightarrow OH + H$	4.71	2.67	26.3	1.5	297–2495	2
3	$H_2 + OH \rightarrow H_2O + H$	8.33	1.51	14.35	1.5	250–2581	3
4	$OH + OH \rightarrow O + H_2O$[c]	11.74	0.00149	0.0	2.5	250–2000	4
5	$H_2 + M \rightarrow H + H + M$[d]	19.93	–1.1	436.7	10	600–2000	4
6	$H + OH + M \rightarrow H_2O + M$	23.14	–2.0	0.0	2	1000–3000	4
7	$H + O_2 + M \rightarrow HO_2 + M$	16.50	0.0	–4.18	2	300–2000	5
8	$H + HO_2 \rightarrow OH + OH$	14.23	0.0	3.64	2	298–773	4
9	$H + HO_2 \rightarrow H_2 + O_2$	13.82	0.0	8.91	2	298–773	4
10	$O + HO_2 \rightarrow OH + O_2$	13.24	0.0	–1.67	1.2	200–400	4
11	$OH + HO_2 \rightarrow H_2O + O_2$	16.16	–1.0	0.0	2	298–1400	4
12	$H_2O_2 + OH \rightarrow H_2O + HO_2$	12.85	0.0	5.98	2	298–800	6
13	$HO_2 + HO_2 \rightarrow H_2O_2 + O_2$	12.93	0.0	17.62	2	750–900	7
14	$OH + OH \rightarrow H_2O_2$	13.88	–0.37	0.0	2	200–1500	8
15	$H_2O_2 + H \rightarrow HO_2 + H_2$	13.68	0.0	33.26	5	283–800	4
16	$H_2O_2 + H \rightarrow H_2O + OH$	13.00	0.0	15.02	3	283–800	6
17	$O + H + M \rightarrow OH + M$	18.67	–1.0	0.0	10	—	4
18	$O + O + M \rightarrow O_2 + M$	14.60	0.0	–7.49	1.3	200–4000	4
19	$H_2O_2 + O \rightarrow OH + HO_2$	6.98	2.0	16.61	3	250–800	4

Table 6.2 **Forward Rate Constants Used in Elementary Reaction Models (YDR91A, YDR91J, YDR91S) for Hydrogen Oxidation in Supercritical Water at 246 bar.**

#	Elementary Reaction	$k = A\,T^b \exp(-E_a/RT)$† log A	b	E_a	UF [a]	Temp. Range[b]	Source
20	$HO_2 \xrightarrow{wall} \frac{1}{2}H_2O + \frac{3}{4}O_2$[e]	8.50	0.5	126.8	—	768–873	9
21	$H_2O_2 \xrightarrow{wall} H_2O + \frac{1}{2}O_2$[e]	6.86	0.5	132.5	—	768–873	9

† Units of kJ, mol, cm^3, s, K.
[a] Uncertainty factor for rate constant.
[b] Valid temperature range for the rate constant expression, in Kelvin.
[c] $k = A \exp(bT)$.
[d] M = third body, assumed to be exclusively H_2O. Rates of all third-body-assisted reactions have been adjusted to include the third-body efficiencies for M = H_2O as recommended by the original sources.
[e] Included in model YDR91S only.

Sources:
1) Pirraglia *et al.* (1989).
2) Sutherland *et al.* (1986).
3) Michael and Sutherland (1988).
4) Tsang and Hampson (1986).
5) Baulch *et al.* (1973).
6) Warnatz (1984).
7) Hippler *et al.* (1990); simplified rate form fit from 750 to 900 K.
8) Brouwer *et al.* (1987).
9) Estimated from Hoare *et al.* (1967) and Hart *et al.* (1963), and fit to data.

Table 6.2 Forward Rate Constants Used in Elementary Reaction Models (YDR91A, YDR91J, YDR91S) for Hydrogen Oxidation in Supercritical Water at 246 bar. Continued.

The final modification of the model was the use of JANAF thermodynamics instead of those recommended by Yetter *et al.* As indicated earlier, the two sets of thermodynamic data differ only in the value of $\Delta H_{f,298}(HO_2)$. This difference affects the model predictions only through the values of two rate constants, and represents a much less significant change than might be expected. Predictions of the modified YDR91 model with JANAF thermodynamics (model YDR91J) are shown in Figure 6.1. The YDR91J model predictions closely follow the behavior of the data, and resemble the predictions of the WT91 model. While the YDR91J model does not necessarily give improved predictions over the WT91 model, the YDR91J model is closely related to a validated gas-phase mechanism and has had very few modifications relative to WT91. With fewer modifications made, YDR91J should provide more unambiguous information as to which rate constants are important and may need to be modified for high pressure. All subsequent modeling was accomplished with the YDR91J model. Rate expressions for the forward rate constants in the YDR91J model are listed in Table 6.2 Expressions for the equilibrium constants K_p were fit from 300 to 1000 K to thermodynamic data from the JANAF tables, and the resulting expressions are given in Table 6.3.

6.4 Modeling Results

6.4.1 Model Predictions

Figure 6.2 shows the conversion of hydrogen, as predicted by model YDR91J, compared to the experimental results from Table 12.3. Given the wide range of conditions represented, the model exhibits quite satisfactory agreement with the data, although the model overpredicts low conversions while underpredicting high conversions. The results of the modeling with YDR91J, as shown in Figures 6.1 and 6.2, were regressed to a

#	Elementary Reaction	$\log_{10} K_p = A + B/T^{\dagger}$	
		A	B
1	$H + O_2 \rightarrow OH + O$	1.2895	–3659.9
2	$O + H_2 \rightarrow OH + H$	0.34432	–406.41
3	$H_2 + OH \rightarrow H_2O + H$	–0.6700	3316.0
4	$OH + OH \rightarrow O + H_2O$	–1.0143	3722.4
5	$H_2 + M \rightarrow H + H + M$	5.5635	–22915.1
6	$H + OH + M \rightarrow H_2O + M$	–6.2335	26231.1
7	$H + O_2 + M \rightarrow HO_2 + M$	–5.1663	11423.6
8	$H + HO_2 \rightarrow OH + OH$	1.2366	7425.3
9	$H + HO_2 \rightarrow H_2 + O_2$	–0.3972	11491.6
10	$O + HO_2 \rightarrow OH + O_2$	–0.05285	11085.2
11	$OH + HO_2 \rightarrow H_2O + O_2$	–1.0672	14807.5
12	$H_2O_2 + OH \rightarrow H_2O + HO_2$	–0.1423	7[illegible]5
13	$HO_2 + HO_2 \rightarrow H_2O_2 + O_2$	–0.9247	72[illegible]8
14	$OH + OH \rightarrow H_2O_2$	–7.3277	11283.9
15	$H_2O_2 + H \rightarrow HO_2 + H_2$	0.5275	4205.88
16	$H_2O_2 + H \rightarrow H_2O + OH$	1.0942	14947.1
17	$O + H + M \rightarrow OH + M$	–5.2192	22508.7
18	$O + O + M \rightarrow O_2 + M$	–6.5087	26168.6
19	$H_2O_2 + O \rightarrow OH + HO_2$	0.8719	3799.47

Table 6.3 Equilibrium Constants for H_2/O_2 Elementary Reactions.

#	Elementary Reaction	$\log_{10} K_p = A + B/T$†	
		A	*B*
20	$HO_2 \xrightarrow{wall} \frac{1}{2}H_2O + \frac{3}{4}O_2$[a]	—	—
21	$H_2O_2 \xrightarrow{wall} H_2O + \frac{1}{2}O_2$[a]	—	—

†Units of bar, K. Source: JANAF Thermochemical Tables (Chase *et al.*, 1985); equilibrium constants fit from 300 to 1000 K.
[a] Irreversible reaction.

Table 6.3 Equilibrium Constants for H_2/O_2 Elementary Reactions. Continued.

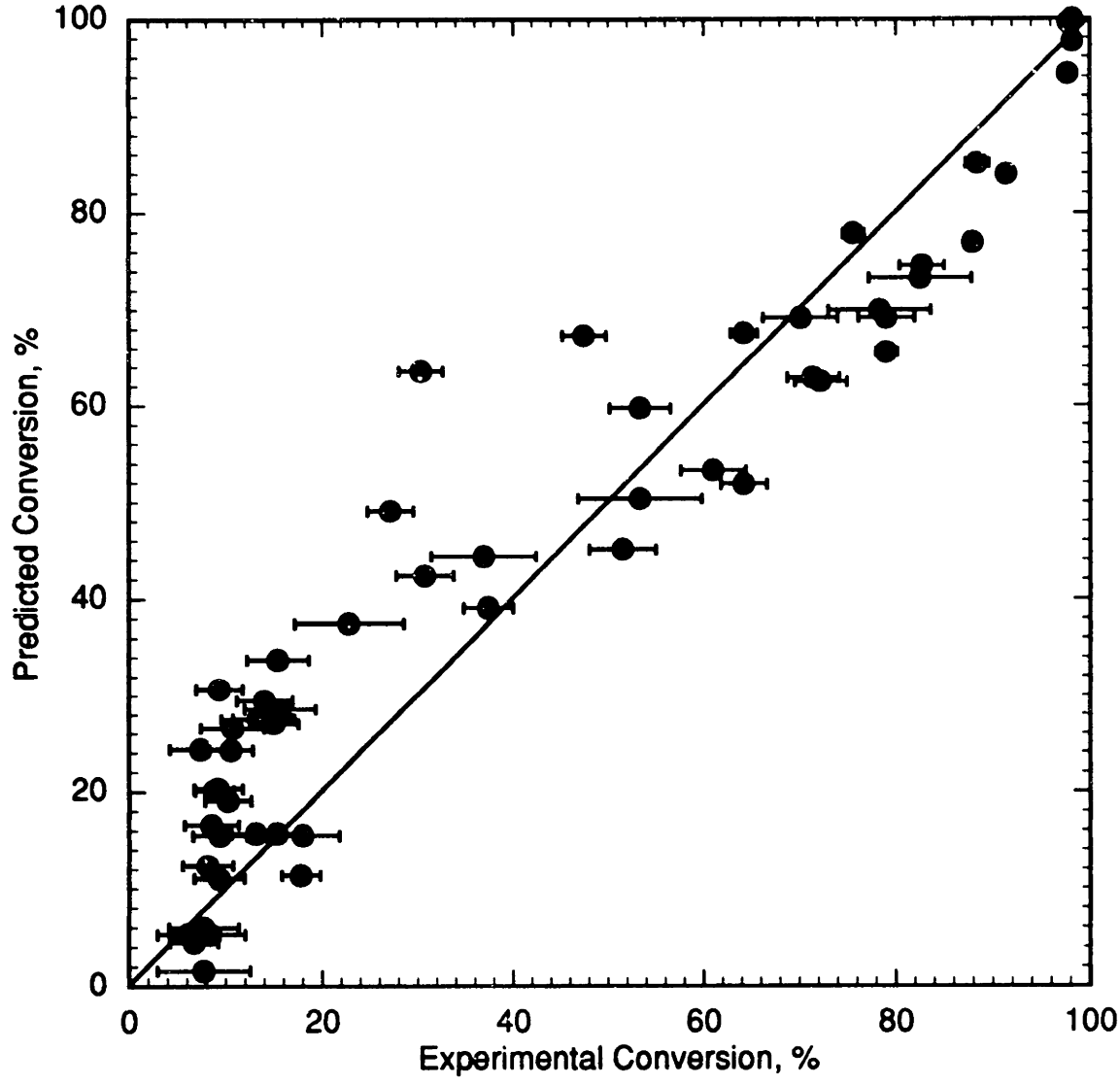

Figure 6.2 **Conversion of Hydrogen Predicted by Elementary Reaction Model YDR91J.**

global rate expression of the form of Equation 5.5, using the same procedure as for the experimental results. The regressed expression was

$$R_{H_2} = 10^{22.7\pm2.7} \exp(-356\pm33/RT)\,[H_2]^{1.11\pm0.12}\,[O_2]^{0.1\pm0.2} \tag{6.9}$$

with the units and confidence intervals corresponding to those given in Equations 5.8, 5.9, and 5.11. Within statistical significance, the reaction orders with respect to hydrogen and oxygen can be set to 1 and 0, respectively, and regression of the data using those values gives

$$R_{H_2} = 10^{20.2\pm1.3} \exp(-329\pm20/RT)\,[H_2] \tag{6.10}$$

The agreement of the elementary reaction model with the experimental results, in terms of both predicted conversions and regressed global parameters, is encouraging, especially since all the model parameters were fixed *a priori* and none was specifically adjusted to fit the data. Both of the overall Arrhenius parameters for the model, as given by Equation 6.10, are within estimation error (at a 95% confidence interval) of the parameters for the data, as given by Equation 5.11. Global reaction orders for the model, including an independence of oxygen concentration, are also in clear accord with the data.

The scatter of the modeling results at 520 and 550 °C in Figure 6.1 indicates that, like the experimental data, the model does not strictly obey a global first-order dependence. Figures 6.3 through 6.5 show the data from Figure 5.3, replotted as hydrogen and oxygen concentration profiles and compared to the predictions of the model for the same initial conditions. The model slightly overpredicts the concentrations

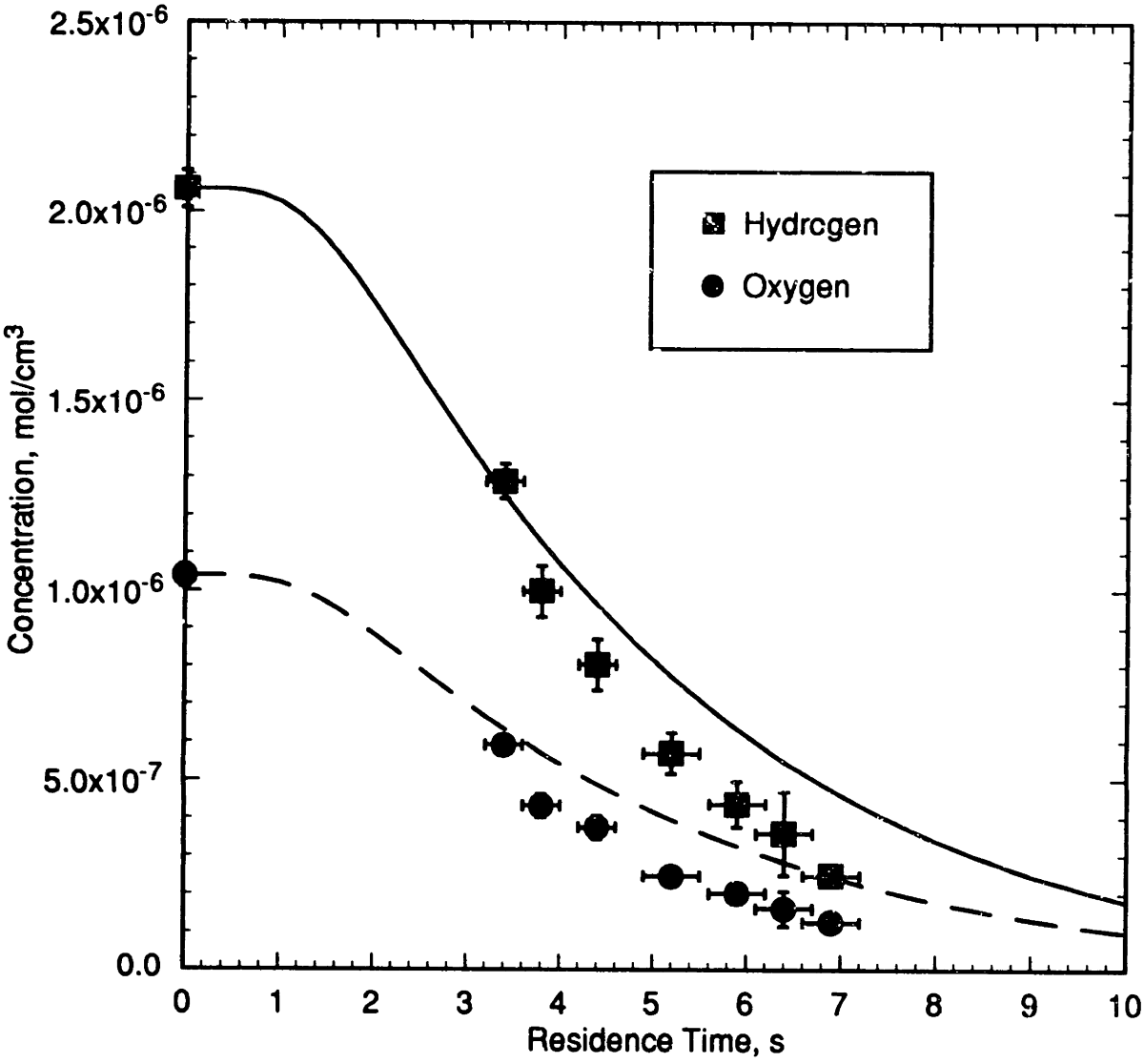

Figure 6.3 **Concentration Profiles for Stoichiometric Hydrogen Oxidation at 550±2 °C.** Symbols: experimental data, $[H_2]_o = (2.06\pm0.02) \times 10^{-6}$ mol/cm^3, $[O_2]_o = (1.04\pm0.01) \times 10^{-6}$ mol/cm^3, $[H_2O] = (4.25\pm0.08) \times 10^{-3}$ mol/cm^3. Curves: predictions of model YDR91J.

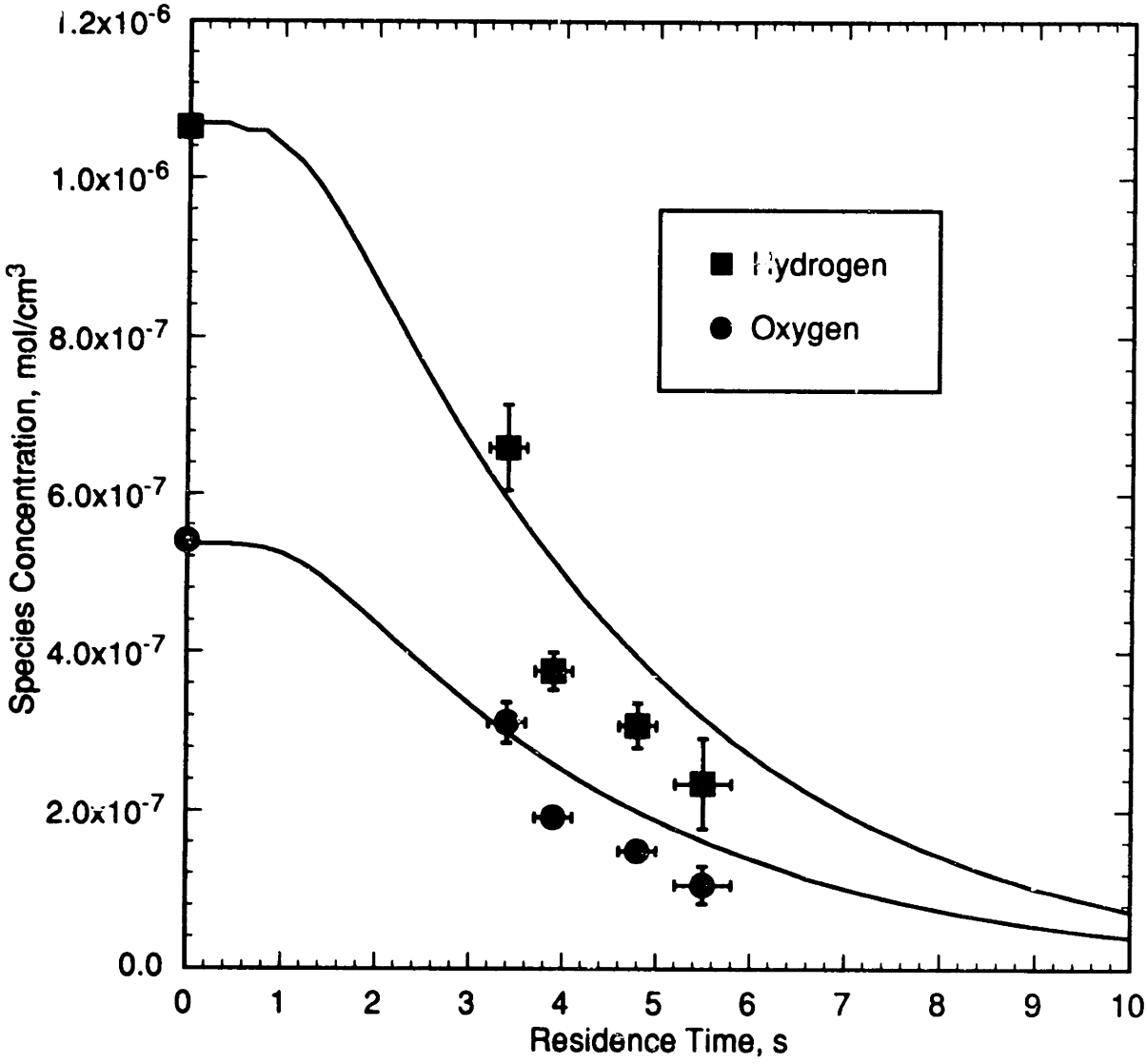

Figure 6.4 **Concentration Profiles for Stoichiometric Hydrogen Oxidation at 550±2 °C.** Symbols: experimental data, $[H_2]_o = (1.065 \pm 0.01) \times 10^{-6}$ mol/cm^3, $[O_2]_o = (0.54 \pm 0.01) \times 10^{-6}$ mol/cm^3, $[H_2O] = (4.25 \pm 0.08) \times 10^{-3}$ mol/cm^3. Curves: predictions of model YDR91J.

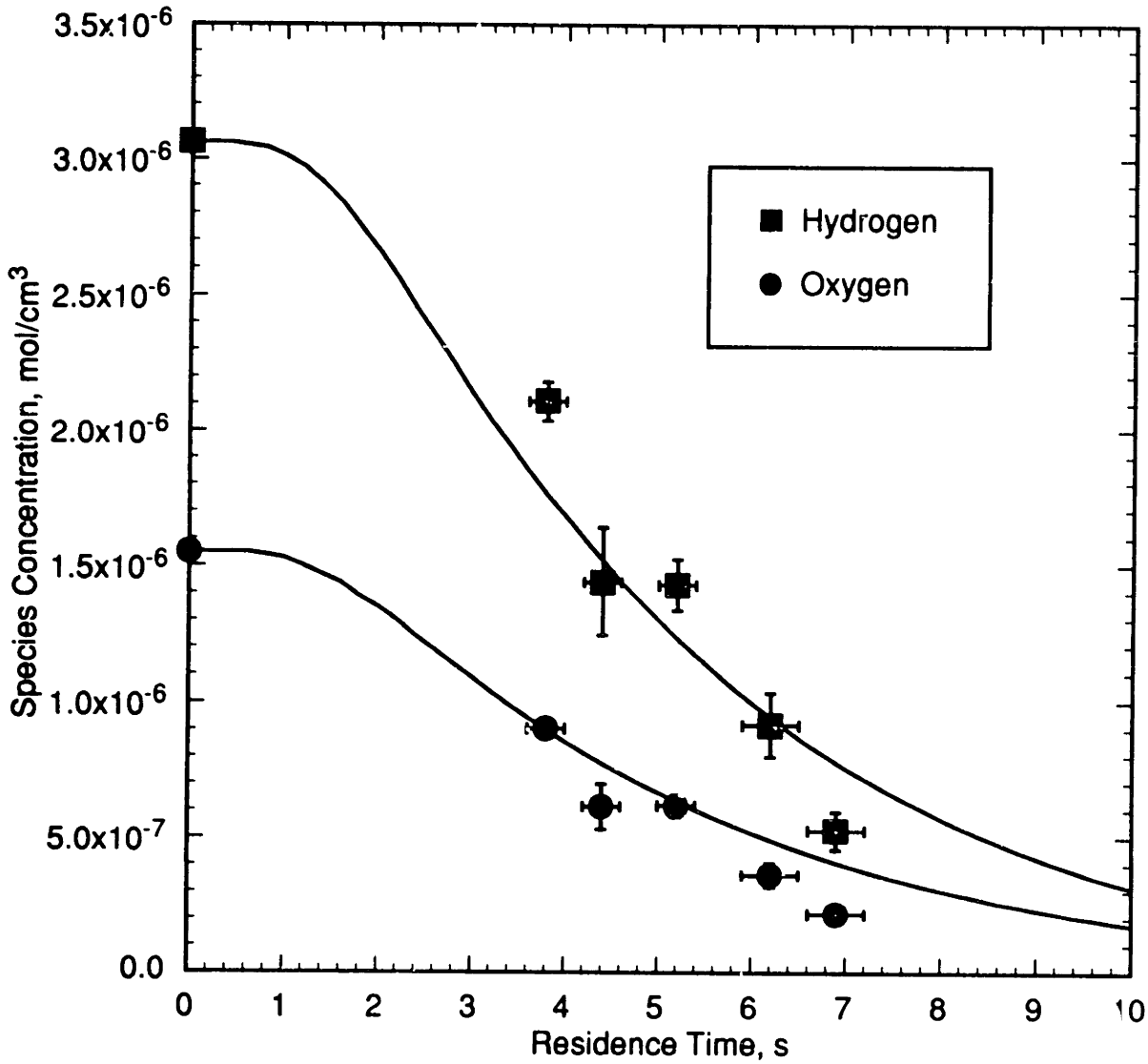

Figure 6.5 **Concentration Profiles for Stoichiometric Hydrogen Oxidation at 550±2 °C.** Symbols: experimental data, $[H_2]_o = (3.06 \pm 0.03) \times 10^{-6}$ mol/cm^3, $[O_2]_o = (1.55 \pm 0.02) \times 10^{-6}$ mol/cm^3, $[H_2O] = (4.25 \pm 0.08) \times 10^{-3}$ mol/cm^3. Curves: predictions of model YDR91J.

over the range of the data, although the model clearly exhibits an induction time similar to the data. The presence of an induction time in the model implies that the model would exhibit the same type of variation in k^* with residence time as was observed in the data in Figure 5.2. Two inaccuracies of the model are apparent in Figures 6.3 through 6.5: first, the decay constant k' for the model is somewhat lower than for the data; and second, the effective induction time τ_{ind} for the model is slightly too short. Following the definitions used earlier in Figures 5.3 and 5.4, values for k' and τ_{ind} can be calculated for the model and compared with those derived from the experimental data. The results are shown in Table 6.4. Note that k' for the model is about 0.27 to 0.31 s^{-1}, compared to 0.40 to 0.44 s^{-1} for the data, and τ_{ind} for the model is 1.6 to 1.8 s, compared to 2.0 to 2.9 s for the data. The combination of these two inaccuracies may result in somewhat fortuitous agreement with the data, since the low k' tends to decrease predicted conversions, while the low τ_{ind} tends to increase predicted conversions. This combination may be the source of the variation noted above in the model's predicted conversions: at low conversions, the shorter τ_{ind} causes the model to overpredict conversion, whereas at high conversion the low k' in the model tends to underpredict conversions.

As discussed earlier, induction times are difficult to measure accurately in an apparatus of our type; other modelers (see, e.g., Yetter *et al.*, 1991a) have avoided the problem of matching induction times by time-shifting their model predictions to match the experimental point of 50% fuel consumption. Were we to perform such time-shifting, however, the model would still not identically match the data, since the kinetic decay constants k' differ somewhat. According to Table 6.4 and as shown in Figure 6.6, the model predicts that k' (the slope of the curves in Figure 6.6) for a stoichiometric mixture should decrease slightly with increasing absolute concentration, while τ_{ind} should increase slightly. These predicted trends are quite subtle and difficult to distinguish

Initial Conditions 10^{-6} mol/cm^3	k', s^{-1} (Exp.)	k', s^{-1} (Model)	τ_{ind}, s (Exp.)	τ_{ind}, s (Model)
$[H_2]_o = 1.06\pm0.02$ $[O_2]_o = 0.54\pm0.01$	0.44±0.11	0.31	2.0±0.6	1.6
$[H_2]_o = 2.06\pm0.02$ $[O_2]_o = 1.04\pm0.01$	0.44±0.02	0.29	2.3±0.2	1.7
$[H_2]_o = 3.06\pm0.03$ $[O_2]_o = 1.55\pm0.02$	0.40±0.07	0.27	2.9±0.7	1.8

Table 6.4 **Comparison of Experimental and Predicted Induction Times and Kinetic Decay Constants for Hydrogen Oxidation at 550 °C and 246 bar.**

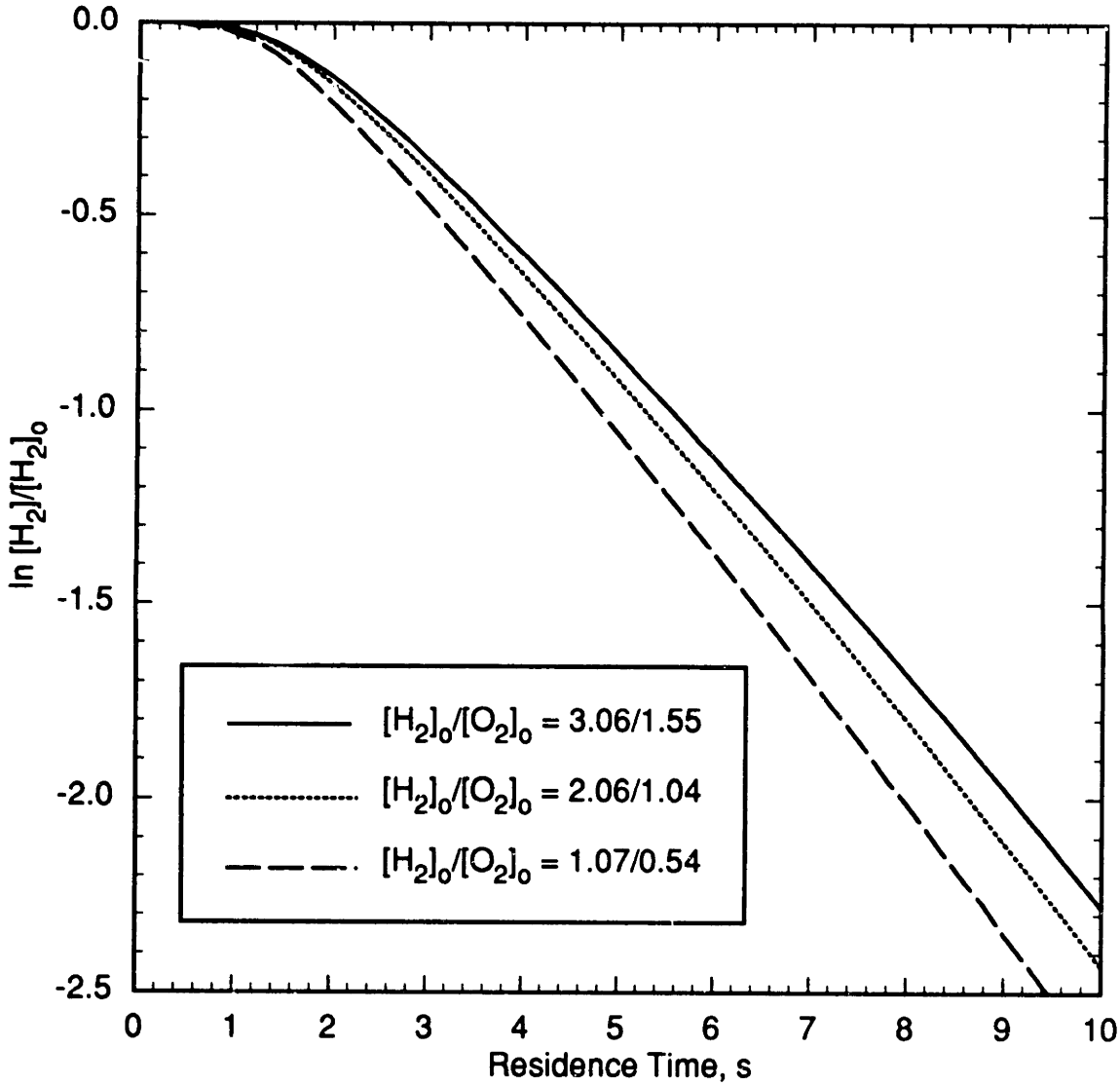

Figure 6.6 **Normalized Hydrogen Profiles from Elementary Reaction Model for Stoichiometric Hydrogen Oxidation at 550 °C.** Initial concentrations (in 10^{-6} mol/cm^3) as given.

experimentally given the scatter in the data; however, the trend of increasing τ_{ind} with increasing concentration appears in the data as well. Note that the model, like the data, does not show a strong dependence of the induction time on the oxygen concentration, contrary to gas-phase observations (Schott and Kinsey, 1958; Skinner and Ringrose, 1965). Despite the admitted shortcomings of the model, the agreement between the YDR91J model and the experimental data must be considered quite good, and certainly more encouraging than the results of earlier elementary reaction modeling efforts.

As noted in Section 5.5, the presence of an induction time in the hydrogen oxidation reaction complicates efforts to derive a simple, global kinetic expression of the form of Equation 5.5, since Equation 5.5 assumes that the reaction begins at $t = 0$. One can imagine an alternative global rate form that incorporates an induction time (Yetter *et al.*, 1986), e.g.,

$$\begin{aligned} \frac{d[H_2]}{dt} &= 0 \qquad t < \tau_{ind} \\ \frac{d[H_2]}{dt} &= -k'[H_2] \quad t \geq \tau_{ind} \end{aligned} \tag{6.11}$$

where k' is given by an Arrhenius rate form and τ_{ind} is also given by an Arrhenius-type expression

$$\tau_{ind} = C \exp(+D/RT) \tag{6.12}$$

where we have anticipated that τ_{ind} will decrease with increasing temperature. The decay of hydrogen concentration is assumed to be first-order, in accordance with the reaction orders regressed earlier (see Equations 6.9 and 6.10). No concentration dependence for τ_{ind} was included, based on the data in Table 6.4. In contrast, induction times do

frequently exhibit a concentration dependence (Yetter *et al.*, 1986). Non-linear regression, to the global form of Equations 6.11 and 6.12, of the predicted conversions from the YDR91J model for the experimental conditions, gave for the decay constant and induction time

$$\begin{aligned} \tau_{ind} &= 10^{-9.2\pm1.9} \exp(+148.\pm29./RT)\ \text{s} \\ k' &= 10^{14.8\pm1.3} \exp(-243.\pm21./RT)\ \text{s}^{-1} \end{aligned} \tag{6.13}$$

with the activation energies in kJ/mol. The F-statistic for Equation 6.13 is very high, 1113, indicating that this global form captures the global kinetic behavior of the model very well. Note that the activation energy for the decay constant in Equation 6.13 (243 kJ/mol) is significantly lower than that for the simpler overall rate constant (329 kJ/mol), given by Equation 6.10. On the other hand, the induction time possesses a fairly strong temperature dependence, which compensates for the lower activation energy for k'. Equation 6.13 predicts an induction time of ~0.5 s at 600 °C, which is still significantly longer than the estimated feed mixing time (Section 4.4.2). Attempts to regress the experimental data to the global form of Equations 6.11 and 6.12 were largely unsuccessful, apparently because the scatter in the data is too great to allow unique determination of the four parameters.

There is generally good agreement between the global behavior of the model and that of the data. Thus, in the absence of *in situ* measurements of radical concentrations for verification, we assume that the elementary reaction model is essentially valid and that it can yield qualitative insights into the fundamental mechanisms of hydrogen oxidation in supercritical water. In our examination of the model, we used conditions of 550 °C, $[H_2]_o = 2.0 \times 10^{-6}$ mol/cm^3, $[O_2]_o = 1.0 \times 10^{-6}$ mol/cm^3, and $[H_2O] = 4.25 \times 10^{-3}$

mol/cm^3, representative of the stoichiometric conditions of the experiments at the same temperature. For these conditions, the radical species concentrations rise rapidly initially, and reach a pseudo-steady state within ~1 second, as shown in Figure 6.7. The radical concentrations vary slightly in this steady state, but the species retain a well-defined hierarchy: H_2O_2 is the unstable species present in the highest concentration (~10^{-9} mol/cm^3), followed by HO_2 (~10^{-10} mol/cm^3), OH (~10^{-13} mol/cm^3), and finally H (~10^{-15} mol/cm^3) and O (~10^{-18} mol/cm^3). The dominance of the HO_2 radical is typical of the intermediate temperatures considered in this work (Westbrook and Dryer, 1984; Yetter *et al.*, 1991a). O atom chemistry is completely unimportant in the model because temperatures are too low. One feature of the predicted concentration profiles is noteworthy: earlier workers defined the induction time for the H_2-O_2 reaction as either the point of maximum OH concentration or the point where the OH concentration reaches 10^{-9} mol/cm^3 (Schott and Kinsey, 1958; Skinner and Ringrose, 1965). In our model, however, the OH concentration never satisfies either criterion, further reinforcing our conclusion that a fundamentally different mechanism controls the induction time under our conditions.

Model predictions are dominated by seven very fast reactions, whose net rate profiles are shown in Figure 6.8. The rates of some of the reactions are indistinguishable on the scale of Figure 6.8, and have been plotted as a single line. The rates shown are net rates, defined as the rate in the forward direction minus the rate in the reverse direction. The remaining reactions in the model all have net rates that are several orders of magnitude slower than these seven. Since the seven fast reactions account for almost the entire reaction flux pathway, the nineteen-reaction mechanism can be approximated by the following abbreviated mechanism:

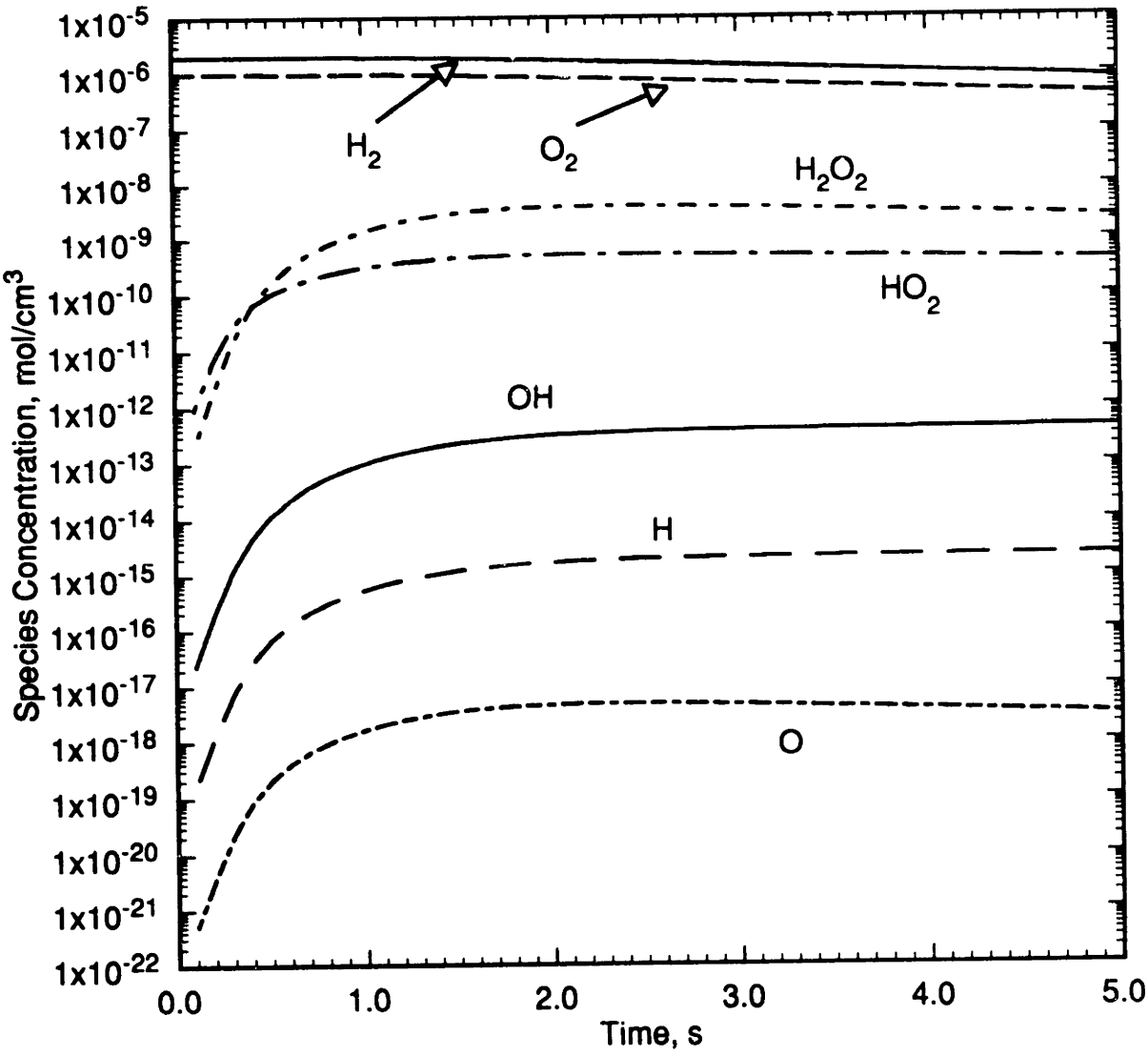

Figure 6.7 **Predicted Species Concentration Profiles from Elementary Reaction Model YDR91J.** Conditions: 550 °C, $[H_2]_o = 2.0 \times 10^{-6}$ mol/cm^3, $[O_2]_o = 1.0 \times 10^{-6}$ mol/cm^3, $[H_2O] = 4.25 \times 10^{-3}$ mol/cm^3.

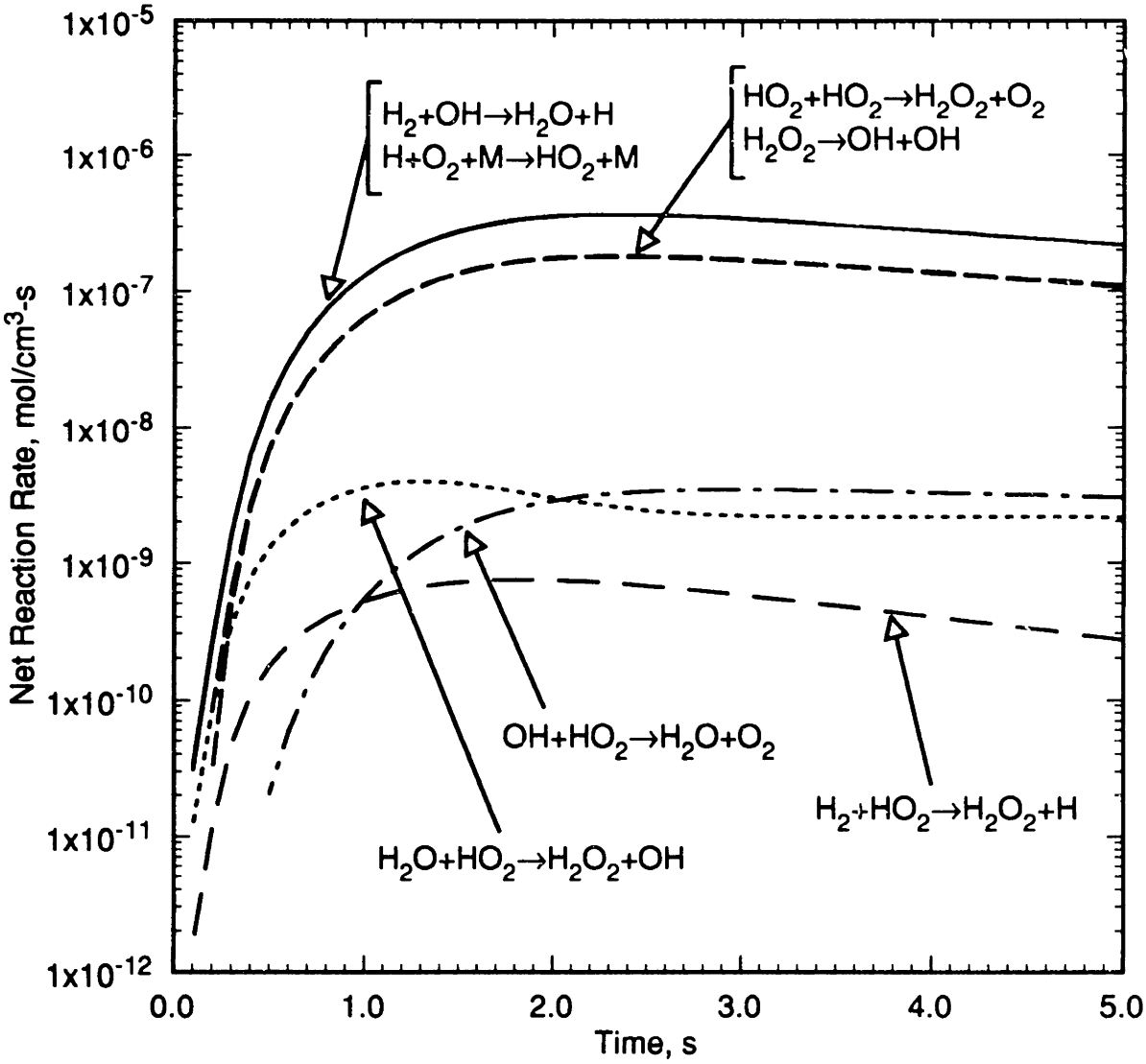

Figure 6.8 **Net Reaction Rate Profiles for Major Reactions as Predicted by Elementary Reaction Model YDR91J.** Conditions: Same as in Figure 6.7.

$$H_2 + OH \rightarrow H_2O + H \qquad (R3)$$

$$H + O_2 + M \rightarrow HO_2 + M \qquad (R7)$$

$$HO_2 + HO_2 \rightarrow H_2O_2 + O_2 \qquad (R13)$$

$$H_2O + HO_2 \rightarrow H_2O_2 + OH \qquad (-R12)$$

$$H_2O_2 \rightarrow OH + OH \qquad (-R14)$$

$$OH + HO_2 \rightarrow H_2O + O_2 \qquad (R11)$$

$$H_2 + HO_2 \rightarrow H_2O_2 + H \qquad (-R15)$$

where the reaction numbers refer to those given in Table 6.2. Primary oxidation of H_2 occurs through (R3), with the H formed in (R3) being rapidly converted to HO_2 in (R7). The large contribution of (R7) is consistent with conventional wisdom regarding hydrogen oxidation (Westbrook and Dryer, 1984; Yetter *et al.*, 1991a), which states that (R7) becomes very important for relatively low temperatures and high pressures. HO_2 radicals can then react via (R13) or (–R12) to form H_2O_2. Of (R13) and (–R12), (–R12) is slower, and the major flux is through (R13). In either case, the H_2O_2 formed undergoes rapid decomposition in (–R14) to OH radicals, which complete the cycle by reacting with H_2 in (R3). (–R15) provides an alternate (but minor) pathway for the oxidation of H_2, and acts as a chain-branching pathway in combination with reactions (R7) and (–R14). (R11) is the primary termination reaction.

The role of (–R12) should not be underestimated. Although its rate is slow compared to (R13), (–R12) provides a direct path from HO_2 to OH and is, in combination with (–R14), a highly efficient branching reaction, effectively forming three OH radicals from a single HO_2 radical. In fact, the branching character of (–R12) makes it very important to the "ignition" of the oxidation. Primary initiation of the reaction occurs with the dissociation of water

$$H_2O + M \rightarrow OH + H + M \qquad (-R6)$$

since dissociation of H_2 and O_2 occurs very slowly at these relatively low temperatures. OH radicals formed in (–R6) react with H_2 in (R3), and the H atoms formed in (–R6) and (R3) react to form HO_2 radicals in (R7). (R3), (R7), and (R13) occur very slowly initially, because radical concentrations are low. The scarcity of radicals makes (–R12) the dominant reaction path for HO_2 radicals, and the branching effect of (–R12) rapidly builds up the radical concentrations until the termination step (R11) becomes fast enough to moderate the growth of the radical pool. Figure 6.8 suggests that the model induction time can be roughly characterized by the transition from net branching via (–R12) to propagation, with (–R12) overtaken by (R11). (–R15) is also a branching reaction, but it is slower than the dominant branching path (–R12) and is less efficient, producing (effectively) only two OH radicals from an HO_2.

The oxidation mechanism predicted by the model at supercritical water conditions is therefore very similar to that for the gas-phase oxidation of hydrogen above the third and extended second explosion limits, as postulated in Section 5.3. A similar straight-chain oxidation mechanism has also been postulated by Baldwin and Mayor (1958). The primary distinction between the gas-phase mechanism and the supercritical-water mechanism is the enlarged role of (–R12) as branching step in supercritical water due to the high concentration of water.

6.4.2 Steady-State Analysis

Figure 6.7 shows that radical species concentrations in the model undergo a rapid initial increase during the induction period, but then level off to relatively constant values. The steady-state assumption for unstable species ($dC_i/dt = 0$) is therefore reasonable under

these conditions. The steady-state behavior of the model is further demonstrated in Figure 6.8, where (R3) and (R7) proceed at identical rates, implying a steady state for the H atom. Similarly, the identical rates of (R13) and (–R14) imply a steady state for H_2O_2. Furthermore, the rate of (R13) is one half that of (R7), as would be expected for steady-state behavior of HO_2. Thus, based on these observations, a steady-state analysis can be used to interpret the mechanism.

Since the dominant hydrogen-oxidizing reaction is (R3), the disappearance of hydrogen may be expressed as

$$-\frac{d[H_2]}{dt} = k_3[H_2][OH] \tag{6.14}$$

This expression is analogous to Equation 6.11, with the decay constant k' defined as

$$k' = k_3[OH]_{ss} \tag{6.15}$$

where $[OH]_{ss}$ is the steady-state OH concentration. Since the OH concentration achieves a constant, steady-state value, k' is constant during the decay of the hydrogen, as evidenced by the straight curves in Figure 6.6. According to Equation 6.15, the value and temperature dependence of k' will depend on the values and temperature dependences of k_3 and $[OH]_{ss}$.

The steady-state OH concentration is maintained primarily by the relative rates of (–R14) and (R3), i.e.,

$$[OH]_{ss} = \frac{2k_{-14}[H_2O_2]}{k_3[H_2]} \tag{6.16}$$

with the steady-state H_2O_2 concentration given almost exclusively by the relative rates of (R13) and (–R14)

$$[H_2O_2]_{ss} = \frac{k_{13}[HO_2]^2}{k_{-14}} \tag{6.17}$$

Similar expressions can be written for the species HO_2 and H. Note that the circular nature of these relationships only describes the *relative* steady-state values of these unstable species. The absolute steady-state values are set at the radical concentrations where chain branching is balanced by chain termination, i.e., where (according to Figure 6.8) the rate of (–R12) equals the rate of (R11). This condition implies

$$[OH]_{ss} = \frac{k_{-12}[H_2O]}{k_{11}} \tag{6.18}$$

such that the steady-state OH concentration is directly proportional to the water concentration.

Since the overall oxidation reaction at steady-state proceeds through a straight-chain mechanism, the activation energy of the overall process will depend on the activation energies of the constituent steps, (R3), (R7), (R13), (–R14). Respectively, the activation energies for these reactions are 18, –4, 14, and 216 kJ/mol. The sum of these, 244 kJ/mol, may be thought of as an overall activation energy for the process, and is virtually identical to the activation energy obtained for the kinetic decay constant in Equation 6.13, 243 kJ/mol. The overall process is by far dominated by the temperature dependence of (–R14), the dissociation of hydrogen peroxide. The same conclusion was reached by Baldwin and co-workers (Baldwin and Mayor, 1958; Baldwin *et al.*, 1960) in

their analysis of a similar straight-chain, gas-phase mechanism. The change in activation energy of the model upon changing the rate expression for (R14) (Section 6.3) is therefore understandable. Furthermore, the (negative) activation energy for the induction time in Equation 6.13, 148 kJ/mol, compares favorably with the activation energy for the reaction (–R12), 150 kJ/mol, since (–R12) is the branching step that largely controls the length of the induction time.

6.4.3 Sensitivity Analysis

Sensitivity analyses were performed on the model for the conditions modeled in Figures 6.7 and 6.8. Results are shown in Figure 6.9 for the sensitivity of the predicted hydrogen concentration (mole fraction) to the model rate constants. Reactions not appearing in Figure 6.9 exhibited sensitivities more than an order of magnitude lower than those shown. Normalized sensitivity gradients, $\partial \ln[H_2]/\partial \ln k_i$, are reported. These quantities can be thought of as the fractional change in the hydrogen concentration ($d\ln[H_2] = d[H_2]/[H_2]$) that results from a fractional change in the value of the rate constant k_i; e.g., if $[H_2]$ is directly proportional to k_i, $\partial \ln[H_2]/\partial \ln k_i = 1$. The SENKIN software used to generate the sensitivity gradients only calculates the sensitivities for the forward rate constants. Sensitivities for the reverse rate constants were generated by interchanging the forward and reverse reactions and repeating the sensitivity calculation.

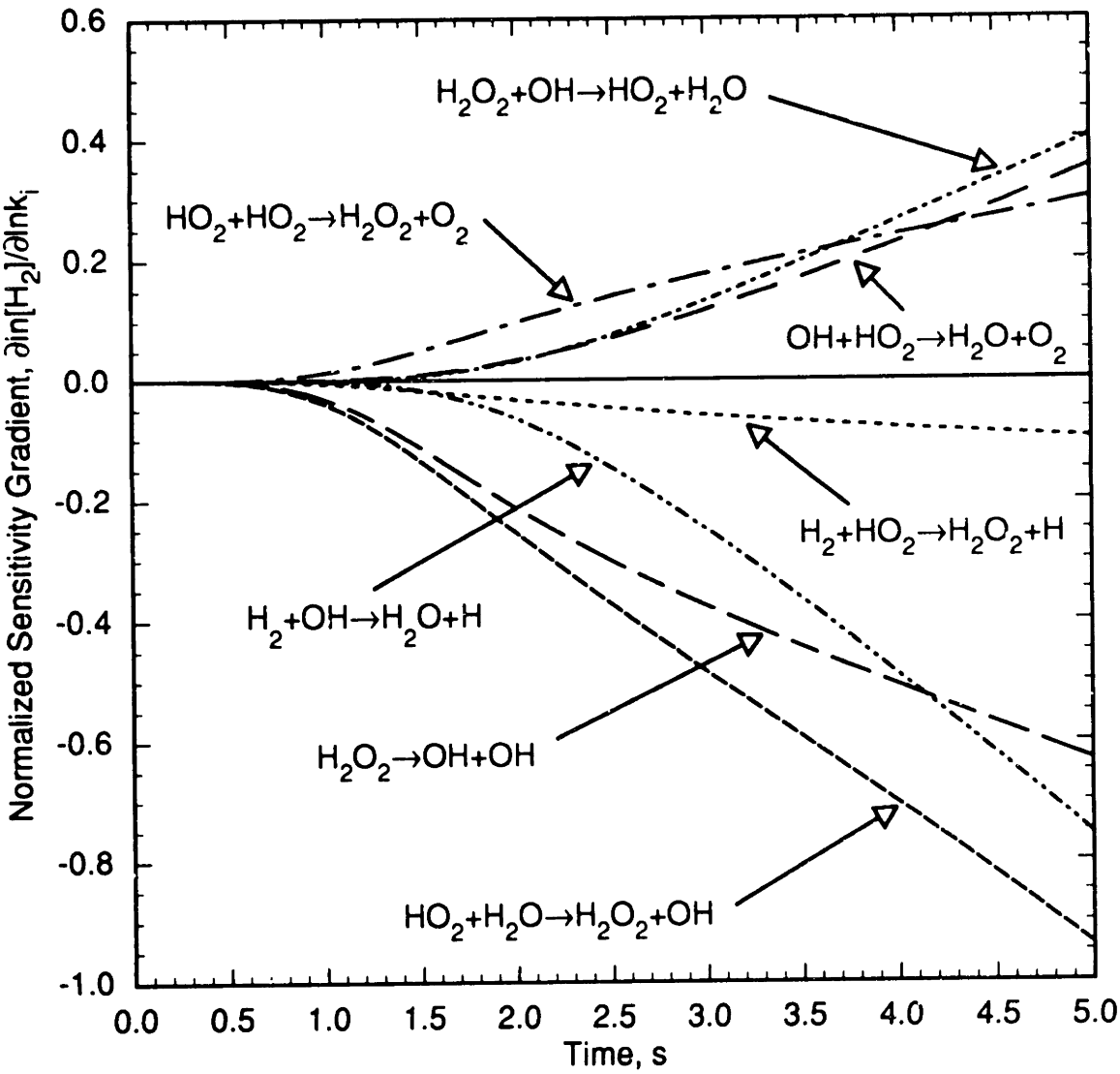

Figure 6.9 **Normalized Sensitivity Gradients for Hydrogen Concentration in Model YDR91J.** Sensitivities of hydrogen mole fraction with respect to rate constants k_i are shown. Conditions: Same as in Figures 6.7 and 6.8.

The high sensitivity of the model to the rate of (R3) is expected, since it is the oxidizing step. The lack of sensitivity to (R7) is somewhat surprising, but indicates that (R3) is the rate-limiting step in the (R3)–(R7) sequence. (R3) is by definition first-order in H_2 and is by far the dominant step for participation of H_2 in the mechanism; thus, the overall reaction is essentially first-order in H_2. By contrast, (R7), the primary step for incorporation of O_2 into the mechanism, is sufficiently fast that the model is unaffected by even large variations in its rate, and the model is globally independent of oxygen concentration, assuming, of course, that sufficient O_2 is present not to limit the reaction. The ultimate effect of changing the oxygen concentration is to change the H-atom concentration; the mechanism thus "regulates" itself such that the overall oxidation rate is unaffected by the O_2 concentration. Results of the analyses of the model are portrayed in Figure 6.10, indicating the cyclic nature of the mechanism and clarifying the roles of the primary elementary reactions.

The sensitivity to (R11) in Figure 6.9 stems from that reaction's importance as a termination step. The positive sensitivity to (R13) is unexpected, since increasing (R13) would presumably increase the oxidation rate and decrease the hydrogen concentration; however, analysis of the model showed that the steady-state OH concentration, which directly affects the oxidation rate, decreases as the rate constant for (R13) is increased. (R13) tends to favor propagation over branching, and an increase in its rate would tend to lower the radical concentration at which propagation overtakes branching via (–R12). Interestingly, the model is sensitive to the forward rate constant for (R12), despite the fact that the net reaction actually proceeds in the reverse direction.

The remaining three reactions in Figure 6.9, (–R12), (–R14), and (–R15), are reverse reactions; rates constants for these reactions are calculated from the forward rate constant and the equilibrium constant. A sensitivity to the reverse rate constant therefore

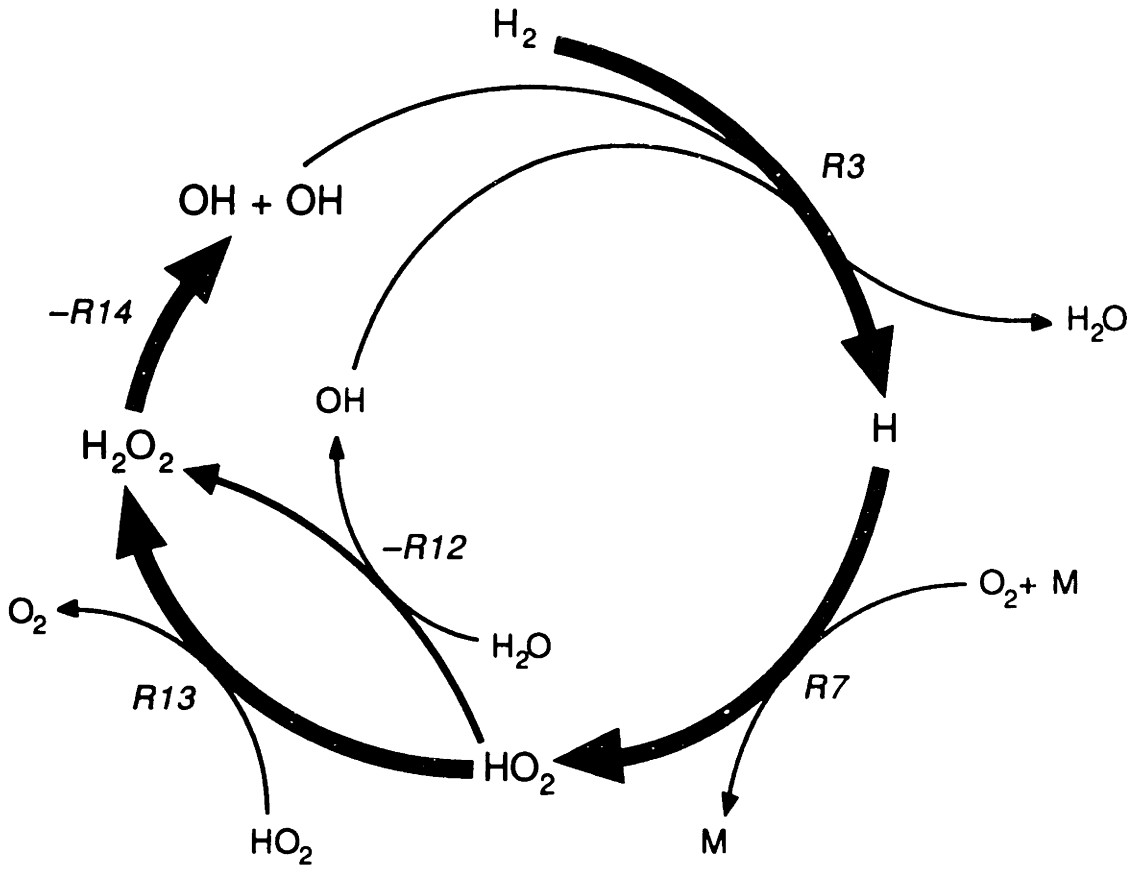

Figure 6.10 **Major Free-Radical Reaction Pathways in Elementary Reaction Model for Hydrogen Oxidation in Supercritical Water.** Arrow thicknesses indicate relative rates of reactions. Reaction numbers refer to Table 6.2.

implies a simultaneous sensitivity to the forward rate constant and the equilibrium constant. The equilibrium constant sensitivities are directly related to the reverse rate constant sensitivities:

$$\frac{\partial \ln[H_2]}{\partial \ln K_{c,i}} = -\frac{\partial \ln[H_2]}{\partial \ln k_{r,i}} \tag{6.19}$$

This relationship is specific to the manner in which the model is formulated and the method of sensitivity analysis; other relationships are obtained for other modeling strategies (Yetter *et al.*, 1985; Dryer, 1991). If the sensitivity to the reverse rate constant is equal to the opposite of the forward rate constant sensitivity, the reaction is at equilibrium (microscopically balanced). For reactions (R13) and (R15), for which the direction of progress is completely in the reverse, the sensitivity to the equilibrium constant results solely from the sensitivity to the reverse rate constant. For (R12), however, there is a simultaneous sensitivity to the forward and reverse rate constants, implying that this reaction is partially equilibrated. (R12) proceeds to a significant extent in both directions, although the dominant direction is the reverse. Whereas the model's sensitivity to the equilibrium constants for (R14) and (R15) could be eliminated if the reverse rate constant could be specified, the model is sensitive to both the forward and reverse rate constants for (R12) and thus the equilibrium-constant sensitivity cannot be eliminated for (R12). Note also that the sensitivity to (–R12) is by far dominant, and retains its dominance to times long beyond the induction time. This extended sensitivity supports the notion that (–R12) not only controls the length of the induction time, but also affects the kinetic decay constant by influencing the ultimate steady-state radical concentrations.

Figure 6.9 shows that the model's sensitivity to the thermodynamics of the HO_2 radical lies in the equilibrium constants for (R12) and, to a lesser extent, (R15). The thermodynamic sensitivity of the model is primarily related to the magnitude of reverse rate constants. In other words, the model's sensitivity to the value of $\Delta H_{f,298}(HO_2)$ is in large part a sensitivity to the rate constants for (–R12) and (–R15). As discussed by Hippler *et al.* (1990) and others, reactions of HO_2 may be significantly affected by the presence of water molecules, and it is not entirely surprising that the rates of those reactions may differ between the gas phase and supercritical water. Unfortunately, there exist no experimental data for (–R12) or for (–R15), and no estimates of the reverse rate constants can be made independently of the thermodynamics.

Only the fast reactions of Figure 6.8 exhibit non-negligible sensitivities; thus there seem to be no slow, rate-limiting reactions that affect the model predictions. Furthermore, the model exhibits virtually no sensitivity to third-body-assisted reactions, indicating that the details of the pressure dependence of those reactions, as predicted by RRKM theory, for example, do not need to be known to any precision. The one exception is the dissociation of hydrogen peroxide, (–R14); since the model is quite sensitive to that rate constant, the validity of the high-pressure-limit assumption has been investigated and verified (Section 12.2). Finally, while sensitivity analysis results are reported only for the YDR91J model, the other models considered exhibited the same general sensitivities shown in Figure 6.9.

The sensitivity analysis of Figure 6.9 reveals sensitivities of a direct model prediction (the hydrogen concentration) to model parameters, but Figures 6.3 through 6.6 suggest that we require information about sensitivities of indirectly predicted "features" of the model such as induction times and decay constants. Yetter *et al.* (1985,1991a) have performed similar "feature sensitivity" analyses for their models. For example, if an

alternative definition for the induction time is used, such that τ_{ind} corresponds to the point where the hydrogen concentration falls to 95% of its original value, the sensitivity of the induction time to the rate constant k_i, $\partial\tau_{ind}/\partial k_i$, is given by (Yetter *et al.*, 1985)

$$\frac{\partial \tau_{ind}}{\partial k_i} = \frac{0.95(\partial[H_2]/\partial k_i)_{t=0} - (\partial[H_2]/\partial k_i)_{t=\tau_{ind}}}{(\partial[H_2]/\partial t)_{t=\tau_{ind}}} \tag{6.20}$$

The sensitivity of the hydrogen concentration to the rate constant at $t = 0$, $(\partial[H_2]/\partial k_i)_{t=0}$,, is by definition zero for all k_i (Yetter *et al.*, 1985; see also Figure 6.9). The rate of H_2 disappearance at τ_{ind}, $(\partial[H_2]/\partial t)_{t=\tau_{ind}}$, is the same for all k_i. The ranking of the induction time sensitivities $\partial\tau_{ind}/\partial k_i$ therefore reduces to a ranking of the simple concentration sensitivities $\partial[H_2]/\partial k_i$ (which are shown in Figure 6.9), evaluated at the induction time (t = ~1.5 s). On the basis of this ranking, Figure 6.9 shows that the induction time is most sensitive to (–R12) and (–R14), followed by (R13). [Note that $\partial\tau_{ind}/\partial k_i$ will have the same sign as $\partial[H_2]/\partial k_i$ because $\partial[H_2]/\partial t$ is negative.] These sensitivities are not surprising, since the branching of (–R12)–(–R14) is the route for formation of the radical pool; the faster these steps occur, the faster the radical pool is established and the shorter the induction time. Note that (R13) exhibits a sensitivity of opposite sign, since it is a chain-propagating step which does not increase the size of the radical pool; hence an increase in its rate slows the pool growth and lengthens the induction time. More surprising is the lack of sensitivity of the induction time to the oxidation step (R3), considering that (R3) performs an integral role in the radical pool generation by converting OH to H for subsequent conversion to HO_2. Examination of the short-time behavior in Figure 6.8 reveals that (R3) is a fast step during the induction

period, with the (–R12)–(–R14) couple limiting the branching rate. The model is therefore not sensitive to the rate of the oxidizing step during the induction period.

The rates of all six reactions in Figure 6.9 affect both the induction time and the decay constant simultaneously, usually tending to increase k' while decreasing τ_{ind}, or vice versa. This behavior is to be expected, since a given change in the hydrogen concentration will affect the induction time and the decay constant oppositely. Figures 6.3 through 6.6 indicate that both k' and τ_{ind} should be larger in our model; clearly it would be difficult to achieve both requirements by varying only one rate constant. Of the high-sensitivity reactions in Figure 6.9, (–R12), (R12) and (R11) are subject to the highest uncertainty, with (R13) more well-defined following the measurements of Hippler *et al.* (1990). Any or all of these reaction rate constants may be slightly in error; according to Figure 6.9, an error of as little as 50% in any of these rate constants (and in the rate constant for (–R12) in particular) could account for the discrepancy between the observed and predicted kinetic decay constants.

6.4.4 Model Assessment

The model predicts accurately both the global (overall reaction orders and Arrhenius parameters) and the local (concentration profiles) behavior of the experimental data quite well. In this respect the hydrogen oxidation model is a significant improvement over earlier modeling efforts. The shortcomings of the model, in particular the underpredicted induction times and kinetic decay constants, are quite minor, all other things being equal.

The primary uncertainty in the model results from the poor state of knowledge of the rate constant for (–R12) and the concurrent high sensitivity of the model to that particular rate constant. All other forward rate constants have been fairly well characterized experimentally, and species thermodynamics (with the exception of HO_2)

are well known. Rate constants for the (R12) reaction, however, have been measured only in the forward direction (whereas we require the reverse rate constant) and are subject to significant uncertainty. A recent compilation of kinetic data (Baulch *et al.*, 1992) shows that the forward rate constant has only been measured up to 670 K (397 °C), and the values measured at the highest temperatures are scattered over a factor of three. Furthermore, scatter in the data at lower temperatures creates significant uncertainty in the activation energy that is magnified when extrapolating to higher temperatures. Only one additional experimental data point for this reaction has become available since the compilation of Warnatz (1984), from which the rate constant in our model was taken: even so, the recommended rate expression from Baulch *et al.* is almost identical to Warnatz's. Hippler *et al.* (1990) have obtained a value of 3×10^{12} cm^3 mol^{-1} s^{-1} for the forward rate constant near 1100 K, which is about 30% lower than the value predicted by Warnatz's recommended rate expression. These recent measurements provide some evidence that the recommended values for the forward rate constants (and thus the reverse rate constants) may be too high.

The uncertainty in the rate constant for (R12) is compounded by the uncertainty in the heat of formation of the hydroperoxyl radical. Our use of the JANAF value for $\Delta H_{f,298}(HO_2)$ should not be construed as verification of its correctness. Rather, the use of the JANAF value was the only possible means for achieving reasonable agreement between the model and the data, and thus may be fortuitously convenient. There is increasing evidence, however, that the JANAF value for $\Delta H_{f,298}(HO_2)$, 2.09 kJ/mol, is too low. Hills and Howard (1984) present convincing experimental evidence for a value of 12.55 kJ/mol, the value chosen by Yetter *et al.* (1991a). Kaufman and Sherwell (1983) adopt a similar value (12 kJ/mol) in their recommendation. Shum and Benson (1983) reviewed the literature for $\Delta H_{f,298}(HO_2)$, and suggest a value of 14.6 kJ/mol. Finally,

Francisco and Zhao (1991) have recently performed *ab initio* calculations and derived an even higher value for $\Delta H_{f,298}(HO_2)$, 21.4 kJ/mol. In the face of this mounting evidence, it seems clear that the JANAF $\Delta H_{f,298}(HO_2)$ value should not be trusted.

Were we to adopt the value of $\Delta H_{f,298}(HO_2)$ favored by Yetter *et al.*, the equilibrium constant for (R12) at 550 °C would decrease from 9.9×10^8 to 2.2×10^8, and the rate constant for the reverse reaction would correspondingly increase by a factor of 4.6. The activation energy of the reverse reaction would also be affected, decreasing from 150 kJ/mol to 139.5 kJ/mol. The large change in the reverse rate constant with the newer $\Delta H_{f,298}(HO_2)$ leads to the extensive branching and fast reaction which are inconsistent with experimental data. To counteract the effect of the decreased equilibrium constant, the forward rate constant would have to be in error by almost a factor of five. Even considering the scatter in the data for the forward rate constant, such a large error seems unlikely.

More complex effects may also be present which influence the rate of (R12) in our system. For example, the reaction of OH and HO_2 radicals (R11) proceeds with an unusually fast rate because of long-range intermolecular interactions (Schwab *et al.*, 1989). In the self-reaction of HO_2, (R13), HO_2 can form complexes with H_2O at low temperatures (Hamilton and Naleway, 1976; Hamilton and Lii, 1977; Cox and Burrows, 1979; Sander *et al.*, 1982; Kircher and Sander, 1984; Mozurkewich and Benson, 1985). (R13) is also known to be pressure-dependent at atmospheric or lower pressures, because it proceeds through a stabilized intermediate (Cox and Burrows, 1979; Sander *et al.*, 1982; Mozurkewich and Benson, 1985); the model of Kircher and Sander (1984) indicates a pressure dependence of (R13) at near-ambient temperatures for pressures as high as 1500 bar. The recent experimental data of Hippler *et al.* (1990), however, indicate that this pressure dependence is unimportant for temperatures of interest in

SCWO. Nevertheless, the reactions of HO_2 radicals are often accompanied by non-ideal effects owing to intermolecular forces. The possibility of the formation of complexes between H_2O and HO_2 radicals under SCWO conditions cannot be ruled out; stabilization of HO_2 by complexation could retard the rate of (–R12), as well as affect the equilibrium constant through a highly non-ideal fugacity coefficient for HO_2. Species which exhibit attractive interactions with water, as HO_2 apparently does, will have a fugacity coefficient greater than one. For example, Webley (1989) found that fugacity coefficients of dilute CO_2 in supercritical water at 500 to 600 °C and 246 bar were 1.5 to 2. An abnormally high fugacity coefficient for HO_2 could increase the value of the equilibrium constant for (R12) and thus decrease the rate constant of (–R12). Consideration of these non-ideal thermodynamic effects was beyond the scope of the present study.

Error is possible in the rate constant for (R11) as well. (R11) serves as the primary termination step in the mechanism, and the oxidation reaction achieves its steady-state (chain-propagating) rate when the rate of (R11) becomes high enough to balance branching through (–R12). If the high value of the rate constant for (R12) is chosen, a corresponding increase in the rate constant for (R11) could compensate for the higher branching rate. However, the (R11) rate constant would need to be a factor of ten higher to accomplish this compensation, and such a large error is outside the range of uncertainty for the rate constant. Moreover, the temperature dependence of (R11) may be slightly negative (Baulch *et al.*, 1992), and a factor of ten increase in the rate constant at 550 °C would necessitate a positive temperature dependence. In addition, induction times are drastically shortened by the higher rate of (–R12), and this effect cannot be compensated by a higher rate for (R11). The rate constants of (R11), (R12), and (R13) could ultimately be treated as simultaneously adjustable in light of their uncertainty, but

this procedure was strictly avoided to prevent a degeneration of the modeling into mere curve fitting.

The sensitivity of the hydrogen oxidation model to reactions and thermodynamics of the HO_2 radical result in a significant uncertainty in several critical model parameters. Similar sensitivities, and corresponding model uncertainties, were noted by Yetter *et al.* (1991c) in their gas-phase modeling study of hydrogen ignition. The current lack of extensive experimental data related to the HO_2 radical represents a significant obstacle to the development of lower-temperature and/or higher-pressure oxidation models where reactions of HO_2 are dominant.

Lastly, we assessed the possible role in our model of radical formation during preheating of the reactor feeds. For modeling purposes, the two feeds were assumed to reach chemical equilibrium at the reactor temperature within the preheating tubing (a conservative estimate which gives an upper limit for the predicted radical concentrations), and the model was "seeded" with the feed radical concentrations predicted by the equilibrium calculation. The addition of the calculated radical concentrations to the reactor "feed" had a negligible effect on the predictions of the model. The presence of even small concentrations of radicals in the reactor feed might be expected to decrease induction times, but the ignition mechanism described earlier involves both H_2 and O_2, and cannot occur to any significant extent without both species present. Without H_2 and O_2 present, there is no rapid path for the conversion of OH to HO_2, and chain branching and radical pool growth are not possible.

6.5 Modeling of Pressure and Density Effects

The next step in the development of the elementary reaction model for hydrogen oxidation is the extension of its predictions beyond the typical operating pressure of 246

bar. The experimental data for varying operating pressure and density (550 °C, 118 to 263 bar, 0.033 to 0.083 g/cm^3) from Section 5.3 provide a basis for comparison of the model's predictions and a means for validating the model's ability to describe the effect of operating pressure on the hydrogen oxidation kinetics.

Operating pressure may influence the model predictions in two ways. First, the change in the density of the reaction medium can affect the rates of pressure-dependent reactions by changing the third-body (water) concentration. The model (YDR91J) contains six such reactions. Of those six, three ((R5), (R17), and (R18)) do not participate in the oxidation mechanism at the low SCWO temperatures (400 to 700 °C). (R6) remains in its low-pressure regime at SCWO pressures and participates in the mechanism as an initiation step, but the model predictions are not sensitive to the value of that rate constant. (R7) and (R14) are the only pressure-dependent reactions that participate to a major extent in the model mechanism. (R14), the recombination to hydrogen peroxide, was shown in Section 12.2 to be at its high-pressure limit at 246 bar, and thus independent of pressure. Calculations for lower pressures, however, revealed that (R14) begins to enter its falloff regime as the operating pressure is decreased below 200 bar (see Section 12.2). Since the YDR91J model showed little sensitivity to the value of the rate constant for (R7), the rate constant was taken to be in its low-pressure limit and more detailed calculations were not carried out. In assesssing the pressure dependence of (R7), however, the rate constant for (R7) was found not to be in the low-pressure region at SCWO conditions, but rather in the falloff region (see Section 12.3). Changes in operating pressure may therefore affect the hydrogen oxidation kinetics through the pressure dependences of (R7) and (R14).

The second effect of changing operating pressure is the change in water concentration. Experiments in Section 5.3 were conducted with constant reactant

concentrations, so that any changes in pressure (density) were directly reflected in the concentration of water in the reactor. Since water is a reactant in many of the elementary reactions, changing the operating pressure has the effect of changing the reactant concentration for certain reactions. In particular, the major branching reaction for the mechanism, (–R12), has water as a reactant, and its rate may therefore be directly altered by the change in water concentration with pressure.

The two pressure-dependent rate constants were incorporated into the model by calculating the rate constants at the particular operating pressure using the models described in Sections 12.2 and 12.3. Since the model in Section 12.2 supplies the rate constant for H_2O_2 dissociation, the model was rearranged to include the dissociation of hydrogen peroxide as the forward reaction; i.e., the direction of (R14) was switched:

$$H_2O_2 \rightarrow OH + OH \qquad \text{(R14)}$$

This inversion of the reaction had no effect on the baseline model predictions at 246 bar, since the dissociation and recombination rate constants for hydrogen peroxide were thermodynamically consistent (see Section 12.2). The predicted pressure dependences of (R7) and (R14) are relatively minor, even over the entire pressure range examined in Section 5.3 (118 to 263 bar). For example, the calculated rate constant for (R7) at 550 °C decreases from 6.2×10^{13} $cm^3mol^{-1}s^{-1}$ at 263 bar to 4.9×10^{13} $cm^3mol^{-1}s^{-1}$ at 118 bar, a decrease of about 20%. Similarly, the calculated rate constant for (R14) at 550 °C declines from 44 s^{-1} at 263 bar to 39 s^{-1} at 118 bar, a decrease of about 10%. By comparison, the water concentration at 550 °C changes dramatically over the same pressure range, from 0.083 g/cm^3 (4.6×10^{-3} mol/cm^3) at 263 bar to 0.033 g/cm^3 (1.8×10^{-3} mol/cm^3) at 118 bar, or by nearly a factor of three.

Figure 6.11 shows the predictions of the model, incorporating the two pressure-dependent reactions, compared to the experimental data from Section 5.3 and Table 12.5. The model clearly captures the majority of the pressure dependence seen in the data. However, the pressure dependence of the model is not quite as strong as that of the data: the apparent first-order rate constant (k^*) from the data increases by almost a factor of ten from the lowest pressure to the highest, while the model predicts a more modest increase by a factor of about 4 to 5. Like the data, the model shows a variation of k^* with residence time at a given pressure because of the presence of an induction time. Despite the slight difference in the magnitudes of the pressure dependence, the model represents well the observed variation in kinetics with pressure, and the model may be used to infer the mechanism of the pressure dependence in the data.

The primary source of the model's pressure dependence must be the change in the water concentration. The small variations in the rate constants for (R7) and (R14) are insufficient to account for the pressure dependence of the overall rate seen in Figure 6.11. Instead, the major effect of changing operating pressure is the corresponding change in water concentration, which affects the model predictions by changing the rate of (–R12)

$$HO_2 + H_2O \rightarrow H_2O_2 + OH \qquad (-R12)$$

Sensitivity analysis of the model in Section 6.4.3 showed that (–R12) is the major chain-branching step in the mechanism. Changes in the water concentration will thus directly affect the rate of branching in the model. Figure 6.12 shows the effect of the change in pressure (water concentration) on the model predictions in going from 263 bar to 118 bar. At the lower pressure, the rate of disappearance of hydrogen is clearly lower, owing to the lower OH radical concentration. The steady-state OH concentration is lowered

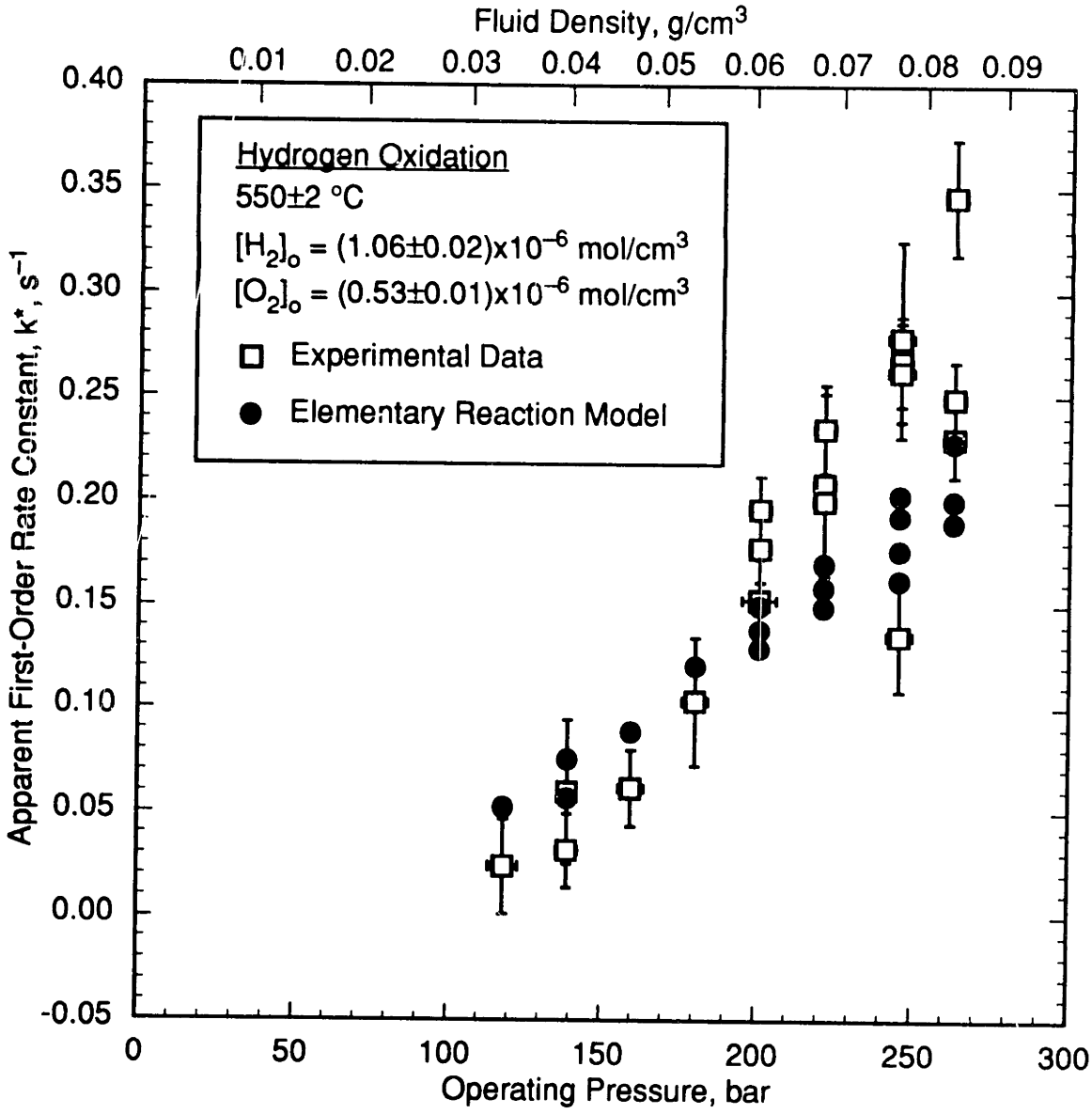

Figure 6.11 **Predicted Effects of Operating Pressure on Apparent First-Order Rate Constant, k^*, for Hydrogen Oxidation.**
□—Experimental data from Figure 5.5;
●—Model predictions.

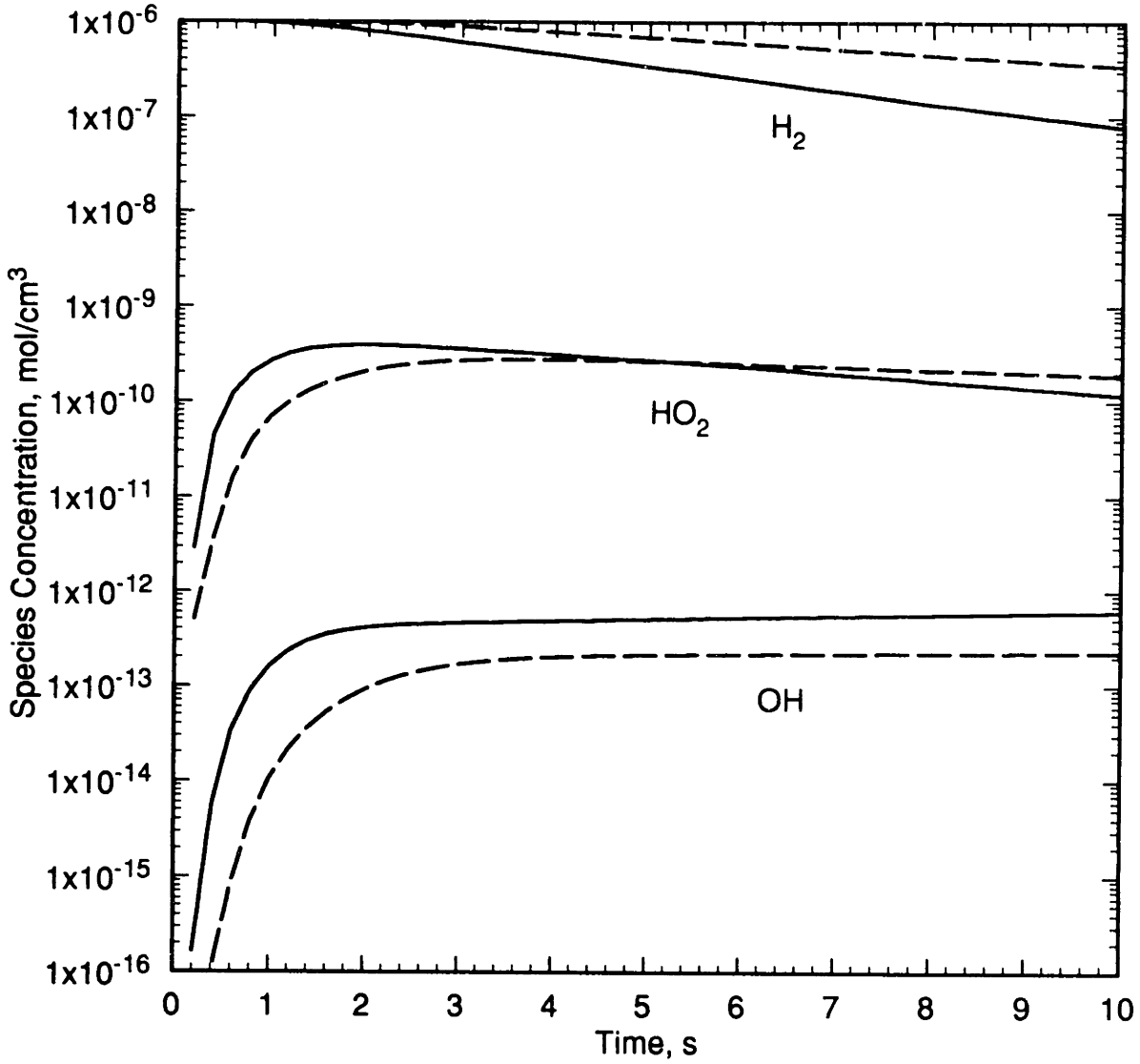

Figure 6.12 **Predicted Hydrogen and Radical Profiles at 263 bar and 118 bar.** Conditions: 550 °C, $[H_2]_o = 1.0 \times 10^{-6}$ mol/cm^3, $[O_2]_o = 0.5 \times 10^{-6}$ mol/cm^3. Solid curves: 263 bar; dashed curves: 118 bar.

because the lower branching rate is balanced by termination via (R11) at a lower concentration of OH radicals. Since the OH concentration is determined by the competition between the rates of termination and branching, and the branching rate is directly proportional to the water concentration, the OH concentration is in turn directly proportional to the water concentration, decreasing by the same factor of three as the water density. This behavior was foreseen in Equation 6.18. Figure 6.12 also indicates that the decreased branching rate at the lower pressure results in a slower approach to the steady-state radical concentrations, and hence a longer induction time. The steady-state HO_2 concentration remains relatively unaffected by the change in pressure, because its formation and destruction are controlled primarily by reactions (R7) and (R13), which have small or no pressure dependences.

Webley (1989), in his elementary reaction modeling studies, arrived at a similar conclusion regarding the role of water in the oxidation mechanism at SCWO conditions; however, he lacked experimental data with which to compare his predictions. The experimental and modeling results from the present study clearly indicate that the primary role of water in the hydrogen oxidation mechanism is as a reactant in the (–R12) chain-branching step.

The slightly stronger pressure dependence seen in the data in Figure 6.11 remains unexplained. Simple changes in either the rates of pressure-dependent reactions or the concentration of water in the present mechanism apparently cannot account for this large an overall pressure dependence. The discrepancy between the observed and predicted rates grows larger at higher pressures, suggesting that the increasing non-ideality of water under those conditions may begin to affect the oxidation kinetics. For example, fugacity coefficients of reactive radical species will deviate more strongly from unity as the pressure is increased, which may affect equilibrium constants and hence reverse reaction

rates (see Sections 6.2 and 6.4). Since fugacity coefficients of unstable species are difficult to estimate reliably under supercritical water conditions, the potential effect of mixture non-idealities on the model predictions was not investigated. An important secondary reaction pathway involving water, not captured in the model, may also be active, such that the rate of the secondary pathway is enhanced at higher pressures.

6.6 Modeling of Surface Reaction Effects

Gas-phase hydrogen oxidation has long been known to be profoundly affected by heterogeneous reactions, with many (non-catalytic) surface influences tending to quench the reaction (von Elbe and Lewis, 1937,1942; Kassel, 1937). Similar effects have been shown to be present in our packed reactor (Section 5.4), although in the tubular reactor the effect is apparently minor. We therefore sought to evaluate the possible influence of surface effects on model predictions, and the potential role of heterogeneous reactions in the overall oxidation mechanism, by estimating surface reaction rates in our system. In this way we hoped to confirm the lack of surface influences in our tubular reactor data.

Kinetic gas theory predicts that the surface rate constant for species i, $k_{wall,i}$, is given by (Hoare *et al.*, 1967; Pitz and Westbrook, 1986)

$$k_{wall,i} = \Gamma_i \left(\frac{surface}{volume} \right)_{reactor} \sqrt{\frac{kT}{2\pi m_i}} \tag{6.21}$$

where the square-root term accounts for the collisional frequency and Γ_i is the efficiency of the surface for destruction of species i, k is Boltzmann's constant, and m_i is the mass of species i. The inherent assumption in the derivation of this rate constant is that the surface in the reactor is dispersed throughout the volume or otherwise arranged such that there are no transport constraints in reaching the surface; the surface rate constants

predicted by Equation 6.21 will therefore appear in the model as homogeneous rate constants. Heterogeneous rates have been incorporated in this fashion into homogeneous models in many previous studies (e.g., Arustamyan *et al.*, 1980; Pitz and Westbrook, 1986; Maas and Warnatz, 1988; Yetter *et al.*, 1991a).

Attempts to use Equation 6.21 to estimate surface reaction rates are frequently limited by the lack of data for Γ_i. Reported values for Γ_{HO_2} at 500 °C range over several orders of magnitude, from 10^{-4} for inert surfaces (such as Pyrex) to 0.1 for highly efficient surfaces (such as PbO); values for $\Gamma_{H_2O_2}$ are typically about $0.01\Gamma_{HO_2}$ (Hoare *et al.*, 1967). Even for the most efficient surfaces, Γ_i is apparently less than unity. Hart *et al.* (1963) indicate that the efficiency of NiO lies somewhere between that of PbO and Pyrex; since our reactor material is Inconel 625, a high-nickel alloy, we can assume that the Γ_i in our system fall between those of PbO and Pyrex. Complicating the estimation of $k_{wall,i}$ is the fact the water can "poison" the surface and inhibit surface destruction of radicals by decreasing Γ_i (Hart *et al.*, 1963).

Surface reaction rates were estimated, using Equation 6.21, for HO_2 and H_2O_2. Only those two species were considered, since they are the dominant unstable species in our model and are particularly susceptible to surface destruction. Stable products (H_2O, O_2) were assumed to form as in Maas and Warnatz (1988). The two estimated rates were then incorporated in the YDR91J model. The presence of the surface reactions tended to extinguish the oxidation reaction over the entire temperature range by lowering the steady-state radical concentrations. Only for surface efficiencies much lower than the reported efficiencies for Pyrex was the model able to predict realistic oxidation rates. Even given the poisoning capacity of water, it is unlikely that our reactor surface is more inert than Pyrex.

Since the surface reactions have a strong tendency to inhibit the oxidation, we incorporated the surface reactions into model YDR91A, which consistently overpredicted oxidation rates, in the hope that the surface reactions would moderate the model's predictions and yield better agreement with the data. Furthermore, the experimental evidence for the Yetter *et al.* (1991a) value for $\Delta H_{f,298}(HO_2)$ seems much more reliable than that for the older value given in the JANAF Tables, and the newer thermodynamics are to be considered more realistic (see Section 6.4.4).

In the absence of a firm basis for estimating surface efficiencies, the Γ_i were taken to be adjustable parameters. In order to fit the data, Γ_i must be made rather strongly temperature-dependent, but such behavior is not inconsistent with earlier studies of surface radical destruction (Hoare *et al.*, 1967; Hart *et al.*, 1963). The resulting fit rate constants are listed in Table 6.2. Fit values of Γ_i were about 10^{-4} for HO_2 and about 10^{-6} for H_2O_2, much lower than reported values for PbO but about the same as for Pyrex. To the extent that Equation 6.21 provides an accurate estimate of surface reacton rates, then, water must have such a strongly inhibiting effect on our reactor material that the surface is made at least as inert as Pyrex. Predictions and behavior of the model containing surface reactions (YDR91S) were virtually identical to those of model YDR91J in almost every detail.

Efforts to identify the role of surface reactions in our model are thus ambiguous. Models with (YDR91S) and without (YDR91J) surface reactions can give equally good agreement with the experimental data from the tubular reactor. The preferable thermodynamics of Yetter *et al.*, and the unlikelihood that surface reactions are completely negligible in our system, tend to favor the YDR91S model. However, sensitivity analysis of the model revealed an extraordinarily high sensitivity to the value of the surface rate constant; a variation of as little as a factor of two in Γ_i could result in

complete suppression of reaction. Such a high sensitivity to surface conditions would suggest that experiments might not be reproducible, yet our data were quite reproducible. More conclusively, an increase in the reactor surface area-to-volume ratio by a factor of 20.5 decreased the observed kinetic decay constant by only a factor of 6 (see Section 5.4). If the predictions of the YDR91S model were accurate, the high amount of surface area in our packed reactor should have essentially extinguished the oxidation reaction. The YDR91S model can only fit the experimental data if terminating surface reactions participate to a sufficient extent to moderate the overall oxidation rate. If the model were fit to the packed reactor data, the predicted oxdiation rates in the tubular reactor would be far too high. Therefore, the YDR91S model is inconsistent with experimental evidence.

Surface reactions could be included successfully in the YDR91J model, if the surface reaction rates were fit to the packed reactor data. The large decrease in surface area in the tubular reactor would then render the surface reactions unimportant and the oxidation would proceed homogeneously. However, this procedure would give fit values of Γ_i much lower than those for Pyrex, and the physical meaningfulness of these values would be suspect.

The attempt to include surface reactions in the model for hydrogen oxidation is therefore inconclusive. The YDR91S model cannot be made consistent with experimental data as long as surface reaction rates are proportional to reactor surface area. The YDR91J model can incorporate surface reactions, but only for very low surface efficiencies. There remains the possibility that the surface reaction model is itself inaccurate. For example, reactor surface area may not be "perfectly accessible," and transport effects may influence heterogeneous rates. Since experimental evidence indicated that the tubular reactor results were likely unaffected by surface reactions,

tubular reactor data were treated as completely homogeneous and more sophisticated models of heterogeneous reactions were not investigated.

Chapter 7

Experimental Studies of Carbon Monoxide Oxidation in Supercritical Water

7.1 Introduction

Kinetic data for the oxidation of model compounds in supercritical water have become available in recent years. Compounds studied have included carbon monoxide (Helling and Tester, 1987), methane (Webley and Tester, 1991), methanol (Webley, 1989; Tester *et al.*, 1992), ammonia (Webley *et al.*, 1990,1991), and acetic acid (Lee and Gloyna, 1990), as well as more complex compounds such as phenol (Thornton and Savage, 1990,1992). Of these, carbon monoxide and ammonia are important because they are intermediates in the oxidation of more complex organics and because their destruction can be the rate-limiting step in the complete conversion of the organic to CO_2 and N_2. Carbon monoxide is also the simplest model organic and its gas-phase oxidation kinetics have been well characterized.

Helling and Tester (1987) were the first to report the oxidation kinetics of carbon monoxide in supercritical water. They observed that CO is converted to CO_2 by two global reaction pathways: direct oxidation (7.1) and the water-gas shift reaction (7.2).

$$CO + {}^1/_2\, O_2 \rightarrow CO_2 \qquad (7.1)$$

$$CO + H_2O \rightarrow CO_2 + H_2 \tag{7.2}$$

Below about 450 °C, the water-gas shift accounted for more than 50% of the total oxidation of CO, as evidenced by the amount of hydrogen produced. The duality of the oxidation pathways complicated the task of obtaining kinetic parameters. In our experimental apparatus, carbon monoxide and oxygen are delivered separately to the reactor as dilute aqueous solutions. Since the water-gas shift can occur without oxygen present, the aqueous carbon monoxide feed could undergo reaction as it was heated to reaction temperature, prior to its entering the reactor. Helling (1986) attempted to calculate the thermal history of the feeds using conventional heat-transfer correlations, but found that the predicted thermal behavior did not agree with that observed experimentally. Furthermore, temperatures at the reactor inlet often differed from the surrounding temperature by as much as 10 to 25 °C, resulting in some degree of reactor nonisothermality.

Despite these experimental limitations, a rate expression for the water-gas-shift reaction pathway was developed by Helling and Tester (1987), on the basis of 21 experiments in which no oxygen was fed to the reactor:

$$R_{WGS} = 10^{1.60\pm3.57} \exp(-62.9\pm8.6/RT)\,[CO]^{0.57\pm0.11} \tag{7.3}$$

where the rate is given in mol/L-s, the concentration is in mol/L, the activation energy is in kJ/mol, and the stated parameter uncertainties are at the 95% confidence level. For the overall oxidation of CO Helling and Tester (1987) obtained the following global expression, based on 39 experiments with oxygen present at stoichiometric or superstoichiometric levels (i.e., $([O_2]/[CO])_{inlet} \geq 0.5$):

$$R_{overall} = 10^{7.25\pm0.53} \exp(-120\pm7.7/RT)\,[CO]^{1.01\pm0.09}\,[O_2]^{0.03\pm0.04} \tag{7.4}$$

with the units and uncertainties as before. In deriving the above expression, all reactions were assumed to have occurred in the reactor, at the reactor inlet temperature. The effects of reaction during preheating were included in Equation 7.3, although the thermal history of the feeds could not be reliably determined.

The objectives of the present study were threefold: first, to reproduce (if possible) the earlier data in an improved apparatus; second, to extend the kinetic measurements to the substoichiometric regime (with $([O_2]/[CO])_{inlet} < 0.5$); and third, to account for reaction during preheating in a rigorous fashion by improving heat-transfer modeling in the preheating tubing. The reactor system of the earlier study was rebuilt and now includes greater reactor temperature measurement capabilities and an improved analytical method for hydrogen, as well as improved feed preheating to insure system isothermality. Heat-transfer experiments in the new system enabled characterization of the temperature profiles within the feed preheaters. These profiles were then incorporated in the data analysis of water-gas-shift experiments, to provide an improved rate expression for that pathway. The water-gas-shift rate expression was then used to quantify the extent of reaction during feed preheating in experiments with oxygen present. In this way the "true" reactor inlet concentrations could be calculated and the effects of preheating accounted for in the data.

The present apparatus is quite similar to that used by Helling and Tester (1987). There are, however, three distinctions relevant to this study. First, the earlier reactor was 4.24 m of 0.635-cm O.D. × 0.211-cm I.D. Inconel 625 tubing, providing a total reactor volume about 25% greater than in the current system, and a surface area-to-volume ratio about 20% smaller. Second, the earlier system used only 2 m of preheating tubing in the reactor sand bath; auxiliary heating was provided by radiative preheaters which have since been removed. To simplify analysis of the thermal history of the feeds and to

minimize reaction during preheating, the auxiliary sand bath in the present system was not used for experiments with carbon monoxide; heating of the feeds was provided entirely by the preheating tubing within the reactor sand bath (see Figure 4.1). Finally, the reactor temperature in the earlier apparatus was measured only at the point of mixing of the feeds. This mixing temperature frequently differed from the sand bath temperature by as much as 10 to 25 °C. Other details regarding the current experimental apparatus and procedures are available in Chapter 4.

The oxidation of carbon monoxide in supercritical water was investigated in 43 experiments at an operating pressure of 246 bar and over the temperature range 420 to 571 °C, at residence times of 5.0 to 12.1 seconds. Inlet concentrations of carbon monoxide ranged from 3.73×10^{-7} to 3.51×10^{-6} mol/cm^3, while inlet oxygen concentrations ranged from 3.81×10^{-7} to 3.87×10^{-6} mol/cm^3. Molar feed ratios of oxygen to carbon monoxide varied between 0.15 and 8.20, both above and below the stoichiometric value of 0.5.

Carbon monoxide oxidation experiments yielded total conversions ranging from 4 to 93%, based on formation of carbon dioxide from carbon monoxide. Average reaction rates, defined as the change in carbon monoxide concentration divided by the residence time, ranged from 5.8×10^{-9} to 1.8×10^{-7} mol/cm^3-s. The conditions and results of the oxidation experiments are listed in Table 12.8. Note that the inlet carbon monoxide concentrations in that table have been corrected for reaction during preheating of the CO feed, as described in Sections 7.3 and 7.4. The carbon monoxide oxidation data are also presented in the form of a first-order Arrhenius plot in Figure 7.1, where they are compared with our earlier data reported by Helling and Tester (1987). The apparent first-order rate constant, k^*, is defined as

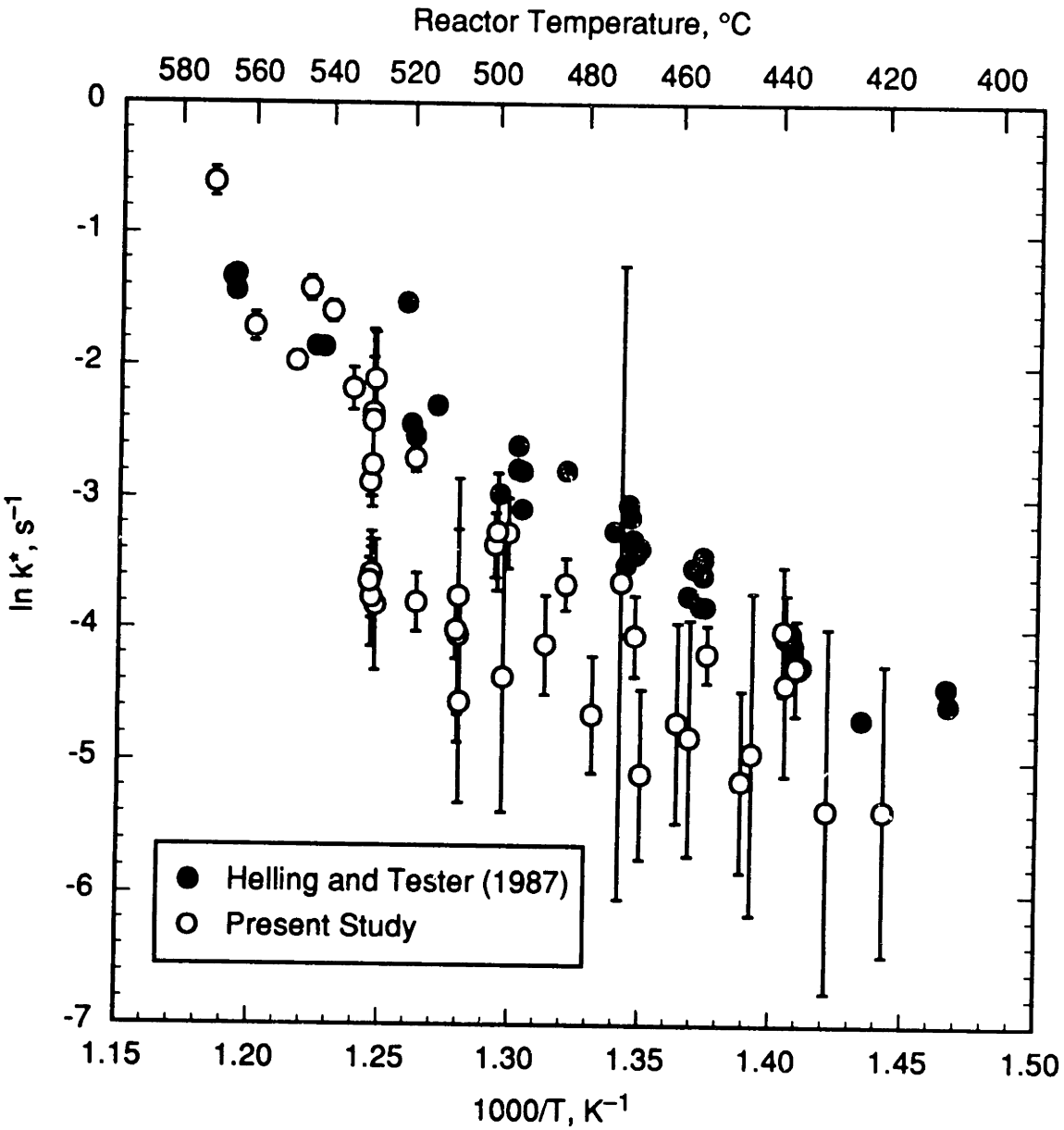

Figure 7.1 **Apparent First-Order Arrhenius Plot of the Overall Oxidation of Carbon Monoxide in Supercritical Water at 246 bars.** Data of Helling and Tester (1987) have been corrected for calculated reactor nonisothermalities (see text for details).

$$k^* = -\ln (1 - X)/\tau \tag{7.5}$$

with X the observed conversion of carbon monoxide and τ the reactor residence time. The reactor temperatures in the earlier experiments (Helling and Tester, 1987) have been adjusted to the sand bath temperature, which is believed to be more representative of the actual temperature within the reactor (see Section 7.2 for details).

Figure 7.2 shows the molar ratio of hydrogen to carbon dioxide in the effluent of the oxidation experiments plotted as a function of reactor temperature. This ratio is a measure of the relative contributions of the water-gas shift and the direct oxidation pathways to the overall conversion of carbon monoxide to carbon dioxide. Previous work (Section 5.1) has demonstrated that the global oxidation of hydrogen proceeds relatively slowly under the conditions of these experiments, so that hydrogen formed by the water-gas shift pathway is unlikely to be oxidized to a significant extent. The H_2/CO_2 ratio is thus an accurate indicator of the contribution of the water-gas shift in these experiments. Both in the earlier data of Helling and Tester and in the data from the present study, the H_2/CO_2 ratio exhibits a clear decreasing trend with increasing reactor temperature, indicating that the relative contribution of the water-gas shift becomes smaller as the temperature increases.

Twenty experiments were conducted to investigate the water-gas shift reaction in supercritical water at 246 bar and from 445 to 593 °C. Residence times in these experiments ranged from 5.1 to 11.1 s, with inlet carbon monoxide concentrations varying from 3.76×10^{-7} to 2.88×10^{-6} mol/cm^3. Oxygen was deliberately excluded from the reactor in these runs; however, it was not possible to eliminate oxygen completely from the system, although the molar feed ratio of oxygen to carbon monoxide never exceeded 0.022. The range of conditions for both the oxidation experiments and the water-gas shift experiments was very similar to that used in earlier experiments

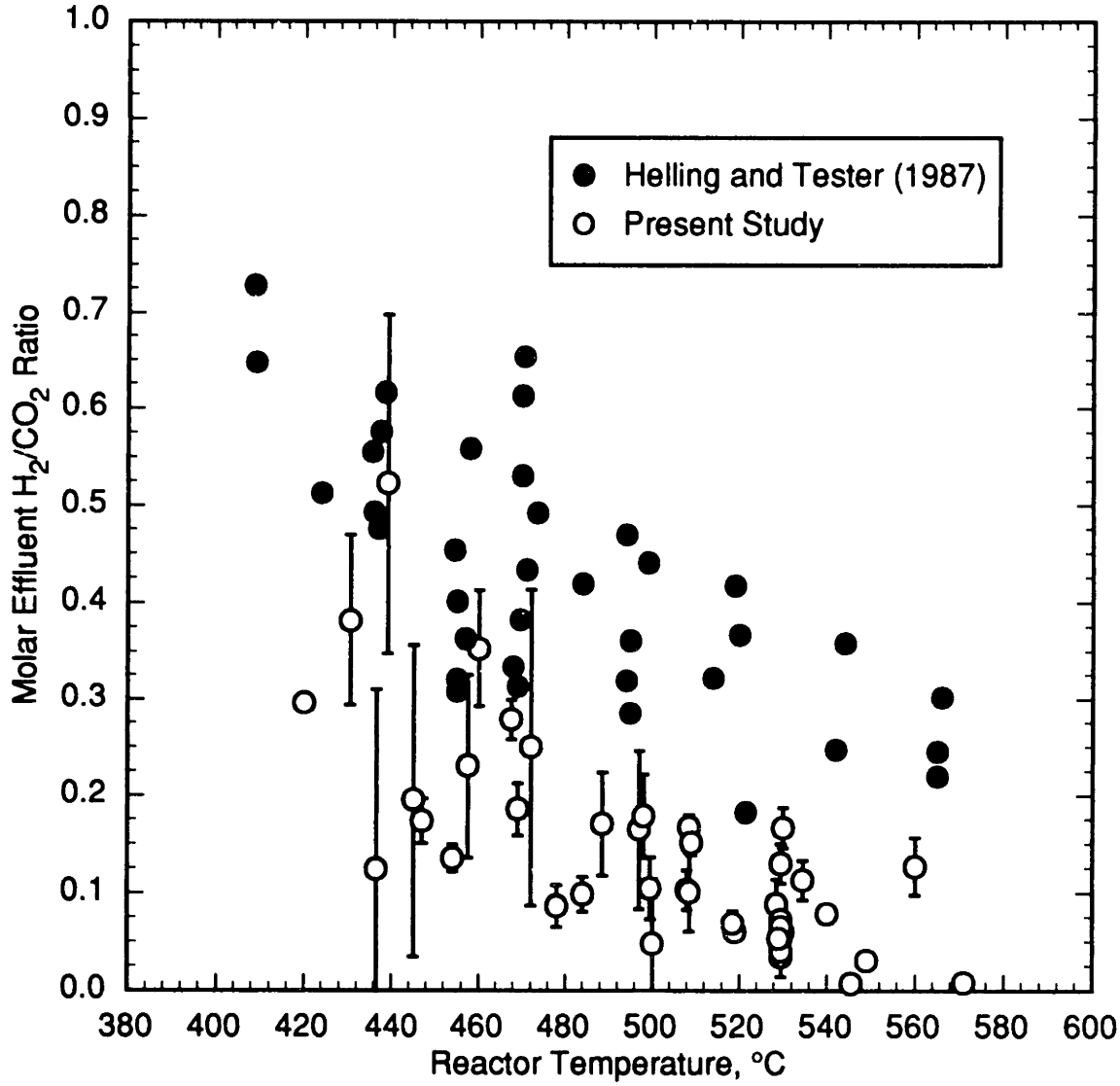

Figure 7.2 **Molar Ratio of Hydrogen to Carbon Dioxide in Effluent of Carbon Monoxide Oxidation Experiments at 246 bars.**

(Helling and Tester, 1987), with the important exception that in this study substoichiometric feed ratios were also investigated in the oxidation experiments.

Water-gas-shift experiments yielded total conversions of 1.4 to 23%. Since oxygen could not be completely excluded from the reactor, some conversion of CO occurred by direct oxidation, as evidenced by effluent H_2/CO_2 ratios that were less than unity. The measured H_2/CO_2 ratios were used to calculate the conversion by the water-gas-shift pathway alone; this calculated conversion varied between 1.4 and 20% in these experiments. Average water-gas-shift reaction rates varied from 1.3×10^{-9} to 3.0×10^{-8} mol/cm^3-s, significantly slower than overall oxidation rates. The conditions and results of the water-gas shift experiments are summarized in Table 12.7. Again, reactor inlet CO concentrations in that table have been corrected for reaction during feed preheating. The water-gas-shift data are also presented in a first-order Arrhenius plot in Figure 7.3, where they are compared with the water-gas-shift data presented earlier by Helling and Tester (1987). As before, the earlier data have been adjusted with respect to reactor temperature.

Several trends are apparent in Figures 7.1 through 7.3. First, the early overall oxidation data seem to indicate somewhat higher observed oxidation rates than in the present study, although the activation energies of the two data sets appear comparable. Similarly, rates in the earlier water-gas-shift data also appear faster than in the current study, although again the activation energies do not seem vastly different. Finally, the effluent H_2/CO_2 ratios in the earlier oxidation data appear consistently higher. Taken together, these three observations suggest that the water-gas shift pathway proceeded faster in the earlier experiments. One possible source of this discrepancy was a difference in the thermal history of the feeds in the two studies. This possibility, along with the importance of quantifying the extent of reaction during feed preheating,

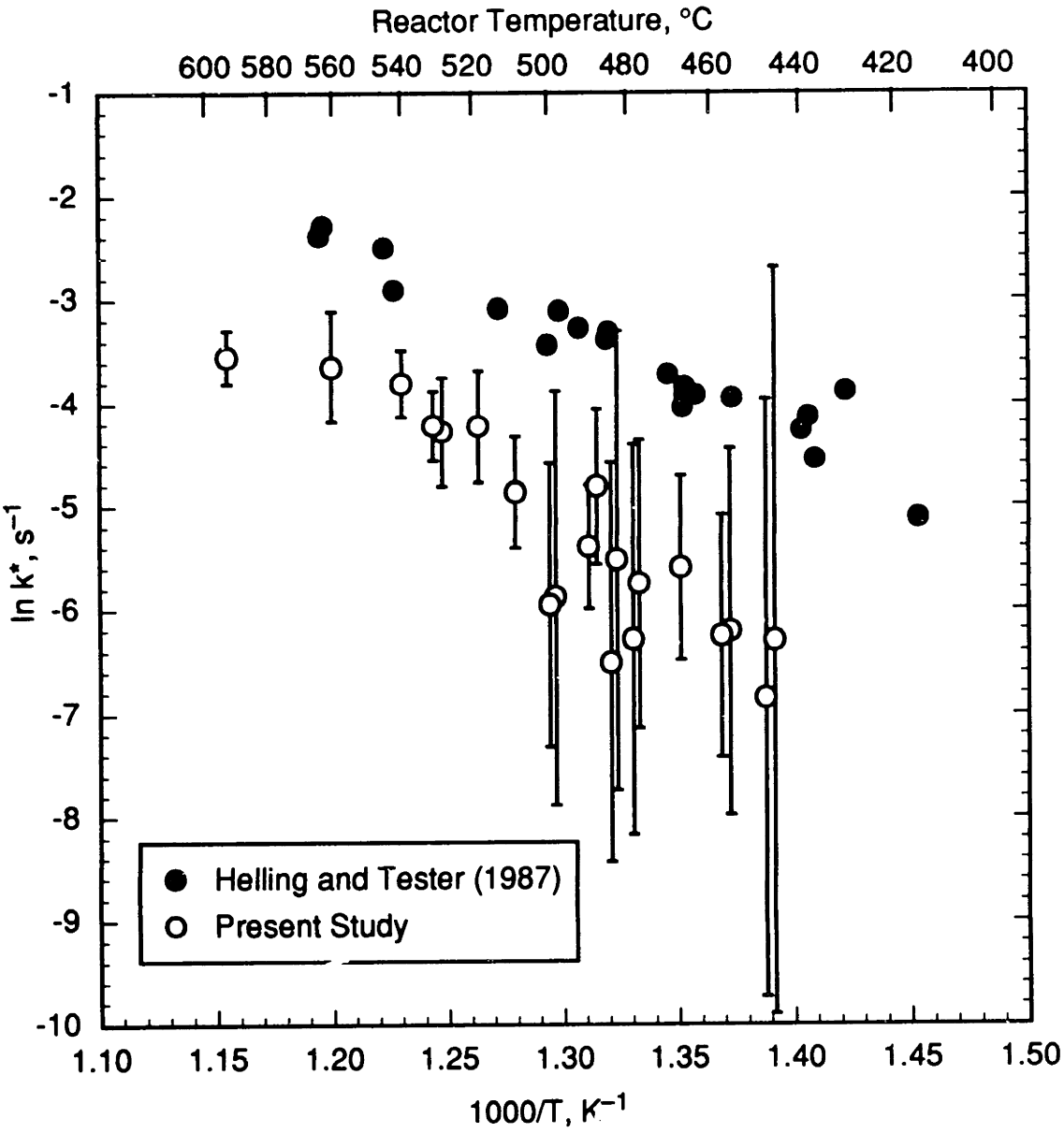

Figure 7.3 **Apparent First-Order Arrhenius Plot for the Water-Gas Shift Reaction in Supercritical Water at 246 bars.** Data of Helling and Tester (1987) have been corrected for calculated reactor nonisothermalities (see text for details).

prompted an investigation of the temperature profiles in the preheating tubing in the current system.

7.2 Heat-Transfer Experiments

Heat-transfer experiments were conducted in the current system to establish temperature profiles in the preheating tubing. In these studies, the mixing temperature of the feeds was measured for varying flow rates and sand bath temperatures, with pure water flowing through the system. Flow rates ranged from 2.8 to 5.1 g/min, with sand bath temperatures of 400 to 575 °C.

Average overall heat-transfer coefficients were determined for the feed preheating tubing in a series of heat-transfer experiments. In these experiments, pure water was used; since the true reactor feeds are very dilute, their thermophysical properties will be very similar to those of pure water. The flow rates of the two feed streams could be controlled independently by varying the feed pump stroke. For a given sand-bath temperature and set of flow rates, the temperature at the point of mixing of the two feeds could be measured. When the two flow rates were identical, the mixing temperature was assumed to be the same as the feed temperatures prior to mixing, as the preheating tubing was the same length for both feed streams. Varying one of the feed flow rates resulted in a change in the mixing temperature; the temperature of each feed immediately prior to mixing could then be determined by an adiabatic, steady-state, First-Law analysis (conservation of enthalpy), as the temperature of the unchanged feed stream would remain constant. Using this simple technique, temperatures at the exit of the preheating tubing were determined for both feed streams.

For a differential element of preheating tubing, the heat transfer from sand bath to feed stream can be described by

$$\dot{m}dH = U_o\,(T_{fsb}-T)\,dA \tag{7.6}$$

where $\dot{m}$ is the mass flow rate of the feed stream, H is the specific enthalpy of the bulk fluid, U_o is the overall heat transfer coefficient from sand bath to feed stream, T_{fsb} is the fluidized sand bath temperature, T is the bulk fluid temperature, and A is the internal surface area of the preheating tubing. If U_o is assumed to have a (constant) characteristic value $\langle U_o \rangle$ over the length of the tubing, Equation 7.6 can be integrated to give

$$\langle U_o \rangle = \frac{\dot{m}}{A} \int_{T_o}^{T_f} \frac{dH}{T_{fsb} - T} \tag{7.7}$$

where T_o is the temperature at the inlet to the preheating tubing (room temperature) and T_f is the temperature at the preheating tubing exit (which was determined experimentally). Using the results of the heat-transfer experiments, average overall heat-transfer coefficients for the preheating tubing, as given by $\langle U_o \rangle$, could be calculated by numerically integrating Equation 7.7 using the enthalpy of water given by the equation of state of Haar *et al.* (1984). This method is admittedly crude, as it essentially infers the thermal history of the feed solely on the basis of the temperature at the preheater exit. On the other hand, the thermal history calculated using the experimentally derived $\langle U_o \rangle$ will, by definition, correctly predict the observed temperature at the preheating tubing exit, where the details of the thermal history are most important for our purposes.

Experimentally derived values for $\langle U_o \rangle$ are shown in Figure 7.4, for various sand bath temperatures and feed-stream flow rates. The experimental conditions were chosen as representative of those encountered in the kinetic experiments. Two pump stroke settings were used, yielding nominal flow rates of 5 and 3 g/min for each feed stream. At a given pump setting, the oxygen-side pump head produces a somewhat lower flow rate (by about 10%) than the organic-side head. Consequently, during an oxidation

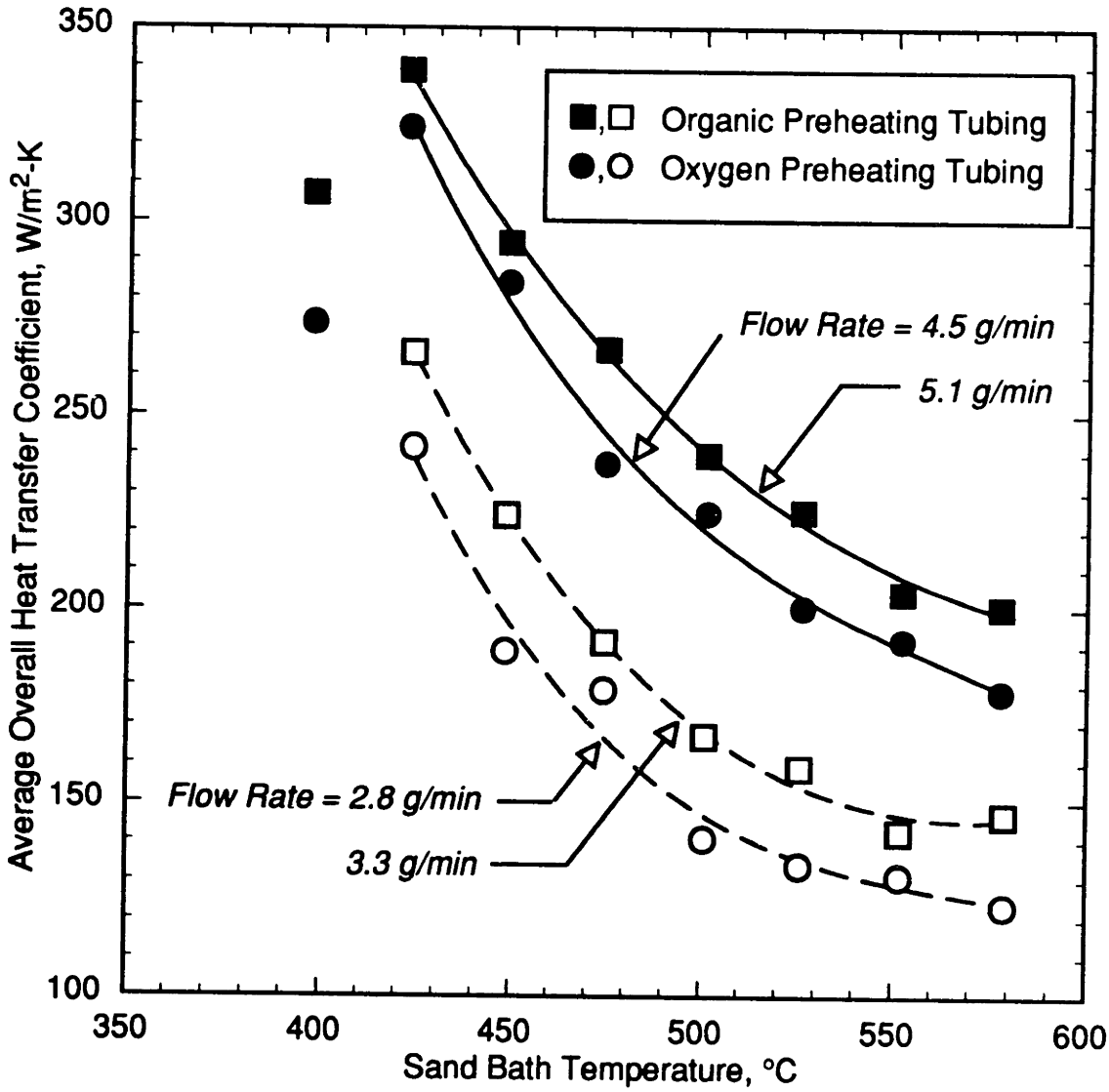

Figure 7.4 **Average Overall Heat-Transfer Coefficients U_o for Preheating Tubing, as Determined Experimentally.**

experiment, the flow rate of the oxygen feed was slightly lower than the flow rate of the organic feed. This small discrepancy in flow rates is reflected in the two pairs of curves in Figure 7.4.

Several features are evident in Figure 7.4. First, $\langle U_o \rangle$ increases with increasing flow rate; this behavior is expected since heat transfer should become more effective as the flow grows more turbulent (or less laminar). In the preheating tubing, the maximum attained Reynolds number increases from 1940 to 3550 as the flow rate increases from 2.8 to 5.1 g/min. Second, $\langle U_o \rangle$ decreases with increasing sand bath temperature, after appearing to peak at a sand-bath temperature of about 425 °C. The reasons for this behavior are less obvious. The reduced heat transfer at the higher temperatures may be the result of a decreasing internal or external heat-transfer coefficient, or both. Finally, the magnitude of the $\langle U_o \rangle$ values should be noted: at 125 to 350 W/m^2-K, the coefficients are not very large, especially considering the manufacturer's quoted value of 600 W/m^2-K for the external sand-bath coefficient.

The ability to calculate an experimental value for U_o in Equation 7.6 rests on the assumption that U_o is constant (and thus may be accurately represented by $\langle U_o \rangle$) over the length of the tubing. The validity of this assumption is not readily apparent, particularly since the feed stream properties vary drastically as the feeds are heated past the pseudocritical point. One might expect the overall heat-transfer coefficient to undergo similarly drastic variations. To test the validity of the constant-U_o assumption, the calculated $\langle U_o \rangle$ values were compared with values predicted using established empirical correlations for heat transfer to fluids flowing in horizontal tubes. These correlations predict only the internal heat-transfer coefficient and typically take the form

$$Nu \equiv h_i D/k = f(Re, Pr, Gz \equiv Re\ Pr\ D/L, \mu_b/\mu_w) \tag{7.8}$$

where *Nu*, *Re*, *Pr*, and *Gz* are the dimensionless Nusselt, Reynolds, Prandtl, and Graetz numbers, respectively, h_i is the internal heat-transfer coefficient, D is the tubing internal diameter, k is the fluid thermal conductivity, and μ_b and μ_w are the viscosities of the fluid in the bulk and at the tubing wall. At the critical point, the Prandtl number of a fluid diverges, and traditional heat-transfer correlations often fail in the near-critical region (Swenson *et al.*, 1965; Yamagata *et al.*, 1972; Perry *et al.*, 1984).

The predictions of three different forced-convection correlations were calculated. The first correlation, given by Perry *et al.* (1984), is really three separate correlations, one for each of the laminar, transition, and turbulent flow regimes. These are the traditional Dittus-Boelter-type correlations which are meant to be generally applicable, without regard for the specific heat-transfer conditions. The second correlation used was that of Swenson *et al.* (1965), which was developed specifically for turbulent flows of supercritical water. Swenson's correlation accounted for the variation in heat capacity and density of the fluid between the wall and the bulk. The third correlation was developed by Yamagata *et al.* (1972), also for turbulent flows of supercritical water. Yamagata's correlation incorporated several correction factors which depended on the nearness of the fluid to the pseudocritical point. Swenson's correlation was based on measurements for a wide variety of heat fluxes relative to fluid flow rates, while Yamagata's correlation was derived from data mostly at low heat fluxes relative to flow rates. Heat transfer to supercritical water is typically less efficient than would be predicted by a traditional correlation of the form of Equation 7.8. In other words, the heat-transfer coefficient does not increase to the same extent as the diverging Prandtl number in the near-critical region. At high heat fluxes, this deterioration is more significant. One should note, however, that the heat-transfer coefficient always increases in the near-critical region; the deterioration affects only the magnitude of the increase.

Both Swenson *et al.* and Yamagata *et al.* conducted experiments with mass velocities on the order of 300 to 2000 kg/m^2-s and heat fluxes of approximately 100 to 2000 kW/m^2; by comparison, in our preheating tubing, mass velocities were about 10 kg/m^2-s and calculated heat fluxes were 20 to 60 kW/m^2. Both studies consider heat flux "high" when the ratio of heat flux to mass velocity is on the order of 1 kW-s/kg. By this rough definition, heat fluxes in our system are high; however, it is not clear whether this definition can be extended from the larger scale of the earlier experiments to the small scale of our preheating tubing. Furthermore, both Swenson *et al.* and Yamagata *et al.* studied heat transfer to highly turbulent supercritical water. In our preheating tubing, the flow conditions are never far beyond the transition region ($Re \leq 3550$). The direct applicability of these empirical correlations to our specific conditions is thus somewhat questionable.

For the calculations using the correlations, a constant external heat-transfer coefficient was assumed, thermodynamic and transport properties were obtained from Haar *et al.* (1984), and tubing thermal-conductivity values were obtained from the manufacturer. A differential-element method was used to determine the internal and external tubing wall temperatures and the bulk fluid temperature on the basis of a radial energy flux balance. Overall heat-transfer coefficients could be calculated from the sum-of-resistances formulation. Typical results from these heat-transfer calculations are presented in Figure 7.5, where the predicted bulk fluid temperature is shown as a function of distance in the preheating tubing. The assumed value for the external coefficient was 190 W/m^2-K for the three correlation calculations; this value was determined by fitting the calculated exit temperature to that observed experimentally. In addition to predictions based on correlations, the temperature profile predicted by the experimentally determined average overall heat-transfer coefficient is also shown. The short plateau at the 1-m point

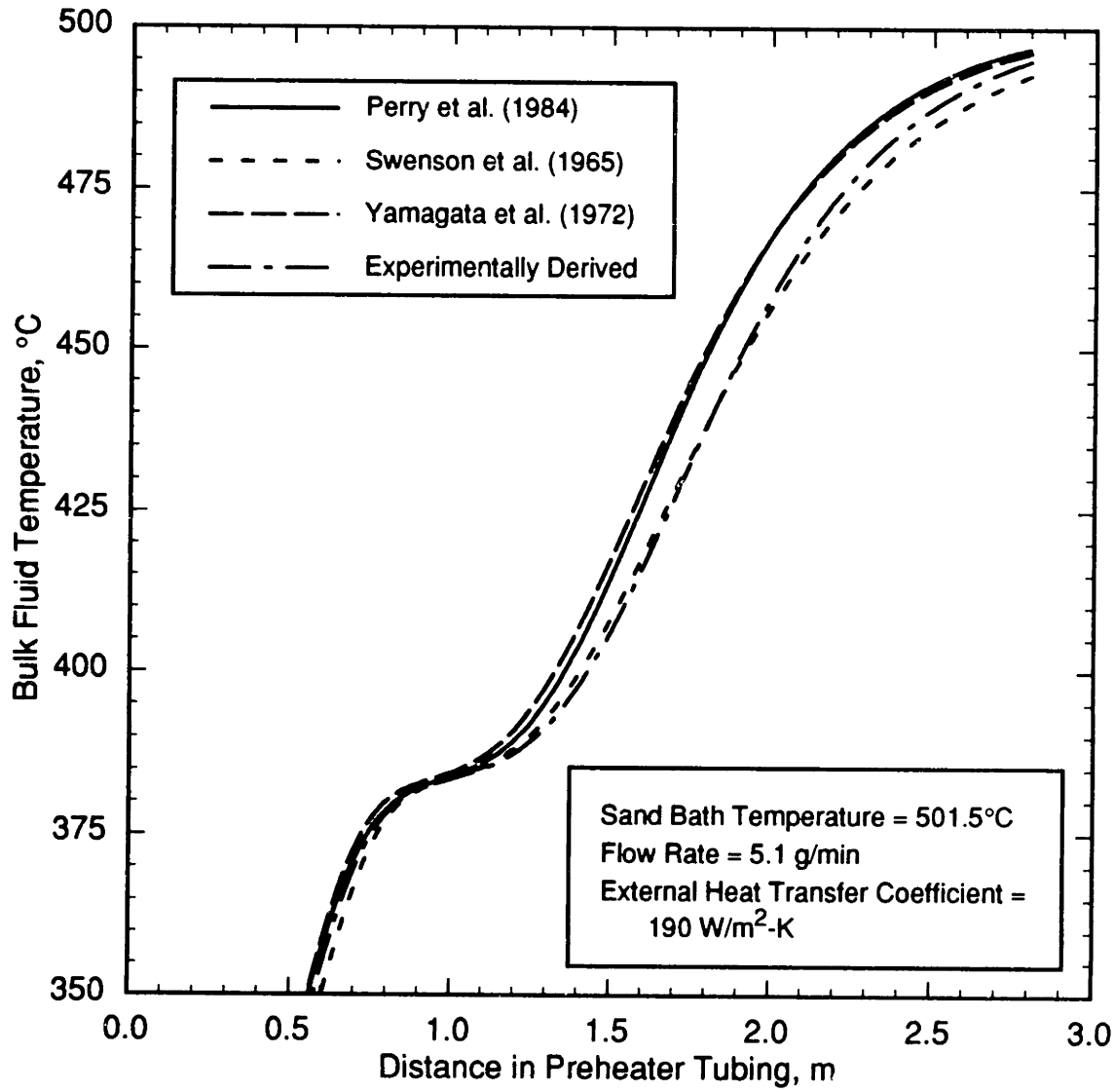

Figure 7.5 **Comparison of Calculated Bulk Fluid Temperature in Preheating Tubing as a Function of Distance for Various Heat-Transfer Models.** Calculations were performed using the heat-transfer correlations of Perry *et al.* (1984), Swenson *et al.* (1965), and Yamagata *et al.* (1972), with the external coefficient shown, and using an experimentally determined average heat-transfer coefficient.

in the tubing is the result of the fluid passing the pseudocritical point, where the fluid heat capacity reaches a maximum. Notable is the close agreement of all four profiles: at a given position, the maximum variation in predicted fluid temperature is 10 °C. Particularly encouraging is the close agreement of the experimentally derived profile with those predicted from correlations, especially the profile that uses the correlation of Swenson *et al.*

Figure 7.6 shows the predicted internal heat-transfer coefficient from the three correlations as a function of bulk fluid temperature; conditions are the same as in Figure 7.5. All of the correlations predict a sharp spike in the heat-transfer coefficient at the pseudocritical temperature (383.5 °C at 246 bar). The discontinuity in the prediction of the Perry *et al.* correlation occurs as the flow enters the transition region and the correlation changes. Interestingly, the Yamagata correlation does not predict lower heat-transfer rates relative to Perry's correlation, while Swenson's correlation predicts a significant decline. This discrepancy may reflect the conditions to which the correlations were fit; Yamagata fit his correlation to largely low-heat-flux conditions, while Swenson also included high-heat-flux conditions, where deterioration is more important. The predicted internal coefficients are much higher than the fitted external coefficient, indicating that the external resistance is controlling in the heat-transfer process. Consequently, despite nearly order-of-magnitude variations in estimates of the internal coefficient, the predicted overall heat-transfer coefficient is relatively insensitive to proper characterization of the details of the internal heat transfer process.

An additional important point is the magnitude of the external heat-transfer coefficient itself. Experimental preheating tubing exit temperatures could be matched by the correlations only by assuming an external coefficient in the range 150 to 250 W/m^2-K. At a given sand bath temperature, all correlations were able to match the

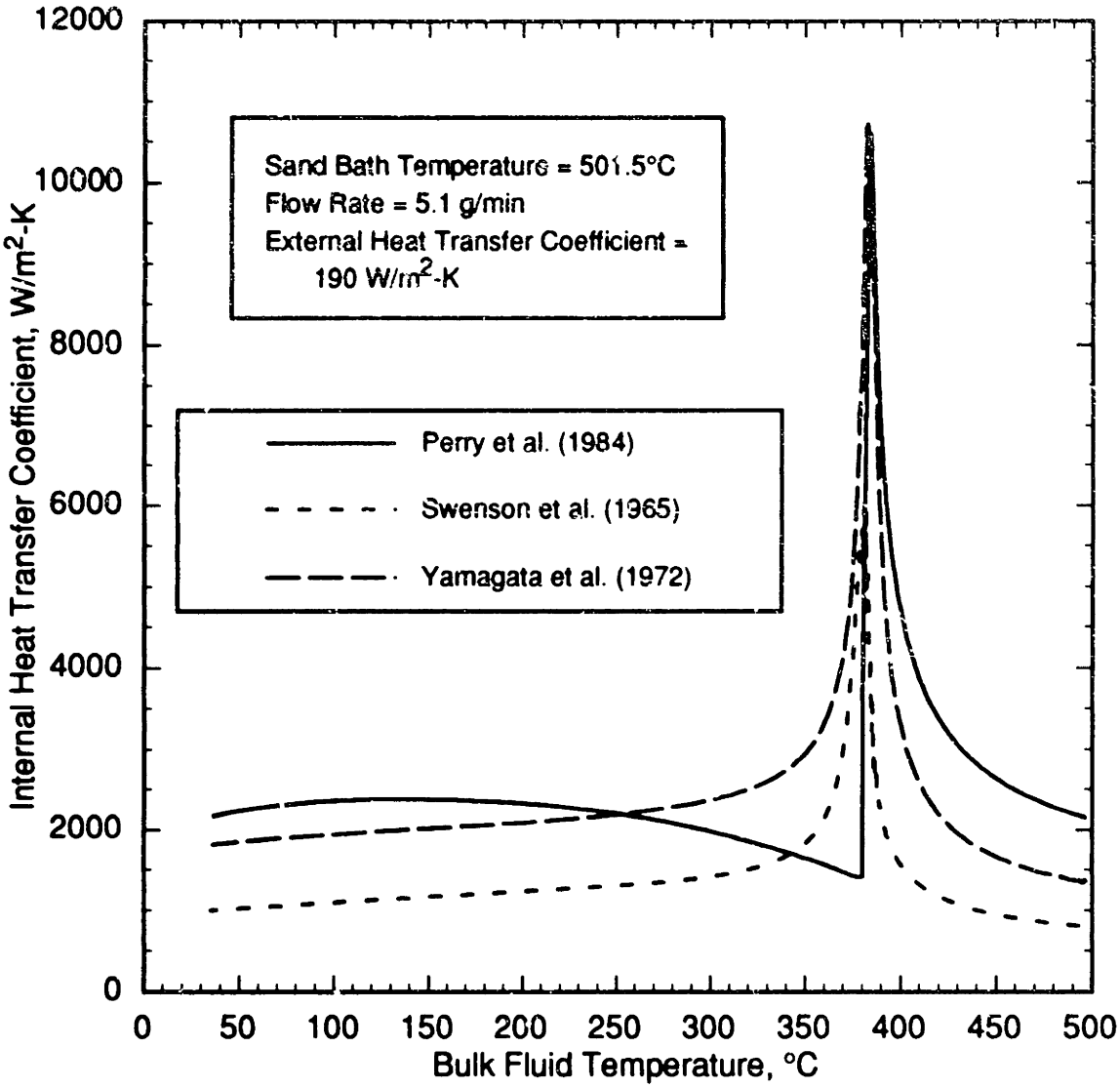

Figure 7.6 **Comparison of Calculated Internal Heat-Transfer Coefficient in Preheating Tubing as a Function of Fluid Temperature for Several Heat-Transfer Correlations.** Correlations used were those of Perry *et al.* (1984), Swenson *et al.* (1965), and Yamagata *et al.* (1972), with the conditions and external coefficient shown.

experimental exit temperature (within ~5 °C) using the same value for the external coefficient; however, the fitted value of the external coefficient decreased with increasing sand bath temperature. At no time did the fitted value of the external coefficient reach the sand bath manufacturer's quoted value of 600 W/m^2-K. One possibile reason for this observed behavior is that the sand bath becomes less efficient at higher temperatures. All heat-transfer experiments were conducted at a constant sand-bath fluidization-air flow rate of 15 L/min, as measured at room temperature. The fluidization rate within the bath would thus increase as the bath temperature was increased, due to the decrease in air density. The increasing fluidization rate could result in a decreased sand-bath heat-transfer coefficient at higher sand bath temperatures, although typically the sand-bath heat-transfer coefficient increases with increasing bath temperature (Kunii and Levenspiel, 1977).

Figure 7.7 shows the calculated overall heat-transfer coefficient U_o as a function of distance in the preheating tubing; conditions are again the same as in Figures 7.5 and 7.6. The experimentally derived coefficient is by definition constant over the length of the tubing. Significantly, the overall coefficients based on heat-transfer correlations are also approximately constant over the length of the tubing, within about ±10%. Predicted values of the overall coefficient are on the order of the external coefficient, further demonstrating that the external coefficient controls the heat transfer. As a result of the controlling external resistance, U_o is only weakly dependent on the internal coefficient, and the experimental assumption of a constant U_o is borne out by the correlations.

The technique for deriving U_o experimentally thus appeared valid, and the experimental values for U_o were used in calculating the temperature profiles within the preheating tubing. Typical results are shown in Figure 7.8 for a variety of sand-bath temperatures (T_{fsb}). Fluid temperature is presented as a function of time rather than

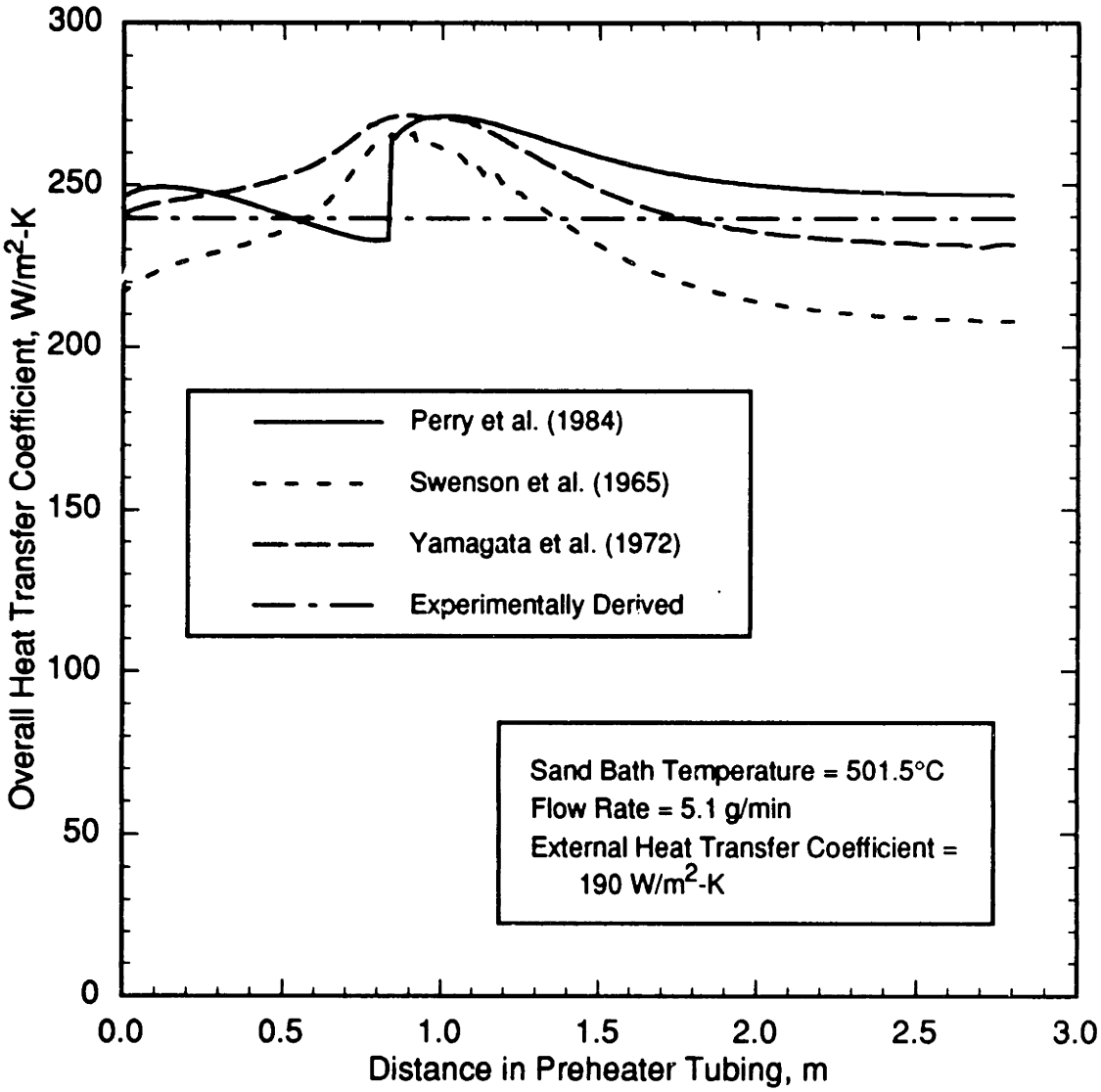

Figure 7.7 **Overall Heat-Transfer Coefficient as a Function of Distance in Preheating Tubing.** For calculations using the correlations of P...y *et al.* (1984), Swenson *et al.* (1965), and Yamagata *et al.* (1972), the listed constant external coefficient was used.

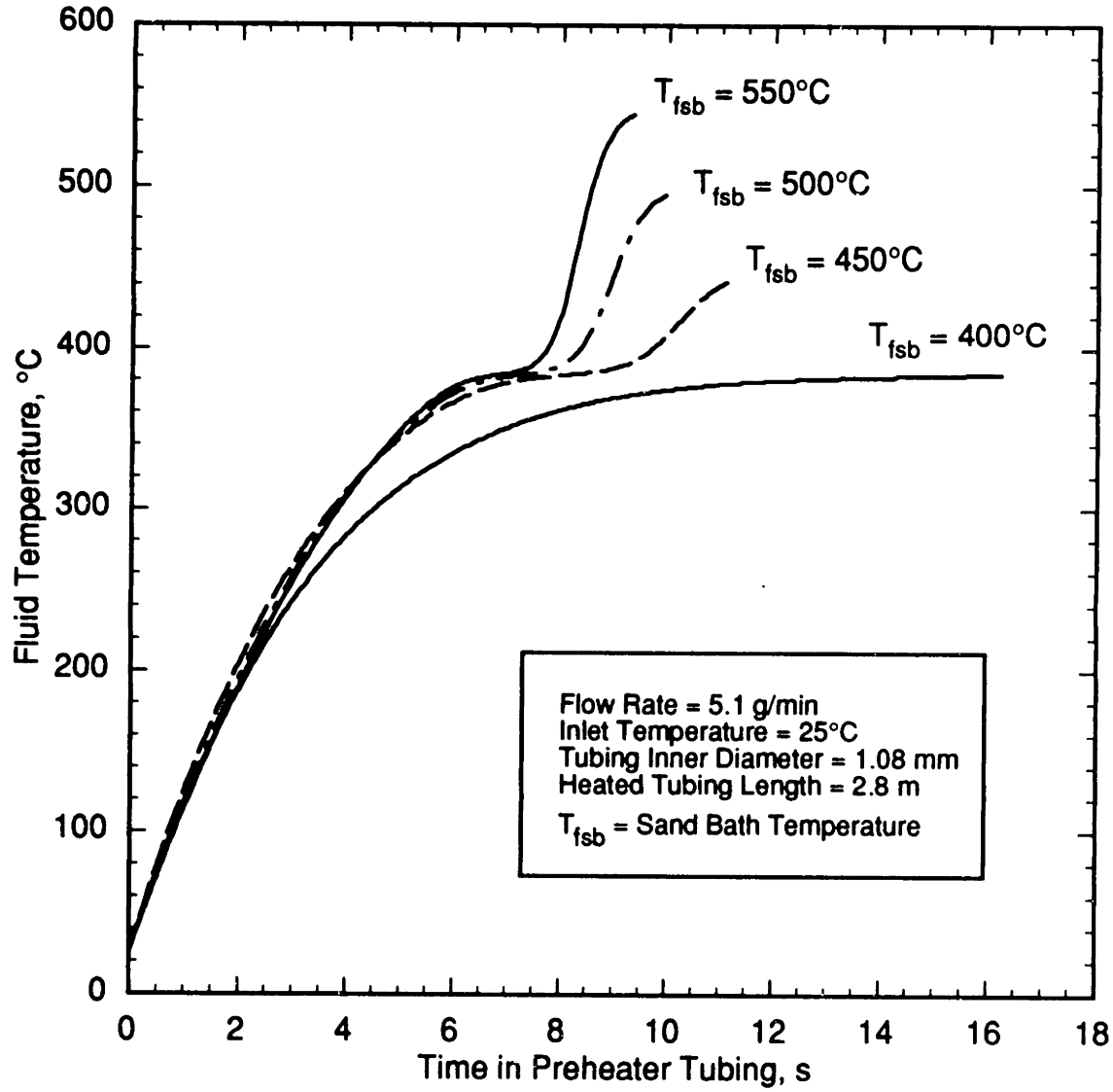

Figure 7.8 **Temporal Variation of Fluid Temperature in Preheating Tubing for Various Fluidized Sand Bath Temperatures.** Temperature profiles based on experimentally determined average overall heat-transfer coefficient; termination of profile indicates fluid has exited preheating tubing.

distance, as time is the more important variable for our purposes. The curves terminate when the fluid exits the preheating tubing and enters the reactor. Several features of Figure 7.8 are noteworthy. First, the residence time in the preheater is significant (9 seconds or longer). At low sand-bath temperatures (low heat fluxes), the time in the preheating tubing near sand-bath (reaction) temperature can be on the order of the reactor residence time; e.g., for T_{fsb} = 400 °C, the fluid in the preheating tubing is within 20 °C of the reactor temperature for about 6 s prior to entering the reactor. Second, as the sand-bath temperature increases, the fluid is heated more rapidly and accelerates through the preheating tubing, reducing both the residence time in the tubing and the time spent near the reactor (sand-bath) temperature. On the other hand, the feed fluid experiences higher temperatures in the preheater at higher sand-bath temperatures, such that reactions may occur to a greater extent than at lower sand-bath temperatures. For example, for sand-bath temperatures of 450 and 550 °C, the fluid in the preheater is above 400 °C for about 2 seconds; however, at the higher sand-bath temperature the fluid experiences higher temperatures during that same 2-second interval, and more reaction is likely to occur. The degree to which any of these profiles affects the extent of reaction during preheating can be estimated using an appropriate reaction rate expression.

The experimental and computational heat-transfer studies have revealed that the sand-bath heat-transfer coefficient is significantly lower than expected. Part of our earlier inability to predict correctly the thermal history of the feeds was our use of the manufacturer's quoted 600-W/m^2-K value for the bath coefficient. Helling's (1986) calculations consequently predicted much faster heating of the feeds than observed experimentally. As previously mentioned, in the earlier experiments the feeds exited the preheating tubing at temperatures 10 to 25 °C lower than the sand bath temperature. Using the new values for the sand-bath (external) heat-transfer coefficient, it is possible

to calculate an approximate temperature profile for the feed mixture within the original reactor. For these calculations we used the internal heat-transfer correlations of Perry *et al.* For the range of sand-bath temperatures employed in the earlier study, and the corresponding range of bath heat-transfer coefficients, we estimate that the reaction mixture was heated to within 1–2 °C of the sand-bath temperature within the first meter of the reactor's 4.24-m length. This estimate is somewhat tentative, as an older, smaller sand bath was used in the earlier studies, and we cannot be sure that the coefficients derived for our sand bath can be directly applied to the earlier apparatus. Realistically, however, it is unlikely that heat-transfer performances in the two baths would differ very significantly. The consequence of these lower heating rates for the reaction mixture is that the temperature at the entrance to the reactor, assumed to be the reactor temperature in earlier studies in our laboratory, is not an accurate estimate of the actual temperature within the majority of the reactor. Rather, the sand bath temperature is more likely to be representative of the reactor temperature. On the basis of this assumption, we have adjusted the earlier data of Helling and Tester (1987), using the sand-bath temperature as the "actual" reactor temperature. All of the data of Helling and Tester presented here have been revised to reflect this adjustment. The revised data, with corrected temperatures, concentrations, and residence times, are listed in Table 12.9.

7.3 Derivation of Water-Gas Shift Rate Expression

One of the main objectives of this study was the quantification of the extent of reaction during preheating of the reactor feeds. Our approach was to estimate the thermal history of the feeds and then use these calculated values to derive kinetic parameters. This method is admittedly somewhat indirect, and its selection deserves some discussion. A more straightforward method might have been to measure the conversion in the

preheating tubing experimentally, by modifying the apparatus to bypass the reactor. However, this approach has two problems. First, conversions in the preheating tubing alone are likely to be quite low (<5%) and thus difficult to measure accurately and reproducibly. Second, two separate experiments are required to obtain a single data point: one experiment to measure conversion in the preheating tubing, and a second to measure total conversion in the reactor and preheating tubing. Conditions in the two experiments would need to be identical, which can be difficult to achieve in practice. For these operational reasons we chose the more indirect approach.

The first step in incorporating the thermal history of the feeds was to use the feed history, in conjunction with the reactor conditions, to derive kinetic parameters for the water-gas-shift pathway. The regression of kinetic parameters to experimental data requires a model which uses measured independent variables to predict a measured dependent variable; the regression process then determines the optimal parameters by minimizing the difference between the measured and calculated values of the dependent variable (see Section 12.1). The model we have used in this case predicts total conversion by the water-gas shift, given the conditions of the experiment. The overall model consists of three equations. Two equations describe the heat- and mass-transfer behavior in the preheating tubing:

$$\frac{dT}{dz} = \frac{2\pi r_i U_o (T_{fsb} - T)}{\dot{m} C_p(T)} \tag{7.9}$$

$$\frac{d[\mathrm{CO}]}{dz} = -\frac{R_{\mathrm{WGS}}(T)\pi r_i^2 \rho(T)}{\dot{m}} + \frac{[\mathrm{CO}]}{\rho(T)} \frac{d\rho(T)}{dT} \frac{dT}{dz} \tag{7.10}$$

where T is the fluid temperature, z is the axial coordinate in the preheating tubing, r_i is the internal tubing radius, C_p is the fluid heat capacity, ρ is the fluid density, and [CO] is the

carbon monoxide concentration. The rate of the water-gas shift reaction is assumed to obey a global kinetic expression of the form

$$R_{WGS} = k\,[CO]^a \tag{7.11}$$

where a is an empirical reaction order and k, the rate constant, is given by an Arrhenius rate form,

$$k = A\exp(-E_a/RT) \tag{7.12}$$

Equation 7.9 describes the heat transfer to the preheating tubing (and hence the temperature profile in the tubing) and is analogous to Equation 7.6. Equation 7.10 describes the carbon monoxide profile in the tubing; the first term accounts for disappearance by reaction, while the second term accounts for changes in concentration as the fluid density decreases upon heating. Since the fluid temperatures at the reactor entrance and exit agree within a few degrees Celsius, the reactor is assumed to be isothermal and is described by the third equation,

$$d[CO]/dt = -R_{WGS} \tag{7.13}$$

Equations 7.9, 7.10 and 7.13 were integrated using two consecutive Runge-Kutta schemes (Press *et al.*, 1986) to yield the carbon monoxide concentration at the reactor exit (and thus the conversion in the system). Fluid properties were calculated from the equation of state of Haar *et al.* (1984), while all other quantities were known (or calculable) from experimental conditions. This model was used as the input to a non-linear regression routine, using a modified Marquardt method (Press *et al.*, 1986), to find best-fit values for the three kinetic parameters (A, E_a, and a) in Equations 7.11 and 7.12.

The selection of the rate form given by Equations 7.11 and 7.12 entails several implicit assumptions. First, we have assumed that a single global rate expression is valid over the range of temperatures encountered in the preheating tubing and reactor, and hence that the reaction does not undergo a change in mechanism as the fluid is heated. This assumption would not be unreasonable for a gas-phase reaction, but in the present case the mixture must pass through the near-critical region as it is heated. As a result, reaction mechanisms are likely to change from predominantly ionic, for temperatures at and below the critical region, to predominantly free-radical, at temperatures above the critical region. The assumption of a single mechanism/single rate expression thus appears questionable. We would argue, however, that any reactions occurring near or below the critical region (for temperatures of 400 °C or lower) are sufficiently slow, because of the relatively low temperatures, that they may be neglected. Experiments conducted at 440 °C or below yielded rates so low as to be almost unmeasurable, providing further evidence for this conclusion. We thus feel that the assumption of a single rate expression is justified.

A second implicit assumption in Equation 7.11 is that the water concentration has no effect on the water-gas-shift rate. In reality, this is probably not true. In our experiments, however, water was by far the major component (mole fraction > 0.999), and its concentration in the reactor was essentially constant during an experiment, independent of any depletion by reaction. One may thus consider the water dependence of the rate to be implicitly included in the rate constant, i.e.,

$$k = \hat{k}[H_2O]^b \tag{7.14}$$

where $\hat{k}$ is the "true" rate constant and b is the order with respect to water. Furthermore, all of our experiments were conducted isobarically. Any variation in water concentration

(density) between experiments was thus directly related to the change in temperature, and the effects of changing water concentration and changing temperature are inseparable. Attempts to regress a value for b resulted in high estimated parameter errors and a high correlation between b and the preexponential factor A. The water dependence was subsequently eliminated from the rate expression.

The water-gas-shift data listed in Table 12.7 and shown in Figure 7.3 reflect only the water-gas-shift portion of the observed overall reaction. Since it was not possible to eliminate oxygen completely from the reactor, a small amount of reaction occurred by the direct-oxidation pathway. Evidence of this contribution was seen in the effluent H_2/CO_2 ratios, which were consistently less than one for the water-gas-shift experiments. If the water-gas shift-pathway alone were operative, the H_2/CO_2 ratios would be unity. Instead, the conversion by the water-gas-shift pathway, X_{WGS}, can be calculated as

$$X_{WGS} = X_{total}(H_2/CO_2)_{effluent} \tag{7.15}$$

Observed values for X_{WGS} are given in Table 12.7, where they are listed as the total conversions. The average value for $(H_2/CO_2)_{effluent}$ in the water-gas-shift experiments was 0.8, so that the direct-oxidation pathway for the most part provided only a minor contribution. Regressions on the water-gas-shift data were performed using only the water-gas-shift portion of the total reaction.

Regression of the water-gas-shift data to the model in Equations 7.9 through 7.13 gave the following rate expression:

$$R_{WGS} = 10^{3.3\pm0.2} \exp(-95\pm3/RT)\,[CO]^{0.71\pm0.08} \tag{7.16}$$

where the units are the same as for previous rate expressions. Parameter uncertainties are at the 95% confidence level as estimated by an ANOVA routine (Press *et al.*, 1986). The

low estimated uncertainties are evidence of the model's sensitivity to the values of the parameters; relatively small changes in parameter values resulted in greatly over- or underpredicted conversions. For the sake of comparison, the corrected water-gas-shift data from the earlier study (Helling and Tester, 1987), shown in Figure 7.3, were regressed to a rate expression of the form of Equations 7.11 and 7.12; the best-fit expression was

$$R_{WGS} = 10^{2.6\pm1.2} \exp(-67\pm11/RT)\,[CO]^{0.61\pm0.19} \qquad (7.17)$$

In deriving Equation 7.17, only the conversion due to water-gas shift was used; in other words, we applied the correction of Equation 7.15 to the earlier data. In the original regression of the earlier water-gas-shift data (Equation 7. 3), all conversion was included in the regression.

Equations 7.3, 7.16, and 7.17 share the common features of a low preexponential factor and an order with respect to carbon monoxide which is less than one. Equations 7.3 and 7.17, the expressions obtained from the uncorrected and corrected data from the earlier study, also share the same activation energy. The reasons for the difference in apparent activation energy between the earlier data and the present study are not clear. A possible explanation is the inclusion of the different preheating tubing effects in the regression of the earlier data, as the calculated time-temperature profiles in the new data were more gradual than the earlier calculated profiles.

Graven and Long (1954) studied the water-gas-shift reaction in the gas phase at temperatures of 875 to 1050 °C and observed rates of similar magnitude to those observed in this study (about 10^{-8} mol/cm^3-s). Their derived rate expression differed markedly from Equation 7.16, however; although they found a fractional-order (0.5) dependence on carbon monoxide, Graven and Long observed a much higher activation

energy, 282 kJ/mol, and a first-order dependence on water. Furthermore, both Graven and Long (1954) and Tingey (1966) noted that the rate of the water-gas shift is strongly affected by the presence of even trace quantities of oxygen. In fact, Tingey noted a decrease from 326 kJ/mol to 164 kJ/mol in the activation energy of the reverse (CO_2 + H_2) reaction below about 800 °C, which was tentatively attributed to an oxygen-facilitated pathway. Given that oxygen could not be completely eliminated from our experimental system, and a certain fraction of the total carbon monoxide conversion occurred by direct oxidation even in the water-gas-shift experiments, we cannot exclude the possibility that the rates we have measured are influenced by the presence of oxygen. Lastly, neither Graven and Long (1954) nor Tingey (1966) report the occurrence of a predominantly heterogeneous reaction over their range of conditions (1 bar, 400 to 1050 °C).

Having obtained a rate expression for the water-gas shift in our current apparatus, we were able to calculate the conversion of carbon monoxide during preheating of the CO feed, both in our water-gas shift and in our oxidation experiments, using Equations 7.9, 7.10 and 7.16. In this way an "actual" reactor inlet concentration of carbon monoxide could be estimated. The calculated feed concentrations are given in Tables 12.7 and 12.8. In all cases the calculated inlet concentration was only slightly smaller (by at most 4%) than the inlet concentration assuming no reaction during preheating. In other words, only a small conversion of CO occurred in the preheating tubing. Table 12.7 lists both total conversion of CO by water-gas shift and conversion within the reactor; the difference between these is the conversion during preheating. In no case was the conversion during preheating more than a few percent. As a result, the correction to the inlet CO concentration was small, almost always within the experimental error of the feed concentration measurement. Interestingly, the correction became larger at higher sand-

bath temperatures, indicating that it was the high-temperature portion of the preheater temperature profile which was important in determining the extent of reaction in the tubing. In retrospect, the conclusion that reaction during preheating was virtually negligible may seem obvious, but one must remember that this conclusion could not be reached *a priori*.

7.4 Derivation of Direct-Oxidation Rate Expression

Of the two pathways for conversion of CO to CO_2, direct oxidation is faster and is of more interest from a process-engineering viewpoint. Unfortunately, the direct oxidation pathway in supercritical water cannot be studied independently from the water-gas-shift pathway. Having quantified the kinetic behavior of the water-gas-shift pathway individually, we sought to use that kinetic information to subtract the water-gas-shift contribution from the overall oxidation, and hence separate the direct-oxidation pathway. The only practical method to accomplish this goal is to assume that the two pathways are independent and that their rates are additive, i.e.,

$$R_{\text{total}} = R_{\text{WGS}} + R_{\text{DO}} \tag{7.18}$$

This separation of pathways is convenient in practice but lacks rigor. Oxidation in a supercritical water environment is likely to proceed via free-radical mechanisms (see Section 6.1). The water-gas shift and direct oxidation pathways are merely empirical, global representations of the much more complex set of reactions occurring, and at a fundamental level the two global pathways are intimately linked through shared elementary reactions. A truly robust model must necessarily incorporate the detailed free-radical mechanism. Unfortunately, implementation of these more complex models can be computationally intensive. When simplicity and ease of use are required,

however, global empirical models can be used with success over a limited range of conditions. Such models have found wide use in the combustion field, where, for example, methane oxidation has been modeled using two global rate expressions, one for methane disappearance and the other for CO oxidation (Dryer and Glassman, 1973). These two "reactions" are again intimately linked, but as an approximation can be treated as two separate global pathways. The global modeling approach is useful when one wants to calculate the formation of certain product or intermediate species, such as carbon monoxide in the combustion example or hydrogen in our case.

A test of the additivity assumption is the comparison of the water-gas shift conversion during oxidation with the conversion calculated to occur using the rate expression obtained for the water-gas shift alone. In other words, the conversion by water-gas shift during an oxidation experiment can be calculated assuming the water-gas shift pathway is unaffected by the simultaneous direct oxidation. Good agreement between these calculated conversions and the observed conversions would indicate that the assumption of additivity of rates is valid. The results of this comparison are shown in Figure 7.9, where the observed conversion by water-gas shift during the oxidation experiments is compared to the conversion calculated using Equation 7.16 (note the expanded scale). In general, there is good agreement between the two, with deviations generally within estimated experimental errors, indicating that the water-gas-shift pathway is neither greatly enhanced nor greatly suppressed in the presence of oxygen. Rather, the water-gas shift appears to proceed under oxidizing conditions at a rate similar to that observed when oxygen is absent. There is in Figure 7.9 a slight trend of overpredicted conversions, but this behavior is likely the result of assuming in the calculations that only the water-gas shift occurred. In reality, the direct-oxidation pathway is also depleting the carbon monoxide concentration, and thus the CO

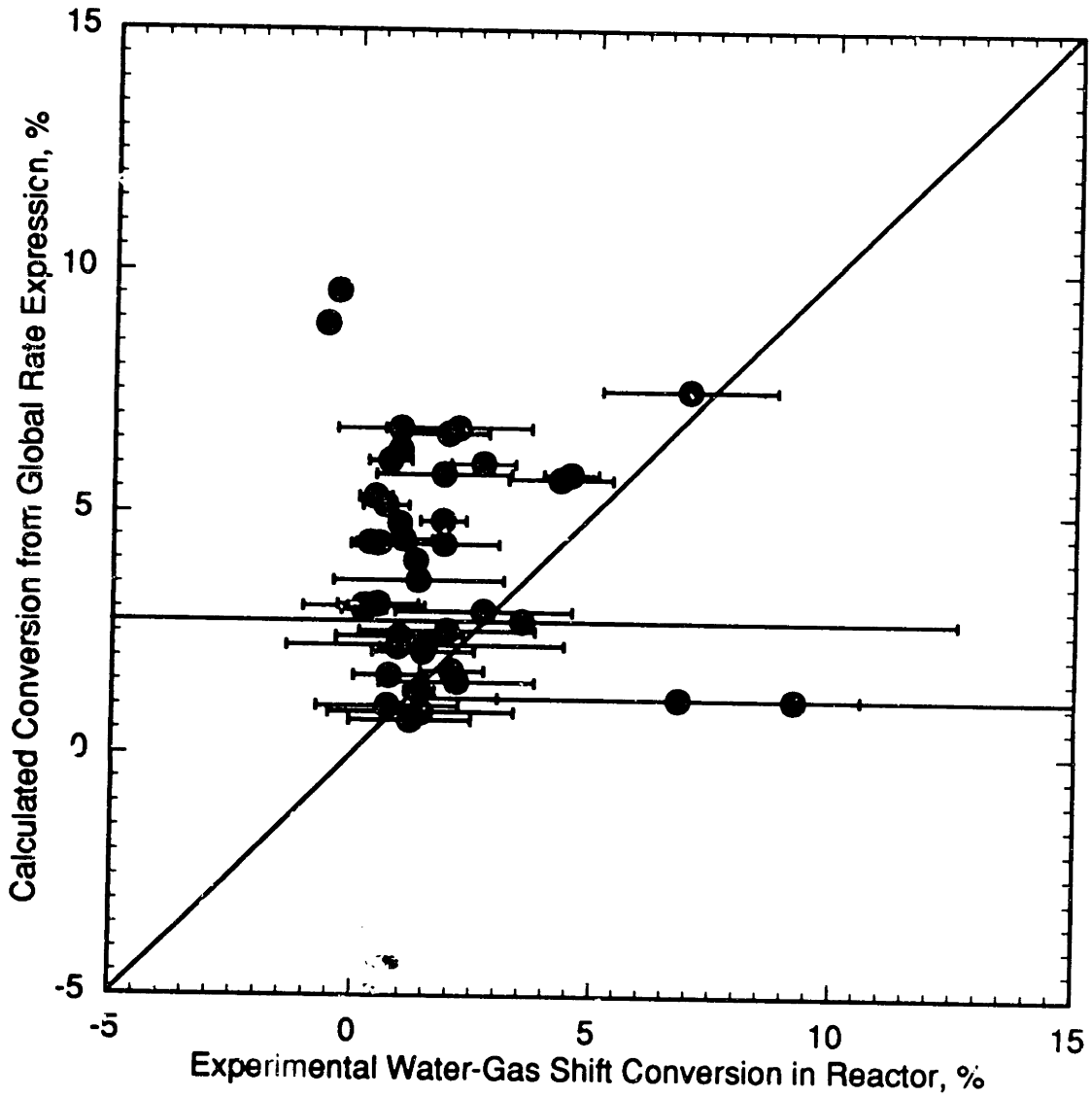

Figure 7.9 **Conversion by Water-Gas Shift Pathway During Oxidation Experiments, as Observed Experimentally and as Calculated Using the Global Rate Expression Developed for the Water-Gas Shift Alone.**

concentration (and hence the reaction rate) will decrease more rapidly than calculated, resulting in a lower conversion than calculated. In any case, the calculations strongly suggest that under these conditions the two reaction pathways can be considered parallel or superimposable.

The apparent independence of the water-gas-shift and direct-oxidation pathways allows us to separate the contributions of the two pathways and thus derive a rate expression for the direct-oxidation pathway from the overall oxidation data. Since both pathways affect the carbon monoxide concentration, the model for the overall oxidation process is more complicated than for a single reaction. In particular, the kinetic behavior is described by

$$d[CO]/dt = -R_{WGS} - R_{DO} \tag{7.19}$$

$$d[O_2]/dt = -{}^1/_2 R_{DO} \tag{7.20}$$

Equation 7.19 is a restatement of Equation 7.18; Equation 7.20 reflects the fact that oxygen is depleted only by direct oxidation, at the stoichiometric ratio of $^1/_2$. R_{WGS} in Equation 7.19 is the water-gas shift rate expression derived earlier (Equation 7.16). For R_{DO} we assume the form

$$R_{DO} = k\,[CO]^a\,[O_2]^b \tag{7.21}$$

where k is again given by an Arrhenius rate form, and we have omitted a dependence on water for the reasons discussed earlier. Equations 7.19 and 7.20 can be integrated using a Runge-Kutta routine (Press *et al.*, 1986) to give a total conversion of carbon monoxide which can be used in a non-linear regression routine (Press *et al.*, 1986) to find optimal values for the four parameters in Equation 7.21. In our regression of the direct-oxidation rate form to the overall oxidation data, we included the oxidation data from the earlier

study. Admittedly the earlier data have not been corrected for reaction during preheating; however, the calculated corrections for the present study were within experimental error of the feed concentrations, and there was a lesser degree of preheating (and thus likely a smaller amount of reaction during preheating) in the earlier study. For these reasons we feel justified in using the earlier data without correcting for reaction during preheating.

An important assumption in the use of the earlier data is that the current water-gas-shift rate expression could describe the water-gas shift in the earlier data. Figures 7.2 and 7.3 suggest that this is not the case: the earlier data contained a larger contribution of the water-gas shift and the water-gas shift appeared to proceed more rapidly in general. The lower rates of the water-gas shift in the current study relative to those in the earlier study are, however, consistent with a global model for methane oxidation (Webley and Tester, 1991) which incorporated the earlier water-gas-shift rate expression. In that modeling effort, the rate of the water-gas-shift reaction was found to be too fast to correctly predict the experimental observations. The experimental methane oxidation study (Webley and Tester, 1991) was carried out in the current apparatus, so it is possible that there is systematic difference between the old and new reactors. Given the similarity of the systems, though, it is unlikely that such a difference could exist, particularly one that would affect the water-gas-shift pathway preferentially. The small effect of reaction during preheating cannot account for the difference between the data sets, particularly since the feeds were preheated to a lesser extent in the earlier study. Preliminary experimental studies in both the old system (Helling and Tester, 1987) and the current system, with the reactor surface area-to-volume ratio increased by as much as a factor of 30, had revealed little or no heterogeneous catalytic (or inhibitory) effects in CO oxidation, although Section 5.4 showed that hydrogen oxidation is retarded in the presence of high surface area. In any case, surface-to-volume ratios in the two systems

differ by only about 20%; any heterogeneous effects should thus be similar in both. The most likely reason for the difference in water-gas-shift behavior was a difference in the analytical method for hydrogen. In the earlier study, sensitivity to hydrogen in the gas chromatograph was not as good as with the present analytical technique. There is some likelihood that hydrogen concentrations measured in the earlier study were consistently too high. In the earlier water-gas-shift study (Helling and Tester, 1987), effluent H_2/CO_2 ratios occasionally reached values as high as 1.15, clearly a non-physical result. In fact, since complete exclusion of oxygen from the reactor is almost impossible, H_2/CO_2 ratios should almost always be *less* than unity. If a systematic analytical error occurred such that hydrogen was consistently overmeasured, the water-gas-shift contribution to the overall oxidation would have been consistently overestimated. The present application of the newer water-gas-shift rate expression to the earlier oxidation data assumes that the water-gas-shift contribution was inaccurately measured in those data.

The best-fit, direct-oxidation rate expression obtained from the regression of all the oxidation data was

$$R_{DO} = 10^{8.5\pm3.3} \exp(-134\pm32/RT)\,[CO]^{0.96\pm0.30}\,[O_2]^{0.34\pm0.24} \qquad (7.22)$$

with the units the same as previously and the estimated errors at the 95% confidence level. Comparison of Equation 7.22 with Equation 7.4 reveals that the preexponential factor and activation energy obtained for the direct oxidation are very similar to those obtained in the earlier study for the overall oxidation. The order with respect to carbon monoxide in Equation 7.22 is essentially one, as it is in Equation 7.4. A technique similar tc that described here was used in the earlier study (Helling and Tester, 1987) to derive a rate expression for the separated direct oxidation. The resulting rate form exhibited a high activation energy (238±24 kJ/mol) and a high order with respect to CO

(1.87±0.02), although the oxygen order was again statistically zero. The source of the large difference in direct oxidation rate expressions is unclear, as is the reason for the good agreement between the current direct-oxidation expression and the earlier overall-oxidation expression.

The oxygen dependence in Equation 7.22 is new; in the earlier study we observed an independence of oxygen over the entire range of experimental conditions. While there is significant error associated with the precise value of the order with respect to oxygen, it is non-zero at a confidence level exceeding 99%.

The kinetic data for the water-gas shift (from the present study) and the direct oxidation (from both studies) are summarized in Figure 7.10, where they are shown with the corresponding best-fit rate expressions. Rate constants in Figure 7.10 were calculated by numerically integrating the plug-flow equation for the data using the regressed values for the reaction orders. The higher activation energy for the direct oxidation relative to the water-gas shift is consistent with the observed decrease in the water-gas shift at higher temperatures (see Figure 7.2). As temperature increases, the rate of the direct oxidation rises more rapidly and its relative contribution increases.

The fractional-order dependence of the direct-oxidation rate form on oxygen is consistent with global rate forms derived for moist carbon monoxide oxidation in earlier low-pressure (0.04 to 2.47 bar), gas-phase combustion studies (Kozlov, 1959; Hottel *et al.*, 1965; Dryer and Glassman, 1973; Howard *et al.*, 1973). A summary of gas-phase global rate expressions is given in Table 7.1, where they are compared with the Equation 7.22. The study of Yetter *et al.* (1986) is a special case, in which elementary reaction modeling results were fit to a global rate expression in order to evaluate the conditions of applicability of a given global rate form. In the gas phase, the global water-gas-shift pathway is virtually negligible and almost all carbon monoxide oxidation occurs by the

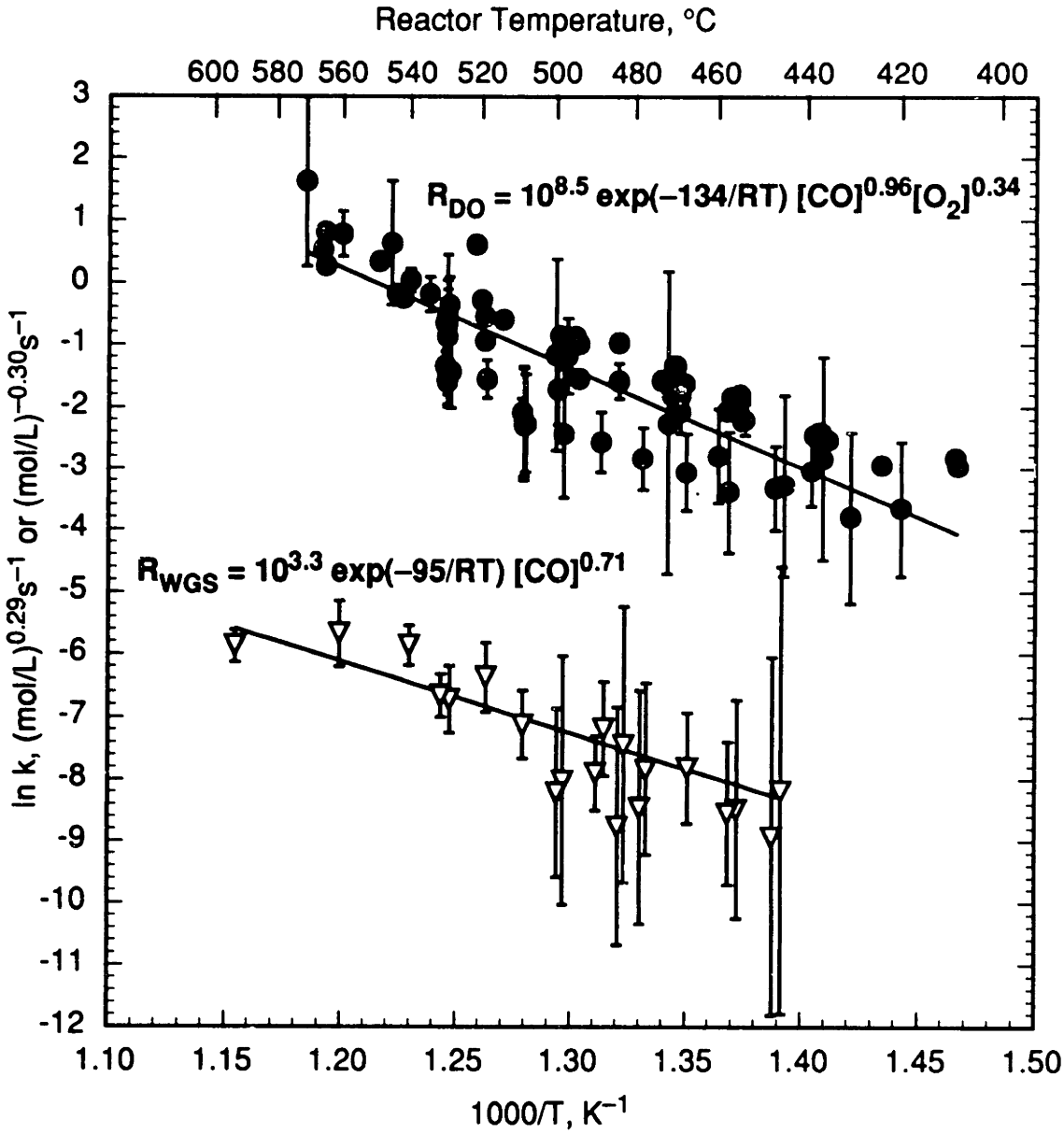

Figure 7.10 **Arrhenius Plot of Direct Oxidation and Water-Gas Shift Data, Including Global Rate Expressions.** Direct oxidation data include both the current data and the data of Helling and Tester (1987).

$$d[CO]/dt = -A \exp(-E_a/RT)\,[CO]^a\,[O_2]^b\,[H_2O]^c$$

Units: kJ, mol, cm³, s, K

Source	Conditions	log *A*	E_a	*a*	*b*	*c*
Kozlov (1958)	1 bar 873–1373 K	12.0	134	1	0.25	0.5
Hottel *et al.* (1965)	0.3–1 bar 1280–1535 K	11.1	66.9	1	0.3	0.5
Dryer and Glassman (1973)	1 bar 1030–1230 K	14.6	167	1	0.25	0.5
Howard *et al.* (1973)	0.04–1 bar 840–2360 K	14.1	126	1	0.5	0.5
Lyon *et al.* (1985)	1.24 bar, 1123–1298 K	10.2	98.7	1	0.25	0.5
	2.47 bar, 1123–1273 K	11.6	127.2	1	0.25	0.5
Yetter *et al.* (1986)	1 bar; 1600–2100 K	11.0	87.9	1	0.25	0.5
	900–1000 K	20.9	289	1	0.25	0.5
	650–750 K	14.8	234	1	0.25	0.5
Present Study (supercritical water)	246 bar 693–843 K	9.4	134	0.96	0.34	0

Table 7.1 **Global Rate Expressions for Low-Pressure, Gas-Phase Moist Carbon Monoxide Oxidation.** Results from the present study in supercritical water at 246 bar are also shown for comparison.

direct-oxidation pathway. All of the studies observed a first-order dependence of the oxidation rate on carbon monoxide concentration, as was observed in the present study. Hottel *et al.* (1965) observed a dependence of the oxidation on oxygen of variable order, approximated as 0.3, while Howard *et al.* (1973) observed a 0.5-order dependence and Dryer and Glassman (1973) and Kozlov (1958) a 0.25-order dependence. The other studies (Lyon *et al.*, 1985; Yetter *et al.*, 1986) used assumed global reaction orders. At a 95% confidence level, the order we determined (0.34±0.24) cannot be distinguished from any of the gas-phase values. Interestingly, the activation energies obtained in four of those studies (167 kJ/mol (Dryer and Glassman, 1973), 134 kJ/mol (Kozlov, 1958), 127 kJ/mol (Lyon *et al.*, 1985), and 126 kJ/mol (Howard *et al.*, 1973)) are also quite similar to that observed in this study (134±32 kJ/mol). On the other hand, observed low-pressure, gas-phase activation energies were as low as 67 kJ/mol and as high as 289 kJ/mol. Furthermore, all four gas-phase studies observed a 0.5-order dependence of the oxidation rate on water concentration; as discussed earlier, no such order can be determined under our conditions and any water dependence in our data must be considered subsumed within the rate constant. Owing to the inclusion of a reaction order with respect to water, preexponential factors in the gas-phase studies were higher (typically 10^9–10^{12} in units of mol, L, and s) than the value obtained here ($10^{8.5}$).

The inclusion of the current data set introduces an oxygen dependence in the rate of the direct oxidation, whereas the earlier data set exhibited no such dependence. The new oxygen dependence may be the result of the inclusion of experiments with substoichiometric oxygen, as implied by the observations of Yetter *et al.* (1991b) In a recent gas-phase study of moist carbon monoxide oxidation, they reported that the rate of disappearance of CO was independent of oxygen concentration for feed ratios of oxygen to carbon monoxide greater than stoichiometric ($[O_2]_o/[CO]_o \geq 0.5$). On the other hand,

for $[O_2]_o/[CO]_o < 0.5$, the first 50% of the carbon monoxide disappeared at the same rate, while the second 50% disappeared at a rate which decreased with decreasing oxygen concentration. Close examination of their data, however, reveals that a more likely explanation is that the oxygen "dependence" results only when the oxygen in the substoichiometric experiments had been depleted. The results of Yetter *et al.* (1991b) thus seem to imply an independence of oxygen under both fuel-rich and fuel-lean conditions. The newly determined oxygen dependence of carbon monoxide oxidation in supercritical water is therefore inconsistent with the results of Yetter *et al.*, but consistent with earlier gas-phase studies. The lack of an observed oxygen dependence in the data of Helling and Tester (1987) is most likely the result of the more limited range of oxygen concentrations examined in that study.

There is considerable variation among the gas-phase global rate expressions for moist carbon monoxide oxidation in Table 7.1. Clearly there is no single rate expression which characterizes the global reaction. In particular, the modeling study of Yetter *et al.* (1986) showed that the global Arrhenius parameters can vary markedly with conditions, even with a change only in temperature: the rate expressions for the three temperature ranges listed in Table 7.1 were obtained with all other model parameters (pressure, concentrations) held constant. These changes in the global parameters are the direct results of changes in the relevant elementary reaction network with changing conditions. As temperature is varied, for example, different reaction subsets of the total mechanism become important, yielding different global oxidation behavior.

The oxidation of carbon monoxide is highly sensitive to the presence of a hydrogenous species, especially molecular hydrogen or water. In fact, there is some doubt whether carbon monoxide can undergo rapid oxidation in the complete absence of

a hydrogen-containing species (Lewis and von Elbe, 1987). The principal oxidizing elementary reaction for CO is

$$CO + OH \rightarrow CO_2 + H \tag{7.23}$$

where one notes that OH radicals cannot form without a hydrogen source. The sensitivity of the oxidation rate to the presence of a hydrogenous species is reflected in the 0.5 order with respect to water in all the rate expressions in Table 7.1. At some level, the concentration of water becomes sufficiently high that it no longer acts to increase the available OH radical pool, but rather affects the oxidation through other mechanisms (Yetter *et al.*, 1991b). The gas-phase studies in Table 7.1, with the exception of Lyon *et al.* (1985), all examined water concentrations of roughly the same order of magnitude or smaller than the carbon monoxide concentration. In the present study, water concentrations are over three or 'ers of magnitude higher than the carbon monoxide concentration. Furthermore, while conditions in our supercritical water oxidation experiments are very dilute in terms of fuel and oxidant mole fractions, the corresponding volumetric concentrations are actually quite similar to those found in high-temperature, atmospheric, gas-phase oxidation studies. For example, a fuel or oxidant concentration of 10^{-6} mol/cm^3, common in our experiments, is equivalent to the concentration of a species present at 1000 K and 1 bar at a mole fraction of 10%. The present experiments may thus be envisioned as a "gas-phase" study in which the water concentration has been increased by several orders of magnitude. Helling and Tester (1987) compared the predictions of several of the gas-phase rate expressions in Table 7.1 to their supercritical water oxidation results, and found that (not surprisingly) the gas-phase expressions drastically

overpredicted the oxidation rate in supercritical water. Clearly the 0.5-order dependence on water cannot hold over orders of magnitude of water concentration.

Several gas-phase studies of moist carbon monoxide oxidation have been conducted at temperatures near those of the present study. Kozlov (1958) found an apparent first-order rate constant ($k^* = -d\ln[CO]/dt$) for gas-phase carbon monoxide oxidation of about 1 s^{-1} at 600 °C, which is very similar to the results shown in Figure 7.1. On the other hand, Khitrin and Solovyeva (1958), for almost identical conditions (2–6% CO in air at 600 °C and 1 bar) but with roughly three times the water concentration (2% vs. 0.6%), observed a first-order rate constant of ~5 s^{-1}, and at 500 °C, the first-order rate constant of Khitrin and Solovyeva was ~1 s^{-1}, considerably higher than the results of Kozlov (1958) and the results of the present study (Figure 7.1). On the other hand, gas-phase oxidation results with H_2 as the hydrogen source (Arustamyan *et al.*, 1980) at 530 to 570 °C and 0.4 to 0.7 bar demonstrated significantly reduced oxidation rates, with first-order rate constants of ~0.02 s^{-1} or less, indicating that H_2 is a less effective hydrogen source than water. Collectively, the observations of these low-pressure, gas-phase studies suggest that carbon monoxide oxidation rates in supercritical water are comparable to, or somewhat slower than, moist gas-phase oxidation rates at comparable temperatures and carbon monoxide concentrations. Thus the ubiquitous 0.5-order dependence of carbon monoxide oxidation cannot hold for the entire range of conditions from the low-density gas phase to the higher-density, supercritical-water phase.

The apparent moderating influence of water under supercritical conditions can most likely be traced to same effects noted in Section 5.3 for hydrogen oxidation. In particular, high water concentrations can alter the branching pathways in the oxidation mechanism, such that regions of fast reaction (explosion limits) are shifted to much higher temperatures. Since the carbon monoxide oxidation reaction is strongly water-

dependent, the explosion limits have not been well defined (Lewis and von Elbe, 1987), and the existence of a third limit or extended second limit, as exist for hydrogen, has not been verified. Nevertheless, the primary oxidizing mechanism for moist CO oxidation is fundamentally the same as that for H_2 oxidation, with reaction (7.23) replacing the H_2 oxidizing step, and a similar mechanism for high-pressure moderation of the oxidation reaction may be expected to occur for carbon monoxide as occurs for hydrogen oxidation (Section 5.3).

7.5 Global Reaction Modeling

The inability of global rate expressions to reveal fundamental mechanistic information has been noted earlier. There are many instances, however, in which mechanistic information is neither available nor required. For example, detailed gas-phase elementary reaction models exist only for relatively simple (C_4 or smaller) compounds. In supercritical water oxidation, there exist even fewer validated models. In cases where there are no detailed models, a simple global mechanism and rate expression must suffice (Westbrook and Dryer, 1981). Furthermore, mechanistic details may be irrelevant for certain applications; a combined kinetic and hydrodynamic model of a supercritical water oxidation reactor, for example, may require only the simple kinetic information that a global model is capable of providing.

Figure 7.11 shows, in first-order form, the global kinetic results which form the basis for a global reaction modeling scheme. A similar figure was presented in Section 2.3; Figure 7.11 includes results of the present study for the oxidation of hydrogen (Equation 5.11) and carbon monoxide (Equation 7.22). Note that hydrogen is quite stable relative to carbon monoxide for temperatures below about 550 °C; hence its appearance as a water-gas shift product even in the presence of oxygen. Since data exist for the

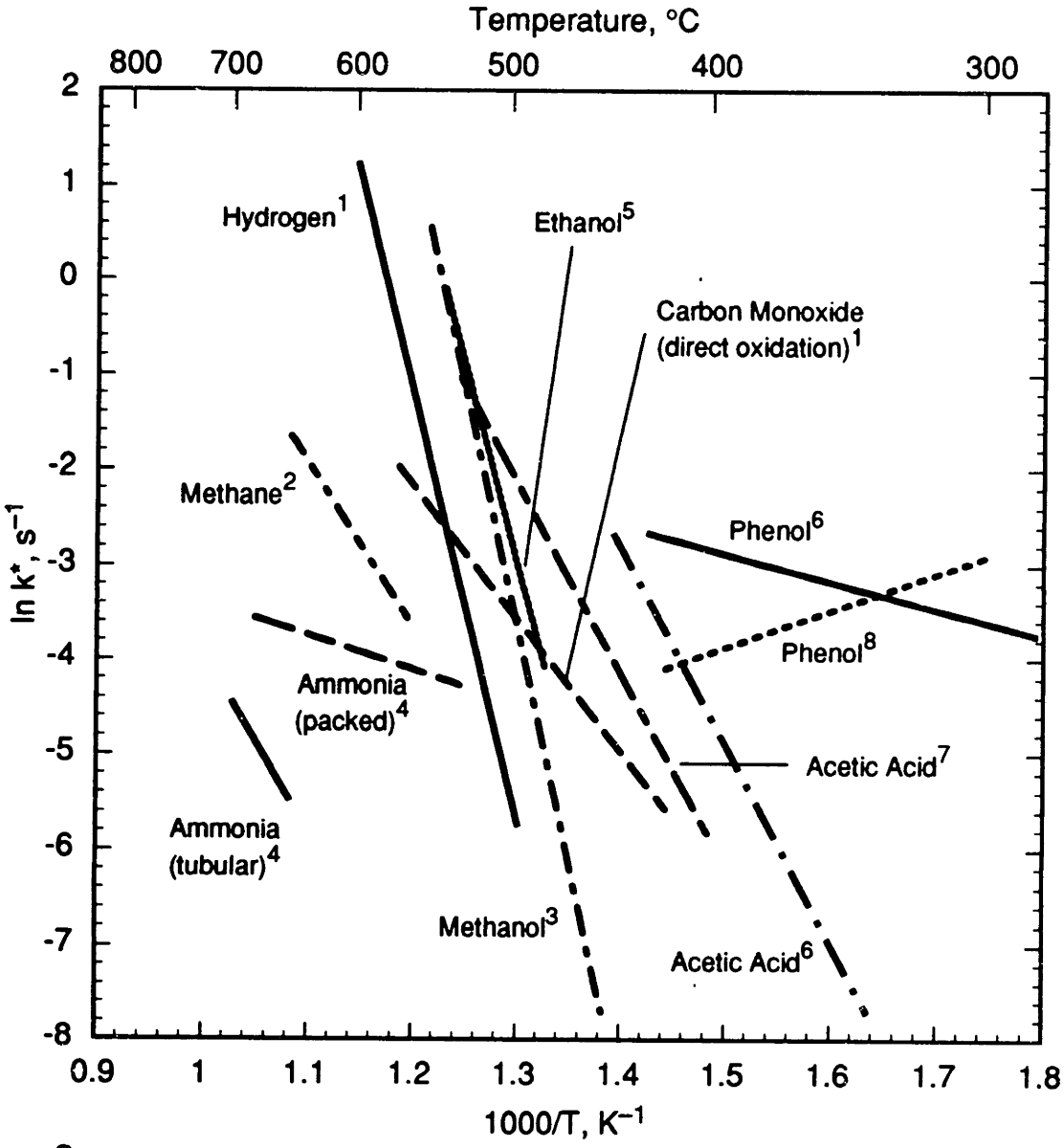

Sources:

[1]Present Study
[2]Webley and Tester (1991)
[3]Webley (1989), Tester *et al.* (1992)
[4]Webley *et al.* (1990,1991)
[5]Helling and Tester (1988)
[6]Wightman (1981)
[7]Lee and Gloyna (1990)
[8]Thornton and Savage (1990)

Figure 7.11 Updated First-Order Arrhenius Plot for Oxidation of Model Compounds in Supercritical Water.

relative yields of carbon monoxide, carbon dioxide, and hydrogen for the oxidation of methane (Webley, 1989; Webley and Tester, 1991) and methanol (Webley, 1989; Tester *et al.*, 1992), those two compounds afford the opportunity for the development and testing of a global, multi-step reaction mechanism. Note that the relative positions of the rate expressions in Figure 7.11 suggest that the rate-limiting step in methane oxidation is the oxidation of methane itself, and not the subsequent oxidation of carbon monoxide. On the other hand, the complete oxidation of methanol is rate-limited by CO oxidation at low temperatures, but by methanol oxidation at higher temperatures.

Figure 7.12 shows the proposed multi-step, global reaction model for the oxidation of methane, methanol, and carbon monoxide. The same global scheme has been used previously (Webley, 1989; Webley and Tester, 1991), but without the newer rate expressions for hydrogen and carbon monoxide oxidation. Methane and methanol are assumed to be oxidized to carbon monoxide, which subsequently undergoes oxidation either by the direct pathway or by the water-gas shift. Hydrogen formed by the water-gas shift may also be oxidized. Rate expressions for the oxidation of methane (Webley and Tester, 1991) and methanol (Webley, 1989; Tester *et al.*, 1992) were taken from previous studies, while Equations 5.11, 7.16, and 7.23 were used for hydrogen oxidation, the water-gas shift, and direct carbon monoxide oxidation, respectively.

7.5.1 Carbon Monoxide Oxidation

The first global model tested was for carbon monoxide oxidation, and comprised three reactions: the two parallel reactive pathways for carbon monoxide and the oxidation of hydrogen (Reactions 3 through 5 in Figure 7.12). The set of coupled ordinary differential equations describing the formation and destruction of the major species (CO, CO_2, O_2, H_2) were solved using a Runge-Kutta routine (Press *et al.*, 1986).

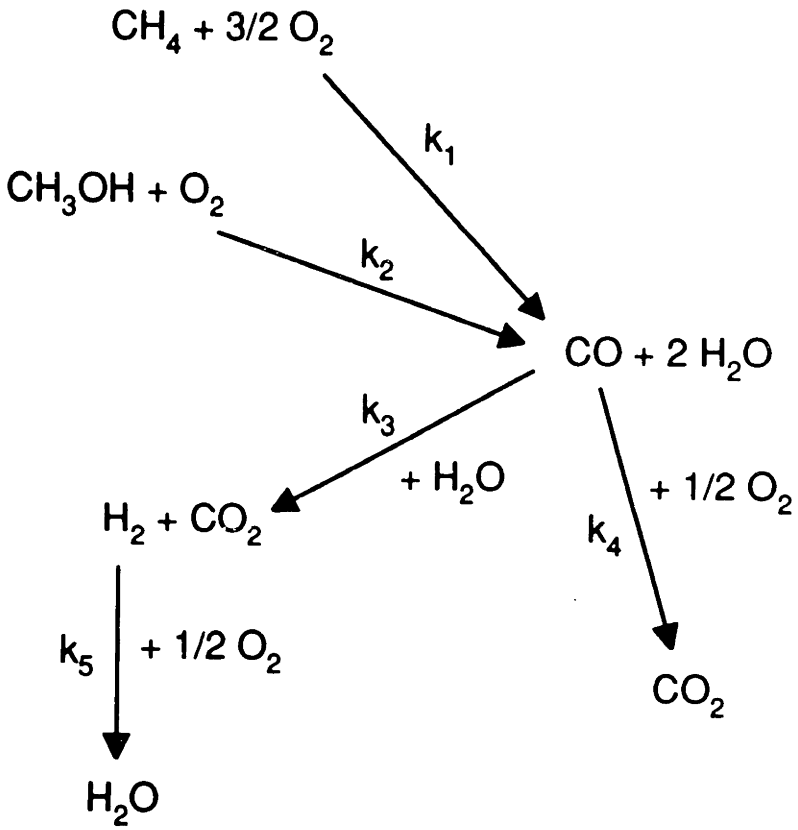

$R_1 = k_1 [CH_4]^{0.99} [O_2]^{0.66}$	$k_1 = 10^{11.4} \exp(-179/RT)$
$R_2 = k_2 [CH_3OH]$	$k_2 = 10^{26.2} \exp(-409/RT)$
$R_3 = k_3 [CO]^{0.71}$	$k_3 = 10^{3.3} \exp(-95/RT)$
$R_4 = k_4 [CO]^{0.96} [O_2]^{0.34}$	$k_4 = 10^{8.5} \exp(-134/RT)$
$R_5 = k_5 [H_2]$	$k_5 = 10^{22.8} \exp(-372/RT)$

Figure 7.12 **Global Reaction Model for Oxidation of Carbon Monoxide, Methane, and Methanol.** Rate expressions have activation energies in kJ/mol, concentrations in mol/L, rates in mol/L-s.

Predictions for the three-step model are shown in Figures 7.13 through 7.17, compared to both the present experimental data (with error bars) and the revised data of Helling and Tester (1987). Figure 7.13 shows the predicted conversion of carbon monoxide, with the newer data corrected for the small amount of reaction during feed preheating. The three-step global model generally reproduces the model well, although the agreement between the model and the data is by no means exact. The model should perform reasonably well in these predictions, since the direct-oxidation rate expression (Equation 7.22) was essentially fit to the conversion data using a two-step model, assuming the water-gas shift occurred in parallel. Hence the only addition with the three-step model is the oxidation of hydrogen, which can only affect the predicted carbon monoxide conversion through depletion of oxygen. Since hydrogen oxidation is relatively slow at the temperatures of the carbon monoxide experiments, the presence of the hydrogen oxidation pathway does not materially affect the predictions of carbon monoxide conversion, and Figure 7.13 is basically a reflection of the fit of the direct oxidation rate expression to the data.

Figures 7.14 through 7.16 show the predicted exit concentrations of carbon monoxide, oxygen, and carbon dioxide. Again, these predictions are essentially a test of the fit of the direct oxidation rate expression. Note that the predictions of the carbon monoxide and oxygen concentrations (Figures 7.14 and 7.15) appear much better than the predictions of conversion and carbon dioxide concentration (Figures 7.13 and 7.16). The reasons for this apparent anomaly are the relative orders of magnitude of the various quantities and the relatively low conversions obtained experimentally. For low-conversion data, the concentration difference across the reactor is small relative to the total concentration; a poor prediction of the conversion corresponds to an error in the small difference between two large quantities, and hence the predicted exit concentration

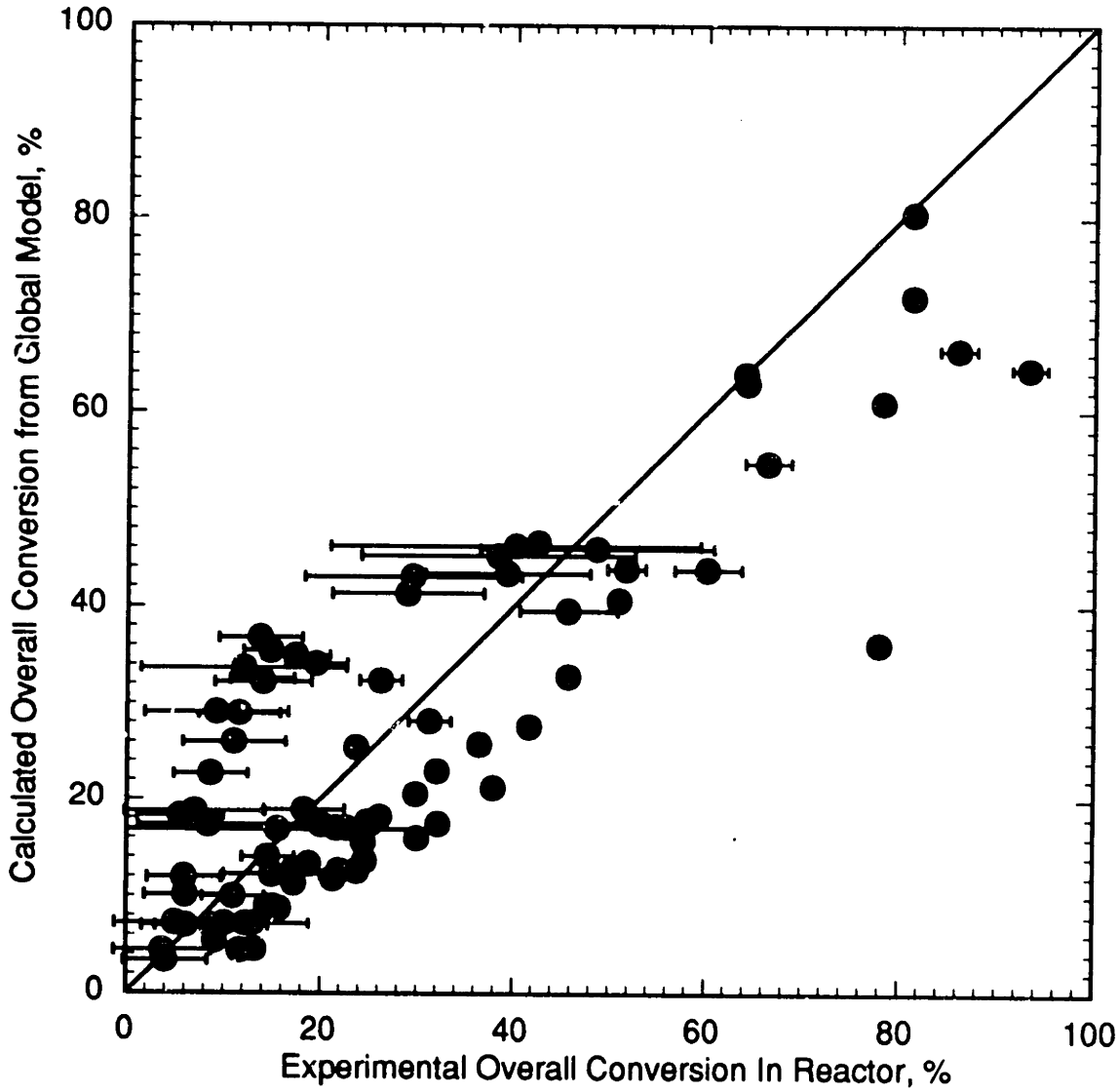

Figure 7.13 **Predicted Conversion from Global Model for Carbon Monoxide Oxidation.**

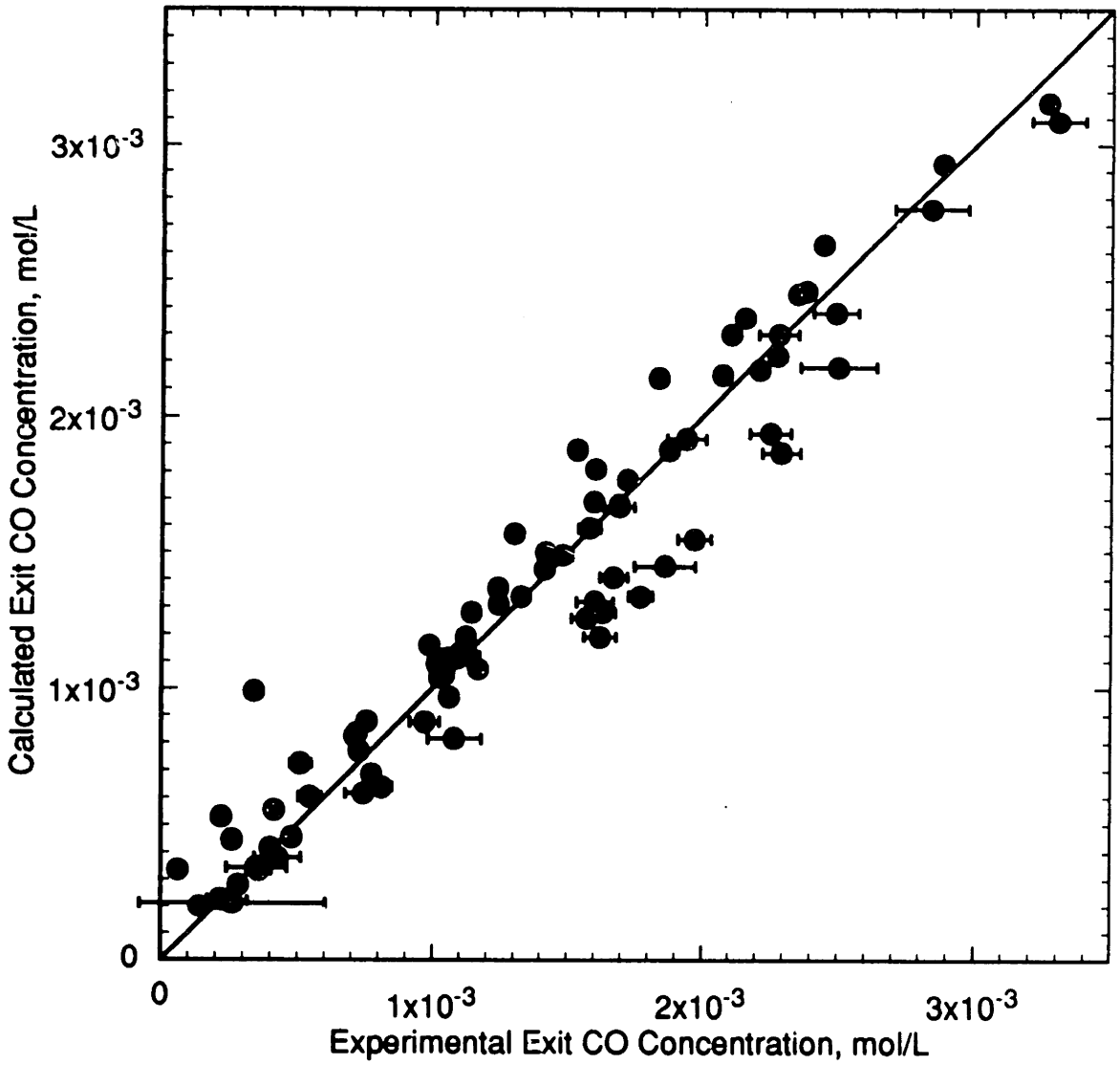

Figure 7.14 **Predicted Carbon Monoxide Concentration from Global Model for Carbon Monoxide Oxidation.**

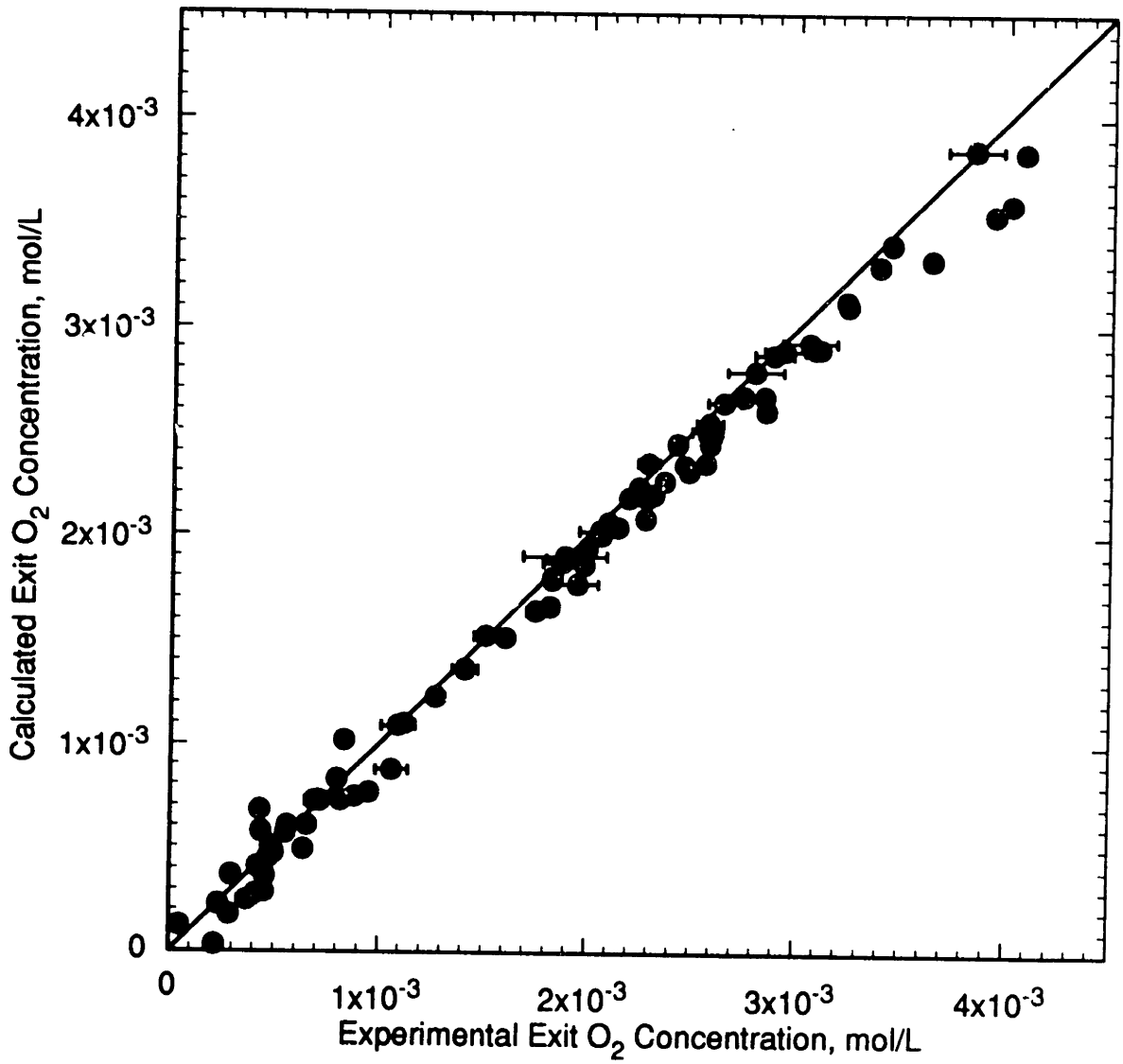

Figure 7.15 **Predicted Oxygen Concentration from Global Model for Carbon Monoxide Oxidation.**

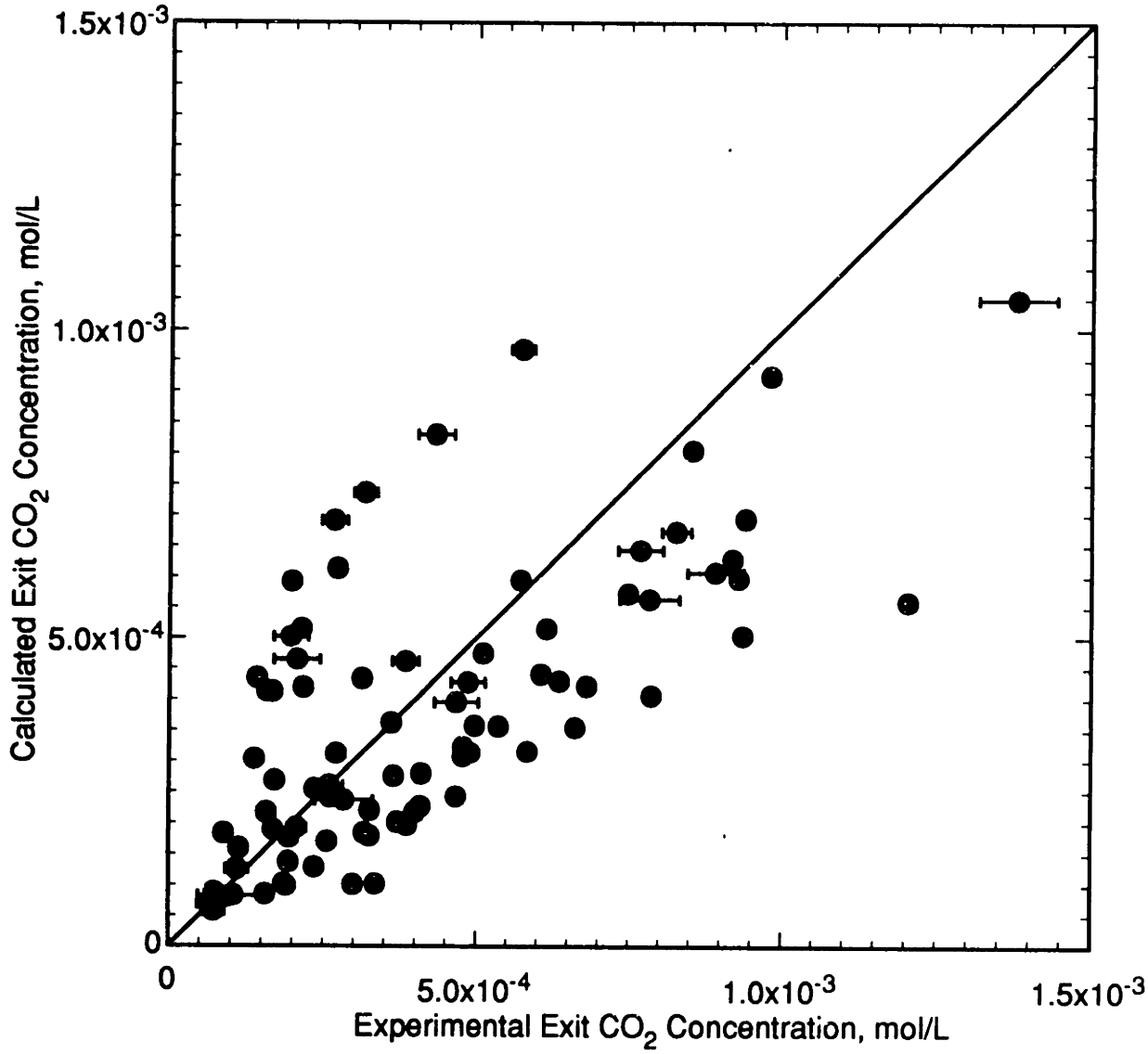

Figure 7.16 **Predicted Carbon Dioxide Concentration from Global Model for Carbon Monoxide Oxidation.**

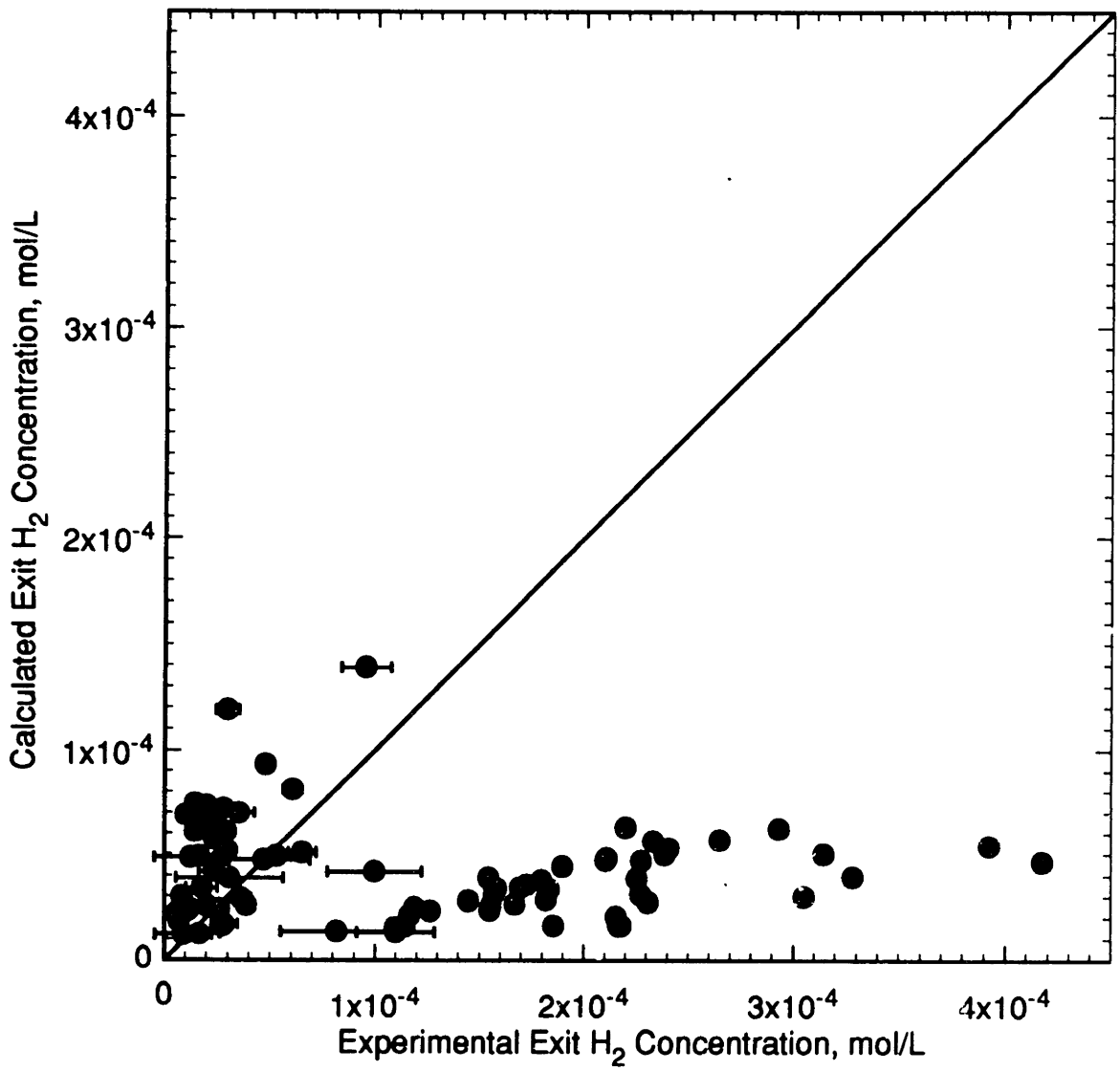

Figure 7.17 Predicted Hydrogen Concentration from Global Model for Carbon Monoxide Oxidation.

of carbon monoxide or carbon dioxide exhibits a very small error relative to the error in the conversion. The same effect is discussed in Section 12.1 in relation to regression of data. Similarly, the predictions of carbon dioxide concentrations (Figure 7.16) appear poorer because the CO_2 concentration is small relative to the CO or O_2 concentrations.

Finally, Figure 7.17 shows the predictions of exit hydrogen concentration. For predictions for the newer data, small concentrations of hydrogen ($\sim 10^{-5}$ mol/L) were added as an initial condition to reflect the calculated formation of hydrogen by the water-gas shift during feed preheating. Two distinct groupings of data exist in Figure 7.17: low-concentration data, which the model largely overpredicts, and higher-concentration data, which the model grossly underpredicts. The high-concentration data are those of Helling and Tester (1987), for which it was concluded that poor analytical measurement sensitivity resulted in overestimated hydrogen concentrations. Thus the underprediction of those data is expected. On the other hand, the overprediction of the newer data implies that either the water-gas-shift rate is too fast or the hydrogen oxidation rate too slow. Still, hydrogen concentrations are very low and the model is at least capable of predicting their approximate magnitude; presumably exact predictions of hydrogen concentrations would not be required for general modeling purposes. In general, then, the three-step global model for carbon monoxide oxidation reproduces the experimental data reasonably well. However, this particular multi-step model does not represent a rigorous test of the modeling methodology, because certain of the model parameters (the direct-oxidation rate expression) were fit directly to the data. Ideally, a multi-step model should be compiled from several independently determined global kinetic expressions.

7.5.2 Methane Oxidation

The existence of both detailed data and a global rate expression for methane oxidation (Webley and Tester, 1991) allows the extension of the multi-step model to a higher level of complexity, as shown in Figure 7.12. The global methane oxidation model now contains four steps: the oxidation of methane to CO and the three subsequent reactions of CO and H_2.

Predicted methane conversions are shown in Figure 7.18. Note that the model generally predicts conversions well, although there is a consistent trend of slightly overpredicted conversions. Similarly, Figure 7.19 shows that methane and oxygen concentrations are consistently underpredicted by a small margin. Figure 7.20, on the other hand, illustrates that carbon dioxide concentrations are predicted quite well, but the carbon monoxide concentrations are uniformly overpredicted. Finally, Figure 7.21 shows that hydrogen concentration predictions are reasonable, considering the high degree of error associated with the experimental data and the very low concentrations present.

Collectively, these predictions suggest that the distribution of carbon in the model is incorrect: there should be less carbon present as carbon monoxide and more present as methane. This incorrect distribution is consistent with a carbon monoxide oxidation rate that is too slow. Since carbon monoxide oxidation consumes oxygen, a too-slow CO oxidation rate decreases the rate of O_2 consumption through that pathway and allows for greater O_2 consumption through the methane oxidation pathway, since the methane oxidation step has a non-zero order with respect to oxygen. This behavior illustrates that the addition of steps that are kinetically "downstream" from the original compound (in this case, methane) can affect the ability of the primary global expression (here, for methane oxidation) to predict conversion of the primary compound.

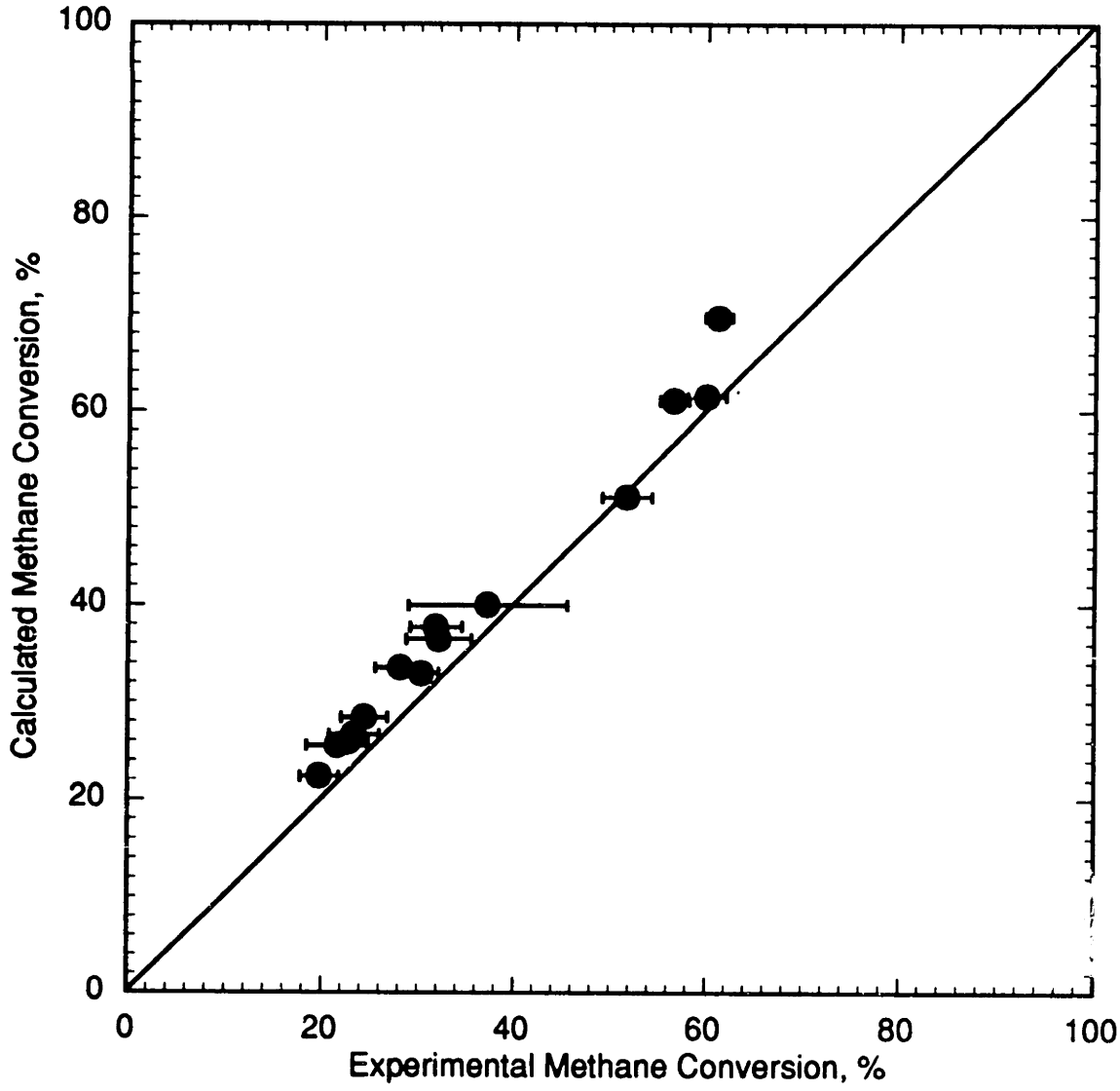

Figure 7.18 Predicted Conversion from Global Model for Methane Oxidation.

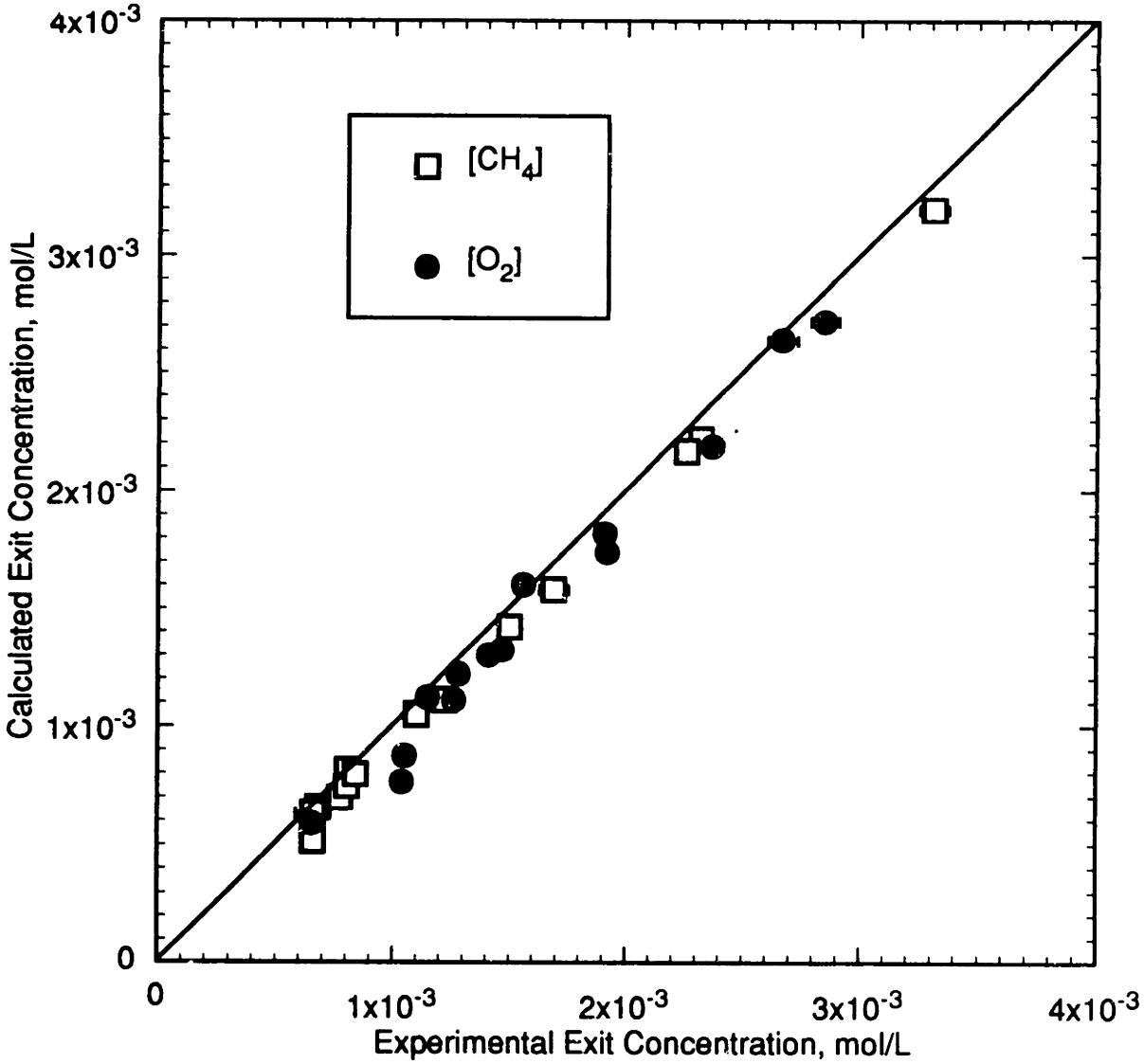

Figure 7.19 Predicted Methane and Oxygen Concentrations from Global Model for Methane Oxidation.

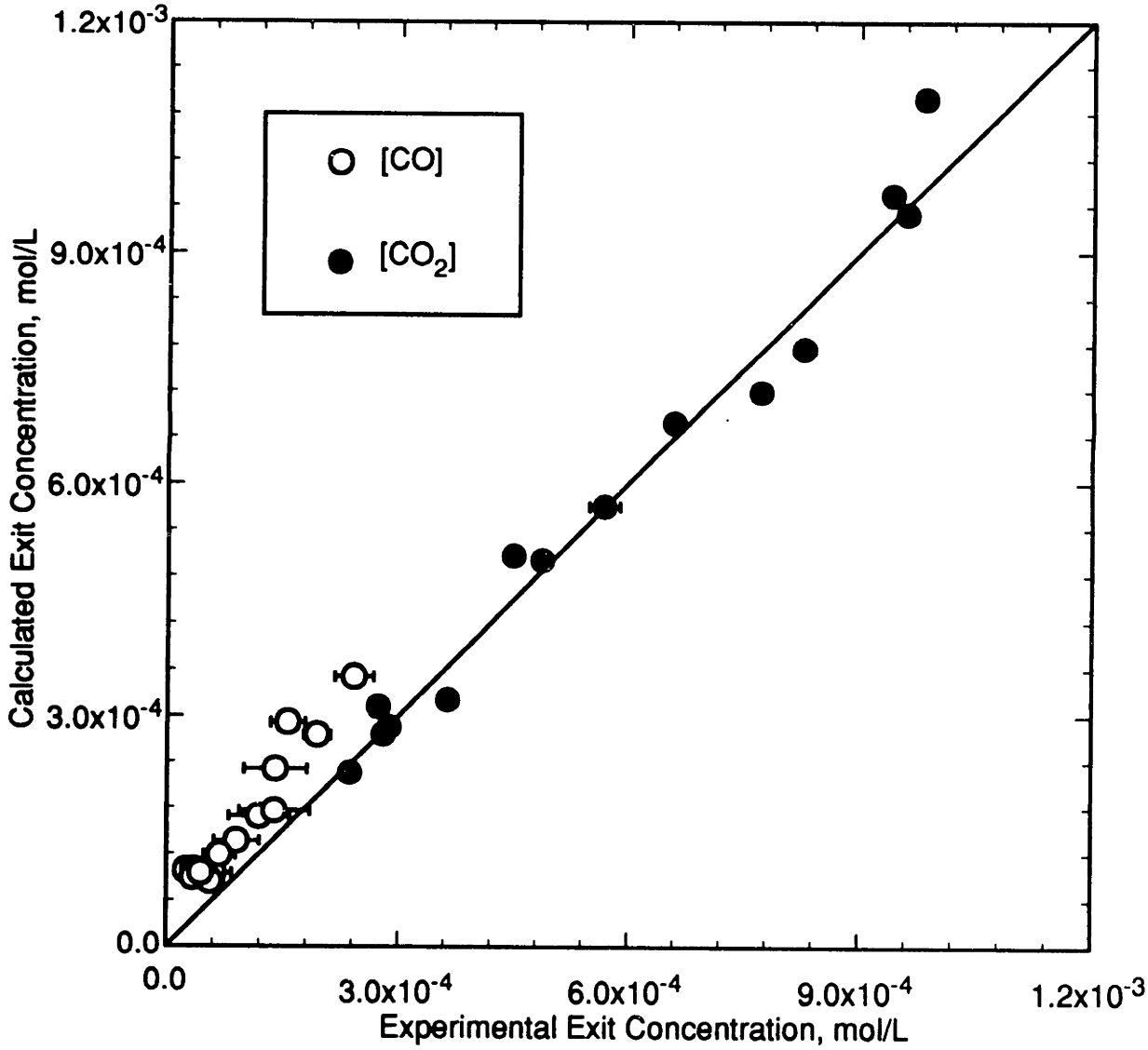

Figure 7.20 Predicted Carbon Monoxide and Carbon Dioxide Concentrations from Global Model for Methane Oxidation.

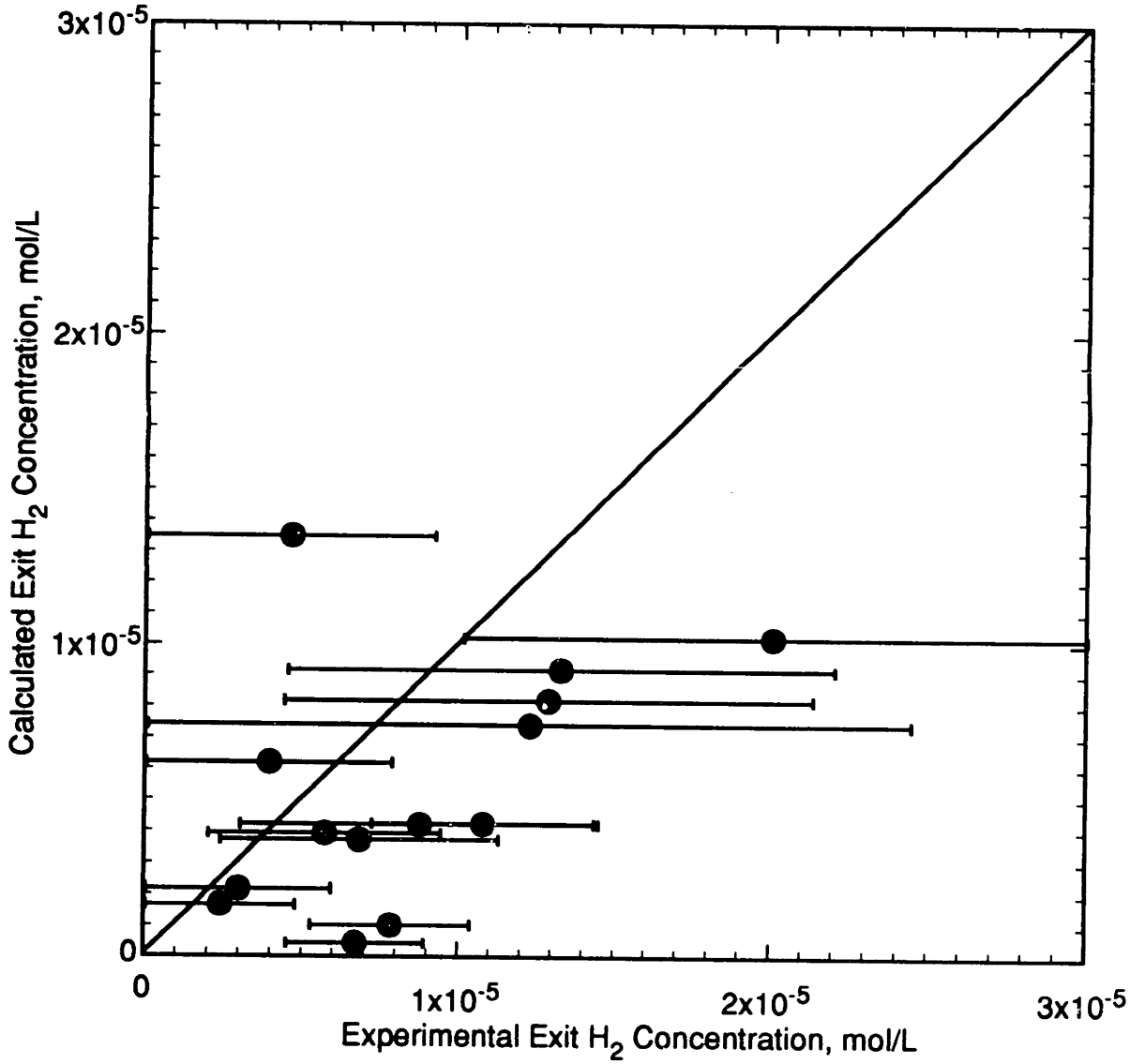

Figure 7.21 **Predicted Hydrogen Concentration from Global Model for Methane Oxidation.**

These results also demonstrate the difficulty in regressing global Arrhenius parameters for the oxidation of more complex compounds when the order with respect to oxygen is non-zero. Since experiments are typically conducted over a range of stoichiometric ratios, the oxygen concentration is not always in large excess and its concentration can vary considerably during an experiment. Regression of kinetic data must take into account the depletion of oxygen as the reaction proceeds. Typically one selects a stoichiometric ratio such that oxygen is depleted in direct proportion to the organic; however, the presence of an oxidation intermediate (for example, carbon monoxide) makes this assumption generally invalid, unless the intermediate is present at uniformly very low concentrations. On the other hand, use of a global multi-step model which does not predict the same, low, intermediate concentrations will partially invalidate the premise upon which the primary kinetic expression was developed, and adversely affect the quality of the primary rate expression. An additional discussion of this point is given in Section 12.1.

In general, the performance of the global multi-step model for methane oxidation is quite good, particularly since methane oxidation rate data (because of the refractory nature of methane) were obtained at temperatures (560 to 650 °C) considerably higher than those at which the carbon monoxide (420 to 590 °C) and hydrogen (495 to 600 °C) oxidation rate data were obtained, and the CO and H_2 rate expressions have been extrapolated outside their range of applicability. Using a similar multi-step model for methane oxidation, but with older rate expressions for carbon monoxide and hydrogen oxidation, Webley and Tester (1991) found that carbon monoxide concentrations were underpredicted and the earlier rate expressions for carbon monoxide destruction were likely too fast; the newer rate expressions (Equations 7.16 and 7.22) are considerably

slower, and account for the higher predicted CO concentrations in the present global model.

7.5.3 Methanol Oxidation

Detailed data and a rate expression for methanol oxidation (Webley, 1989; Tester *et al.*, 1992) allow the development of a multi-step global model for this compound as well. Like the methane oxidation model, the global methanol oxidation model contains four steps, as indicated in Figure 7.12. Predictions of the methanol model are shown in Figures 7.22 through 7.25.

The predicted conversion of methanol, shown in Figure 7.22, demonstrates reasonable agreement with the data. Since the methanol oxidation rate expression is independent of oxygen concentration, the predictions of the methanol oxidation step are completely unaffected by the presence of reactions kinetically downstream; Figure 7.22 thus merely reflects the fit of the methanol oxidation rate expression to the data. Predicted methanol and oxygen concentrations are shown in Figure 7.23; again the agreement with the data is good. On the other hand, predicted carbon monoxide and carbon dioxide concentrations, shown in Figure 7.24, are less satisfactory. Carbon monoxide concentrations are generally overpredicted, while carbon dioxide concentrations are underpredicted. As in the global methane oxidation model, there is an indication that the predicted rate of carbon monoxide oxidation is too slow. The effect is somewhat more pronounced in the methanol model, with the most obvious failure of the model occurring for low methanol conversions (low carbon monoxide concentrations), where carbon monoxide oxidation is not rate-limiting. Note that the methanol oxidation rate expression was obtained over essentially the same temperature range (450 to 550 °C) as the carbon monoxide (420 to 590 °C) and hydrogen (495 to 600 °C) oxidation

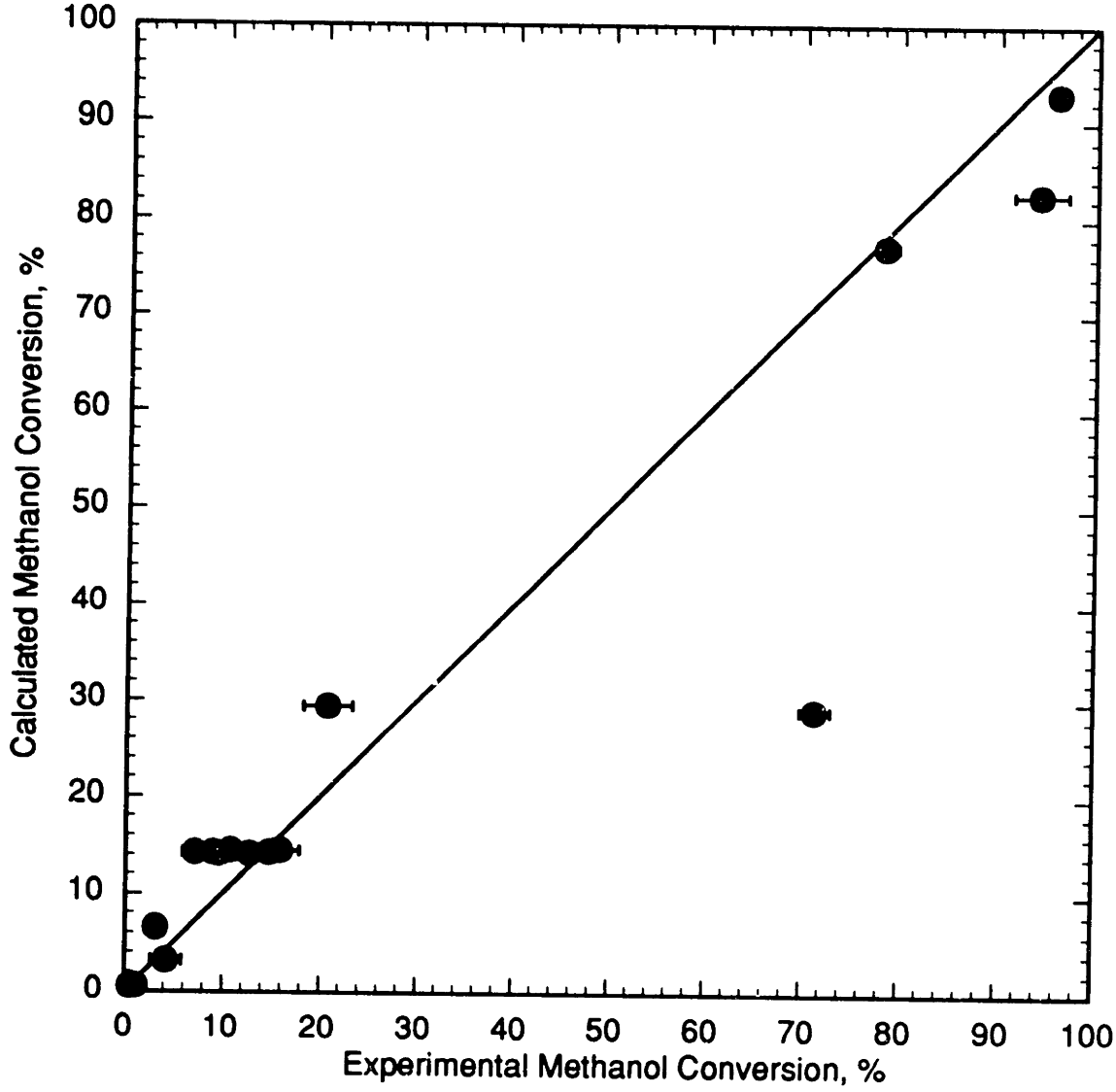

Figure 7.22 Predicted Conversion from Global Model for Methanol Oxidation.

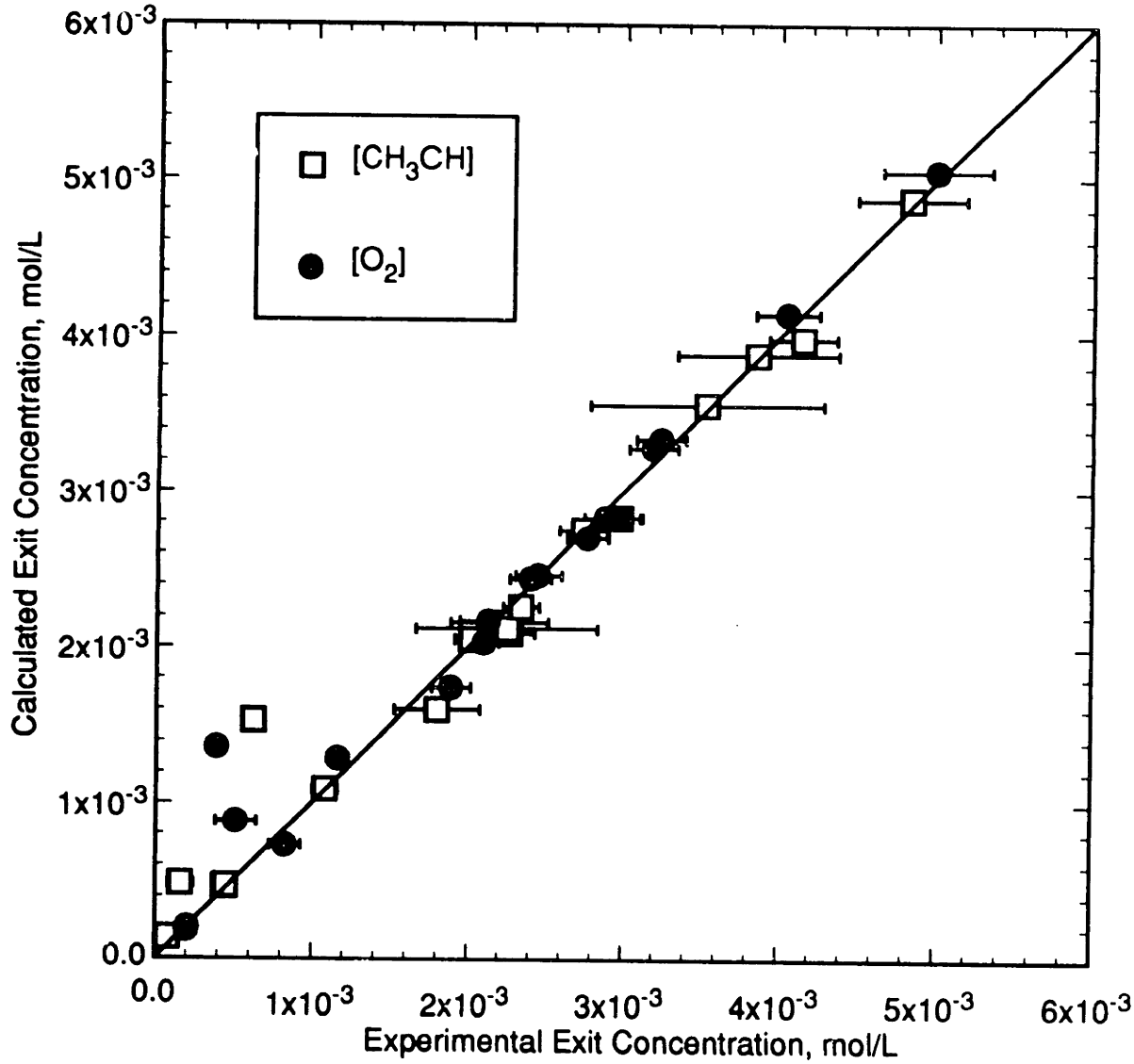

Figure 7.23 **Predicted Methanol and Oxygen Concentrations from Global Model for Methanol Oxidation.**

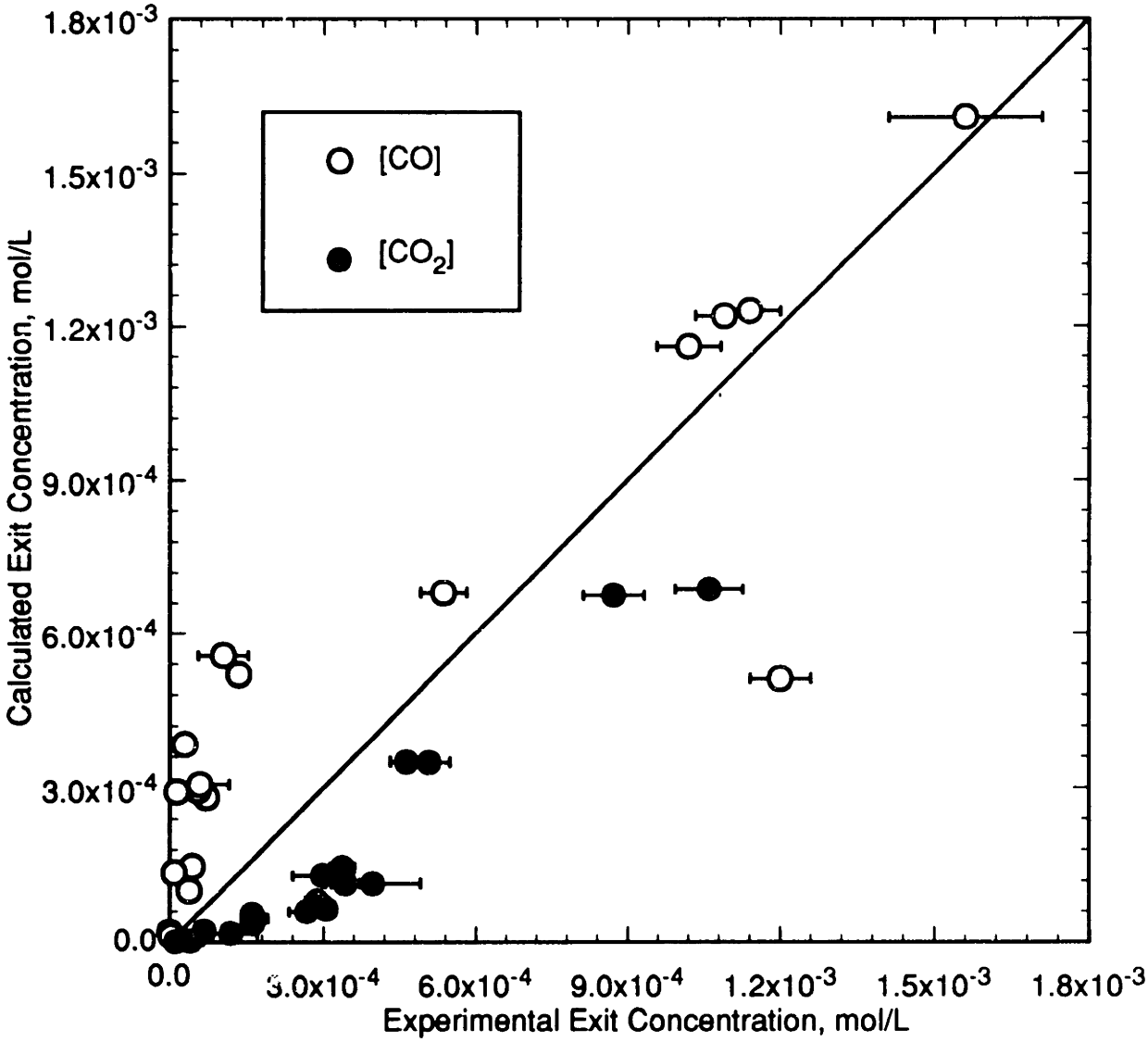

Figure 7.24 Predicted Carbon Monoxide and Carbon Dioxide Concentrations from Global Model for Methanol Oxidation.

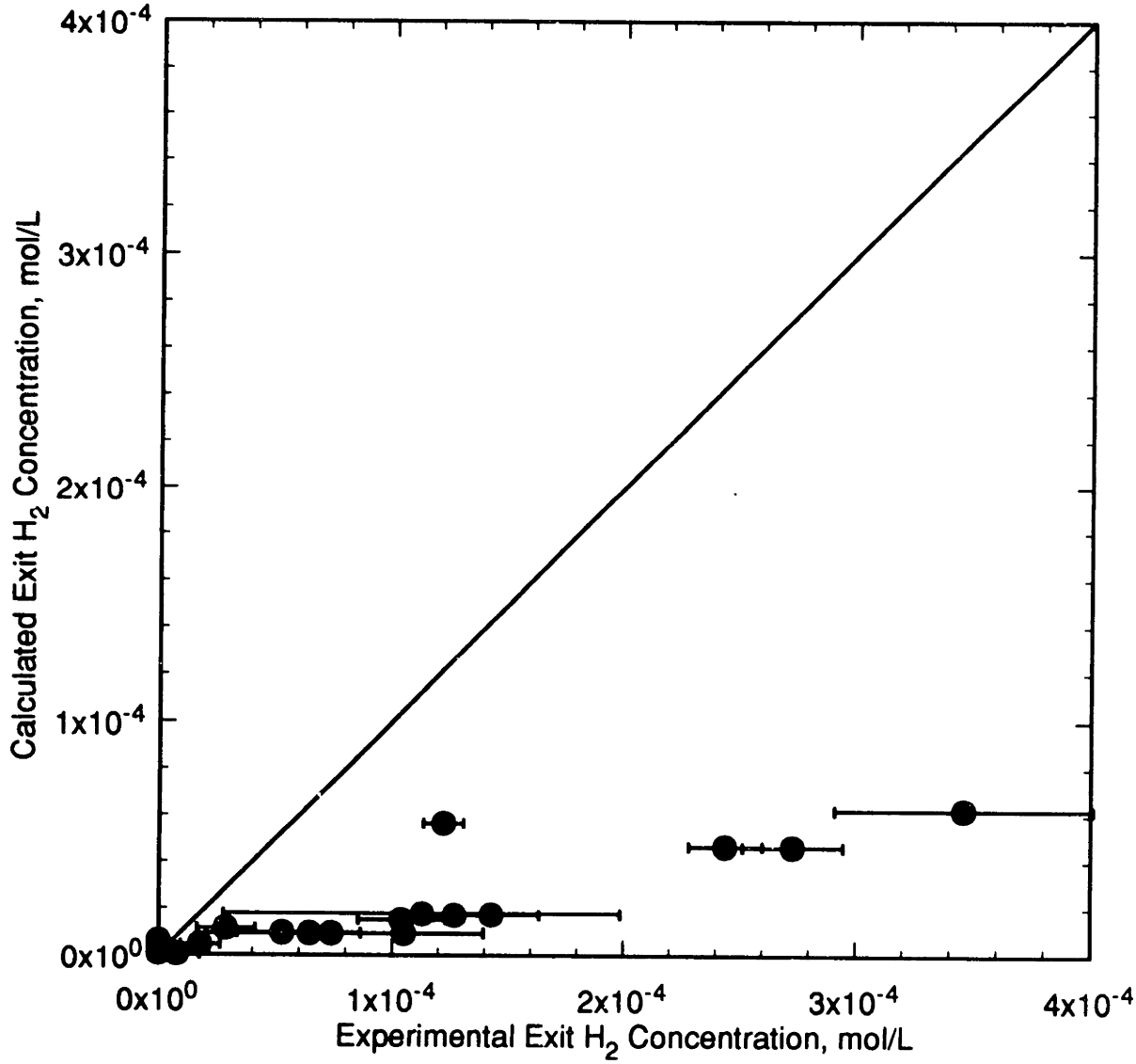

Figure 7.25 Predicted Hydrogen Concentration from Global Model for Methanol Oxidation.

expressions, and thus application of the latter rate expressions to the methanol model involved little or no extrapolation.

Finally, Figure 7.25 shows the predicted hydrogen concentration from the global methanol model. Note that observed hydrogen concentrations in the methanol oxidation experiments are much higher (by an order of magnitude) than those observed in the methane oxidation experiments (Figure 7.21). Figure 7.25 shows that the hydrogen concentration is severely underpredicted over the entire range of the methanol data. This behavior may be caused by a water-gas-shift rate that is too slow in the model. However, the global water-gas-shift expression tended to overpredict hydrogen concentrations (disregarding the earlier, suspect data) in the carbon monoxide experiments (Figure 7.17). A more complex effect is thus likely responsible for this discrepancy. In particular, Webley (1989) and Tester *et al.* (1992) have noted the existence of a minor pyrolysis pathway for methanol, in which CO and H_2 are formed. Evidence therefore exists that a pathway for H_2 formation directly from methanol may be operative. Any such pathway cannot be described by the present multi-step global model.

The performance of the global methanol model must be considered somewhat less satisfactory than that of the model for methane oxidation. The data suggest that, in contrast to the model, carbon monoxide oxidation occurs more rapidly when it occurs simultaneously with methanol oxidation (when methanol oxidation is rate-limiting, e.g., for the low-CO-concentration data in Figure 7.24); when carbon monoxide oxidation is rate-limiting (i.e., for the high-CO-concentration data in Figure 7.24), CO oxidation occurs subsequent to methanol oxidation, at a rate that is reasonably well described by the global model.

7.5.4 General Applicability of Multi-step Global Models

The behavior of the global methanol oxidation model with regard to the oxidation of carbon monoxide is suggestive of similar behavior encountered in gas-phase global models, and illustrates the inherent difficulties in constructing an accurate, multi-step global model. For example, in low-pressure gas-phase studies of moist carbon monoxide oxidation, both Hottel *et al.* (1965) and Dryer and Glassman (1973) observed that the reaction was correlated by different global parameters if the CO oxidation occurred in isolation or in the presence a more complex fuel such as propane (Hottel *et al.*, 1965) or methane (Dryer and Glassman, 1973), with CO oxidation occurring more slowly when it was part of the oxidation of a larger fuel. Dryer and Glassman also noted that the rate of carbon monoxide oxidation increased to its higher "isolation" rate when the methane had been largely depleted. Evidence from gas-phase studies therefore indicates that the rate of carbon monoxide oxidation in the presence of other compounds cannot always be described by the rate of carbon monoxide oxidation in isolation, and in fact the CO oxidation rate is suppressed in the presence of other fuels.

This behavior is identical to that observed in the global models for methane and methanol oxidation in supercritical water. For all of the methane data and for the low-conversion methanol data, carbon monoxide oxidation is not rate-limiting, and organic is present at high concentrations while CO oxidation is occurring. For the high-conversion methanol data, however, CO oxidation is the rate-limiting step and methanol oxidation largely occurs prior to CO oxidation; for those data, the model predicts the data reasonably well. Thus rate expressions obtained for individual reactions cannot always be accurately applied to more complex systems. This inflexibility in global rate expressions reflects the inherent interconnectedness of the fundamental oxidation

mechanisms through common free-radical species and shared elementary reactions. The implicit assumption of the model in Figure 7.12, that the reactions occur essentially in parallel as if in isolation, cannot be strictly true. This assumption is only a good approximation when reactions occur in essentially a sequential manner, such that the reaction environments are nearly the same as for the isolated reactions.

The presence of multiple, simultaneously reacting compounds may necessitate the inclusion in the global model of additional effects that are unimportant for the individual reactions. For example, in a two-step global model of a methane-air flame, Westbrook and Dryer (1981) found it necessary to add a third step (a reverse CO oxidation step) to reflect the fact that CO and CO_2 can become equilibrated in the flame. Presumably this effect would not have been important for CO oxidation alone, since total carbon (and thus carbon dioxide) concentrations would have been much lower. With methane present, the possibility exists to build up high CO_2 concentrations which can then equilibrate with the CO. The existence of these complicating effects suggests that any global, multi-step models under development should be checked against data, and modified if necessary, before their predictions are accepted as accurate.

7.6 Species Profiles

Subsequent to the carbon monoxide oxidation experiments which were used to determine global rate expressions for the direct-oxidation and water-gas-shift pathways, additional carbon monoxide oxidation experiments were conducted to obtain species concentrations profiles of the type obtained earlier for hydrogen oxidation (Figures 5.3 and 6.3 through 6.5). These profiles were of interest because of the induction time observed for hydrogen oxidation; similar induction times were considered likely to be present in carbon monoxide oxidation as well, but their existence could only be ascertained from

concentration profile data. Furthermore, concentration profiles provide a much more rigorous and detailed test of elementary reaction model predictions than mere conversion data, because concentration decay (or growth) rates may be directly compared. Finally, concentration profiles afford the opportunity to observe changes in product distributions with time, which is important for organics which give multiple products (e.g., CO_2 and H_2 from CO); these data are also important for modeling comparisons.

7.6.1 Effects of Initial Conditions

Four sets of experiments were conducted, one at 550 °C and three at 560 °C. Experimental temperatures were somewhat constrained by the need to resolve kinetic features over the range of accessible residence times (roughly 3.4 to 11 seconds), which were in turn constrained by the maximum pump flow rate and the desire to maintain turbulent flow within the reactor. As noted earlier, residence times in the current experimental system (at constant temperature and pressure) must be varied by varying the flow rate through the reactor. The two temperatures examined, 550 and 560 °C, were found to give oxidation rates of a magnitude that allowed species profiles to be spread over a moderately large range of residence times while still providing a broad range of conversions (species concentrations). All concentration profile data were obtained at a constant pressure of 246 bar, consistent with the earlier CO oxidation experiments (Sections 7.1 through 7.4). Numerical data for the concentration profiles are given in Table 12.10. Carbon and oxygen balances on the four sets of data showed excellent closure, typically within about 3%. Reaction of the carbon monoxide during preheating was neglected, in accordance with the conclusions of Sections 7.3 and 7.4.

The initial set of experiments was conducted at 550 °C with nominally stoichiometric concentrations of CO and O_2 (1×10^{-6} mol/cm^3 and 0.5×10^{-6} mol/cm^3,

respectively). The results are shown in Figure 7.26. Note that the carbon monoxide, oxygen, and carbon dioxide profiles suggest that, like hydrogen oxidation, carbon monoxide oxidation proceeds after a pronounced induction time. Also notable in Figure 7.26 is the hydrogen concentration, which increases continuously with residence time. This behavior suggests that hydrogen continues to be formed while carbon monoxide is being oxidized, and thus the rate of hydrogen oxidation remains slower than the rate of the water-gas-shift pathway under these conditions. Note also the magnitude of the hydrogen concentrations; hydrogen is effectively a trace component, present at levels about 30 times lower than that of the major product, CO_2.

Figure 7.27 shows the results of a similar set of experiments, but with the temperature raised 10 °C to 560 °C. Initial concentrations of carbon monoxide and oxygen were maintained at the same stoichiometric values. Note that carbon monoxide disappears markedly faster, even though the temperature increase was relatively modest. Again, the major species profiles suggest a pronounced induction time. Interestingly, the hydrogen concentration seems to have peaked at approximately 2×10^{-8} mol/cm^3 at 4 s residence time, and at longer residence times the hydrogen concentration decreases, indicating that hydrogen oxidation becomes faster than the water-gas shift pathway at carbon monoxide conversions greater than about 80%. These observations are completely consistent with the profiles in Figure 7.26; the faster rates at the higher temperature enable us to observe the higher-conversion behavior of the hydrogen profile, which was not accessible at the lower temperature because it occurs at inaccessibly long residence times. The profiles in Figures 7.26 and 7.27 thus indicate an initial rise in hydrogen concentration (net hydrogen formation) at low carbon monoxide conversions, followed by a decrease (net hydrogen oxidation) at higher carbon monoxide conversions.

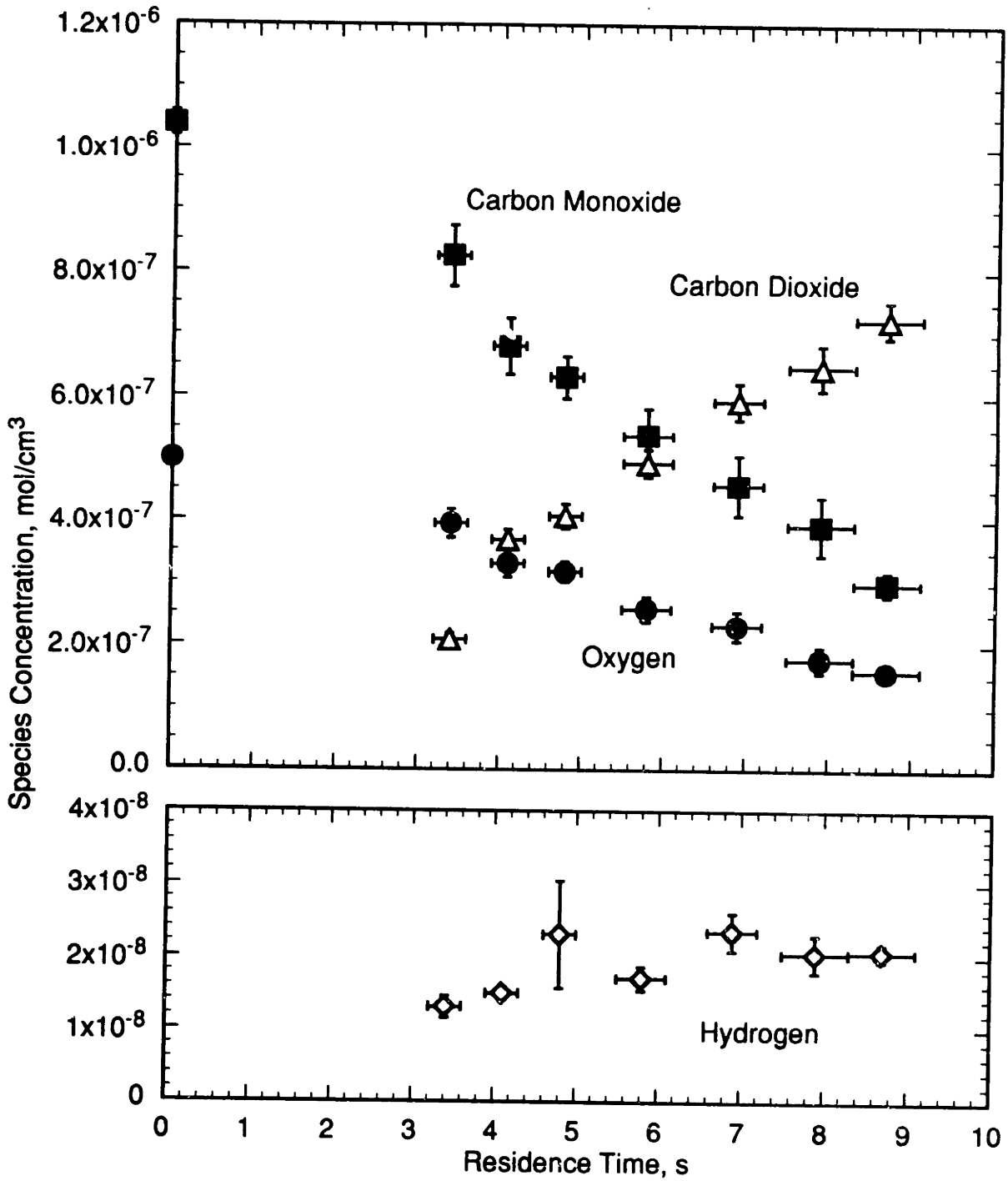

Figure 7.26 **Major Species Profiles for Stoichiometric Carbon Monoxide Oxidation at 550±2 °C.** $[CO]_o = (1.04\pm0.02) \times 10^{-6}$ mol/cm^3, $[O_2]_o = (0.50\pm0.01) \times 10^{-6}$ mol/cm^3, $[H_2O] = (4.25\pm0.08) \times 10^{-3}$ mol/cm^3

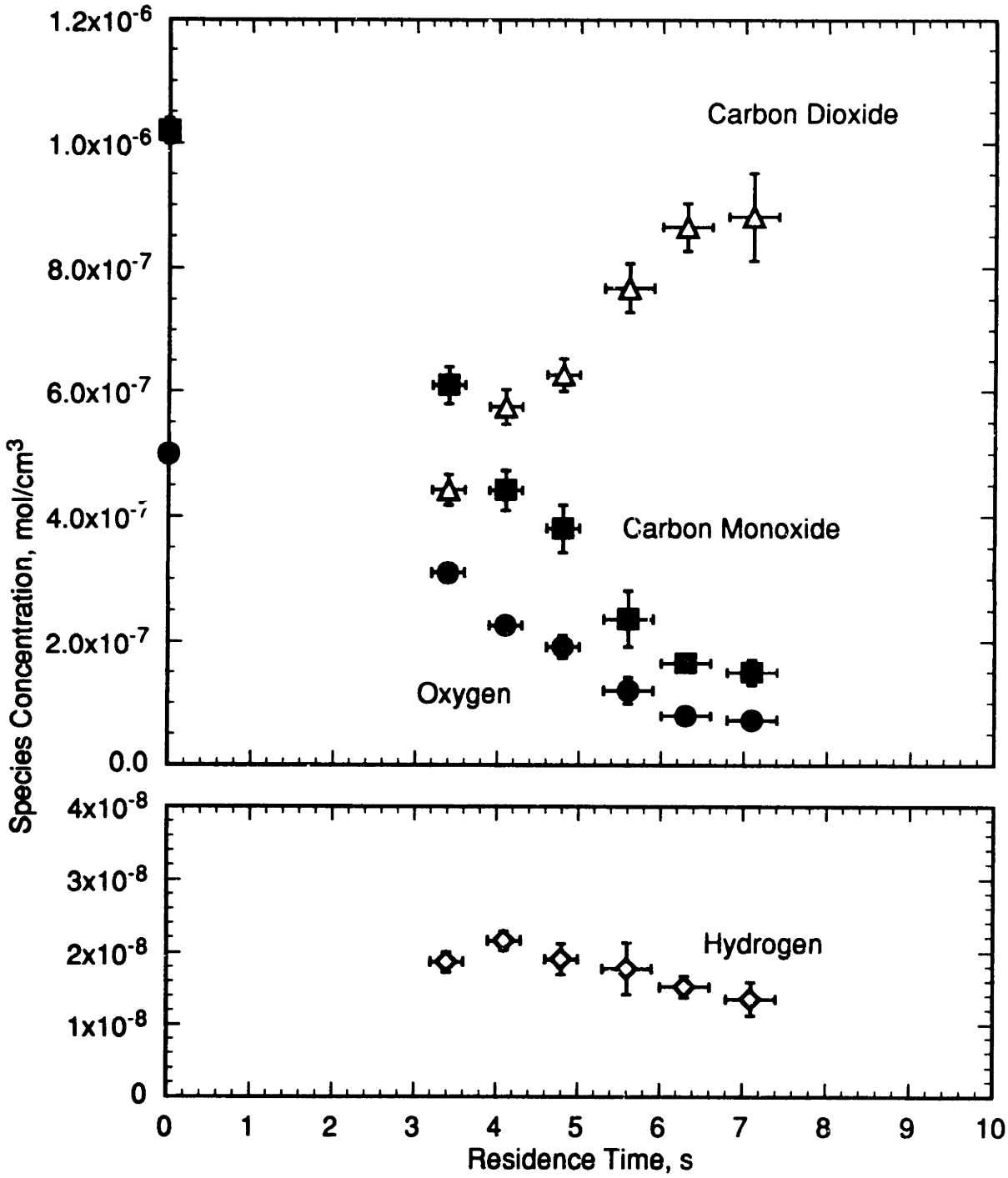

Figure 7.27 **Major Species Profiles for Stoichiometric Carbon Monoxide Oxidation at 560±2 °C.** $[CO]_o = (1.02 \pm 0.02) \times 10^{-6}$ mol/cm^3, $[O_2]_o = (0.50 \pm 0.01) \times 10^{-6}$ mol/cm^3, $[H_2O] = (4.16 \pm 0.07) \times 10^{-3}$ mol/cm^3.

Results for a substoichiometric (fuel-rich) CO-O_2 mixture at 560 °C are shown in Figure 7.28; initial concentrations were nominally 2×10^{-6} mol/cm^3 and 0.5×10^{-6} mol/cm^3 for CO and O_2 respectively, or a fuel equivalence ratio ($\phi = [CO]_o/2[O_2]_o$) of 2. The concentration profiles for these fuel-rich conditions are markedly different from those for the stoichiometric conditions in Figure 7.27. First, the oxygen becomes completely depleted at a residence time of about 6 seconds; reaction at subsequent residence times is therefore oxygen-limited. However, note the high hydrogen concentrations, even prior to the oxygen depletion: hydrogen concentrations in the presence of oxygen are a factor of five higher than for the comparable stoichiometric experiment (Figure 7.27), rising to an order of magnitude higher once oxygen has been depleted. This behavior suggests that the extent of hydrogen formation is strongly dependent on equivalence ratio, to an extent that cannot be explained by simple parallel direct-oxidation and water-gas-shift pathways. For example, the global model for CO oxidation from Section 7.5.1 predicts only about a factor of two increase in hydrogen concentration upon doubling the CO concentration. The behavior in Figure 7.28 thus reveals an inadequacy in the global model.

The lack of apparent reaction at long residence times in Figure 7.28 suggests that the mixture may be equilibrated. A simple ideal-gas calculation using thermodynamic data for the water-gas-shift reaction from the JANAF tables (Chase *et al.*, 1985) showed, however, that under these conditions the forward direction of the water-gas shift equilibrium is favored to over 99% conversion; non-ideal effects would have to change the equilibrium constant K_c by a factor of over 10^4 to cause the mixture in Figure 7.28 to be equilibrated, which is physically highly unlikely. Thus the lack of observable reaction following oxygen depletion reflects a kinetic limitation, rather than the attainment of equilibrium. While it was recognized earlier that the water-gas-shift pathway proceeds

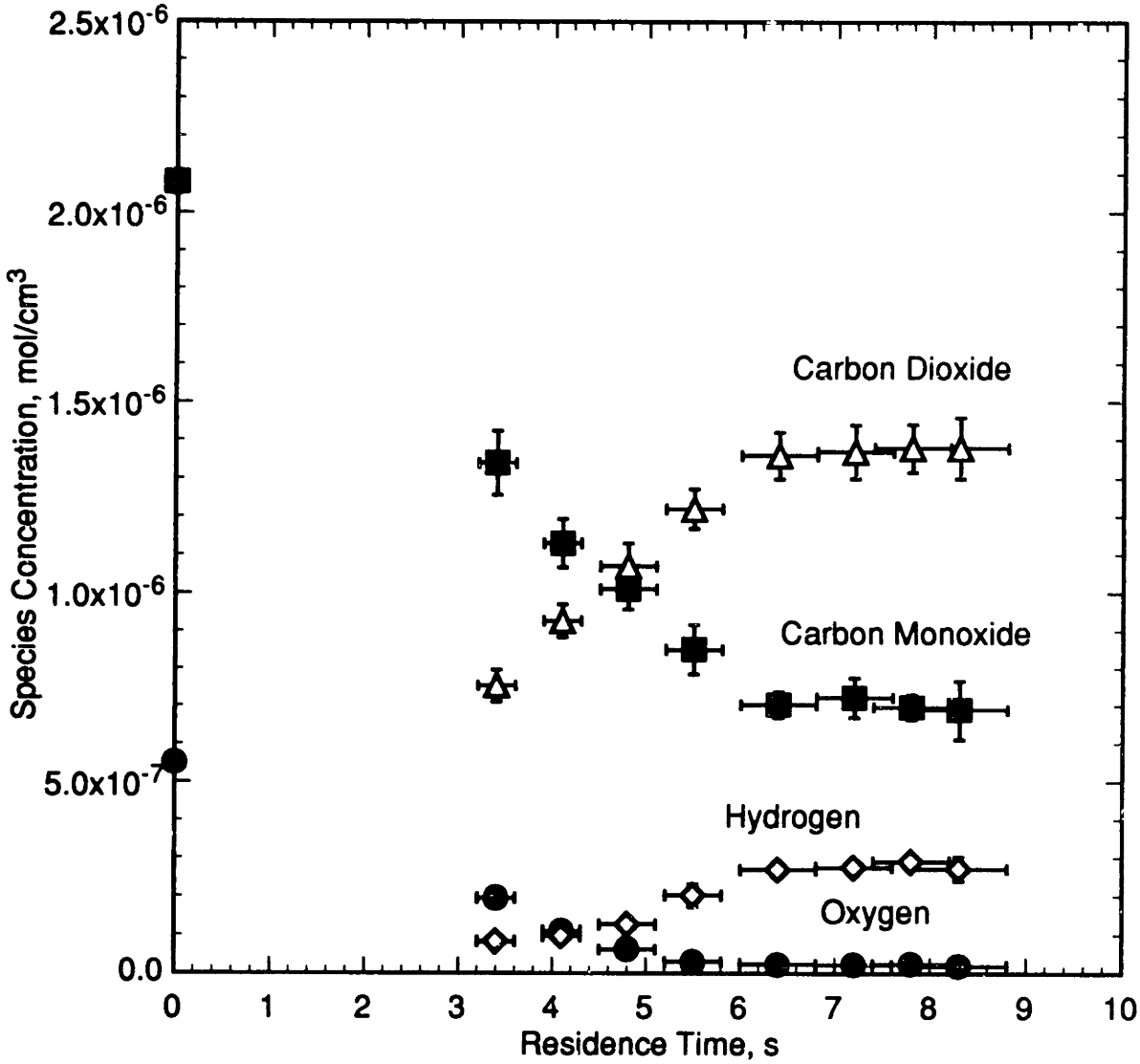

Figure 7.28 **Major Species Profiles for Substoichiometric (Fuel-Rich) Carbon Monoxide Oxidation at 560±3 °C.** $[CO]_o = (2.08 \pm 0.03) \times 10^{-6}$ mol/cm^3, $[O_2]_o = (0.55 \pm 0.01) \times 10^{-6}$ mol/cm^3, $[H_2O] = (4.16 \pm 0.14) \times 10^{-3}$ mol/cm^3.

slowly relative to direct oxidation, the short-residence-time data in Figure 7.28 indicate that the water-gas-shift pathway had been proceeding at a significant rate prior to oxygen depletion. Once oxygen has been depleted, however, the water-gas-shift pathway appears to cease completely. This behavior indicates that the water-gas-shift pathway is distinctly facilitated in the presence of oxygen.

Finally, a set of experiments was conducted at 560 °C for superstoichiometric (fuel-lean) conditions, with nominally the same initial concentration of 1×10^{-6} mol/cm^3 for both CO and O_2, or a fuel equivalence ratio of 0.5. The results are shown in Figure 7.29. Note that under these conditions the carbon monoxide is oxidized virtually to completion within about eight seconds. The hydrogen concentration decreases steadily for all residence times, indicating its formation occurred within the first three seconds and there is net oxidation of hydrogen for longer residence times. Note also the extremely low concentrations of hydrogen present at the longer residence times ($\sim 2 \times 10^{-9}$ mol/cm^3); these concentrations are *over two orders of magnitude lower* than the hydrogen concentrations under fuel-rich concentrations. The dependence of hydrogen concentration on fuel equivalence ratio is thus very strong; fuel-rich conditions favor hydrogen formation to a much greater extent than fuel-lean conditions. Observed hydrogen concentrations thus decrease significantly with increasing oxygen concentration, although oxygen-free conditions tend to dramatically decrease the rate of hydrogen formation. A similar effect of fuel equivalence ratio on hydrogen formation was seen in a gas-phase study of formaldehyde oxidation (Hochgreb *et al.*, 1990), in which low fuel equivalence ratios suppressed hydrogen formation.

The strong dependence of hydrogen formation on equivalence ratio, combined with the apparently very slow reaction by water-gas shift in the absence of oxygen, raises the possibility that the measured rates of the water-gas shift reaction (Section 7.3) do not

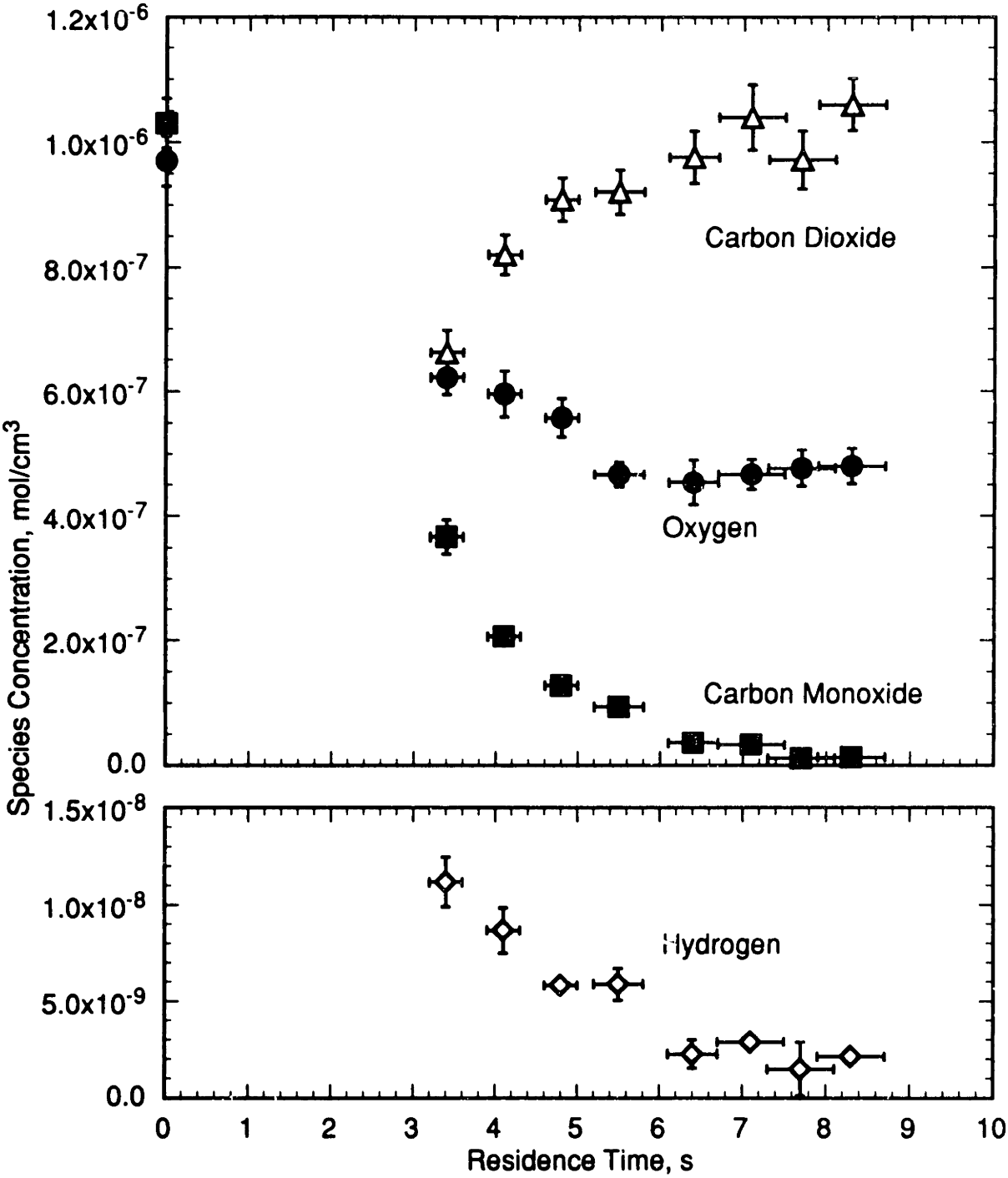

Figure 7.29 **Major Species Profiles for Superstoichiometric (Fuel-Lean) Carbon Monoxide Oxidation at 560±2 °C.** $[CO]_o = (1.03 \pm 0.04) \times 10^{-6}$ mol/cm^3, $[O_2]_o = (0.97 \pm 0.04) \times 10^{-6}$ mol/cm^3, $[H_2O] = (4.16 \pm 0.09) \times 10^{-3}$ mol/cm^3.

truly reflect the rate of the reaction in an oxygen-free environment. For example, all water-gas shift data in Table 12.7 exhibited a lower hydrogen yield than the carbon dioxide yield, indicating that oxygen was present in the reactor in all of the experiments. Thus the "water-gas shift" results may be more accurately characterized as an "oxidative pyrolysis," that is, oxidation at very high fuel equivalence ratios (Hochgreb *et al.*, 1990). Experimental limitations prevented the attainment of a strictly oxygen-free environment in the reactor for the water-gas shift experiments. However, future experiments under fuel-rich conditions, at higher temperatures and/or longer residence times, could provide a direct measurement of the water-gas-shift rate by allowing observation of the rate of reaction of CO under oxygen-depleted conditions (e.g., the long-residence-time behavior in Figure 7.28).

The data of Figures 7.26 through 7.29 have been recast in Figures 7.30 and 7.31 in the form of carbon monoxide profiles normalized by the initial concentrations. Note that there are four distinct profiles in Figure 7.30, and thus the carbon monoxide decay constant is different for each of the sets of data. Figure 7.30 shows the normalized profiles with exponential fits; Figure 7.31 linearizes the normalized profiles logarithmically and shows straight-line fits to the data. Note that the curve fits in both figures, when extrapolated back to the initial concentration, indicate an induction time of approximately 2 seconds in all the profiles. Figures 7.30 and 7.31 thus permit the determination of decay constants and induction times for the carbon monoxide profiles. Although the fuel-rich profiles are shown without curve fits because the data deviate from a smooth decay when oxygen becomes depleted, an approximate decay constant and induction time can be derived for the fuel-rich conditions using only the first four data points.

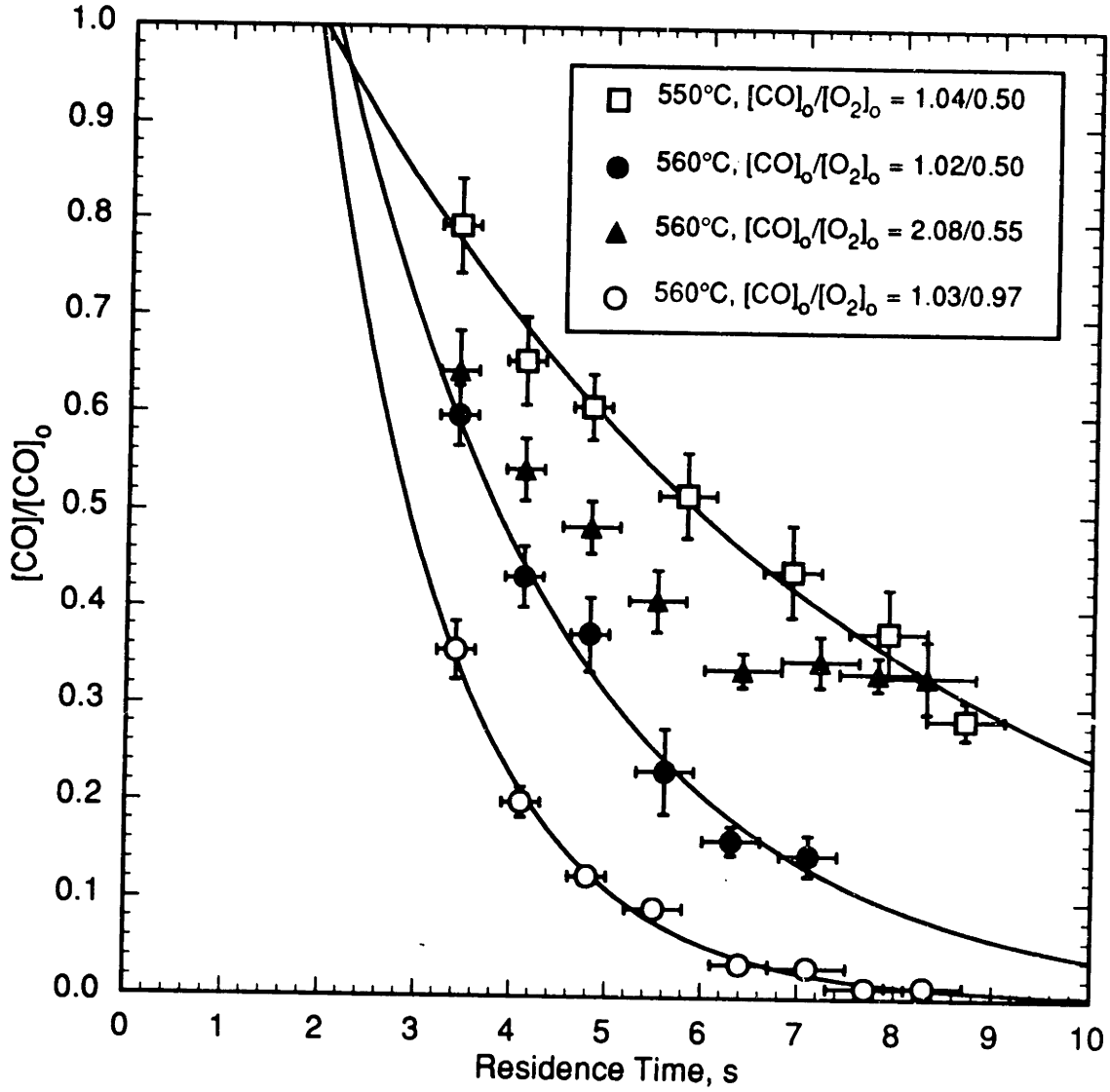

Figure 7.30 **Normalized Carbon Monoxide Decay Profiles Demonstrating Effective Induction Times and Decay Constants.**
Experimental conditions:
□—550±2 °C, $[CO]_o = (1.04\pm0.02) \times 10^{-6}$ mol/cm^3, $[O_2]_o = (0.50\pm0.01) \times 10^{-6}$ mol/cm^3 $[H_2O] = (4.25\pm0.08) \times 10^{-3}$ mol/cm^3,
●—560±2 °C, $[CO]_o = (1.02\pm0.02) \times 10^{-6}$ mol/cm^3, $[O_2]_o = (0.50\pm0.01) \times 10^{-6}$ mol/cm^3, $[H_2O] = (4.16\pm0.07) \times 10^{-3}$ mol/cm^3;
▲—560±3°C, $[CO]_o = (2.08\pm0.03) \times 10^{-6}$ mol/cm^3, $[O_2]_o = (0.55\pm0.01) \times 10^{-6}$ mol/cm^3, $[H_2O] = (4.16\pm0.14) \times 10^{-3}$ mol/cm^3;
○—560±2 °C, $[CO]_o = (1.03\pm0.04) \times 10^{-6}$ mol/cm^3, $[O_2]_o = (0.97\pm0.04) \times 10^{-6}$ mol/cm^3, $[H_2O] = (4.16\pm0.09) \times 10^{-3}$ mol/cm^3.
Curves are exponential fits to data.

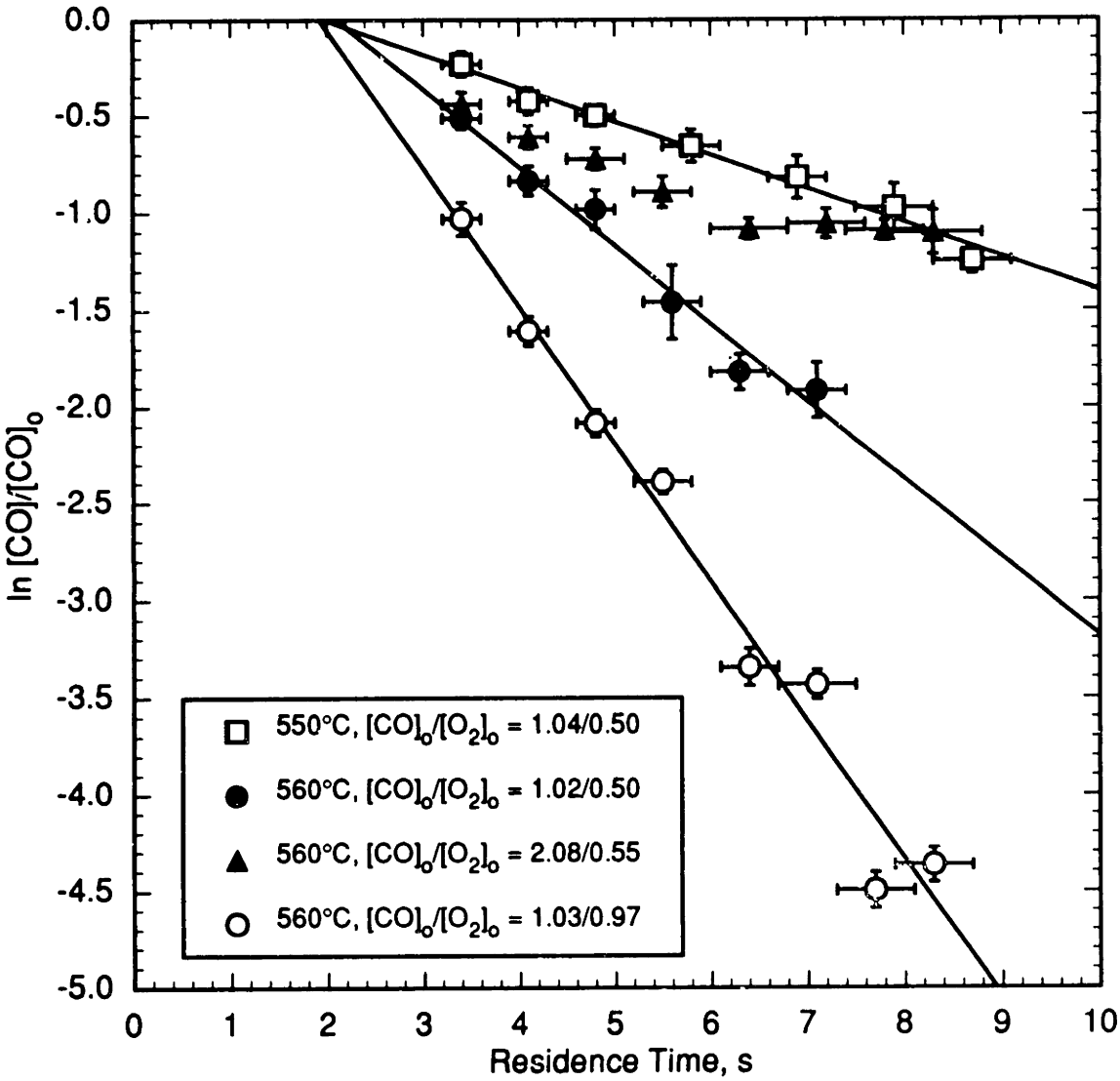

Figure 7.31 **Normalized Carbon Monoxide Decay Profiles Demonstrating Effective Induction Times and Decay Constants.** Symbols and conditions as in Figure 7.30, but concentration scale is logarithmic. Lines are linear fits to data.

Table 7.2 summarizes the kinetic decay constants and induction times for the four data sets, as determined from both the carbon monoxide profiles and the oxygen profiles; quoted errors are one standard deviation. Note that only stoichiometric conditions give the same decay constants and induction times for both the CO and the O_2 profiles; for off-stoichiometric conditions, the two profiles yield different values. Table 7.2 shows that the carbon monoxide decay constant more than doubles for stoichiometric conditions when the temperature is raised from 550 to 560 °C, reflecting a strong temperature dependence. For these two conditions, the activation energy for the carbon monoxide decay constant is approximately 488 kJ/mol, which is much higher than the activation energy regressed for carbon monoxide oxidation in Section 7.4, 134±32 kJ/mol. On the other hand, the induction time in Table 7.2 remains essentially constant (within estimation error) at approximately 2 seconds as temperature is raised from 550 to 560 °C. Accurate estimation of the decay constant and induction time for the fuel-rich profile at 560 °C is difficult because oxygen becomes depleted; however, the decay constant under fuel-rich conditions clearly decreases relative to that under stoichiometric conditions at the same temperature. The fuel-rich induction time may be somewhat shorter, but remains roughly 2 seconds. The fuel-lean profile at 560 °C exhibits a decay constant significantly higher than the corresponding stoichiometric profile; the three profiles at 560 °C thus suggest a dependence on oxygen of the disappearance of carbon monoxide, consistent with the global rate expression (Equation 7.22). The fuel-lean induction time is also about 2 s, indicating that the induction time is independent of fuel equivalence ratio. A dependence of CO disappearance on oxygen is consistent with the earlier, gas-phase, global rate expressions (Table 7.1), but is in contrast to the more recent gas-phase results at 1030 K (757 °C) of Yetter *et al.* (1991b), who observed an independence of oxygen of CO disappearance.

Initial Conditions 10^{-6} mol/cm^3	k', s^{-1} (CO)	k', s^{-1} (O_2)	τ_{ind}, s (CO)	τ_{ind}, s (O_2)
550±2 °C				
$[CO]_o$ = 1.04±0.02	0.17±0.01	0.17±0.01	2.0±0.3	1.9±0.3
$[O_2]_o$ = 0.50±0.01				
560±2 °C				
$[CO]_o$ = 1.02±0.02	0.40±0.03	0.42±0.03	2.1±0.3	2.3±0.3
$[O_2]_o$ = 0.50±0.01				
560±3 °C				
$[CO]_o$ = 2.08±0.03	0.21±0.01	0.86±0.03	1.3±0.1	2.2±0.1
$[O_2]_o$ = 0.55±0.01				
560±2 °C				
$[CO]_o$ = 1.03±0.04	0.71±0.05	0.13±0.03	1.9±0.3	0.3±0.4
$[O_2]_o$ = 0.97±0.04				

Table 7.2 **Apparent Induction Times and Decay Constants for Carbon Monoxide Oxidation at 246 bar.**

Comparison of the values in Table 7.2 for carbon monoxide oxidation with the corresponding values for hydrogen oxidation in Table 5.1 reveals several interesting trends. First, for identical conditions of temperature (550 °C) and stoichiometric concentrations, the decay constant for carbon monoxide (0.17 s^{-1}) is less than half the decay constant for hydrogen (0.44 s^{-1}). The ratio of these two decay constants is very close to the ratio of the rate constants of the primary oxidizing elementary reactions, i.e.,

$$\frac{k'(\mathrm{CO},550°\mathrm{C})}{k'(\mathrm{H_2},550°\mathrm{C})} = 0.39 \cong \frac{k_{\mathrm{CO+OH\rightarrow CO_2+H}}(550°\mathrm{C})}{k_{\mathrm{H_2+OH\rightarrow H_2O+H}}(550°\mathrm{C})} = 0.45 \qquad (7.24)$$

where the rate constants for the CO and H_2 oxidizing reactions have been taken from Section 12.4 and Michael and Sutherland (1988), respectively. Under the same conditions at 550 °C, then, hydrogen oxidation in supercritical water proceeds more rapidly than carbon monoxide oxidation. At 560 °C, the decay constant for carbon monoxide oxidation is approximately the same as that for hydrogen oxidation at 550 °C. This observation is consistent with the global kinetic behavior in Figure 7.11. On the other hand, the observed induction times of both carbon monoxide oxidation and hydrogen oxidation at 550 °C are approximately 2 s. The induction time thus appears to be independent of the particular fuel for these conditions.

7.6.2 Verification of Global Reaction Order(s)

The oxygen dependence of the carbon monoxide decays in Figures 7.30 and 7.31 enable a determination of the global order of the oxidation reaction with respect to oxygen. Note that data in both Figure 7.30 and 7.31 have been fit with exponentials; all of the data sets follow an exponential decay quite closely, implying that the oxidation reaction is strictly first-order in carbon monoxide. Clearly this is at odds with the change in the carbon

monoxide decay (and hence the exponential decay constant) upon changing the oxygen concentration. Questions then remain regarding the significance of the data following an exponential decay: how unique is this fit, and does the appearance of an exponential decay truly imply a first-order reaction?

Figure 7.32 shows the data for the carbon monoxide concentration profile for stoichiometric CO oxidation at 560 °C, originially shown in Figure 7.27. In Figure 7.32 these data are compared with the concentration profiles predicted by the global rate expression

$$-d[\mathrm{CO}]/dt = k\,[\mathrm{CO}]^a\,[\mathrm{O_2}]^b \qquad (7.25)$$

where the overall order of the reaction has been varied from simple first order ($a = 1$, $b = 0$) to 0.5-order in oxygen ($a = 1$, $b = 0.5$). [Note that the data in Figure 7.32 have been shifted in time by 2.1 s to eliminate the induction time.] For this analysis, we have assumed that the reaction is first-order in carbon monoxide and we have not treated a as a variable. All three curves in Figure 7.32 fit the data well, and the "best fit" certainly cannot be identified, given the scatter in the data. The fit is even more ambiguous if one recognizes that the derived induction time is actually somewhat dependent, through extrapolation, on the shape of the curve used to fit the data. Thus the curves in Figure 7.32 should be allowed to float with time; if this allowance is made, all three curves give equally good fits. Note also that the three curves retain their similarity for residence times at least up to 10 seconds, and additional data at those longer residence times would not help in discriminating among the reaction orders. One should also realize that the reaction order may be varied only by simultaneously varying the value of the rate constant, k. Since the fit of the rate expression (Equation 7.25) is seemingly equally for a

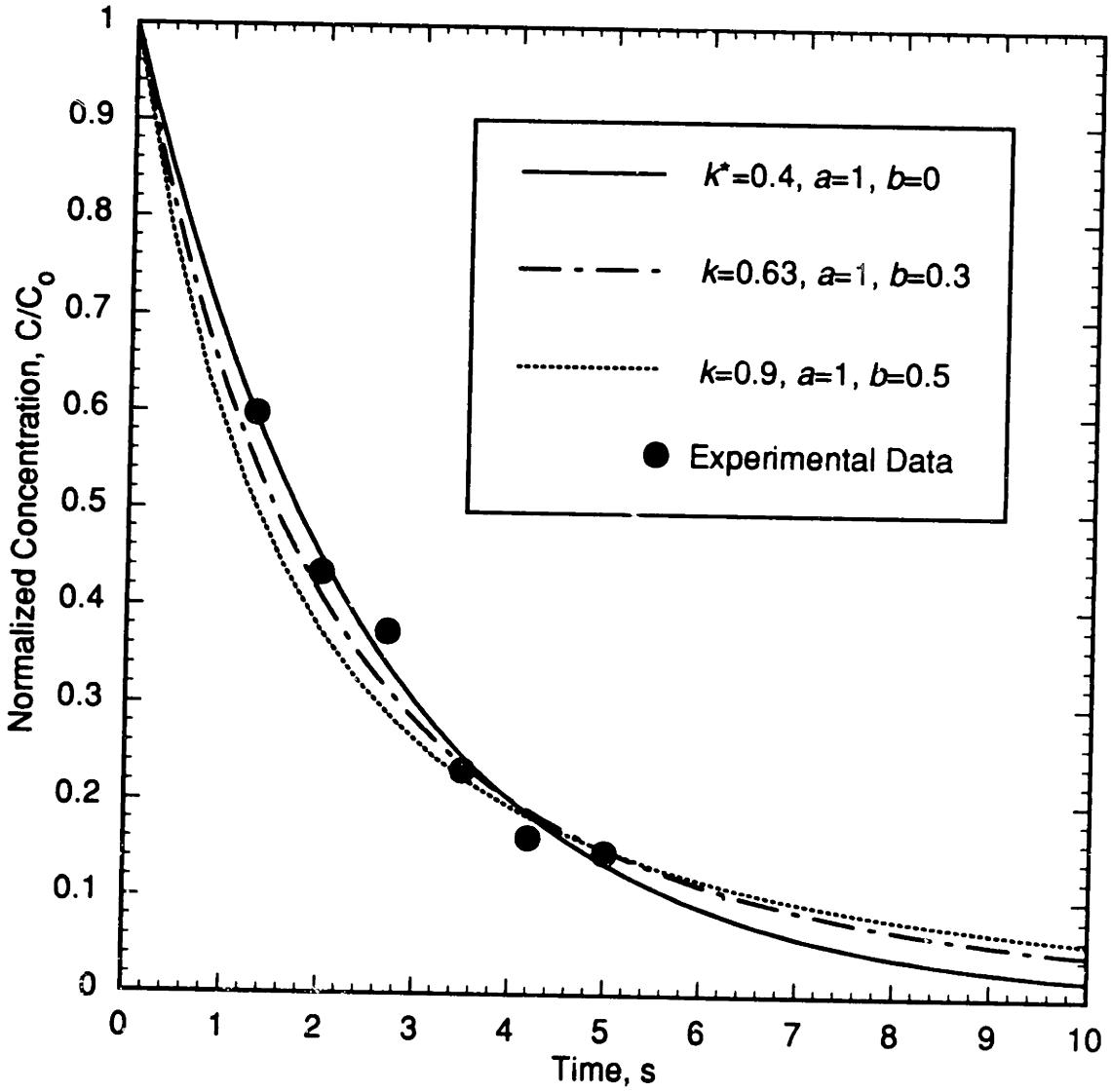

Figure 7.32 **Normalized Concentration Profiles for Reactions of Varying Global Order.** Experimental CO profile shown is from Figure 7.27; curves are calculated assuming a stoichiometric feed ratio (O_2/CO) of 0.5. Data are time-shifted backward 2.1 s to eliminate induction time.

large number of combinations of k and b, these two parameters are highly coupled and it is almost impossible to determine unique values for k and b from a single concentration profile.

Some discrimination among reaction orders is afforded by examining the concentration profile on a logarithmic scale, as shown in Figure 7.33. In that figure, the same three predicted curves for stoichiometric conditions from Figure 7.32 are shown, along with a curve for $b = 0.5$ and superstoichiometric conditions ($[O_2]_o/[CO]_o = 1$). Note that the three stoichiometric curves in Figure 7.33 remain indistinguishable for $\ln C/C_o > -2$, or conversions less than about 86%. The first-order curve becomes clearly distinguishable from the higher-order curves for $\ln C/C_o < -3$, or conversions greater than 95%; unfortunately, extensive data are rarely available in that conversion range. Furthermore, the higher-order curves remain similar even at those high conversions. More interestingly, the superstoichiometric curve, with a 0.5-order dependence on oxygen, remains linear (exponential) over essentially the entire range of conversions. Hence the superstoichiometric curve appears to follow a first-order decay, despite its significant dependence on oxygen. The oxygen dependence of the reaction is only evident when the superstoichiometric curve is compared to the stoichiometric curve for the same parameters; the two curves, if fit with an exponential, would be distinguished by markedly different exponential decay constants. Figure 7.33 thus clearly shows that the appearance of an exponential decay in a concentration profile is by no means a clear indication of a first-order reaction; rather, the profile must be compared to other profiles obtained at different fuel equivalence ratios.

Comparison of the three profiles at 560 °C in Figures 7.30 and 7.31 shows that carbon monoxide oxidation possesses an oxygen dependence, despite the apparent first-order behavior of the individual curves, because the exponential decay constant varies

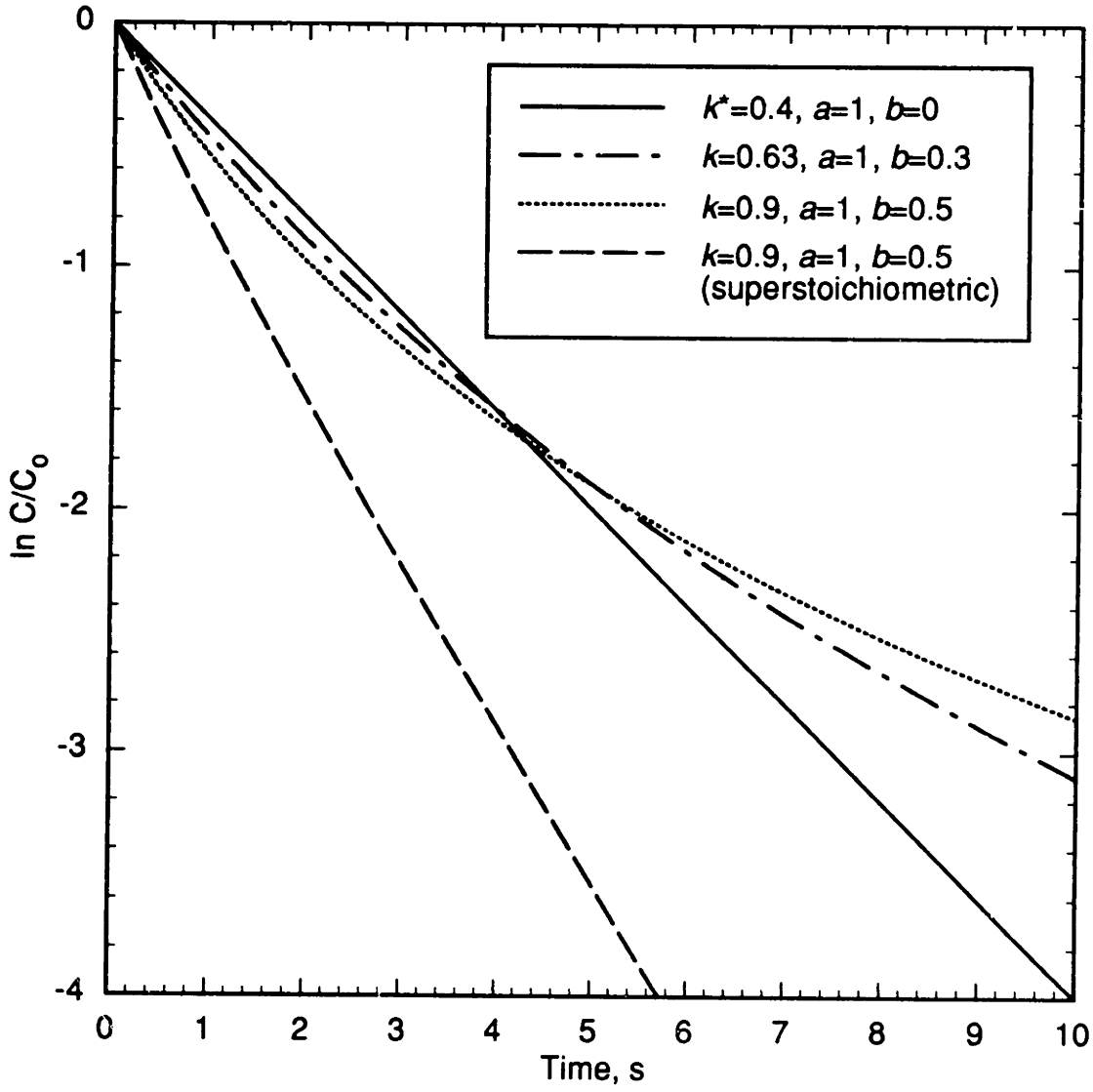

Figure 7.33 Normalized Concentration Profiles for Reactions of Varying Global Order, Logarithmic Scale. First three curves are for stoichiometric mixtures ($[O_2]/[CO] = 0.5$); superstoichiometric curve is for $[O_2]/[CO] = 1$.

with fuel equivalence ratio. Recognizing that the rate constant for the three curves should be identical since the same reactor temperature was used for each, the decays of the stoichiometric and superstoichiometric curves can only be reconciled by a reaction order with respect to oxygen of approximately 0.5. Figure 7.34 shows the concentration profiles and the fit curves for the stoichiometric and superstoichiometric data at 560 °C. One should note that the selection of $k = 0.9$, $b = 0.5$ is not strictly unique, and small perturbations of those values might produce a better fit. The predicted curves have both been assumed to start at a time of 2.1 s; as discussed earlier, these curves should not necessarily be fixed in time, but should be allowed to float to achieve the best fit to the data. The fit of the stoichiometric curve to the data could be improved by shifting the curve to slightly longer time (increasing slightly the stoichiometric induction time).

The analysis of the concentration decays in Figure 7.30 and 7.31 thus reveals a global dependence of carbon monoxide oxidation on oxygen of approximately 0.5-order. This derived order is in good agreement with the order obtained earlier in the regression of the data, 0.34±0.24. The two sets of data are thus consistent with regard to the global oxygen dependence.

7.7 Effects of Operating Pressure (Fluid Density)

An additional set of experiments was conducted to evaluate the effect of operating pressure on the rate of carbon monoxide oxidation. The same approach was taken in these experiments as was used in the earlier studies of operating-pressure effects in hydrogen oxidation (Section 5.3). That is, experiments were performed at a constant temperature, 570 °C, and constant, stoichiometric reactant concentrations of nominally 1×10^{-6} mol/cm^3 for carbon monoxide and 0.5×10^{-6} mol/cm^3 for oxygen, such that the only effect of changing the operating pressure was a change in the concentration (density)

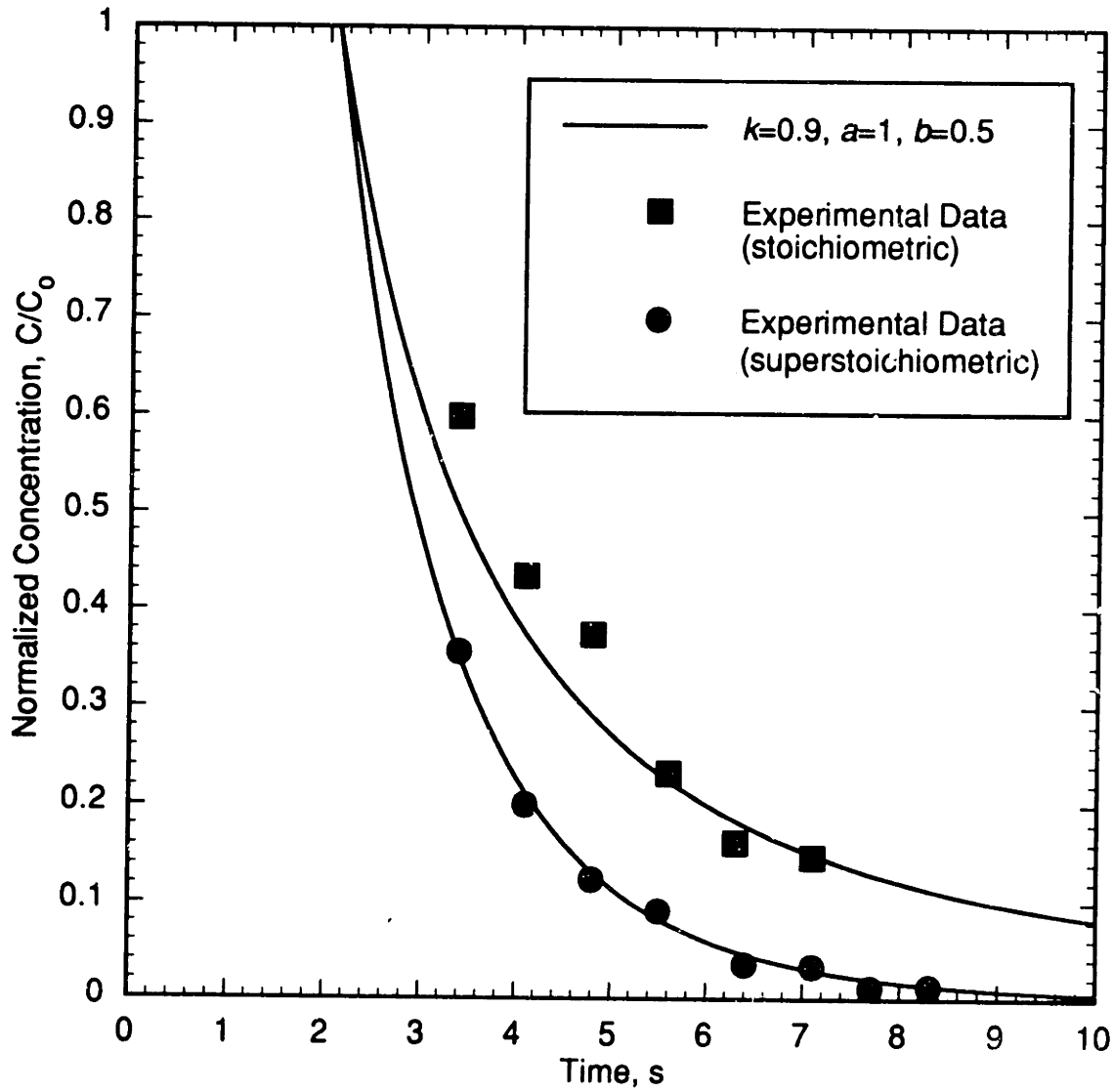

Figure 7.34 **Normalized Concentration Profiles for Stoichiometric and Superstoichiometric Mixtures.** Experimental CO profiles are from Figures 7.27 and 7.29; calculated curves are time-shifted forward 2.1 s to simulate experimental induction time.

of water in the reactor. As in the hydrogen experiments, these conditions were chosen to allow observation of significant changes in conversion with operating pressure. Furthermore, recognition of the complicating effect of residence time in the results for hydrogen oxidation at varying pressure led to an effort to maintain a constant residence over the range of pressures investigated. For pressures ranging from 118 to 263 bar in one set of experiments, it was possible to maintain a constant residence time of 4.1 s. When possible, experiments were also conducted for each pressure at a residence time of 3.4 s.

Results of the variable-pressure results are shown in Figure 7.35, where the apparent first-order rate constant, k^*, is shown as a function of operating pressure (water density). The data are also compiled numerically in Table 12.11. Observed carbon monoxide conversions ranged from about 30% to 80%. A datum point for 263 bar and 3.4 s residence time was not obtainable owing to feed-pump flow limitations. Note that k^* is consistently higher for the 4.1-s results than for the 3.4-s results, the result of the induction time identified earlier. Figure 7.35 shows unambiguously that the rate of carbon monoxide oxidation increases uniformly (and almost linearly) with operating pressure or water density, from subcritical to supercritical pressures. Over the range of pressures studied, from 118 to 263 bar, the apparent first-order rate constant for CO oxidation increases by a factor of more than three. Figure 7.36 shows the concentrations of the major species in the reactor effluent as a function of operating pressure for a constant residence time of 4.1 s. Clearly all species concentrations increase similarly with pressure, including those for hydrogen and carbon dioxide, indicating that the increase in operating pressure (water density) does not affect the direct-oxidation or water-gas shift pathways preferentially.

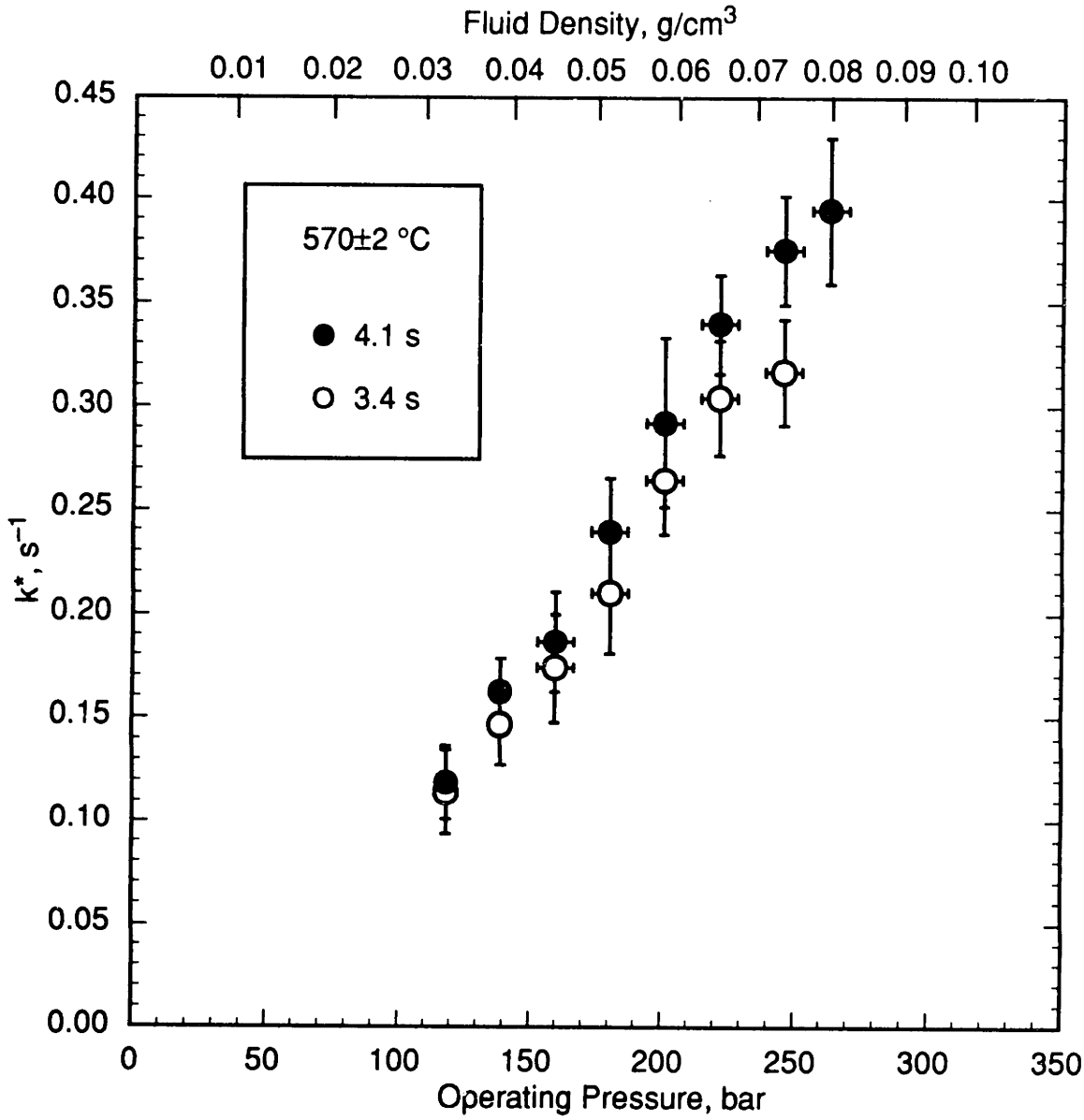

Figure 7.35 **Effects of Operating Pressure (Fluid Density) on Apparent First-Order Rate Constant, k^*, for Carbon Monoxide Oxidation at 570 °C.** Experimental conditions: 570±2 °C, $[CO]_o = (1.03 \pm 0.01) \times 10^{-6}$ mol/cm^3, $[O_2]_o = (0.51 \pm 0.01) \times 10^{-6}$ mol/cm^3. Results for two residence times (3.4 s, 4.1 s) are shown.

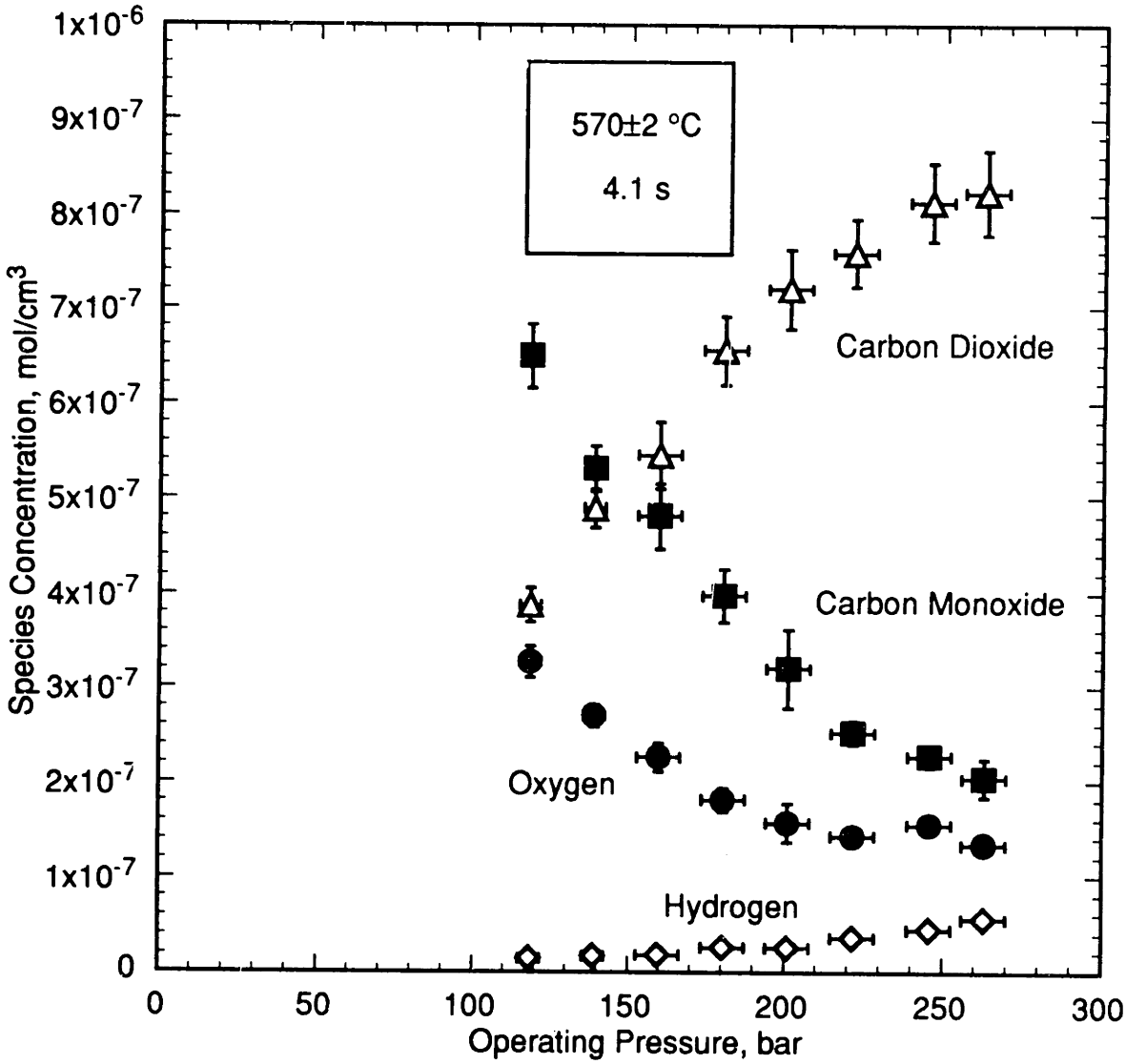

Figure 7.36 Variation with Operating Pressure (Fluid Density) of Major Species Concentrations at 570 °C and 4.1-s Residence Time. Initial conditions as in Figure 7.35.

The availability of data at two residence times at the same operating pressure permits the elimination of the residence time effect on k^*. In other words, a decay constant k' can be derived at each pressure from the conversions (X_{CO}) at the two residence times, using the definition of k':

$$k' = -\frac{d\ln[CO]}{dt} = -\frac{d\ln(1-X_{CO})}{dt} \tag{7.26}$$

Equation 7.26 gives values of k' ranging from 0.16 s^{-1} at 118 bar to 0.66 s^{-1} at 246 bar, or about a fourfold increase in k' with increasing pressure. If the decay constant k' is assumed to depend on pressure (water concentration) in a power-law fashion, i.e.,

$$k' = \hat{k}'[H_2O]^a \tag{7.27}$$

where $\hat{k}'$ is the "water-free" decay constant, then the data in Figure 7.35, when regressed linearly as ln k' vs. ln $[H_2O]$, exhibit an order with respect to water of approximately 1.7. This water dependence is much stronger than the 0.5-order dependence observed in many gas-phase studies (Table 7.1).

The strong dependence of the oxidation rate on water concentration seen here clearly cannot be extraploated to gas-phase conditions, just as the gas-phase 0.5-order dependence cannot be extrapolated to supercritical water conditions. As noted earlier, gas-phase studies of moist CO oxidation at temperatures similar to the present investigation (570 °C) observed an oxidation rate of similar magnitude to the rates observed in the high-pressure supercritical water phase. For the oxidation rates in the two environments to be similar, yet with rates in the two environments dependent on water concentration, there must exist a region, between the low-density gas phase and the high-

density supercritical-water phase, where increasing water concentration decreases the oxidation rate. Clearly this region exists somewhere between about 1 and 118 bar. The existence of such a "negative water dependence" region is consistent with the theory of the extended second explosion limit for hydrogen oxidation, as described by Yetter *et al.* (1989,1991c). In that concept, at low pressures water enhances oxidation rates by improving the production of OH radicals. At higher pressures (water concentrations), formation of more slowly reacting HO_2 radicals becomes favored, chain branching is reduced, and the reaction rate decreases. At still higher pressures, different chain-branching steps become important and the reaction again increases with increasing pressure (water concentration).

The implications of the pressure (water-concentration) dependence of carbon monoxide oxidation for the commercial SCWO process are clear: operation at lower water concentrations entails a penalty in terms of oxidation rate. However, the relationship between water concentration and operating pressure is less direct in the process than it is in these experiments, because water is a much less dominant component in the process stream. For a concentrated, high-heating-value waste with air as the oxidant, water may account for less than 30 wt% of the reactor fluid. A decrease in operating pressure at these lower water contents will have a much less dramatic effect on the water concentration than if water were the dominant component, as in our experimental system. The strong decrease in oxidation rate with decreasing pressure seen in Figure 7.35 is thus likely an overestimate of the effect of decreasing operating pressue in the SCWO process. Results for carbon monoxide oxidation under practical process conditions (595 to 600 °C, 160 to 260 bar), as reported by Hong (1992), therefore showed a much less pronounced effect of the operating pressure on the oxidation rate.

7.8 Reactor Surface Effects

A limted series of experiments was conducted to evaluate the potential influence of reactor surface on observed kinetics. In these experiments, a stoichiometric $CO\text{-}O_2$ mixture, with nominal initial concentrations of 1×10^{-6} and 0.5×10^{-6} mol/cm^3, respectively, was reacted at 560 °C in the packed reactor, which had a 20.5-fold higher surface-to-volume ratio than the open tubular reactor. Conditions were thus essentially identical to those used in Figure 7.27 in the tubular reactor, with the exception that longer residence times were studied owing to the larger volume of the packed reactor. Results of these experiments are shown in Figure 7.37, where the major species profiles from the packed reactor are compared to the profiles from the comparable tubular reactor experiments. Numerical data for the packed-reactor experiments are given in Table 12.12.

Figure 7.37 indicates that the oxidation of carbon monoxide, like the oxidation of hydrogen, is significantly inhibited in the presence of additional Inconel surface area. All four of the major species profiles are extended to longer times. In particular, the hydrogen profile, which peaks slightly at 4 s and then decreases steadily, has not reached its peak concentration for a residence time of over 10 s in the packed reactor. The magnitudes of the two hydrogen profiles are in good agreement, indicating that the water-gas-shift pathway is not preferentially inhibited (or catalyzed) in the presence of additional reactor surface.

Figure 7.38 shows only the carbon monoxide and oxygen profiles for the two reactors, with exponential fits to all four profiles. The kinetic decay constant for the carbon monoxide profile in the packed reactor, 0.057 s^{-1}, is markedly smaller than the decay constant in the tubular reactor, 0.40 s^{-1}. However, if the observed decay constant

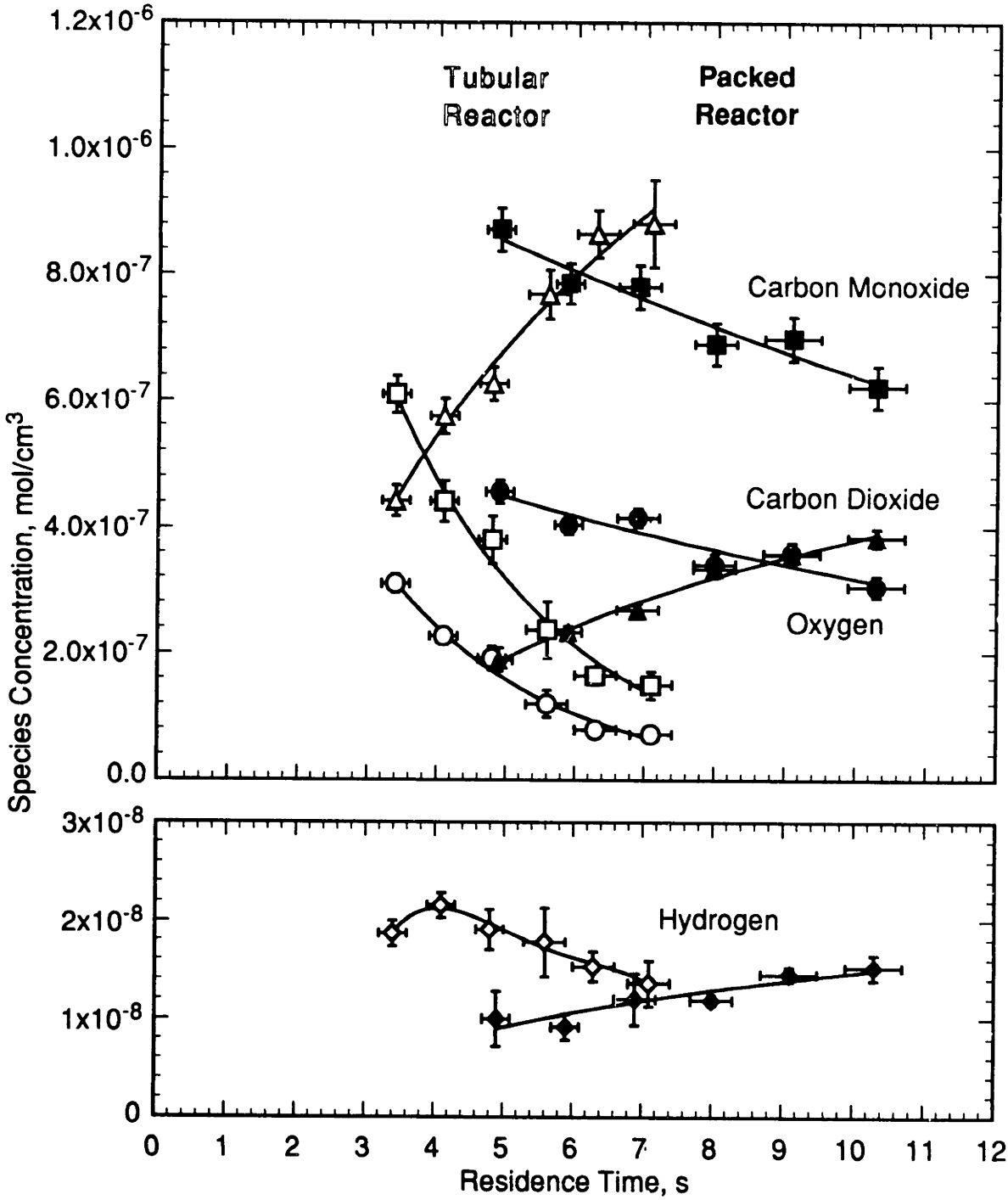

Figure 7.37 **Comparison of Major Species Profiles for CO Oxidation at 560 °C and 246 bar in Tubular and Packed-Bed Reactors.** Nominal experimental conditions: 560 °C, $[CO]_o = 1 \times 10^{-6}$ mol/cm^3, $[O_2]_o = 0.5 \times 10^{-6}$ mol/cm^3. Squares: carbon monoxide; circles: oxygen; triangles: carbon dioxide; diamonds: hydrogen. Open symbols: tubular reactor; filled symbols: packed reactor.

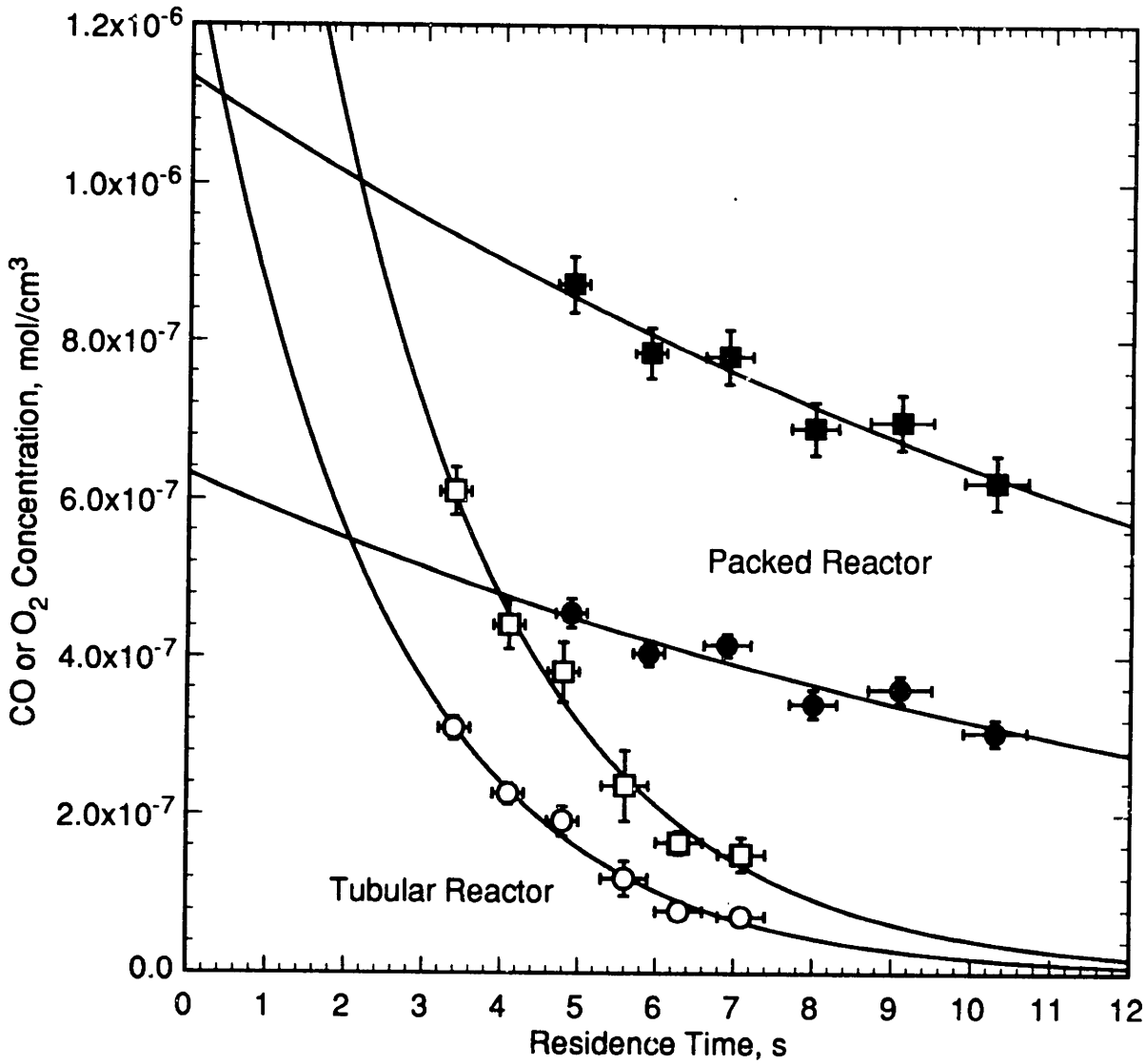

Figure 7.38 Comparison of CO and O_2 Profiles for CO Oxidation at 560 °C and 246 bar in Tubular and Packed-Bed Reactors. Conditions as in Figure 7.37. Squares: carbon monoxide; circles: oxygen. Open symbols: tubular reactor; filled symbols: packed reactor.

is assumed to be linearly proportional to the surface area-to-volume ratio in the reactor, extrapolation of the decay constant to the limit of zero reactor surface area gives a value for k' of 0.42 s^{-1},which is very similar to the tubular-reactor value. Using the logic presented in Section 5.4, the similarity of the decay constants for the tubular reactor and the zero-surface-area case implies that the tubular reactor results, at least at 560 °C, may be treated as reflective of *homogeneous* reaction rates. As noted in Section 5.4, however, this conclusion is strictly true only for the higher temperatures examined, and heterogeneous reactions may increase in importance at lower temperatures. While there was no evidence of a corresponding change in activation energy for hydrogen oxidation, such a change cannot be ruled out for carbon monoxide oxidation (see Section 7.6). The importance of surface reactions in the low-temperature results for carbon monoxide oxidation thus has not been completely ruled out, and further studies of heterogeneous effects under those conditions may be necessary to resolve the issue.

Finally, note that the intersection of the decay curves for the tubular and packed reactors in Figure 7.38 occurs almost exactly at the initial concentration and at the tubular-reactor induction time. As in the case of hydrogen oxidation, the induction time for carbon monoxide oxidation appears to be insensitive to the amount of surface area in the reactor.

Chapter 8

Elementary Reaction Modeling of Carbon Monoxide Oxidation

8.1 Model Development

Elementary reaction modeling of carbon monoxide oxidation was initiated using the successful model for hydrogen oxidation (see Chapter 6) as a starting point. The success of the earlier model for hydrogen oxidation indicated that the model correctly captured many of the fundamental mechanisms of the overall oxidation reaction, and implied that the H_2/O_2 subset of the carbon monoxide oxidation mechanism was well characterized.

Reactions and forward rate constants for the participation of carbon-containing species in the $CO/O_2/H_2O$ mechanism were taken initially from the validated gas-phase mechanism of Yetter *et al.* (1991a). For consistency with the earlier hydrogen oxidation model, species thermodynamic data were taken from the JANAF Thermochemical Tables (Chase *et al.*, 1985). Preliminary modeling showed that oxidation rates were in general underpredicted by the carbon monoxide oxidation model. Furthermore, hydrogen concentrations (formed through the global water-gas-shift pathway) were drastically underpredicted, as they had been in earlier elementary reaction models for supercritical water oxidation (Helling, 1986; Webley, 1989; Webley and Tester, 1991). Following these initial modeling results, five modifications were made to the carbon monoxide model.

1. The rate of the primary carbon-monoxide-oxidizing reaction

$$CO + OH \rightarrow CO_2 + H \tag{8.1}$$

is known to be pressure-dependent (Overend and Paraskevopoulos, 1977; Biermann *et al.*, 1978; Hofzumahaus and Stuhl, 1984; Paraskevopoulos and Irwin, 1984; DeMore, 1984; Hynes *et al.*, 1986) and its rate constant for the conditions of interest (246 bar, 400 to 600 °C) was calculated using the model of Larson *et al.* (1988). According to the model, at 246 bar the rate constant varies by only about 15% over the entire temperature range, and has a value of about 3×10^{11} $cm^3mol^{-1}s^{-1}$ (see Section 12.4 for details). The recommended rate expression of Baulch *et al.* (1976), used in the model of Yetter *et al.* (1991a), predicts that the rate constant varies from 1.2×10^{11} to 1.5×10^{11} $cm^3mol^{-1}s^{-1}$ over this temperature range and is independent of pressure; the incorporation of the pressure-dependent rate constant from the Larson *et al.* (1988) model thus increases the rate of the primary oxidizing reaction in the model (by about a factor of two) and increases the predicted carbon monoxide oxidation rates. While the excellent agreement between their model and experimental data lends strong support to selection of the Yetter *et al.* (1991a) rate constant expression, one should note that a more recent evaluation by Baulch *et al.* (1992) recommends a different rate expression for the CO + OH reaction which predicts a slightly higher rate constant (about 1.6×10^{11} to 2.2×10^{11} $cm^3mol^{-1}s^{-1}$) over the range 400 to 600 °C. For the present modeling study, the higher values for the rate constant, as predicted by the pressure-dependent model, are preferred.

2. The rate constant for the formation of the hydroperoxyl radical

$$H + O_2 (+ M) \rightarrow HO_2 (+ M) \tag{8.2}$$

was found to affect the predicted hydrogen concentration, and its value was more carefully scrutinized. The hydrogen oxidation model at 246 bar was virtually insensitive to the value of this rate constant, and the rate constant was assumed to be in the low-pressure regime. Modeling of the pressure dependence of hydrogen oxidation (and the concurrent examination of pressure-dependent rate constants), however, showed that the rate constant was not in the low-pressure regime at supercritical-water conditions, but rather in the falloff regime (see Section 12.3 for details). The carbon monoxide model was sensitive to the value of the rate constant for reaction 8.2; thus, the low-pressure rate expression used in the hydrogen model was replaced by the falloff rate expression calculated in Section 12.3.

3. Pressure-dependence calculations (Section 12.2) showed that the dissociation of hydrogen peroxide

$$H_2O_2\ (+\ M) \rightarrow OH + OH\ (+\ M) \tag{8.3}$$

is very near its high-pressure limit at 400 to 600 °C and 246 bar. The hydrogen oxidation model used the high-pressure limit expression for the reverse (recombination) reaction rate constant from Brouwer *et al.* (1987). In the carbon monoxide model, the high-pressure recombination rate constant was replaced with the dissociation rate constant (from Section 12.2) for consistency with modeling of oxidation at varying operating pressures. Since the calculated rate constant is very close to its high-pressure limit, this modification has a negligible effect on the model predictions.

4. The rate constant for the self-reaction (disproportionation) of HO_2

$$HO_2 + HO_2 \rightarrow H_2O_2 + O_2 \tag{8.4}$$

is known to exhibit non-Arrhenius behavior, with a minimum in its rate constant at about 700 K (Hippler *et al.*, 1990), such that the temperature dependence of the rate constant can be expressed as the sum of two exponentials. For the hydrogen oxidation model, all experimental data were obtained at temperatures (495 to 600 °C or 768 to 873 K) sufficiently above the range in which the minimum occurs that the rate constant could be expressed in simple Arrhenius form for modeling purposes. The temperature range of the carbon monoxide experiments (420 to 593 °C), however, spans the range of the rate-constant minimum, and a modified Arrhenius form (incorporating a temperature exponent) was needed to capture the curvature in the temperature dependence of the rate constant. The recommended rate expression of Hippler *et al.* (1990) was subsequently fit to such a form in the temperature range 400 to 600 °C for modeling of carbon monoxide oxidation.

5. The initial carbon monoxide oxidation model exhibited a small sensitivity to the rate constant for the reaction of carbon monoxide with an oxygen atom

$$CO + O\ (+ M) \rightarrow CO_2\ (+ M) \tag{8.5}$$

The low-pressure-limit rate constant for this reaction, as recommended by Warnatz (1984) and used by Yetter *et al.* (1991a), has a value of about 3×10^{12} $cm^3mol^{-1}s^{-1}$ for temperatures of 400 to 600 °C and water concentrations of approximately 4×10^{-3} mol/cm^3 (supercritical water conditions at 246 bar). However, this reaction exhibits strong non-Arrhenius behavior, with a positive activation energy at low temperatures (below ~1000 K) and a negative activation energy at high temperatures, and a resulting maximum in the rate constant at about 1000 K (Westmoreland *et al.*, 1986). The expression from Warnatz (1984) adequately describes the high-temperature regime, yet

the temperatures of the present study are actually in the lower-temperature regime; extrapolation of the high-temperature behavior to the lower temperatures will overestimate the low-temperature rate constant. Furthermore, the high-pressure-limit rate constant for this reaction, in the 400 to 600 °C temperature range, is about 4×10^9 $cm^3mol^{-1}s^{-1}$ (Troe, 1974), or about three orders of magnitude lower than the extrapolated low-pressure rate constant. The rate constant for this reaction thus appears to be at its high-pressure limit for supercritical water conditions, and the high-pressure rate expression recommended by Troe (1974), encompassing both the low- and high-temperature regimes, was used in the carbon monoxide model. Substitution of the high-pressure rate constant in the model had a negligible effect on predicted carbon monoxide oxidation rates.

The final, modified elementary reaction network for carbon monoxide oxidation in supercritical water is given in Tables 8.1 and 8.2. Table 8.1 lists the rate expressions used in calculating the forward rate constants in the model. Note the highly unusual parameters for the HO_2 self-reaction (reaction 13); those parameters were obtained strictly by curve fitting (see above) and should be accorded no physical significance. Table 8.2 lists equilibrium constants (K_p) for the reactions, with thermodynamic data taken from the JANAF Tables (Chase *et al.*, 1985) and fit to a Gibbs-Helmholtz form. Reverse rate constants are calculated from the forward rate constants (Table 8.1) and the equilibrium constants (Table 8.2) by microscopic reversibility as described in Section 6.2. The model was integrated using the Acuchem kinetic software (Braun *et al.*, 1988) with sensitivity analysis provided by SENKIN (Lutz *et al.*, 1988).

#	Elementary Reaction	$k = A\,T^b \exp(-E_a/RT)$† log A	b	E_a	UF [a]	Temp. Range[b]	Source
1	$H + O_2 \rightarrow OH + O$	14.28	0.0	68.8	2	962–2577	1
2	$O + H_2 \rightarrow OH + H$	4.71	2.67	26.3	1.5	297–2495	2
3	$H_2 + OH \rightarrow H_2O + H$	8.33	1.51	14.35	1.5	250–2581	3
4	$OH + OH \rightarrow O + H_2O$[c]	11.74	0.00149	0.0	2.5	250–2000	4
5	$H_2 + M \rightarrow H + H + M$[d]	19.93	−1.1	436.7	10	600–2000	4
6	$H + OH + M \rightarrow H_2O + M$	23.14	−2.0	0.0	2	1000–3000	4
7	$H + O_2 \rightarrow HO_2$	13.68	0.0	−1.61	2	673–873	5
8	$H + HO_2 \rightarrow OH + OH$	14.23	0.0	3.64	2	298-773	4
9	$H + HO_2 \rightarrow H_2 + O_2$	13.82	0.0	8.91	2	298–773	4
10	$O + HO_2 \rightarrow OH + O_2$	13.24	0.0	−1.67	1.2	200–400	4
11	$OH + HO_2 \rightarrow H_2O + O_2$	16.16	−1.0	0.0	2	298–1400	4
12	$H_2O_2 + OH \rightarrow H_2O + HO_2$	12.85	0.0	5.98	2	298–800	6
13	$HO_2 + HO_2 \rightarrow H_2O_2 + O_2$	−38.77	15.43	−87.8	2	673–873	7
14	$H_2O_2 \rightarrow OH + OH$	14.89	0.0	208.7	2	673–873	5
15	$H_2O_2 + H \rightarrow HO_2 + H_2$	13.68	0.0	33.26	5	283–800	4
16	$H_2O_2 + H \rightarrow H_2O + OH$	13.00	0.0	15.02	3	283–800	6
17	$O + H + M \rightarrow OH + M$	18.67	−1.0	0.0	10	—	4
18	$O + O + M \rightarrow O_2 + M$	14.60	0.0	−7.49	1.3	200–4000	4
19	$H_2O_2 + O \rightarrow OH + HO_2$	6.98	2.0	16.61	3	250–800	4
20	$CO + OH \rightarrow CO_2 + H$[c]	11.25	0.0006285	0.0	2	673–873	5

Table 8.1 **Forward Rate Constants Used in Elementary Reaction Model for Carbon Monoxide Oxidation in Supercritical Water.**

#	Elementary Reaction	$k = A\ T^b \exp(-E_a/RT)$† log A	b	E_a	UF [a]	Temp. Range[b]	Source
21	$CO + O \rightarrow CO_2$	10.26	0.0	10.17	4	298–3500	8
22	$CO + O_2 \rightarrow CO_2 + O$	12.40	0.0	199.54	2	1500–3000	4
23	$CO + HO_2 \rightarrow CO_2 + OH$	13.78	0.0	96.03	3	700–1000	9
24	$HCO + M \rightarrow H + CO + M$	18.54	−1.0	71.13	5	637–832	10
25	$HCO + O_2 \rightarrow CO + HO_2$	12.38	0.0	1.72	5	295–713	11
26	$HCO + H \rightarrow CO + H_2$	13.86	0.0	0.0	2	296–418	12
27	$HCO + O \rightarrow CO + OH$	13.48	0.0	0.0	3	—	4
28	$CO + H_2O \rightarrow HCO + OH$	13.48	0.0	0.0	3	—	4

† Units of kJ, mol, cm^3, s, K.
[a] Uncertainty factor for rate constant.
[b] Valid temperature range for the rate constant expression, in Kelvin.
[c] $k = A \exp(bT)$.
[d] M = third body, assumed to be exclusively H_2O. Rates of all third-body-assisted reactions have been adjusted to include the third-body efficiencies for M = H_2O as recommended by the original sources.

Sources:
1) Pirraglia *et al.* (1989).
2) Sutherland *et al.* (1986).
3) Michael and Sutherland (1988).
4) Tsang and Hampson (1986).
5) Pressure-dependence calculation for 246 bar (see text and Sections 12.2 to 12.4).
6) Warnatz (1984).
7) Hippler *et al.* (1990); simplified rate form fit from 673 to 873 K.
8) Troe (1974).
9) Atri *et al.* (1977).
10) Timonen *et al.* (1987a).
11) Timonen *et al.* (1988).
12) Timonen *et al.* (1987b).

Table 8.1 Forward Rate Constants Used in Elementary Reaction Model for Carbon Monoxide Oxidation in Supercritical Water. Continued.

#	Elementary Reaction	$\log_{10} K_p = A + B/T^{\dagger}$	
		A	B
1	$H + O_2 \rightarrow OH + O$	1.2895	–3659.9
2	$O + H_2 \rightarrow OH + H$	0.34432	–406.41
3	$H_2 + OH \rightarrow H_2O + H$	–0.6700	3316.0
4	$OH + OH \rightarrow O + H_2O$	–1.0143	3722.4
5	$H_2 + M \rightarrow H + H + M$	5.5635	–22915.1
6	$H + OH + M \rightarrow H_2O + M$	–6.2335	26231.1
7	$H + O_2 \rightarrow HO_2$	–5.1663	11423.6
8	$H + HO_2 \rightarrow OH + OH$	1.2366	7425.3
9	$H + HO_2 \rightarrow H_2 + O_2$	–0.3972	11491.6
10	$O + HO_2 \rightarrow OH + O_2$	–0.05285	11085.2
11	$OH + HO_2 \rightarrow H_2O + O_2$	–1.0672	14807.5
12	$H_2O_2 + OH \rightarrow H_2O + HO_2$	–0.1423	7521.85
13	$HO_2 + HO_2 \rightarrow H_2O_2 + O_2$	–0.9247	7285.68
14	$H_2O_2 \rightarrow OH + OH$	7.3277	–11283.9
15	$H_2O_2 + H \rightarrow HO_2 + H_2$	0.5275	4205.88
16	$H_2O_2 + H \rightarrow H_2O + OH$	1.0942	14947.1
17	$O + H + M \rightarrow OH + M$	–5.2192	22508.7
18	$O + O + M \rightarrow O_2 + M$	–6.5087	26168.6
19	$H_2O_2 + O \rightarrow OH + HO_2$	0.8719	3799.47

Table 8.2 Equilibrium Constants for $CO/O_2/H_2O$ Elementary Reactions.

#	Elementary Reaction	$\log_{10} K_p = A + B/T^{\dagger}$	
		A	*B*
20	$CO + OH \rightarrow CO_2 + H$	–2.6273	5383.08
21	$CO + O \rightarrow CO_2$	–7.8465	27891.8
22	$CO + O_2 \rightarrow CO_2 + O$	–1.3379	1723.22
23	$CO + HO_2 \rightarrow CO_2 + OH$	–1.3907	12808.4
24	$HCO + M \rightarrow H + CO + M$	4.9983	–3482.32
25	$HCO + O_2 \rightarrow CO + HO_2$	–0.1680	7941.23
26	$HCO + H \rightarrow CO + H_2$	–0.5652	19432.8
27	$HCO + O \rightarrow CO + OH$	–0.2209	19026.4
28	$HCO + OH \rightarrow CO + H_2O$	–1.2352	22748.8

†Units of bar, K. Source: JANAF Thermochemical Tables (Chase *et al.*, 1985); equilibrium constants fit from 300 to 1000 K.

Table 8.2 Equilibrium Constants for $CO/O_2/H_2O$ Elementary Reactions. Continued.

8.2 Modeling Results

Since certain modifications to the carbon monoxide oxidation model had the potential to affect the predictions of the hydrogen oxidation subset, modeling calculations using the carbon monoxide model were carried out for the hydrogen oxidation data. The modifications to the H_2/O_2 subset of reactions had a negligibly small effect on the predicted hydrogen oxidation behavior. The modified carbon monoxide model thus does not violate the principle of a hierarchical model. The predictions of the model, denoted YDR91J for consistency with the earlier hydrogen oxidation model, were subsequently compared to the experimental data for carbon monoxide oxidation.

8.2.1 Model Predictions

Figure 8.1 compares the predictions of the YDR91J model with the experimental carbon monoxide oxidation data from the present study (listed in Table 12.8), in the form of a first-order Arrhenius plot. Calculated first-order rate constants in Figure 8.1 are based on the total conversion of carbon monoxide in the reactor, i.e., conversion by both the direct-oxidation and the water-gas shift pathways has been included, and the inlet carbon monoxide concentration has been corrected for reaction during preheating. While the model and the data show reasonable agreement at the higher temperatures, the deviation is considerable at lower temperatures, and the model exhibits a significantly higher global activation energy than the data (428±31 kJ/mol vs. 180±38 kJ/mol). Note that the global activation energy for the lumped, first-order reaction of carbon monoxide, 180±38 kJ/mol, is within statistical error of the activation energy obtained in Equation 7.22 for the oxygen-dependent, direct-oxidation pathway, 134±32 kJ/mol. On the other hand, the global activation energy of the model, 428±31 kJ/mol, compares more favorably with the activation energy obtained in Section 7.6 for the stoichiometric carbon monoxide decay

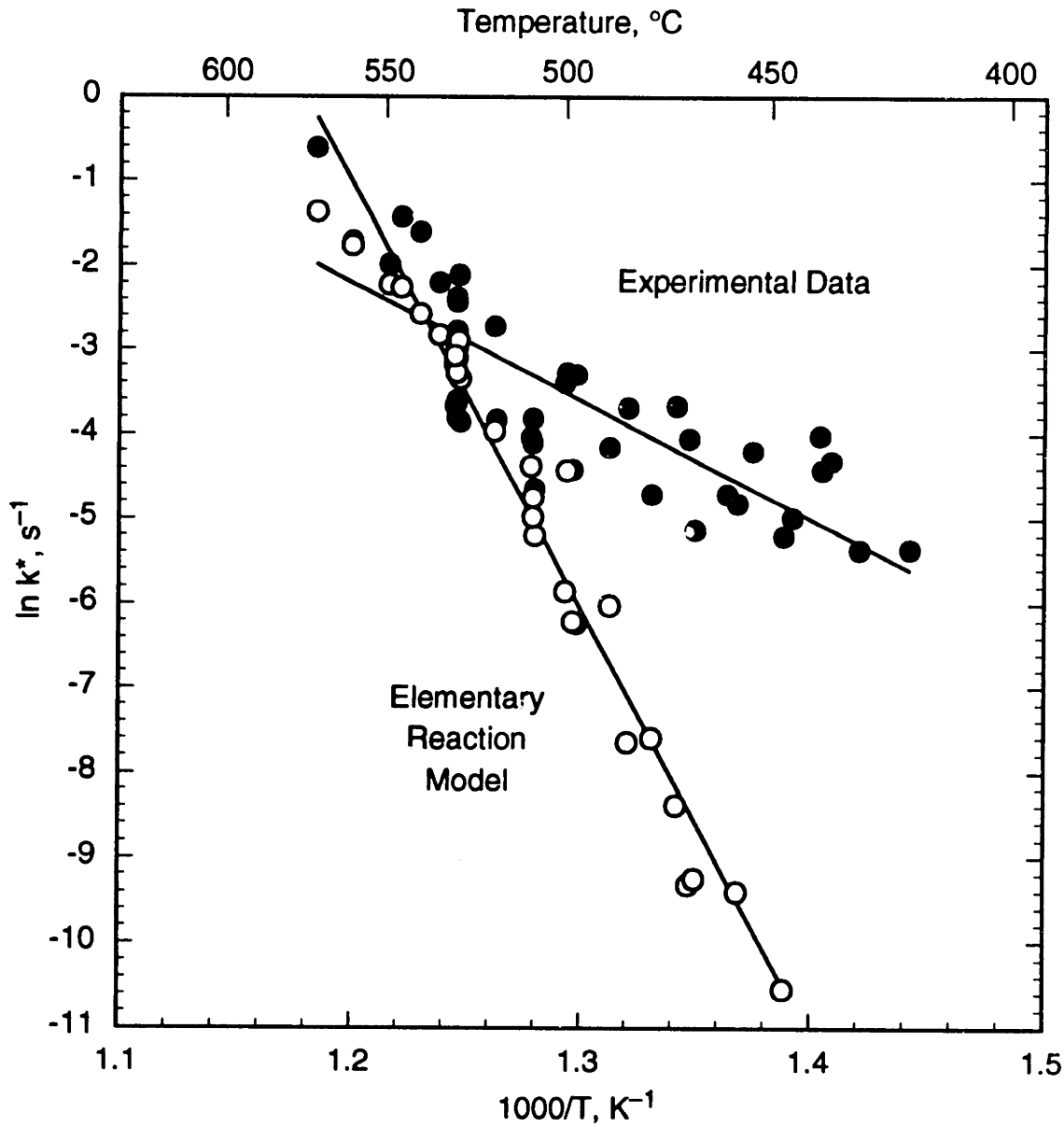

Figure 8.1 **Arrhenius Plot for Experimental Data and Elementary Reaction Model for Carbon Monoxide Oxidation in Supercritical Water at 246 bar.** Experimental data are from the present study only.

constants at 550 and 560 °C, 488 kJ/mol. The same data and model predictions from Figure 8.1 are compared in Figure 8.2, where observed and predicted conversions of carbon monoxide are shown. Low conversions are seriously underpedicted, while higher conversions show better agreement. Predicted effluent $[H_2]/[CO_2]$ ratios in general ranged from about 3 to 15%, in reasonable agreement with the magnitudes observed experimentally (Holgate *et al.*, 1992).

The data thus show some evidence of a change in activation energy at about 500 °C. As noted above, the two stoichiometric curves in Figure 7.30, at 550 and 560 °C, imply an activation energy of 488 kJ/mol for the CO decay constant, which is similar to the model activation energy but much higher than the overall activation energy for the data in Figure 8.1. A different low-temperature mechanism for carbon monoxide oxidation, possibly involving heterogeneous reactions, cannot be ruled out.

Predicted carbon monoxide conversions from the model for water-gas shift experiments are compared to the data (from Table 12.7) in Figure 8.3. As noted in Section 7.3, it was impossible to completely exclude oxygen from the reactor, and there was consequently always a direct-oxidation contribution to the conversion of carbon monoxide in the water-gas shift experiments. The modeling calculations in Figure 8.3 were performed with a small feed concentration of oxygen, as calculated from experimental effluent conditions. Carbon monoxide conversions reported in Figure 8.3 include the contribution of the direct-oxidation pathway. Note that the model predicts the experimental conversions reasonably well, in some cases even *overestimating* conversions by a considerable margin. At the same time, predicted effluent $[H_2]/[CO_2]$ ratios were roughly 0.8 to 0.9, in good agreement with experimental observations and clearly indicating that the dominant reactive pathway was the water-gas shift. The ability of the present model to predict conversion by the water-gas-shift pathway contrasts

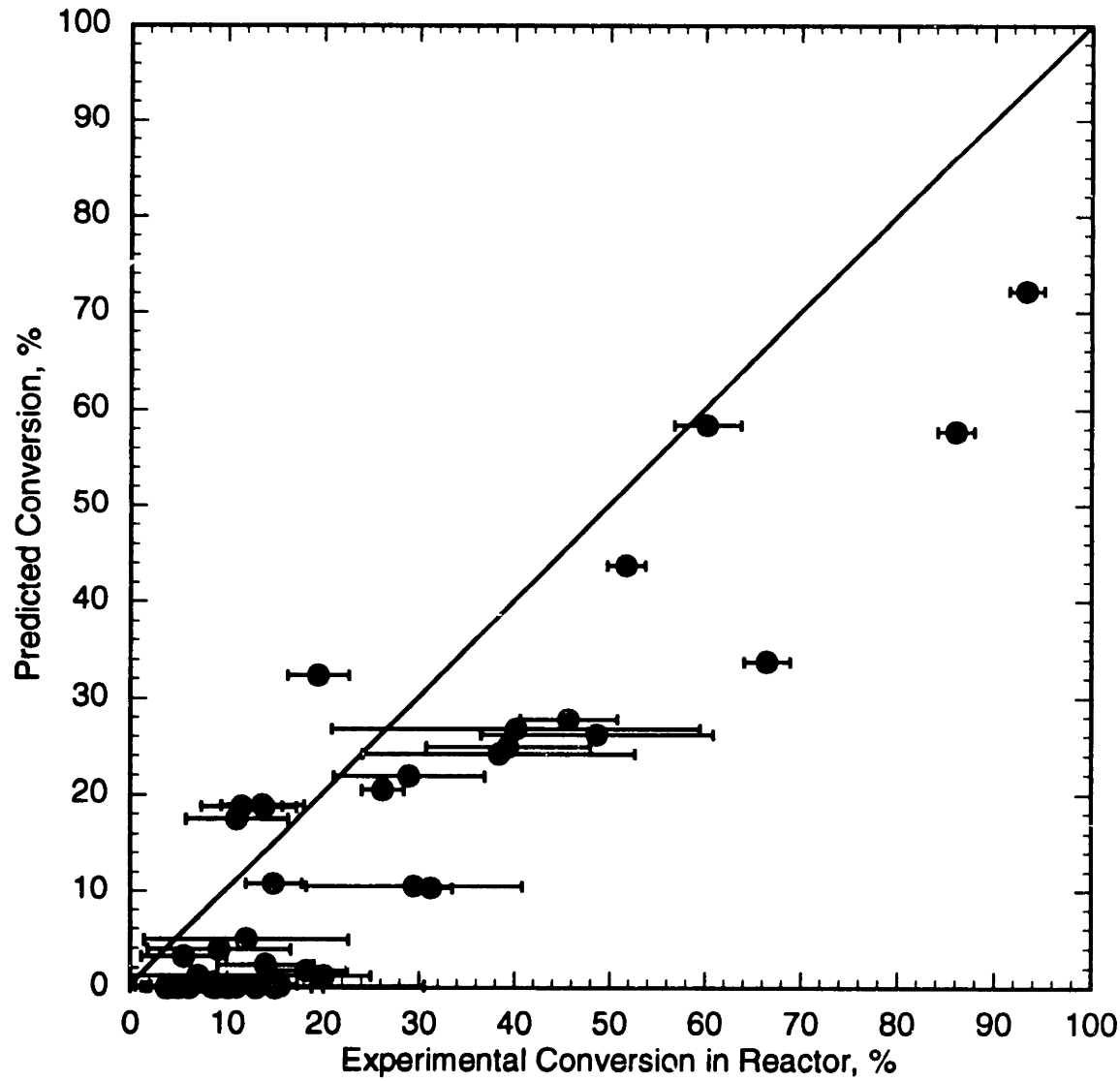

Figure 8.2 **Predicted Conversion of Carbon Monoxide from Elementary Reaction Model (Oxidation Experiments).** Experimental data are from the present study only.

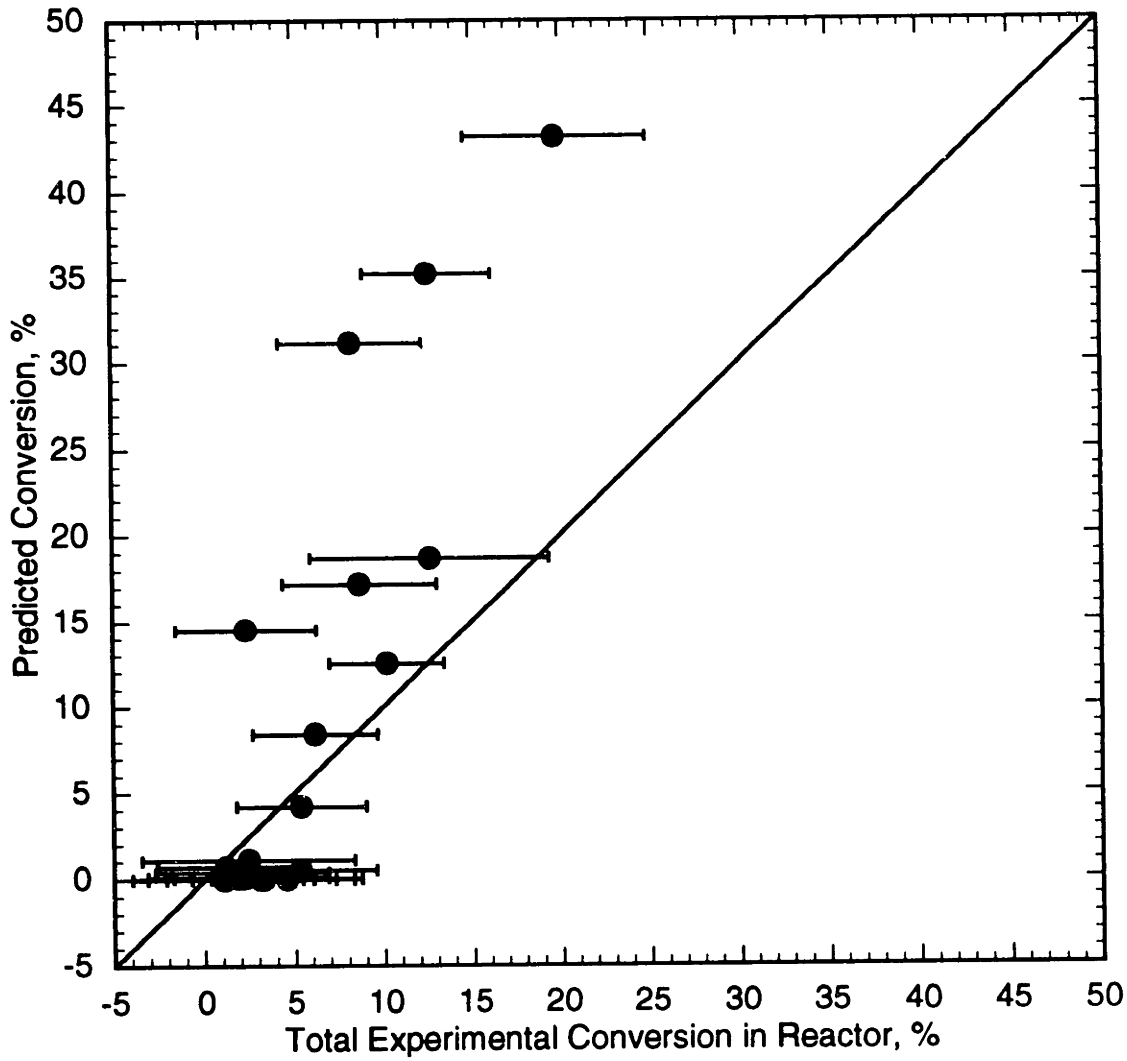

Figure 8.3 **Predicted Conversion of Carbon Monoxide from Elementary Reaction Model (Water-Gas Shift Experiments).** Experimental data are from the present study only.

sharply with earlier elementary reaction models (Helling, 1986; Webley, 1989; Webley and Tester, 1991), which were uniformly unable to predict hydrogen formation. However, the present model predicts negligibly slow reaction rates in the complete absence of oxygen, indicating that the water-gas-shift pathway is in some way enhanced or "catalyzed" by the presence of oxygen, and cannot occur to any measurable extent in the absence of oxygen.

The prediction of an oxygen-catalyzed water-gas-shift pathway is consistent with experimental observations in our laboratory and elsewhere. For example, Figure 7.28 showed that under fuel-rich conditions, when the oxygen has been completely depleted, the reaction (disappearance) of carbon monoxide ceases. Since our experimental environment cannot be made oxygen-free, no observations of the pure water-gas shift pathway are possible. A strong influence of oxygen on the gas-phase water-gas shift reaction has been identified, with even traces of oxygen tending to greatly enhance reaction rates (Hadman *et al.*, 1932; Graven and Long, 1954; Tingey, 1966); in the absence of oxygen, the gas-phase water-gas shift occurs very slowly. The model predictions thus raise the possibility, supported by experimental evidence, that all experimental observations in the present study of conversion by the isolated water-gas shift reaction (Section 7.3 and Table 12.7) are an artifact of the unavoidable traces of oxygen present in the reactor.

Higher-temperature carbon monoxide oxidation data, including the major-species profiles from Figures 7.26 through 7.29 for 550 and 560 °C, are quite well described by the model, as shown in Figures 8.4 through 8.7. For the model predictions in these figures, experimental reaction of carbon monoxide (and concurrent hydrogen formation) during feed preheating was neglected; initial conditions for the model calculations were those listed in Table 12.10. Figure 8.4 shows the model predictions for a stoichiometric

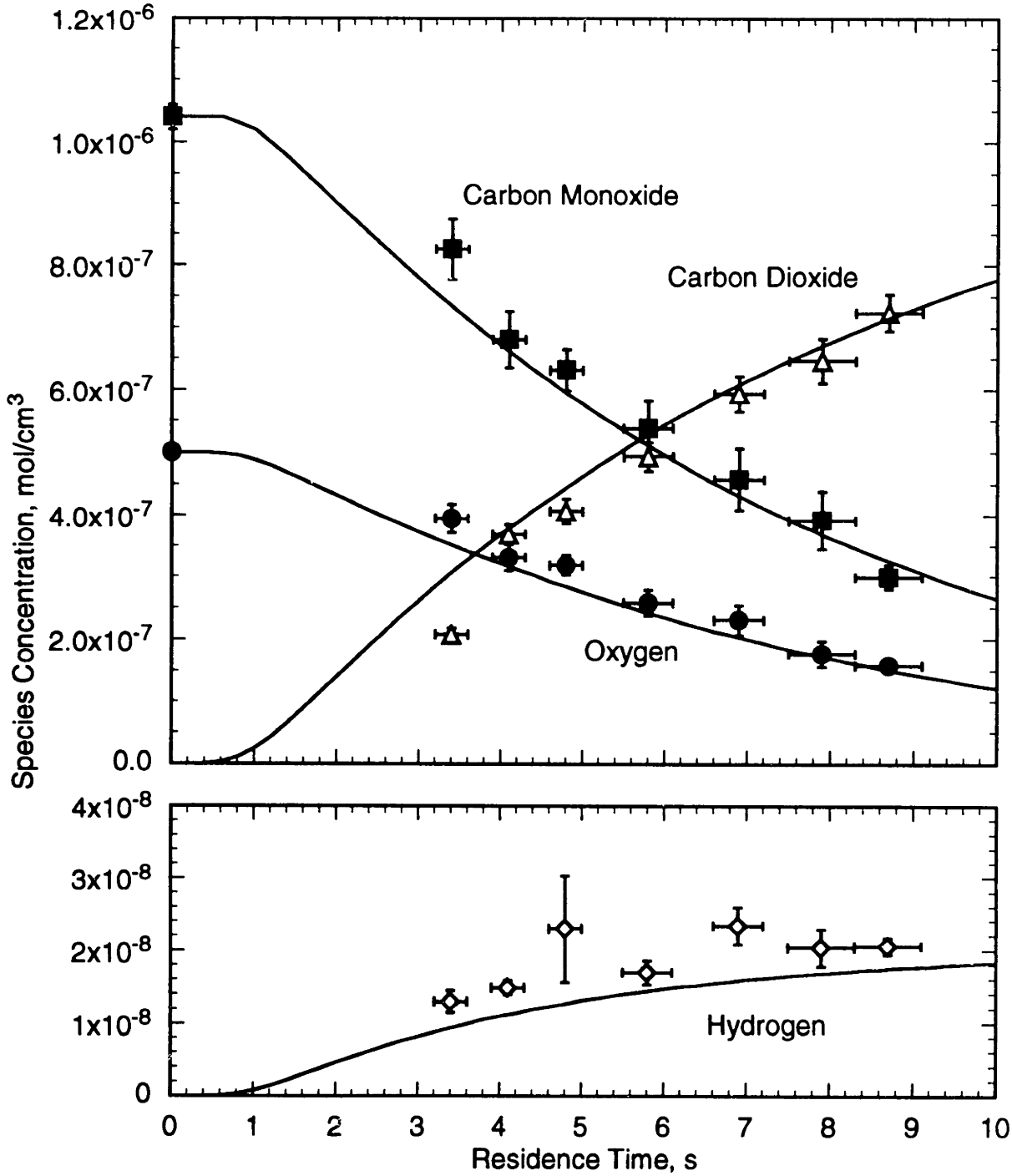

Figure 8.4 **Major Species Profiles for Stoichiometric Carbon Monoxide Oxidation at 550±2 °C.** Symbols: experimental data, $[CO]_o$ = (1.04±0.02) × 10^{-6} mol/cm^3, $[O_2]_o$ = (0.50±0.01) × 10^{-6} mol/cm^3, $[H_2O]$ = (4.25±0.08) × 10^{-3} mol/cm^3. Curves: predictions of model YDR91J.

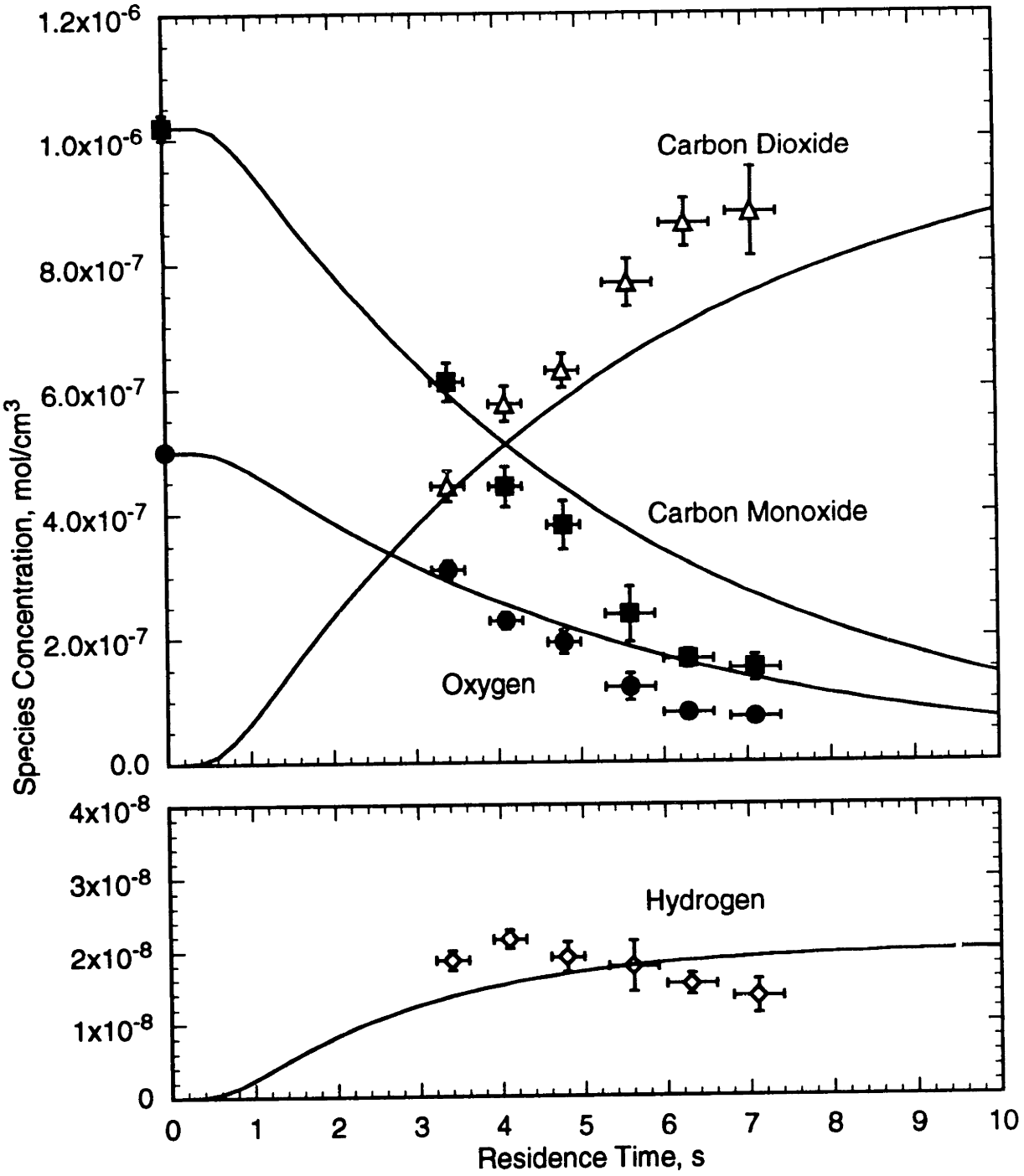

Figure 8.5 **Major Species Profiles for Stoichiometric Carbon Monoxide Oxidation at 560±2 °C.** Symbols: experimental data, $[CO]_o$ = $(1.02\pm0.02) \times 10^{-6}$ mol/cm^3, $[O_2]_o = (0.50\pm0.01) \times 10^{-6}$ mol/cm^3, $[H_2O]$ = $(4.16\pm0.07) \times 10^{-3}$ mol/cm^3. Curves: predictions of model YDR91J.

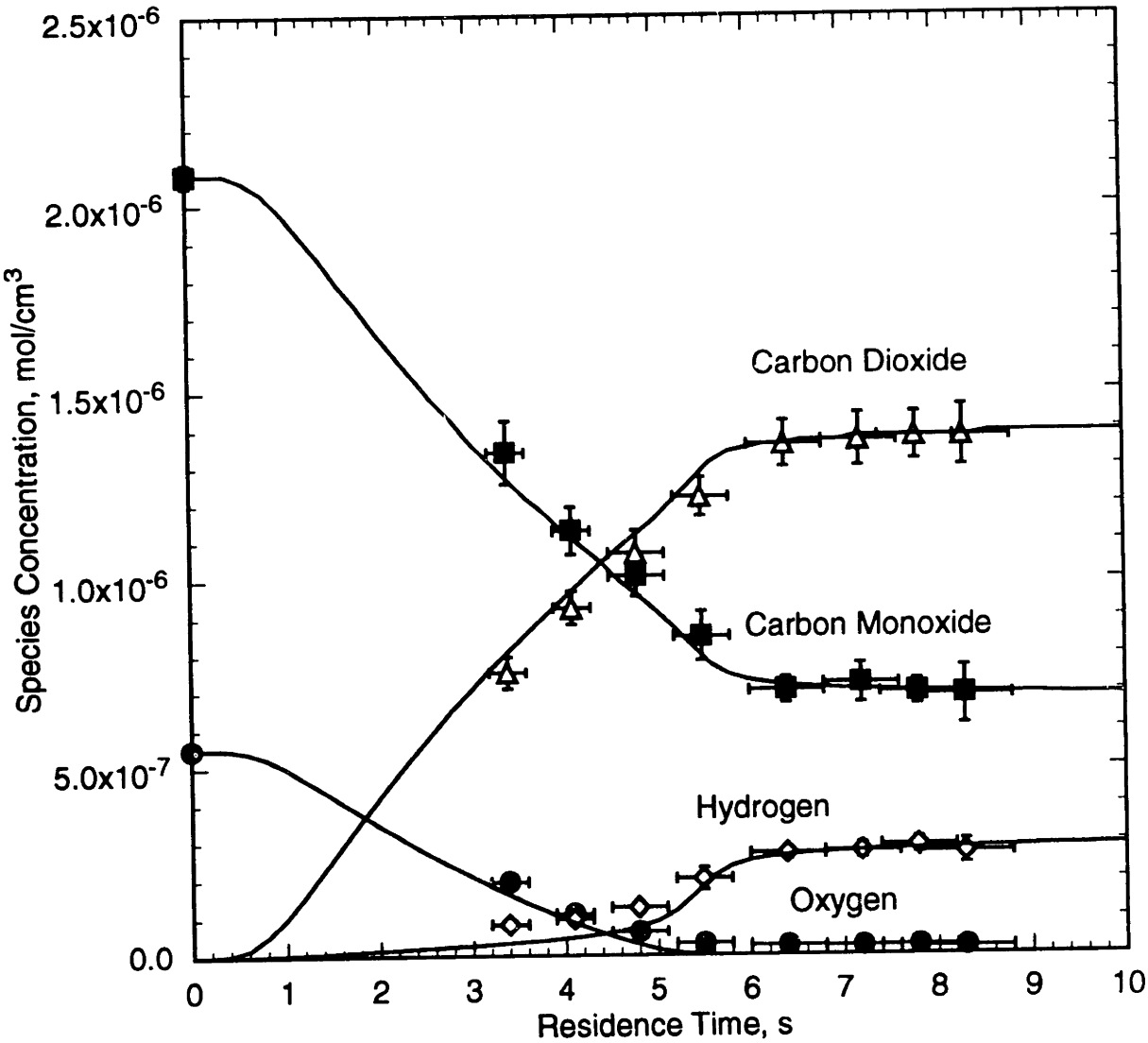

Figure 8.6 **Major Species Profiles for Substoichiometric (Fuel-Rich) Carbon Monoxide Oxidation at 560±3 °C.** Symbols: experimental data, $[CO]_o$ = (2.08±0.03) × 10^{-6} mol/cm^3, $[O_2]_o$ = (0.55±0.01) × 10^{-6} mol/cm^3, $[H_2O]$ = (4.16±0.14) × 10^{-3} mol/cm^3. Curves: predictions of model YDR91J.

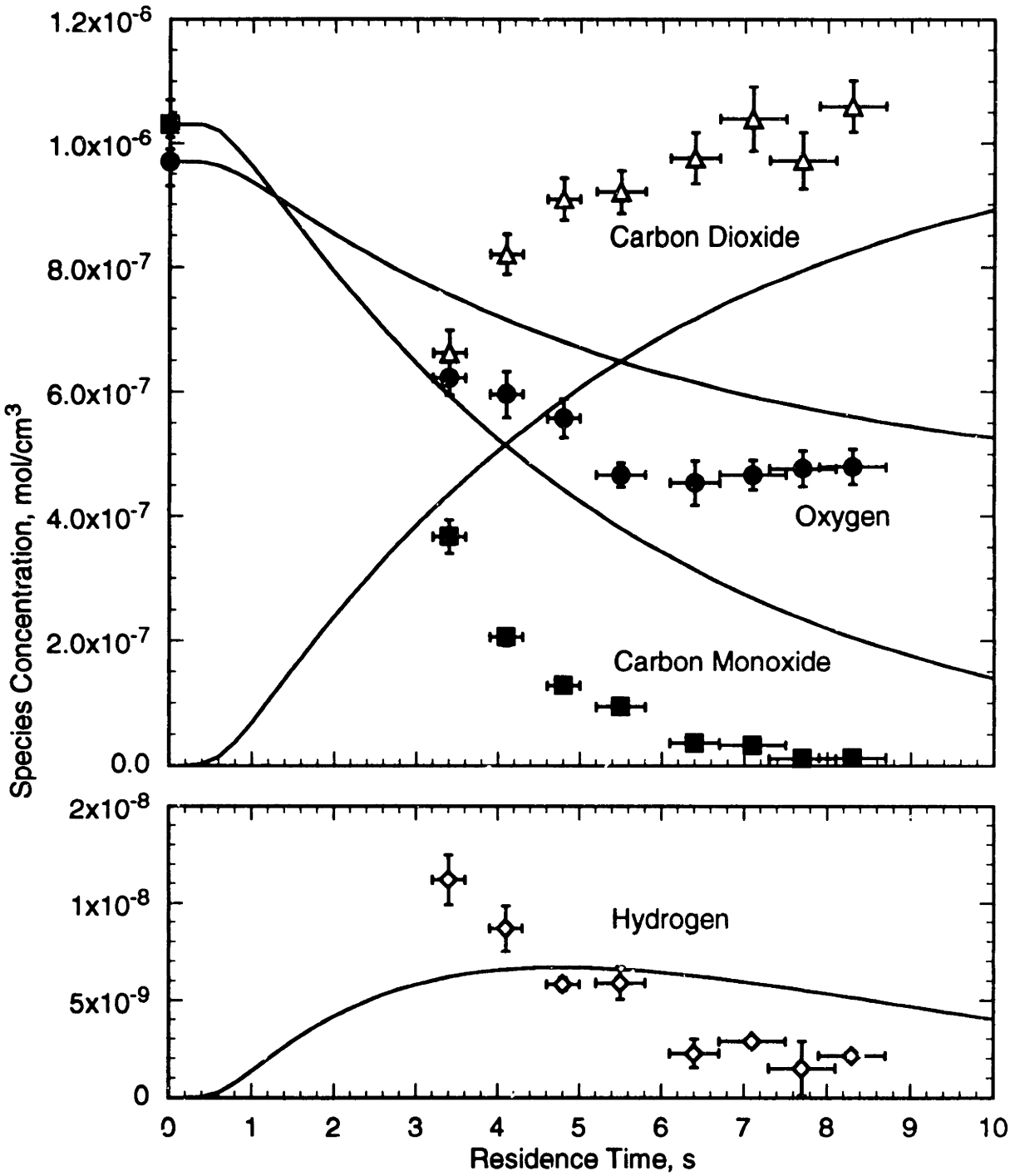

Figure 8.7 **Major Species Profiles for Superstoichiometric (Fuel-Lean) Carbon Monoxide Oxidation at 560±2 °C.** Symbols: experimental data, $[CO]_o$ = (1.03±0.04) × 10^{-6} mol/cm^3, $[O_2]_o$ = (0.97±0.04) × 10^{-6} mol/cm^3, $[H_2O]$ = (4.16±0.09) × 10^{-3} mol/cm^3. Curves: predictions of model YDR91J.

CO-O_2 mixture at 550 °C. Note that the shapes and ıgnitudes of all four major-species profiles are correctly predicted by the model. Of particular note is the correct prediction of the hydrogen concentration profile, which (as noted earlier) had not been achieved in previous models. Recall also that no rate constants have been adjusted specifically to fit the experimental data, and the predicted profiles have not been shifted in time to match the experimental profiles.

Figure 8.5 shows the model predictions for a stoichiometric CO-O_2 mixture at 560 °C. In this case the agreement between model and experiment is somewhat less satisfactory, with the model underpredicting reaction rates. This behavior is consistent with the overall activation energy for the model (428±31 kJ/mol) being lower than the activation energy implied by the carbon monoxide profile in Figures 8.4 and 8.5 (488 kJ/mol). Note that the model again predicts the correct magnitude of the hydrogen concentration, even if the shape of the hydrogen profile is not quite correctly predicted.

Predictions for a fuel-rich ($\phi = 2$) CO-O_2 mixture at 560 °C are shown in Figure 8.6. The model shows excellent agreement with the data. The hydrogen concentration is again correct, and the model shows the characteristic, significant reduction in reaction rate following oxygen depletion, as discussed earlier.

Finally, Figure 8.7 shows the model predictions for a fuel-lean ($\phi = 0.5$) CO-O_2 mixture at 560 °C. Here the agreement between model and experiment is markedly poorer, with the model predicting much slower reaction rates than observed. The approximate magnitude of the hydrogen concentration is reproduced by the model, and the general shape of the hydrogen profile, including a maximum and subsequent decrease is correct, although the model appears to predict a much slower development of the profile than is observed.

The predictions in Figures 8.4 through 8.7 show that the present model is quite capable of correctly reproducing both the magnitude and the shape of the hydrogen concentration profiles in carbon monoxide oxidation experiments, without fitting of rate constants or time-shifting the model predictions. Furthermore, the model incorporates only traditional, well-accepted, gas-phase elementary reactions with theoretically consistent corrections for the effects of high pressure (density). Thus, we have demonstrated that it is possible to predict the observed contribution of the global water-gas shift pathway without invoking new reactions, such as a molecular water-gas shift pathway proceeding via a formic acid intermediate, as has been proposed by Melius and co-workers (Melius *et al.*, 1990).

Figure 8.8 shows the predicted carbon monoxide concentration profiles from Figures 8.4 through 8.7, normalized by the initial concentration. All three predicted CO profiles at 560 °C exhibit essentially the same shape, at least until the oxygen is depleted in the fuel-rich case. This behavior indicates that the model does not predict an oxygen dependence of the CO oxidation rate; thus while the model shows excellent agreement with the experimental fuel-rich profile (Figure 8.6), the model predictions become increasingly unsatisfactory for leaner mixtures (Figures 8.5 and 8.7), since the observed increase in oxidation rate for lean conditions is not predicted. The inability of the model to capture the observed oxygen dependence is its major shortcoming.

Predicted decay constants and induction times for carbon monoxide oxidation, as obtained from Figure 8.8, are summarized and compared with data in Table 8.3. The predicted kinetic decay constants for the stoichiometric profile at 550 °C is in very good agreement with the experimental value. Induction times are uniformly overpredicted by the model, as they were for hydrogen oxidation. The model gives the same kinetic decay constant for all three profiles at 560 °C, contrary to the observed behavior but expected

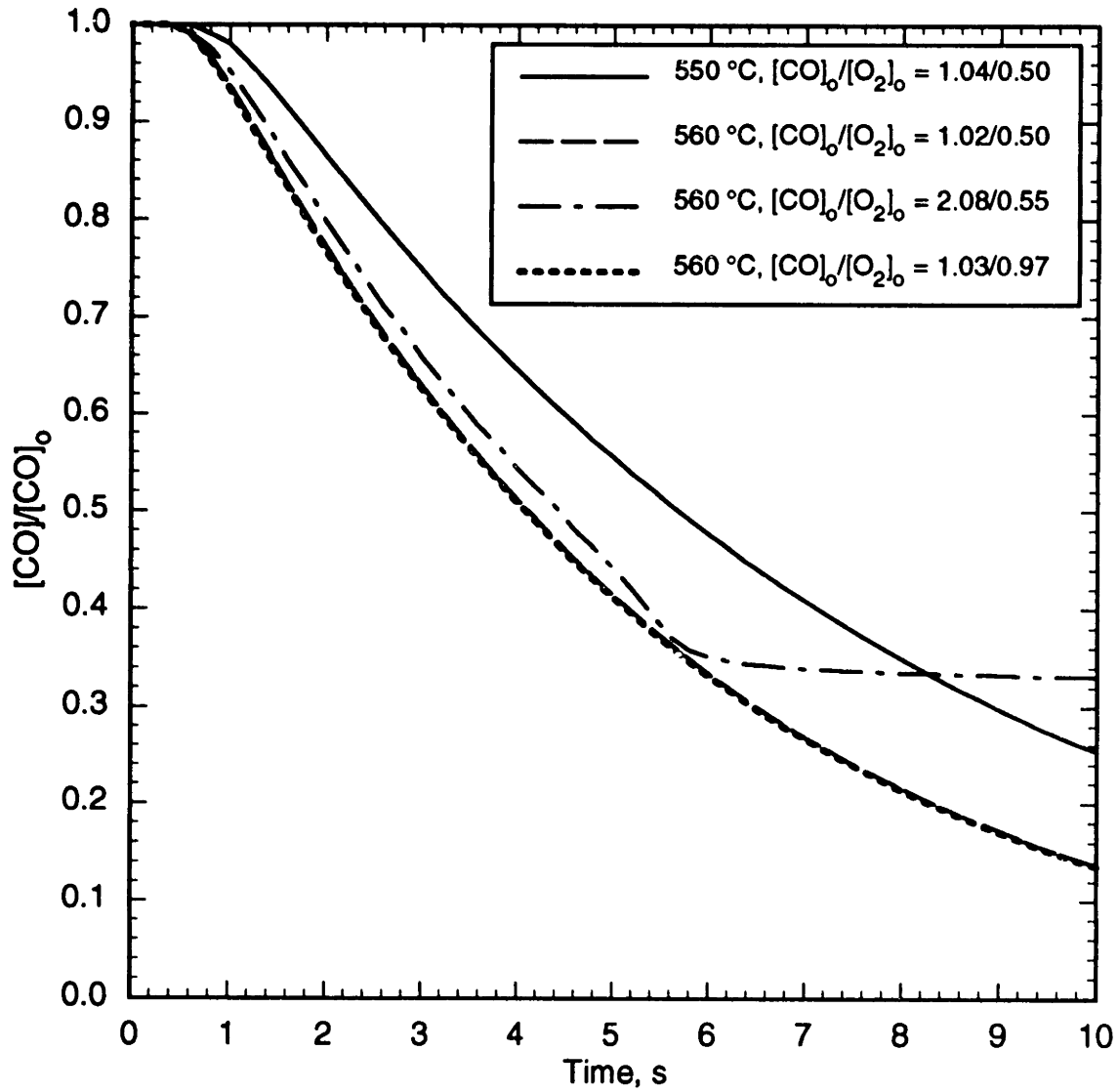

Figure 8.8 **Normalized Carbon Monoxide Profiles from Elementary Reaction Model for Carbon Monoxide Oxidation at 550 and 560 °C.** Initial concentrations (in 10^{-6} mol/cm^3) as given.

Initial Conditions 10^{-6} mol/cm^3	k', s^{-1} (Exp.)	k', s^{-1} (Model)	τ_{ind}, s (Exp.)	τ_{ind}, s (Model)
550±2 °C				
$[CO]_o$ = 1.04±0.02	0.17±0.01	0.15	2.0±0.3	1.1
$[O_2]_o$ = 0.50±0.01				
560±2 °C				
$[CO]_o$ = 1.02±0.02	0.40±0.03	0.22	2.1±0.3	0.89
$[O_2]_o$ = 0.50±0.01				
560±3 °C				
$[CO]_o$ = 2.08±0.03	0.21±0.01	0.19	1.3±0.1	0.84
$[O_2]_o$ = 0.55±0.01				
560±2 °C				
$[CO]_o$ = 1.03±0.04	0.71±0.05	0.22	1.9±0.3	0.87
$[O_2]_o$ = 0.97±0.04				

Table 8.3 Comparison of Experimental and Predicted Induction Times and Kinetic Decay Constants for Carbon Monoxide Oxidation at 246 bar.

from the lack of oxygen dependence of the model in Figure 8.8. The model also predicts the same induction time for the three profiles, indicating an independence of equivalence ratio for the induction time, as was seen in the hydrogen experiments and model. [The anomalously low induction time observed for the fuel-rich profile most likely results from the smaller number of data points available for estimation of the induction time.] Comparison of the model predictions for a stoichiometric $CO\text{-}O_2$ mixture at 550 °C with the predictions for hydrogen oxidation under identical conditions (Table 6.4) shows that the predicted kinetic decay constant for hydrogen oxidation (0.31 s^{-1}) is about twice that for carbon monoxide oxidation (0.15 s^{-1}). These predictions are consistent with experimental observations and with the fact that the rate constant for the primary hydrogen-oxidizing reaction ($H_2 + OH \rightarrow H_2O + H$) at 550 °C is about twice that for the primary carbon-monoxide-oxidizing reaction ($CO + OH \rightarrow CO_2 + H$), as discussed in Section 7.6. On the other hand, the predicted induction time for carbon monoxide oxidation at 550 °C (1.1 s) is slightly shorter than the induction time for hydrogen oxidation under identical conditions (1.6 s), indicating that the behavior of the model during the induction period is not completely insensitive to the identity of the fuel. Experimental induction times were about 2.0 s for both carbon monoxide and hydrogen, suggesting a fuel-independent induction chemistry; however, uncertainties in the derived experimental values make it difficult to identify the subtle variations in induction times predicted by the model.

Figures 8.9 and 8.10 illustrate the model's detailed predictions for stoichiometric carbon monoxide oxidation at 560 °C. In Figure 8.9, the predicted species concentration profiles are shown. As in the hydrogen oxidation model, the concentrations of the unstable species rapidly establish a well-defined hierarchy which is retained throughout the consumption of carbon monoxide. Hydrogen peroxide and hydroperoxyl radicals are

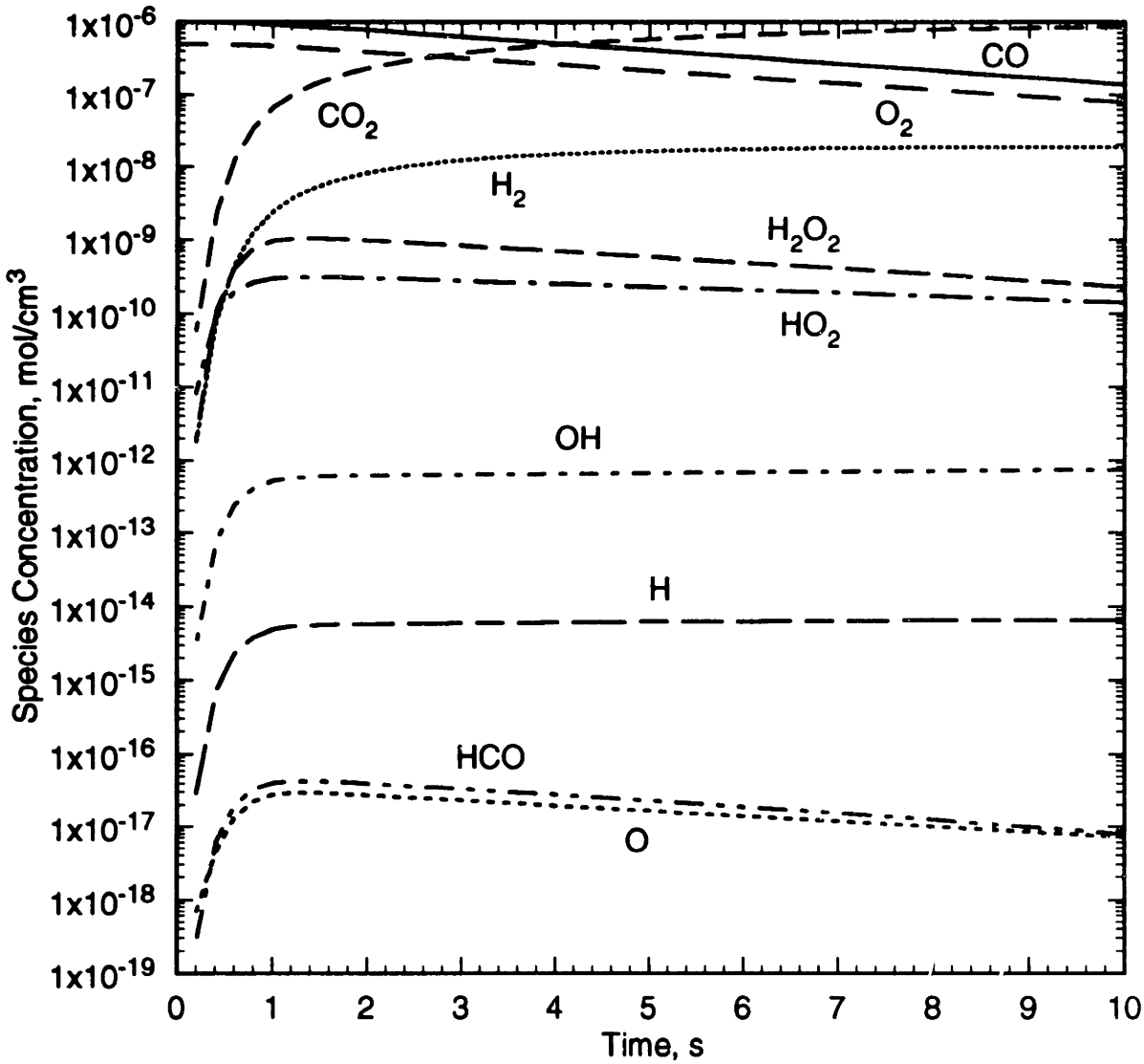

Figure 8.9 **Predicted Species Concentration Profiles from Elementary Reaction Model YDR91J.** Conditions: 560 °C, $[CO]_o = 1.0 \times 10^{-6}$ mol/cm^3, $[O_2]_o = 0.5 \times 10^{-6}$ mol/cm^3, $[H_2O] = 4.16 \times 10^{-3}$ mol/cm^3.

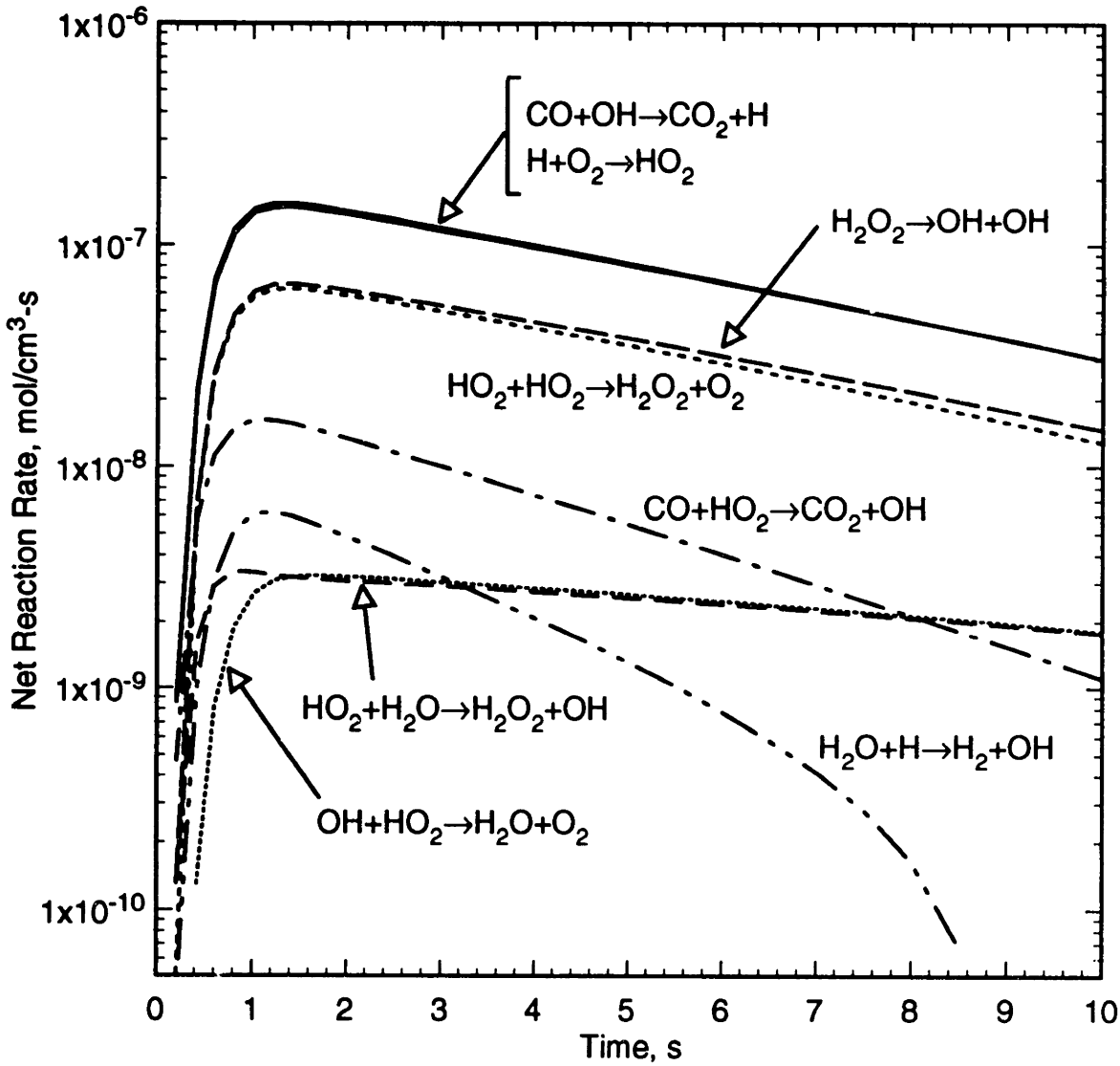

Figure 8.10 **Net Reaction Rate Profiles for Major Reactions as Predicted by Elementary Reaction Model YDR91J.** Conditions: Same as in Figure 8.9.

the dominant unstable species, with the concentration of the oxidizing hydroxyl radical about two orders of magnitude lower and the hydrogen-atom concentration still lower. Oxygen-atom chemistry remains unimportant at these temperatures in the carbon monoxide model, and the formyl radical (HCO) is present at very low concentrations. The OH radical and H atom also closely approximate steady-state behavior over most of the extent of reaction seen in Figure 8.9, even though hydrogen peroxide and the hydroperoxyl radical reach a maximum and then steadily decrease.

Net reaction rate profiles for the fast reactions in the model are shown in Figure 8.10. The dominant reactions are

$$CO + OH \rightarrow CO_2 + H \qquad \text{(R20)}$$

$$H + O_2 \rightarrow HO_2 \qquad \text{(R7)}$$

$$H_2O_2 \rightarrow OH + OH \qquad \text{(R14)}$$

$$HO_2 + HO_2 \rightarrow H_2O_2 + O_2 \qquad \text{(R13)}$$

$$CO + HO_2 \rightarrow CO_2 + OH \qquad \text{(R23)}$$

$$HO_2 + H_2O \rightarrow H_2O_2 + OH \qquad \text{(–R12)}$$

$$OH + HO_2 \rightarrow H_2O + O_2 \qquad \text{(R11)}$$

$$H_2O + H \rightarrow H_2 + OH \qquad \text{(–R3)}$$

where the reaction numbers refer to those cited in Table 8.1. The similarity of the rate profiles in Figure 8.10 to those in the hydrogen model (Figure 6.8) is striking, as is the cyclic nature of the carbon monoxide oxidation mechanism. Carbon monoxide is oxidized rapidly to CO_2 by (R20), with the hydrogen atom formed being converted immediately to HO_2 by reaction with oxygen in (R7). HO_2 is converted by self-reaction in (R13) to H_2O_2, which quickly decomposes in (R14) to two hydroxyl radicals, which

complete the cycle by reacting with carbon monoxide in (R20). (R23) provides an alternate, minor pathway for oxidation of carbon monoxide, and is analogous to (–R15) for hydrogen oxidation. The induction time again seems to be characterized by the point where the rate of termination via (R11) becomes sufficiently fast to balance branching via (–R12), with steady-state (straight-chain) oxidation of carbon monoxide occurring when the two rates are equal. (–R3) is the pathway for formation of hydrogen in the mechanism; note that the net rate of this reaction sharply decreases at longer times as the oxidation of hydrogen (R3) becomes faster and eventually overcomes the rate of hydrogen formation.

8.2.2 Sensitivity Analysis

Figure 8.11 shows the normalized sensitivity coefficients for the carbon monoxide concentration, for the same model conditions used in Figures 8.9 and 8.10. The dominant, fast reactions listed above (with the exception of (R7) and (–R3)) are the same reactions to whose rate constants the carbon monoxide concentration is most sensitive. The magnitude and hierarchy of the sensitivity coefficients in Figure 8.11 are very similar to those for hydrogen oxidation (Figure 6.9), with reactions (R20) and (R23) for CO oxidation replacing (R3) and (–R15) for H_2 oxidation, implying that the fundamental pathways are the same in both oxidation mechanisms. In particular, the lack of sensitivity to (R7) shows that the incorporation of O_2 into the mechanism again occurs in a fast step, and the predicted, overall carbon monoxide oxidation rate is consequently insensitive to the oxygen concentration. Furthermore, the carbon monoxide model is sensitive to both the forward and reverse rate constants for (R12), indicating a partial equilibration of this reaction, although the reverse direction remains dominant. The primary carbon monoxide oxidation mechanism is thus completely analogous to the

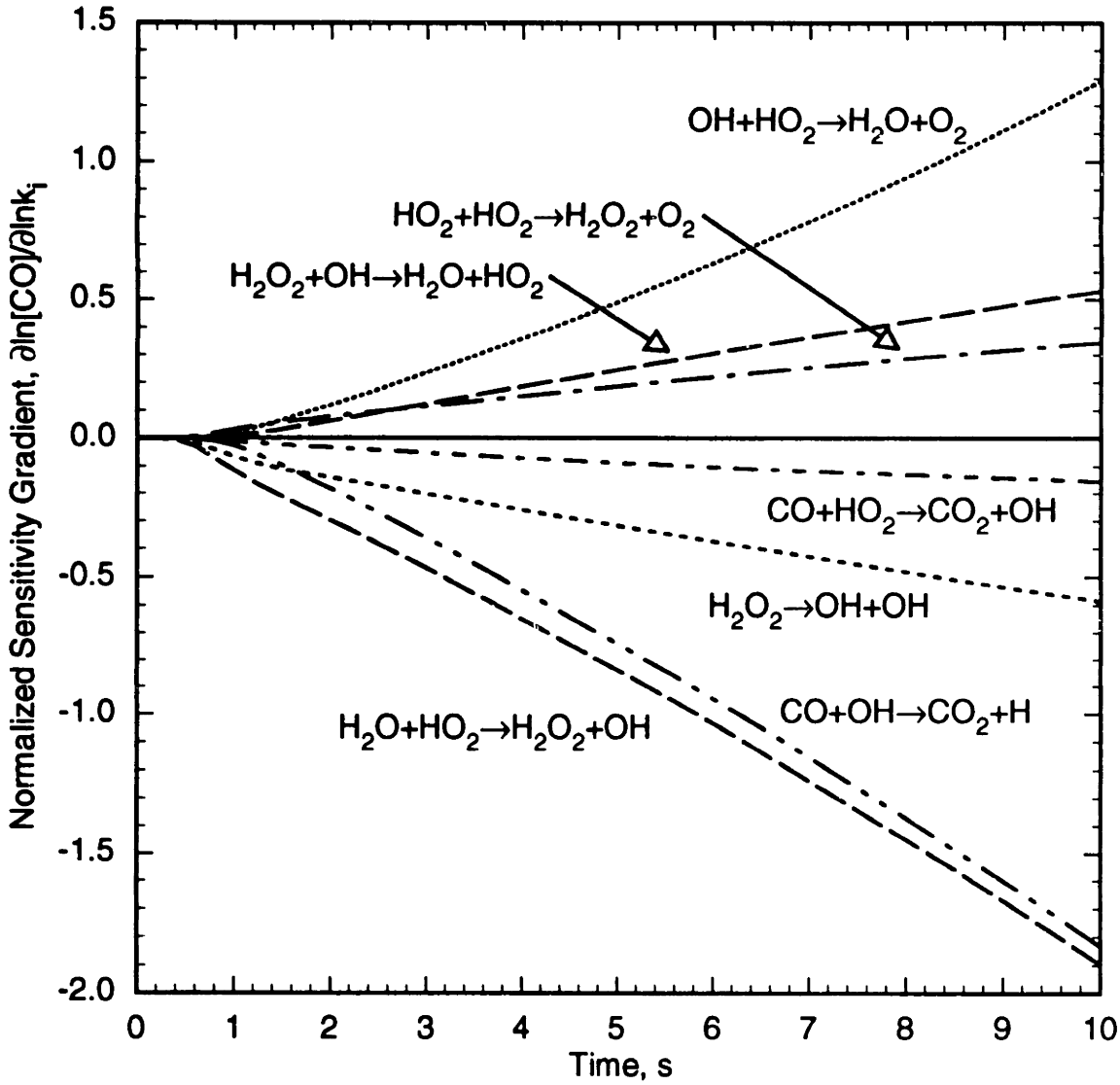

Figure 8.11 Normalized Sensitivity Gradients for Carbon Monoxide Concentration in Model YDR91J. Sensitivities of carbon monoxide mole fraction with respect to rate constants k_i are shown. Conditions: Same as in Figures 8.9 and 8.10.

primary hydrogen oxidation mechanism from Section 6.4. Since the predicted hydrogen oxidation mechanism was insensitive to the oxygen concentration, so too is the predicted carbon monoxide oxidation mechanism.

The dominant sensitivities during the induction period for carbon monoxide oxidation are to the reaction rate constants for (–R12), (R13), and (R14), the same as for hydrogen oxidation. The length of the induction period is thus almost insensitive to the rate of the oxidizing reaction, and the induction periods for both carbon monoxide oxidation and hydrogen oxidation are very similar, despite the factor-of-two difference in the rate constants for the oxidizing reactions ($CO + OH \rightarrow CO_2 + H$ or $H_2 + OH \rightarrow H_2O + H$). Primary buildup of OH radicals occurs through the (–R12)–(R14) branching reaction sequence, with the oxidizing reaction serving only to regenerate H atoms from OH radicals.

The relatively weak sensitivity to the $CO + HO_2 \rightarrow CO_2 + OH$ reaction, (R23), is somewhat surprising. An earlier model of moist gas-phase carbon monoxide oxidation at 550 °C demonstrated a very high sensitivity to the rate constant of (R23) (Yetter *et al.*, 1991a). Models of the high-pressure gas-phase oxidation of methane, at 330 to 430 °C and 100 bar (Vedeneev *et al.*, 1988), and of ethane and methanol at 1100 to 1900 °C and 20 to 60 bar (Grouset *et al.*, 1986), also showed very high sensitivity to the rate of (R23), owing to the increasing importance of HO_2 radicals at lower temperatures and higher pressures.

The submechanism in the carbon monoxide model for hydrogen formation (and destruction) deserves further discussion, since it has been deficient in earlier models. Figure 8.12 shows the normalized sensitivity gradients for the hydrogen concentration in the carbon monoxide model, for the same conditions as in Figures 8.9 through 8.11. The high, early sensitivities are related to the establishment of the steady-state radical pool:

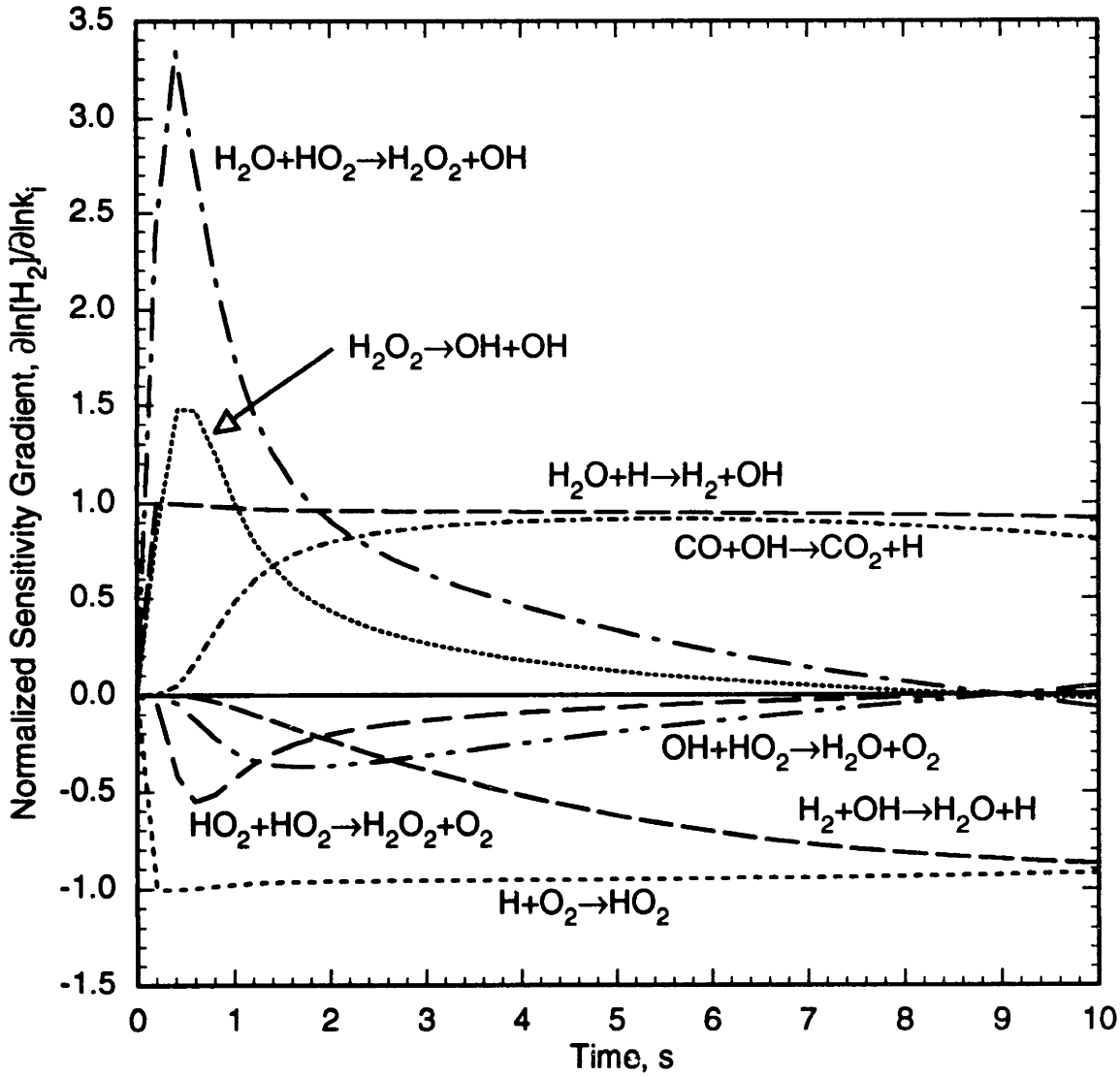

Figure 8.12 Normalized Sensitivity Gradients for Hydrogen Concentration in Model YDR91J for Carbon Monoxide Oxidation. Sensitivities of hydrogen mole fraction with respect to rate constants k_i are shown. Conditions: Same as in Figures 8.9 through 8.11.

the primary hydrogen-forming step, (–R3), has a hydrogen atom as a reactant, and the concentration of hydrogen atoms during the induction period is directly affected by the rates of the primary radical-pool-forming reactions. Note that once the steady-state radical pool has been established (beyond about 2 seconds), the (–R12)–(R14) branching reaction sequence decreases in importance while the (R20) oxidizing step increases in prominence. At longer times, as the net reaction rate for hydrogen shifts from formation to consumption, (R3), the hydrogen-oxidizing step, becomes important. During the majority of the carbon monoxide consumption (from 3 to 10 seconds), the hydrogen concentration exhibits approximately unit sensitivity ($|\partial \ln[H_2]/\partial \ln k_i| = \sim 1$) to the rate constants for three reactions, (–R3), (R20), and (R7). This condition indicates that the hydrogen concentration is essentially proportional (or inversely proportional) to the values of those three rate constants. Figure 8.13 summarizes in schematic form the major pathways for carbon monoxide oxidation and hydrogen formation.

8.2.3 Steady-State Analysis

The steady-state behavior of the H-atom concentration was noted earlier in Figures 8.9 and 8.10. Since the dominant reaction pathways for the hydrogen atom are (R20) and (R7), the steady-state H-atom concentration is set by the relative rates of those two reactions, i.e.,

$$[H]_{ss} \approx \frac{k_{20}[CO][OH]}{k_7[O_2]} \tag{8.6}$$

Meanwhile, Figure 8.9 shows that the molecular hydrogen concentration achieves an approximate steady state for times longer than about 3 seconds. Under those conditions, the hydrogen concentration is given by

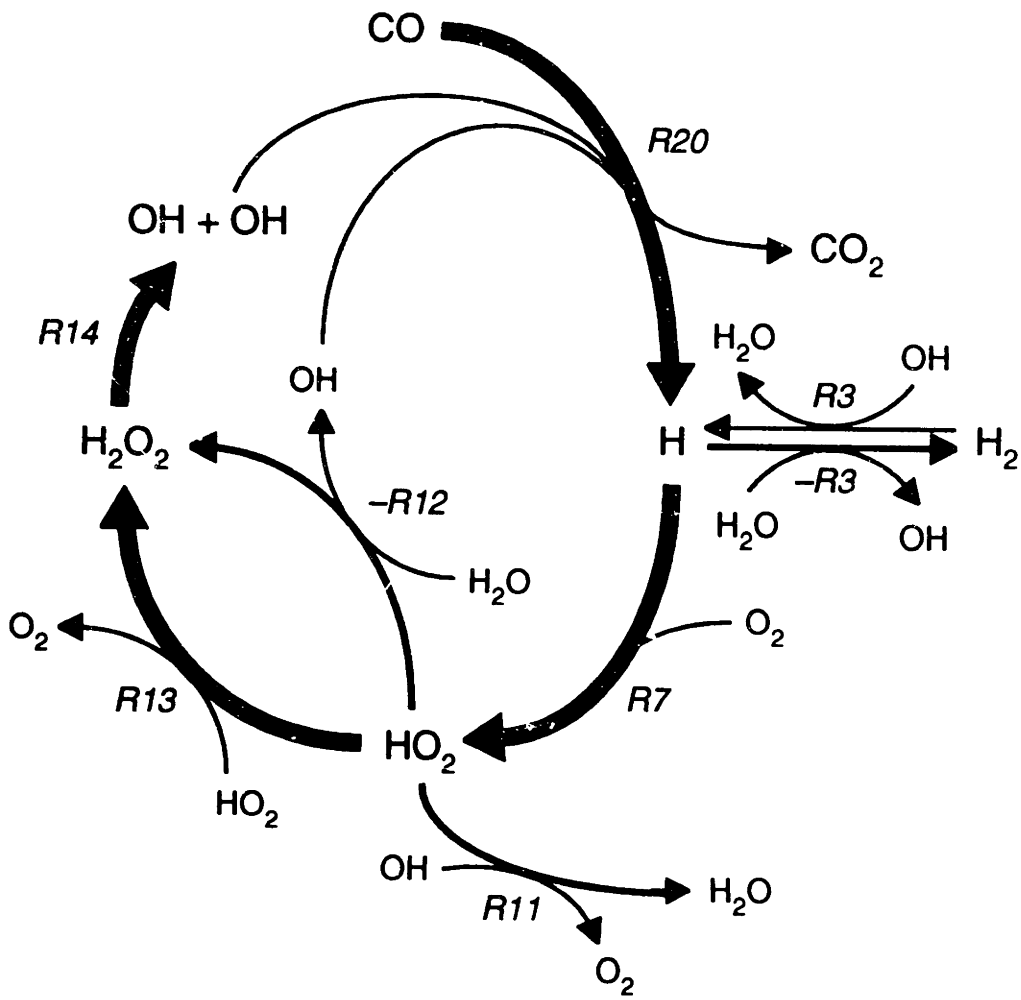

Figure 8.13 **Major Free-Radical Reaction Pathways in Elementary Reaction Model for Carbon Monoxide Oxidation in Supercritical Water.** Arrow thicknesses indicate relative rates of reactions. Reaction numbers refer to Table 8.1.

$$[H_2]_{ss} \approx \frac{k_{-3}[H_2O][H]}{k_3[OH]} = \frac{[H_2O][H]}{K_{c,3}[OH]} \tag{8.7}$$

where we have made use of the fact that $K_{c,3} = k_3/k_{-3}$. Combining Equations 8.6 and 8.7, one obtains for the steady-state molecular hydrogen concentration

$$[H_2]_{ss} \approx \frac{k_{20}}{K_{c,3}k_7}\frac{[H_2O][CO]}{[O_2]} \tag{8.8}$$

which conforms to the expectations from Figure 8.12: the hydrogen concentration is indeed proportional to k_{20}, k_7, and, through $K_{c,3}$, k_{-3}. Strictly speaking, Equation 8.8 holds only for long times, when (R3) has become equilibrated; however, for shorter times, when there is net hydrogen formation, the rate of hydrogen formation remains directly related to k_{20}, k_7, and k_{-3} through the rate of (-R3). The inability of earlier models (Helling and Tester, Webley, 1989; Webley and Tester, 1991) to predict hydrogen formation is directly traceable to the value of the rate constant for (R7), $H + O_2 \rightarrow HO_2$. For example, the low-pressure rate expression used by Webley and Tester (1991) predicts a rate constant (at 560 °C and 246 bar) *two orders of magnitude higher* than the falloff rate constant used here (see Table 8.1 and Section 12.3); hydrogen concentrations were thus two orders of magnitude too low in the earlier model. Proper incorporation of the pressure dependence of (R7) is therefore crucial to the model's ability to predict hydrogen formation correctly.

Equation 8.8 also shows that the hydrogen concentration is directly related to the fuel equivalence ratio ($\phi = [CO]_o/2[O_2]_o$). At 560 °C and 246 bar, Equation 8.8 reduces to

$$[H_2]_{ss} \approx 1 \times 10^{-8}\ [CO]/[O_2]\ \text{mol/cm}^3 \tag{8.9}$$

where the rate constants and equilibrium constant have been evaluated from Tables 8.1 and 8.2 and the water density (concentration) is 4.16×10^{-3} mol/cm^3. For a stoichiometric mixture, the $[CO]/[O_2]$ ratio remains approximately constant at 2 throughout the CO consumption, implying that the hydrogen concentration should likewise be constant, with a value of about 2×10^{-8} mol/cm^3. Figure 8.5 shows that, for the stoichiometric conditions at 560 °C, the model in fact predicts a relatively constant hydrogen concentration of 2×10^{-8} mol/cm^3, in good agreement with experimental observations. Note that for non-stoichiometric conditions, Equation 8.9 indicates that the hydrogen concentration should change over time. For example, a superstoichiometric (fuel-lean) mixture ($\phi < 1$) will grow increasingly deficient in carbon monoxide as the reaction progresses, and the hydrogen concentration should correspondingly decrease with time. Figure 8.7 shows that this is the case experimentally, but the trend in the model predictions is less pronounced. Furthermore, for the fuel-lean conditions of Figure 8.7, the predicted maximum hydrogen concentration is limited to lower values than under stoichiometric conditions, since the maximum $[CO]/[O_2]$ ratio is smaller (and decreases continuously) for $\phi < 1$. On the other hand, substoichiometric (fuel-rich) mixtures ($\phi > 1$) grow increasingly enriched in carbon monoxide as the reaction proceeds, implying a continuously increasing hydrogen concentration. This trend is clear in Figure 8.6, at least until the oxygen is completely depleted; at that point, carbon monoxide oxidation ceases, the supply of H atoms is terminated, and the inherent assumptions in Equations 8.8 and 8.9 break down.

This simple steady-state analysis provides a clear explanation for the mechanism of hydrogen formation during carbon monoxide oxidation. The carbon-monoxide-oxidizing step, (R20), creates relatively high H-atom concentrations which, in combination with the high water concentrations in the experiments, are sufficient to drive the equilibrium of (R3) in the reverse direction, toward formation of molecular hydrogen. The magnitude of these superequilibrium H-atom concentrations, and hence the amount of hydrogen formation, is strongly dependent on the oxygen concentration (and fuel equivalence ratio), which controls the rate of H-atom consumption in (R7). Net oxidation of hydrogen can only occur for stoichiometric or fuel-lean conditions where the H-atom concentration is maintained at a sufficiently low level that the importance of (–R3) is reduced. Similarly, as CO consumption nears completion, the production of H-atoms (and hence their concentration) decreases and hydrogen is oxidized.

Note that the production of hydrogen can occur in the complete absence of oxygen, but the rate of production must be greatly reduced because there is no fast source of OH radicals or H atoms. Instead, OH radicals must be formed initially by a slow initiation step, such as the dissociation of water, (–R6). The OH radicals may then react with CO in (R20), generating H atoms which can form hydrogen in (–R3) and regenerate the OH radical. The net reaction is the water-gas shift, $CO + H_2O \rightarrow CO_2 + H_2$. However, the (R20)–(–R6) reaction sequence is a straight chain, and there is no mechanism for chain branching in the absence of oxygen. The rate of the oxygen-free water-gas shift is therefore constrained by the slow initiation step, and there is thus little net reaction on the time scales of interest.

Finally, the extent to which the equilibrium of (R3) is driven towards hydrogen formation is explicitly dependent on the water concentration (Equation 8.8). The amount of hydrogen formation is thus directly related to the amount of water present. At the

experimental conditions of this study, water concentration is by far the largest of all components in the reaction mixture (mole fraction greater than 0.999). Recall from Figure 7.35 and Table 12.11 that the hydrogen concentration at 570 °C and a 4.1-s residence time increased steadily with increasing operating pressure (increasing water concentration). This observed behavior provides direct experimental evidence for the dependence of hydrogen formation on water concentration predicted by Equation 8.8.

Under practical SCWO process conditions, however, water is not present in the same high concentrations as in the experiments, because a major fraction of the reaction mixture is taken up by organic (or CO_2) and oxygen, and nitrogen if the oxidant is air. Thus the reaction mixture may typically only be about 30% water, and at a given temperature and pressure the water concentration in the process is significantly lower than the water concentration during our experiments. The lower water concentration in the process will directly affect the amount of hydrogen produced by the water-gas shift, and hydrogen formation may thus be expected to be much less important under normal process conditions.

8.3 Modeling of Pressure and Density Effects

The working model for carbon monoxide oxidation was subsequently extended to pressures other than the typical experimental operating pressure of 246 bar. The experimental data for varying operating pressures and densities (570 °C, 118 to 263 bar, 0.032 to 0.079 g/cm^3) from Section 7.7 and Table 12.11 provided a basis for comparison of the model predictions with experimental observations.

Section 6.5 discussed the two mechanisms by which operating pressure or water density may affect oxidation kinetics: 1) by pressure-dependent reaction rate constants, and 2) by changing the concentration of a reactant (water). The reactions added to the

model for carbon monoxide oxidation include only one overtly pressure-dependent reaction, the formation/decomposition of the formyl radical (HCO)

$$HCO + M \rightarrow H + CO + M \qquad \text{(R24)}$$

Sensitivity analyses of the carbon monoxide model showed that the predicted carbon monoxide consumption was completely insensitive to the rate constant for this reaction, and in fact the reaction could be completely removed from the mechanism without noticeable effect. Helling and Tester (1987) also noted the unimportance of formyl radical reactions in their CO oxidation model. Since the model was insensitive to the rate constant for (R24), its pressure dependence was not investigated in any detail. Furthermore, (R24) appeared to be equilibrated under model conditions, implying that the important parameter for this reaction is not the rate constant but rather the equilibrium constant, which is known rather well (Timonen *et al.*, 1987a). The important pressure-dependent recombination/dissociation rate constants in the carbon monoxide model thus remain the same as in the hydrogen model, namely, the rate constants for (R7) and (R14). The calculated pressure dependences for these reaction rate constants were examined in detail in Sections 12.2 and 12.3.

The carbon monoxide model also includes the more weakly pressure-dependent reaction (R20), as discussed in Section 8.1. The pressure dependence of this reaction was treated in Section 12.4. The three important pressure-dependent reactions in the carbon monoxide model are thus (R7), (R14), and (R20). At 570 °C and 118 to 263 bar, however, the rate constants for these reactions undergo only modest variations. For example, the rate constant for (R7) varies from 6.1×10^{13} $cm^3mol^{-1}s^{-1}$ at 263 bar to 4.8×10^{13} $cm^3mol^{-1}s^{-1}$ at 118 bar, a decrease of about 20%. Similarly, the calculated

rate constant for (R14) decreases from 90.6 s^{-1} at 263 bar to 80.2 s^{-1} at 118 bar, or by about 10%; and the rate constant for (R20) decreases from 3.0×10^{11} $cm^3mol^{-1}s^{-1}$ to 2.9×10^{11} $cm^3mol^{-1}s^{-1}$, about a 3% decrease from 263 bar to 118 bar. Meanwhile, the observed, overall, first-order rate constant for carbon monoxide oxidation decreases by about a factor of three or four when pressure is decreased from 263 to 118 bar, with all other conditions the same (see Figure 7.35). The model is not sufficiently sensitive to the rate constants for (R7), (R14), and (R20) that the small decreases in these rate constants can translate into such a large effect on the overall oxidation rate. Rather, the majority of the pressure dependence of the overall, first-order rate constant must lie in the changing water concentration. At 570 °C and 118 to 263 bar, the density of water varies from 0.032 to 0.079 g/cm^3 (1.8×10^{-3} to 4.4×10^{-3} mol/cm^3), or by nearly a factor of three.

Figure 8.14 shows the predictions of the carbon monoxide model, incorporating both the pressure-dependent rate constants and the varying water concentration, compared to the experimental data from Section 7.7 and Table 12.11. The CO oxidation model, like the hydrogen oxidation model, clearly exhibits the same general pressure or density dependence as the data, although the model is not as strongly density-dependent as the data. Since the fundamental oxidation mechanism for carbon monoxide oxidation is completely analogous to that for hydrogen oxidation, the source of the density dependence in the carbon monoxide mechanism is the same as that discussed in Section 6.5. Namely, the primary effect of density is in the changing water concentration and the corresponding change in the branching rate of (–R12), as in Equation 6.18; the pressure-dependence of reaction rate constants are of only minor importance. Using the methodology of Section 7.7, an effective "order" of the model with respect to water can be derived from the model predictions in Figure 8.14. Linear regression of ln k' vs. ln $[H_2O]$ for the model gives an order with respect to water of 0.95, consistent with

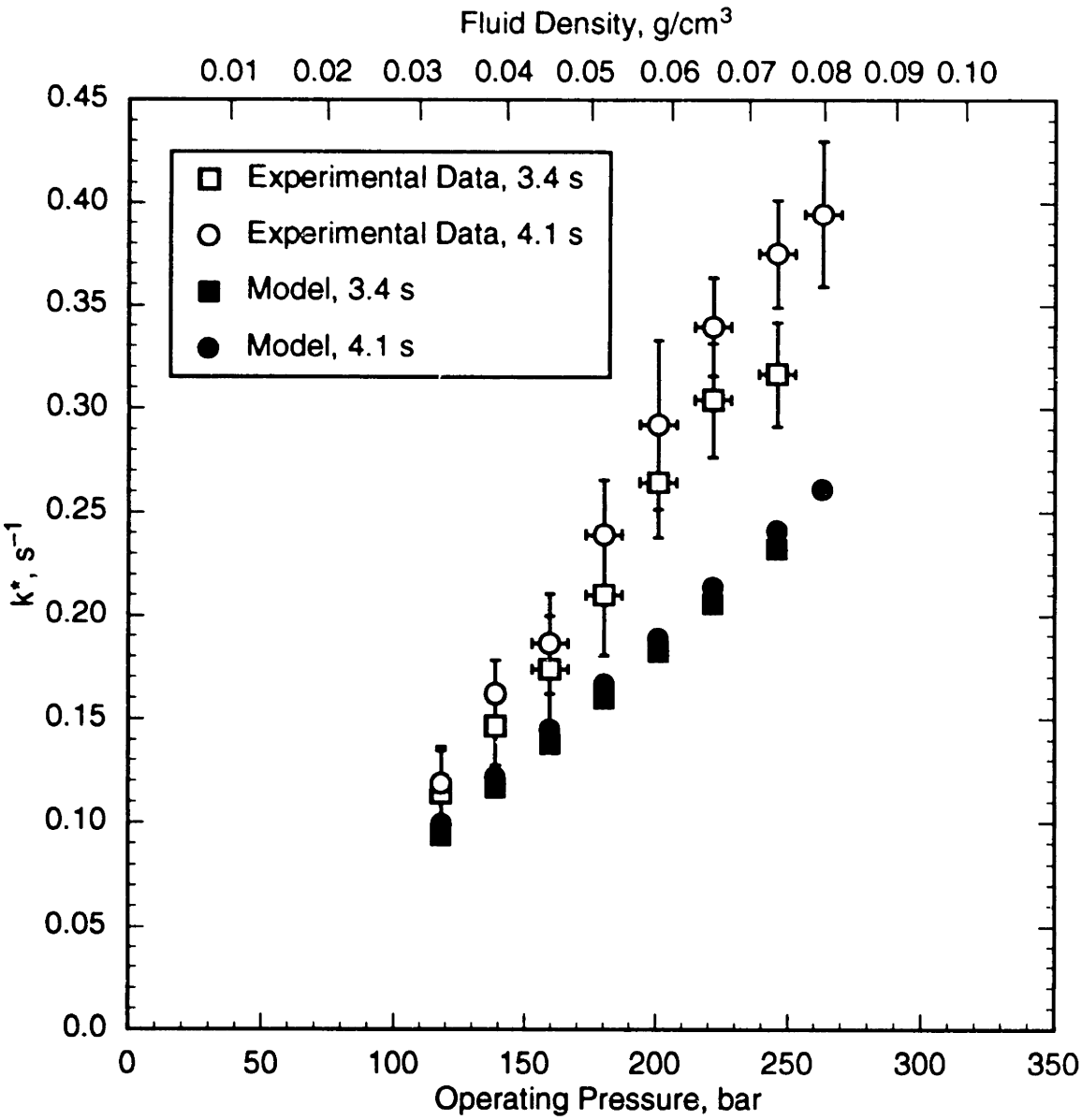

Figure 8.14 **Predicted Effects of Operating Pressure on Apparent First-Order Rate Constant, k^*, for Carbon Monoxide Oxidation.**
□,○—Experimental data from Figure 7.35;
■,●—Model predictions.

Equation 6.18; in other words, the model decay constant for carbon monoxide increases almost linearly with water density. The experimental data, on the other hand, indicate a stronger water dependence of about 1.7-order (see Section 7.7).

The model predictions for the two pressure extremes, 118 and 263 bar, are shown in Figure 8.15. As in the hydrogen model, the steady-state HO_2 radical concentration remains relatively unaffected by the change in pressure (water density), whereas the steady-state OH concentration decreases in direct proportion to the decrease in the water density. Coincident with the lower OH concentration, the carbon monoxide oxidation rate decreases. Both the lower OH concentration and the apparently longer induction time at the lower pressure are the direct result of the slower branching rate via

$$HO_2 + H_2O \rightarrow H_2O_2 + OH \qquad (-R12)$$

which results from the lower water concentration. The major effect of the high-density, supercritical-water medium, for both hydrogen oxidation and carbon monoxide oxidation, is increased branching by (–R12) due to the high water concentration.

8.4 Model Assessment

Even with the modifications made in this study, the major shortcoming of the carbon monoxide model is its inability to predict the oxygen dependence of the oxidation rate observed experimentally. Since the predicted mechanism for carbon monoxide oxidation is analogous to that for hydrogen oxidation, it is reasonable that the carbon monoxide mechanism should mimic the oxygen independence of the hydrogen mechanism. However, the experimental data clearly indicate that the carbon monoxide oxidation reaction possesses an oxygen dependence. Owing to the similarity of the two oxidation mechanisms, it is very difficult to modify the carbon monoxide mechanism (so as to

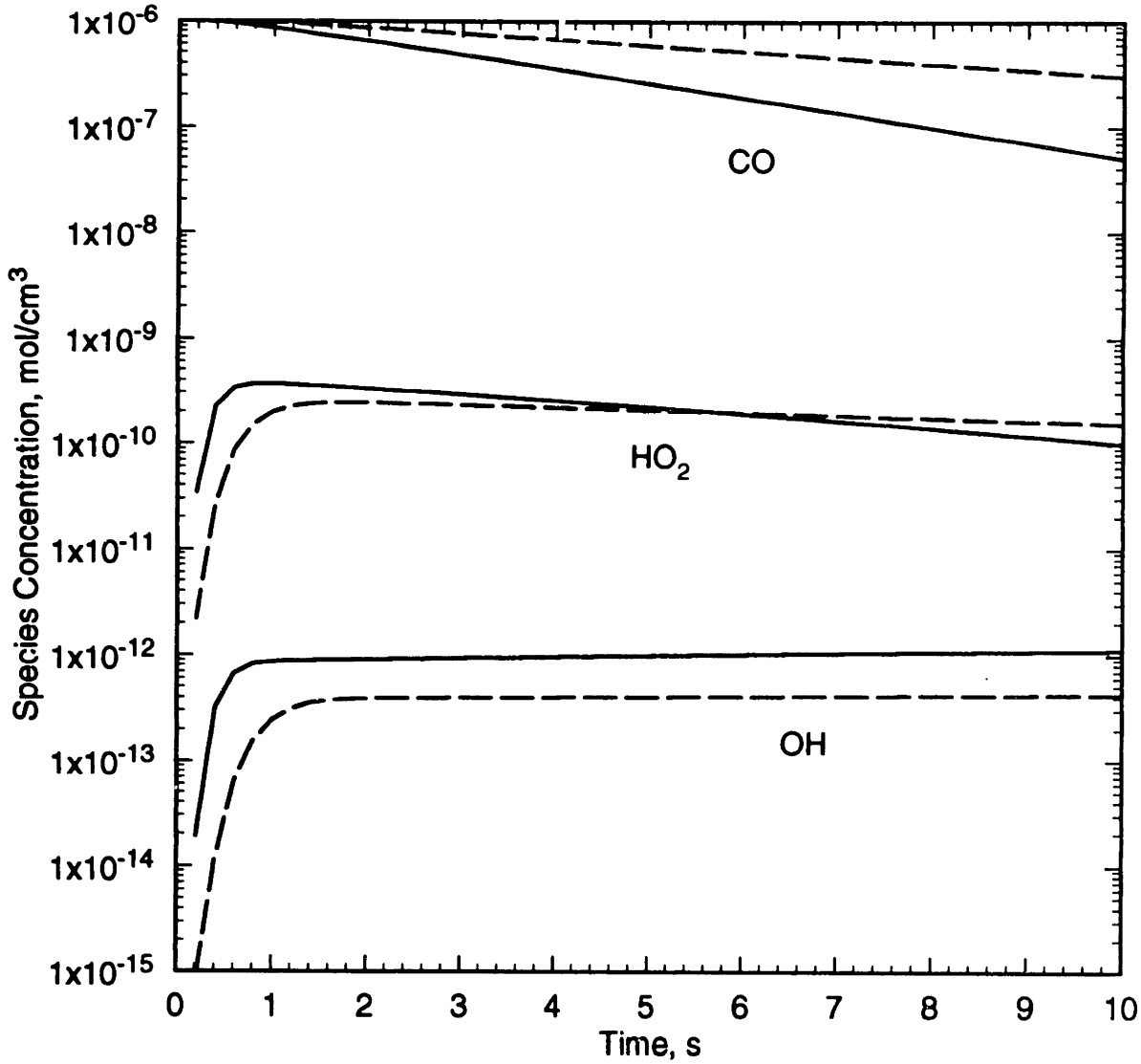

Figure 8.15 **Predicted Carbon Monoxide and Radical Profiles at 263 bar and 118 bar.** Conditions: 570 °C, $[CO]_o = 1.0 \times 10^{-6}$ mol/cm^3, $[O_2]_o = 0.5 \times 10^{-6}$ mol/cm^3. Solid curves: 263 bar; dashed curves: 118 bar.

introduce an oxygen dependence) without simultaneously affecting the hydrogen mechanism in such a way as to render it invalid. Furthermore, although not shown, the carbon monoxide sensitivity profiles are virtually identical for the three fuel equivalence ratios in Figures 8.5 through 8.7. Thus any attempt to modify a sensitive rate constant to bring the fuel-lean predictions into better agreement with the data will simultaneously worsen the agreement of the fuel-rich predictions. For example, increasing the rate constants of (R20) or (R23) or decreasing the rate constant for (R13) increases the predicted rate of CO disappearance uniformly for all three fuel equivalence ratios. Reactions involving carbon monoxide that do not appear as sensitive reactions in Figure 8.11 would need to have their rate constants adjusted by several orders of magnitude to elicit any response from the model.

Fractional-order oxygen dependences observed in earlier gas-phase studies of carbon monoxide oxidation were explained on the basis of simultaneous equilibria of several elementary reactions involving O, OH, and O_2 (Hottel *et al.*, 1965; Dryer and Glassman, 1973; Howard *et al.*, 1973). However, none of the equilibrated reactions cited in those studies is equilibrated in our model, nor are reactions of O atoms important for our reduced temperatures. In addition, the extent of the observed oxygen dependence of low-pressure, gas-phase CO oxidation appears to be a function of temperature. As the temperature is varied, the oxidation mechanism varies in such a way that the OH concentration becomes more strongly or more weakly coupled to the oxygen concentration; the stronger the relationship, the more oxygen-dependent the reaction (Yetter *et al.*, 1991a). At temperatures of about 800 K and at 1 bar, gas-phase carbon monoxide oxidation, as modeled by Yetter *et al.* (1991a), exhibits an oxygen dependence. Unfortunately, the gas-phase mechanism for this oxygen dependence cannot be

extrapolated to the higher-pressure, supercritical-water regime, because branching routes and pathways for oxygen incorporation change drastically with increasing pressure.

The model's insensitivity to variations of particular rate constants suggests that the absence of an oxygen dependence is probably caused by the combined effects of several incorrect rate constants and/or equilibrium constants, assuming of course that the reaction network is complete. Trial-and-error adjustment of rate constants may imporve the fit to the data but will not reveal the source of the model's deficiency; instead, a detailed analysis of the oxidation mechanism, including comparisons to oxygen-dependent gas-phase models, is necessary to elucidate the required modifications to the model.

The high global activation energy of the model (see Figure 8.1) appears incorrect, but cannot be immediately dismissed as erroneous. Experimental evidence, in the form of the two stoichiometric profiles at 550 and 560 °C (Figures 8.4 and 8.5), supports an overall activation energy greater than 400 kJ/mol at the high-temperature end of the data range. The lower overall activation energy for the experimental data, when all the data are considered, may indicate a change in activation energy (and mechanism) for the overall reaction at about 500 °C. If such is the case, the model clearly does not incorporate the low-temperature mechanism properly. The higher experimental rates relative to the predicted rates implies that the low-temperature mechanism either involves heterogeneous *catalysis* (as opposed to the inhibition observed experimentally at 560 °C) or an alternative homogeneous pathway for CO oxidation which is not correctly included in the model. The experimental data at the lower temperatures require verification in a lower-surface-area reactor to insure the lack of heterogeneous effects, while the model (and its constituent parameters) needs to be examined for uncertainties, either in rate constants or in thermodynamic data.

The carbon monoxide model exhibits the same high sensitivity to the rate of branching via (–R12), and concurrently to the thermodynamics of the HO_2 radical, seen in the hydrogen model. The sensitivity to the HO_2 thermodynamics is not augmented in the carbon monoxide model, because rate constants for the important CO reactions may be calculated directly from rate expressions or through equilibrium constants not involving HO_2. Nevertheless, the carbon monoxide model retains the sensitivity to model parameters for the HO_2 radical that was present in the H_2/O_2 submechanism, and emphasizes the need for improved rate-constant and thermodynamic data for the HO_2 species.

The addition of heterogeneous radical-termination reactions to the carbon monoxide model was not explored, owing to the failure of such reactions to describe the experimental observations for hydrogen oxidation (Section 6.6). The experimental lack of an apparent influence of reactor surface on oxidation kinetics in the tubular reactor (at least at higher temperatures) implies that heterogeneous reactions are largely unimportant. The current experimental data do not warrant a more detailed modeling treatment of surface effects.

Finally, the failure of the current elementary reaction network to describe the full extent of the pressure dependence of the data, either for hydrogen oxidation or carbon monoxide oxidation, suggests that we have not completely captured the chemical effect of the increased water concentration (density). A more detailed examination, both experimentally and theoretically, of the effects of the high water concentrations is warranted.

In all cases, the effect of the water concentration is one of enhancement. Higher water densities could produce highly non-ideal fugacity coefficients for unstable species such as HO_2, which can influence the model predictions by affecting the equilibrium

constants (and hence the calculated reverse rate constants) for certain reactions. Of particular interest is the main branching reaction, (–R12), whose rate constant must be calculated using the equilibrium constant. Additional reactions may also be pressure-dependent under supercritical water conditions, such as (R13); however, the magnitude of the unexplained pressure dependence in Figure 8.14 appears too great to be explained solely on the basis of pressure-dependent rate constants. Experiments at pressures below 118 bar, and perhaps as low as 20 bar, could provide important validation of the essential mechanism of oxidation while minimizing or eliminating any non-ideal effects associated with a high-pressure aqueous phase. Such low-pressure experiments could also provide vital information about the role of water over orders of magnitude of density, and could identify the "turnover" region hypothesized in Section 7.7.

Chapter 9

Glucose Hydrolysis and Oxidation in Supercritical Water

9.1 Introduction

Supercritical water oxidation is an attractive alternative for the treatment of aqueous wastes with high solids contents, including activated sludges (Shanableh and Gloyna, 1991), pulp mill sludges (Hossain and Blaney, 1991; Modell *et al.*, 1992), and human waste (Takahashi *et al.*, 1989). For wastes with a solids content as low as 10 wt%, complete oxidation to CO_2, N_2, and H_2O by SCWO can be carried out without addition of auxiliary fuel, and a significant fraction of the heating value of the waste can be recovered. Furthermore, SCWO treatment of this class of waste is more economical than incineration, since burning a high-water-content waste requires dewatering of the sludge combined with addition of auxiliary fuel to supplement the heating value of the waste. In some cases, SCWO of sludges may even be cheaper than the common disposal method of landfilling (Modell *et al.*, 1992). Supercritical water oxidation has also demonstrated the ability to destroy quickly and efficiently dioxins and furans, which are frequently present as trace contaminants in pulp mill sludges (Hossain and Blaney, 1991; Modell *et al.*, 1992). In addition, SCWO conditions can be controlled to give only partial oxidation of nitrogenous waste constituents to ammonia, while carbon-containing species are oxidized completely to CO_2 and H_2O; human waste can thus be converted to a clean fertilizer for

plants, a critical capability for controlled ecological life support systems (Takahashi *et al.*, 1989).

A common feature of sludges and human waste is their high fiber content, most of which is cellulose. In the case of pulp mill sludges, the waste will also contain significant amounts of lignin. Sludges and human waste are typically at least somewhat acidic, and heating of aqueous cellulose under acidic conditions hydrolyzes and depolymerizes cellulose to its monomer, glucose (Skaates *et al.*, 1981). Yields of glucose from cellulose hydrolysis, however, are by no means 100%. Instead, secondary destructive pathways exist, which reduce the glucose yield either by hydrolyzing the glucose (Saeman, 1945) or by converting the cellulose to a non-glucose product (Bobleter and Bonn, 1983; Mok *et al.*, 1992). Nevertheless, a significant fraction of the cellulosic waste in the reactor is likely to decompose to glucose, and glucose is thus an appropriate model compound for sludges and human waste.

Despite the potentially widespread application of SCWO to this class of waste, relatively few studies have been conducted to investigate the destruction characteristics or oxidation kinetics of glucose. Rather, most studies have been concerned with proving the ability of SCWO to treat these wastes with high efficiency (Takahashi *et al.*, 1989; Hossain and Blaney, 1991; Modell *et al.*, 1992). Several kinetic studies of glucose oxidation have been carried out under wet-air oxidation conditions, however (Ploos van Amstel and Rietema, 1970; Brett and Gurnham, 1973; Skaates *et al.*, 1981). In those studies, oxidation rates were determined by the reduction in glucose concentration or in chemical oxygen demand (COD). Since wet-air oxidation occurs at temperatures and pressures much lower than those used in the SCWO process, the applicability to SCWO of kinetic results obtained under wet-air oxidation conditions is suspect. None of the wet-air oxidation studies made an extensive effort to ascertain identities or yields of oxidation

products, however, although Ploos van Amstel and Rietema (1970) reported that the hydrolysis products of glucose were more refractory than glucose itself, while Skaates *et al.* (1981) listed several identified oxidation products, with acetic acid the major product.

The oxidation of glucose in supercritical water, as a model for the oxidation of more complex cellulosic wastes, remains poorly understood. A brief study of the oxidation characteristics of glucose in supercritical water was therefore undertaken. Initial experiments revealed that hydrolysis of glucose occurred rapidly, and subsequent glucose experiments examined both the hydrolysis and oxidation reactive pathways. Previous experimental results for glucose pyrolysis and hydrolysis were examined to obtain anticipated indentities for the products of the hydrolysis and oxidation of glucose in supercritical water.

9.2 Previous Experimental Studies of Glucose Hydrolysis/Pyrolysis

While relatively few studies have examined glucose oxidation, there exists an extensive literature concerning the pyrolysis and hydrolysis of cellulose and glucose. Much of this work has been directed toward the utilization of biomass through its conversion to liquid fuels or chemical feedstocks. Efforts to maximize product yields have led to the examination of a wide range of reaction conditions.

Biomass pyrolysis, in which biomass is heated and decomposed in an inert atmosphere or under a vacuum, has been reviewed by Antal (1982). Pyrolysis of cellulosic carbohydrates leads to a variety of smaller compounds, including liquid organics, light gases, and char (Antal, 1982; Evans and Milne, 1987). Destruction of cellulose by pyrolytic reactions proceeds through an intermediate species, levoglucosan (1,6-anhydro-β-D-glucopyranose), which is distinct from the glucose formed from cellulose hydrolysis. Levoglucosan is apparently formed through intramolecular

condensation, although the mechanism is not well understood, with evidence for both heterolytic (ionic) and homolytic (free-radical) pathways found experimentally (Theander and Nelson, 1978; Antal, 1982; Evans and Milne, 1987). Evans and Milne (1987) recently identified by mass spectrometry over 80 products of the pyrolysis of wood, including many phenolics which were attributed to the pyrolysis of lignin.

Hydrolysis of glucose has been the subject of experimental studies for over a century. Many studies were concerned with the role of glucose hydrolysis in the discoloration of sugar solutions; aqueous, liquid solutions of glucose at 100 to 250 °C were found to form 5-hydroxymethylfurfural, which subsequently either hydrolyzed to levulinic acid and formic acid or polymerized to form colored products (Wolfrom *et al.*, 1948; Singh *et al.*, 1948; Newth, 1951; Mednick, 1962). More recently, Antal and co-workers (Antal and Mok, 1988; Antal *et al.*, 1990a,b,1991) have studied the hydrolysis of fructose, sucrose and xylose, both with and without an acid catalyst, at 250 °C and 345 bar. The hexoses (fructose, sucrose) produced significant yields of 5-hydroxymethyl-furfural and smaller quantities of furfural, while the pentose (xylose) produced furfural. Small yields of other products were also found, including formic acid, lactic acid, levulinic acid, pyruvaldehyde,and glyceraldehyde (Antal *et al.*, 1990a,1991). Product formation was explained on the basis of ionic, acid-catalyzed mechanisms.

Modell and co-workers were the first to study the hydrolysis of glucose in near- and supercritical water (Amin *et al.*, 1975; Woerner, 1976; Modell, 1985b). Amin *et al.* (1975) reported that, for temperatures below the critical temperature (374 °C), glucose hydrolysis produced liquid organics and char, with little formation of gas. On the other hand, for temperatures above the critical temperature and at 221 bar, gasification of the glucose (after 30 to 60 min.) increased significantly (up to 20%), while char formation was suppressed, and most of the hydrolyzed glucose appeared as furans or furan

derivatives (furfurals). The gaseous product consisted mostly of carbon monoxide, carbon dioxide, and hydrogen, with smaller amounts of methane and C_2 (two-carbon) gases. Woerner (1976) found similar results in his continuation of the same work.

Most recently, Antal *et al.* (1992) have studied the reactions of glucose in supercritical water at 345 bar and 450 to 650 °C. At 600 °C, the glucose was completely gasified for a residence time of 20 s, with the major products being carbon dioxide and hydrogen. At a given temperature, the yield of gases showed little sensitivity to residence time, whereas gasification increased markedly with increasing temperature. Both the extent of gasification and the composition of the gas produced were found to be sensitive to the reactor material, with Inconel 625 favoring gasification to a greater extent than Hastelloy C276. Inconel also appeared to catalyze the water-gas shift pathway, such that carbon monoxide yields decreased sharply while hydrogen and carbon dioxide yields increased in the Inconel reactor (Antal *et al.*, 1992).

With the exception of the work of Modell and co-workers (Modell, 1985b) and Antal *et al.* (1992), little of the prior work on glucose pyrolysis and hydrolysis is directly relevant to the conditions in the supercritical water oxidation process. Glucose pyrolysis studies lack the presence of water as a reactive medium at relevant densities and temperatures. Glucose hydrolysis studies are carried out in liquid water, typically with acid catalysis, such that ionic chemistry is dominant; in the SCWO process, ionic chemistry is likely to be of much more minor (if any) importance. Nevertheless, the foregoing studies provide a framework within which to develop an expectation of the types and identities of products which may be formed during the reactions (hydrolysis and oxidation) of glucose in supercritical water.

9.3 Product Identification

Experiments for glucose hydrolysis and oxidation were conducted over a temperature range of 425 to 600 °C at a constant pressure of 246 bar. Compositional analyses of the reactor effluents were accomplished by gas chromatography (GC) for the gaseous effluent and high-performance liquid chromatography (HPLC) for the liquid effluent; see Section 4.2 for analytical details.

Gas-phase analyses and product identifications were relatively straightforward owing to the limited number of possible products. Species identified in the gas-phase effluent included hydrogen, carbon monoxide, carbon dioxide, methane, ethane, and ethylene. No acetylene was detected. Higher-molecular-weight gases, e.g., three-carbon and higher, were not specifically searched for, but had they been present they should have caused spurious peaks during the consecutive sample analyses. No such peaks were observed, and furthermore, under conditions where the glucose was completely converted to gaseous species, carbon-balance closures were excellent (within 3 to 5%). These observations led us to conclude that C_3 (or higher) gases were formed to a negligible extent under all of our experimental conditions.

Product identifications for the liquid-phase effluent presented more of a challenge. A list of suspected products was obtained from earlier studies of glucose pyrolysis and hydrolysis (Woerner, 1976; Shallenberger and Birch, 1975; Antal, 1982; Evans and Milne, 1987; Antal *et al.*, 1990a,1991). This list was then condensed on the basis of commercial availability (for calibration purposes) and the importance (abundance) of the products in the earlier studies. The resulting list of almost forty suspected products is shown in Table 9.1. Suspected compounds were tested by injection of authentic standard

Compound	RT[a], min	λ[b], nm	Present in Effluent from Hydrolysis	Oxidation
Acetaldehyde	15.9	290	✓	✓
Acetic Acid	13.1	210	✓	✓
Acetol (Hydroxyacetone)	10.4,14.8	210	?	
Acetone	18.3	290		
Acetonylacetone (2,5-Hexanedione)	19.75	210	✓	✓
2-Acetylfuran	42.9	290	✓	
Crotonaldehyde	28.9	210	?	?
Crotonic Acid	21.7	210	?	
2-Cyclopenten-1-one	29.7	210	?	?
3,4-Dihydro-2H-pyran	ND[c]	—		
Dihydroxyacetone	11.9	210		
2,5-Dimethylfuran	M[d]	—		
Formaldehyde	ND	—		
Formic Acid	11.8	210	✓	
Furfuryl Alcohol	36.1	290		
2-Furaldehyde (Furfural)	35.8	290	✓	✓
Furan	31.9	210	?	?
2,5-Furandimethanol	M	—		
2-(5H)-Furanone	23.1	210		
2-Furoic Acid	22.9	210		
Glucaric (Saccharic) Acid	6.8	210		
Gluconic Acid	8.0	210		
Gluconic Acid Lactone	8.0	210		
Glucose	ND	—	✓	✓
Glyceraldehyde	10.1	210	?	
Hydroxyacetic (Glycolic) Acid	10.7	210	?	
5-Hydroxymethylfurfural	25.1	290	✓	✓
Lactic Acid	11.1	210	✓	
Levulinic Acid	13.7	210		
5-Methyl-2(3H)-furanone	M	210		
2-Methyl-2-cyclopenten-1-one	41.7	210		
2-Methylfuran	ND	—		
5-Methylfurfural	51.9	290	✓	
Oxalic Acid	5.2	210		
Propenal (Acrolein)	21.0	210		
Propenoic (Acrylic) Acid	15.6	210	✓	✓
Propionaldehyde	19.6	290		
Propionic Acid	15.3	210		
Succinic Acid	10.1	210	?	

[a]Retention time.
[b]Wavelength for detection/maximum absorbance.
[c]Not detectable at either 210 or 290 nm.
[d]Gives multiple unidentified peaks.

Table 9.1 Summary of Compounds Tested as Possible Liquid-Phase Products.

solutions in the HPLC, and observed retention times for the standards were compared with retention times of peaks in a sample of the liquid-phase effluent.

Peak detection was accomplished by UV absorption at two different wavelengths, 210 and 290 nm. Analysis at dual wavelengths enabled discrimination between peaks by functional group, and allowed identification of additional species not detectable at a single wavelength. For example, UV absorption by a compound requires the presence of a double bond, either C=C or C=O. Carboxylic acids have their maximum UV absorbance at approximately 210 nm, as do unsaturated or conjugated ketones and aldehydes. On the other hand, saturated aldehydes and ketones have their maximum absorbance at about 290 nm. Extended conjugation of aldehydes and ketones shifts the maximum absorbance back toward 290 nm from 210 nm, while conjugated carboxylic acids maintain their maximum absorbance at about 210 nm (Silverstein *et al.*, 1991). Consequently, detection at a single wavelength (e.g., 210 nm) limits the ability to identify all species: at 210 nm, simple aldehydes have virtually no absorbance, while carboxylic acids have no absorbance at 290 nm. Furthermore, for compounds which absorb at both 210 and 290 nm, the wavelength that maximizes sensitivity (with maximum absorption) can be chosen. For example, furaldehydes may be detected in the liquid effluent at concentrations as low as 10^{-7} mol/L by absorbance at 290 nm. The ability to discriminate on the basis of functional group is illustrated by acetaldehyde and propenoic (acrylic) acid in Table 9.1 Both compounds have almost the same retention time, but propenoic acid absorbs exclusively at 210 nm while acetaldehyde absorbs only at 290 nm. Thus the two compounds may be "separated" by the dual-wavelength analysis, even though their peaks overlap. Table 9.1 lists the better of the two wavelengths for the detection of each test compound. Detection by UV absorption has the disadvantage of not allowing determination of compounds that lack a double bond, such as methanol, which may be

present in the liquid effluent; should detection of such species be desired, alternative analytical methods would be required.

Note that not all of the test compounds in Table 9.1 have an associated retention time. In those cases, clear assignment of a retention time for a standard solution was not possible. In some cases, detection of the compound was not possible, even though in principle the compounds should have been detectable. For example, glucose was not detectable, indicating that in aqueous solution glucose does not exist in its straight-chain, aldohexose form (with a detectable aldehyde group), but rather in its cyclic, hemiacetal (glucopyranose) form, which lacks the aldehyde group and which therefore cannot be detected by UV absorption. Fortunately, an alternate enzymatic method is available for glucose determinations (see Section 4.2). Formaldehyde was similarly not detectable, indicating that it, like glucose, exists in solution in a form (formalin, or methanediol) which lacks the C=O group and which is thus not capable of UV absorption.

Other test compounds in Table 9.1 were detectable, but gave multiple peaks even for ostensibly pure standard solutions. In these cases, the test compound apparently undergoes reaction while standing in aqueous solution, and it is difficult to determine which of the peaks corresponds to the "parent" molecule, and what the identities of the secondary species might be. A compound that is sufficiently labile to undergo hydrolysis in room-temperature water may not be stable under reactor conditions, although the compound may represent an important step in a degradative pathway, and the room-temperature hydrolysis products may well be present in the reactor effluent.

Figure 9.1 shows two HPLC chromatograms, with detection at 210 nm, for hydrolysis and oxidation of glucose in supercritical water at 500 °C and 246 bar, with nominal initial conditions of 1×10^{-6} mol/cm^3 glucose, 6×10^{-6} mol/cm^3 oxygen (for the oxidation experiment), and a 6-second reactor residence time. Peak identities, when

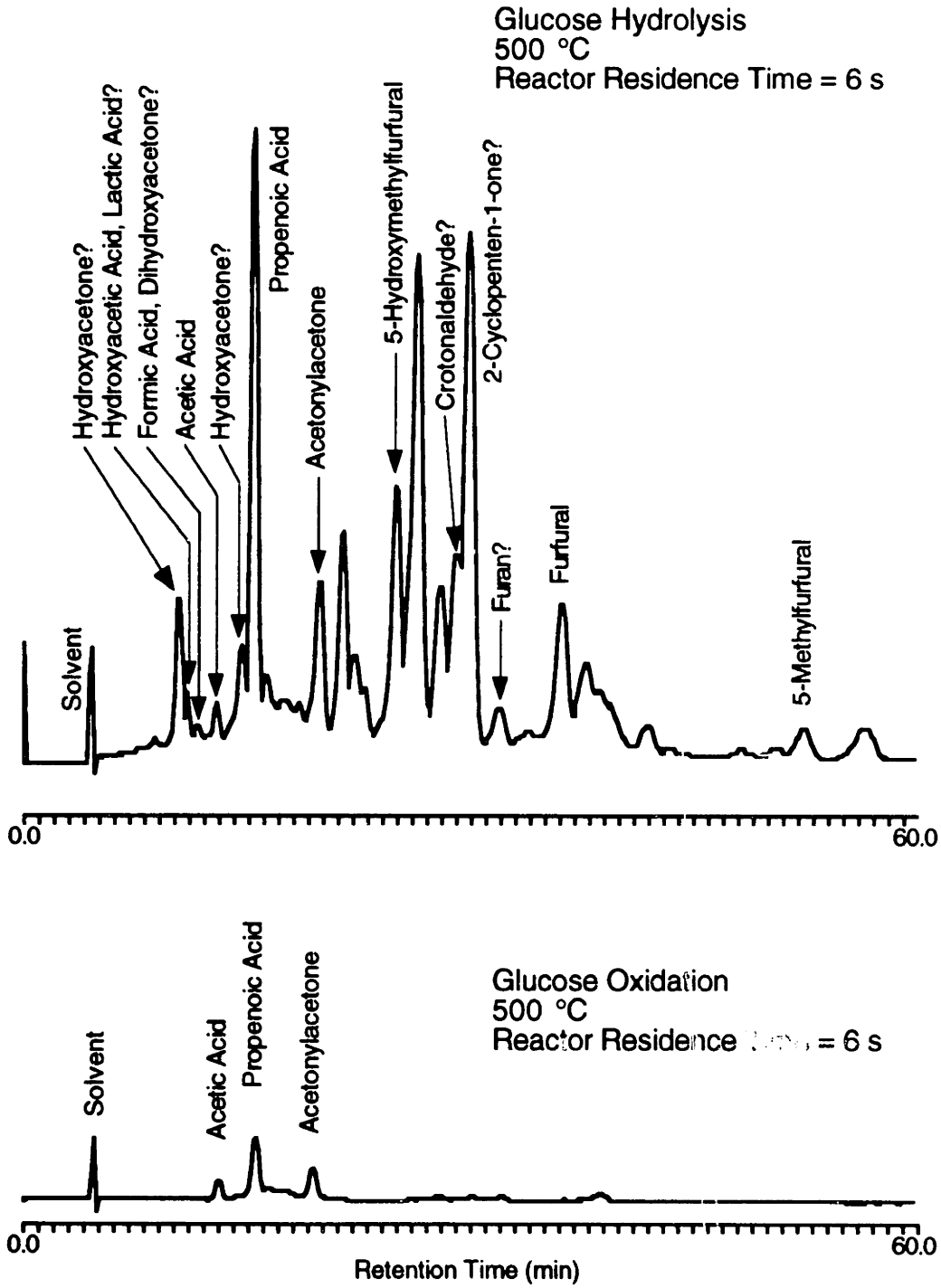

Figure 9.1 **Comparison of HPLC Chromatograms of Liquid Effluent from Glucose Hydrolysis and Oxidation in Supercritical Water.** Nominal initial conditions: 500 °C, 1×10^{-6} mol/cm^3 glucose, 6×10^{-6} mol/cm^3 oxygen (for oxidation), 6 s reactor residence time. UV detection at 210 nm.

known or suspected, have been indicated. Clearly the number of liquid-phase products is greatly reduced under oxidizing conditions.

Many peaks formed during glucose hydrolysis remain unidentified, as Figure 9.1 shows. Of the 26 or more peaks detected in the hydrolysis effluent, only half have been identified, with many of those identifications tentative. Positive identifications were made for acetaldehyde (not shown in Figure 9.1 because it can only be detected at 290 nm), acetic acid, acetonylacetone (2,5-hexanedione), 2-acetylfuran (present in very low concentrations and not quantified), formic acid, furfural (2-furaldehyde), 5-hydroxymethylfurfural, lactic acid, 5-methylfurfural, and propenoic (acrylic) acid. Structures of the positively identified compounds are shown in Figure 9.2. The rationale for these identifications, whether tentative or positive, deserves further elaboration.

Formic acid and dihydroxyacetone have virtually identical retention times (11.8 vs. 11.9 min.; see Table 9.1). However, dihydroxyacetone has a much lower absorbance than formic acid, and the peak at this retention time should be considered to be formic acid, in accordance with Antal *et al.* (1990a,1991). No matter what the peak's identity, it appears to be fairly unstable and disappears from the hydrolysis effluent for temperatures above 500 °C.

Acetol (hydroxyacetone) gives two peaks (at 10.4 and 14.8 min.), indicating that it undergoes rearrangement in solution, most likely forming 2-hydroxypropanal. The HPLC method in this work was based on the method of Antal *et al.* (1991) for detection and quantification of the products of xylose hydrolysis; comparison of relative retention times from their work indicates that the peak observed here at 14.8 min. probably corresponds to acetol; the peak at 10.4 min. is probably 2-hydroxypropanal.

A cluster of peaks with similar retention times exists near the 10-min. mark. Compounds eluting in this narrow retention-time range include glyceraldehyde, succinic

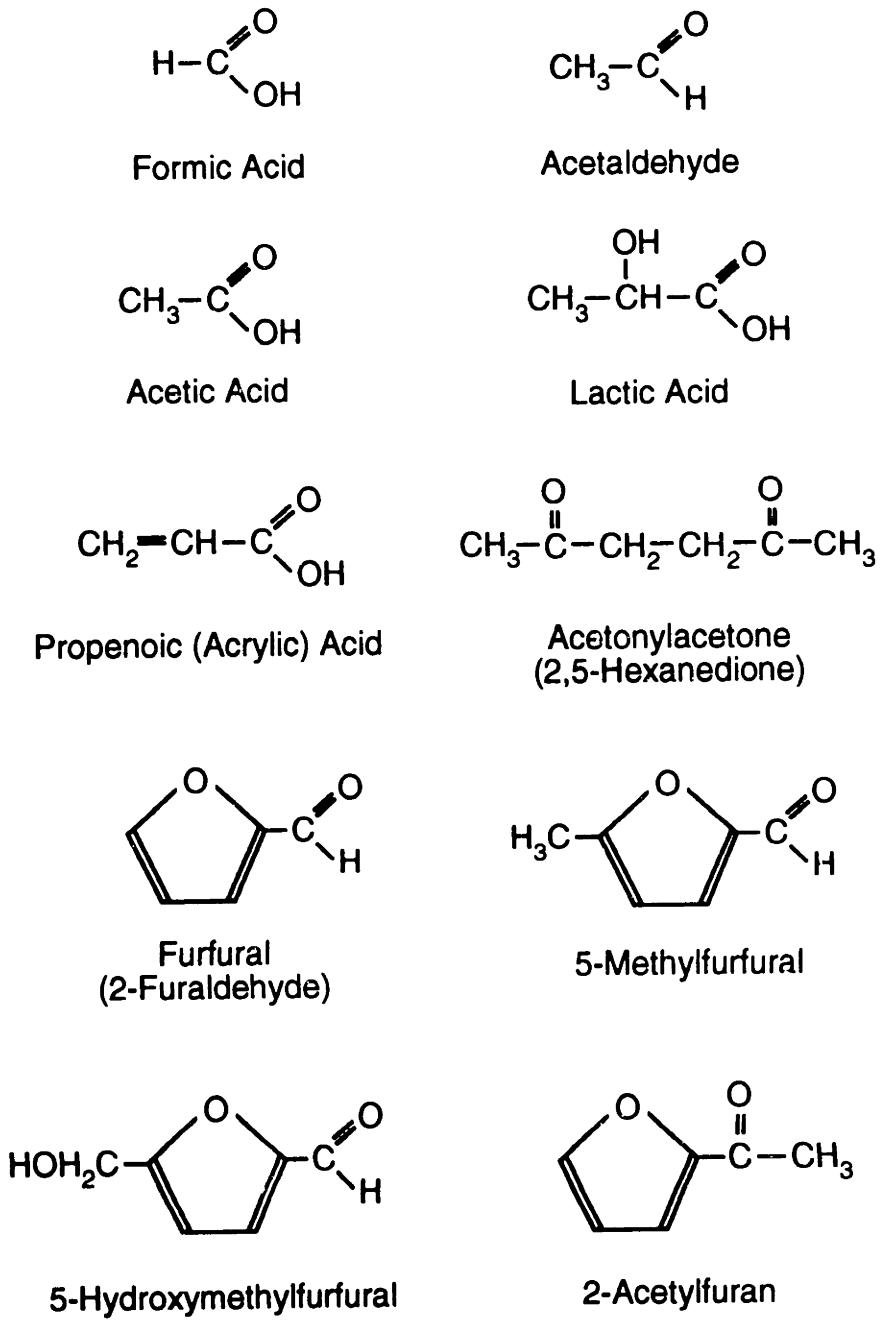

Figure 9.2 **Compounds Identified in Liquid Effluent of Glucose Hydrolysis and/or Oxidation.**

acid, hydroxyacetic acid, and (tentatively) 2-hydroxypropanal. With the natural drift in retention times between samples, these peaks are not adequately resolved and no positive identifications are possible. At higher temperatures, these peaks are unimportant. Under oxidizing conditions, the peaks disappear at 450 °C and above. For hydrolysis conditions, the peaks persist to higher temperatures, but disappear at 525 °C and above. The identification of lactic acid at a retention time of 11.1 min. may not be positive, since Antal *et al.* (1991) indicate that glycolaldehyde (which was not tested here) elutes at the same time as lactic acid; however, Antal *et al.* (1990a) did not detect glycolaldehyde during fructose hydrolysis at 250 °C and 345 bar. Like the peaks at ~10 min., the lactic acid peak disappears at higher temperatures.

Propenoic (acrylic) acid and propionic (propanoic) acid have very similar retention times; the very tall peak at ~15.5 min. present in effluent samples could belong to either compound. However, the height of the peak suggests that it is probably propenoic acid, because of its much higher absorption due to conjugation. To create such large peaks, propionic acid would have to be present at concentrations so unphysically large that carbon-balance closures on the reactor would be adversely affected. The tall peak is therefore attributed to propenoic acid.

Crotonaldehyde, crotonic acid, and 2-cyclopenten-1-one all exhibit retention times near those of peaks observed in effluent samples. Unfortunately, retention times are not sufficiently close to warrant a positive assignment of identity to the peaks. Furthermore, a peak at ~30 min. exists in the effluent samples for detection at both 210 nm and 290 nm. If the peak at 210 nm is 2-cyclopenten-1-one, then the peak at 290 nm must correspond to another unknown species, since 2-cyclopenten-1-one does not absorb at 290 nm.

The peak in the effluent samples at ~36 min. was quantified as furfural rather than furfuryl alcohol, since furfuryl alcohol did not absorb at 210 nm and gave a small peak at 290 nm; the peak in the effluent sample, on the other hand, occurred at both 210 and 290 nm and was large at 290 nm, consistent with the behavior of the furfural peak.

Acetonylacetone was identified since it appears to be a hydrolysis product of 2,5-dimethylfuran, which has been detected among the products of cellulose pyrolysis (Antal, 1982) and glucose caramelization (Shallenberger and Birch, 1975). A path to acetonylacetone from glucose through 2,5-dimethylfuran therefore apparently exists. Acetonylacetone was also listed as a suspected product by Woerner (1976) for hydrolysis of glucose in near-critical water. However, oxidation experiments in the present study at 450 and 475 °C gave in excess of 100% carbon recovery (118% and 111%, respectively), and indicated that the acetonylacetone peak may have been improperly assigned. Were the peak a C_3 instead of a C_6, carbon-balance closures would have been much improved. The assignment of the acetonylacetone peak must therefore be regarded as the most tenuous of the positive identifications.

Phenolics or other six-membered aromatics were not tested as possible products. Note that without synthesis or condensation pathways, compounds larger than phenolics cannot form since glucose is only a six-carbon molecule. The results of Antal and co-workers for hydrolysis of sugars (Antal *et al.*, 1990a,b,1991) indicate that furans, furaldehydes and their derivatives are the dominant products, while Evans and Milne (1987) attribute the presence of phenolics among the products of biomass pyrolysis to the decomposition of lignin, not cellulose. Phenolics were therefore not tested as possible products in the present study. However, Antal *et al.* (1990b) have noted that 1,4-butanediol may form tetrahydrofuran with acid catalysis, while West and Gray (1987) observed the formation of dioxanes from 1,4-butanediol in supercritical water. Similarly,

Theander and Nelson (1978) indicate that dihydroxyacetone may form aromatics (hydroxybenzenes) in acid solution. These results suggest that phenols or other condensation products cannot be completely eliminated from consideration as possible products, and future studies of glucose reactions may wish to consider these species.

Finally, larger condensation products, such as oligomers of 5-hydroxymethyl-furfural or dibenzofurans cannot be ruled out *a priori* as possible products. HPLC chromatograms were run for retention times as long as 90 min., however, without detecting any peaks beyond retention times of 60 min. In addition, detection by UV absorption should be highly sensitive to these conjugated species, and if the compounds were present even in minute quantities they should produce peaks. Furthermore, any long-retention-time peaks should eventually appear during the consecutive sample analyses, and should create spurious peaks in the sample chromatograms. No spurious peaks were seen, however, and consecutive chromatograms showed excellent reproducibility. From these observations we concluded that there were no products of high molecular weight present in the liquid reactor effluent.

9.4 Product Distributions for Glucose Hydrolysis and Oxidation

The global hydrolysis or "reforming" of glucose

$$C_6H_{12}O_6 + 6\ H_2O \rightarrow 6\ CO_2 + 12\ H_2 \qquad (9.1)$$

can produce significant quantities of hydrogen, if complete reaction to CO_2 and H_2 is achievable, and provides the motivation for the research of Antal *et al.* (1992). The global oxidation of glucose

$$C_6H_{12}O_6 + 6\ O_2 \rightarrow 6\ CO_2 + 6\ H_2O \qquad (9.2)$$

is of more relevance to SCWO treatment of cellulosic wastes, where complete destruction of organics is desired. Since glucose hydrolysis occurs at significant rates at supercritical-water temperatures and pressures, oxidation of glucose via reaction 9.2 cannot occur without a simultaneous contribution from reaction 9.1. In the present study, glucose hydrolysis and oxidation were examined at conditions relevant to the SCWO process (246 bar, 425 to 600 °C) to evaluate the relative contributions of the two reactive pathways.requires a large amount of oxygen to achieve stoichiometric conditions.

In a series of experiments, an initial concentration (at reactor conditions) of 1×10^{-6} mol/cm^3 of glucose was used at a fixed residence time of 6 seconds and over the temperature range 425 to 600 °C. Experiments with and without stoichiometric (6×10^{-6} mol/cm^3) oxygen present were conducted, in order to distinguish the products and rates of the hydrolysis and oxidation pathways. The concentration of oxygen required to achieve a stoichiometric glucose/oxygen ratio was high and was limited by solubility constraints in the oxygen saturator. The upper limit of oxygen concentration restricted the maximum glucose concentration, since the glucose concentration was to be the same during both oxidation and hydrolysis experiments. The concentrations used reflect the highest attainable oxygen concentration over the range of reactor temperatures studied.

Hydrolysis and oxidation experiments were performed in pairs. Following heatup of the system, only the organic (glucose) feed was switched on, and a hydrolysis experiment was begun. After data had been collected for the hydrolysis experiment, the oxygen feed was switched on and an oxidation experiment was begun. In this manner the hydrolysis and oxidation pathways could be examined under otherwise identical conditions. Switching to the oxygen feed perturbed reaction conditions slightly, since the high-pressure oxygen saturator solution causes the oxygen-side pump head to increase its flow rate, diluting the glucose feed somewhat and slightly decreasing the overall reactor

residence time. These perturbations were very minor, however, and conditions of the hydrolysis and oxidation experiments were essentially identical except for the presence or absence of oxygen.

Even at the lowest temperature studied (425 °C), glucose concentrations in the liquid effluent (as determined enzymatically) indicated a conversion of glucose *by hydrolysis* of 97%, demonstrating the high reactivity of glucose even in the absence of oxygen. Measurements of the kinetics of glucose consumption by either global pathway were therefore not feasible at these temperatures and pressures.

Both hydrolysis and oxidation of glucose produced large quantities of gas, as shown in Figure 9.3. The extent of gasification in Figure 9.3 is defined as the moles of carbon present in the gaseous effluent divided by the moles of carbon fed to the reactor. Gasification was obviously more prevalent under oxidizing conditions, with 60% of the glucose carbon appearing in the gaseous effluent at 425 °C, increasing to virtually 100% for temperatures of 500 °C and higher. Under hydrolysis conditions, gasification was less extensive at low temperatures (~12% at 450 °C), but rose quickly to 100% at 575 to 600 °C. The large error in the extent of hydrolytic gasification at high temperatures stems from the very high gas flow rates (~40 mL/min) caused by the large amounts of gas produced (18 moles of gas per mole of glucose; see Equation 9.1); in the present system, high gas flow rates are difficult to measure precisely.

Figure 9.4 shows the yields of major identified products from the glucose hydrolysis experiments. In this and subsequent figures, the product yield is defined as the moles of product divided by the moles of glucose reacted. Thus the maximum yield of carbon dioxide is 6, while the maximum yield of hydrogen is 12. Since the conversion of glucose was 97% or higher in all experiments, the product yield on a per-mole-reacted basis, as used here, is essentially the same as the yield on a per-mole-fed basis. Figure

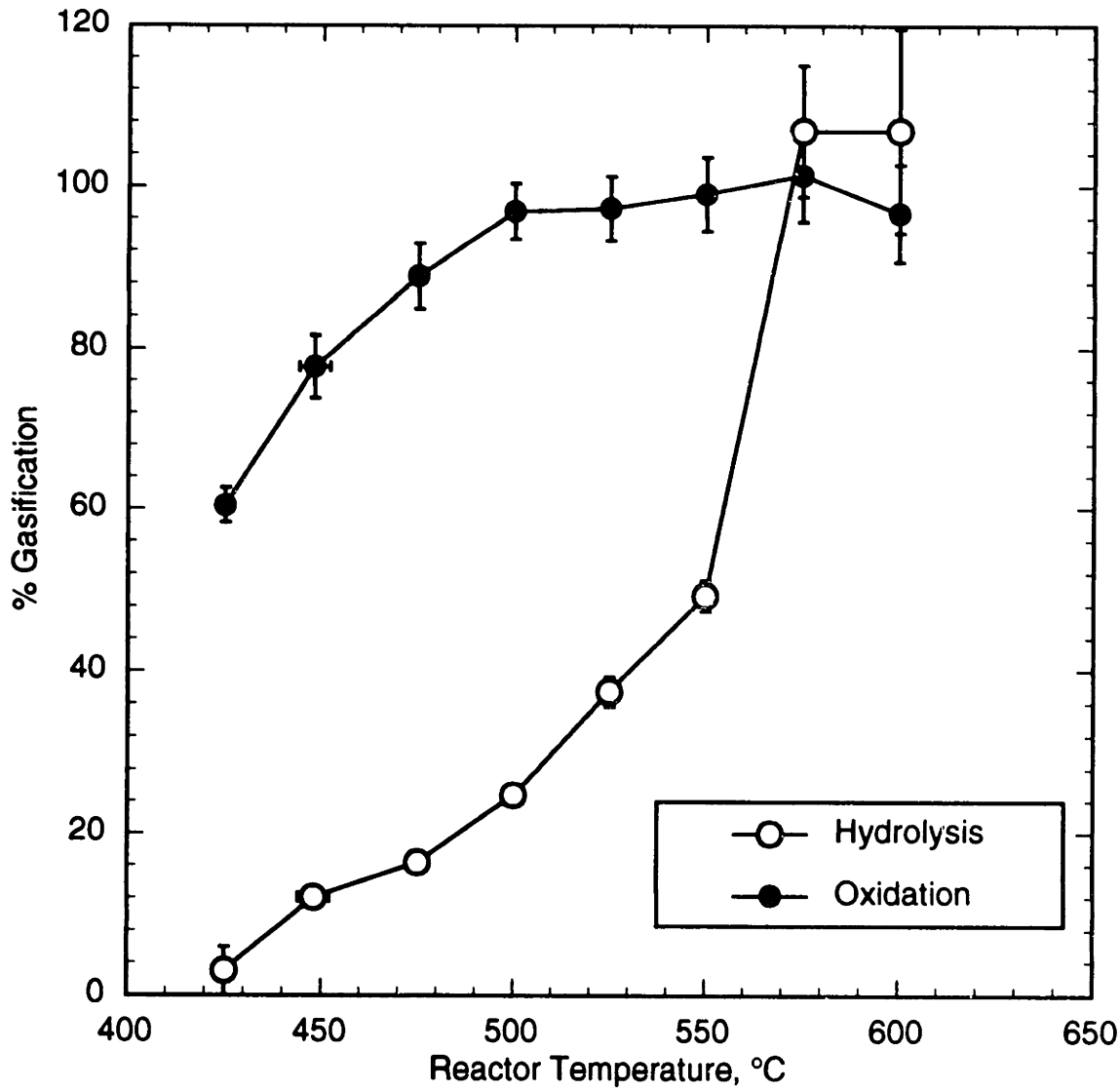

Figure 9.3 **Variation of Extent of Glucose Gasification with Temperature During Hydrolysis and Oxidation.** Nominal initial conditions: 1×10^{-3} mol/L glucose, 6×10^{-3} mol/L oxygen; 6 s reactor residence time.

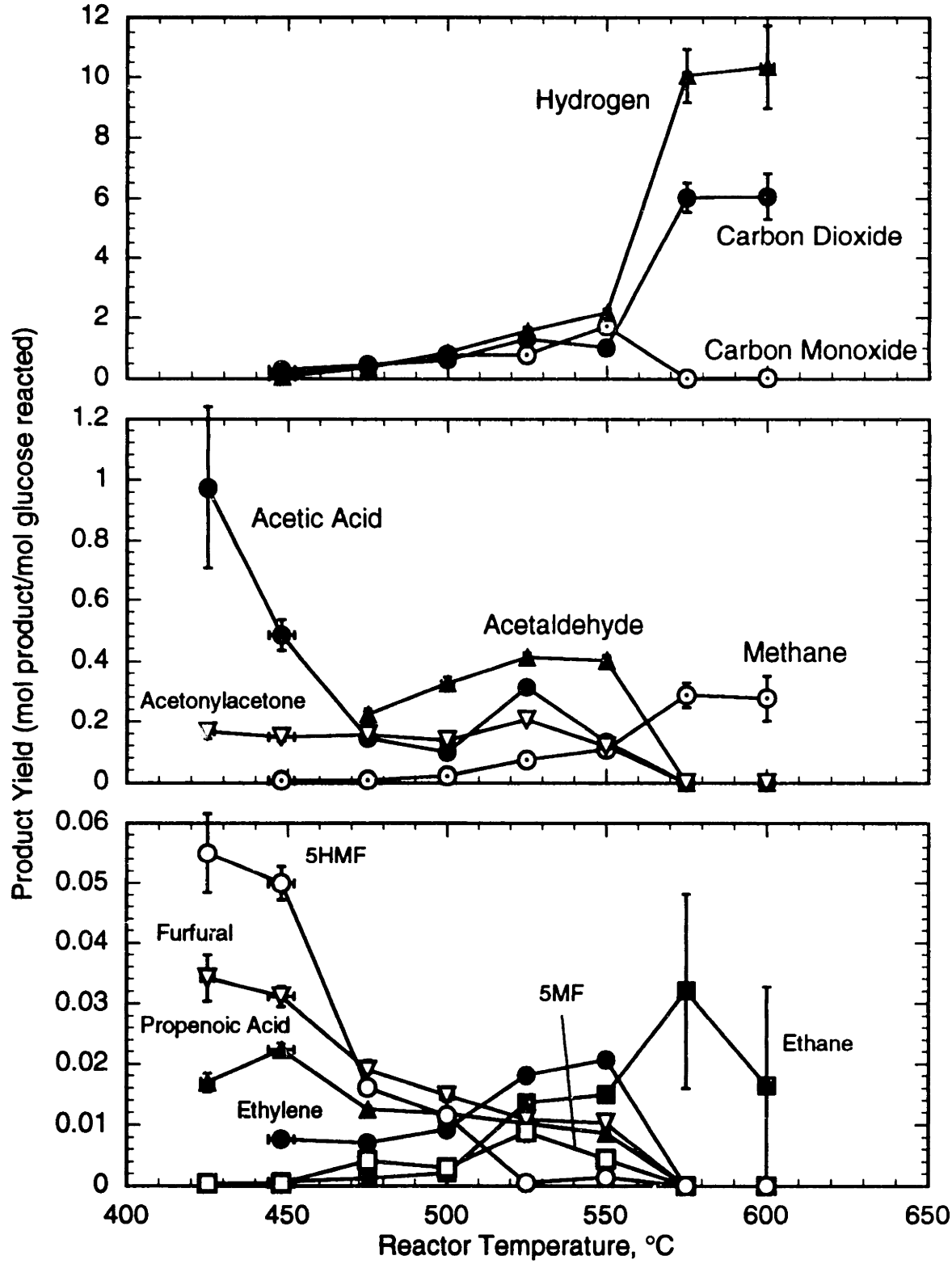

Figure 9.4 **Variation of Product Yields with Temperature for Glucose Hydrolysis at 246 bar.** Experimental conditions: $(1.02\pm0.02) \times 10^{-6}$ mol/cm^3 glucose, 6.1±0.3 s reactor residence time.

9.4 indicates that the major constituents of the gaseous product of glucose hydrolysis are carbon dioxide, carbon monoxide, hydrogen, and methane, with smaller quantities of ethylene and ethane. As noted in Section 4.2, small quantities of ethylene in the presence of large quantities of carbon dioxide (e.g., at the higher hydrolysis temperatures) may be lost due to inadequate GC peak separation; thus the disapprearance of ethylene at 575 and 600 °C may be an artifact of analytical error. Hydrolysis at the highest temperatures yielded a gaseous effluent consisting almost exclusively of hydrogen and carbon dioxide in a 1.7:1 ratio, indicating the presence of a fast, water-gas-shift-type pathway. These observations are generally consistent with the recently reported results of Antal and co-workers (Antal *et al.*, 1992).

Hydrolytic reactions of glucose also tended to produce large numbers of products present in the liquid effluent. At the lowest temperatures, the majority of these products was unidentified, and the carbon balance closure for those experiments was consequently poor (about 50%). As temperature was increased, the extent of gasification increased and the carbon balance improved, with complete closure at 575 to 600 °C, where the glucose was completely gasified and no liquid-phase products remained. The identified liquid-phase products of glucose hydrolysis were acetic acid, acetaldehyde, acetonylacetone, 5-hydroxymethylfurfural (5HMF), furfural, propenoic acid, and 5-methylfurfural (5MF). Acetaldehyde was not detectable below 475 °C because its HPLC peak was obscured by a large, broad peak of unknown origin. Note that the yields of all of the liquid-phase products decrease steadily with increasing temperature, indicating that the stability of those species decreases sharply with increasing temperature The exceptions are 5MF and acetaldehyde, whose formation is apparently favored at 475 to 550 °C; these species may be intermediates in the destruction (hydrolysis) of more complex species. Similarly, the yields of methane, ethane, and ethylene increase steadily with temperature up to the

highest temperatures, implying that these small gases are products of the hydrolysis of liquid-phase intermediates.

Yields of identified products from the corresponding glucose oxidation experiments are shown in Figure 9.5. Yields of liquid-phase products are greatly reduced compared to hydrolysis conditions, and decrease with increasing oxidation temperature, with no liquid-phase products detected at temperatures above 550 °C. Temperatures above 550 °C are thus sufficient to insure complete destruction of all intermediates produced from glucose, including acetic acid and furan derivatives. At the highest temperatures, glucose is converted almost entirely to carbon dioxide, with small quantities of hydrogen and methane also present. Ethylene may also be present at the highest temperatures, but it was not resolved by the GC from the high concentration of carbon dioxide. The average carbon-balance closure for the oxidation experiments was $103.4 \pm 7.1\%$. The stability of methane even at the highest temperatures is consistent with the methane oxidation study of Webley and Tester (1991), who found methane to be one of the more refractory species (see also Figure 7.11).

The pH of the liquid effluent from the hydrolysis experiments ranged from 3.5 at the lowest temperatures to 4.75 at 600 °C, while the pH of the oxidation effluent ranged from 4.25 at 425 °C to 4.75 at 600 °C. The seemingly low pH values at the high temperatures are consistent with the presence of dissolved CO_2 in the liquid effluent. At the lower temperatures, the lower pH values for the hydrolysis experiments indicate that the yield of organic acids is higher than in the oxidation experiments, consistent with the yields in Figures 9.4 and 9.5.

The potential exists for reaction (hydrolysis) of the glucose during feed preheating in these experiments. Using the heat-transfer coefficients derived in Section 7.2, the residence time of the glucose feed in the feed preheating tubing is estimated to range

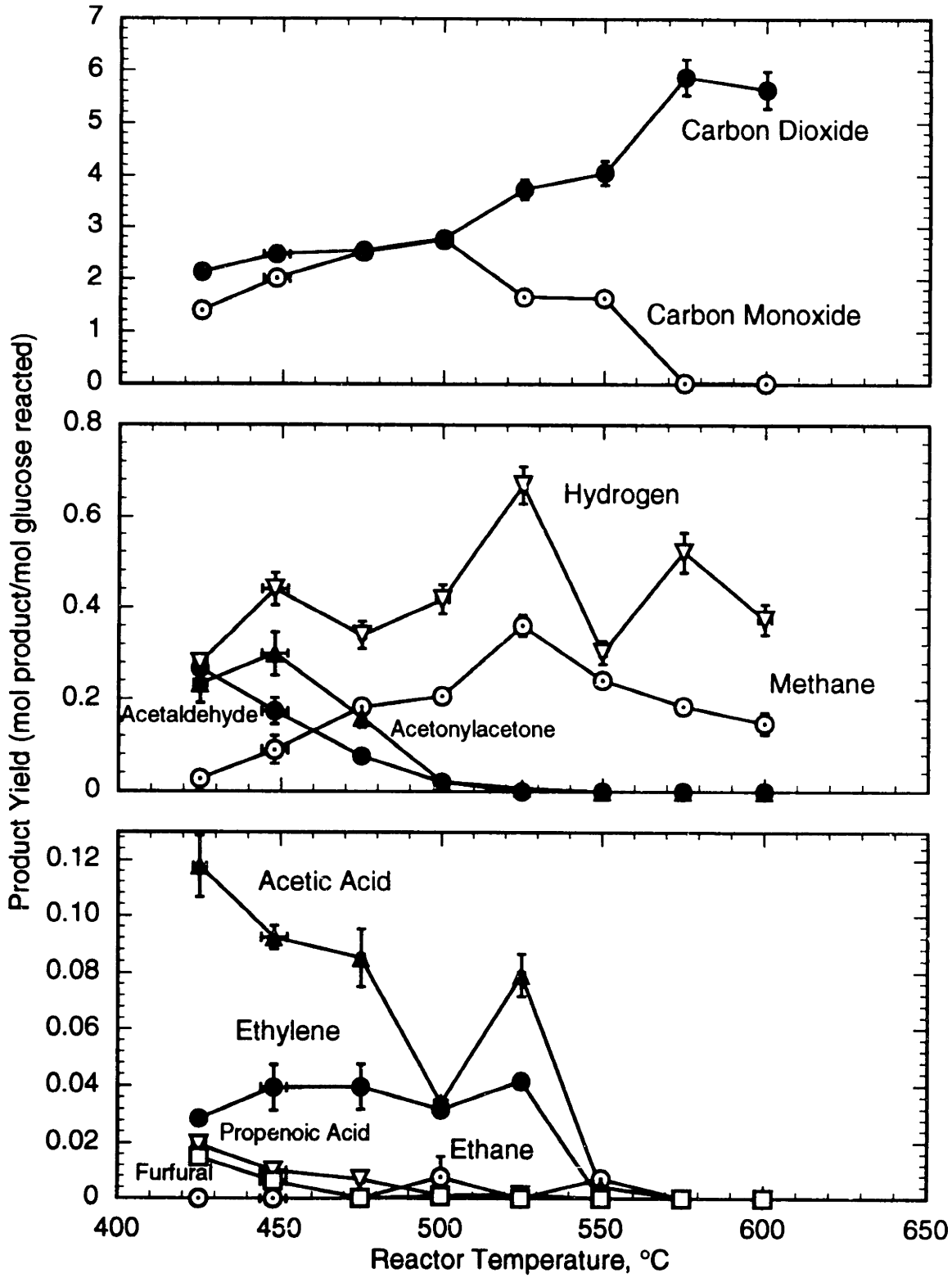

Figure 9.5 **Variation of Product Yields with Temperature for Glucose Oxidation at 246 bar.** Experimental conditions: $(0.99\pm0.02) \times 10^{-6}$ mol/cm^3 glucose, $(6.2\pm0.2) \times 10^{-6}$ mol/cm^3 oxygen, 5.9±0.3 s reactor residence time.

from 14.7 s at 600 °C to 11.7 s at 425 °C. A significant fraction of this residence time (~4 s) is spent near the reaction temperature, such that the actual reaction time may be over 50% longer than the reactor residence time. In the oxidation experiments, the glucose may undergo hydrolysis prior to mixing with oxygen; the high efficiency of the oxidation indicates that any pre-hydrolysis of the glucose does not produce compounds which are refractory relative to oxidation.

Figure 9.6 shows the results of a series of stoichiometric oxidation experiments conducted at 500 °C in order to evaluate the effect of reactor residence time on the observed product yields. In these experiments,the average extent of gasification was 89.1%, with an average of 101.7% carbon-balance closure. All products were thus well accounted for in these experiments. Comparison of the yields at 6 s in Figure 9.6 with the yields at 500 °C in Figure 9.5 demonstrates the good agreement between the two sets of data (with the exception of the acetic acid yield), despite the fact that the two sets of results were obtained in different experiments. Figure 9.6 shows that over a five-second span of residence times, the yields of the major products do not change markedly, indicating that reactions (oxidation) of these species occur relatively slowly at this temperature. In fact, the range of residence times is effectively expanded by the need to change the flow rate to change the reactor residence time, combined with the effects of the changing flow rate on feed preheating. For example, at the longest reactor residence time (9.9 s), heat-transfer calculations indicate that the glucose feed spends an additional 16 s in the preheating tubing, with an additional 3 s at ~500 °C. At the shortest reactor residence time (5.1 s), the glucose feed spends an additional 9 s in the preheating tubing, with only an additional 1 s at ~500 °C. Thus the residence times at reaction temperature effectively range from 6.1 to 12.9 s. The lack of a pronounced change in species yields over this range of times is remarkable, but is in accordance with the observations of Antal

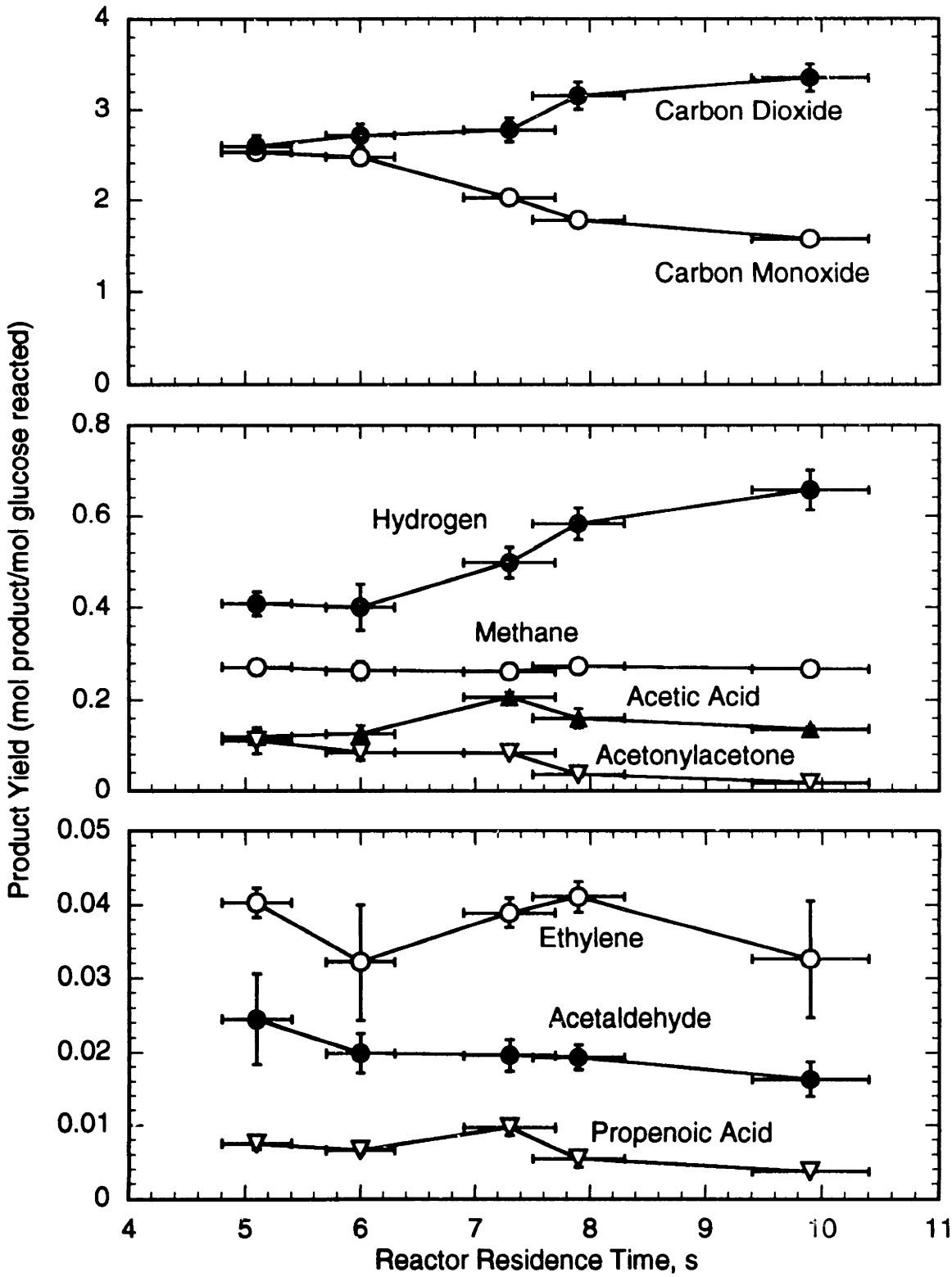

Figure 9.6 **Variation of Product Yields with Residence Time for Glucose Oxidation at 500±2 °C and 246 bar.** Experimental conditions: $(1.01\pm0.02) \times 10^{-6}$ mol/cm^3 glucose, $(6.1\pm0.2) \times 10^{-6}$ mol/cm^3 oxygen.

et al. (1992). On the other hand, primary decomposition/oxidation of glucose, as well as secondary destruction of the more complex intermediates, must occur quite rapidly, in the first 5 to 6 s and/or during preheating of the glucose feed. The compounds shown in Figure 9.6 therefore represent the destruction-limiting species for treatment of glucose.

9.5 Mechanistic Implications of Product Spectra

The data in Figures 9.4 through 9.6 allow certain conclusions to made regarding the mechanisms of glucose hydrolysis and oxidation in supercritical water. First, the absence of levulinic acid from the liquid effluent in all experiments is significant. Levulinic acid is typically formed from the ionic, acid-catalyzed hydrolysis of 5-hydroxymethylfurfural (Kuster and Temmink, 1977). While 5-hydroxymethylfurfural (5HMF) is present in the effluent of hydrolysis experiments, the absence of levulinic acid suggests that it either is not formed or is rapidly hydrolyzed. Experiments by Amin *et al.* (1975) and Woerner (1976) indicate that levulinic acid is relatively stable, and we thus conclude that the acid-catalyzed hydrolysis of 5HMF is not an operative pathway in supercritical water. Disappearance of 5HMF must occur through another, possibly free-radical, mechanism.

The presence of propenoic acid among the products both of hydrolysis and of oxidation is consistent with the work of Mok *et al.* (1989), provided that lactic acid is first formed to a significant extent. Lactic acid is at least formed at lower temperatures and is identifiable in the effluent; at higher temperatures, lactic acid formation may continue, but degradative pathways may render the lactic acid concentration too low to be quantified. According to Mok *et al.* (1989), lactic acid undergoes parallel free-radical pathways, decarboxylation to CO_2, H_2, and acetaldehyde, and dehydration to propenoic acid. The acetaldehyde may then undergo further free-radical reactions to form acetic acid, acetone, and methane. Methane (along with carbon monoxide) is also a primary

product of the gas-phase pyrolysis and oxidation of acetaldehyde (Colket *et al.*, 1975,1976). Furthermore, propenoic acid may decarboxylate to ethylene and CO_2. Note that in Figures 9.4 and 9.5 the yields of methane and ethylene at the high temperatures are approximately equivalent to the yields of acetaldehyde and propenoic acid, respectively, at lower temperatures. This behavior supports the notion that methane is formed from acetaldehyde while ethylene is formed from propenoic acid.

Under the conditions of the present study, the pathway for formation of acetic acid from acetaldehyde does not appear to be operative, or acetic acid is significantly less stable than acetaldehyde. For example, once the decline in acetaldehyde yield begins, acetic acid concentrations are very low; if acetic acid is a major product of acetaldehyde decomposition, it must subsequently degrade quickly. Gas-phase studies of acetic acid decomposition (oxidation studies are virtually non-existent) suggest that acetic acid decarboxylates to methane and carbon dioxide (Bamford and Dewar, 1949; Blake and Jackson, 1969). A consecutive pathway, in which acetaldehyde first formed acetic acid which then rapidly formed methane, would be indistinguishable from the direct formation of methane from acetaldehyde. The precise relationship between acetic acid, acetaldehyde, and methane unfortunately cannot be determined from the present data.

Figure 9.4 indicates that between 550 and 575 °C a fast water-gas-shift-type pathway becomes important, with carbon monoxide quickly converted to carbon dioxide for temperatures of 575 °C and above. This behavior contrasts with the observations of the water-gas shift in Chapter 7, where it was noted that the water-gas-shift reaction pathway is actually quite slow, even at temperatures approaching 600 °C. The mechanism for this accelerated water-gas shift remains unexplained.

The limited response of the product yields in Figure 9.6 to increases in residence time, combined with the yield behavior in Figures 9.4 and 9.5, suggests that there are

three kinetic regimes for the reactions of glucose in supercritical water. First, glucose undergoes rapid hydrolysis or oxidation to form a wide array of products, the more stable of which include acetic acid, acetaldehyde, acetonylacetone, propenoic acid, and others. The secondary reactions of these species are slower, and result in the formation of small quantities of stable light gases, including methane and ethylene. The tertiary destruction of these trace light gases ultimately limits the complete conversion of glucose to carbon dioxide and water.

While this limited study of glucose hydrolysis and oxidation in supercritical water was not able to provide global kinetic data, important products of both pathways have been characterized. The identified products were frequently the most refractory products formed, indicating that their destruction may, under certain circumstances, limit complete destruction of glucose; for this reason alone, the identification of these species was important. Future experiments at lower temperatures may be able to provide more quantitative kinetic information.

Chapter 10

Conclusions

1. Measurements of oxidation kinetics. The oxidation kinetics of hydrogen in supercritical water have been examined at 246 bar and 495 to 600 °C. Over the range of conditions studied, the reaction is first order in hydrogen and independent of oxygen concentration, with a global activation energy of 372±34 kJ/mol. The kinetics of carbon monoxide oxidation, both via the direct oxidation and the water-gas shift pathways, have been re-investigated at 246 bar and 420 to 593 °C, over an extended range of concentrations and fuel equivalence ratios. Reaction of the carbon monoxide during preheating of the reactor feeds was found to be unimportant for the experimental conditions studied. Regression of the carbon monoxide oxidation data to a global rate form revealed a fractional-order dependence on oxygen concentration, which had not been observed earlier. The global reaction was first-order in carbon monoxide, with an activation energy of 134±32 kJ/mol.

2. Identification of induction times. Hydrogen oxidation in supercritical water possesses a distinct induction time, which is a strong indication of a free-radical mechanism. Observed induction times for stoichiometric hydrogen oxidation at 550 °C were about 2 s and increased slightly as concentrations were increased by a factor of three. Additional studies of carbon monoxide oxidation showed that the reaction, like hydrogen oxidation, possesses an induction time. The induction time for carbon

monoxide oxidation is the same or slightly shorter than that for hydrogen oxidation, and was independent of fuel equivalence ratio at 560 °C. These observations represent the first reported identification of an induction time in supercritical water oxidation kinetics.

3. Hydrogen formation by the water-gas shift pathway. Hydrogen formation during carbon monoxide oxidation is facilitated by the presence of oxygen, and is very slow in the absence of oxygen. Hydrogen formation is strongly dependent on the fuel equivalence ratio, with fuel-rich conditions favoring its formation. Higher water concentrations favor hydrogen formation, and the water-gas shift pathway is expected to be less important under supercritical water oxidation process conditions where water concentrations are lower.

4. Global reaction modeling. The presence of an induction time complicates, and partially invalidates, global reaction modeling efforts. Attempts to extend global models for single compounds to multi-step global models for more complex compounds (methane, methanol) were not completely successful. In the absence of validated elementary reaction models, however, global reaction models remain useful.

5. Effects of operating pressure (fluid density). The oxidation of hydrogen and carbon monoxide, at 550 and 570 °C, respectively, is strongly pressure (water-density) dependent over the range 118 to 263 bar, with higher pressures favoring higher oxidation rates. The effective order with respect to water for stoichiometric carbon monoxide oxidation at 570 °C was 1.7. This dependence suggests that a slight kinetic penalty is incurred for operation of the supercritical water oxidation process at lower pressures or lower water concentrations.

6. Effects of reactor surface. Limited studies of hydrogen and carbon monoxide oxidation in a packed reactor showed that the additional Inconel 625 surface area tends to inhibit oxidation, most likely through termination of free radicals. The inhibitory effect of the surface was not so severe, however, suggesting that tubular-reactor kinetic results at higher temperatures are representative of a homogeneous reaction pathway.

7. Elementary reaction modeling. An elementary reaction model for hydrogen oxidation, with certain modifications for high pressure, was largely successful in reproducing the experimentally observed kinetic behavior, including the global reaction orders and Arrhenius parameters and the effect of pressure. A similar model for carbon monoxide oxidation was somewhat less successful, exhibiting a higher overall activation energy than the data and lacking an oxygen dependence. High-temperature data under stoichiometric and fuel-rich feed conditions were reproduced well. However, results for fuel-lean conditions were not correctly predicted by the carbon monoxide model. The principal effects of the high pressure (water concentration) on the oxidation mechanism are threefold: a) the dissociation of hydrogen peroxide ($H_2O_2 \rightarrow OH + OH$) is at or near its high-pressure limit; b) the dissociation (recombination) of the hydroperoxyl radical ($H + O_2 \rightarrow HO_2$) approaches its high-pressure limit; and c) the rate of the $HO_2 + H_2O \rightarrow H_2O_2 + OH$ branching reaction is greatly accelerated by the high water concentrations (densities) present in supercritical water relative to typical gas-phase oxidation conditions. The majority of the pressure (density) dependence of the oxidation reactions is accounted for by the effect of the changing water concentration on the rate of the branching reaction. The models for hydrogen and carbon monoxide oxidation are both highly sensitive to the rate constant of the $HO_2 + H_2O \rightarrow H_2O_2 + OH$ reaction.

Experimental data could be reproduced with the assumed reaction network only if the value of this rate constant under supercritical water conditions is significantly lower than its most probable gas-phase value.

8. Glucose hydrolysis and oxidation. Glucose hydrolysis proceeds rapidly and completely in supercritical water. The products formed are diverse but also undergo hydrolysis; at 600 °C and a 6-second reactor residence time, glucose is converted completely to gases, even in the absence of oxygen. The presence of oxygen accelerates the destruction of the intermediate products, with no liquid-phase products found above 550 °C at a 6-second reactor residence time. The major, persistent intermediate products of glucose hydrolysis and oxidation are acetic acid, acetonylacetone (2,5-hexanedione), propenoic (acrylic) acid, and acetaldehyde in the liquid effluent, and carbon monoxide, methane, ethane, ethylene, and hydrogen in the gaseous effluent. Methane and hydrogen are present in the effluent at temperatures up to 600 °C at a reactor residence time of 6 seconds.

Chapter 11

Recommendations

1. Improvement of experimental capabilities. Modifications to the experimental apparatus are necessary to increase the range of operating conditions (concentrations, residence times, and possibly pressures) and to maximize the flexibility of the system. The range of accessible residence times needs to be extended to allow the determination of temporal concentration profiles over a wider range of temperatures and pressures. This may entail upgrading the flow capacity of the feed pump, improving the heating capability of the fluidized sand bath, and/or constructing new tubular reactors of varying sizes. In addition, a larger-diameter (lower surface area relative to fluid volume) reactor should be tested to confirm the lack of a surface influence on the kinetic data obtained in the present tubular reactor.

2. Concentration profile characterization. Temporal concentration profiles should be obtained for hydrogen oxidation under sub- and superstoichiometric conditions, and, if possible, for both carbon monoxide and hydrogen over an extended temperature range. These profiles should then be used for further validation of the elementary reaction models. Similar profiles should also be obtained for more complex compounds such as methane and methanol, since simple conversion data are insufficient for verification of elementary reaction models.

3. Expansion of elementary reaction modeling. With the existing model for carbon monoxide and hydrogen oxidation as a basis, and with additional concentration-profile data, elementary reaction models should be extended to more complex model compounds. A hierarchical modeling effort with proper validation is necessary.

4. Examination of specific elementary reactions. The high sensitivity of elementary reaction models to the rate constant of the $HO_2 + H_2O \rightarrow H_2O_2 + OH$ branching reaction necessitates a more detailed examination of the rate of this reaction. In particular, to the extent possible, efforts should be made to evaluate the influence on the rate constant (through the equilibrium constant) of intermolecular forces, including the possibility of HO_2–H_2O complex formation and highly non-ideal fugacity coefficients for HO_2. Experiments at relatively low pressures (e.g., 50 bar), in a high-pressure, gas-phase environment, could minimize non-ideal effects and provide validation of the fundamental high-pressure oxidation mechanism.

5. Extension of glucose oxidation data. More extensive glucose experiments are needed to quantify the global oxidation kinetics and the optimum treatment conditions for cellulosic wastes. Experiments under hydrolysis conditions and at subcritical temperatures and pressures may be desirable to identify (in terms of by-product formation) the implications of operating under conditions more typically encountered in wet-air oxidation. Positive identification of intermediates and products may require more sophisticated analytical techniques, such as liquid chromatography with mass spectrometry.

6. Studies of additional model compounds. The kinetics of oxidation of additional model compounds should be studied. In particular, acetic acid and acetaldehyde represent the next level of molecular complexity and are frequently found to be persistent intermediates. Compounds containing nitrogen, chlorine, sulfur, and phosphorus heteroatoms represent an important class of wastes whc oxidation kinetics in supercritical water have not been fully investigated or characterized; selection and examination of simple model compounds from this class are a logical step in the extension of the reaction kinetics database.

7. Exploration of hydrogen peroxide as an oxidant. Elementary reaction models have clearly demonstrated the important role of the hydroxyl radical in oxidation in supercritical water. Hydrogen peroxide added to the reactor feed, as a source of these radicals, has been shown to enhance oxidation. Careful experimental examination of this enhancement, with corresponding elementary reaction modeling, may provide important verification of the fundamental oxidation mechanisms.

Chapter 12

Appendices

12.1 Regression of Global Rate Parameters

Rate parameters are typically derived from experimental data through a least-squares regression of the k kinetic parameters ($\boldsymbol{p} = [p_1, p_2, \ldots, p_k]$). As in any regression, such a procedure requires the selection of an objective function f which is to be minimized. In general, the experimental data are a collection of m individual experiments, each of which yields n observable quantities (temperature, residence time, conversion, etc.). The data may thus be thought of as an $m \times n$ matrix of observables, $\boldsymbol{O}$, and the value of the objective function will depend on both the parameter values and the observables: $f = f(\boldsymbol{O};\boldsymbol{p})$. For a fixed set of experimental results, $\boldsymbol{O}$, the objective function depends only on the parameter values: $f = f(\boldsymbol{p})$.

The approach in this work, and in most work of this kind, has been to choose an objective function which is the sum (over the m experiments) of the squared differences between the predicted jth observable for the ith experiment, O'_{ij}, and the corresponding experimental value, O_{ij}. In other words,

$$f(\boldsymbol{O};\boldsymbol{p}) = \sum_{i=1}^{m} (O'_{ij} - O_{ij})^2 \qquad (12.1)$$

By nature, the O'_{ij} are a function of $\boldsymbol{p}$ and the other $n-1$ observables; this functional relationship is specific to the type of experiments being conducted. One should note that the objective function need not be based on a quantity that is directly observable (such as conversion), but could equally well be based on some quantity which is immediately calculable from experimental observables. For example, f might be based on the first-order rate constant, k^*, which is directly related to the experimental conversion X and residence time τ. This type of objective function is implicitly used when one performs a linear regression to a first-order Arrhenius plot; in that case, $f = \Sigma\ (\ln k^{*\prime}_i - \ln k^*_i)^2$, with $k^*_i = -\ln(1-X_i)/\tau_i$ (the "observable") and $k^{*\prime}_i = A \exp(-E_a/RT_i)$ (the predicted value, based on the parameter values A and E_a and the other observable, T).

The functional relationship among the observables in our system is assumed to be described by the plug-flow equation. In its most common and general form, the plug-flow equation is written as

$$\frac{\tau}{[C]_o} = \int_0^X \frac{dX}{R_c} \tag{12.2}$$

where τ is the reactor residence time, $[C]_o$ is the initial concentration of the organic compound C, X is the conversion of C, and R_c is the rate of disappearance of C, which typically depends on X. The reaction rate is usually given by the expression

$$R_c = k\,[C]^a\,[O_2]^b \tag{12.3}$$

with k, the rate constant, given by an Arrhenius rate form,

$$k = A \exp(-E_a/RT) \tag{12.4}$$

Since by definition $[C] = [C]_o(1-X)$, Equation 12.2 may be rewritten using Equation 12.3 as

$$k[C]_o^{a+b-1}\tau = \int_0^X \frac{dX}{(1-X)^a(F-SX)^b} \tag{12.5}$$

where it has been implicitly assumed that the rate of disappearance of oxygen is directly proportional to the rate of disappearance of C, with the proportionality given by the stoichiometric O_2/C ratio, S. Furthermore, the initial oxygen concentration is given by $F[C]_o$, where F is the feed O_2/C ratio. For the special case $a=1$, $b=0$, Equation 12.5 reduces to the well-known first-order expression, $k = -\ln(1-X)/\tau$. For arbitrary values of a and b, Equation 12.5 must be solved numerically.

One should note that, mathematically, Equation 12.5 is completely equivalent to the coupled ordinary differential equations (ODEs)

$$\begin{aligned} d[C]/dt &= -k\,[C]^a\,[O_2]^b \\ d[O_2]/dt &= -S\,d[C]/dt \end{aligned} \tag{12.6}$$

with the initial conditions $[C](t=0) = [C]_o$, $[O_2](t=0) = F\,[C]_o$. Equation 12.6 can be integrated to give $[C](t=\tau)$, or X. Consequently, both Equation 12.5 and Equation 12.6 describe the relationship among the experimental variables in a plug-flow reactor, and either form can be used to establish the objective function f for regression purposes. The statement that data have been regressed to the plug-flow equation does not automatically distinguish between the integral (Equation 12.5) and differential (Equation 12.6) forms of

the plug-flow equation, and more information is required to completely characterize the regression that has been performed.

Operationally, the selection of Equation 12.5 or 12.6 will affect the nature of the objective function. The available experimental variables in this work are temperature (T), inlet organic concentration ($[C]_o$), O_2/C feed ratio (F) or inlet oxygen concentration ($[O_2]_o$), residence time (τ), and conversion (X). Physically, X is the dependent variable, with its value set by the choice of the other variables: $X = X(T, [C]_o, F, \tau)$. The form of Equation 12.5, however, suggests that for the integral form of the plug-flow equation X cannot be used as a dependent (predicted) variable. More specifically, the right-hand side of Equation 12.5 cannot be evaluated without *a priori* knowledge of both X and F (S is set by the stoichiometry of the reaction and is not strictly a variable). Consequently, the use of Equation 12.5 precludes the use of X as the predicted variable, and one of the variables T (through k), $[C]_o$, or τ must instead be chosen. On the other hand, selection of Equation 12.6 requires that X be the predicted variable, since all other quantities (T, $[C]_o$, F, τ) must be known to solve the coupled ODEs.

Equation 12.6 might be regarded as the preferable functional relationship, since it more accurately reflects the physical situation. However, solution of the ODEs requires more intensive computation than the numerical integration of Equation 12.5. Also, it is not clear that X is the preferable predicted variable for the regression. The objective function in Equation 12.1 seeks to minimize the difference between predicted and observed values, without regard to the absolute magnitude of the values themselves. If all of the values are of the same order of magnitude, there is no problem in this approach. On the other hand, if the values vary over an order magnitude or more, this type of objective function can yield skewed results. For example, experimental conversions can vary from roughly 5% (0.05) to 95% (0.95), or more than a factor of ten. The objective

function of Equation 12.1 considers a difference of 0.02 (2%) between the predicted and observed conversions to be no worse in either case. Depending on the ultimate use of the regression, however, a 2% difference in conversion at 5% conversion can be a much more serious error than a 2% difference at, say, 80% conversion.

Consider the first-order rate constant, $k^* = -\ln(1-X)/\tau$. Experimental data are often presented in the form of an Arrhenius plot, with $\ln k^*$ plotted against $1/T$; the best-fit regressed rate expression should presumably give a straight line through the data. The fractional error in k^* ($\partial \ln k^*$) due to error in X (∂X) is given by

$$\frac{\partial \ln k^*}{\partial X} = \frac{-1}{(1-X)\ln(1-X)} \tag{12.7}$$

For $X = 0.80$ (80%), an error of 0.02 (2%) in X gives an error of about 6% in k^*; on the other hand, for $X = 0.05$ (5%), an error of 0.02 gives an error of over 40% in k^*! If low-conversion data tend to occur at lower temperatures, as is frequently the case owing to experimental limitations, choosing X as the predicted variable can effectively weight higher-temperature (higher-conversion) data more heavily, potentially yielding a rate expression which, on an Arrhenius plot, does not pass through all the data. In the case of a first-order reaction, this problem can be overcome by choosing the first-order rate constant as the predicted variable; for more complicated cases, though, the problem remains. One technique to correct the problem is to introduce a weighting in Equation 12.1. Traditional weightings (Héberger *et al.*, 1987) use $(1/\sigma_i)^2$, with σ_i the standard deviation (error) of the measured variables (in this case, X_i). In the case of conversion, the absolute error in the measured value is likely to be the same (or larger) at low conversions as at high conversions, and this type of weighting does not improve the fit. Rather, a weighting of $(1/X_i)^2$ may be more appropriate, such that the *relative*

(normalized) errors between the predicted and observed values are minimized. The non-linear regression routine used in this work (Press *et al.*, 1986) did not incorporate weighting, however, and the normalization approach was not tested.

The problem of improper weighting in the objective function can be overcome by choosing a different predicted variable, i.e., using Equation 12.5 as the plug-flow functional relationship. The choice of variables is thus T (through k), $[C]_o$, or τ. Of these, τ is known to only limited precision, and is thus not likely a sufficiently sensitive variable for minimization, and $[C]_o$, while known to greater precision, suffers from the same problem as conversion, in that it can vary over an order of magnitude and the least-squares minimization cannot account for relative errors. Temperature, however, is known to relatively high precision, and the temperature varies over a relatively small range in most sets of kinetic experiments. Even over our entire operating range, from 400 to 700 °C, the temperature varies by only a factor of about 1.8. As a result, a given difference between experimental and predicted temperature will be equivalent to roughly the same relative error, regardless of the actual value of the temperature; the differences are effectively normalized. The plug-flow regressions performed in Chapters 5 and 6 thus used the functional relationship of Equation 12.5, with T the predicted variable: $T = f([C]_o, F, X, \tau)$. For the regressions presented in Chapter 7, where X for the reaction of interest was not known precisely because of the complicating effect of a parallel reaction pathway, it was necessary to use X as the predicted variable.

The choice of Equation 12.5 vs. 12.6 may also affect the values of the regressed parameters, as well as the estimates of standard errors for the regressed parameter values. Parameter errors are typically estimated by means of estimates of the curvature in the objective function at the minimum in the function: $\partial^2 f(\boldsymbol{p}_o)/\partial p_i^2$, with $\boldsymbol{p}_o$ the optimum parameter values. The objective function is usually approximated by a Taylor-series

expansion about $\boldsymbol{p}_o$, with accurate estimates of parameter errors relying on the objective function behaving quadratically in the vicinity of the minimum (Press *et al.*, 1986; Draper and Smith, 1981). Even though Equations 12.5 and 12.6 are mathematically equivalent representations of the plug-flow relationship, the shape (curvature) of the objective function will likely be different for the two functional forms, with the minimum in f lying in somewhat different positions (different values of $\boldsymbol{p}_o$) with somewhat different local curvatures. Furthermore, the correlation between parameters (related to $\partial^2 f(\boldsymbol{p}_o)/\partial p_i \partial p_j$) may also vary with the functional form. Ideally, regression using either Equation 12.5 or 12.6 should give virtually identical results; realistically, both the nature of the experimental data and the implicit weighting discussed above will produce some variation in the regression results. A clear example is shown by the methanol oxidation data analyzed by Tester *et al.* (1992). In that paper, a full, four-parameter, non-linear regression was performed, using Equation 12.5 as the (integral) form of the plug-flow equation with T the predicted variable. The resulting rate expression was

$$-\frac{d[CH_3OH]}{dt} = 10^{28.8\pm10.5} \exp(-447.\pm125./RT)[CH_3OH]^{0.89\pm0.69}[O_2]^{0.12\pm0.66} \quad (12.8)$$

where the activation energy is in kJ/mol, the concentrations in mol/L, and the stated errors are at the 95% confidence level. Non-linear regression of the same kinetic data, but with Equation 12.6 as the (differential) form of the plug-flow equation and with X the predicted variable, gives for the rate expression

$$-\frac{d[CH_3OH]}{dt} = 10^{29.2\pm26.3} \exp(-450.\pm334./RT)[CH_3OH]^{1.05\pm1.34}[O_2]^{0.02\pm0.80} \quad (12.9)$$

with the units and errors as before. Clearly there is significant error associated with the parameter estimations in both cases, but the differential form of the plug-flow equation results in much larger estimates of parameter error (by a factor of 2 to 3) than the integral form, even though both functional forms give optimal parameter values that are in quite close agreement.

As a final note, the value for S (the stoichiometric ratio) in Equations 12.5 and 12.6 deserves mention. For a "simple" reactive system such as hydrogen/oxygen, where there are no stable intermediates, the appropriate value for S (1/2) is unambiguous. For more complex systems, such as methane/oxygen or methanol/oxygen, the stoichiometric ratio is typically defined by the amount of oxygen needed to completely convert the organic to CO_2 and H_2O; for methane, $S = 2$ by this definition; for methanol, $S = 1.5$. Experimentally, methane and methanol oxidation are observed to proceed through CO, which is subsequently oxidized to CO_2 (Webley and Tester, 1991; Tester *et al.*, 1992); as a result, it may be possible to oxidize all of the methane or methanol without completely converting them to CO_2. Using $S = 2$ in Equation 12.5 or 12.6 does not acknowledge this fact, and may lead to incorrect predictions of O_2-limited organic conversions when in fact it is the carbon monoxide conversion that is O_2-limited. Thus the appropriate value for S is not that for complete conversion of the organic to CO_2, but rather that for complete conversion to CO and H_2O (for methane and methanol, small amounts of hydrogen are also formed, but the hydrogen concentrations are sufficiently small that the contribution of hydrogen oxidation to the oxygen demand may be neglected). For even more complicated systems, where the number and/or identities of the stable intermediates may not be known, Thornton and Savage (1990) have correctly pointed out that it is not possible to choose a value for S *a priori*, and experiments must be conducted under

excess oxygen conditions, where the oxygen concentration remains essentially constant during the experiments and the kinetic results are independent of S.

12.2 Pressure Dependence of H_2O_2 Dissociation

Like most unimolecular dissociation reactions, the decomposition of hydrogen peroxide can be represented as

$$H_2O_2 (+ M) \rightarrow OH + OH (+ M) \tag{12.10}$$

and exhibits an experimental dependence on pressure under certain conditions. At low pressures, collisional excitation of the H_2O_2 molecules by third-body species (M) is slow and the excitation process limits the decomposition; under such conditions, the decomposition reaction is first-order in both H_2O_2 and M, such that the apparent first-order decomposition rate constant increases linearly with pressure or, equivalently, the third-body concentration [M] (the low-pressure limit). At sufficiently high pressures, the excitation process becomes faster than the intrinsic (transition-state theory) decomposition process for the activated complex, and the reaction becomes first-order in H_2O_2 alone and independent of pressure (the high-pressure limit). The pressure dependence of this type of reaction between these two limiting cases is a complex function of molecular and collisional properties, and has been the subject of much study. The most commonly used theoretical framework for this pressure dependence is the Rice-Ramsperger-Kassel-Marcus (RRKM) theory (Robinson and Holbrook, 1972; Gilbert and Smith, 1990).

Elementary reaction modeling of supercritical water oxidation, both in this work (Chapters 6 and 8) and in earlier studies (Webley and Tester, 1991; Schmitt *et al.*, 1991), shows the decomposition of hydrogen peroxide to be an important step in the oxidation

mechanism, with model predictions sensitive to the value of the decomposition rate constant. Extrapolation of the low-pressure-limit (pressure-dependent) rate constant for this reaction (Warnatz, 1984; Tsang and Hampson, 1986) to SCWO conditions gives an unrealistic value of the rate constant that is many times higher than the high-pressure limit. Consequently, in earlier studies researchers have set the value of this rate constant to its high-pressure limit (Webley and Tester, 1991; Schmitt *et al.*, 1991). The validity of this assumption has never been tested; the breadth of the falloff curve might be such that the high-pressure limit is not reached at SCWO conditions. Furthermore, some of our experiments have been conducted at pressures as low as half the typical SCWO operating pressure, and the high-pressure limit, while possibly achieved at the higher operating pressures of approximately 250 bar, may not be reached at the lower pressures studied. Detailed RRKM calculations were thus undertaken to describe the full pressure dependence of the hydrogen peroxide dissociation rate constant.

Parameters used for the RRKM calculations are given in Table 12.1. All calculations were performed using the UNIMOL collection of programs (Gilbert *et al.*, 1990). The majority of the parameters are taken from two earlier modeling studies (Wardlaw and Marcus, 1985; Brouwer *et al.*, 1987) which employed the statistical adiabatic channel model (SACM), an alternative to RRKM theory for barrierless fission/recombination reactions which does not require detailed characterization of the transition state (Quack and Troe, 1974; Troe, 1981). The geometry of the H_2O_2 reactant was taken from Wardlaw and Marcus (1985), as was the threshold energy for dissociation. The value for the threshold energy given by Wardlaw and Marcus (49.5 kcal/mol) is virtually identical to that (49.6 kcal/mol) used by Brouwer *et al.* (1987). Vibrational frequencies were taken from Brouwer *et al.* For these calculations, the OH

Parameter	Reactant HOOH	Transition State HO···OH
r_{H-O}, Å	0.965[1]	0.971[1]
r_{O-O}, Å	1.462[1]	4.1[2]
∠HOO	100°[1]	180°
Dihedral Angle	120°[1]	—
Symmetry Number	1	2
Threshold (Dissociation) Energy, kcal/mol	49.5[1]	—
Rotational Constants, cm^{-1} (Symmetry, Dimension)		
$B_{\text{inactive external}}$[3]	0.8566 (1,2)	0.1103 (2,2)
$B_{\text{active external}}$[3]	10.114 (1,1)	—
$B_{\text{active internal}}$[4]	—	18.871 (1,2) × 2
β_{HO-OH} (Morse Parameter), $Å^{-1}$	—	2.425[1,4]
Vibrational Frequencies, cm^{-1}		
O–H stretch[4]	3599	3735 × 2
O–H stretch[4]	3611	
OOH bend[4]	1387	
OOH bend[4]	1266	
O–O stretch[4]	875	
Torsion (hindered internal rotation)	150[2]	
Lennard-Jones Parameters[5]		
σ, Å	4.196	—
ε/k, K	289.3	—

Sources:
[1]Wardlaw and Marcus (1985)
[2]Adjusted; see text for details.
[3]Calculated from molecular geometry using program GEOM (Gilbert *et al.*, 1990).
[4]Brouwer *et al.* (1987)
[5]Reid *et al.* (1987)

Table 12.1 RRKM Parameters for $H_2O_2 + M \rightarrow OH + OH + M$.

moieties in the transition state (activated complex) were assumed to have the same properties (O–H separation, vibrational frequency, moment of inertia/rotational constant) as the free hydroxyl radical, as given by Brouwer *et al.* (1987). The transition-state configuration was taken to be linear, with the OOH bend and HOOH torsion frequencies in the reactant being converted to rotation of the OH moieties in the transition state. For O–O separations greater than about 3.9 Å, these two-dimensional OH rotations are unhindered. The O–O stretch in the reactant is the reaction coordinate and that vibrational frequency disappears in the activated complex. The reactant, with the geometry given by Wardlaw and Marcus (1985), is not quite symmetric and its symmetry number was taken to be 1; other studies have used the approximate symmetry number 2 (e.g., Brouwer *et al.*, 1987). The linear activated complex has a symmetry number of 2.

The O–O separation in the transition state was determined by canonical variation (Gilbert and Smith, 1990). That is, the O–O distance was varied to find the separation which gave the minimum calculated high-pressure rate coefficient. This O–O separation corresponds to a maximum on the potential energy surface between the OH moieties, and is determined by the balance between the natural HO–OH attractive potential and the effective repulsive potential created by the centrifugal force of the rotation of the activated complex. Both Wardlaw and Marcus (1985) and Brouwer *et al.* (1987) described the attractive potential using a Morse potential function; the two studies used slightly different values for the Morse parameter β, and a median value of 2.425 $Å^{-1}$ was chosen for use here. For each variation in the O–O separation, moments of inertia (rotational constants) for the activated complex were calculated using the program GEOM (Gilbert *et al.*, 1990). Rotational constants for the reactant were calculated in the same way using the fixed geometry of Wardlaw and Marcus (1985). Two of the external rotations of the reactant were taken to be inactive (unable to contribute energy to the

reaction), while the third rotation, roughly about the O–O axis, was considered active (Gilbert and Smith, 1990). The reactant had no internal rotations, since the hindered relative rotation of the OH groups was taken to be a torsional frequency. The external rotations of the linear transition state were considered inactive, with the internal rotations of the OH moieties active. Canonical variation of the O–O separation revealed a shallow minimum in the high-pressure rate coefficient for $r_{O-O} = 4.1$ Å, and this distance was used to determine the final transition-state configuration. This separation is sufficiently large that the two internal OH rotations are completed unhindered.

The final step in setting the RRKM parameters was the comparison of the predicted high-pressure Arrhenius parameters for dissociation, $A_{diss,\infty}$ and $E_{diss,\infty}$, with experimental values. Unfortunately, high-pressure Arrhenius parameters for H_2O_2 dissociation have never been measured experimentally; however, Brouwer *et al.* (1987) deduced the temperature dependence of the recombination rate constant on the basis of SACM modeling and extrapolation of the experimental data of Zellner *et al.* (1988) for the recombination reaction. The derived rate expression for the high-pressure-limit recombination rate constant, in the temperature range 200–1500 K, was

$$k_{rec,\infty} = 10^{-10.82}(T/300)^{-0.37} \text{ cm}^3\text{molecule}^{-1}\text{s}^{-1} \qquad (12.11)$$

with T in Kelvins (Brouwer *et al.*, 1987). Using species thermodynamics for the equilibrium constant from the JANAF Thermochemical Tables (Chase *et al.*, 1985), the dissociation rate constant can be calculated from the recombination rate constant by microscopic reversibility. The dissociation equilibrium constant in pressure units (bar), for 1-bar, ideal-gas standard states, can be expressed as

$$\log K_{p,diss} = 7.3277 - 11284./T \tag{12.12}$$

and can be converted to concentration units by the relationship

$$K_{c,diss} = K_{p,diss}(RT)^{-1} \tag{12.13}$$

In Arrhenius form, the dissociation rate constant is then given by

$$k_{diss,\infty} = k_{rec,\infty}K_{c,diss} = 10^{14.93}\exp(-50.23/RT) \ \ s^{-1} \tag{12.14}$$

such that the high-pressure dissociation Arrhenius parameters are $A_{diss,\infty} = 10^{14.93}$ s^{-1}, $E_{diss,\infty} = 50.23$ kcal/mol. To match $A_{diss,\infty}$, the value of the torsional frequency in the reactant was changed to 150 cm^{-1}, from the value of 243 cm^{-1} given by Wardlaw and Marcus (1985). An alternative approach would have been to treat the torsional motion as a hindered rotation. With the modified value for the torsional frequency, the RRKM parameters in Table 12.1 reproduced the high-pressure dissociation Arrhenius parameters quite well, with the calculations giving $A_{diss,\infty} = 10^{15.02}$ s^{-1}, $E_{diss,\infty} = 50.41$ kcal/mol.

Having established appropriate RRKM parameters, full pressure-dependence (falloff) calculations were performed. Lennard-Jones parameters for the reactant, as well as for the bath gases M = N_2 (σ = 3.798 Å, ε/k = 71.4 K) and M = H_2O (σ = 2.641 Å, ε/k = 809.1 K), were obtained from Reid *et al.* (1987). Binary Lennard-Jones interaction parameters were calculated with the standard mixing rules, $\sigma_{ij} = (\sigma_i + \sigma_j)/2$, $\varepsilon_{ij} = (\varepsilon_i\varepsilon_j)^{1/2}$, and were used in the calculation of the reactant-bath gas collision rate (Troe, 1979). For the theoretical calculations with M = N_2, a weak-collision model has been used, with collisional energy transfer between reactant and bath gas described by the "exponential down" model (Gilbert and Smith, 1990). The single parameter in this model is the

average downward collisional energy transferred, $\langle \Delta E \rangle_{down}$, which was treated as adjustable in order to fit the experimental low-pressure data. The results of the calculations at 298 K are shown in Figure 12.1, where predictions for M = N_2 are compared to the experimental data of Zellner *et al.* (1988), which have been converted from recombination rate constants to dissociation rate constants using Equations 12.12 through 12.14. The theoretical predictions are clearly in good agreement with the experimental data, although it is apparent that conclusions regarding the high-pressure region of the rate constant necessarily entail a significant amount of extrapolation.

The chosen value for $\langle \Delta E \rangle_{down}$ for the M = N_2 data in Figure 12.1 was 300 cm^{-1} (~0.9 kcal/mol), which gave for the low-pressure rate constant ($k_{diss,o}$) a value of 3.3×10^{-18} $cm^3 mol^{-1} s^{-1}$, in reasonable agreement with the experimental value (converted from the measured recombination rate constant) of $(2.9^{+0.6}_{-1.1}) \times 10^{-18}$ $cm^3 mol^{-1} s^{-1}$ (Zellner *et al.*, 1988). The collisional efficiency β_c for a bath gas is defined as the ratio between the weak-collision low-pressure rate coefficient k_o and the corresponding strong-collision rate coefficient k_o^{SC}, i.e. (Troe, 1977a):

$$\beta_c \equiv k_o / k_o^{SC} \tag{12.15}$$

The chosen value of $\langle \Delta E \rangle_{down}$ gives a value for β_c for N_2 of 0.44, in close agreement with the value of 0.43 derived by Zellner *et al.* (1988).

Predictions for M = H_2O at 298 K are also shown in Figure 12.1. For these calculations, the strong collision assumption was used, such that $\beta_c = 1$, since water is known to have a high collisional efficiency. Thus, at any pressure below the high limiting value, the rate constant for M = H_2O is higher than that for M = N_2; in particular, for the low-pressure rate constant, calculations gave $k_o^{SC}(M = H_2O) = 9.9 \times 10^{-18}$

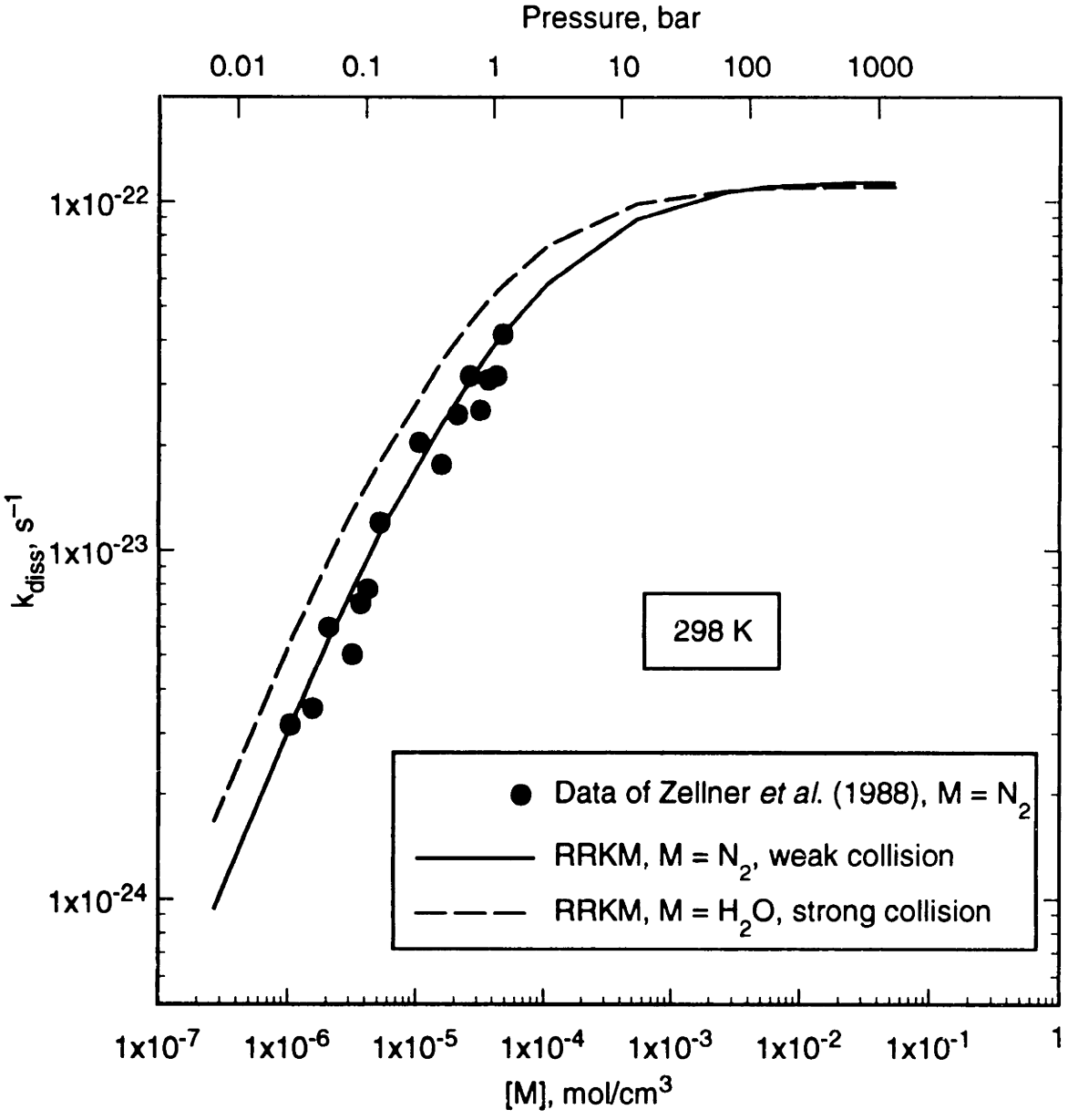

Figure 12.1 Comparison of Experimental Data and RRKM Predictions for Pressure Dependence of H_2O_2 Dissociation at 298 K.

$cm^3mol^{-1}s^{-1}$, approximately three times the value for M = N_2. On the other hand, Zellner *et al.* (1988), on the basis of experiments in which water was present at low levels, derived a value at 298 K for $k_o(H_2O)$ of $(1.7^{+0.6}_{-0.8}) \times 10^{-17}$ $cm^3mol^{-1}s^{-1}$, a factor of 5.7 higher than the experimental value for M = N_2 and almost twice the present calculated value. Additional studies (Hoare *et al.*, 1959; Baldwin and Brattan, 1960) have reported similar values (4.3 to 6.0) for the relative collisional efficiencies, i.e., $k_o(H_2O)/k_o(N_2)$. Zellner *et al.* also performed a strong-collision calculation, and similarly found that the strong-collision result, using a Lennard-Jones collision frequency, was a factor of 1.7 lower than the experimental value for M = H_2O, implying a non-physical collisional efficiency for water greater than unity. The observation of an experimental rate coefficient for M = H_2O which apparently exceeds (by a considerable amount) the Lennard-Jones-based strong-collision limit has previously been made by Hsu *et al.* (1987) for the reaction H + O_2 + M → HO_2 + M. In that study, low-pressure experimental results were a factor of 2.6 higher than the strong-collision rate, calculated using slightly different Lennard-Jones parameters for water than those used here. There is thus some question regarding the ability of the Lennard-Jones collision rate to accurately predict the strong-collision rate for M = H_2O. Given the complex intermolecular potential interactions of the water molecule, it is not surprising that the simplified Lennard-Jones potential is not able to capture the true collisional behavior. One should thus consider the strong-collision calculations for M = H_2O to be only an approximation, most likely providing a low estimate of the actual rate coefficient.

Figure 12.2 shows pressure-dependence predictions for H_2O_2 dissociation at three temperatures relevant to the current experimental study; rate constants have been normalized with respect to the high-pressure limit to better illustrate the approach to that limit. For simplicity, in these calculations the strong-collision assumption has been

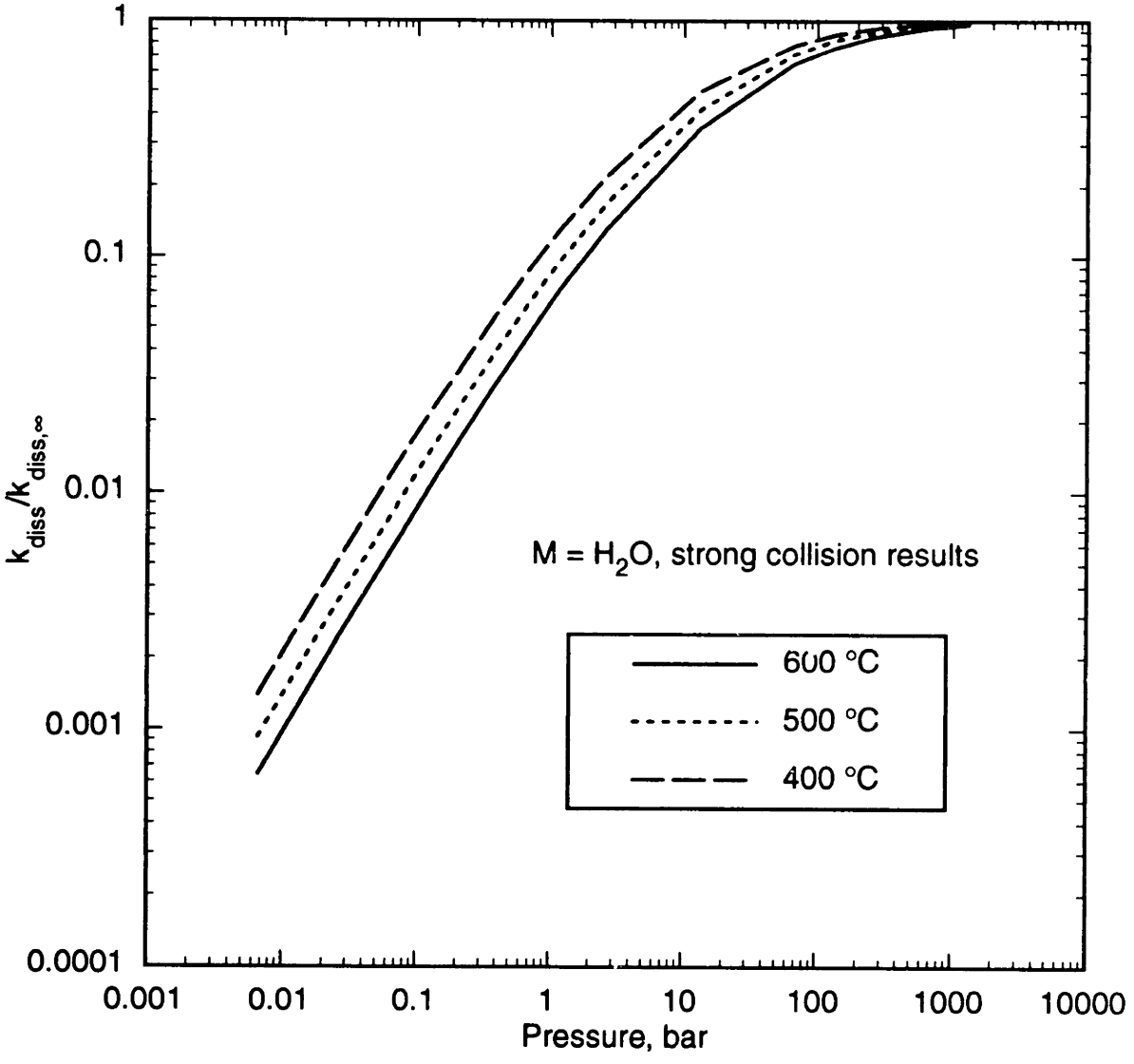

Figure 12.2 Predicted Pressure and Temperature Dependence of H_2O_2 Dissociation.

employed. Figure 12.2 shows that the approach to the high-pressure limit occurs more rapidly at lower temperatures, since the thermodynamic (high-pressure) rate coefficient increases more rapidly with temperature than the rate of the collisional activation process. Nevertheless, the nearness of the rate constant to the high-pressure value is apparent for pressures of 200 to 300 bar and higher, implying that the use of the high-pressure limit rate constant is reasonable under those conditions. The approach is likely even closer than indicated by Figure 12.2, owing to the tendency of the Lennard-Jones collision frequency to underestimate rate constants for M = H_2O.

Additional calculations were performed to evaluate the effect of "realistic" collisional energy transfer on the predictions of Figure 12.2. The strong-collision assumption, while apparently good for water at room temperature, may fail at higher temperatures. In particular, the collisional efficiency typically decreases with increasing temperature. Reasons for this behavior can be found in the alternative approximate expression for β_c (Troe, 1977b; Tardy and Rabinovitch, 1977)

$$\frac{\beta_c}{1-\sqrt{\beta_c}} \approx \frac{-\langle \Delta E \rangle}{F_E RT} \tag{12.16}$$

where $\langle \Delta E \rangle$ is the average *overall* energy transferred (both upward and downward) and F_E is a factor close to unity related to the energy dependence of the density of states of the reactant molecule (Troe, 1977b). $\langle \Delta E \rangle$ is negative because the net energy transfer is downward; hence $\langle \Delta E \rangle_{down} > -\langle \Delta E \rangle$, and the two quantities are related by the approximate expression (Tardy and Rabinovitch, 1977; Hippler *et al.*, 1983)

$$-\langle \Delta E \rangle \approx \frac{\langle \Delta E \rangle_{down}^2}{\langle \Delta E \rangle_{down} + RT} \tag{12.17}$$

Experimental studies have shown $-\langle\Delta E\rangle$ to have a relatively weak temperature dependence (Tardy and Rabinovitch, 1977), and Equation 12.16 indicates that β_c should thus decrease markedly with increasing temperature. Zellner *et al.* (1988) used Equation 12.16 and their experimental data to derive a value of 3.7 kJ/mol (~300 cm^{-1}) for $-\langle\Delta E\rangle$ for N_2 at 298 K. Water, a more effective collision partner, will have a larger (but finite) value for $-\langle\Delta E\rangle$; note that the strong-collision assumption ($\beta_c = 1$) implies that $-\langle\Delta E\rangle$ is infinite. Experimental studies of collisional energy transfer confirm the effectiveness of H_2O, but are in disagreement regarding the value of $-\langle\Delta E\rangle$ for H_2O relative to N_2. For example, studies of complex molecules such as toluene (Hippler *et al.*, 1983) and azulene (Hippler *et al.*, 1985) have found $-\langle\Delta E\rangle$ for H_2O to be a factor of 2 to 3 larger than that for N_2, while a study of CS_2 (Dove *et al.*, 1985) found $-\langle\Delta E\rangle$ for H_2O to be almost an order of magnitude larger than for N_2.

Given the uncertainty in the relative amounts of energy transferred, two cases were chosen, one in which $-\langle\Delta E\rangle$ for H_2O was 3000 cm^{-1} (~36 kJ/mol), ten times that for N_2, the second in which it was five times (1500 cm^{-1}). These $-\langle\Delta E\rangle$ values were taken to be constant from 298 K to temperatures of interest here, and were converted using Equation 12.17 to $\langle\Delta E\rangle_{down}$ values for use in RRKM calculations. The results for 600 °C are shown in Figure 12.3, where they are compared to the strong-collision results. Clearly the use of more "realistic" values for collisional energy transfer does not have a dramatic effect on the predicted pressure dependence, although use of a weak-collision model does entail a significantly higher computational burden since the master equation must then be solved (Gilbert and Smith, 1990). The experimental collisional energy transfer data thus strongly suggest that water as a third body quite closely approaches the strong-collision limit, even at elevated temperatures. The error introduced by the strong-collision assumption is certainly small relative to other errors, such as the Lennard-Jones

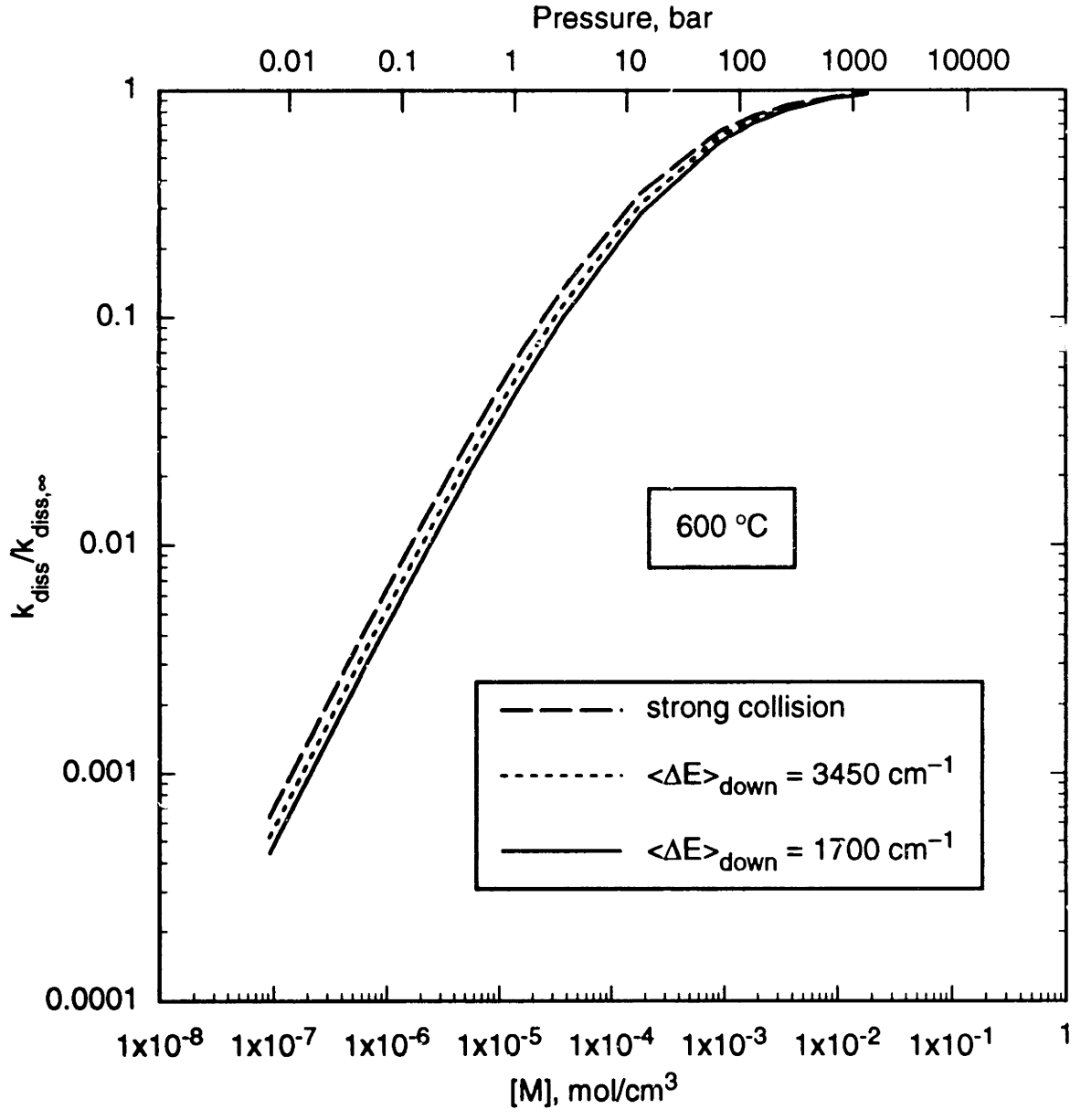

Figure 12.3 Effect of Collisional Energy Transfer on Pressure Dependence of H_2O_2 Dissociation.

collisional rate, and a more detailed treatment of collisional energy transfer is therefore not warranted.

One should also note that pressures and third-body concentrations [M] in Figures 12.1 and 12.3 are related by the ideal-gas law: [M] = P/RT. Strictly speaking, however, at relevant SCWO temperatures (400 to 700 °C) the ideal-gas law (especially for water) begins to fail for pressures of about 100 bar, and becomes increasingly worse at higher pressures and at lower temperatures. Under those conditions, the compressibility factor of the medium (bath gas), Z, must be used to accurately estimate [M], i.e., [M] = P/ZRT. Alternatively, [M] may be defined with respect to an effective ideal-gas pressure, P_{eff}, such that the ideal-gas relationship ([M] = P_{eff}/RT) still holds; P_{eff} is then given by $P_{eff} = P/Z$. For the "standard" operating pressure in this work, 246 bar, P_{eff} varies from almost 500 bar at 400 °C to about 265 bar at 700 °C (Haar *et al.*, 1984), decreasing with increasing temperature as water becomes less non-ideal and more like an ideal gas. The non-ideal relationship between [M] and P accelerates the approach of the rate constant (with respect to pressure) to the high-pressure limit, particularly at lower temperatures, and the higher effective pressure must be taken into account when locating the appropriate point on the falloff curves (Figure 12.2).

With proper accounting for the non-ideality in the P-[M] relationship, the calculated rate constant for dissociation of hydrogen peroxide in supercritical water at 246 bar and 400 to 600 °C can be represented quite accurately by the expression

$$k_{diss}\ (s^{-1}) = 10^{14.89} \exp(-49.9/RT) \qquad (12.18)$$

with the activation energy in kcal/mol. Comparison with Equation 12.14 shows that the calculated, pressure-dependent rate constant is very close to its high-pressure limit.

Calculated rate constant values are within about 10% of the high-pressure value, over the temperature range of interest, for effective pressures of 250 bar or higher. The assumption that the hydrogen peroxide dissociation is at its high-pressure limit thus appears to be valid under those conditions. For lower effective pressures, however, the deviation from the high-pressure limit becomes significant, with the rate constant decreasing by 20 to 30% or more for effective pressures of 150 bar or less. For lower operating pressures, then, the high-pressure limit assumption for H_2O_2 dissociation is weak, and a more detailed examination of the falloff behavior is required owing to the sensitivity of elementary reaction models to the value of this rate constant. Falloff curves of the type shown in Figure 12.2 were thus calculated at 550 and 570 °C for use in modeling the pressure dependences of hydrogen and carbon monoxide oxidation (Sections 6.5 and 8.3).

12.3 Pressure Dependence of HO_2 Dissociation/Recombination

Like the dissociation of hydrogen peroxide, the recombination of a hydrogen atom and molecular oxygen to form the hydroperoxyl radical

$$H + O_2 (+ M) \rightarrow HO_2 (+ M) \qquad (12.19)$$

exhibits an experimental pressure dependence which can be described by RRKM theory. Unlike hydrogen peroxide dissociation, hydroperoxyl formation by recombination has received relatively little attention from SCWO modelers, since models are not necessarily sensitive to the value of the rate constant (see Section 6.4). On the other hand, the model for CO oxidation in supercritical water was found to be highly sensitive to the recombination rate constant, in that the predicted molecular hydrogen concentration was directly related to the rate constant (see Section 8.2).

In the gas phase, the hydroperoxyl recombination reaction is typically treated as being in the low-pressure (third-order) limit, even at pressures of up to several atmospheres. This assumption was validated by a recent study of the reaction at pressures as high as 200 bar (Cobos *et al.*, 1985); the recombination appeared to be close to the low-pressure limit over a wide range of pressures, and the authors estimated that the high-pressure limit would not be approached except for pressures over 2000 bar. The data and modeling of Cobos *et al.* do however suggest that the recombination reaction is likely not still in the low-pressure limit at SCWO pressures (several hundred bar), but rather that the rate constant lies in the intermediate falloff regime at those pressures. Estimations of the extent of the falloff behavior of the hydroperoxyl recombination reaction at SCWO pressures were thus made using a semi-empirical model with parameters given by Cobos *et al.* (1985).

Troe and co-workers (Troe, 1977a,b,1979,1983; Gilbert *et al.*, 1983) have developed a formalism for describing the pressure dependence of unimolecular reactions in terms of "reduced falloff curves." In this formalism, the recombination (or dissociation) rate constant is expressed relative to the high-pressure limit as

$$\frac{k_{rec}}{k_{rec,\infty}} = \left(\frac{P_r}{1+P_r}\right) F^{SC} F^{WC} \tag{12.20}$$

where P_r is a "reduced pressure," defined as the ratio of the low-pressure-limit rate constant to the high-pressure-limit rate constant (Troe, 1983):

$$P_r \equiv k_{rec,o}/k_{rec,\infty} \tag{12.21}$$

and F^{SC} and F^{WC} are "broadening factors" which reflect the contributions of strong and weak collisions to the shape of the falloff curve. Without F^{SC} and F^{WC}, Equation 12.20 is the simplified Lindemann-Hinshelwood model for unimolecular reactions. F^{SC} and F^{WC} incorporate more complex effects, and can be written as (Troe, 1979)

$$\log F^{SC}F^{WC} \approx \left[1+\left(\frac{\log P_r}{N}\right)^2\right]^{-1} \log F_{cent} \tag{12.22}$$

with N given by

$$N \approx 0.75 - 1.27 \log F_{cent} \tag{12.23}$$

F_{cent}, the "center broadening factor," can be factored into strong- and weak-collision contributions

$$F_{cent} = F_{cent}^{SC} F_{cent}^{WC} \tag{12.24}$$

with the weak-collision contribution calculated straightforwardly from the collisional efficiency of the particular bath gas (Troe, 1979):

$$\log F_{cent}^{WC} \approx 0.14 \log \beta_c \tag{12.25}$$

The strong-collision factor F_{cent}^{SC} is a more complicated empirical function (given by Troe (1979)) of S_K and B_K, the so-called Kassel parameters, which are related to the properties of the activated complex. S_K is related to the activated complex partition function $Q^{\ddagger}$

$$S_K = 1 - \frac{1}{T}\frac{\partial \ln Q^{\ddagger}}{\partial(1/T)} \tag{12.26}$$

and hence, through transition-state theory, to the high-pressure-limit rate constant (Troe, 1983; Cobos *et al.*, 1985):

$$Q^{\ddagger} = \frac{h}{kT} k_{diss,\infty} Q_{vib} Q_{rot} \exp(E_o / kT) \tag{12.27}$$

where Q_{vib} and Q_{rot} are the vibrational and rotational partition functions of the dissociating molecule (HO_2) and E_o is the dissociation energy at 0 K. B_K is then related to S_K by

$$B_K = \frac{S_K - 1}{s - 1}\left(\frac{E_o + a(E_o)E_z}{kT}\right) \tag{12.28}$$

with s the number of oscillators in the reactant (3 for HO_2), $a(E_o)$ the Whitten-Rabinovitch correction for the density of states (Troe, 1977b), and E_z the zero-point energy for the s oscillators (Troe, 1979).

Equations 12.20 and 12.22 through 12.28 contain a variety of approximations, simplifications, and empiricisms; the original sources should be consulted for details. Nevertheless, the information required to use the formalism is similar to that required for a complete falloff calculation, and much of the true falloff behavior is captured accurately by the simplified model. On the other hand, computational requirements are much reduced and the model may be solved repeatedly without extensive calculational effort. Furthermore, the accuracy of the formalism is greatly enhanced by the existence of experimental data for input to the model, as is the case with the hydroperoxyl radical

recombination. The reduced-falloff approach thus provides a quite satisfactory description of pressure dependences with minimal effort.

For the present calculations, model parameters were taken largely from Cobos *et al.* (1985). Vibrational frequencies for HO_2 are 3436, 1392, and 1098 cm^{-1}; E_o is 201.25 kJ/mol. The high-pressure recombination rate constant was given by Cobos *et al.* as

$$k_{rec,\infty} = 4.5 \times 10^{13} \, (T / 300 \text{ K})^{0.6} \text{ cm}^3\text{mol}^{-1}\text{s}^{-1} \qquad (12.29)$$

and can be converted to $k_{diss,\infty}$ using the equilibrium constant, giving a high-pressure dissociation activation energy of 205.3 kJ/mol (Cobos *et al.*, 1985); this value alone determines the contribution of $k_{diss,\infty}$ to S_K in Equations (12.26) and (12.27). Hsu *et al.* (1989) measured the low-pressure rate constant for M = N_2 and derived the rate expression

$$k_{rec,o}(N_2) = (2.36 \pm 0.80) \times 10^{15} \exp[(680 \pm 110)/T] \text{ cm}^6\text{mol}^{-2}\text{s}^{-1} \qquad (12.30)$$

which agrees very well with the experimental value of Cobos *et al.* (1985) for M = N_2 at 298 K, $k_{rec,o} = 2.36 \times 10^{16}$ $cm^6mol^{-2}s^{-1}$, corresponding to a β_c value for N_2 of 0.29. Hsu *et al.* (1989) also determined a rate expression for M = H_2O

$$k_{rec,o}(H_2O) = (6.89 \pm 3.26) \times 10^{15} \exp[(1050 \pm 140)/T] \text{ cm}^6\text{mol}^{-2}\text{s}^{-1} \qquad (12.31)$$

As discussed in Section 12.2, Equation 12.31 implies a β_c for H_2O greater than 1 if the Lennard-Jones collisional rate is used (Hsu *et al.*, 1987,1989). Equations 12.29 through 12.31 have all been determined over a somewhat limited temperature range: 200 to 400 K for Equation 12.29, 298 to 639 K for Equations 12.30 and 12.31. Extrapolation to higher

temperatures thus involves some uncertainty, but Equation 12.30 correctly predicts the observations of Slack (1977) for temperatures of 980 to 1176 K. For the present calculations, we have assumed Equations 12.29 through 12.31 to be valid to 600 °C (873 K).

With these input parameters, Equation 12.20 can be solved to give the pressure dependence of the hydroperoxyl recombination. The use of experimental data for $k_{rec,o}$ eliminates the inaccuracies that apparently arise when the Lennard-Jones collisional rate is used for M = H_2O. Information regarding collisional efficiency (β_c) is still required, but data are available for N_2 and β_c can evidently be set to unity for H_2O without loss of accuracy (see Section 12.2). One should note that Equations 12.30 and 12.31 give a relative efficiency for H_2O, $k_{rec,o}(H_2O)/k_{rec,o}(N_2)$, of about 10, in contrast to the relative efficiency for H_2O_2 decomposition, which is about 6. This change in relative efficiency with reactant conflicts with the traditional use of the same Lennard-Jones parameters for HO_2 as for H_2O_2 (Troe, 1977b; Cobos *et al.*,1985); more complex effects are apparently present which cause the HO_2-H_2O collisional rate to be nearly twice the H_2O_2-H_2O rate.

Figure 12.4 compares the experimental data at 298 K of Cobos *et al.* (1985) with the predictions from the model for M = N_2, β_c = 0.29. The model accurately captures the trend of the data, even at pressures of around 100 bar, where the falloff regime becomes important. As observed by Cobos *et al.*, the approach to the high-pressure limit is slow, with attainment of the limit requiring pressures of several thousand bar for M = N_2. For M = H_2O, β_c = 1, the approach to the high-pressure limit in Figure 12.4 occurs much more rapidly owing to the high relative efficiency of H_2O. Note that both curves must be correct at the high- and low-pressure limits, since data for $k_{rec,o}$ and $k_{rec,\infty}$ were used in the model.

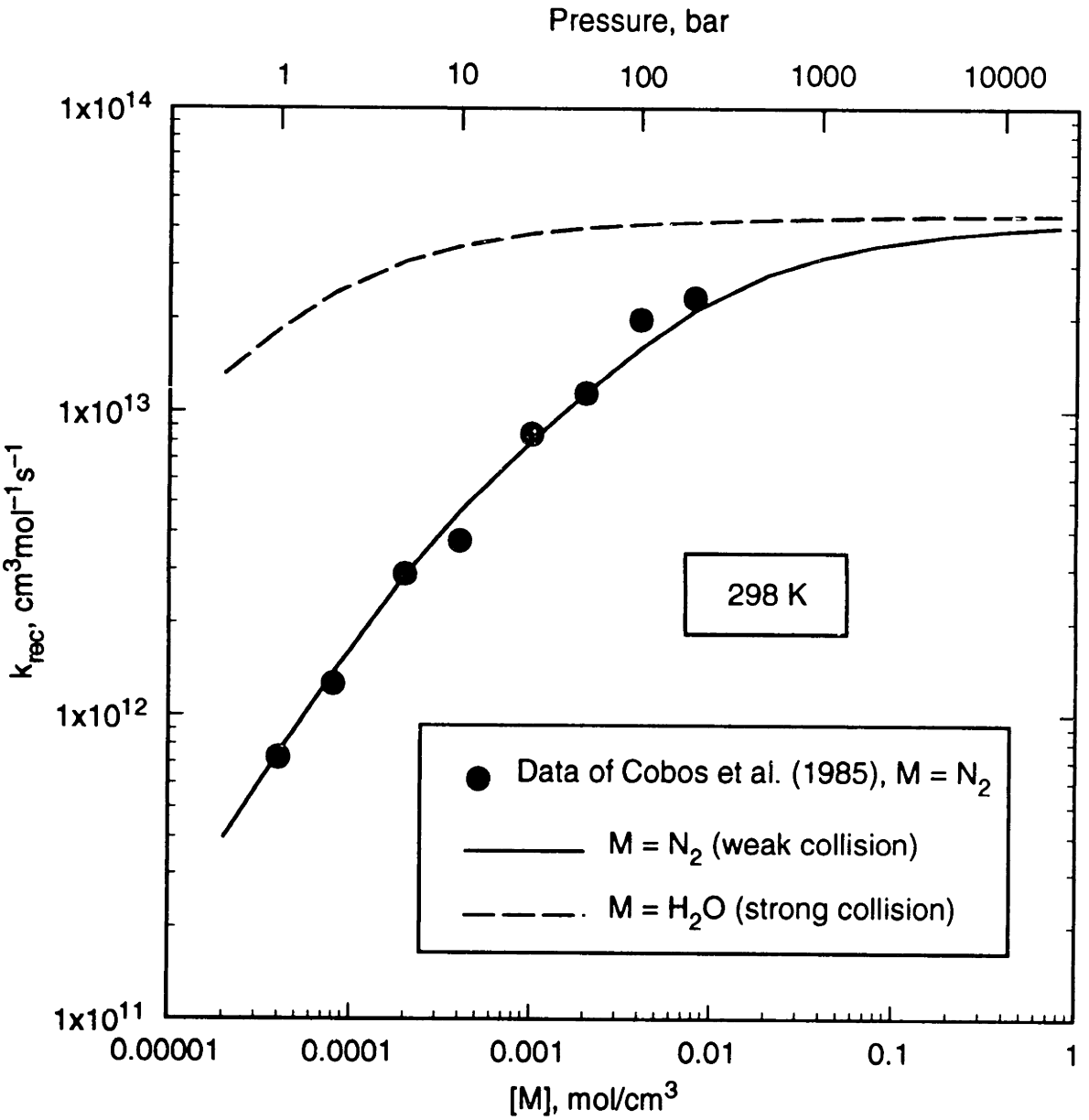

Figure 12.4 Comparison of Experimental Data and Model Predictions for Pressure Dependence of HO_2 Recombination at 298 K.

Figure 12.5 shows the model predictions for M = H_2O, $\beta_c = 1$, for SCWO temperatures, with Equations 12.29 and 12.31 extrapolated to those conditions. As noted in Section 12.2, the pressure in Figure 12.5 (as well as in Figure 12.4) is an effective ideal-gas pressure, which can be significantly higher than the actual experimental SCW pressure. Figure 12.5 clearly illustrates that the approach to the high-pressure limit is slower for HO_2 recombination than for H_2O_2 dissociation; at effective pressures of several hundred bar, the rate constant is still about 20 to 30% below the high-pressure value. At a real pressure of 246 bar, with proper accounting of the variation of the effective pressure with temperature, the rate constant for HO_2 recombination at 400 to 600 °C is approximately constant, and can be expressed as

$$k_{rec}(H_2O) \approx 10^{13.68} \exp(193.4/T) \text{ cm}^3\text{mol}^{-1}\text{s}^{-1} \tag{12.32}$$

For lower operating pressures, the recombination rate constant is well into the falloff regime, with $k_{rec}/k_{rec,\infty} \sim 0.5$ for $P = 100$ bar. The model was solved for the full pressure dependence of k_{rec} for the temperatures (550 and 570 °C) and range of pressures required to model the experimental effects of pressure on hydrogen and carbon monoxide oxidation (Sections 6.5 and 8.3).

12.4 Pressure Dependence of CO + OH → CO_2 + H

The reaction of carbon monoxide with a hydroxyl radical to form carbon dioxide and a hydrogen atom

$$CO + OH \rightarrow CO_2 + H \tag{12.33}$$

is the primary oxidizing step for CO in combustion and atmospheric chemistry, and

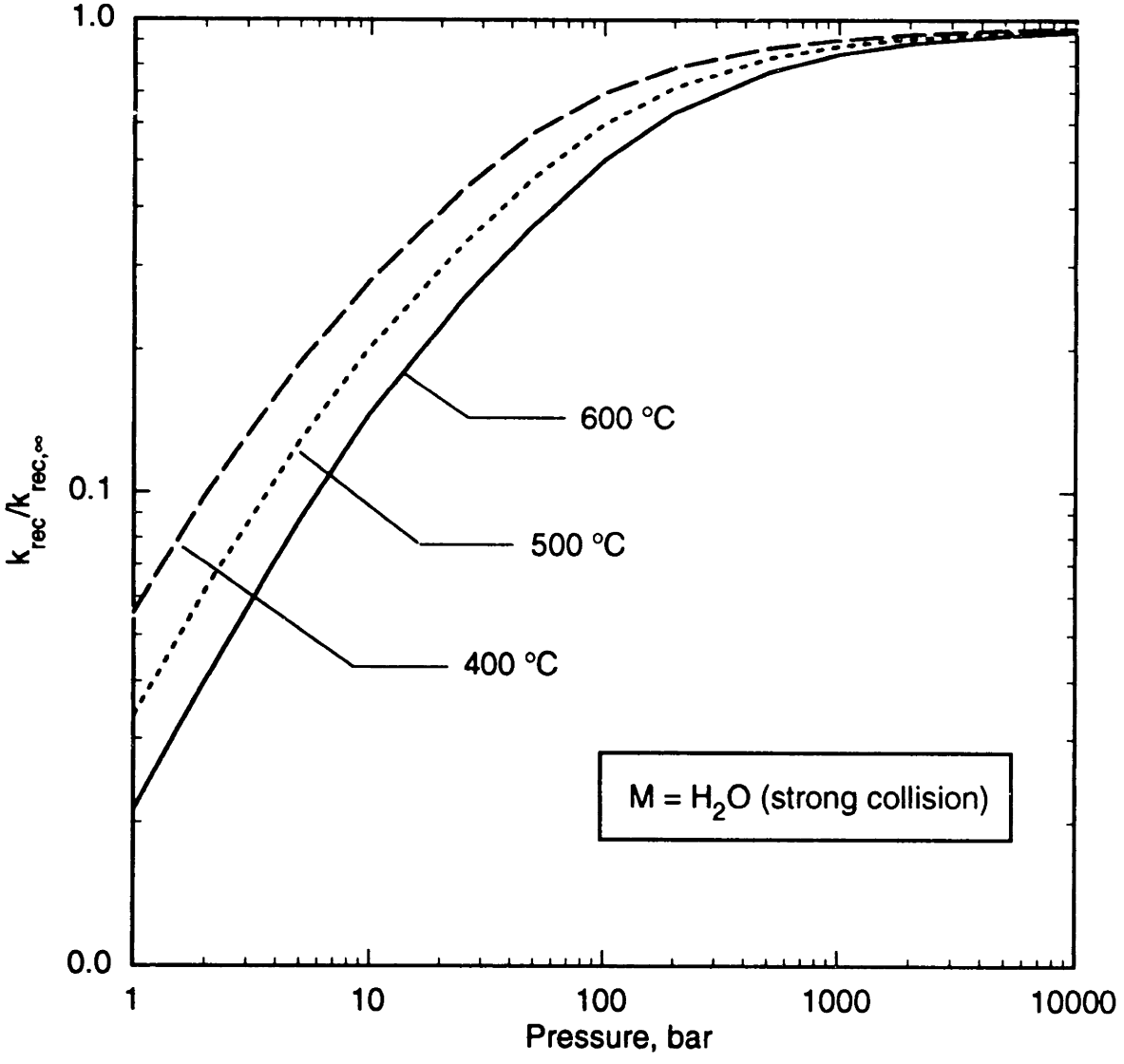

Figure 12.5 Predicted Pressure and Temperature Dependence of HO_2 Recombination.

accounts for the majority of the heat release during combustion owing to its high exothermicity. Numerous experimental studies have determined that this reaction shows a distinct pressure dependence at ambient temperature for pressures at or below atmospheric (Overend and Paraskevopoulos, 1977; Biermann *et al.*, 1978; Hofzumahaus and Stuhl, 1984; Paraskevopoulos and Irwin, 1984; DeMore, 1984; Hynes *et al.*, 1986). Furthermore, experimental data for the temperature dependence of the reaction show that the rate coefficient is essentially constant from 250 to 500 K, but then increases markedly for temperatures over 500 K (Westenberg and deHaas, 1973; Ravishankara and Thompson, 1983; Jonah *et al.*, 1984). Theoretical analysis of this unusual behavior suggests that the reaction is not strictly bimolecular, but rather proceeds through formation of an intermediate complex with a finite lifetime that can be stabilized collisionally (Overend and Paraskevopoulos, 1977; Smith, 1977; Mozurkewich *et al.*, 1984; Brunning *et al.*, 1988). The mechanism of the CO + OH reaction can thus be conceptually represented as (Larson *et al.*, 1988)

$$\begin{aligned} \mathrm{CO + OH} &\underset{k_{-a}}{\overset{k_a}{\rightleftarrows}} \mathrm{HOCO^*} \\ \mathrm{HOCO^* + M} &\xleftrightarrow{\beta_c \omega} \mathrm{HOCO + M} \\ \mathrm{HOCO^*} &\xrightarrow{k_b} \mathrm{H + CO_2} \end{aligned} \tag{12.34}$$

where the first step is the formation (from CO + OH) of an excited intermediate, HOCO*, which can undergo collisional stabilization in the second step (with collisional rate ω and collisional efficiency β_c) or can decompose to products (CO_2 + H) in the third step. Note that the excited complexes in the first and third steps are probably not identical, but rather represent a reactant-like intermediate (with an elongated C–O bond) and a product-like

intermediate (with an elongated O–H bond), respectively. The configurations of these complexes, as well as that of the stable HOCO intermediate itself, have been the subject of much theoretical scrutiny (Mozurkewich *et al.*, 1984; Brunning *et al.*, 1988; Larson *et al.*, 1988; Kudla *et al.*, 1991).

Larson *et al.* (1988) have chosen to rewrite the mechanism in the form of two unimolecular decomposition (recombination) processes and a chemical activation process:

$$\begin{aligned} \mathrm{HOCO} &\underset{k_{-1}}{\overset{k_1}{\rightleftarrows}} \mathrm{CO + OH} \\ \mathrm{HOCO} &\underset{k_{-2}}{\overset{k_2}{\rightleftarrows}} \mathrm{CO_2 + H} \\ \mathrm{CO + OH} &\xrightarrow{k^{ca}} \mathrm{CO_2 + H} \end{aligned} \tag{12.35}$$

Using assumed configurations and molecular parameters for HOCO and for the two (reactant- and product-like) activated complexes, Larson *et al.* performed dual-channel strong-collision RRKM calculations, and fit the results to an expression of the form of the Troe formalism (Troe, 1977a,b,1979,1983) to derive values for F_c^{SC}. The resulting values for the strong-collision rate constants and F_c^{SC} were then fit to empirical three-parameter expressions. Parameters for the empirical expressions in this model are reproduced in Table 12.2, since the original reference contained errors which have been subsequently corrected by the authors. Strong-collision rate constants are converted to weak-collision rate constants in the usual manner, $k^{WC} = \beta_c k^{SC}$ (Equation 12.15), and $F_c^{WC} = F_c^{SC}\beta_c^{0.14}$. The collisional efficiency β_c was calculated by means of Equation 12.16; Larson *et al.* (1988) used a temperature-independent value of 535 cal/mol for $\langle \Delta E \rangle$ for M = N_2 and a calculated value of F_E. In the case of the chemical

Unimolecular Reactions: $k = 10^a T^b \exp(-c/T)$

$F_c^{SC} = f \exp(-g/T) + \exp(-T/h)$

	k_o^{SC}/[M] $cm^3mol^{-1}s^{-1}$			k_∞ s^{-1}			F_c^{SC}		
	a	*b*	*c*	*a*	*b*	*c*	*f*	*g*	*h*
k_1	23.34	–1.89	17750.	12.77	0.53	17100.	1.37	4110.	2676.
k_2	26.36	–3.024	17650.	12.24	0.307	16570.	2.49	5755.	1601.

Chemical Activation Process: $k^{ca} = 10^a T^b \exp(-c/T)$

$F_c = f \exp(-g/T) + \exp(-T/h)$

	k_o^{ca} $cm^3mol^{-1}s^{-1}$			$[M]k_\infty^{ca}$ s^{-1}			F_c		
	a	*b*	*c*	*a*	*b*	*c*	*f*	*g*	*h*
k^{ca}	7.068	1.354	–364.8	–2.610	3.684	–621.0	1.391	2365.	2020.

Equilibrium Constants: K_c (mol/cm^3) $= 10^\alpha T^\beta \exp(-\gamma/T)$

	α	β	γ
$K_{c,1}$	5.87	–1.32	17420.
$K_{c,2}$	–0.910	–0.01	4378.

Table 12.2 Model Parameters for Pressure and Temperature Dependence of CO + OH → CO_2 + H from Larson *et al.* (1988).

activation process, the low-pressure rate constant is independent of pressure while the high-pressure limit is pressure dependent; thus $k_{\infty}^{ca,WC}$ $k_{\infty}^{ca,SC} / \beta_c$. Rate constants for the reverse reactions are calculated from the forward rate constants using the equilibrium constants, e.g., $k_{-1} = k_1/K_{c,1}$.

Strictly speaking, the mechanism of Equations 12.34 and 12.35 implies that the observed, overall rate constant for CO + OH will exhibit transient (time-dependent) behavior. If it is assumed, however, that thermal decomposition (collisional destabilization) of the HOCO intermediate occurs rapidly, the overall rate constant, k(CO + OH), can be expressed as an algebraic function of the "microscopic" rate constants in Equation 12.35, which can be calculated from the parameters in Table 12.2:

$$k(\mathrm{CO} + \mathrm{OH}) = k^{ca} + k_2 \frac{k_1}{k_1 + k_2} \frac{1}{K_{c,1}} \tag{12.36}$$

Predictions of the temperature dependence of CO + OH from the model of Larson *et al.* (1988), with P = 1 bar and M = N_2 (with the $\langle \Delta E \rangle$ used by the authors), are shown in Figure 12.6, where they are compared with a variety of experimental data and recommended rate expressions. The collection of experimental data is by no means comprehensive, but is representative of the general trends observed.

The experimental data at low temperatures appear to be quite scattered because of the pressure dependence of the reaction under those conditions. For example, the plotted data of Hynes *et al.* (1986), Paraskevopoulos and Irwin (1984), DeMore (1984), and Hofzumahaus and Stuhl (1984) were all obtained at pressures of about 1 bar (each of these studies also obtained data at lower pressures, which have been omitted from Figure 12.6 for clarity). By contrast, the data of Smith and Zellner (1973), Westenberg and deHaas (1973), and Ravishankara and Thompson (1983) were obtained at considerably

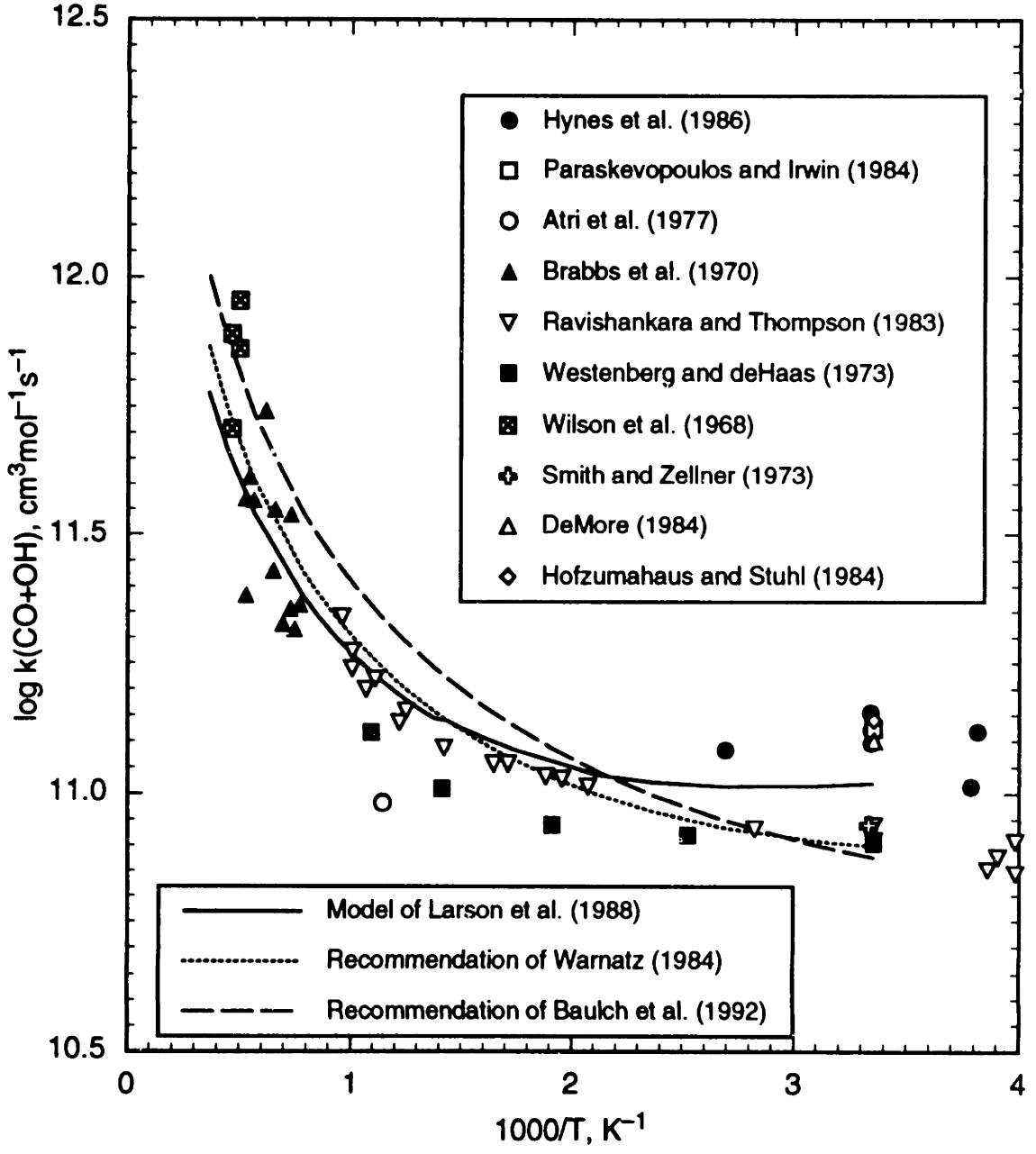

Figure 12.6 Comparison of Model Predictions and Experimental Data for CO + OH → CO_2 + H. Model predictions based on P = 1 bar, M = N_2; see text for discussion of data.

lower pressures (~0.01–0.1 bar or less). Thus the discrepancy in the lower-temperature data can be attributed to the reaction's pressure dependence; for example, the study of Hynes *et al.* (1986) also examined comparably low pressures and obtained rate constants in good agreement wih the low-pressure data shown here. At higher temperatures, the pressure dependence of the reaction becomes less significant, such that the rate constant is virtually pressure-independent above 1000 K. The high-temperature data of Wilson *et al.* (1968), Brabbs *et al.* (1970), and Ravishankara and Thompson (1983) thus demonstrate good agreement, even though the data were obtained at widely varying pressures (0.05 bar, ~0.9–1.5 bar, and ~0.1 bar, respectively).

The model of Larson *et al.* (1988) can be seen to accurately capture the curvature in the data in Figure 12.6, although the model does appear to underpredict the atmospheric rate data. The inability of the model to capture the complete pressure dependence at low temperatures was noted by the authors; while the model does predict a linear dependence of the rate constant on pressure at low temperatures, as is observed experimentally (Paraskevopoulos and Irwin, 1984; DeMore, 1984; Hynes *et al.*, 1986), the model predicts a weaker dependence than is observed. On the other hand, the model reproduces the atmospheric-pressure and ambient-temperature data much more reliably than either of the recommended rate expressions, which seem to be heavily weighted toward the lower-pressure data. The recommendation of Baulch *et al.* (1992) also seems to overemphasize the higher values at the higher temperatures. The earlier recommendation by Baulch *et al.* (1976) gives essentially the same curve as the model, since the model parameters were chosen to reproduce that recommended rate expression.

The ability of the model to capture the temperature dependence of the rate data is encouraging, although the failure to reproduce the full low-temperature pressure dependence is somewhat troublesome from the perspective of the present study. The

model does however appear to contain the major features of the kinetic behavior, and, in the absence of suitable experimental data, can be expected to provide a reasonable estimate of higher-pressure behavior. More detailed and rigorous models have been developed (Brunning *et al.*, 1988; Kudla *et al.*, 1991), but those models require much more extensive information and computational effort, and they have not proven to be any more accurate than the simple form used here. The model of Larson *et al.* (1988) was therefore used to obtain an estimate of the rate constant for CO + OH under SCWO conditions. For these calculations, β_c was taken to be 1, which appears to be a reasonable assumption for M = H_2O (see Section 12.2). In any case, results for $\beta_c = 1$ were not substantially different from results for β_c as low as ~0.5. Model predictions for the pressure dependence of the rate constant for 400 to 600 °C are shown in Figure 12.7. While the pressure dependence is quite non-linear, the predicted rate constant varies by less than a factor of two from 1 to 1000 bar (note the expanded scale in Figure 12.7). Similarly, the temperature dependence of the rate constant is quite weak, and, to a reasonable approximation, the rate coefficient could be treated as constant over the entire range of pressure and temperature examined experimentally in the present research. For elementary reaction modeling purposes, then, the details of the pressure and temperature dependences of the rate constant are less important than the absolute value of the rate constant, which has been assumed to be predicted correctly by the model.

At an operating pressure of 246 bar and temperatures of 400 to 600 °C, with proper inclusion of the compressibility factor Z to account for the non-ideal behavior of water, the overall rate constant for CO + OH → CO_2 + H, as predicted by the model of Larson *et al.* (1988), can be expressed in the form

$$k(\mathrm{CO + OH}) = 1.783 \times 10^{11} \exp(0.0006285T) \ \mathrm{cm^3 mol^{-1} s^{-1}} \qquad (12.37)$$

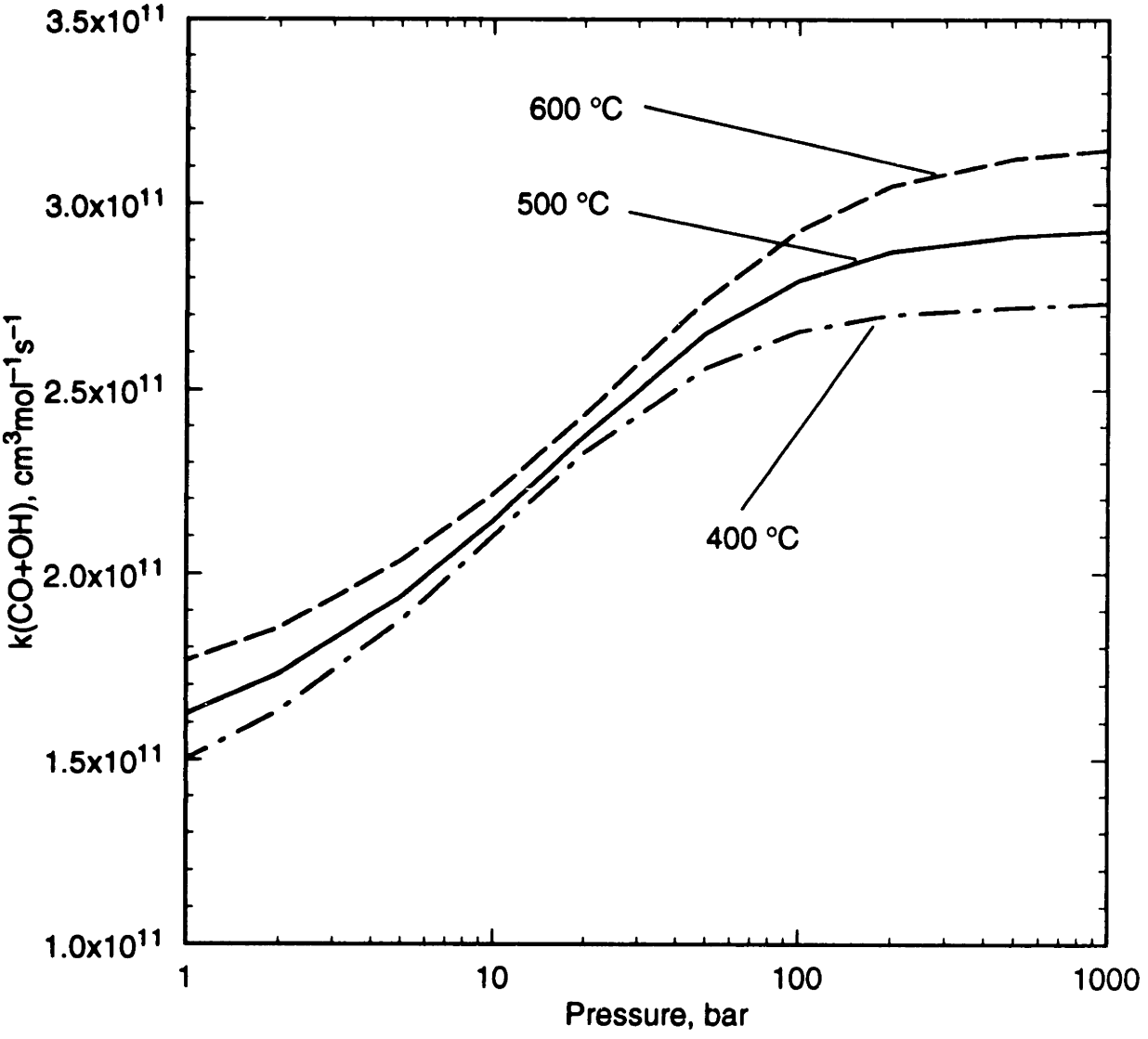

Figure 12.7 Predicted Pressure and Temperature Dependence of CO + OH → CO_2 + H.

This rate form was used in the model calculations for the isobaric kinetic experiments (Chapter 8). Over the temperature range, the rate constant varies from 2.7×10^{11} to 3.1×10^{11} $cm^3mol^{-1}s^{-1}$, consistent with the temperature-invariant value (3.2×10^{11}) used by Webley and Tester (1991) in their modeling study. For elementary reaction modeling of variable-pressure data in the present study (Section 8.3), the model was used to determine the appropriate rate constant values. As expected from Figure 12.7, the predicted rate constant varies less than 4% over the entire range of pressures studied experimentally.

12.5 Tabulated Experimental Data

The following tables contain the numerical experimental data obtained in this study for hydrogen and carbon monoxide oxidation in supercritical water. The corrected data for carbon monoxide oxidation from Helling (1986) are also included. While not all experimental quantities are listed in the tables, the data given are sufficient for modeling purposes and should allow calculation of quantities not listed (e.g., conversion or exit concentration, first-order rate constant, Reynolds number) if such information is required.

Run numbers with the suffix "A" indicate duplicates of earlier experiments; the results of the original experiments were not used, either because mass-balance closures were poor or because experimental conditions were not maintained at their desired values.

Run No.	Temperature °C	$[H_2]_o$ 10^{-6} mol/cm^3	$[O_2]_o$ 10^{-6} mol/cm^3	Residence Time, s	Conversion %	Mass Balance Closure, %
11	499±1	1.29±0.03	1.18±0.03	6.0±0.3	7.7±4.8	98.9
12	600±1	0.977±0.02	0.814±0.02	4.7±0.2	98.2±0.8	97.6
14	520±1	1.21±0.02	1.05±0.03	5.7±0.3	18.0±3.8	103.2
16	560.5±1	1.12±0.02	0.944±0.03	5.2±0.2	88.4±1.2	100.8
17	581±1	1.00±0.02	0.934±0.03	4.5±0.2	98.2±0.5	96.1
18	550±1	1.16±0.02	0.997±0.03	5.2±0.2	47.4±2.3	97.1
19	571±1	1.06±0.02	1.02±0.03	5.0±0.2	97.7±0.7	93.2
21	509.5±1	1.29±0.03	1.22±0.03	5.8±0.3	8.4±3.6	94.3
22	529±1	1.21±0.03	1.15±0.03	5.5±0.3	15.6±3.7	92.9
23	540±1	1.24±0.03	1.13±0.03	5.4±0.2	27.1±2.4	98.4
24	509±1	1.30±0.03	1.19±0.03	5.9±0.3	6.1±3.2	97.6
25	556±1	1.15±0.02	1.04±0.03	5.2±0.2	75.6±1.1	99.1
27	495±1	1.35±0.03	1.11±0.04	11.0±0.5	7.7±3.6	94.7
28	520±1	2.92±0.05	0.714±0.02	5.9±0.3	17.8±2.0	105.7
31	520±1	1.22±0.02	3.05±0.07	5.6±0.3	15.3±2.2	104.5
32	520±1	1.24±0.03	2.42±0.06	5.6±0.3	9.4±2.8	101.7
33	521±1	1.21±0.02	1.66±0.04	5.6±0.3	8.5±2.8	100.7
34	520±1	1.22±0.02	3.12±0.07	5.6±0.3	13.1±2.5	105.6
36	520±1	2.38±0.04	1.03±0.03	5.6±0.3	9.3±2.6	95.9
37	521±1	2.26±0.04	1.05±0.03	5.6±0.3	8.1±2.6	96.9
38	520±1	1.27±0.03	0.992±0.04	7.7±0.4	13.3±3.8	96.8
39	520±1	1.26±0.03	1.04±0.04	7.7±0.4	13.8±3.1	99.1
40	600±1	1.06±0.02	0.913±0.03	3.5±0.2	97.8±0.1	98.3
41	570±1	1.09±0.03	0.939±0.03	3.7±0.2	91.4±0.4	101.0
42	559±1	1.16±0.02	1.00±0.03	3.8±0.2	64.2±1.4	101.4
43	520±1	0.671±0.02	1.09±0.05	7.7±0.4	15.4±3.2	100.9
44	521±1	1.22±0.03	3.51±0.11	7.5±0.4	14.0±2.9	102.5
45	539±1	1.21±0.03	0.985±0.03	7.3±0.3	30.3±2.3	100.7
46	500±1	1.34±0.03	1.12±0.03	8.1±0.4	6.7±2.5	100.1
47	520±1	2.97±0.07	1.01±0.03	7.6±0.4	9.2±2.5	89.7
48	520±1	3.08±0.06	1.01±0.03	7.6±0.4	8.8±2.0	89.6
	520±1	3.69±0.07	0.994±0.03	7.6±0.4	10.2±2.4	87.3

Table 12.3 Experimental Data for Hydrogen Oxidation at 246 bar.

Run No.	Temperature °C	$[H_2]_o$ 10^{-6} mol/cm^3	$[O_2]_o$ 10^{-6} mol/cm^3	Residence Time, s	Conversion %	Mass Balance Closure, %
50	520±1	1.84±0.04	0.999±0.03	7.7±0.4	10.5±2.3	102.4
51	520±1	0.909±0.02	1.02±0.03	7.7±0.4	9.3±2.4	100.3
52	520±1	1.29±0.04	0.409±0.02	7.7±0.4	10.7±3.3	90.5
54	520±1	1.28±0.03	0.702±0.02	7.7±0.4	15.0±2.5	97.3
117	558±4	1.06±0.03	0.541±0.02	3.8±0.2	79.0±1.1	98.7
118	550±1	1.05±0.03	0.546±0.02	3.9±0.2	64.2±2.4	97.0
119	550±1	2.06±0.05	1.03±0.03	3.8±0.2	51.5±3.5	93.5
120	550±1	2.05±0.05	1.03±0.03	5.2±0.3	72.2±2.7	96.1
121	550±1	2.06±0.05	1.04±0.03	4.4±0.2	61.0±3.4	96.5
122	550±1	2.06±0.05	1.04±0.03	6.4±0.3	82.5±5.3	97.2
123	525±2	3.68±0.09	0.459±0.02	7.2±0.3	7.4±3.2	102.0
125	550±2	2.06±0.05	1.06±0.03	3.4±0.2	37.4±2.6	91.8
126	550±1	2.07±0.04	1.05±0.03	5.9±0.3	79.0±2.9	97.2
127	550±1	2.06±0.05	1.06±0.03	6.9±0.3	87.9±0.8	97.1
130	520±1	0.385±0.13	4.55±0.12	7.2±0.4	22.8±5.7	95.3
138	550±1	1.08±0.03	0.523±0.02	5.5±0.3	78.3±5.3	101.2
139	550±1	1.08±0.03	0.530±0.02	4.8±0.2	71.4±2.7	100.8
140	550±2	1.05±0.03	0.543±0.02	3.4±0.2	36.9±5.5	92.5
148	550±3	3.05±0.08	1.54±0.05	3.8±0.2	30.7±3.0	87.5
149	550±2	3.06±0.06	1.54±0.04	6.2±0.3	70.1±3.9	93.0
150	550±2	3.08±0.07	1.55±0.04	4.4±0.2	53.3±6.5	92.2
151	550±1	3.06±0.06	1.55±0.04	5.2±0.2	53.3±3.2	92.1
152	550±1	3.05±0.06	1.55±0.05	6.9±0.3	82.7±2.3	95.1
63	600±1	1.04±0.02	<0.07±0.01	4.8±0.2	2.0±2.6	—

Table 12.3 Experimental Data for Hydrogen Oxidation at 246 bar. Continued.

Initial Conditions: 550±2 °C
$[H_2]_o = (3.06 \pm 0.03) \times 10^{-6}$ mol/cm^3
$[O_2]_o = (1.55 \pm 0.02) \times 10^{-6}$ mol/cm^3

Run No.	Residence Time, s	$[H_2]$ 10^{-6} mol/cm^3	$[O_2]$ 10^{-7} mol/cm^3	% Mass Closure
148	3.8±0.2	2.11±0.07	9.03±0.3[illegible]	87.5
150	4.4±0.2	1.44±0.20	6.14±0.84	92.2
151	5.2±0.2	1.43±0.09	6.18±0.40	92.1
149	6.2±0.3	0.92±0.12	3.62±0.45	93.0
152	6.9±0.3	0.53±0.07	2.17±0.27	95.1

Table 12.4 Experimental Data for Hydrogen Species Profiles at 550 °C and 246 bar.

Initial Conditions: 550±2 °C
$[H_2]_o = (2.06 \pm 0.02) \times 10^{-6}$ mol/cm^3
$[O_2]_o = (1.04 \pm 0.01) \times 10^{-6}$ mol/cm^3

Run No.	Residence Time, s	$[H_2]$ 10^{-6} mol/cm^3	$[O_2]$ 10^{-7} mol/cm^3	% Mass Closure
125	3.4±0.2	1.29±0.05	5.93±0.22	91.8
119	3.8±0.2	1.00±0.07	4.33±0.30	93.5
121	4.4±0.2	0.81±0.07	3.76±0.31	96.5
120	5.2±0.3	0.57±0.05	2.48±0.23	96.1
126	5.9±0.3	0.44±0.06	2.03±0.27	97.2
122	6.4±0.3	0.36±0.11	1.63±0.46	97.2
127	6.9±0.3	0.25±0.02	1.27±0.08	97.1

Table 12.4 Experimental Data for Hydrogen Species Profiles at 550 °C and 246 bar. Continued.

Initial Conditions: 550±2 °C
$[H_2]_o = (1.06 \pm 0.02) \times 10^{-6}$ mol/cm^3
$[O_2]_o = (0.54 \pm 0.01) \times 10^{-6}$ mol/cm^3

Run No.	Residence Time, s	$[H_2]$ 10^{-7} mol/cm^3	$[O_2]$ 10^{-7} mol/cm^3	% Mass Closure
140	3.4±0.2	6.60±0.55	3.12±0.25	92.5
118	3.9±0.2	3.76±0.24	1.92±0.12	97.0
139	4.8±0.2	3.08±0.28	1.49±0.12	100.8
138	5.5±0.3	2.35±0.58	1.06±0.24	101.2

Table 12.4 Experimental Data for Hydrogen Species Profiles at 550 °C and 246 bar. Continued.

Initial Conditions: 550±2 °C
$[H_2]_o = (1.06\pm0.02) \times 10^{-6}$ mol/cm^3
$[O_2]_o = (0.53\pm0.01) \times 10^{-6}$ mol/cm^3

Run No.	Pressure bar	Residence Time, s	$[H_2]$ 10^{-7} mol/cm^3	$[O_2]$ 10^{-7} mol/cm^3	% Mass Closure
141	118.2±4.8	3.6±0.2	9.64±0.61	4.81±0.30	100.5
134	138.9±3.4	3.1±0.2	9.39±0.41	4.14±0.18	89.0
142	138.9±2.8	3.9±0.2	8.21±1.09	3.89±0.51	96.0
135	159.6±4.1	3.7±0.2	8.42±0.48	3.78±0.22	94.5
132	180.3±4.1	4.3±0.2	6.67±0.85	2.83±0.35	90.4
200A	201.0±3.4	3.8±0.2	5.42±0.21	2.73±0.12	101.0
199A	201.0±3.4	4.2±0.2	4.63±0.20	2.35±0.11	101.6
136	200.9±5.5	4.9±0.3	5.02±0.41	2.25±0.21	97.0
203A	221.6±3.4	3.8±0.2	4.95±0.50	2.47±0.24	99.1
204A	221.6±3.4	4.2±0.2	3.98±0.26	2.08±0.13	100.7
137	221.6±3.4	4.8±0.2	3.89±0.79	1.78±0.34	95.7
140	245.8±4.1	3.4±0.2	6.60±0.55	3.12±0.25	92.5
118	245.8±3.4	3.9±0.2	3.76±0.24	1.92±0.12	97.0
139	245.8±4.1	4.8±0.2	3.08±0.28	1.49±0.12	100.8
138	245.8±4.1	5.5±0.3	2.35±0.58	1.06±0.24	101.2
202A	263.0±3.4	3.8±0.2	4.41±0.25	2.19±0.12	97.0
201A	263.0±3.4	4.2±0.2	3.75±0.18	1.92±0.09	97.5
133	263.0±3.4	6.0±0.3	1.35±0.18	0.60±0.07	97.9

Table 12.5 Experimental Data for Hydrogen Oxidation at 550 °C and 118 to 263 bar.

Initial Conditions: 550±2 °C
$[H_2]_o = (1.04 \pm 0.01) \times 10^{-6}$ mol/cm^3
$[O_2]_o = (0.55 \pm 0.01) \times 10^{-6}$ mol/cm^3

Run No.	Residence Time, s	$[H_2]$ 10^{-7} mol/cm^3	$[O_2]$ 10^{-7} mol/cm^3	% Mass Closure
238	4.9±0.2	7.91±0.29	4.28±0.17	97.1
235	5.5±0.2	7.82±0.46	4.30±0.24	103.7
232	6.4±0.2	7.14±0.35	4.03±0.19	104.8
236	7.7±0.3	6.48±0.33	3.94±0.22	105.7
234	8.7±0.3	6.41±0.60	3.79±0.35	104.9
237	9.5±0.3	5.45±0.71	3.11±0.38	102.0
233	10.4±0.4	5.37±0.52	3.30±0.31	104.1

Table 12.6 Experimental Data for Hydrogen Oxidation at 550 °C and 246 bar in the Packed Reactor.

Run No.	T, °C	$[CO]_o$,[a] 10^{-3} mol/L	τ,[b] s	X,[c] %	X_{rxr},[d] %	ln k^*[e]	ln k[f]	Carbon Balance Closure, %
85	560.5	1.350	5.1	12.5	11.2	–3.64	–5.67	108.0
86	498.0	1.740	6.1	1.7	1.1	–5.88	–8.03	99.8
87	540.0	1.120	5.4	11.4	10.6	–3.80	–5.87	98.8
88	477.0	1.360	6.5	2.1	1.3	–5.75	–7.85	97.7
89	518.5	0.8920	5.7	8.0	7.3	–4.22	–6.37	98.4
90	455.5	1.150	7.1	1.4	1.4	–6.21	–8.49	95.7
91	508.5	0.7520	5.9	4.4	3.8	–4.87	–7.13	96.3
92	467.0	0.8640	6.8	2.5	2.0	–5.60	–7.82	96.7
93	528.5	0.3760	5.6	7.5	6.5	–4.27	–6.72	87.7
94	487.5	0.4320	6.3	5.0	4.3	–4.81	–7.19	86.1
95	482.5	2.260	6.3	2.5	2.1	–5.52	–7.45	105.5
96	445.5	2.670	7.4	1.4	1.0	–6.30	–8.19	104.2
97	593.0	0.7610	7.6	19.7	16.3	–3.54	–5.87	97.0
98	457.5	1.170	11.1	2.1	1.3	–6.25	–8.55	95.2
99	531.0	0.4080	8.7	12.0	10.3	–4.22	–6.66	89.3
100	489.5	0.4630	9.8	4.4	3.3	–5.39	–7.90	89.6
101	484.0	2.440	9.8	1.5	0.6	–6.51	–8.77	100.3
102	447.5	2.880	11.4	1.2	0.9	–6.85	–8.93	99.2
103	499.5	1.740	9.4	2.4	1.9	–5.95	–8.22	97.2
104	478.5	1.900	10.1	1.9	1.3	–6.29	–8.46	95.4

[a]Inlet CO concentration, corrected for reaction during preheating.
[b]Reactor residence time.
[c]Total conversion of carbon monoxide by water-gas shift pathway.
[d]Conversion of carbon monoxide in reactor by water-gas shift pathway.
[e]First-order rate constant, $k^* = -\ln(1-X)/\tau$.
[f]Rate constant from regressed rate expression (Equation 7.16).

Table 12.7 Experimental Data for the Water-Gas Shift Reaction at 246 bar.

Run No.	Temp. °C	$[CO]_o$,[a] 10^{-3} mol/L	F[b]	τ,[c] s	X,[d] %	H_2/CO_2[e]	ln k^*[f]	ln k_{DO}[g]	Mass Balance Closure, % C	O
6	438.5	1.19	2.168	7.7	8.8	—	–4.43	—	92.5	106.9
7	540.0	1.23	2.171	5.4	66.4	0.0789	–1.60	0.04	102.4	94.3
8	439.0	1.20	2.233	7.7	13.0	0.5230	–4.01	–3.04	91.1	102.5
9	500.0	1.38	0.491	6.0	18.2	0.0482	–3.40	–1.16	95.2	101.1
10	497.0	1.37	0.440	6.1	20.0	0.1652	–3.31	–1.18	94.9	100.8
55	469.0	1.77	0.450	6.7	11.0	0.1859	–4.05	–2.08	97.8	94.8
56	454.0	1.91	0.462	7.1	10.1	0.1354	–4.20	–2.20	94.8	93.0
57	519.0	1.52	0.520	5.7	31.3	0.0603	–2.72	–0.55	97.0	83.6
58	484.0	1.73	0.479	6.3	14.5	0.0989	–3.69	–1.58	93.2	92.9
59	549.0	1.47	0.454	5.3	51.7	0.0306	–1.99	0.34	94.9	96.4
60	530.0	1.43	0.457	5.5	26.2	0.0603	–2.90	–0.66	98.8	96.8
61	420.0	2.38	0.471	8.7	4.0	0.2960	–5.36	–3.65	97.4	97.0
62	430.5	2.01	0.567	8.1	3.7	0.3817	–5.37	–3.79	103.9	90.6
66	534.5	1.00	0.899	5.5	45.7	0.1131	–2.20	–0.19	99.0	103.3
67	460.0	1.80	0.254	7.0	6.1	0.3525	–4.71	–2.80	97.3	96.6
68	508.0	2.38	0.182	5.9	5.5	0.1031	–4.65	–2.27	102.2	82.2
69	528.5	1.79	0.213	5.5	11.0	0.0887	–3.85	–1.44	98.3	95.7
70	560.0	1.29	0.303	5.1	60.2	0.1271	–1.71	0.78	101.6	86.6
71	571.0	0.944	0.930	5.0	93.3	0.0080	–0.61	1.62	102.0	102.5
72	472.0	0.414	6.812	6.6	15.5	0.2501	–3.67	–2.26	91.8	104.9
73	445.0	2.98	0.711	7.5	5.0	0.1955	–4.99	–3.27	107.1	98.3
74	508.5	2.04	1.000	5.8	9.2	0.1011	–4.10	–2.29	97.1	108.8
75	529.5	1.88	0.633	5.5	13.6	0.0597	–3.62	–1.60	101.0	104.3
76	529.5	1.89	0.406	5.5	13.8	0.0727	–3.61	–1.44	100.8	108.5
77	529.5	1.05	1.486	5.5	28.9	0.0531	–2.78	–0.87	95.6	127.3
78	529.5	0.589	2.767	5.5	39.3	0.0346	–2.40	–0.53	82.9	124.5
79	529.5	0.412	4.757	5.5	40.2	0.0403	–2.37	–0.60	69.0	109.2

Table 12.8 Experimental Data for Carbon Monoxide Oxidation at 246 bar.

Run No.	T, °C	$[CO]_o$,[a] 10^{-3} mol/L	F[b]	τ,[c] s	X,[d] %	H_2/CO_2[e]	ln k^*[f]	ln k_{DO}[g]	Mass Balance Closure, % C	O
80	529.5	0.694	2.925	5.5	38.4	0.0653	-2.43	-0.68	84.0	105.9
81	529.0	0.420	4.738	5.5	48.6	0.0534	-2.11	-0.37	69.6	105.7
82	498.0	2.68	0.360	6.0	7.0	0.1790	-4.42	-2.44	106.1	94.0
83	529.5	1.78	0.284	5.5	11.5	0.1301	-3.81	-1.54	105.4	98.2
84	508.5	1.23	2.537	5.8	12.0	0.1674	-3.82	-2.24	89.6	111.9
105	499.5	0.373	7.882	9.3	29.5	0.1048	-3.28	-1.71	95.5	104.8
106	436.5	0.472	8.199	12.1	14.9	0.1244	-4.31	-2.84	98.3	103.5
107	509.0	2.08	0.524	9.1	14.8	0.1512	-4.04	-2.09	100.0	93.2
108	447.0	2.65	0.506	11.4	6.0	0.1737	-5.21	-3.32	98.7	95.1
109	545.5	1.58	0.962	8.2	86.0	0.0072	-1.43	0.63	92.8	97.4
110	478.0	1.82	1.000	10.0	8.6	0.0867	-4.71	-2.84	99.1	98.4
111	488.5	0.944	2.786	9.6	14.0	0.1708	-4.16	-2.57	105.2	100.4
112	457.5	1.06	2.802	10.9	8.4	0.2306	-4.82	-3.38	106.1	99.9
113	530.0	2.84	0.161	8.5	19.4	0.1666	-3.67	-1.34	101.4	77.7
114	467.5	3.51	0.153	10.4	5.9	0.2786	-5.14	-3.06	100.2	82.4
116	518.5	2.38	0.275	8.8	17.3	0.0690	-3.84	-1.55	97.6	98.0

[a]Inlet CO concentration, corrected for reaction during preheating.
[b]Feed ratio, $[O_2]_o/[CO]_o$.
[c]Reactor residence time.
[d]Conversion of carbon monoxide in reactor.
[e]Molar ratio of hydrogen to carbon dioxide in reactor effluent.
[f]First-order rate constant, $k^* = -\ln(1-X)/\tau$.
[g]Rate constant for direct oxidation, from regressed rate expression (Equation 7.22).

Table 12.8 Experimental Data for Carbon Monoxide Oxidation at 246 bar. Continued.

Run No.	Temp. °C	$[CO]_o$[a] 10^{-3} mol/L	$[O_2]_o/[CO]_o$[b]	Tau[c] s	$[H_2]/[CO_2]$[d]	Conv. %	ln k^*[e] s^{-1}
1	495.0	2.171	1.154	7.28	0.2849	41.7	−2.60
2	484.0	2.384	0.851	7.76	0.4189	37.9	−2.79
3	470.0	2.552	0.832	8.26	0.5307	30.0	−3.14
4	455.0	2.676	0.961	8.66	0.3079	21.3	−3.59
5	470.0	2.048	1.381	8.17	0.6123	25.1	−3.34
6	470.5	1.402	1.750	8.16	0.6534	32.1	−3.05
7	455.0	1.575	1.758	8.72	0.4014	23.8	−3.47
8	468.0	2.720	0.869	8.24	0.3341	24.4	−3.38
9	455.0	1.482	2.360	8.82	0.3203	24.5	−3.44
10	469.5	1.594	2.037	7.89	0.3827	24.8	−3.32
11	454.5	2.819	1.225	8.72	0.4534	17.3	−3.83
12	469.0	2.588	1.285	7.93	0.3132	22.6	−3.43
13	455.5	2.756	0.798	8.64	0.3150	17.2	−3.82
14	495.0	1.499	1.100	5.73	0.3613	29.9	−2.78
15	437.0	2.986	0.721	15.96	0.4748	21.3	−4.20
16	457.0	1.725	1.498	8.48	0.3630	21.9	−3.53
17	435.5	3.159	0.747	9.60	0.5549	12.4	−4.28
18	494.0	2.441	0.849	7.41	0.3188	36.5	−2.79
19	436.0	1.808	1.060	9.62	0.4927	12.3	−4.30
20	424.0	3.335	0.714	10.24	0.5126	9.1	−4.68
21	471.0	1.618	1.431	8.10	0.4334	21.6	−3.51
22	437.0	2.074	1.896	9.60	0.4880	14.5	−4.12
23	437.5	1.140	2.578	9.58	0.5757	15.7	−4.03
24	409.0	2.267	1.599	11.94	0.6468	13.2	−4.44
25	438.5	1.148	2.561	9.55	0.6156	15.1	−4.06
26	514.0	1.409	1.633	7.14	0.3216	51.0	−2.30
27	408.5	2.322	1.544	11.89	0.7287	11.6	−4.57
28	494.0	1.432	2.443	5.90	0.4688	23.6	−3.09
29	473.5	0.944	2.386	7.82	0.4920	26.1	−3.25
30	458.0	1.664	1.527	8.75	0.5586	18.7	−3.74
31	499.0	1.411	0.528	7.50	0.4404	32.0	−2.97
32	520.0	1.314	0.503	7.03	0.3668	45.7	−2.44
33	519.0	1.278	2.244	6.97	0.4172	42.5	−2.53
34	521.5	1.545	0.597	6.97	0.1826	78.0	−1.53
35	542.0	1.265	2.165	6.58	0.2471	64.0	−1.86
36	544.0	0.754	2.495	6.60	0.3587	64.3	−1.86
37	565.0	1.147	2.205	6.25	0.2198	81.3	−1.32
38	565.0	1.138	0.492	6.43	0.2453	78.3	−1.44
39	566.0	0.715	1.363	6.36	0.3019	81.3	−1.33

[a]Inlet CO concentration. [b]Inlet O_2/CO ratio. [c]Reactor residence time.
[d]Exit H_2/CO_2 ratio. [e]Apparent first-order rate constant.

Table 12.9 Corrected Experimental Data for Carbon Monoxide Oxidation from Helling (1986).

Initial Conditions: 550±2 °C
$[CO]_o = (1.04 \pm 0.02) \times 10^{-6}$ mol/cm^3
$[O_2]_o = (0.50 \pm 0.01) \times 10^{-6}$ mol/cm^3

Run No.	Residence Time, s	[CO] 10^{-7} mol/cm^3	[O_2] 10^{-7} mol/cm^3	[CO_2] 10^{-7} mol/cm^3	[H_2] 10^{-8} mol/cm^3	% Mass Closure C	% Mass Closure O
160	3.4±0.2	8.26±0.49	3.95±0.23	2.08±0.10	1.30±0.15	102.2	104.5
155	4.1±0.2	6.81±0.45	3.31±0.22	3.69±0.16	1.49±0.10	102.4	103.2
157	4.8±0.3	6.32±0.33	3.18±0.16	4.07±0.20	2.30±0.74	101.6	102.6
156	5.8±0.3	5.39±0.44	2.58±0.20	4.94±0.23	1.70±0.16	104.8	104.5
158	6.9±0.3	4.58±0.49	2.31±0.23	5.94±0.29	2.34±0.26	101.1	100.8
161	7.9±0.4	3.92±0.47	1.77±0.21	6.47±0.36	2.04±0.26	103.4	102.7
159	8.7±0.4	2.99±0.19	1.58±0.08	7.24±0.29	2.06±0.11	103.9	101.9

Table 12.10 Experimental Data for Carbon Monoxide Species Profiles at 246 bar.

Initial Conditions: 560±2 °C
$[CO]_o = (1.02 \pm 0.02) \times 10^{-6}$ mol/cm^3
$[O_2]_o = (0.50 \pm 0.01) \times 10^{-6}$ mol/cm^3

Run No.	Residence Time, s	[CO] 10^{-7} mol/cm^3	[O_2] 10^{-7} mol/cm^3	[CO_2] 10^{-7} mol/cm^3	[H_2] 10^{-8} mol/cm^3	% Mass Closure C	% Mass Closure O
169	3.4±0.2	6.10±0.30	3.10±0.14	4.43±0.24	1.87±0.14	98.7	99.2
166	4.1±0.2	4.42±0.32	2.27±0.13	5.75±0.28	2.16±0.13	104.3	102.1
164	4.8±0.2	3.81±0.38	1.92±0.19	6.27±0.27	1.91±0.21	102.4	100.3
168	5.6±0.3	2.37±0.45	1.20±0.21	7.68±0.39	1.78±0.36	104.2	103.1
167	6.3±0.3	1.65±0.15	0.79±0.07	8.65±0.38	1.53±0.15	103.1	101.6
165	7.1±0.3	1.50±0.21	0.72±0.10	8.82±0.70	1.36±0.23	100.9	97.4

Table 12.10 Experimental Data for Carbon Monoxide Species Profiles at 246 bar. Continued.

Initial Conditions: 560±3 °C
$[CO]_o = (2.08 \pm 0.03) \times 10^{-6}$ mol/cm^3
$[O_2]_o = (0.55 \pm 0.01) \times 10^{-6}$ mol/cm^3

Run No.	Residence Time, s	[CO] 10^{-7} mol/cm^3	[O_2] 10^{-7} mol/cm^3	[CO_2] 10^{-6} mol/cm^3	[H_2] 10^{-7} mol/cm^3	% Mass Closure C	% Mass Closure O
190	3.4±0.2	1.34±0.08	1.96±0.16	0.75±0.04	0.84±0.10	99.7	96.7
186	4.1±0.2	1.13±0.06	1.11±0.08	0.93±0.04	0.98±0.12	100.5	96.2
183	4.8±0.3	1.01±0.05	0.64±0.10	1.07±0.06	1.28±0.12	100.2	96.6
189	5.5±0.3	0.85±0.07	0.32±0.06	1.22±0.05	2.03±0.29	100.5	96.1
187	6.4±0.4	0.70±0.03	0.25±0.06	1.36±0.06	2.70±0.16	99.8	88.3
184	7.2±0.4	0.72±0.05	0.23±0.08	1.37±0.07	2.76±0.19	99.0	89.2
188	7.8±0.4	0.70±0.03	0.25±0.08	1.38±0.06	2.91±0.20	99.7	87.0
185	8.3±0.5	0.69±0.08	0.21±0.05	1.38±0.08	2.72±0.32	100.7	88.1

Table 12.10 Experimental Data for Carbon Monoxide Species Profiles at 246 bar. Continued.

Initial Conditions: 560±2 °C
$[CO]_o = (1.03 \pm 0.04) \times 10^{-6}$ mol/cm^3
$[O_2]_o = (0.97 \pm 0.04) \times 10^{-6}$ mol/cm^3

Run No.	Residence Time, s	[CO] 10^{-7} mol/cm^3	[O_2] 10^{-7} mol/cm^3	[CO_2] 10^{-6} mol/cm^3	[H_2] 10^{-8} mol/cm^3	% Mass Closure C	% Mass Closure O
198	3.4±0.2	3.67±0.27	6.22±0.27	0.66±0.04	1.12±0.13	100.0	106.7
196	4.1±0.2	2.06±0.13	5.96±0.36	0.82±0.03	0.87±0.12	101.8	101.2
194	4.8±0.2	1.28±0.07	5.58±0.31	0.91±0.03	0.58±0.03	99.0	99.2
191	5.5±0.3	0.94±0.04	4.67±0.20	0.92±0.04	0.59±0.08	100.5	106.5
197	6.4±0.3	0.36±0.03	4.54±0.36	0.98±0.04	0.23±0.07	103.0	107.5
192	7.1±0.4	0.33±0.02	4.67±0.24	1.04±0.05	0.29±0.01	94.7	100.4
195	7.7±0.4	0.12±0.01	4.77±0.29	0.97±0.05	0.15±0.14	104.5	103.7
193	8.3±0.4	0.13±0.01	4.80±0.28	1.06±0.04	0.22±0.01	94.0	99.5

Table 12.10 Experimental Data for Carbon Monoxide Species Profiles at 246 bar. Continued.

Initial Conditions: 570±3 °C
$[CO]_o = (1.04 \pm 0.02) \times 10^{-6}$ mol/cm^3
$[O_2]_o = (0.51 \pm 0.02) \times 10^{-6}$ mol/cm^3
Residence Time = 3.4±0.1 s

Run No.	Pressure bar	[CO] 10^{-7} mol/cm^3	[O_2] 10^{-7} mol/cm^3	[CO_2] 10^{-7} mol/cm^3	[H_2] 10^{-8} mol/cm^3	% Mass Closure C	% Mass Closure O
172	118.2±3.4	7.02±0.37	3.57±0.17	3.16±0.15	1.54±0.15	102.3	101.4
170	138.9±3.4	6.30±0.29	3.11±0.14	4.01±0.20	1.79±0.24	99.4	98.7
174	159.6±6.9	5.75±0.37	2.72±0.18	4.61±0.32	1.73±0.24	103.0	105.6
176	180.3±6.9	5.05±0.39	2.35±0.17	5.29±0.29	2.36±0.20	102.0	104.5
179	200.9±6.9	4.28±0.27	2.09±0.12	6.18±0.32	2.51±0.17	98.5	100.3
180	221.6±6.9	3.67±0.20	1.96±0.10	6.70±0.32	3.78±0.30	100.5	99.8
163A	245.8±4.1	3.59±0.17	2.15±0.09	6.77±0.45	4,52±0.79	102.6	100.4

Table 12.11 Experimental Data for Carbon Monoxide Oxidation at 570 °C and 118 to 263 bar.

Initial Conditions: 570±3 °C
$[CO]_o = (1.03 \pm 0.02) \times 10^{-6}$ mol/cm^3
$[O_2]_o = (0.51 \pm 0.01) \times 10^{-6}$ mol/cm^3
Residence Time = 4.1±0.2 s

Run No.	Pressure bar	[CO] 10^{-7} mol/cm^3	[O_2] 10^{-7} mol/cm^3	[CO_2] 10^{-7} mol/cm^3	[H_2] 10^{-8} mol/cm^3	% Mass Closure C	% Mass Closure O
173	118.2±3.4	6.49±0.33	3.27±0.17	3.88±0.18	1.47±0.14	101.0	99.7
171	138.9±3.4	5.31±0.24	2.70±0.12	4.89±0.20	1.73±0.08	100.1	99.3
175	159.6±6.9	4.81±0.34	2.26±0.15	5.45±0.36	1.84±0.15	104.4	105.3
177	180.3±6.9	3.98±0.28	1.81±0.12	6.55±0.36	2.64±0.42	100.6	102.8
178	200.9±6.9	3.20±0.42	1.57±0.20	7.20±0.43	2.59±0.34	98.8	100.7
181	221.6±6.9	2.52±0.12	1.43±0.07	7.59±0.36	3.66±0.19	102.7	101.6
162A	245.8±6.9	2.27±0.12	1.55±0.08	8.13±0.41	4.51±0.32	102.2	100.3
182	263.0±6.9	2.04±0.20	1.34±0.07	8.23±0.44	5.60±0.68	100.0	96.4

Table 12.11 Experimental Data for Carbon Monoxide Oxidation at 570 °C and 118 to 263 bar. Continued.

Initial Conditions: 560±1 °C
$[CO]_o = (1.04 \pm 0.02) \times 10^{-6}$ mol/cm^3
$[O_2]_o = (0.52 \pm 0.02) \times 10^{-6}$ mol/cm^3

Run No.	Residence Time, s	[CO] 10^{-7} mol/cm^3	[O_2] 10^{-7} mol/cm^3	[CO_2] 10^{-7} mol/cm^3	[H_2] 10^{-8} mol/cm^3	% Mass Closure C	% Mass Closure O
227	4.9±0.2	8.72±0.35	4.57±0.18	1.90±0.18	1.00±0.28	99.2	96.0
230	5.9±0.2	7.85±0.32	4.05±0.16	2.33±0.10	0.92±0.13	102.5	99.5
226	6.9±0.3	7.80±0.34	4.16±0.15	2.68±0.10	1.20±0.26	100.7	96.2
229	8.0±0.3	6.90±0.33	3.41±0.18	3.34±0.14	1.19±0.05	102.0	100.8
228	9.1±0.4	6.98±0.34	3.59±0.17	3.57±0.13	1.45±0.07	100.3	98.6
231	10.3±0.4	6.22±0.34	3.05±0.17	3.84±0.15	1.52±0.13	105.1	104.9

Table 12.12 Experimental Data for Carbon Monoxide Oxidation at 560 °C and 246 bar in the Packed Reactor.

12.6 Nomenclature

A	Arrhenius preexponential factor
C_i	concentration of species i
C_p	heat capacity
$\mathcal{D}$	diffusivity
D	tubing diameter
$\mathcal{D}_m$	molecular diffusivity
D_p	particle diameter
$\mathcal{D}_t$	turbulent (eddy) diffusivity
E_a	Arrhenius activation energy
F	oxygen/fuel (organic) feed ratio
H	enthalpy
h_i	internal heat-transfer coefficient
k	reaction rate constant; thermal conductivity; Boltzmann's constant
k^*	apparent first-order rate constant
K_c	equilibrium constant, concentration units
k_{diss}	dissociation rate constant
k_o	low-pressure-limit rate constant for elementary reaction
K_p	equilibrium constant, pressure units
k_{rec}	recombination rate constant
k'	kinetic decay constant
k_∞	high-pressure-limit rate constant for elementary reaction
R	gas constant; tubing radius
r	radial coordinate
R_i	reaction rate for species/reaction i
S	oxygen/fuel (organic) stoichiometric ratio
U_o	overall heat-transfer coefficient
v	fluid velocity
X	conversion
Z	compressibility factor
z	axial coordinate

Greek Letters

β	Morse potential parameter
β_c	collisional efficiency
ε	Lennard-Jones well depth; dielectric constant
ϕ	fuel/oxygen equivalence ratio
ϕ_i	fugacity coefficient of species *i*
Γ_i	surface efficiency for destruction of radical species *i*
μ	viscosity
ρ	density
σ	Lennard-Jones diameter
τ	reactor residence time
τ_{ind}	induction time

Chapter 13

References

Amin, S., Reid, R.C., and Modell, M. (1975) "Reforming and decomposition of glucose in an aqueous phase." ASME Paper #75-ENAs-21, Intersociety Conference on Environmental Systems, San Francisco, CA, July 21-24.

Antal, M.J. Jr. (1982) "Biomass pyrolysis: A review of the literature. Part 1—Carbohydrate pyrolysis." *Adv. Solar Energy* **1**, 61-111.

Antal, M.J. Jr. and Mok, W.S. (1988) "A study of the acid catalyzed dehydration of fructose in near-critical water." In *Research in Thermochemical Biomass Conversion*, A.V. Bridgwater and J.L. Kuester, eds. New York: Elsevier Applied Science, pp. 464-472.

Antal, M.J. Jr., Brittain, A., DeAlmeida, C., Ramayya, S., and Roy, J.C. (1987) "Heterolysis and homolysis in supercritical water." *ACS Symp. Ser. 329: Supercritical Fluids: Chemical and Engineering Principles and Applications*, T.G. Squires and M.E. Paulaitis, eds. Washington, DC: American Chemical Society, pp. 77-86.

Antal, M.J. Jr., Leesomboon, T., Mok, W.S.L., and Richards, G.N. (1991) "Mechanism of formation of 2-furaldehyde from D-xylose." *Carbohydr. Res.* **217**, 71-85.

Antal, M.J. Jr., Manarungson, S., and Mok, W.S.L. (1992) "Hydrogen production by steam reforming glucose in supercritical water." Presented at the Advances in Thermochemical Biomass Conversion Conference, Interlaken, Switzerland, May 11-15.

Antal, M.J. Jr., Mok, W.S.L., and Richards, G.N. (1990a) "Mechanism of formation of 5-(hydroxymethyl)-2-furaldehyde from D-fructose and sucrose." *Carbohydr. Res.* **199**, 91-109.

Antal, M.J. Jr., Mok, W.S.L., and Richards, G.N. (1990b) "Four-carbon model compounds for the reactions of sugar in water at high temperatures." *Carbohydr. Res.* **199**, 111-115.

Armellini, F.J. and Tester, J.W. (1990) "Salt separation during supercritical water oxidation of human metabolic waste: Fundamental studies of salt nucleation and growth." SAE Technical Paper Series #901313, 20th Intersociety Conference on Environmental Systems, Williamsburg, VA, July 9-12.

Armellini, F.J. and Tester, J.W. (1991) "Experimental methods for studying salt nucleation and growth from supercritical water." *J. Supercritical Fluids* **4**(4), 254-264.

Armellini, F.J. and Tester, J.W. (1992) "Solubility of sodium chloride in sub- and supercritical water vapor." Accepted for publication in *Fluid Phase Equilibria.*

Arustamyan, A.M., Shakhnazaryan, I.K., Philipossyan, A.G., and Nalbandyan, A.B. (1980) "The kinetics and the mechanism of the oxidation of carbon monoxide in the presence of hydrogen." *Int. J. Chem. Kinet.* **12**, 55-75.

Atri, G.M., Baldwin, R.R., Jackson, D., and Walker, R.W. (1977) "The reaction of OH radicals and HO_2 radicals with carbon monoxide." *Combust. Flame* **30**, 1-12.

Azatyan, V.V. (1972) "Study on gas-phase reactions in a jet, with allowance being made for longitudinal diffusion." *Doklady Akad. Nauk SSSR* **203**(1), 137-140.

Baldwin, R.R. and Brattan, D. (1960) "Homogeneous gas-phase decompositon of hydrogen peroxide." *Symp. (Int.) Combust. (Proc.) 8th*, 110-119.

Baldwin, R.R. and Mayor, L. (1958) "The slow reaction and second limit of the hydrogen-oxygen reaction in boric acid coated vessels." *Symp. (Int.) Combust. (Proc.) 7th*, 8-16.

Baldwin, R.R., Doran, P., and Mayor, L. (1960) "The dissociation of hydrogen peroxide and its role in the hydrogen-oxygen reaction." *Symp. (Int.) Combust. (Proc.) 8th*, 103-109.

Bamford, C.H. and Dewar, M.J.S. (1949) "The thermal decomposition of acetic acid." *J. Chem. Soc.*, 2877-2882.

Barner, H.E., Yuang, C.Y., Johnson, T., Jacobs, G., Martch, M.A., and Killilea, W.R. (1992) "Supercritical water oxidation: An emerging technology." *J. Haz. Mat.* **31**, 1-17.

Baulch, D.L., Cobos, C.J., Cox, R.A., Esser, C., Frank, P., Just, Th., Kerr, J.A., Pilling, M.J., Troe, J., Walker, R.W., and Warnatz, J. (1992) "Evaluated kinetic data for combustion modelling." *J. Phys. Chem. Ref. Data* **21**(3), 411-734.

Baulch, D.L., Drysdale, D.D., Duxbury, J., and Grant, S.J. (1976) *Evaluated Chemical Kinetic Data for High Temperature Reactions, Volume 3: Homogeneous Gas Phase Reactions of the O_2-O_3 System, the CO-O_2-H_2 System, and of Sulphur-Containing Species.* Boston: Butterworths.

Baulch, D.L., Drysdale, D.D., Horne, D.G., and Lloyd, A.C. (1972) *Evaluated Chemical Kinetic Data for High Temperature Reactions, Volume 1: Homogeneous Gas Phase Reactions of the H_2-O_2 System.* Cleveland, OH: CRC Press.

Benson, B.B., Krause, D. Jr., and Peterson, M.A. (1979) "The solubility and isotopic fractionation of gases in dilute aqueous solution. I. Oxygen." *J. Solution Chem.* **8**(9), 655-690.

Biermann, H.W., Zetzsch, C., and Stuhl, F. (1978) "On the pressure dependence of the reaction of HO with CO." *Ber. Bunsenges. Phys. Chem.* **82**, 633-639.

Blake, P.G. and Jackson, G.E. (1969) "High- and low-temperature mechanisms in the thermal decomposition of acetic acid." *J. Chem. Soc. (B)*, 94-96.

Bobleter, O. and Bonn, G. (1983) "The hydrothermolysis of cellobiose and its reaction-product D-glucose." *Carbohydr. Res.* **124**, 185-193.

Bondarenko, G.V., Gorbatyi, Yu.E., and Édel'shtein, V.M. (1974) "Effect of temperature and pressure on the vibrational-rotational spectra of the supercritical phase of water." *Doklady Akad. Nauk SSSR* **14**(2), 365-368.

Bosworth, R.C.L. (1949) "Distribution of reaction times for turbulent flow in cylindrical reactors." *Phil. Mag. VII* **40**, 314-324.

Brabbs, T.A., Belles, F.E., and Brokaw, R.S. (1970) "Shock-tube measurements of specific reaction rates in the branched-chain H_2-CO-O_2 system. *Symp. (Int.) Combust. (Proc.) 13th*, 129-136.

Bramlette, T.T., Mills, B.E., Hencken, K.R., Brynildson, M.E., Johnston, S.C., Hruby, J.M., Feemster, H.C., Odegard, B.C., and Modell, M. (1990) "Destruction of DOE/DP surrogate wastes with supercritical water oxidation technology." Sandia National Laboratories Report SAND90-8229, November.

Braun, W., Herron, J.T., and Kahaner, D.K. (1988) "Acuchem: a computer program for modeling complex chemical reaction systems." *Int. J. Chem. Kinet.* **20**, 51-62.

Brelvi, S.W. and O'Connell, J.P. (1972) "Corresponding states correlations for liquid compressibility and partial molal volumes of gases at infinite dilution in liquids." *AIChE J.* **18**(6), 1239-1243.

Brett, R.W.J. and Gurnham, C.F. (1973) "Wet air oxidation of glucose with hydrogen peroxide and metal salts." *J. Appl. Chem. Biotechnol.* **23**, 239-250.

Brouwer, L., Cobos, C.J., Troe, J., Dübal, H.-R., and Crim, F.F. (1987) "Specific rate constants *k(E,J)* and product state distributions in simple bond fission reactions. II. Application to HOOH → OH + OH." *J. Chem. Phys.* **86**(11), 6171-6182.

Brown, R.L. (1978) "Tubular flow reactors with first-order kinetics." *J. Res. Natl. Bur. Stand.* **83**(1), 1-8.

Brunning, J., Derbyshire, D.W., Smith, I.W.M., and Williams, M.D. (1988) "Kinetics of OH(v=0,1) and OD(v=0,1) with CO and the mechanism of the OH + CO reaction." *J. Chem Soc., Faraday Trans. 2* **84**(1), 105-119.

Butler, P.B., Bergan, N.E., Bramlette, T.T., Pitz, W.J., and Westbrook, C.K. (1991) "Oxidation of hazardous waste in supercritical water: A comparison of modeling and experimental results for methanol destruction." Presented at the Spring Meeting of the Western States Section of the Combustion Institute, Boulder, CO, March 17-19.

Chase Jr., M.W., Davies, C.A., Downey Jr., J.R., Frurip, D.J., McDonald, R.A., and Syverud, A.N. (1985) *JANAF Thermochemical Tables*, Third Edition. *J. Phys. Chem. Ref. Data* **14**, Supplement No. 1.

Christoforakos, M. and Franck, E.U. (1986) "An equation of state for binary fluid mixtures to high temperatures and pressures." *Ber. Bunsenges. Phys. Chem.* **90**, 780-789.

Cleland, F.A. and Wilhelm, R.H. (1956) "Diffusion and reaction in viscous-flow tubular reactor." *AIChE J.* **2**(4), 489-497.

Cobos, C.J., Hippler, H., and Troe, J. (1985) "High-pressure falloff curves and specific rate constants for the reactions H + O_2 ⇔ HO_2 ⇔ HO + O." *J. Phys. Chem.* **89**(2), 342-349.

Colket, M.B. III, Naegeli, D.W., and Glassman, I. (1975a) "High-temperature pyrolysis of acetaldehyde." *Int. J. Chem. Kinet.* **7**, 223-247.

Colket, M.B. III, Naegeli, D.W., and Glassman, I. (1975b) "High temperature oxidation of acetaldehyde." *Symp. (Int.) Combust. (Proc.) 16th*, 1023-1039.

Connolly, J.F. (1966) "Solubility of hydrocarbons in water near the critical solution temperatures." *J. Chem. Eng. Data* **11**(1), 13-16.

Cox, R.A. and Burrows, J.P. (1979) "Kinetics and mechanism of the disproportionation of HO_2 in the gas phase." *J. Phys. Chem.* **83**(20), 2560-2568.

Cutler, A.H., Antal, M.J. Jr., and Jones, M. Jr. (1988) "A critical evaluation of the plug-flow idealization of tubular-flow reactor data." *Ind. Eng. Chem. Res.* **27**(4), 691-697.

DeMore, W.B. (1984) "Rate constant for the OH + CO reaction: pressure dependence and the effect of oxygen." *Int. J. Chem. Kinet.* **16**, 1187-1200.

Denbigh, K. (1965) *Chemical Reactor Theory: An Introduction.* Cambridge: Cambridge University Press.

Dougherty, E.P. and Rabitz, H. (1980) "Computational kinetics and sensitivity analysis of hydrogen-oxygen combustion." *J. Chem. Phys.* **72**(12), 6571-6586.

Dove, J.E., Hippler, H., and Troe, J. (1985) "Direct study of energy transfer of vibrationally highly excited CS_2 molecules." *J. Chem. Phys.* **82**(4), 1907-1919.

Draper, N. and Smith, H. (1981) *Applied Regression Analysis*, Second Edition. New York: John Wiley and Sons, Inc.

Dryer, F.L. (1991) "The phenomenology of modeling combustion chemistry." In *Fossil Fuel Combustion: A Source Book*, W. Bartok and A.F. Sarofim, eds. New York: John Wiley and Sons, Inc., pp. 121-213.

Dryer, F.L. and Glassman, I. (1973) "High-temperature oxidation of CO and CH_4." *Symp. (Int.) Combust. (Proc.) 14th*, 987-1003.

Dudziak, K.H. and Franck, E.U. (1966) "Messungen der Viskosität des Wassers bis 560°C und 3500 bar." *Ber. Bunsenges. Phys. Chem.* **70**(9-10), 1120-1128.

Evans, R.J. and Milne, T.A. (1987) "Molecular characterization of the pyrolysis of biomass. 1. Fundamentals." *Energy & Fuels* **1**(2), 123-137.

Francisco, J.S. and Zhao, Y. (1991) "A re-examination of the heat of formation of HO_2 using *ab initio* molecular orbital theory." *Mol. Phys.* **72**(5), 1207-1208.

Franck, E.U. (1970) "Water and aqueous solutions at high pressures and temperatures." *Pure Appl. Chem.* **24**, 13-30.

Franck, E.U. (1976) "Properties of water." In *High Temperature, High Pressure Electrochemistry in Aqueous Solutions*, D. de G. Jones and R.W. Staehle, chairmen. Houston, TX: National Association of Corrosion Engineers, pp. 109-116.

Franck, E.U. (1991) "High pressure combustion and flames in supercritical water." Proceedings of the Second International Symposium on Supercritical Fluids, Boston, MA, May 20-22, pp. 91-96.

Franck, E.U., Rosenzweig, S., and Christoforakos, M. (1990) "Calculation of the dielectric constant of water to 1000°C and very high pressures." *Ber. Bunsenges. Phys. Chem.* **94**, 199-203.

Gibson, C.H. and Hinshelwood, C.N. (1928) "The homogeneous reaction between hydrogen and oxygen." *Proc. Royal Soc. A* **119**, 591-606.

Gilbert, R.G. and Smith, S.C. (1990) *Theory of Unimolecular and Recombination Reactions*. Boston: Blackwell Scientific Publications.

Gilbert, R.G., Jordan, M.J.T., and Smith, S.C. (1990) "UNIMOL: A program for the calculation of rate coefficients for unimolecular and recombination reactions." Department of Theoretical Chemistry, Sydney University, Sydney, Australia.

Gilbert, R.G., Luther, K., and Troe, J. (1983) "Theory of thermal unimolecular reactions in the fall-off range. II. Weak collision rate constants." *Ber. Bunsenges. Phys. Chem.* **87**, 169-177.

Golodets, G.I. (1983) *Studies in Surface Science and Catalysis 15: Heterogeneous Catalytic Reactions Involving Molecular Oxygen.* Amsterdam: Elsevier Science Publishers B.V.

Gorbaty, Yu.E. and Demianets, Yu.N. (1983) "The pair-correlation functions of water at a pressure of 1000 bar in the temperature range 25-500°C." *Chem. Phys. Lett.* **100**(5), 450-454.

Graven, W.M. and Long, F.J. (1954) "Kinetics and mechanism of the two opposing reactions of the equilibrium $CO + H_2O = CO_2 + H_2$." *J. Am. Chem. Soc.* **76**(10), 2602-2607.

Grouset, D., Plion, P., Znaty, E., and Galant, S. (1986) "Development of a variational method for chemical kinetic sensitivity analysis." *Symp. (Int.) Combust. (Proc.) 21st*, 795-807.

Haar, L., Gallagher, J.S., and Kell, G.S. (1984) *NBS/NRC Steam Tables.* New York: Hemisphere Publishing Corp.

Hadman, G., Thompson, H.W., and Hinshelwood, C.N. (1932) "The oxidation of carbon monoxide." *Proc. R. Soc. London A* **137**, 87-101.

Hamilton, E.J. Jr. and Lii, R.-R. (1977) "The dependence on H_2O and on NH_3 of the kinetics of the self-reaction of HO_2 in the gas-phase formation of $HO_2 \cdot H_2O$ and $HO_2 \cdot NH_3$ complexes." *Int. J. Chem. Kinet.* **9**, 875-885.

Hamilton, E.J. Jr. and Naleway, C.A. (1976) "Theoretical calculation of strong complex formation by the HO_2 radical: $HO_2 \cdot H_2O$ and $HO_2 \cdot NH_3$." *J. Phys. Chem.* **80**(18), 2037-2040.

Hart, A.B., McFadyen, J., and Ross, R.A. (1963) "Solid-oxide-catalyzed decomposition of hydrogen peroxide vapour." *Trans. Faraday Soc.* **59**, 1458-1469.

Héberger, K., Kemény, S., and Vidóczy, T. (1987) "On the errors of Arrhenius parameters and estimated rate constant values." *Int. J. Chem. Kinet.* **19**, 171-181.

Heger, K., Uematsu, M., and Franck, E.U. (1980) "The static dielectric constant of water at high pressures and temperatures to 500 MPa and 550°C." *Ber. Bunsenges. Phys. Chem.* **84**, 758-762.

Helling, R.K. (1986) "Oxidation kinetics of simple compounds in supercritical water: carbon monoxide, ammonia, and ethanol." Doctoral thesis, Department of Chemical Engineering, Massachusetts Institute of Technology, Cambridge, MA.

Helling, R.K. and Tester, J.W. (1987) "Oxidation kinetics of carbon monoxide in supercritical water." *Energy & Fuels* **1**, 417-423.

Helling, R.K. and Tester, J.W. (1988) "Oxidation of simple compounds and mixtures in supercritical water: carbon monoxide, ammonia and ethanol." *Environ. Sci. Technol.* **22**(11), 1319-1324.

Henzler, H.-J. (1978) "Untersuchungen zum Homogenisieren von Flüssigkeiten oder Gasen." *VDI-Forsch.-Heft* **587**, 1-60.

Hidaka, Y., Takahashi, S., Kawano, H., Suga, M., and Gardiner, W.C. Jr. (1982) "Shock-tube measurement of the rate constant for excited $OH(A^2\Sigma^+)$ formation in the hydrogen-oxygen reaction." *J. Chem. Phys.* **86**(8), 1429-1433.

Hills, A.J. and Howard, C.J. (1984) "Rate coefficient temperature dependence and branching ratio for the OH + ClO reaction." *J. Chem. Phys.* **81**(10), 4458-4465.

Hippler, H., Lindemann, L., and Troe, J. (1985) "Collisional energy transfer of vibrationally highly excited molecules. V. UV absorption of azulene." *J. Chem. Phys.* **83**(8), 3906-3912.

Hippler, H., Troe, J., and Wendelken, H.J. (1983) "Collisional deactivation of vibrationally highly excited polyatomic molecules. II. Direct observations for excited toluene." *J. Chem. Phys.* **78**(11), 6709-6717.

Hippler, H., Troe, J., and Willner, J. (1990) "Shock wave study of the reaction $HO_2 + HO_2 \rightarrow H_2O_2 + O_2$: Confirmation of a rate constant minimum near 700 K." *J. Chem. Phys.* **93**(3), 1755-1760.

Hoare, D.E., Peacock, G.B., and Ruxton, G.R.D. (1967) "Efficiency of surfaces in destroying hydrogen peroxide and hydroperoxy radicals." *Trans. Faraday Soc.* **63**, 2498-2503.

Hoare, D.E., Protheroe, J.B., and Walsh, A.D. (1959) "The thermal decomposition of hydrogen peroxide vapour." *Trans. Faraday Soc.* **55**, 548-557.

Hochgreb, S., Yetter, R.A., and Dryer, F.L. (1990) "The oxidation of CH_2O in the intermediate temperature range (943-995 K)." *Symp. (Int.) Combust. (Proc.) 23rd*, 171-177.

Hofzumahaus, A. and Stuhl, F. (1984) "Rate constant of the reaction HO + CO in the presence of N_2 and O_2." *Ber. Bunsenges. Phys. Chem.* **88**, 557-561.

Holgate, H.R., Webley, P.A., Tester, J.W., and Helling, R.K. (1992) "Carbon monoxide oxidation in supercritical water: The effects of heat transfer and the water-gas shift reaction on observed kinetics." *Energy & Fuels* **6**(5), 586-597.

Hong, G.T. (1992) "Process for oxidation of materials in water at supercritical temperatures and subcritical pressures." United States patent # 5,106,513, April 21.

Hong, G.T., Fowler, P.K., Killilea, W.R., and Swallow, K.C. (1987) "Supercritical water oxidation: Treatment of human waste and system configuration tradeoff study." SAE Technical Paper Series #871444, 17th Intersociety Conference on Environmental Systems, Seattle, WA, July 13-15.

Hong, G.T., Killilea, W.R., and Thomason, T.B. (1988) "Supercritical water oxidation: Space applications." In *Engineering, Construction, and Operation in Space: Proceedings of Space '88*, Albuquerque, NM, August 29-31, S.W. Johnson and J.P. Wetzel, eds. New York: American Society of Civil Engineers.

Hong, G.T., Killilea, W.R., and Thomason, T.B. (1989) "Method for solids separation in a wet oxidation type process." United States patent # 4,822,497, April 18.

Hossain, S.U. and Blaney, C.A. (1991) "Method for removing polychlorinated dibenzodioxins and polychlorinated dibenzofurans from paper mill sludge." United States patent # 5,075,017, December 24.

Hottel, H.C., Williams, G.C., Nerheim, N.M., and Schneider, G.R. (1965) "Kinetic studies in stirred reactors: Combustion of carbon monoxide and propane." *Symp. (Int.) Combust. (Proc.) 10th*, 111-121.

Howard, J.B., Williams, G.C., and Fine, D.H. (1973) "Kinetics of carbon monoxide oxidation in postflame gases." *Symp. (Int.) Combust. (Proc.) 14th*, 975-986.

Hsu, K.-J., Anderson, S.M., Durant, J.L., and Kaufman, F. (1989) "Rate constants for H + O_2 + M from 298 to 639 K for M = He, N_2, and H_2O." *J. Phys. Chem.* **93**(3), 1018-1021.

Hsu, K.-J., Durant, J.L., and Kaufman, F. (1987) "Rate constants for H + O_2 + M at 298 K for M = He, N_2, and H_2O." *J. Phys. Chem.* **91**(7), 1895-1899.

Hynes, A.J., Wine, P.H., and Ravishankara, A.R. (1986) "Kinetics of the OH + CO reaction under atmospheric conditions." *J. Geophys. Res.* **91**(D11), 11,815-11,820.

Japas, M.L. and Franck, E.U. (1985a) "High pressure phase equilibria and PVT-data of the water-nitrogen system to 673 K and 250 MPa." *Ber. Bunsenges. Phys. Chem.* **89**, 793-800.

Japas, M.L. and Franck, E.U. (1985b) "High pressure phase equilibria and PVT-data of the water-oxygen system including water-air to 673 K and 250 MPa." *Ber. Bunsenges. Phys. Chem.* **89**, 1268-1275.

Johnston, J.B., Hannah, R.E., Cunningham, V.L., Daggy, B.P., Sturm, F.J., and Kelly, Robert M. (1988) "Destruction of pharmaceutical and biopharmaceutical wastes by the MODAR supercritical water oxidation process." *Bio/Technology* **6**, 1423-1427.

Jonah, C.D., Mulac, W.A., and Zeglinski, P. (1984) "Rate constants for the reaction of OH + CO, OD + CO, and OH + methane as a function of temperature." *J. Phys. Chem.* **88**, 4100-4104.

Josephson, J. (1982) "Supercritical fluids." *Environ. Sci. Technol.* **16**(10), 548A-551A.

Kalinichev, A.G. (1991) "Monte Carlo simulation of water under supercritical conditions. I. Thermodynamics and structural properties." *Z. Naturforsch.* **46A**, 433-444.

Kassel, L.S. (1937) "The mechanism of the combustion of hydrogen." *Symp. (Int.) Combust. (Proc.) 2nd*, 175-182.

Kaufman, M. and Sherwell, J. (1983) "Kinetics of gaseous hydroperoxyl radical reactions." *Prog. React. Kinet.* **12**, 1-53.

Kee, R.J., Rupley, F.M., and Miller, J.A. (1989) "CHEMKIN-II: A Fortran chemical kinetics package for the analysis of gas-phase chemical kinetics." Sandia National Laboratories Report SAND89-8009, September; Version 2.6, December 1990.

Khitrin, L.N. and Solovyeva, L.S. (1958) "Homogeneous-heterogeneous combustion of carbon monoxide in narrow tubes (channels)." *Symp. (Int.) Combust. (Proc.) 7th*, 532-538.

Killilea, W.R., Hong, G.T., Swallow, K.C., and Thomason, T.B. (1988) "Supercritical water oxidation: Microgravity solids separation." SAE Technical Paper Series #881038, 18th Intersociety Conference on Environmental Systems, San Francisco, CA, July 11-13.

Killilea, W.R., Swallow, K.C., and Hong, G.T. (1992) "The fate of nitrogen in supercritical-water oxidation." *J. Supercritical Fluids* **5**(1), 72-78.

Kircher, C.C. and Sander, S.P. (1984) "Kinetics and mechanism of HO_2 and DO_2 disproportionations." *J. Phys. Chem.* **88**(10), 2082-2091.

Kohl, W., Lindner, H.A., and Franck, E.U. (1991) "Raman spectra of water to 400 °C and 3000 bar." *Ber. Bunsenges. Phys. Chem.* **95**(12), 1586-1593.

Kozlov, G.I. (1958) "On high-temperature oxidation of methane." *Symp. (Int.) Combust. (Proc.) 7th*, 142-149.

Krader, T. and Franck, E.U. (1987) "The ternary systems H_2O-CH_4-NaCl and H_2O-CH_4-$CaCl_2$ to 800 K and 250 MPa." *Ber. Bunsenges. Phys. Chem.* **91**, 627-634.

Kramers, H. and Westerterp, K.R. (1963) *Elements of Chemical Reactor Design and Operation.* New York: Academic Press, Inc.

Kudla, K., Schatz, G.C., and Wagner, A.F. (1991) "A quasiclassical trajectory study of the OH+CO reaction." *J. Chem. Phys.* **95**(3), 1635-1647.

Kunii, D. and Levenspiel, O. (1977) *Fluidization Engineering.* New York: Robert E. Krieger Publishing Co., Inc.

Kuster, B.F.M. and Temmink, H.M.G. (1977) "The influence of pH and weak-acid anions on the dehydration of D-fructose." *Carbohydr. Res.* **54**, 185-191.

Lamb, W.J., Hoffman, G.A., and Jonas, J. (1981) "Self-diffusion in compressed supercritical water." *J. Chem. Phys.* **74**(12), 6875-6880.

Larson, C.W., Stewart, P.H., and Golden, D.M. (1988) "Pressure and temperature dependence of reactions proceeding via a bound complex. An approach for combustion and atmospheric modelers. Application to HO + CO → [HOCO] → H + CO_2." *Int. J. Chem. Kinet.* **20**, 27-40.

Lee, D.-S. and Gloyna, E.F. (1990) "Supecritical water oxidation of acetamide and acetic acid." Center for Research in Water Resources, Bureau of Engineering Research, University of Texas at Austin, Technical Report CRWR 209.

Lee, D.-S. and Gloyna, E.F. (1992) "Hydrolysis and oxidation of acetamide in supercritical water." *Environ. Sci. Technol.* **26**(8), 1587-1593.

Lee, D.-S., Gloyna, E.F., and Li, L. (1990) "Efficiency of H_2O_2 and O_2 in supercritical water oxidation of 2,4-dichlorophenol and acetic acid." *J. Supercritical Fluids* **3**(4), 249-255.

Lewis, B. and von Elbe, G. (1987) *Combustion, Flames, and Detonations of Gases, Third Edition.* Orlando, FL: Academic Press, Inc.

Li, L., Chen, P., and Gloyna, E.F. (1991) "Generalized kinetic model for wet oxidation of organic compounds." *AIChE J.* **37**(11), 1687-1697.

Lutz, A.E., Kee, R.J., and Miller, J.A. (1988) "SENKIN: A Fortran program for predicting homogeneous gas-phase kinetics with sensitivity analysis." Sandia National Laboratories Report SAND87-8248, February; Version 1.6, September 1990.

Lyon, R.K., Hardy, J.E., and Von Holt, W. (1985) "Oxidation kinetics of wet CO in trace concentrations." *Combust. Flame* **61**, 79-86.

Maas, U. and Warnatz, J. (1988) "Ignition processes in hydrogen-oxygen mixtures." *Combust. Flame* **74**, 53-69.

Marshall, W.L. (1976) "Predicting conductance and equilibrium behavior of aqueous electrolytes at high temperatures and pressures." In *High Temperature, High Pressure Electrochemistry in Aqueous Solutions*, D. de G. Jones and R.W. Staehle, chairmen. Houston, TX: National Association of Corrosion Engineers, pp. 117-130.

Marshall, W.L. and Franck, E.U. (1981) "Ion product of water substance, 0-1000°C, 1-10,000 bars: New international formulation and its background." *J. Phys. Chem. Ref. Data* **12**(2), 295-304.

Martynova, O.I. (1976) "Solubility of inorganic compounds in subcritical and supercritical water." In *High Temperature, High Pressure Electrochemistry in Aqueous Solutions*, D. de G. Jones and R.W. Staehle, chairmen. Houston, TX: National Association of Corrosion Engineers, pp. 131-138.

Mather, A.E., and Franck, E.U. (1992) "Phase equilibria in the system carbon dioxide-water at elevated pressures." *J. Phys. Chem.* **96**(1), 6-8.

Mednick, M.L. (1962) "The acid-base-catalyzed conversion of aldohexose into 5-(hydroxymethyl)-2-furfural." *J. Org. Chem.* **27**, 398-403.

Melius, C.F., Bergan, N.E., and Shepherd, J.E. (1990) "Effects of water on combustion kinetics at high pressure." *Symp. (Int.) Combust. (Proc.) 23rd*, 217-223.

Michael, J.V. and Sutherland, J.W. (1988) "Rate constant for the reaction of H with H_2O and OH with H_2 by the flash photolysis-shock tube technique over the temperature range 1246-2297 K." *J. Phys. Chem.* **92**, 3853-3857.

Modell, M. (1982) "Processing methods for the oxidation of organics in supercritical water." United States patent # 4,338,199, July 6.

Modell, M. (1985a) "Processing methods for the oxidation of organics in supercritical water." United States patent # 4,543,190, September 24.

Modell, M. (1985b) "Gasification and liquefaction of forest products in supercritical water." In *Fundamentals of Thermochemical Biomass Conversion*, R.P. Overend, T.A. Milne, and L.K. Mudge, eds. New York: Elsevier Applied Science Publishers, pp. 95-119.

Modell, M. (1989) "Supercritical-water oxidation." In *Standard Handbook of Hazardous Waste Treatment and Disposal*, H.M. Freeman, ed. New York, NY: McGraw-Hill, pp. 8.153-8.168.

Modell, M., Larson, J., and Sobczynski, S.F. (1992) "Supercritical water oxidation of pulp mill sludges." *Tappi J.* June, 195-202.

Modell, M., Gaudet, G.G., Simson, M., Hong, G.T., and Biemann, K. (1982) "Supercritical water: testing reveals new process holds promise." *Solid Wastes Management*, August.

Mok, W.S.-L., Antal, M.J. Jr., and Jones, M. Jr. (1989) "Formation of acrylic acid from lactic acid in supercritical water." *J. Org. Chem.* **54**, 4596-4602.

Mok, W.S.-L., Antal, M.J. Jr., and Varhegyi, G. (1992) "Productive and parasitic pathways in dilute acid-catalyzed hydrolysis of cellulose." *Ind. Eng. Chem. Res.* **31**(1), 94-100.

Moore, J.C., Battino, R., Rettich, T.R., Handa, Y.P., and Wilhelm, E. (1982) "Partial molar volumes of 'gases' at infinite dilution in water at 298.15 K." *J. Chem. Eng. Data* **27**, 22-24.

Mozurkewich, M. and Benson, S.W. (1985) "Self-reaction of HO_2 and DO_2: Negative temperature dependence and pressure effects." *Int. J. Chem. Kinet.* **17**, 787-807.

Mozurkewich, M., Lamb, J.J., and Benson, S.W. (1984) "Negative activation energies and curved Arrhenius plots. 2. OH + CO." *J. Phys. Chem.* **88**, 6435-6441.

Mulcahy, M.F.R. and Pethard, M.R. (1963) "Errors in determining the rate constant of a first-order gaseous reaction by the flow method." *Aust. J. Chem.* **16**, 527-543.

Newth, F.H. (1951) "The formation of furan compounds from hexoses." *Adv. Carbohydr. Chem.* **5**, 83-106.

Norton, T.S. (1990) "The combustion chemistry of simple alcohol fuels." Doctoral thesis, Department of Mechanical and Aerospace Engineering, Princeton University, Princeton, NJ.

Overend, R. and Paraskevopoulos, G. (1977) "The question of a pressure effect in the reaction OH + CO at room temperature." *Chem. Phys. Lett.* **49**(1), 109-111.

Paraskevopoulos, G. and Irwin, R.S. (1984) "The pressure dependence of the rate constant of the reaction of OH radicals with CO." *J. Chem. Phys.* **80**(1), 259-266.

Perry, R.H., Green, D., and Maloney, J.O., eds. (1984) *Perry's Chemical Engineers' Handbook, Sixth Edition.* New York: McGraw-Hill.

Pirraglia, A.N., Michael, J.V., Sutherland, J.W., and Klemm, R.B. (1989) "A flash photolysis-shock tube kinetic study of the H atom reaction with O_2: $H + O_2 \leftrightarrow OH + O$ ($962\ K \leq T \leq 1705\ K$) and $H + O_2 + Ar \rightarrow HO_2 + Ar$ ($746\ K \leq T \leq 987\ K$)." *J. Phys. Chem.* **93**(1), 282-291.

Pitz, W.J. and Westbrook, C.K. (1986) "Chemical kinetics of the high pressure oxidation of n-butane and its relation to engine knock." *Combust. Flame* **63**, 113-133.

Ploos van Amstel, J.J.A. and Rietema, K. (1970) "Naßoxidation von Abwasserschlamm. Teil I: Oxidation von Glucose als Modellsubstanz." *Chem.-Ing.-Tech.* **42**(15), 981-990.

Poirier, R.V. and Carr, R.J. Jr. (1971) "The use of tubular flow reactors for kinetic studies over extended pressure ranges." *J. Phys. Chem.* **75**(10), 1593-1601.

Press, W.H., Flannery, B.P., Teukolsky, S.A., and Vetterling, W.T. (1986) *Numerical Recipes: The Art of Scientific Computing.* New York: Cambridge University Press.

Quack, M. and Troe, J. (1974) "Specific rate constants of unimolecular processes II. Adiabatic channel model." *Ber. Bunsenges. Phys. Chem.* **78**(3), 240-252.

Ramayya, S.V. and Antal, M.J. Jr. (1989) "Evaluation of systematic error incurred in the plug flow idealization of tubular flow reactor data." *Energy & Fuels* **3**, 105-108.

Ravishankara, A.R. and Thompson, R.L. (1983) "Kinetic study of the reaction of OH with CO from 250 to 1040 K." *Chem. Phys. Lett.* **99**(5/6), 377-381.

Reid, R.C., Prausnitz, J.M., and Poling, B.E. (1987) *The Properties of Gases and Liquids, Fourth Edition*. New York: McGraw-Hill.

Rettich, T.R., Battino, R., and Wilhelm, E. (1982) "Solubility of gases in liquids. 15. High-precision determination of Henry coefficients for carbon monoxide in liquid water at 278 to 323 K." *Ber. Bunsenges. Phys. Chem.* **86**, 1128-1132.

Rettich, T.R., Handa, Y.P., Battino, R., and Wilhelm, E. (1981) "Solubility of gases in liquids. 13. High-precision determination of Henry's constants for methane and ethane in liquid water at 275 to 328 K." *J. Phys. Chem.* **85**, 3230-3237.

Robinson, P.J. and Holbrook, K.A. (1972) *Unimolecular Reactions*. New York: Wiley-Interscience.

Rofer, C.K. and Streit, G.E. (1988) "Kinetics and mechanism of methane oxidation in supercritical water." Los Alamos National Laboratory Report LA-11439-MS.

Rofer, C.K. and Streit, G.E. (1989) "Phase II final report: Oxidation of hydrocarbons and oxygenates in supercritical water." Los Alamos National Laboratory Report LA-11700-MS.

Saeman, J.F. (1945) "Kinetics of wood saccharification: Hydrolysis of cellulose and decomposition of sugars in dilute acid at high temperature." *Ind. Eng. Chem.* **37**(1), 43-52.

Sander, S.P., Peterson, M., Watson, R.T., and Patrick, R. (1982) "Kinetics studies of the HO_2 + HO_2 and DO_2 + DO_2 reactions at 298 K." *J. Phys. Chem.* **86**(8), 1236-1240.

Schilling, W. and Franck, E.U. (1988) "Combustion and diffusion flames at high pressures to 2000 bar." *Ber. Bunsenges. Phys. Chem.*, **92**, 631-636.

Schmitt, R.G., Butler, P.B., Bergan, N.E., Pitz, W.J., and Westbrook, C.K. (1991) "Destruction of hazardous wastes in supercritical water. Part II: A study of high-pressure methanol oxidation kinetics." Presented at the Fall Meeting of the Western States Section of the Combustion Institute, University of California at Los Angeles, October 13-15.

Schott, G.L. and Kinsey, J.L. (1958) "Kinetic studies of hydroxyl radicals in shock waves. II. Induction times in the hydrogen-oxygen reaction." *J. Chem. Phys.* **29**(5), 1177-1182.

Schwab, J.J., Brune, W.H., and Anderson, J.G. (1989) "Kinetics and mechanism of the OH + HO_2 reaction." *J. Phys. Chem.* **93**(3), 1030-1035.

Sengers, J.V. and Watson, J.T.R. (1986) "Improved international formulation for the viscosity and thermal conductivity of water substance." *J. Phys. Chem. Ref. Data* **15**(4), 1291-1314.

Seward, T.M. and Franck, E.U. (1981) "The system hydrogen-water up to 440°C and 2500 bar pressure." *Ber. Bunsenges. Phys. Chem.* **85**, 2-7.

Shallenberger, R.S. and Birch, G.G. (1975) *Sugar Chemistry*. Westport, CT: Avi Publishing Co., Inc.

Shanableh, A. and Gloyna, E.F. (1991) "Supercritical water oxidation—wastewaters and sludges." *Water Sci. Technol.* **23**(1-3), 389-398.

Shaw, R.W., Brill, T.R., Clifford, A.A., Eckert, C.A., and Franck, E.U. (1991) "Supercritical water: a medium for chemistry." *Chem. Eng. News* **69**(51), 26-39.

Sherwood, T.K., Pigford, R.L., and Wilke, C.R. (1975) *Mass Transfer*. New York: McGraw-Hill, Inc.

Shum, L.G.S. and Benson, S.W. (1983) "Review of the heat of formation of the hydroperoxyl radical." *J. Phys. Chem.* **87**(18), 3479-3482.

Silverstein, R.M., Bassler, G.C., and Morrill, T.C. (1991) *Spectrometric Identification of Organic Compounds, Fifth Edition* New York: John Wiley and Sons.

Singh, B., Dean, G.R., and Cantor, S.M. (1948) "The role of 5-(hydroxymethyl)-2-furfural in the discoloration of sugar solutions." *J. Am. Chem. Soc.* **70**, 517-522.

Skaates, J.M., Briggs, B.A., Lamparter, R.A., and Baillod, C.R. (1981) "Wet oxidation of glucose." *Can. J. Chem. Eng.* **59**, 517-521.

Skinner, G.B. and Ringrose, G.H. (1965) "Ignition delays of a hydrogen-oxygen-argon mixture at relatively low temperatures." *J. Chem. Phys.* **42**(6), 2190-2192.

Slack, M.W. (1977) "Rate coefficient for $H + O_2 + M = HO_2 + M$ evaluated from shock tube measurements of induction times." *Combust. Flame* **28**, 241-249.

Smith, G.K., Krieger, B.B., and Herzog, P.M. (1980) "Experimental and analytical study of wall reaction and transport effects in fast reaction systems." *AIChE J.* **26**(4), 567-576.

Smith, I.W.M. (1977) "The mechanism of the OH + CO reaction and the stability of the HOCO radical." *Chem. Phys. Lett.* **49**(1), 112-115.

Smith, I.W.M. and Zellner, R.L. (1973) "Rate measurements of reactions of OH by resonance absorption. Part 2.—Reactions of OH with CO, C_2H_4 and C_2H_2." *J. Chem. Soc., Faraday Trans. 2* **69**, 1617-1627.

Staszak, C.N., Malinowski, K.C., and Killilea, W.R. (1987) "The pilot-scale demonstration of the MODAR oxidation process for the destruction of hazardous waste materials." *Environ. Prog.* **6**(1), 39-43.

Steeper, R.R., Rice, S.F., Brown, M.S., and Johnston, S.C. (1992) "Methane and methanol diffusion flames in supercritical water." Sandia National Laboratories Report SAND92-8474, June.

Sutherland, J.W., Michael, J.V., Pirraglia, A.N., Nesbitt, F.L., and Klemm, R.B. (1986) "Rate constant for the reaction of $O(^3P)$ with H_2 by the flash photolysis-shock tube and flash photolysis-resonance fluorescence techniques; $504K \leq T \leq 2495K$." *Symp. (Int.) Combust. (Proc.) 21st*, 929-941.

Swallow, K.C., Killilea, W.R., Hong, G.T., and Lee, H. (1990) "Supercritical water oxidation: Behavior of heavy metal compounds in the oxidation process." SAE Technical Paper Series #901314, 20th Intersociety Conference on Environmental Systems, Williamsburg, VA, July 9-12.

Swallow, K.C., Killilea, W.R., Malinowski, K.C., and Staszak, C. (1989) "The MODAR process for the destruction of hazardous organic wastes—field test of a pilot-scale unit." *Waste Management* **9**, 19-26.

Swenson, H.S., Carver, J.R., and Kakarala, C.R. (1965) "Heat transfer to supercritical water in smooth-bore tubes." *J. Heat Transfer* **87**(11), 477-484.

Takahashi, Y., Wydeven, T., and Koo, C. (1989) "Subcritical and supercritical water oxidation of CELSS model wastes." *Adv. Space Res.* **9**(8), (8)99-(8)110.

Tanger, J.C. IV and Pitzer, K.S. (1989) "Calculation of the ionization constant of H_2O to 2,273 K and 500 MPa." *AIChE J.* **35**(10), 1631-1638.

Tardy, D.C. and Rabinovitch, B.S. (1977) "Intermolecular vibrational energy transfer in thermal unimolecular systems." *Chem. Rev.* **77**(3), 369-408.

Tester, J.W., Holgate, H.R., Armellini, F.J., Webley, P.A., Killilea, W.R., Hong, G.T., and Barner, H.E. (1991) "Oxidation of hazardous organic wastes in supercritical water: A review of process development and fundamental research." Presented at the Third Annual Symposium on Emerging Technologies for Hazardous Waste Management, Atlanta, GA, October 1-3, Paper 113.2; to appear in an ACS Symposium Series volume, *Emerging Technologies for Hazardous Waste Management III*.

Tester, J.W., Webley, P.A., and Holgate, H.R. (1992) "Revised global kinetic measurements of methanol oxidation in supercritical water." Submitted for publication in *Ind. Eng. Chem. Res.*, July.

Theander, O. and Nelson, D,A, (1978) "Aqueous, high-temperature transformation of carbohydrates relative to utilization of biomass." *Adv. Carbohydr. Chem. Biochem.* **46**, 273-326.

Thomason, T.B. and Modell, M. (1984) "Supercritical water destruction of aqueous wastes." *Haz. Waste* **1**(4), 453-467.

Thomason, T.B., Hong, G.T., Swallow, K.C., and Killilea, W.R. (1990) "The MODAR supercritical water oxidation process." In *Innovative Hazardous Waste Treatment Technology Series, Volume 1: Thermal Processes*, H.M. Freeman, ed. Lancaster, PA: Technomic Publishing, pp. 31-42.

Thornton, T.D. and Savage, P.E. (1990) "Phenol oxidation in supercritical water." *J. Supercritical Fluids* **3**(4), 240-248.

Thornton, T.D. and Savage, P.E. (1992) "Kinetics of phenol oxidation in supercritical water." *AIChE J.* **38**(3), 321-327.

Thornton, T.D., LaDue, D.E. III, and Savage, P.E. (1991) "Phenol oxidation in supercritical water: Formation of dibenzofuran, dibenzo-*p*-dioxin, and related compounds." *Environ. Sci. Technol.* **25**(8), 1507-1510.

Timberlake, S.H., Hong, G.T., Simson, M., and Modell, M. (1982) "Supercritical water oxidation for wastewater treatment: preliminary study of urea destruction." SAE Technical Paper Series #820872, 12th Intersociety Conference on Environmental Systems, San Diego, CA, July 19-21.

Timonen, R.S., Ratajczak, E., and Gutman, D. (1987) "Kinetics of the reaction between formyl radicals and atomic hydrogen." *J. Phys. Chem.* **91**(3), 692-694.

Timonen, R.S., Ratajczak, E., and Gutman, D. (1988) "Kinetics of the reactions of the formyl radical with oxygen, nitrogen dioxide, chlorine, and bromine." *J. Phys. Chem.* **92**(3), 651-655.

Timonen, R.S., Ratajczak, E., Gutman, D., and Wagner, A.F. (1987) "The addition and dissociation reaction H + CO ⇔ HCO. 2. Experimental studies and comparison with theory." *J. Phys. Chem.* **91**(20), 5325-5332.

Tingey, G.L. (1966) "Kinetics of the water-gas equilibrium reaction. I. The reaction of carbon dioxide with hydrogen." *J. Phys. Chem.* **70**(5), 1406-1412.

Tödheide, K. (1972) "Water at high temperatures and pressures." *Water: A Comprehensive Treatise*, F. Franks, ed. New York: Plenum Press, Inc., pp. 463-514.

Tödheide, K. and Franck, E.U. (1963) "Das Zweiphasengebiet und die kritische Kurve im System Kohlendioxid-Wasser bis zu Drucken von 3500 bar." *Z. Phys. Chem. N.F.* **37**, 387-401.

Troe, J. (1974) "Thermal dissociation and recombination of polyatomic molecules." *Symp. (Int.) Combust. (Proc.) 15th*, 667-680.

Troe, J. (1977a) "Theory of thermal unimolecular reactions at low pressures. I. Solution of the master equation." *J. Chem. Phys.* **66**(11), 4745-4757.

Troe, J. (1977b) "Theory of thermal unimolecular reactions at low pressures. II. Strong collision rate constants. Applications." *J. Chem. Phys.* **66**(11), 4758-4775.

Troe, J. (1979) "Predictive possibilities of unimolecular rate theory." *J. Phys. Chem.* **83**(1), 114-126.

Troe, J. (1981) "Theory of thermal unimolecular reactions at high pressures." *J. Chem. Phys.* **75**(1), 226-237.

Troe, J. (1983) "Theory of thermal unimolecular reactions in the fall-off range. I. Strong collision rate constants." *Ber. Bunsenges. Phys. Chem.* **87**, 161-169.

Tsang, W. and Hampson, R.F. (1986) "Chemical kinetic data base for combustion chemistry. Part I. Methane and related compounds." *J. Phys. Chem. Ref. Data* **15**(3), 1087-1279.

Uematsu, M. and Franck, E.U. (1980) "Static dielectric constant of water and steam." *J. Phys. Chem. Ref. Data* **9**(4), 1291-1306.

Uhl, V.W. and Gray, J.B. (1986) *Mixing: Theory and Practice, Volume III.* New York: Academic Press, Inc.

Vedeneev, V.I., Gol'denberg, M.Ya., Gorban, N.I., and Teitel'boim, M.A. (1988) "Quantitative model of the oxidation of methane at high pressures. II. The mechanism of autoacceleration." *Kinet. Katal.* **29**(1), 14-20.

Vermeersch, M.L. (1991) "A variable pressure flow reactor for chemical kinetic studies: Hydrogen, methane and butane oxidation at 1 to 10 atmospheres and 880 to 1,040 K." Doctoral thesis, Department of Mechanical and Aerospace Engineering, Princeton University, Princeton, NJ.

von Elbe, G. and Lewis, B. (1937) "The reaction between hydrogen and oxygen above the upper explosion limit." *J. Am. Chem. Soc.* **59**, 656-662.

von Elbe, G. and Lewis, B. (1942) "Mechanism of the thermal reaction between hydrogen and oxygen." *J. Chem. Phys.* **10**, 366-393.

Walker, R.E. (1961) "Chemical reaction and diffusion in a catalytic tubular reactor." *Phys. Fluids* **4**(10), 1211-1216.

Wardlaw, D.M. and Marcus, R.A. (1985) "Unimolecular reaction rate theory for transition states of any looseness. II. Implementation and analysis with applications to NO_2 and C_2H_6 dissociations." *J. Chem. Phys.* **83**(7), 3462-3480.

Warnatz, J. (1984) "Rate coefficients in the C/H/O system." In *Combustion Chemistry*, W.C. Gardiner, Jr., ed. New York: Springer-Verlag, pp. 197-360.

Webley, P.A. (1989) "Fundamental oxidation kinetics of simple compounds in supercritical water." Doctoral thesis, Department of Chemical Engineering, Massachusetts Institute of Technology, Cambridge, MA.

Webley, P.A. and Tester, J.W. (1988) "Fundamental kinetics and mechanistic pathways for oxidation reactions in supercritical water." SAE Technical Paper Series #881039, 18th Intersociety Conference on Environmental Systems, San Francisco, CA, July 11-13.

Webley, P.A. and Tester, J.W. (1989) "Fundamental kinetics of methanol oxidation in supercritical water." *ACS Symp. Ser. 406: Supercritical Fluid Science and Technology*, K.P. Johnston and J.M.L. Penninger, eds. Washington, D.C.: American Chemical Society, pp. 259-275.

Webley, P.A. and Tester, J.W. (1991) "Fundamental kinetics of methane oxidation in supercritical water." *Energy & Fuels* **5**, 411-419.

Webley, P.A., Holgate, H.R., Stevenson, D.M., and Tester, J.W. (1990) "Oxidation kinetics of model compounds of metabolic waste in supercritical water." SAE Technical Paper Series #901333, 20th Intersociety Conference on Environmental Systems, Williamsburg, VA, July 9-12.

Webley, P.A., Tester, J.W., and Holgate, H.R. (1991) "Oxidation kinetics of ammonia and ammonia-methanol mixtures in supercritical water in the temperature range 530-700°C at 246 bar." *Ind. Eng. Chem. Res.* **30**(8), 1745-1754.

West, M.B. and Gray, M.R. (1987) "Pyrolysis of 1,3-butanediol as a model reaction for wood liquefaction in supercritical water." *Can J. Chem. Eng.* **65**, 645-650.

Westbrook, C.K. and Dryer, F.L. (1979) "A comprehensive mechanism for methanol oxidation." *Combust. Sci. Technol.* **20**, 125-140.

Westbrook, C.K. and Dryer, F.L. (1981) "Simplified reaction mechanisms for the oxidation of hydrocarbon fuels in flames." *Combust. Sci. Technol.* **27**, 31-43.

Westbrook, C.K. and Dryer, F.L. (1984) "Chemical kinetic modeling of hydrocarbon combustion." *Prog. Energy Combust. Sci.* **10**, 1-57.

Westbrook, C.K., Dryer, F.L., and Schug, K.P. (1982) "A comprehensive mechanism for the pyrolysis and oxidation of ethylene." *Symp. (Int.) Combust. (Proc.) 19th*, 153-166.

Westenberg, A.A. and deHaas, N. (1973) "Rates of CO + OH and H_2 + OH over an extended temperature range." *J. Chem. Phys.* **58**(10), 4061-4065.

Westmoreland, P.R., Howard, J.B., Longwell, J.P., and Dean, A.M. (1986) "Prediction of rate constants for combustion and pyrolysis reactions by bimolecular QRRK." *AIChE J.* **32**(12), 1971-1979.

Wightman, T.J. (1981) "Studies in supercritical wet air oxidation." Masters Thesis, Department of Chemical Engineering, University of California at Berkeley, Berkeley, CA.

Wilhelm, E., Battino, R., and Wilcock, R.J. (1977) "Low-pressure solubility of gases in liquid water." *Chem. Rev.* **77**(2), 219-262.

Wilmanns, E.G. and Gloyna, E.F. (1990) "Supercritical water oxidation of volatile acids." Center for Research in Water Resources, Bureau of Engineering Research, University of Texas at Austin, Technical Report CRWR 218.

Wilson, W.E. Jr., O'Donovan, J.T., and Fristrom, R.M. (1968) "Flame inhibition by halogen compounds." *Symp. (Int.) Combust. (Proc.) 12th*, 929-942.

Woerner, G.A. (1976) "Thermal decomposition and reforming of glucose and wood at the critical conditions of water." Masters thesis, Department of Chemical Engineering, Massachusetts Institute of Technology, Cambridge, MA.

Wolfrom, M.L., Schuetz, R.D., and Cavalieri, L.F. (1948) "Chemical interactions of amino compounds and sugars. III. The conversion of D-glucose to 5-(hydroxymethyl)-2-furaldehyde." *J. Am. Chem. Soc.* **70**, 514-517.

Yamagata, K., Nishikawa, K., Hasegawa, S., Fujii, T., and Yoshida, S. (1972) "Forced convective heat transfer to supercritical water flowing in tubes." *Int. J. Heat Mass Transfer* **15**, 2575-2593.

Yang, H.H. and Eckert, C.A. (1988) "Homogeneous catalysis in the oxidation of *p*-chlorophenol in supercritical water." *Ind. Eng. Chem. Res.* **27**, 2009-2014.

Yetter, R.A., Dryer, F.L., and Rabitz, H. (1985) "Some interpretive aspects of elementary sensitivity gradients in combustion kinetics modeling." *Combust. Flame* **59**, 107-133.

Yetter, R.A., Dryer, F.L., and Golden, D.M. (1989) "Pressure effects on the kinetics of high speed chemically reacting flows." Contribution to A Workshop on High Speed Combustion, Institute for Computer Applications in Science and Engineering, Newport News, VA, October.

Yetter, R.A., Dryer, F.L., and Rabitz, H. (1986) "Complications of one-step kinetics for moist CO oxidation." *Symp. (Int.) Combust. (Proc.) 21st*, 749-760.

Yetter, R.A., Dryer, F.L., and Rabitz, H. (1991a) "A comprehensive reaction mechanism for carbon monoxide/hydrogen/oxygen kinetics." *Combust. Sci. Technol.* **79**, 97-128.

Yetter, R.A., Dryer, F.L., and Rabitz, H. (1991b) "Flow reactor studies of carbon monoxide/hydrogen/oxygen kinetics." *Combust. Sci. Technol.* **79**, 129-140.

Yetter, R.A., Rabitz, H., and Hedges, R.M. (1991c) "A combined stability-sensitivity analysis of weak and strong reactions of hydrogen/oxygen mixtures." *Int. J. Chem. Kinet.* **23**, 251-278.

Zellner, R., Ewig, F., Paschke, R., and Wagner, G. (1988) "Pressure and temperature dependence of the gas-phase recombination of hydroxyl radicals." *J. Phys. Chem.* **92**, 4184-4190.